Einstein gravitational wave Telescope

Conceptual Design Study

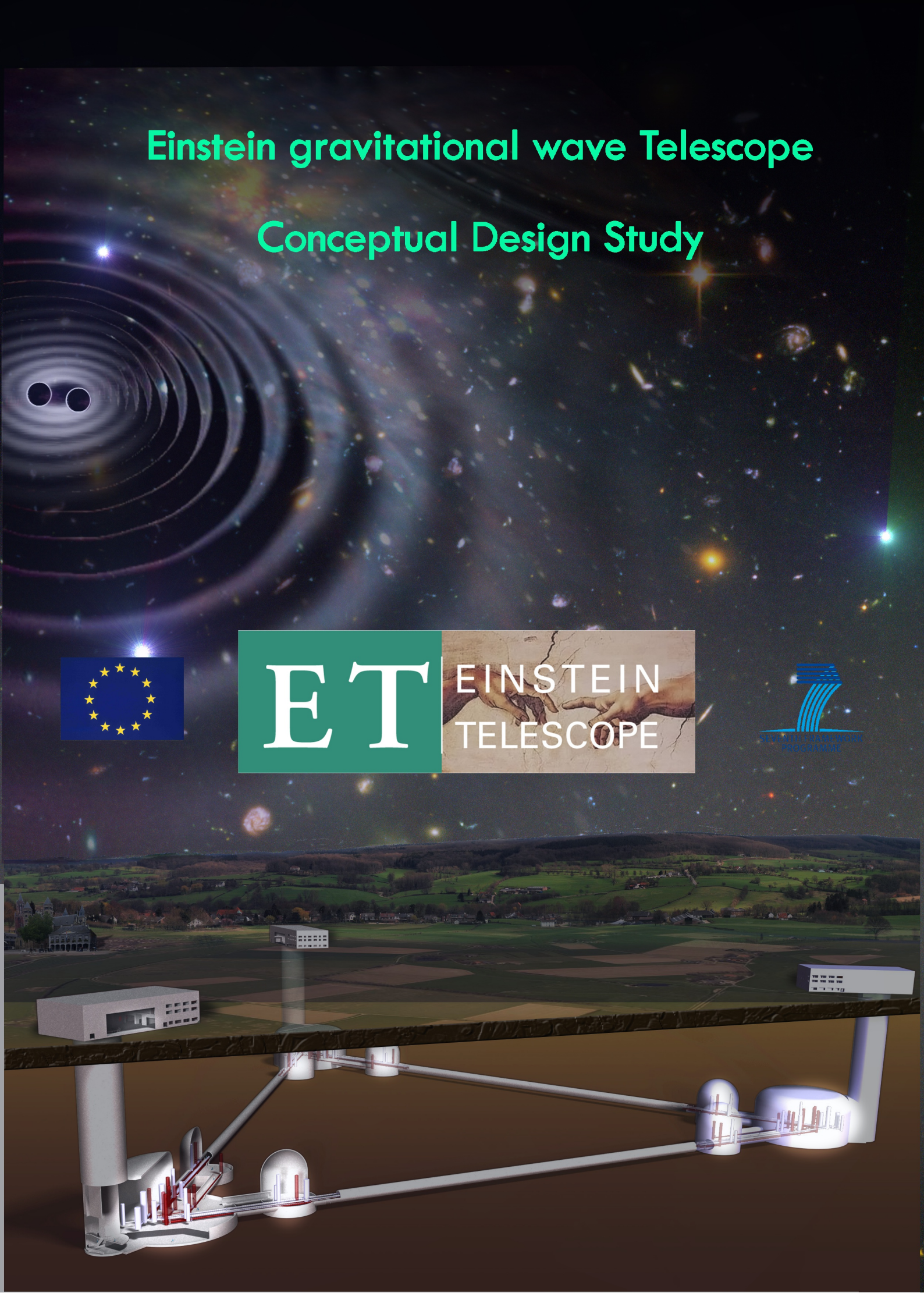

dedicated in memory of Stefano Braccini, a colleague who greatly contributed to the ET project and a friend who left us.

European Commission
FP7, Grant Agreement 211743

Einstein gravitational wave Telescope conceptual design study

ET-0106C-10

The research leading to these results has received funding from the European Community's Seventh Framework Programme (FP7/2007–2013) under grant agreement n 211743.

Author list: **ET Science Team**

M Abernathy[1], F Acernese[2,3], P Ajith[30], B Allen[4], P Amaro-Seoane[54,32], N Andersson[5], S Aoudia[54], P Astone[6,7], B Krishnan[4], L Barack[5], F Barone[2,3], B Barr[1], M Barsuglia[8], M Bassan[9,10], R Bassiri[1], M Beker[11], N Beveridge[1], M Bizouard[12], C Bond[13], S Bose[14], L Bosi[15], S Braccini[16], C Bradaschia[16,17], M Britzger[4], F Brueckner[18], T Bulik[19], H J Bulten[20], O Burmeister[4], E Calloni[2,21], P Campsie[1], L Carbone[13], G Cella[16], E Chalkley[13], E Chassande-Mottin[8], S Chelkowski[13], A Chincarini[22], A Di Cintio[6], J Clark[26], E Coccia[9,10], C N Colacino[16], J Colas[17], A Colla[6,7], A Corsi[30], A Cumming[1], L Cunningham[1], E Cuoco[17], S Danilishin[23], K Danzmann[4], E Daw[28], R De Salvo[25], W Del Pozzo[11], T Dent[26], R De Rosa[2,21], L Di Fiore[2], M Di Paolo Emilio[9], A Di Virgilio[16], A Dietz[27], M Doets[11], J Dueck[4], M Edwards[26], V Fafone[9,10] S Fairhurst[26], P Falferi[29,56], M Favata[30], V Ferrari[6,7], F Ferrini[17], F Fidecaro[17,51], R Flaminio[31], J Franc[31], F Frasconi[16], A Freise[13], D Friedrich[4], P Fulda[13], J Gair[57], M Galimberti[31], G Gemme[22], E Genin[17], A Gennai[16], A Giazotto[16,17], K Glampedakis[40], R Gouaty[27], C Graef[4], W Graham[1], M Granata[8], H Grote[4], G Guidi[33,34], J Hallam[13], G Hammond[1], M Hannam[26], J Harms[30], K Haughian[1], I Hawke[5], D Heinert[18], M Hendry[1], I Heng[1], E Hennes[11], S Hild[1], J Hough[1], D Huet[17], S Husa[55], S Huttner[1], B Iyer[38], I Jones[5], G Jones[1], I Kamaretsos[26], C Kant Mishra[38], F Kawazoe[4], F Khalili[39], B Kley[18], K Kokeyama[13], K Kokkotas[40], S Kroker[18], R Kumar[1], K Kuroda[41], B Lagrange[31], N Lastzka[4], T G F Li[11], M Lorenzini[33], G Losurdo[33,17], H Lück[4], E Majorana[6], V Malvezzi[9,10], I Mandel[42,13], V Mandic[36], S Marka[50], F Marin[33], F Marion[27], J Marque[17], I Martin[1], D Mc Leod[26], D Mckechan[26], M Mehmet[4], C Michel[31], Y Minenkov[9], N Morgado[31], A Morgia[9], S Mosca[2,21] L Moscatelli[6], B Mours[27], H Müller-Ebhardt[4], P Murray[1], L Naticchioni[6,7], R Nawrodt[18], J Nelson[1], R O' Shaughnessy[43], C D Ott[30], C Palomba[6], A Paoli[17], G Parguez[17], A Pasqualetti[17], R Passaquieti[16], D Passuello[16], M Perciballi[6], F Piergiovanni[33,34], L Pinard[31], M Pitkin[1], W Plastino[44], M Plissi[1], R Poggiani[16], P Popolizio[17], E Porter[8], M Prato[22], G Prodi[45,56], M Punturo[15,17], P Puppo[6], D Rabeling[20], I Racz[46], P Rapagnani[6,7], V Re[9], J Read[37], T Regimbau[47], H Rehbein[4], S Reid[1], L Rezzolla[54], F Ricci[6,7], F Richard[17], A Rocchi[9], R Romano[2], S Rowan[1], A Rüdiger[4], A Samblowski[4], L Santamaría[30], B Sassolas[31], B Sathyaprakash[26], R Schilling[4], P Schmidt[26], R Schnabel[4], B Schutz[26,54], C Schwarz[18], J Scott[1], P Seidel[18], A M Sintes[55], K Somiya[48], C F Sopuerta[49], B Sorazu[1], F Speirits[1], L Storchi[15], K Strain[1], S Strigin[23], P Sutton[26], S Tarabrin[4], B Taylor[4], A Thürin[4], K Tokmakov[1], M Tonelli[16,51], H Tournefier[27], R Vaccarone[17], H Vahlbruch[4], J F J van den Brand[11,20], C Van Den Broeck[11], S van der Putten[11], M van Veggel[1], A Vecchio[13], J Veitch[26], F Vetrano[33,34], A Vicere[33,34], S Vyatchanin[23], P Weßels[52], B Willke[4], W Winkler[4], G Woan[1], K Wojcik[26], A Woodcraft[53], K Yamamoto[35]

Issue: 4

Date: June 28, 2011

[1] Department of Physics and Astronomy, The University of Glasgow, Glasgow, G12 8QQ, UK
[2] INFN, Sezione di Napoli, Italy
[3] Università di Salerno, Fisciano, I-84084 Salerno, Italy
[4] Max–Planck–Institut für Gravitationsphysik und Leibniz Universität Hannover, D-30167 Hannover, Germany

[5] University of Southampton, Southampton SO17 1BJ, UK
[6] INFN, Sezione di Roma 1, I-00185 Roma, Italy
[7] Università 'La Sapienza', I-00185 Roma, Italy
[8] Laboratoire AstroParticule et Cosmologie (APC), Universitè Paris Diderot, CNRS: IN2P3, CEA:DSM/IRFU, Observatoire de Paris, 10 rue A.Domon et L.Duquet, 75013 Paris - France
[9] INFN, Sezione di Roma Tor Vergata I-00133 Roma, Italy
[10] Università di Roma Tor Vergata, I-00133, Roma, Italy
[11] Nikhef, Science Park, Amsterdam, the Netherlands
[12] LAL, Université Paris-Sud, IN2P3/CNRS, F-91898 Orsay, France
[13] University of Birmingham, Birmingham, B15 2TT, UK
[14] Washington State University, Pullman, WA 99164, USA
[15] INFN, Sezione di Perugia, Italy
[16] INFN, Sezione di Pisa, Italy
[17] European Gravitational Observatory (EGO), I-56021 Cascina (Pi), Italy
[18] Friedrich–Schiller–Universität Jena PF 07737 Jena, Germany
[19] Astronomical Observatory, University of Warsaw, 00-478, Warszawa, Poland
[20] VU University Amsterdam, De Boelelaan 1081, 1081 HV, Amsterdam, The Netherlands
[21] Università di Napoli 'Federico II', Complesso Universitario di Monte S. Angelo, I-80126 Napoli, Italy
[22] INFN, Sezione di Genova, I-16146 Genova, Italy
[23] Moscow State University, Moscow, 119992, Russia
[24] INFN, Laboratori Nazionali del Gran Sasso, Assergi l'Aquila, Italy
[25] Università degli Studi del Sannio, Benevento, Italy
[26] Cardiff University, Cardiff, CF24 3AA, UK
[27] LAPP-IN2P3/CNRS, Université de Savoie, F-74941 Annecy-le-Vieux, France
[28] University of Sheffield, UK
[29] Istituto di Fotonica e Nanotecnologie, CNR-Fondazione Bruno Kessler, 38123 Povo, Trento, Italy
[30] Caltech–CaRT, Pasadena, CA 91125, USA
[31] Laboratoire des Matériaux Avancés (LMA), IN2P3/CNRS, F-69622 Villeurbanne, Lyon, France
[32] Institut de Ciències de l'Espai, Campus UAB, Torre C-5, parells, 2na plantaES-08193 Bellaterra (Barcelona)
[33] INFN, Sezione di Firenze, I-50019 Sesto Fiorentino, Italy
[34] Università degli Studi di Urbino 'Carlo Bo', I-61029 Urbino, Italy
[35] INFN, Sezione di Padova, Italy
[36] University of Minnesota, Minneapolis, MN 55455, USA
[37] Department of Physics and Astronomy, University of Mississippi, Oxford, US
[38] Raman research institute, Bangalore, India
[39] Moscow State University, Moscow, 119992, Russia
[40] Theoretical Astrophysics (TAT) Eberhard-Karls-Universität Tübingen, Auf der Morgenstelle 10, D-72076 Tübingen, Germany
[41] Institute for Cosmic Ray Research, University of Tokyo, Kashiwa, Chiba, Japan
[42] MIT Kavli Institute, Cambridge, MA 02139, US
[43] The Pennsylvania State University, University Park, PA 16802, USA
[44] INFN, Sezione di Roma Tre and Università di Roma Tre-Dipartimento di Fisica, I-00146 Roma, Italy
[45] Università di Trento, Trento, Italy
[46] KFKI Research Institute for Particle and Nuclear Physics, Budapest, Hungary
[47] Université Nice 'Sophia–Antipolis', CNRS, Observatoire de la Côte d'Azur, F-06304 Nice, France
[48] Department of Physics, Tokyo Institute of Technology, Tokyo, Japan
[49] Institute of Space Sciences (CSIC-IEEC), Campus UAB, 08193 Bellaterra, Barcelona, Spain
[50] Department of Physics, Columbia University, New York, US
[51] Dipartimento di Fisica, Università di Pisa, Pisa, Italy
[52] Laser Zentrum Hannover e.V., Hollerithallee 8, D-30419 Hannover, Germany
[53] Royal Observatory, Blackheath Avenue, Greenwich, SE10 8XJ, UK
[54] Max–Planck–Institut für Gravitationsphysik, D-14476 Potsdam, Germany
[55] Departament de Fisica, Universitat de les Illes Balears, Cra. Valldemossa Km. 7.5, E-07122 Palma de Mallorca, Spain
[56] INFN, Gruppo Collegato di Trento, Italy
[57] Institute of Astronomy, University of Cambridge, Cambridge, CB3 0HA, UK

Abstract

This document describes the Conceptual Design of a third generation gravitational wave observatory named Einstein Telescope ("ET"). The design of this new research infrastructure has been realised with the support of the European Community's Seventh Framework Programme (FP7/2007-2013) under grant agreement n 211743. In this document are described the fundamental design options, the site requirements, the main technological solutions, a rough evaluation of the costs and a schematic time plan.

Contents

1 Introduction to the ET project

1.1 Prologue

The first generation of interferometric gravitational wave (GW) detectors (GEO600 [1], LIGO [2], TAMA [3], Virgo [4]) have reached or approached their design sensitivities, and thus demonstrated the effectiveness of the working principle. The major detectors currently operative are enhanced versions of the first generation (Virgo+ and eLIGO), with higher laser power and some technological improvements.

Advanced detectors (like "Advanced LIGO" ([5], [6]) and "Advanced Virgo" ([7])), also called the second generation, will show a sensitivity improved roughly by a factor of ten with respect to the initial interferometers. They are based on technologies currently available, sometimes tested in reduced scale prototypes, but still to be implemented in full scale. According to the current models of GW sources, the sensitivity of the advanced interferometers is expected to guarantee the detection of signals generated by astrophysical sources within months to a year at most. For example, at the nominal sensitivity of the advanced detectors, the expected detection rate of the GW signal generated by a binary system of coalescing neutron stars is about a few tens per year. But apart from extremely rare events, the expected signal-to-noise ratio (SNR) of these detections obtained with the advanced detectors is too low for precise astronomical studies of the GW sources and for complementing optical and X–ray observations in the study of fundamental systems and processes in the Universe.

These considerations led the GW community to start investigating a new (third) generation of detectors. In particular, the European Commission supported the institutions in Table 1 to realise this design study within the Seventh Framework Programme (FP7-Capacities). With a considerably improved sensitivity, such new machines of the third-generation will open the era of routine GW astronomy and with the Einstein Telescope (ET) project Europe will lead this scientific revolution. Since the first detection of a GW signal is expected to occur in the advanced interferometers, the evaluation of the scientific impact of ET it is especially focused on the observational aspects rather than on the detection capabilities.

To realise a third-generation GW observatory with a significantly enhanced sensitivity (we defined a target of a factor of ten improvement in sensitivity for ET with respect to the advanced detectors over a wide frequency range), several limitations of the technologies adopted in the advanced interferometers must be overcome and new solutions to be developed are proposed in this document to reduce the fundamental and technical noises that will limit the next generation machines.

However, the first and main target of this document is the definition of the requirements and of the main characteristics of the site hosting ET, the design of the key elements of the research infrastructure, the rough evaluation of the costs and of the timeline of its implementation. To understand the importance and the need of the site and infrastructures in the ET design it is worth to recall the history of the current GW detector infrastructures, shown in Fig. 1.

Table 1: Institutions participating ("Beneficiaries") to the ET design study.

Institute	Country
European Gravitational Observatory	Italy–France
Istituto Nazionale di Fisica Nucleare	Italy
Max-Planck-Gesellschaft zur Förderung der Wissenschaften e.V., acting through Max-Planck-Institüt für Gravitationsphysik	Germany
Centre National de la Recherche Scientifique	France
University of Birmingham	United Kingdom
University of Glasgow	United Kingdom
NIKHEF	The Netherlands
Cardiff University	United Kingdom

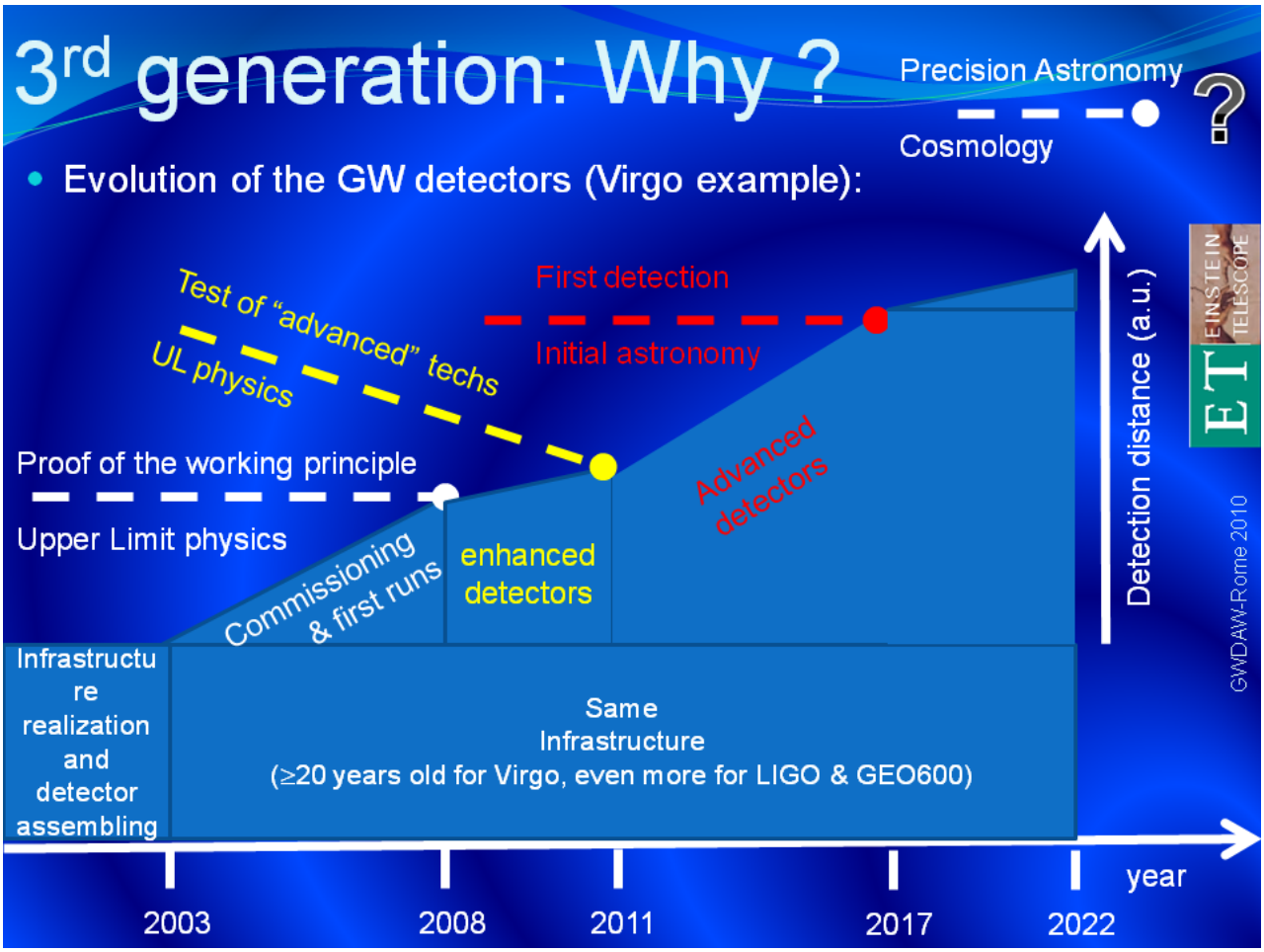

Figure 1: Evolution of the first and second generation GW detectors. Time is on the horizontal axis, detector performance in the vertical one. When the advanced detectors will be operative the hosting infrastructures will be more than 20 years old and any further improvement of performance (sensitivity) will be suppressed by the limitation imposed by the infrastructures. (slide presented by M. Punturo at the GWDAW meeting, Rome Jan. 2010).

Current and advanced detectors are using the same infrastructure that will be about 20 years old when the second generation will be online. Further improvements of the sensitivity will be limited by the constraints of the site and infrastructure (arm length, local seismic noise, absence of cryogenic apparatus, vacuum pipe size . . .). Indeed, in order to realise a third-generation GW observatory like ET, an infrastructure hosting several detectors that evolve for many decades is crucial.

Box 1.1: The Einstein Telescope at a glance

The *Einstein gravitational–wave Telescope* will be an observatory of the third generation aiming to reach a sensitivity for GW signals emitted by astrophysical and cosmological sources about a factor of 10 better than the advanced detectors currently being built. An observatory with such a level of sensitivity will open the era of routine GW astronomy.

An artist's impression of ET is given in Fig. 2, below. The main purpose of the ET project is the realisation of an infrastructure (an "observatory") capable of hosting more than one GW detector. This infrastructure will be usable for many decades, while the implemented detectors will undergo successive upgrades or replacements according to the current state of the art of interferometer technologies.

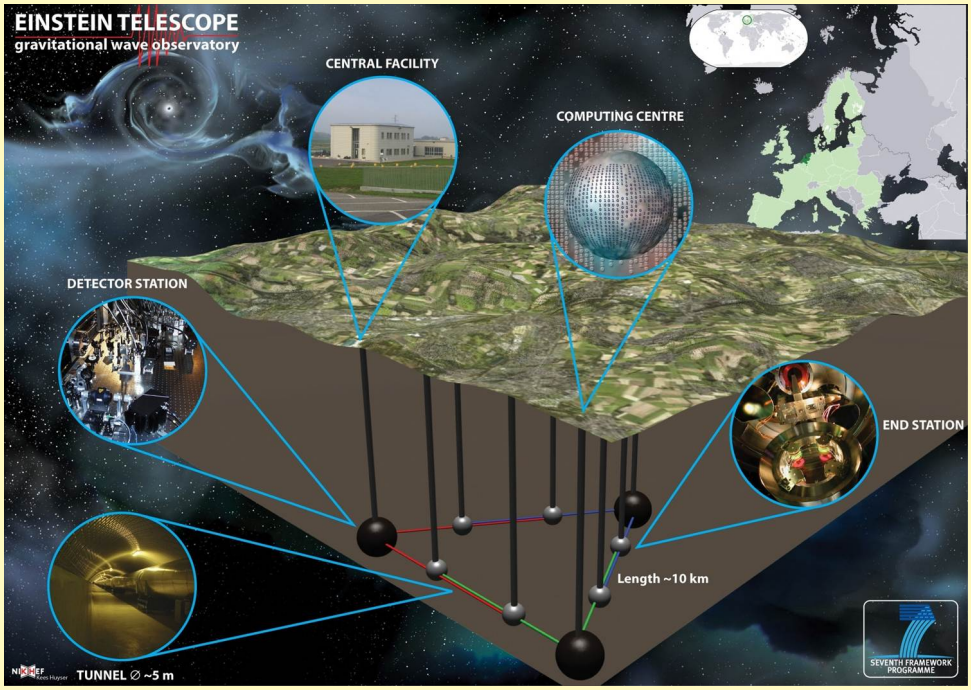

Figure 2: Artist's view of the Einstein Telescope

To reduce the effect of the residual seismic motion, thus allowing a better sensitivity at low frequencies (between 3 and 100 Hz), ET will be located underground at a depth of about 100 m to 200 m and, in the complete configuration, it will consist of three nested detectors, each in turn composed of two interferometers (*xylophone* configuration). The topology of each interferometer will be the dual-recycled Michelson layout with Fabry–Perot arm cavities, with a length of about 10 km. The xylophone configuration of each detector devotes one interferometer to the detection of the low-frequency components of the GW signal (2–40 Hz) while the other is dedicated to the high-frequency components, each interferometer adopting different, optimal technologies. In the former (ET-LF), operating at cryogenic temperature, the thermal, seismic, gravity gradient and radiation pressure noise sources will be particularly suppressed; in the latter (ET-HF) the sensitivity at high frequencies will be improved through the high laser light power circulating in the Fabry–Perot cavities, and through the use of frequency-dependent squeezed light technologies. The target sensitivity of the ET observatory, at the current level of understanding, is shown in figure 7.

Box 1.2: Detecting Gravitational Waves

Gravitational waves change distances between objects, while the objects themselves locally remain at rest, by changing the metric of space-time. These changes occur with opposing sign for orthogonal directions, as illustrated in figure 3 for one polarisation of a gravitational wave incident perpendicular to the paper (h_+: see box 2.2 for more details).

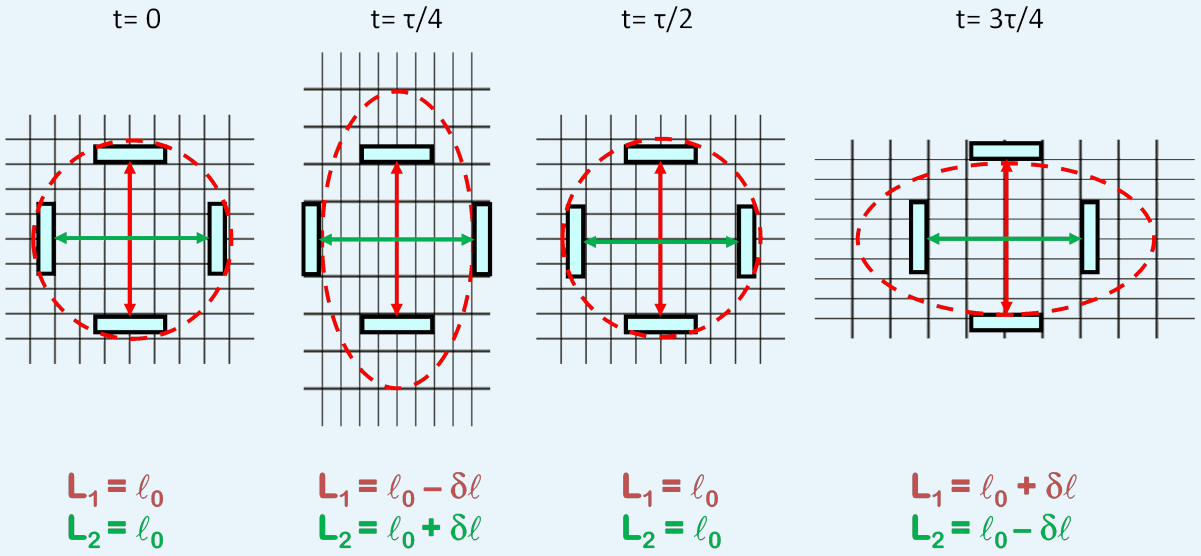

Figure 3: The effect of gravitational waves on the distances between objects. While the mirrors remain locally at rest the metric gets changed by the gravitational wave. The figure shows the effect of a sinusoidal gravitational wave with period τ, for different times t. The distances measured between the mirrors change by $\pm\delta\ell$.

A Michelson interferometer is ideally suited to measuring this effect. The measurement principle is shown in figure 4. A laser beam is split into two partial beams, sent along the interferometer arms, where it experiences a phase shift by the metric change of the gravitational wave, is reflected at the end and returns to the beam splitter, where it is recombined. The interference condition at the beam splitter, i.e. the phase relation of the two returning beams, determines the intensity on the photo detector. Three different phase relations are shown in figure 4. The relative length change of the interferometer arms can hence be detected by measuring the power at the output port. Although the measurement principle is very simple, for getting the best possible sensitivity all influences that change the geometrical or optical arm length or that cause a signal in the detected photo-current mimicking a gravitational wave have to be minimised, resulting in very sophisticated and complex instruments.

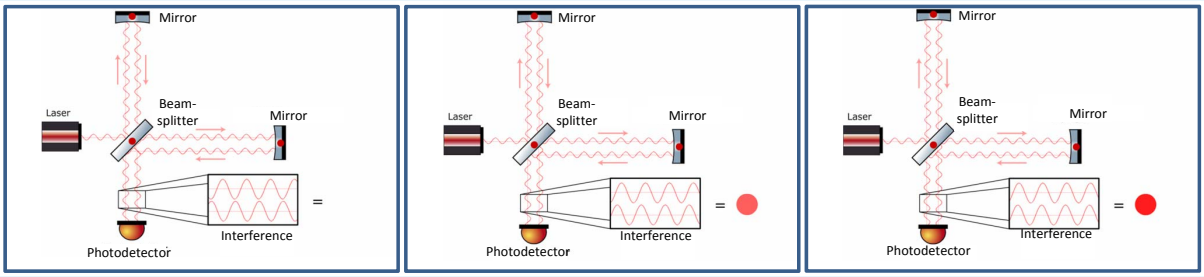

Figure 4: Michelson interferometer principle for gravitational wave detection, showing three different interference conditions resulting in different brightness at the output port.

1.2 Scientific targets of the ET observatory

1.2.1 Fundamental physics

Astronomical sources of gravitational waves are essentially systems where gravity is extremely strong, and are often characterized by relativistic bulk motion of massive objects. The emitted radiation carries an uncorrupted signature of the nature of the space-time geometry, and is thus an invaluable tool to understand the behaviour of matter and geometry in extreme conditions of density, temperature, magnetic fields and relativistic motion. Here are some examples of how GW observations can impact fundamental physics.

In Einstein's theory, gravitational radiation travels at the speed of light and has two polarization states. In alternative theories of gravity one or both of these properties might not hold, owing to the presence of massive gravitons, or a scalar field mediating gravity in addition to the tensor field. Current experimental tests of gravity, as well those afforded by the data from the Hulse-Taylor binary, are consistent with both Einstein's theory and one of its alternatives called the Brans-Dicke theory. Gravitational wave detectors will bring these theories vis-a-vis observations that could decisively rule out one or the other.

According to Einstein's gravity the space-time in the vicinity of black holes is described by a unique geometry called the Kerr solution. Observation of the radiation from the infall of stellar-mass black holes into intermediate-mass black holes will make it possible to test such uniqueness theorems. X-ray astronomy has provided firm indirect evidence that intense sources of X-rays may well host a black hole. An unambiguous signature of the black hole geometry, however, could eventually be provided by the detection of black hole quasi-normal modes: gravitational radiation with characteristic frequencies and decay times that depend only on the mass and spin angular momentum of the black hole. Failure to detect such radiation from, for example, a newly formed black hole would mean that gravity is more exotic than we currently believe, and might reveal new phases of matter at extremely high densities.

The most attractive versions of string theory require a ten- or eleven-dimensional space-time, far above those that we perceive. In certain phenomenological models at the interface of string theory and cosmology, what we perceive as a four-dimensional Universe could be one part, or "brane", within a higher dimensional "bulk" Universe. The extra spatial dimensions may be compact and sub-millimetre-scale, or even macroscopically large, if their geometry has properties known as "warping". The key feature of brane-world theories is that gravitational interactions, and in particular gravitational waves, propagate in the bulk, while other interactions are restricted to the brane, which partly explains why gravity is so weak. Third-generation detectors offer the exciting possibility of observing radiation from the bulk and thereby exploring whether the Universe has large extra dimensions.

1.2.2 Relativistic Astrophysics

Astronomy has revealed a Universe full of diverse and exotic phenomena that remain enigmas decades after their discovery. Supernovae are the end-states of stellar evolution, resulting in gravitational collapse followed by a huge explosion of the formerly infalling matter. Gamma-ray bursts are intense sources of gamma radiation that last only a few seconds to minutes yet emit more energy than a star does in its entire lifetime. Radio pulsars are compact objects as massive as the Sun but only about 10 km in size, and the regularity of their radio pulses and occasional glitches in that regularity have remained puzzles for a long time after their discovery three decades ago. Transient radio sources thousands of light years away are associated with magnetic fields so strong that the emitted radiation could break down terrestrial radio stations.

The source in question in each case is believed to be couched in dense environs and strong gravitational fields and, therefore, a potential source of gravitational radiation. For example, gamma-ray bursts could be produced by colliding neutron stars which are electromagnetically invisible for most of their lives but are very powerful emitters of GWs. Transient radio sources could be the result of quakes in neutron stars with concomitant emission of GWs. Observing such 'multi-messengers' (sources that are strong emitters of both EM and GW radiation) will help understand phenomena that have remained puzzles for decades.

The centre of every galaxy is believed to host a compact object a million to a billion times as massive as our Sun, a powerful emitter of optical, radio and other radiation. What is the nature of this object? How and when did it form? Did it form from small 100-solar-mass seeds and then grow by accreting gas and other compact objects? What is its relation to the size of the galaxy as a whole? These are some of the questions which a model of the formation of structure in the Universe must answer. While electromagnetic observations have provided valuable data, ET can explore the population of stellar mass and intermediate mass black holes as a function of redshift and shed light on black hole demographics, their mass distribution and growth.

ET will also be sensitive to a population of sources at very high redshifts, helping us study cosmological evolution of sources, the history of star formation and its dependence on the matter content of the Universe, and the development of large-scale structure in the Universe.

1.2.3 Cosmology

The twentieth century was the golden age of cosmology. With the advent of radio and microwave astronomy it was possible to finally address key questions about the origin of the Universe. The cosmic microwave background (CMB) is a relic radiation from the hot Big Bang that is believed to have been the initial condition for primordial nucleosynthesis. Since the early Universe was very dense, this radiation was in thermal equilibrium with matter for about 380,000 years after the Big Bang and cannot directly reveal the conditions in the very early phases of the Universe's history. The most direct way of observing the primeval Universe is via the gravitational window with a network of two or more detectors. From fairly general assumptions one can predict the production of a stochastic background of GWs in the early Universe, which travel to us unscathed as a consequence of their weak coupling to matter.

The most amazing aspect of the Universe is that only about 4% of its energy density appears in the form of visible matter, the rest being dark matter and dark energy. In order to understand the behaviour of these 'dark' contents it is necessary to have a standard candle—a population of sources whose distance from Earth can be inferred from their luminosity. Compact binaries are an astronomer's ideal standard candle. By measuring the signature of the gravitational radiation they emit, it is possible to infer their intrinsic parameters (e.g. the masses and spins of the component objects) and accurately deduce their luminosity distance. In fact, compact binaries eliminate the need to build a cosmic distance ladder—the process by which standard candles at different distances are calibrated in astronomy since there is no source that is suitable at all distances.

The synergy of multi-messenger astronomy is nowhere more apparent than in the use of standard sirens of gravity to test the concordance model of cosmology. ET might detect several hundred compact binary coalescence events each year in coincidence with short-hard gamma-ray bursts, provided, of course, the two are related. While gravitational observations would provide an unambiguous measure of the luminosity distance, the host galaxy of the GRB could be used to measure the redshift. By fitting the observed population to a cosmological model, it will be possible to measure the Hubble parameter, dark matter and dark energy densities, as well as the dark energy equation-of-state parameter.

The early history of the Universe may have witnessed several phase transitions as the temperature decreased through the energy scales of a Grand Unified Theory (GUT) and electroweak symmetry-breaking, and eventually to the current state in which we see four different fundamental interactions. During some phase transitions, cosmic strings form as one-dimensional topological defects at the boundaries of different phases. Vibrations of these strings at the speed of light can sometimes form a kink that emits a burst of gravitational radiation. The spectrum of such radiation has a unique signature that can help us detect cosmic strings and measure their properties, and thus provide a glimpse of the Universe as it underwent phase transitions.

Perhaps the most exciting discovery of the new window will be none of the above. If astronomical history is any example, gravitational astronomy should unveil phenomena and sources never imagined in the wildest theories—a possibility of any new observational tool.

1.3 Layout of the detector

The sensitivity of gravitational wave detectors improved considerably from the bar detectors to the first generation of interferometric detectors, which are currently being upgraded to the 'advanced' generation. The corresponding sensitivities are shown in figure 5. In order to achieve the scientific goals stated above, the sensitivity in comparison to the second generation of gravitational wave detectors must be improved by about an order of magnitude over the entire detection frequency band ranging from 10 Hz to about 10 kHz. Frequent observation of low-frequency sources, e.g. intermediate mass black holes, requires an extension of the detection range towards lower frequencies.

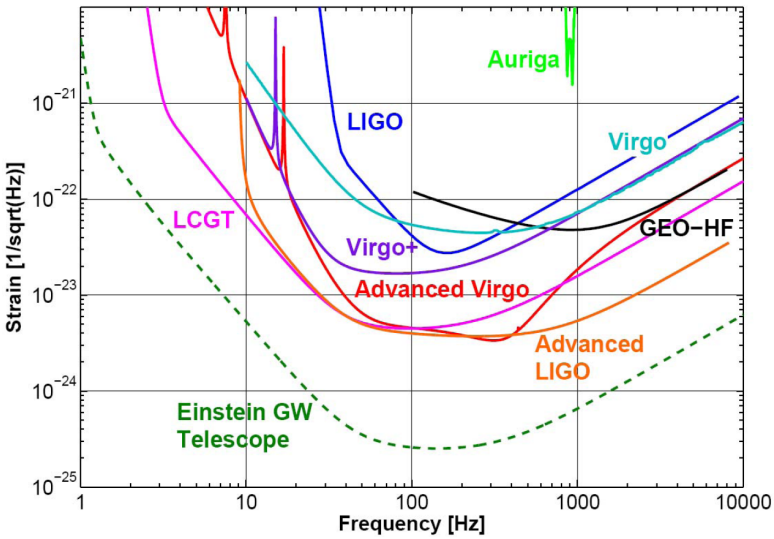

Figure 5: Sensitivities of gravitational wave detectors from the first to the third generation.

The initial sensitivity goal for the Einstein Telescope, estimated at the start of the Design Study, as shown in figure 5, was driven by the need to get frequent high Signal to Noise Ratio (SNR) events for routine gravitational wave astronomy. The high-frequency sensitivity was given by the maximum power feasible, the mid-frequency range was governed by thermal noises and the low-frequency range by either thermal or seismic noises. The initial estimates have been refined during the design study and finally resulted in the sensitivity shown in figure 13.

1.3.1 Size, shape and layout

The conceptual design of a project of this financial scale (see table 212) has to be based on well proven and experimentally tested techniques. To achieve the sensitivity that the Einstein Telescope project aims for, on the other hand, it will be necessary to exploit all state-of-the-art technologies and drive them to their physical limits. This sensitivity can only be reached by significantly increasing the size of the detector beyond the size of currently available instruments (i.e. 3 km for Virgo and 4 km for LIGO) and going to an underground location, where the seismic noise is lower than at the surface. Only by increasing the arm length to 10 km can the influence of unavoidable displacement noises be lowered to a tolerable level.

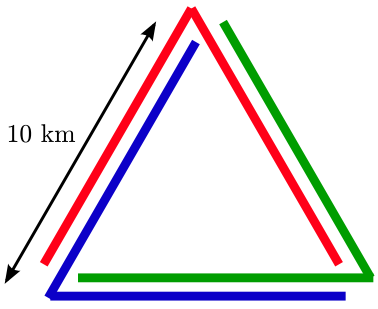

Figure 6: Three nested detectors in a triangular arrangement will form the final Einstein Telescope geometry.

In its final construction stage the Einstein Telescope will consist of three nested detectors, which will be arranged in a triangular pattern as shown in figure 6. In contrast to the traditional L-shaped geometry of the first and second generations of gravitational wave detectors this arrangement is equally sensitive for both polarisations of the gravitational wave. Additionally it shows a more isotropic antenna pattern compared to the L-shaped detectors, as shown in figure 16. The overall frequency range covered will reach from a few Hertz to about 10 kHz.

Each individual detector in turn will comprise two interferometers, one specialised for detecting low-frequency gravitational waves and the other one for the high-frequency part. The sensitivity goal for each interferometer

is shown in figure 7. Each individual interferometer has a classical dual-recycled Michelson topology with arm cavities. This is a mature technique, well tested in laboratory experiments, and currently being set up for the second-generation detectors, Advanced LIGO and Advanced Virgo. More elaborate topologies like Sagnac interferometers or optical bars using Quantum Non-Demolition (QND) techniques do not promise significant advantages and have not yet reached the level of maturity required for a project of this scale.

1.3.2 Quantum Noise

In order to achieve a sufficient sensitivity at high frequencies the light power in the arms of the high-frequency interferometer needs to be increased to the megawatt range. Thermal noise considerations on the other hand require cryogenic optics to reach the sensitivity goal at low frequencies.

Operating cryogenic optics at a level of several megawatt of light power presents a serious technological challenge which is extremely hard to master. Even for the best mirrors that state-of-the-art coating technology can produce, the residual absorption of only about one ppm leads to an absorbed power of several Watt at a circulating light power level in the megawatt range. The resulting thickness of the suspension fibres, which would be needed to remove the heat, would spoil the performance of the ultra low loss suspension. The Einstein Telescope will therefore be realised in what we call a 'xylophone' arrangement, where each single detector is split into two interferometers, leading to sensitivities as shown in figure 7. The one dedicated for detecting high-frequency gravitational waves in the range from about 30 Hz to 10 kHz will be operated at room temperature, use fused silica optics with a diameter of about 60 cm and a mass of about 200 kg each, have a light power of about 3 MW in the interferometer arms, and run with broadband tuned signal recycling. The cryogenic, low-frequency one, operated at a temperature of 10 K and aimed at the frequency range from 1.5 Hz to 30 Hz, will use detuned signal recycling, have a light power of 18 kW in the interferometer arms, and silicon mirrors with a diameter of about 40 cm and a mass of about 200 kg. The cryogenic optics will either be made of sapphire or, more likely, of silicon. The dimensions will partly be determined by the maximum available bulk material size and otherwise be comparable to the room temperature ones. A summary of the main parameters for the high and low temperature interferometers is given in table 10.

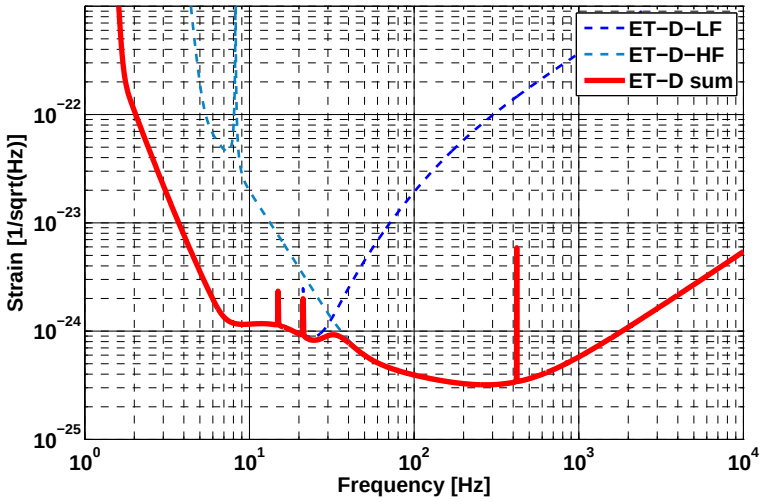

Figure 7: Sensitivity of the Einstein Telescope in the 'xylophone' configuration. The sensitivity of the low-frequency cryogenic interferometer is shown in the dashed dark blue curve and the one of the high-frequency room temperature one in a dashed blue-green tone. The sum of both is given by the solid bright red curve.

The high mirror mass will not only keep radiation pressure effects low but also allow larger sized beam spots on the mirror surfaces for lowering thermal noise effects. This split detector arrangement also offers an elegant solution for the challenge that radiation pressure noise and shot noise scale in opposite ways with light power and cannot individually be optimised in a single interferometer. In an interferometer using classical states of light the so-called Standard Quantum Limit (SQL) determines the lower limit for the quantum noise. For each frequency there is a different optimal compromise between shot noise and radiation pressure noise, meaning that in a single interferometer the SQL cannot be reached for all frequencies simultaneously.

It can only be overcome if non-classical light with correlations between the phase and the amplitude quadratures is used, so-called squeezed light. In the shot noise dominated frequency range squeezed light is used, which shows lower phase fluctuations at the cost of the amplitude fluctuations in comparison to classical laser light in the interferometer arms. In the low-frequency, radiation pressure dominated range the fluctuations need to be lowered in the amplitude quadrature. This goal can be achieved by reflecting squeezed light off a filter cavity (see figure 165).

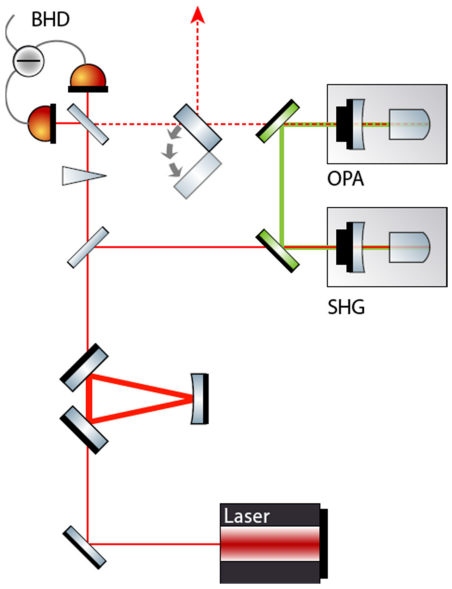

Figure 8: Scheme for generating squeezed light. For details see section 5.5.3

The usage of squeezed light is currently tested in the existing gravitational wave detectors and is foreseen as an add-on to the second generation. Squeezing levels over the full observation band width of up to 10 dB, and stable long-term operation and best squeezing values of almost 13 dB have been demonstrated [8]. For the Einstein Telescope we assume 15 dB initial squeezing level at the squeezing source and an effective squeezing level of 10 dB to be available (equivalent in shot noise reduction to a laser power increase of a factor of 10).

The squeezing level, and with it the sensitivity improvement that can be reached, depends on the optical losses in the squeezer, the filtering optics, the interferometer, and all optical devices on the way to the photodetector, including the photodetector efficiency itself. Optical losses easily add vacuum fluctuations to the squeezed quadrature and hence reconvert squeezed light into classical light. It will therefore be essential to keep the optical losses as low as possible. Optical losses of 75 ppm per round trip are currently achievable with state-of-the-art techniques and are used as a conservative estimate for the filter cavities.

1.3.3 Thermal Noise

Reaching the sensitivity goal at low frequencies requires a significant reduction of thermal noises compared to the first and second generations of gravitational-wave detectors, which can be achieved by operating the mirrors at cryogenic temperatures as low as 10 K.

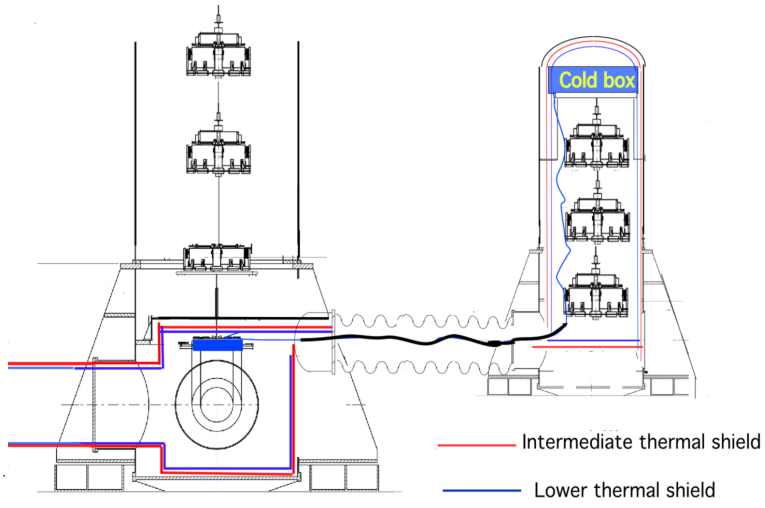

Figure 9: Scheme for cooling the mirrors. For details see section 3.9

Cryogenic operation is also foreseen for the final stage of the planned Japanese gravitational wave detector LCGT. At these low temperatures fused silica has a low mechanical quality factor and becomes unusable. Silicon and sapphire show excellent low-temperature behaviour (see section E) and are good candidates for cryogenic gravitational wave detectors. Its availability in large quantities and good purity through the semiconductor industry makes silicon a promising candidate for the Einstein Telescope cryogenic optics. Some quantities such as the temperature dependence of the refractive index at low temperatures and the residual optical absorption in ultra pure silicon, although assumed to be good enough for use in ET, are currently not known and need to be investigated in R&D activities.

Removing the heat generated by laser light being absorbed at the mirror surfaces without introducing excess vibration levels poses another technical challenge. As thermal radiation does not provide sufficient coupling at cryogenic temperatures this heat removal has to be done by thermal conduction of the suspension fibres. The resulting requirement for the thickness of the silicon suspension fibres needs to be balanced against good seismic isolation properties of thin fibres. The vibration level of cryo coolers, which could be placed close to the optics, threatens the low-frequency sensitivity (see section 3.9.3). R&D in active and passive vibration suppression is still required to sufficiently cut the remaining noise level down for use in the Einstein Telescope. Cryo fluids, like superfluid Helium II, which are cooled down at a remote location above ground, are available as a seismically more quiet alternative (see section 3.9.6). The final operating temperature for ET remains to be fixed in a technical design phase. The cooling capabilities foreseen so far will allow mirror temperatures as low as 10 K.

1.3.4 Seismic Isolation

The main optics for the Einstein telescope need to be very well isolated against seismic ground motion. For the second generation of gravitational wave detectors both active and passive isolation strategies are being pursued. In the advanced LIGO detectors a two stage system actively isolates a platform from ground motion, from which the main optics are suspended by quadruple pendulums. The passive strategy employed at the Virgo detector demonstrated an excellent performance over the full frequency range (see figure 117) and is foreseen as the reference solution for the Einstein telescope. The horizontal isolation is achieved with a six-stage pendulum system, whereas for the vertical degree of freedom cantilever springs are used. The pendulum suspension system itself is supported by a platform resting on an inverted pendulum, which provides additional horizontal seismic isolation (see figure 115). All mechanical resonances of the whole structure are actively damped to avoid resonant mechanical amplification of ground motion. The overall height of the suspension system is about 17 m, requiring correspondingly tall vacuum chambers and caverns.

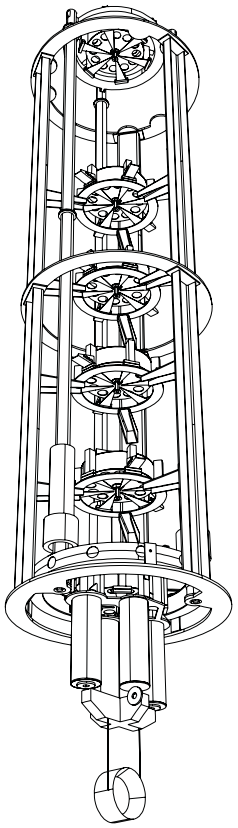

Figure 10: Schematic view of the Virgo Superattenuator. See also section 4

1.3.5 Newtonian gravity gradient noise

Newtonian gravitational interactions between the optics and the surrounding soil provide a direct coupling mechanism of ground motion to the interferometer test masses (see also section 3.5). As the resulting, so-called gravity gradient noise cannot be shielded from the mirrors, a location has to be found where this seismic motion is minimal and the surrounding soil as homogeneous as possible. This goal can be achieved in an underground location in a seismically quiet region. Preliminary measurements show that a depth of 100 to 200 m in a remote location with low population density provides sufficiently low seismic motion. The potential of measuring the ambient seismic motion, feeding it into a gravity gradient noise model, and then subtracting the predicted effect from the interferometer output signal has been investigated. Initial results are promising, and are interesting also for the second generation of gravitational wave detectors, but investigations need to be continued in an R&D programme (see section 3.5.3).

1.3.6 Vacuum

The space between the mirrors in the interferometer arms has to be evacuated to very low residual partial gas pressures to keep the apparent length changes caused by fluctuations of the refractive index sufficiently low. The tolerable maximum pressure is on the order of 10^{-8} Pa (see paragraph 3.8.2).

Some technical parameters will remain "to be defined" in this design study document. At this stage of the conceptual design these parameters are not important and will be worked out in a future technical design phase.

1.3.7 Noise budget

The xylophone strategy, i.e. the division of each detector into a low-frequency and a high-frequency interferometer, allows to pursue different strategies in optimising the noise for each frequency range. The noise budget for the high-frequency interferometer is shown in the upper part of figure 11.

In the frequency range from about 7 Hz to 30 Hz the sensitivity is limited by suspension thermal noise, resulting from the interferometer being operated at room temperature. At frequencies above 500 Hz the dominating noise source is photon shot noise. Between these two frequency ranges mirror thermal noise is limiting the overall sensitivity. In the noise budget for the low-frequency interferometer, shown in the lower part of figure 11, quantum noise is limiting the sensitivity over the entire frequency range above 7 Hz. Due to the operation at cryogenic temperatures the influence of suspension thermal noise in the frequency range above 7 Hz can be cut down to a sufficiently low level. Below 7 Hz the sensitivity is limited by comparable amounts of quantum noise, gravity gradient noise, and suspension thermal noise. Due to the good performance of the multistage pendulum suspensions the influence of seismic noise can be limited to the frequency range below 2 Hz. Investigations of new quantum non-demolition techniques in a planned R&D program will show whether it is possible to cut down the quantum noise contributions to an even lower level in the frequency range from 7 Hz to 30 Hz.

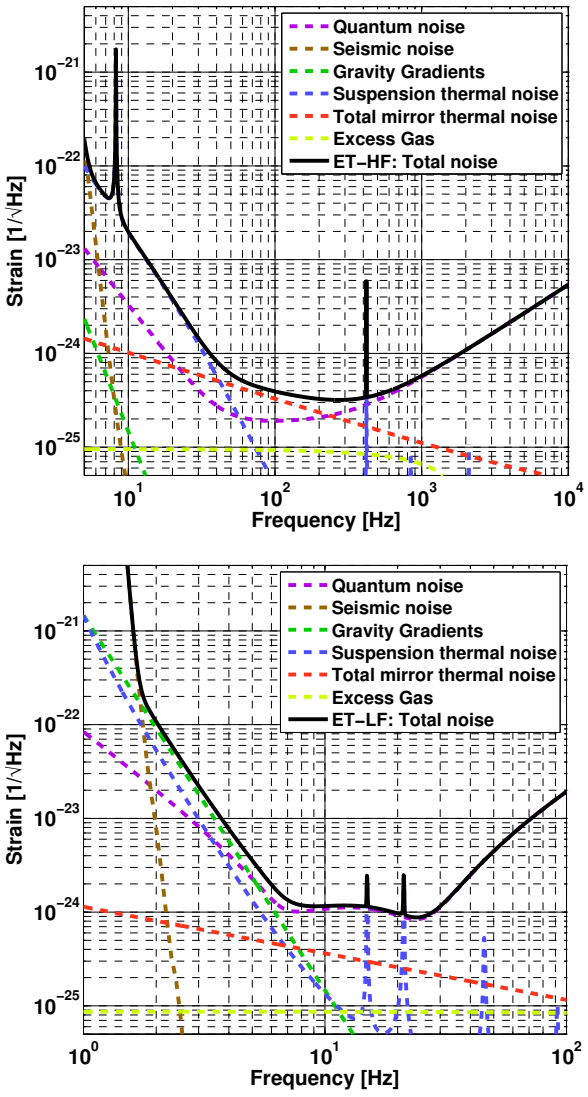

Figure 11: Noise budget for the low- and high-frequency interferometer for the parameters used for the ET-D sensitivity curve as stated in table 10.

1.4 Layout of the observatory

As a consequence of the extremely demanding seismic requirements the Einstein Telescope will be located underground at a depth of about 100 m to 200 m and will, in the complete configuration, consist of three nested detectors, each in turn composed of two interferometers. Selecting the geometry of an equilateral triangle, where each side of the triangle is simultaneously used by two detector arms, allows to determine the polarisation of the gravitational wave and optimises the usage of the tunnels. The topology of each interferometer will be the dual-recycled Michelson layout with Fabry-Perot arm cavities. An artist's impression of the Einstein Telescope is shown in figure 2.
Underground seismic measurements at eight different European locations have been performed within this design study and additional measurements from external sources have also been evaluated. Satisfactory seismic performance has been found in several locations.

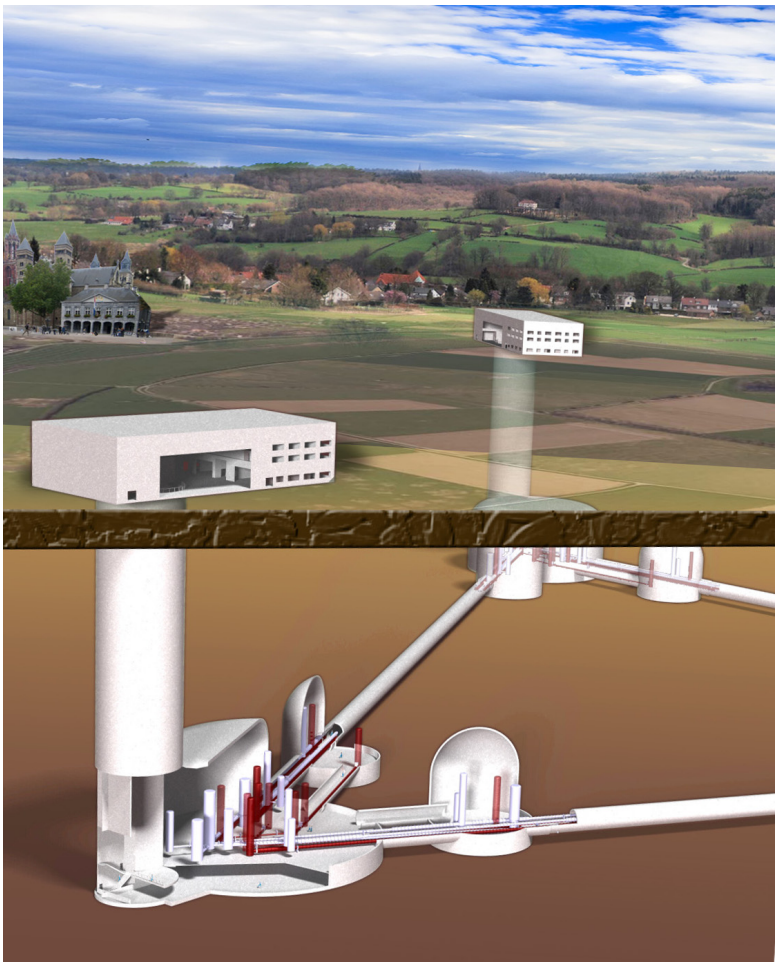

Figure 12: Artistic view of the arrangement of buildings, access shafts and underground caverns.

For the final site selection long-term seismic noise measurements including seasonal effects like variable wind speeds and ocean wave height need to be made, and other nonscientific factors of influence (e.g. political, financial, interest of local parties, vicinity to research institutions) have to be included in the decision process.

The sensitivity curve shown in figure 7 gives the sensitivity for a single detector with 10 km arm length and an angle of 90° between the arms. This is done for better comparison with the existing detectors and their 'advanced' versions. ET will in fact have three 10 km detectors and the angles between the arms will be 60°. The resulting sensitivity in comparison with a single 90° detector depends on the source location in the sky and its orientation, as the angular antenna pattern (see figure 161) and the polarization dependence (independent in the triangular case) influence the signal strength differently for different detector layouts. On average the sensitivity of the triple 60° detector is slightly better than a single, optimally oriented 90° one.

Box 1.3: Sensitivity curves for the Einstein Telescope

As the understanding of the achievable sensitivity of the Einstein Telescope evolved throughout the Design Study, different sensitivity curves are used in this document, named from ET-B to ET-D (see figure 13).
The very first, preliminary sensitivity curve ET-A was a crude, early estimate and will hence not be used in this document. ET-B is the sensitivity curve where each detector is built from a single interferometer, where the high power needed to achieve good high-frequency performance compromises the low-frequency performance. Over a wide frequency range from a few Hertz to a few times 10 Hz the sensitivity is limited by radiation pressure noise, whereas above a few hundred Hertz the sensitivity is limited by shot noise.
The next evolutionary step is the sensitivity curve ET-C, where each detector is split into two interferometers, each dedicated to a distinct frequency range (the xylophone configuration). Some technical details, such as losses inside optical resonators are not fully included in this sensitivity curve.
The latest sensitivity curve is given by ET-D, where imperfections like optical losses in cavities are included in the computations. As the later sensitivity curves became available only during the Design Study, some of the subsection results are still based on earlier versions, which will be indicated by the sensitivity curve acronym.
In the cost optimisation phase towards the end of the design study some parameters have been changed with respect to the ET-D sensitivity parameters, e.g. the lengths of the filter cavities for the high frequency interferometers, but have only an insignificant (<10%) influence on the overall sensitivity.

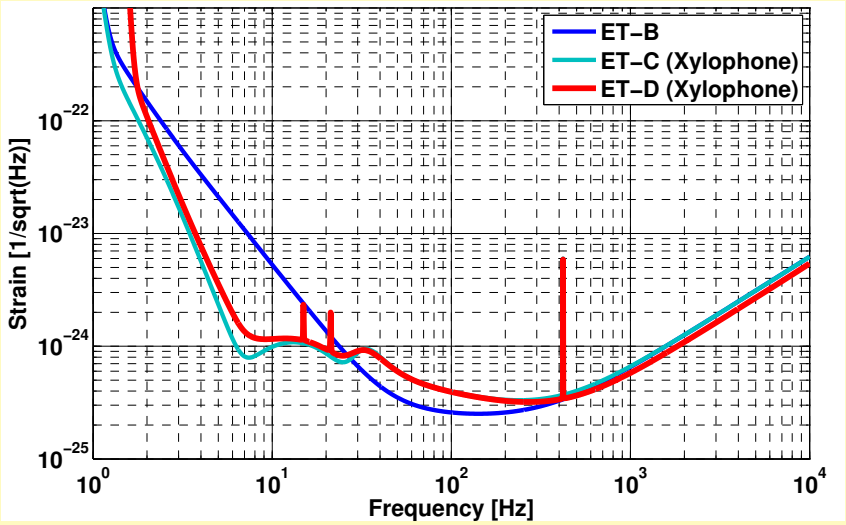

Figure 13: Sensitivity curves for ET used in this document. For details see text.

For the desired sensitivity an overall side length of the triangle of about 10 km is required. More specifically in this document we assume 10 km for the arm cavity length as depicted in figure 71 and figure 163 and an additional 300 m of tunnel length for telescopes for mode matching the large beam size from the interferometer arms to smaller beams in the beam splitter area. This gives a total triangle side length of 10.3 km and an overall tunnel length for the Einstein Telescope Observatory of 30.9 km. This length of 300 m from the "vertex station" to the "satellite station" is also used for the filter cavities for the high-frequency interferometer housed in a separate tunnel, which simultaneously serves as a safety escape route from the "satellite caverns" (see figure 40 and figure,42.

The main ≃10 km tunnels that connect two satellite stations (see section 3.7.3) will have an inner diameter of 5.5 m, which will locally be increased to 6.0 m wherever the insulation for cryogenic operation requires more space. The three vertex caverns and six satellite caverns will house the vacuum vessels and must be about 25 m high (see section 3.7.2). Access to the underground detectors is foreseen via vertical shafts (see figure 70). It remains to be explored in a technical design phase after site selection whether horizontal access is favourable. This option may, for instance, be advantageous if the Observatory is built inside a mountain.

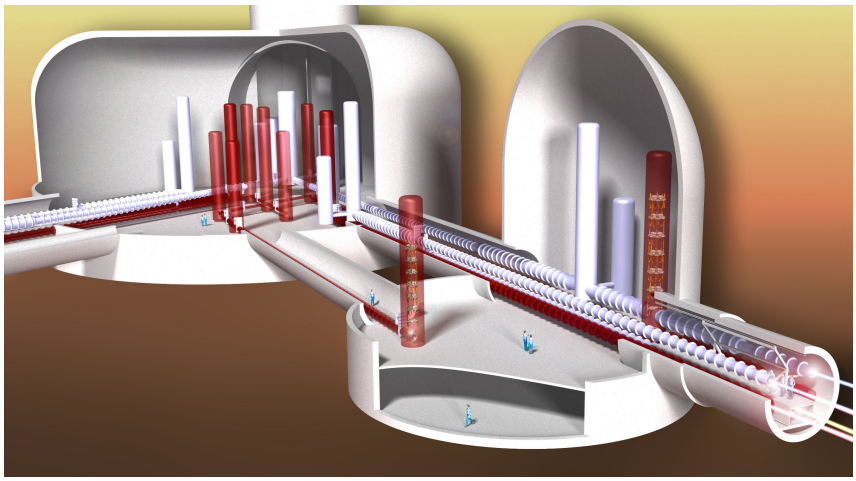

Figure 14: Artistic impression of the underground arrangement of tunnels and caverns. For details see sections 3.7.3 and 3.7.2

The ET infrastructure will house the observatory for many decades, during which the interferometers will receive upgrades as technology advances. Some of these changes may result in the necessity to change mirror positions and with it vacuum tank positions as we now see in the upgrades from the 'initial' to the 'advanced' generation of gravitational wave detectors. Hence we plan to build large caverns where the tanks can be placed at arbitrary positions, instead of building an inflexible system of short tunnels connecting narrow but tall caverns housing a single vacuum tank each.

Above ground, at the entrance to the vertical axis shafts, facilities housing workshops, offices, apartments, technical facilities providing cryogenic fluids, air conditioning and venting, emergency electricity generators, etc. will be set up, as shown in figure 70. One major aspect of the design of the total infrastructure is to provide an environment able to house not only the basic initial version of the Einstein telescope that we describe in this Design Study document but also be versatile enough to accommodate upgraded versions in the following decades to come.

1.5 Observatory timeline

The realization of the ET observatory will be the final step of a long path and the initial act of a new scientific adventure. Several steps have been necessary (see Sec. 6.1) to allow the realization of this conceptual design study document and few other important achievements are needed to reach the readiness condition for the observatory realization. The design of the new detector must evolve from the current conceptual phase to the technical design phase, successful R&D activities must confirm the feasibility of the solutions proposed in this document, but, first of all, it is crucial that advanced detectors confirm the effectiveness of their new technologies and that a gravitational wave signal is detected in these interferometers. The detection of gravitational waves is regarded as a prerequisite for the start of construction of the Einstein Telescope. For this reason the excavation of the ET site cannot start before 2017, and hence 2018 is here taken as the initial time (t_0) for the ET observatory realization. ET being an observatory that will be *on line* for decades, priority in construction will be attributed to the site and infrastructures realization, selecting a modular philosophy for the detectors that will allow to implement the different interferometers composing each detector with a schedule stretched in time. In this way, after about 6 years of construction, installation and commissioning, the first detector of the ET observatory could be operative at the end of the first half of the next decade.

1.6 Observatory costs

At this stage of the conceptual design the costs of the Observatory have to be regarded as a rough estimate. A summary of the estimated costs is shown in figure 212. More details on the costing are explained in section 6.2. The overall costs of an underground facility like the Einstein Telescope Observatory are dominated by excavation costs and construction of the underground tunnels and caverns. These costs depend significantly on the location and type of soil. In this design study a rather conservative assumption of 260 €/m^3 has been made. The costs listed in the figure 212 assume a single detector to be implemented first. The costs include spares for each individual item. In most instances the spares will remain unused and can act as spares for the subsequent installation of the other two detectors, reducing their price tags somewhat.

2 Science case

2.1 Introduction

Some three hundred years after Galileo observed the Jovian satellites, the twentieth century heralded a new era in observational astronomy with radio and microwave antennas and gamma- and X-ray detectors, which revolutionized astronomy and opened the entire electromagnetic spectrum for observing and understanding the Universe. Each new spectral window has unveiled a new source or phenomenon that could not have been discovered in any other way. A remarkable revelation coming from these observations is that about 96 percent of our Universe is invisible and that gravitational interaction powers the most luminous and spectacular objects and phenomena such as quasars, gamma-ray bursts, ultra luminous X-ray sources, pulsars, and the evolution of the early Universe. Gravity has, so far, played a passive role. But that is about to change.

Einstein's General Theory of Relativity is among the most successful physical theories of the 20th century. It has passed with flying colours all laboratory-based experiments and solar system tests. It predicts that dynamical systems in strong gravitational fields will release vast amounts of energy in the form of gravitational radiation (see Box 2.1 for a brief introduction to gravitational waves). This radiation has the potential to open a new window on the Universe, complementing the electromagnetic window. Russell Hulse and Joseph Taylor were awarded the 1993 Nobel Prize in Physics for their discovery of a binary consisting of two neutron stars in close orbit, in which indirect evidence for the emission of gravitational waves (GWs) was found.

2.2 Executive Summary

Gravitational waves interact weakly with matter because gravity itself is very weak. Detectable amounts of gravitational radiation cannot be produced in a laboratory but catastrophic astronomical events could be the source of strong GWs. The first attempts to detect cosmic gravitational radiation were made in the 60's by Joseph Weber, who built resonant bar detectors, but they were not sensitive enough to even the most energetic sources of gravitational waves, such as a nearby supernova. Over the past four decades, progress in technology has led to the construction of ever more sensitive instruments, culminating in long-baseline laser interferometric detectors such as the European GEO 600 and Virgo and the American LIGO.

Interferometric detectors that are currently taking data, and advanced detectors that will be built over the next five to ten years, will be the first steps in establishing the field of *gravitational astronomy*. Advanced Virgo and LIGO are expected to observe several tens of inspiralling and merging binaries of neutron stars (NSs) and black holes (BHs) each year. They could also detect occasional Galactic sources such as transients associated with supernovae, glitching pulsars, or soft gamma-ray bursts. This phase of observation will, for the first time, test Einstein's theory in the dissipative regime beyond the basic quadrupole approximation, verify the existence of binary black holes (BBHs), measure the speed of gravitational radiation relative to the speed of light and map the expansion rate of the Universe on scales of hundreds of megaparsec (Mpc), providing a completely independent estimate of the Hubble parameter.

Advanced Virgo and LIGO will be sensitive to binary neutron stars (BNSs) at a distance of 200 Mpc and to stellar mass BBHs at a red shift of $z = 0.5$. The lower frequency cutoff of a detector places an upper limit on the total mass of binary systems they can detect. A lower frequency cutoff of 20 Hz in the case of Virgo and LIGO limits the total mass to be less than about $200\,M_\odot$. ET plans to improve the amplitude sensitivity by an order of magnitude and extend the frequency sensitivity down to 1 Hz. This will allow astronomers to explore binaries at cosmological distances and unveil new sources: ET would observe BNS up to a redshift of $z \sim 2$, stellar-mass BBH population at the edge of the Universe ($z \sim 15$) and intermediate-mass (10^2–$10^4\,M_\odot$) BBH out to a typical redshift limit $z \sim 5$. ET will be sensitive to supernovae out to a distance of 15 million light years within which one might expect to observe an event every year.

An observatory with the capability of ET will produce tremendous scientific payoffs. ET will make it possible to observe a greater variety of phenomena and provide a new tool for expanding our knowledge of fundamental physics, cosmology and relativistic astrophysics. ET's key science objectives are:

Fundamental Physics and Gravity

1. *Is the nature of gravitational radiation as predicted by Einstein's theory?*

   ET will allow a test of the wave generation formula beyond the quadrupole approximation and check whether there are only two polarizations as predicted by Einstein's theory or six as in scalar tensor theories. It could accurately measure the GW propagation speed by coincident observation of GW and EM radiation from BNS coalescences at $z \sim 2$ and constrain the graviton mass.

2. *Are black hole spacetimes uniquely given by the Kerr geometry?*

   By measuring different quasi-normal modes, ET will test if the spacetime geometry of a BH is uniquely described by its mass and spin. Additionally, ET can measure the multipole moments of a source from the radiation emitted as a stellar-mass BH spirals into an intermediate-mass BH and confirm if the different moments depend only on the massive BH's mass and spin.

3. *What is the physics of gravitational collapse?*

   ET can study supernovae and explore if they leave behind a massive object that is trapped inside an event horizon or lead to a naked singularity, or some other exotic object. ET could well reveal a new class of objects and phenomena, for instance *silent supernovae* [9] and other gravitationally unstable transients.

4. *What is the equation of state of matter at supra-nuclear densities as might be found in NS cores?*

   The equation of state (EoS) of NSs affects the late-time evolution of BNS and neutron star-black hole (NSBH) binaries. By matching the observed radiation from the coalescence of such sources to theoretical predictions, ET will deduce the EoS of NS cores.

5. *What is the maximum mass of a neutron star?*

   The maximum mass of a white dwarf is $\sim 1.4\,M_\odot$ as determined by the electron degeneracy pressure. The maximum mass of a NS is an additional test of the nature of matter at extremely high densities; it is currently unknown and should be determined by accurately constructing their mass function from millions of BNS systems observable in ET.

Cosmology

1. *What are the true luminosity distances of cosmological sources?*

   BBH and BNS binaries are an astronomer's ideal *standard candles* or, more appropriately, *sirens*. Gravitational wave observations alone can determine both the apparent and absolute luminosity of a source. With ET these standard sirens can be used to calibrate the cosmic distance ladder.

2. *What is the EoS of dark energy and how does it vary with redshift?*

   ET could observe thousands of coalescing BNS and NSBH systems in coincidence with optical or gamma-ray observations and hence measure both the luminosity distance and redshift. ET will, therefore, facilitate precision measurement of the dark energy EoS and its variation with redshift.

3. *How did black holes at galactic nuclei form and evolve?*

   ET can verify if seeds of galaxy formation were intermediate BHs of hundreds to thousands of solar masses and map their merger history up to redshifts of $z \sim 5$–15 depending on the total mass and mass ratio of progenitor binaries.

4. *What were the physical conditions in the primeval Universe and what phase transitions occurred in its early history?*

   Stochastic GW backgrounds could be produced by quantum processes in the primordial Universe or during phase transitions in its early history. ET will be sensitive to background densities $\rho_{\rm GW} \gtrsim 10^{-12}\,\rho_c$, where ρ_c is the critical density of the Universe.

Astrophysics and Multimessenger Astronomy

1. *What is the mass function of BHs and NSs and their redshift distribution?*

   ET will measure masses and spins of millions of NSs and BHs in binary systems and will thereby obtain a census of these objects as a function of redshift. This will be a very valuable database for understanding a host of questions in astronomy related to redshift evolution of compact objects.

2. *What are the progenitors of gamma-ray bursts?*

   Gamma-ray bursts (GRBs) are the most luminous electromagnetic sources in the Universe. While advanced detectors might provide some clues as to their origin, ET will provide a large statistical sample of events that could be used to understand GRB progenitors and to test their astrophysical models.

3. *How do compact binaries form and evolve?*

   The process by which main sequence binary stars evolve into compact binaries (that is, BNS and BBH) could be understood by ET's observation of millions of coalescing binaries with different masses, mass ratios and spins and mapping the observed population to astrophysical models.

4. *What is the physical mechanism behind supernovae and how asymmetric is the gravitational collapse that ensues?*

   Supernovae are complex processes whose modelling requires many different inputs, including relativistic magneto-hydrodynamics, general relativity and nuclear and particle physics. ET's observation of supernovae in coincidence with EM afterglows and neutrinos could provide the data necessary to constrain models and help understand the process by which stars collapse to form NSs and BHs.

5. *Do relativistic instabilities occur in young NSs and if so what is their role in the evolution of NSs?*

   Non-linearities of general relativity could cause instabilities in NSs that lead to parametric amplification of GWs. ET's observations of the formation of NSs can explore if such instabilities occur in young NSs and how that might affect their spin frequencies.

6. *Why are spin frequencies of NSs in low-mass X-ray binaries bounded?*

   ET will verify if gravitational radiation back-reaction torque is responsible for the observed upper limit on NS spin frequencies in low-mass X-ray binaries.

7. *What is the nature of the NS crust and its interaction with the core?*

   ET should detect NS ellipticities that are few $\times 10^{-10}$ or larger depending on their spin frequency. This can be used to deduce the property of NS crusts. ET might also detect GWs that are expected to be emitted when pulsars glitch and magnetars flare and thereby help understand crust-core interaction that is believed to transfer angular momentum from the core to crust.

8. *What is the population of GW sources at high redshifts?*

   A large population of point sources would produce a confusion background that would be detectable by ET if the energy density of the background is large enough. Detection of confusion backgrounds can be used to understand the nature and population of GW sources in the Universe.

Gravitational radiation is an essential prediction of any relativistic theory of gravity. It will be a new tool for observing the most energetic processes in the Universe—processes originating in such extremely dense environs that all other forms of radiation and particles might be trapped. In this chapter we will look at what new science is enabled by ET and how its low frequency ($< 10\,\mathrm{Hz}$) sensitivity will be critical in achieving its key science objectives.

Box 2.1: Gravitational Waves

At a sufficiently large distance from cosmic sources, GWs can be described as a small perturbation to a flat spacetime. The spacetime can thus be described by a metric $g_{\alpha\beta} = \eta_{\alpha\beta} + h_{\alpha\beta}$, $|h_{\alpha\beta}| \ll 1$, where $\eta_{\alpha\beta} = \mathrm{Diag}(-1, 1, 1, 1)$ is the flat Minkowski metric and $h_{\alpha\beta}$ is the perturbation due to GWs. In a suitable coordinate system and gauge, $h_{\alpha\beta}$ has only two independent components conventionally called the "plus" and "cross" polarizations h_+ and $h_\times$, respectively: $h_+ \equiv h_{xx} = -h_{yy}$, $h_\times \equiv h_{xy} = h_{yx}$, all other components being zero, $h_{0\alpha} = h_{z\alpha} = 0$.

The apparent luminosity of radiation $\mathcal{F}$, at great distances from the source and in geometrical units in which $c = G = 1$, is related to the time-derivative of the amplitude by [10]:

$$\mathcal{F} \sim |\dot{h}|^2/(16\pi). \tag{1}$$

If a source at a distance D radiates away energy E in a time T, predominantly at a frequency f, then writing $\dot{h} = 2\pi f h$ and noting that $\mathcal{F} \sim E/(4\pi D^2 T)$, the amplitude of GWs is

$$h \sim \sqrt{E/T}/(\pi f D). \tag{2}$$

Gravitational waves cause a strain in space as they pass. The distance L between two masses will be altered by an amount δL that is proportional to a linear combination of the two polarizations. Figure 15 below depicts how a ring of free particles responds to the two polarizations.

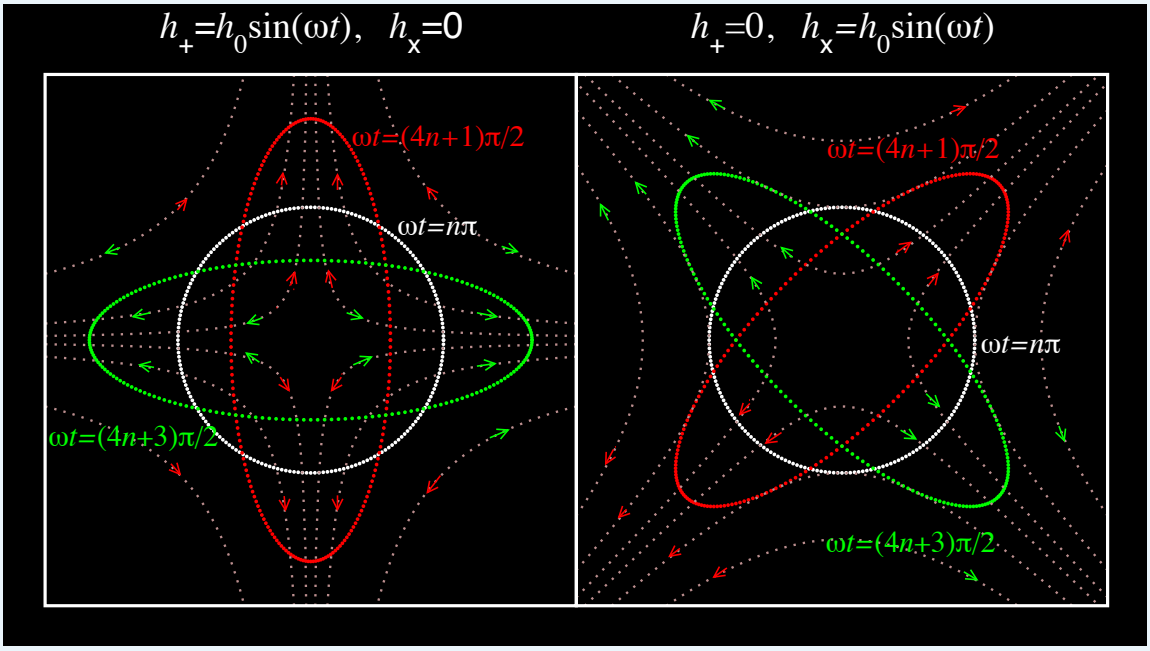

Figure 15: Response of a circular ring of free particles to a passing sinusoidal GW of plus (left) or cross (right) polarization. The tidal field of the waves on the ring is indicated by light dotted lines. The direction of the force reverses sign each half-period of the wave as indicated by the red and green arrows. The ring oscillates between the red and green ellipses over one period of the wave, the maximum eccentricity of the ellipses being the wave amplitude h_+ or $h_\times$. A general wave is a linear combination of the two polarizations.

A sinusoidal wave incident perpendicular to the plane of the ring tidally deforms it into an ellipse over the first quarter of the wave's period, back to the ring over the next quarter, to an ellipse oriented orthogonally to the first over the third quarter, and back to the ring over the fourth quarter.

2.3 Sources of gravitational waves in ET

The goal of this Section is to give an overview of the sources expected to be observed by ET and the problems that were addressed in the context of the Design Study. A brief description of how ET responds to an incident GW is given in Box 2.2. ET will observe GWs from a variety of different astronomical sources such as BNSs, BBHs, supernovae, spinning NSs, glitching pulsars, flaring magnetars, and, perhaps, a primordial stochastic background. We will first give a brief introduction to the types of sources expected to be routinely observed by ET. This will be followed by a discussion of the fundamental physics, astrophysics and cosmology enabled by ET. Recent reviews on sources and science can be found in Sathyaprakash and Schutz [11] and Andersson et al [12].

Box 2.2: ET's Response to Gravitational Waves

A single interferometric gravitational-wave detector cannot measure both polarizations of GW, but only a linear combination of the two, called the *response* $h(t)$, given by

$$h(t) = F_+(\theta, \varphi, \psi)h_+(t) + F_\times(\theta, \varphi, \psi)h_\times(t). \tag{3}$$

Here, F_+ and $F_\times$ are the detector antenna pattern functions, ψ is the polarization angle, and (θ, φ) are angles describing the location of the source on the sky (see *e.g.* Ref. [11] for details). The various angles can be treated as constants for transient sources, but must be taken to be time-dependent for sources that last for more than about 30 min, after which Doppler modulation of the signal due to the relative motion of the source and detector cannot be neglected.

It is expedient to write the response as

$$h(t) = F(t)\,(\cos\xi\, h_+ + \sin\xi\, h_\times)\,, \quad F = \sqrt{F_+^2 + F_\times^2}, \quad \tan\xi = F_\times/F_+. \tag{4}$$

It turns out that F is independent of the polarization angle and so measures the sensitivity of the detector to different locations on the sky. Figure 16 below plots $F(\theta, \varphi)$ for an L-shaped interferometer such as Virgo (panel on the left) and for a triangular ET (panel on the right). Since ET consists of a triangle of three detectors, it is a factor $\sqrt{3}$ more sensitive than a single detector; but, since the opening angles of the arms are $\pi/3$, the sensitivity is smaller by a factor $\sin(\pi/3) = \sqrt{3}/2$ compared to an L-shaped detector—an overall factor of 3/2, as can be seen in Fig. 16.

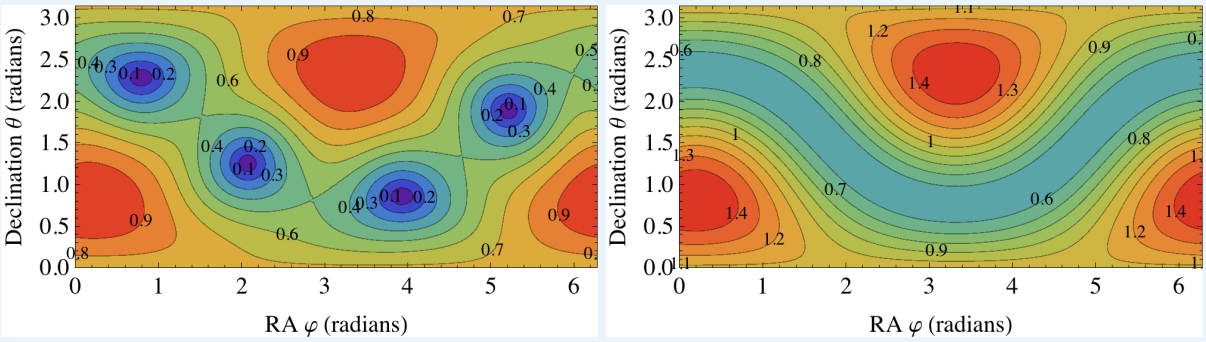

Figure 16: Antenna pattern of ET (right panel) compared to that of Virgo (left panel). ET is assumed to be at the same location as Virgo. Note that Virgo is a *single* L-shaped detector while ET consists of *three* V-shaped interferometers rotated relative to one other by 120 deg . The combined antenna pattern of the three detectors in ET (defined as $F^2 = \sum_{A=1}^{3} F_A^2$, where F_1, F_2, F_3 are the individual antenna pattern functions) makes the response the same for all sources whose sky location makes the same angle to the plane formed by ET (see *e.g.* contours marked 0.6).

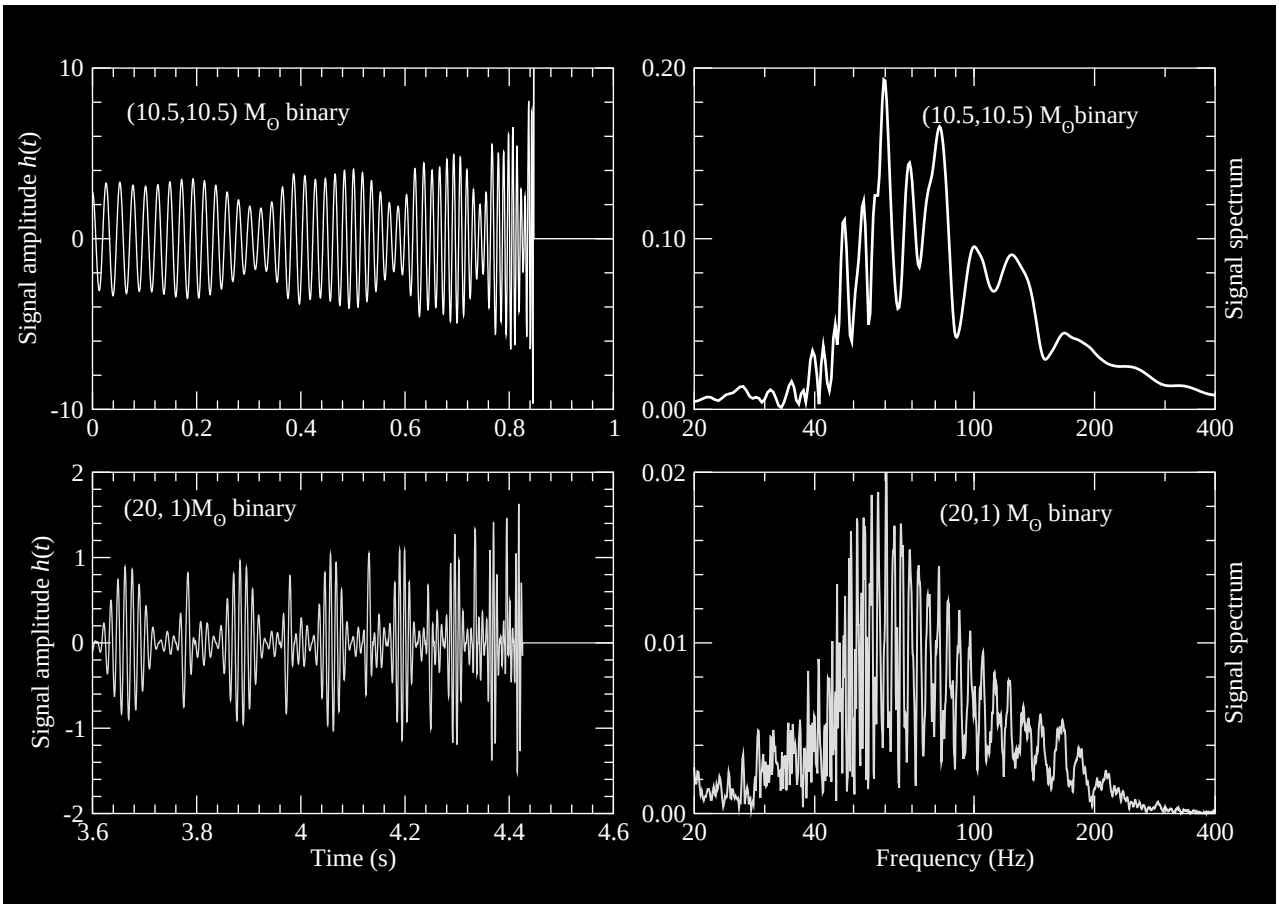

Figure 17: The waveforms from two compact binary systems that ET could detect. Left panels show the time-domain waveforms (for clarity only the last second is plotted), right panels show the frequency spectrum. The upper two panels show a binary composed of two equal masses; the waveform's modulation is due to interaction between the spins of the bodies and the orbital angular momentum. The lower panels show a binary composed of a neutron star and a black hole. In this case, the signal amplitude is smaller, the duration is longer due to the larger mass ratio, and the signal modulation is stronger as the spin-orbit precession of the orbital plane is greater.

2.3.1 Compact binary coalescences

A compact binary, consisting of NSs and/or BHs, evolves by emitting gravitational radiation which extracts rotational energy and angular momentum from the system. This causes the two bodies to inspiral toward each other and eventually merge. The dynamics of a compact binary can be described in three phases:

- The *inspiral phase* in which the system spends hundreds of millions of years. During this phase the luminosity in GW is low and the dynamics can be solved using approximation methods — the most popular being the post-Newtonian (PN) approximation (see Box 2.3). The two polarizations are given at the lowest order approximation by Equations (5), Box 2.3. At the dominant PN order, the frequency of the emitted signal is twice the orbital frequency; the signal has a characteristic shape, with slowly increasing amplitude and frequency, called a *chirp* waveform. A BNS system will stay in ET's sensitivity band for nearly a week starting from 1 Hz, 20 hours starting from 2 Hz, and a little less than 2 hours starting from 5 Hz. For the same lower frequency limits the duration of a BBH signal from a pair of 10 $M_\odot$ BHs is 2 days, 45 minutes and 4 minutes, respectively. Such long durations, owing primarily to the low frequency sensitivity of ET, are crucial in obtaining very accurate estimates of a binary system's parameters, which

is essential to achieve some of the scientific goals of ET.

When the binary companions are spinning, the signal is modulated due to spin-orbit and spin-spin couplings as in Fig. 17. These modulations encode the parameters of sources (their masses, spins, inclination of the orbit, etc.) most of which can be extracted very accurately [13–16] by matching the observed signals onto general relativistic predictions.

At higher PN orders, the signal also contains other harmonics of the orbital frequency and including these in the estimation of parameters has proved to be extremely important, especially for localizing the source on the sky [17–19].

Box 2.3: Post-Newtonian Description of the Inspiral Signal

The adiabatic evolution of a compact binary, during which the emission of GWs causes the component stars of the system to *slowly* spiral in towards each other, can be computed very accurately using the PN expansion of the Einstein equations. Currently, the dissipative dynamics is known to order (v^7/c^7), where v is the characteristic velocity in the system.

For a binary consisting of two stars of masses m_1 and m_2 (total mass $M \equiv m_1 + m_2$ and symmetric mass ratio $\nu \equiv m_1 m_2/M^2$), at a luminosity distance $D_{\rm L}$, the dominant parts of the two polarizations are given by

$$h_+(t) = \frac{2\nu M}{D_{\rm L}}(1+\cos^2\iota)\,[M\omega(t;t_0,M,\nu)]^{\frac{2}{3}}\cos\left[2\Phi(t;t_0,M,\nu)+\Phi_0\right], \tag{5a}$$

$$h_\times(t) = \frac{2\nu M}{D_{\rm L}}2\cos\iota\,[M\omega(t;t_0,M,\nu)]^{\frac{2}{3}}\sin\left[2\Phi(t;t_0,M,\nu)+\Phi_0\right], \tag{5b}$$

where ι is the angle of inclination of the binary's orbital angular momentum with the line-of-sight, $\omega(t)$ is the angular velocity of the equivalent one-body system around the binary's centre-of-mass and $\Phi(t;\,t_0,M,\nu)$ is the corresponding orbital phase. Parameters t_0 and Φ_0 are constants giving the epoch of merger and the orbital phase of the binary at that epoch, respectively. The orbital dynamics, and hence the phase Φ, are known to order (v^7/c^7).

The above expressions for h_+ and $h_\times$ contain only the dominant terms which oscillate at twice the orbital frequency. Higher order amplitude corrections contain other harmonics (*i.e.* phase terms depending on $k\,\Phi(t)$, $k = 1, 3, 4, \ldots$). The above expressions are written down for a system consisting of non-spinning components on a quasi-circular orbit. In reality, we can assume neither to be true. Waveforms for binaries on an eccentric inspiral orbit are known, as are those with spin effects, but we shall not discuss them here.

- The *merger* phase when the two stars are moving at around a third of the speed of light and experiencing extreme gravitational fields. A post-Newtonian approximation is not accurate when the two stars get close to each other. To predict the dynamics of the bodies during this phase requires the full non-linear structure of Einstein's equations, as the problem involves strong relativistic gravity and tidal deformation and disruption. The merger signal lasts for a very short duration (milliseconds in the case of stellar mass BHs, to seconds in the case of the heaviest systems ET is likely to detect). Yet BBH have the greatest possible luminosity of all sources one can conjure up, exceeding the luminosity of the entire Universe in EM radiation in that short duration.

  Numerical simulations of BBH mergers have been highly successful, and analytical and phenomenological models of the merger dynamics have been developed. Following breakthroughs in 2005 [20–22], it is now possible to numerically solve the full Einstein equations for the last orbits that include the merger and ringdown phases, for coalescing BBH systems with comparable component masses, and to calculate the

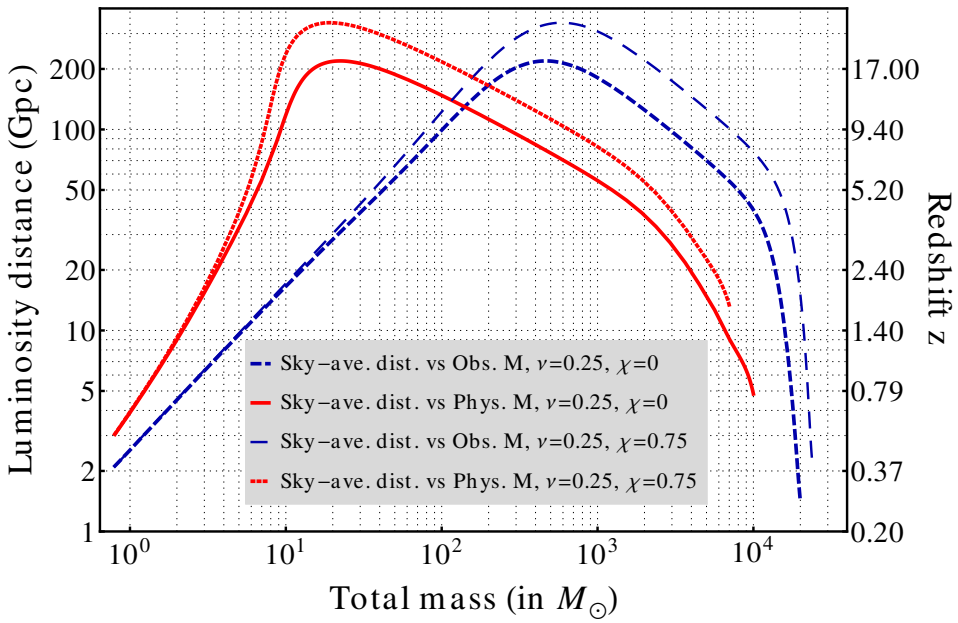

Figure 18: ET's distance reach for signals from coalescing compact binaries as a function of the *intrinsic* (red curves) and *observed* (blue curves) total mass, averaged over sky position and binary's orientation relative to the line-of-sight. We assume that a source is visible if it produces an SNR of at least 8 in ET. Solid red and short-dashed blue curves correspond to binaries composed of non-spinning objects. Dotted red and long-dashed blue curves correspond to binaries composed of objects whose spins are aligned with the orbital angular momentum of the binary, with spin parameter $\chi = 0.75$.

GW signal emitted. Subsequent dramatic progress has led both to simulations of increasing numerical accuracy and physical fidelity, and to the inclusion of larger numbers of GW cycles before merger, allowing full GR waveforms to be in principle useful in searching for BBHs of ever lower mass (see *e.g.* Fig. 3 in [23]).

Currently efforts are focussed on understanding the full parameter space of BBHs of arbitrary spins and mass ratios. In the case of BNSs the merger phase is not well understood, as it is complicated by a number of unknown physical effects, such as the EoS of NSs and their magnetic fields.

- The *ringdown* phase when the two systems have merged to form either a NS or BH, settling down to a quiescent state by radiating the deformations inherited during the merger. The emitted radiation can be computed using perturbation theory and it consists of a superposition of quasi-normal modes of the compact object that forms after merger. These modes carry a unique signature that depends only on the mass and spin angular momentum in the case of BH, but depends also on the EoS of the supra-nuclear matter in the case of NS. Just as in the merger phase, here too the signal lasts for a very short duration (of milliseconds to seconds depending on the mass of the final object) and consistst of two to three cycles. However, the superposition of different modes means that the signal can have an interesting and characteristic structure.

The merger and ringdown parts of the signal last only for a short duration yet carry tremendous luminosity. Their inclusion in a matched filter search for binary systems dramatically increases the distance reach of ET, relative to the reach obtained with the inspiral phase alone. As we shall see below, having observational access to these later stages of the coalescence process will lead to key insights into the structure of NS; in the case of BH it will open up the possibility of testing gravity in genuinely strong-field dynamics of spacetime.

ET's distance reach and mass range A standard measure of the reach of a detector is the horizon distance D_h, defined as the distance at which a detector measures an SNR of 8 for an optimally-oriented and optimally-

located binary, *i.e.* overhead from the detector and with a face-on orbit. Sub-optimally located and oriented sources are detected with an SNR of 8 at closer distances.

The sky-position averaged distance up to which a 3-detector ET observatory would detect signals from coalescing binaries with an SNR of 8 is shown in Fig. 18, for the ET-B sensitivity curve (see Box 1.3). The range is plotted both as a function of the intrinsic (red lines) and observed (blue lines) total mass. The two are related by the redshift function $z(D_{\rm L})$ as we will describe later. The binary systems are modeled by the phenomenological waveforms of [24] which comprise the inspiral, merger and ringdown stages of the coalescence. Fig. 18 shows the reach associated with two physical configurations of the binary: equal-mass, non-spinning and equal-mass, spin-aligned configuration with spins $\chi_1 = \chi_2 = \chi = 0.75$.

A neutron star binary composed of two $1.4\,M_\odot$ NSs would be observed by ET from a redshift of $z \simeq 2$. A NS-BH system comprising a $1.4\,M_\odot$ NS and a $10\,M_\odot$ BH would be observed from $z \simeq 4$. Binaries formed by stellar-mass BH will be visible at much larger distances, allowing ET to explore their populations at cosmological distances of $z \simeq 10$ and further. ET is also sensitive to intermediate-mass BBHs of total mass in the range $[10^2, 10^4]M_\odot$ over the redshift range $z \sim 1$–15. ET-D's better sensitivity at lower frequencies compared to ET-B is important in all cases, but particularly so for systems with total mass in the range 500–$10^4\,M_\odot$, for which the reach is a factor 2–10 greater for ET-D than ET-B.

Table 2: Expected coalescence rates per Mpc^3 per Myr in the local universe ($z \simeq 0$). Also shown are predicted event rates in Advanced LIGO (aLIGO) and ET.

Source	BNS	NS-BH	BBH
Rate ($\mathrm{Mpc}^{-1}\ \mathrm{Myr}^{-1}$)	0.1–6	0.01–0.3	2×10^{-3}–0.04
Event Rate (yr^{-1}) in aLIGO	0.4–400	0.2–300	2–4000
Event Rate (yr^{-1}) in ET	$\mathcal{O}(10^3$–$10^7)$	$\mathcal{O}(10^3$–$10^7)$	$\mathcal{O}(10^4$–$10^8)$

Expected coalescence rates Black holes and neutron stars are expected to form after Type II supernovae, which occur roughly once a century in galaxies like our own. Most stars seem to form in binaries; a fraction of compact binary progenitors will survive the kicks that supernovae impart, and roughly half of the remaining low-mass binaries (NSBH, BNS) will inspiral and eventually merge through the gradual emission of radiation. With roughly one Milky Way-like galaxy per $100\,\mathrm{Mpc}^3$, we anticipate a rate per comoving volume ρ_c large enough to permit many detections even for advanced detectors (see Table 2). For example, the binary pulsar population in the Milky Way implies a local BNS merger rate $\rho_c^{(\mathrm{NS-NS})} \simeq 0.2 - 6\,\mathrm{Myr}^{-1}\,\mathrm{Mpc}^{-3}$ [25–27]. With its vastly greater sensitivity, ET will reach deep back into the universe. Due to an enhanced star formation rate between $z \simeq 1 - 3$ [28], ET will probe a regime of possibly significantly enhanced compact object merger rates [29–31]. We give an illustration of this for BNS systems in Appendix A.1.

Lacking direct observational input, predictions for BBH and NSBH merger rates rely entirely on theory. However, recent observational evidence for BBH progenitors (see below) have allowed, for the first time, an astronomical estimate of BBH rates.

Studies of isolated binary evolution in the Milky Way [32–35] and local universe [30] lead to expected event rates in the ranges shown in Table 2, depending on the assumptions adopted in the model. As with the BNS rate, the NSBH merger rate is roughly proportional to the star formation rate [31] and therefore also increases substantially with redshift; many detections are expected.

The BBH merger rate is even more uncertain. First, long expected delays between BBH birth and merger imply BH born in the early universe could merge now [30]. Second, BH masses depend strongly on the metallicity of the gas from which the progenitor star forms, low metallicity environments form both more binaries and binaries that can be detected farther away [36, 37]. Even restricting attention to the local universe, low-metallicity environments should be significantly over-represented in the present-day detection rate [38]. For example, the nearby BBH progenitor binaries IC10 X-1 and NGC300 X1 lie in a low metallicity environment and suggest a high BBH detection rate for initial LIGO of 1 per two years, strongly dependent on survey selection effects (see

[39]). Further, in the early universe, where fewer generations of stars have produced metals, massive binaries could form very frequently [37]. Third, being the most massive compact objects, BH can *mass segregate* in interacting protoclusters. If enough protoclusters persist long enough for this process to occur, the BBH binary merger rate could be vastly enhanced [40–42]. As a practical matter, theory provides no useful upper bound; the local merger rates of stellar mass BBH are constrained only by existing GW measurements.

Standard Sirens of Gravity Cosmologists have long sought for standard candles that can work on large distance scales without being dependent on the lower rungs of the cosmic distance ladder. In 1986, Schutz [43] pointed out that gravitational astronomy can provide such a candle, or, more appropriately, a *standard siren*, in the form of a chirping signal from the coalescence of compact stars in a binary. The basic reason for this is that the gravitational-wave amplitude depends only on the ratio of a certain combination of the binary masses and the luminosity distance. For chirping signals observations can measure both the amplitude of the signal and the masses very accurately and hence infer the luminosity distance.

Box 2.4: Coalescing Binaries: Self-Calibrating Standard Sirens

The response of ET to a signal from a coalescing binary can be found by using the two polarizations in Eq. (5) in Eq. (3). The resulting expression can then be written as:

$$h(t) = \frac{2\nu M}{D_{\rm eff}}\,[M\omega(t)]^{\frac{2}{3}}\cos[2\Phi(t)+\Phi_0'], \tag{6}$$

where $D_{\rm eff}$ is the effective distance to the binary, which is a combination of the true luminosity distance $D_{\rm L}$ and the antenna pattern functions F_+ and $F_\times$, and Φ_0' is a constant phase involving the various angles:

$$D_{\rm eff} \equiv \frac{D_{\rm L}}{\left[F_+^2\,(1+\cos^2\iota)^2 + 4\,F_\times^2\,\cos^2\iota\right]^{1/2}}, \quad \Phi_0' \equiv \Phi_0 + \arctan\left[-\frac{2\,F_\times\cos\iota}{F_+(1+\cos^2\iota)}\right]. \tag{7}$$

Thus, for non-spinning binaries on a quasi-circular orbit, the signal is characterized by nine parameters in all: $(M, \nu, t_0, \Phi_0, \theta, \varphi, \psi, \iota, D_{\rm L})$. Since the phase $\Phi(t)$ of the signal is known to a high order in PN theory, matched filtering can be employed to extract the signal, and in the process accurately measure the two mass parameters (M, ν) that completely determine the phase evolution, and the two fiducial parameters (t_0, Φ_0).

The response of a single GW observatory is not sufficient to disentangle the luminosity distance from the angular parameters. A network of three non-colocated interferometers (say, ET and two advanced detectors), can measure three independent combinations of the polarizations and two time delays, and hence measure the remaining five parameters and thereby extract the luminosity distance.

The detector response depends only upon a small number of signal parameters, which can all be measured either directly or indirectly. The signal is insensitive to the composition of the component stars, and there is no complicated modelling required of the structure of the stars or their environments. Consequently, the measurement of the luminosity distance is precise, except for statistical errors whose magnitude depends on the SNR, and systematic errors due to weak gravitational lensing. We will discuss the magnitude of these errors later.

Although the inspiral signal from a compact binary is a standard siren, there is no way of inferring from it the redshift of a source. The mappings $M \to (1+z)M$, $\omega \to \omega/(1+z)$, and $D_{\rm L} \to (1+z)D_{\rm L}$ for redshifted sources in Eq. (5) leave the signal invariant. Note that a source with an intrinsic (*i.e.* physical) total mass $M_{\rm phys}$ at a redshift z will appear to an observer to be a binary of total mass $M_{\rm obs} = (1+z)M_{\rm phys}$. One must optically identify the host galaxy to measure its redshift. Thus, there is synergy in GW and EM observations which

can make precision cosmography possible, without the need to build a cosmic distance ladder. Later in this document we will explore how to exploit compact binaries for fundamental physics and cosmography.

Cosmological evolution of compact object populations The Einstein Telescope will provide a large sample of coalescences with the precise measurement of their masses and luminosity distances. This will be an extremely valuable tool for the analysis of cosmic compact object formation history. The measurement of their masses will yield information on the metallicity evolution as well as the evolution of the most massive stars. ET will yield a cosmic compact object census up to redshift $z = 2$, and will yield information about BH and NS formed at even earlier epochs because of the delays between formation and coalescence.

Contribution of intermediate-mass black holes Globular clusters may host intermediate-mass black holes (IMBHs) with masses in the range $[100, 1000]\,M_\odot$: see [44, 45] for reviews on IMBHs, and [46] for an announcement of a recently discovered ultra-luminous X-ray source that represents a possible IMBH detection. These may contribute to binary merger rates observable by ET in two ways.

Since an IMBH will be the most massive object in the cluster, it will readily sink to the center and substitute into a binary with a compact-object companion. The binary will then harden (i.e. its separation shrinks and the system becomes more gravitationally bound) through three-body interactions and eventually merge via an intermediate-mass-ratio inspiral (IMRI) on timescales of less than one billion years [47]. The number of detectable mergers depends on the unknown distribution of IMBH masses and their typical companions. According to Ref. [48], 300 events could be detected per year out to $z = 1.5$ for $100\,M_\odot$ (redshifted) primaries and $10\,M_\odot$ (redshifted) secondaries, but the range and rates drop for higher-mass primaries and lower-mass secondaries.

If the stellar binary fraction in a globular cluster is sufficiently high, two or more IMBHs can form [49]. These IMBHs then sink to the center in a few million years, where they form a binary and merge via three-body interactions with cluster stars followed by gravitational radiation reaction [49, 50]. Then ET could detect $2000\left(\frac{g}{0.1}\right)\left(\frac{g_{\rm cl}}{0.1}\right)$ mergers per year, where g is the fraction of all globular clusters hosting pairs of IMBHs, and $g_{\rm cl}$ is the fraction of star forming clusters. Mergers between pairs of globular clusters containing IMBHs can increase this rate by up to a factor of ~ 2 [51].

2.3.2 Continuous wave sources

Continuous wave sources that are discussed in this section are so-named because these sources last for at least a few weeks, but typically for months or years, and produce signals with roughly constant amplitude and frequency varing relatively slowly over the observation time. Such signals are expected to be produced by rapidly rotating non-axisymmetric NSs which are either isolated or in binary systems. A description of the signal emitted by such sources is given in Box 2.5. There are a number of mechanisms which may cause the star to emit GWs. These include deformations of the NS crust, precession, magnetic fields, and internal oscillation modes of the NS fluid.

Isolated neutron stars There are at present almost 2000 pulsars known from either radio or X-ray observations. The parameters of many of these systems, i.e. the sky location and frequency evolution, have been accurately measured. In this case we talk of *targeted searches* for known NSs. We assume the GW phase evolution to be tightly correlated with the rotational phase as inferred from electromagnetic observations. For GW emission due to a non-negligible ellipticity, the GW emission occurs at twice the rotational frequency of the star. These two assumptions constrain the expected gravitational waveform up to an unknown initial phase ϕ_0, amplitudes $A_{+,\times}$ and polarization angle ψ. Methods have been developed to search over these unknown parameters [52] and to either measure the amplitude h_0, or in the case that no signals are detected, to set upper limits on it. The main issue in the analysis is how to compensate accurately for the Doppler shift due to the source-detector relative motion (and other relativistic effects), and the intrinsic spin-down of the source.

The benchmark for these searches is the indirect upper bound on h_0 set by assuming that all of the kinetic energy of the star lost in the spin-down is channeled into gravitational radiation as illustrated in Appendix A.2. This assumption is not expected to hold for any of the known pulsars where electromagnetic braking explains most of the spin-down. Nevertheless, the spin-down limit is still a very useful benchmark for identifying astrophysically relevant targets and quantifying search results. Setting an upper limit below the spin-down limit constrains the fraction of spin-down energy that is emitted as GWs.

Initial interferometers have now set upper limits on a number of known pulsars using data from the LIGO, GEO and Virgo detectors [53–55]. One highlight from these results is beating the spin-down limit for the Crab pulsar [55] where the GW luminosity is constrained to be less than 2% of the spin-down luminosity [56]. ET will be able to detect continuous waves from Crab even if it emits one millionth of the spin-down luminosity in GWs.

Box 2.5: Continuous Gravitational Waves

In the case of continuous waves, the waveforms for the two polarizations are given by

$$h_+(t) = A_+ \cos\Phi(t), \qquad h_\times(t) = A_\times \sin\Phi(t), \tag{8}$$

where t is the time in the frame of the moving, accelerating detector and $\Phi(t)$ is the phase of the GW; the amplitudes $A_{+,\times}$ depend on the other pulsar parameters, such as its rotational frequency, moments of inertia, the orientation of its rotation axis and its distance from Earth. The phase Φ takes its simplest form when the time coordinate used is τ, the proper time in the rest frame of the NS:

$$\Phi(\tau) = \phi_0 + 2\pi \sum_{n=0}^{s} \frac{f_{(n)}}{(n+1)!}\tau^{n+1}. \tag{9}$$

Here ϕ_0, $f_{(0)}$ and $f_{(n)}$ $(n \geq 1)$ are respectively the phase, instantaneous frequency and the spin-down parameters in the rest frame of the star at the fiducial start time $\tau = 0$, s is the number of spin-down parameters included in the model, and ι denotes the angle between the line-of-sight to the star and its rotation axis. It is useful to write the amplitudes $A_{+,\times}$ in terms of a single number h_0

$$A_+ = \frac{1}{2}h_0(1+\cos^2\iota)\,, \qquad A_\times = h_0\cos\iota\,. \tag{10}$$

The exact expression of the overall amplitude h_0 depends on the specific mechanism producing the continuous signal. For instance, in the case of a tri-axial NS rotating with frequency f_{rot} around a principal axis of inertia we have

$$h_0 = \frac{4\pi^2 G}{c^4}\frac{I_{zz}\epsilon f^2}{d}, \tag{11}$$

where I_{zz} is the star's moment of inertia with respect to the rotation axis, the equatorial ellipticity ϵ is defined in terms of pricipal axis of inertia as $\epsilon = \frac{I_{xx}-I_{yy}}{I_{zz}}$, d is the distance to the star and $f = 2f_{rot}$ is the signal frequency.

The maximum expected signal frequency is below 2 kHz. Potentially interesting sources are within the Galaxy, thus the distance $d \simeq 10$ kpc. The standard value of the moment of inertia is $I = 10^{38}\,\mathrm{kg\,m^2}$, although values in the range $(1-3)\times 10^{38}\,\mathrm{kg\,m^2}$ are considered plausible. The typical values of ellipticity are largely unknown; the maximum value allowed by standard equations of state for NS matter is $\sim 5\times 10^{-6}$. Some exotic equations of state imply maximum values even two orders of magnitude larger.

The minimum signal amplitude detectable by a given targeted search depends directly on the detector sensitivity and scales with the square root of the observation time, as discussed in Appendix A.3.

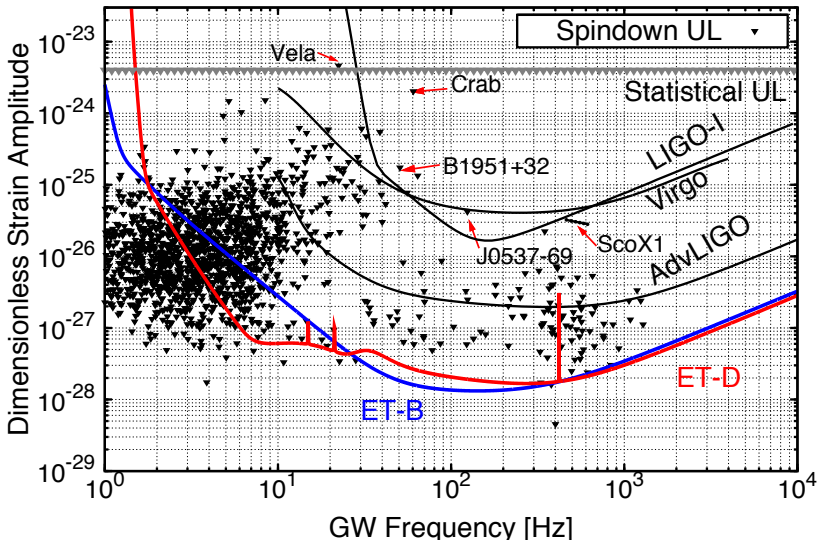

Figure 19: Upper limits and spin-down limits for known pulsars. The detector sensitivity curves plot the minimum detectable amplitude of the GW averaged over sky positions and pulsar orientations. A detection threshold based on a false alarm rate of 1% and a false dismissal rate of 10% is assumed. The spin-down limits assume the NS to have a moment of inertia in the range $1\text{-}3\times10^{38}\,\mathrm{kg\,m^2}$ and a $\pm10\%$ uncertainty in its distance. Initial LIGO and Virgo curves assume an integration time of 2 years while the rest assume 5 years. Initial LIGO consists of the H1, L1 and H2 detectors, Virgo is a single detector, aLIGO, ET-B and ET-D are assumed to consist of three detectors. ET-D's better sensitivity, compared to ET-B, at frequencies below 20 Hz helps target a number of known pulsars.

It is informative to compare detectable values of $h_{0,\mathrm{min}}$ with the spin-down limits for a number of known pulsars. Figure 19 shows the detectable amplitude for Initial and Advanced LIGO, Virgo and ET, and the spin-down limits for various known pulsars. It is clear that the better low-frequency sensitivity of ET-D allows it to reach the spin-down rate of almost all pulsars with spin frequencies greater than 3 Hz (corresponding to a GW frequency of 6 Hz).

Let us turn now to the *wide parameter space searches*. Here, instead of targeting a known pulsar, the aim is to search for unknown sources in as large a portion of the parameter space (sky location, frequency, frequency derivatives) as possible. Potential GW sources could be invisible in the EM band, either because their radio pulses are not beamed towards us or because their EM emission is dim due to having a very low magnetic field. Such searches are computationally limited because the number of templates increases much faster than linearly with the observation time T_{obs}. The large number of templates affects the search sensitivity in three basic ways. The first and most obvious one is simply the discreteness of the template grid: SNR is lost by searching for a GW signal with a template that does not exactly match. Secondly, it leads to a large number of statistical trials, which increases the false alarm rate and thus leads to a larger SNR threshold for detection. Finally, and most importantly, it limits the largest observation time that can be considered; even given the increase in computer power following Moore's law, this limitation will most likely still apply in the ET era.

The problem of computational cost is addressed by the so-called *semi-coherent* methods. These rely on breaking up the full data set into shorter segments of duration T_{coh}, analyzing the segments coherently and combining the power from the different segments incoherently. There are a number of different techniques available for performing the incoherent combination. For these searches, the sensitivity, incorporating all the effects mentioned above, is proportional to the square root of the total observation time and is given by Eq. (135), Appendix A.3. Typically, the output of a wide-area search is a set of *candidates*, i.e. points in the source parameter space with values of a given statistic above a threshold. These candidates are then analyzed in a deeper way *e.g.* by making coincidences with another set of candidates coming from a different dataset, followed by a full coherent

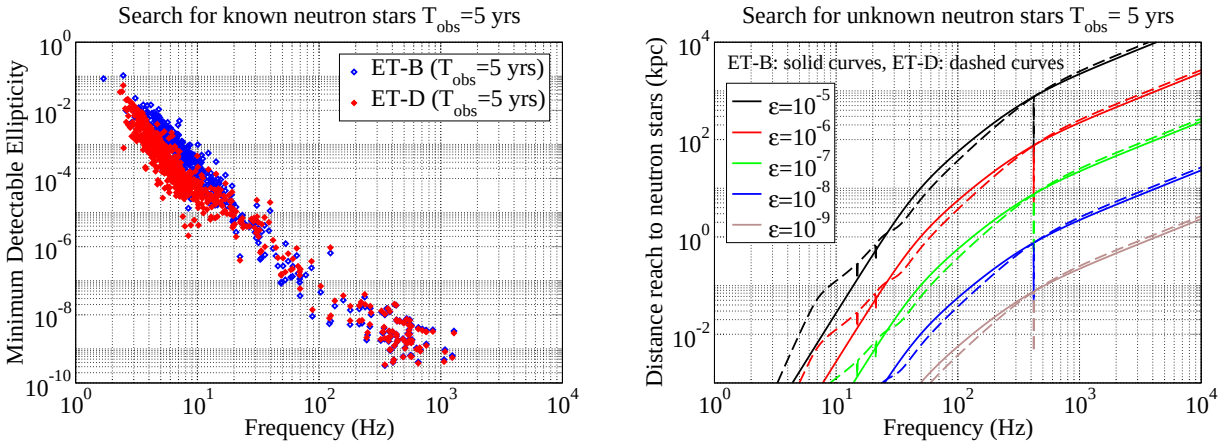

Figure 20: Left: Minimum detectable ellipticity for known pulsars for ET-B and ET-D sensitivities. The search parameters are the same as for Fig. 19. Right: Maximum distance of an unknown source in order to be selected among the candidates of an all-sky search with ET-B and ET-D sensitivities. Search parameters are given in the text.

analysis on the surviving candidates, in order to confirm or reject them.

Comparing prospects of detection for ET-B and ET-D sensitivities ET-B has a better sensitivity at extremely low frequencies, below ~ 2 Hz. ET-D, on the other hand, has a better sensitivity in the low frequency range, say between 2 Hz and 20 Hz. At intermediate frequencies, between ~ 30 Hz and ~ 300 Hz, ET-B has a slightly better sensitivity. The sensitivities of the two configurations are basically the same in the high frequency range. Fig. 19 plots the minimum detectable amplitude, assuming ET-B sensitivity (continuous blue line) and ET-D sensitivity (dashed red line), with an observation time $T_{\rm obs} = 5$ yr, a false alarm probability of 1% and a false dismissal probability of 10% (see Eq. (134)), versus the spin-down limit of the known pulsars taken from the ATNF Catalogue at `http://www.atnf.csiro.au/research/pulsar/psrcat/`. For comparison, the upper limit reached by Initial and Advanced LIGO and Virgo are also shown but assuming an integration time of 2 yrs for all except Advanced LIGO, for which an integration time of 5 yrs is assumed.

We note that no pulsar has yet been found that could emit a detectable signal with frequency below ~ 2.5 Hz. Thus there is no gain in having a good sensitivity at extremely low frequencies. On the other hand, having a better sensitivity around 10 Hz impacts positively on the possibility of detecting a continuous GW signal.

This can be seen also in Fig. 20, left panel, where the ellipticity corresponding to the minimum detectable amplitude is plotted but only for those pulsars for which the spin-down limit can be beaten in an observation time of $T_{\rm obs} = 5$ yr. Not only is the number of pulsars for which the spin-down limit can be beaten far larger for ET-D but, more importantly, the minimum ellipticity needed to produce a detectable signal is almost one order of magnitude lower in the 10 Hz range. For instance, with ET-B we typically need ϵ in the range $(0.1-5)\times 10^{-4}$ for pulsars emitting around 10 Hz, while $\epsilon \sim (0.1-5)\times 10^{-5}$ is enough with ET-D. There are just a couple of pulsars at frequencies below ~ 3 Hz for which the spin-down limit could be beaten with ET-B, but not with ET-D, with corresponding ellipticity in the 10^{-2} range, a value difficult to reach even assuming an exotic equation of state for NS matter.

We must, however, keep in mind that the number of pulsars increases with decreasing frequency, and so also the probability that extremely deformed, EM-dim, NSs exist, provided such large deformations are attainable in nature. At high frequency, in contrast, there is no relevant difference between the two detector configurations and fast spinning pulsars with ellipticity less than $\sim 5\times 10^{-8}$ could be detected.

Next, we consider the *blind* search for unknown NSs. In this case we plot in Fig. 20, right panel, the maximum

distance of a source to be selected among the candidates of an all-sky, semi-coherent search, for different values of the NS ellipticity. An observation time $T_{\rm obs} = 5\,{\rm yr}$ and a coherent length $T_{\rm coh} = 24\,{\rm hr}$ are assumed. Moreover, the threshold for the selection of candidates is chosen in order to have 10^9 candidates.

In practice, we do not expect detections for signal frequencies below $\sim 10\,{\rm Hz}$ for $\epsilon < 10^{-5}$ (the corresponding r_{max} becomes unrealistically small). And also considering extremely deformed NSs ($\epsilon > 10^{-5}$) signal frequencies below $\sim 3\,{\rm Hz}$ are basically excluded. Then, having a better sensitivity at very low frequencies gives basically no gain. On the other hand, having a better sensitivity around 10 Hz somewhat increases the possibility of detection: for instance, assuming $\epsilon = 10^{-5}$, the maximum distance that a search can reach, goes from $\sim 10\,{\rm pc}$ with ET-B to $\sim 80\,{\rm pc}$ with ET-D at 8 Hz, while it goes from $\sim 30\,{\rm pc}$ to $\sim 150\,{\rm pc}$ at 10 Hz. On the contrary, in the range $\sim 30 - 100\,{\rm Hz}$ with ET-B the distance reach is about a factor of 2 greater.

These conclusions do not significantly change assuming a longer coherent step (compatible with the computing power believed to be available in the ET era), because the sensitivity increases only as $T_{\rm coh}^{1/4}$, see Eq. (135), Appendix A.3.

2.3.3 Burst sources

Many transient astronomical phenomena, such as supernovae, gamma-ray bursts and glitching pulsars, could produce bursts of gravitational waves that last for as short as a few milliseconds (*e.g.* supernovae) to several minutes or longer (*e.g.* certain instabilities of NSs, discussed below). Detecting such waves, especially in coincidence with optical, X-ray, gamma-ray radiation or neutrinos could help resolve decades-old problems in astronomy. Gravitational waves will be a very powerful addition to multi-messenger astronomy (see [57] for a review), allowing a view into the dark and dense cores of sources that are inaccessible to other windows of observation.

Gravitational wave bursts from gravitational collapse Neutron stars and BHs are formed from the gravitational collapse of a highly evolved star or the core collapse of an accreting white dwarf. In either case, if the collapse is non-spherical, perhaps induced by strong rotation or magnetic field, then GWs could carry away some of the binding energy and angular momentum, depending on the geometry of the collapse. Gravitational collapse events are the progenitors of supernovae of various types. Supernovae of Type II are believed to occur at a rate of between 0.01 and 0.1 per year in a Milky Way equivalent galaxy; thus, within 5 Mpc, we might expect an event rate of about 1 per 2 years [58].

Simulating gravitational collapse is a very active area of numerical astrophysics. Most simulations also predict the energy and spectral characteristics of the emitted GWs [59, 60]. However, it is still beyond the capabilities of computers to simulate a gravitational collapse event with all the physics that might be necessary to give reliable predictions: three-dimensional hydrodynamics, neutrino transport, realistic nuclear physics, magnetic fields, rotation. In fact, it is still by no means clear why Type II supernovae explode at all: simulations typically have great difficulty reversing the inflow and producing an explosion with the observed light-curves and energetics. It may be that the answer lies in some of the physics that has to be oversimplified in order to be used in current simulations, or in some neutrino physics that we do not yet know.

In a typical supernova, simulations suggest that GWs might extract between about 10^{-11} and 10^{-7} of the total available mass-energy [61–64], and the waves could come off in a burst whose frequency might lie in the range of ~ 200–$1000\,{\rm Hz}$. Using representative values for a supernova in our galaxy, lying at $D = 10\,{\rm kpc}$, emitting the energy equivalent of $E = 10^{-8}\,M_\odot$ at a frequency of $f = 1\,{\rm kHz}$, and lasting for $T = 2\,{\rm ms}$, the observed amplitude would be (cf. 2)

$$h \sim 1.5 \times 10^{-21} \left(\frac{E}{10^{-7}\,M_\odot}\right)^{1/2} \left(\frac{1\,{\rm ms}}{T}\right)^{1/2} \left(\frac{1\,{\rm kHz}}{f}\right) \left(\frac{10\,{\rm kpc}}{D}\right). \tag{12}$$

This amplitude is large enough for current ground-based detectors to observe with a reasonably high confidence, but of course the event rate within 10 kpc is expected to be far too small to make an early detection likely.

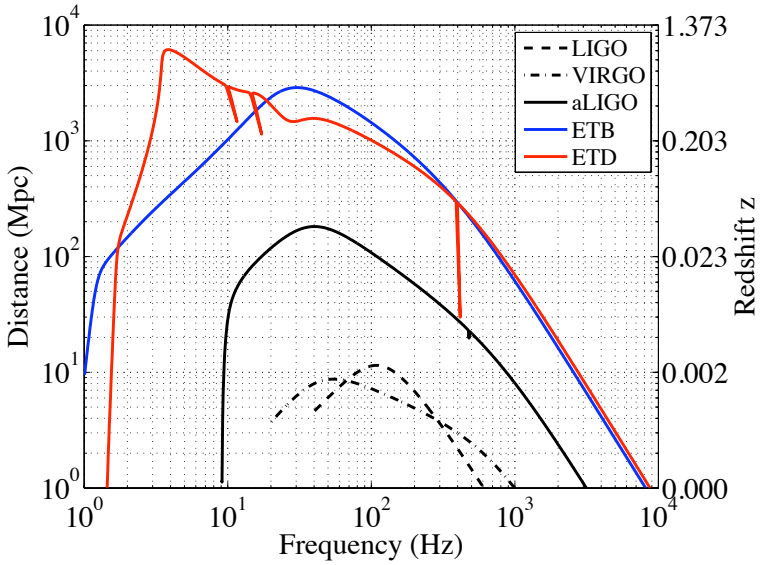

Figure 21: 90%-confidence lower limit on distance for GRB burst sources assuming a GRB energy emission of $E_{\rm GW}^{\rm iso} = 0.05\,M_\odot c^2 \sim 9\times10^{52}$ergs. A redshift correction of $(1+z)$ has been used in computing the lower limit.

ET can detect an amplitude that is two orders of magnitude smaller or from a distance of 1 Mpc. ET might, therefore, see a supernova collapse once per four or six years.

Gamma-ray bursts There is increasing evidence that gravitational collapse also produces some of the observed gamma-ray bursts [65] in *hypernovae* and *collapsars* [66, 67]. As we shall discuss in more detail, several different classes of GRBs are now known although their cause is not yet completely understood. There are no reliable GW emission models from collapsars or hypernovae although some estimates give as large as $10^{-2}M_\odot$ for isotropic GW emission for GRB progenitors. BNS and NSBH mergers (the likely progenitors of most short GRBs) will have isotropic-equivalent emission on the order of (0.01-0.1) $M_\odot$ in the 100 to 200 Hz band. For long GRBs, fragmentation of the accretion disk [68–70] could produce inspiral-like chirps with (0.001-0.01) $M_\odot$ emission in GW. The suspended accretion model [71] also predicts an energy emission of up to (0.01-0.1)$M_\odot$ in this band.

A GRB at a distance of $D = 4.2\,$Gpc (a redshift of $z \simeq 0.7$) emitting the energy equivalent of $E = 5\times10^{-2}\,M_\odot$ at a frequency of $f = 1\,$kHz, and lasting for $T = 1\,$ms, produces an amplitude of [57]

$$h \sim 10^{-23}\left(\frac{E}{5\times10^{-2}\,M_\odot}\right)^{1/2}\left(\frac{1\,\mathrm{ms}}{T}\right)^{1/2}\left(\frac{1\,\mathrm{kHz}}{f}\right)\left(\frac{4.2\,\mathrm{Gpc}}{D}\right), \tag{13}$$

Figure 21 shows the distance reach of Initial and Advanced LIGO, Virgo and two possible noise curves considered for ET (ET-B and ET-D) to such a GRB. The waveform emitted in the process is not known with any certainty and so the distance reach is calculated by assuming that GW bursts are detected by search algorithms that look for excess energy in a time-frequency map. While aLIGO might detect rare closeby GRBs, ET could probe GRBs at cosmological distances, assuming GWs extract about $0.05\,M_\odot$ in the process.

Pulsar glitches and magnetar flares Neutron stars have a rich spectrum of non-radial normal modes, which which can be classified according to key key restoring force that affects the fluid motion. In the context of GW astrophysics f-, g-, p-, w-, and r-modes have all been studied [72, 73]. Just as in the case of BHs, these normal modes are a superposition of damped sinusoids, but in the NS case the frequencies and damping times depend on the complex physics of NS interiors. Modelling the NS oscillation spectrum requires physics beyond what is within reach for laboratory experiments. This sets a severe challenge, but at the same time

it is a key reason why the problem is important. It also provides ample motivation for attempts to provide observations that can be used to test various theoretical models, e.g. concerning the state of matter at extreme densities. A promising, at least in principle, strategy follows the very successful asteroseismology programme for normal stars. In the case of the sun, the matching of inferred non-radial oscillation modes to theoretical predictions has led to a much improved understanding of the interior conditions. Similarly, one may expect that GW observations of oscillating NSs may place useful constraints both on bulk parameters like mass and radius, and hence the overall EoS, and detailed physics, like internal composition gradients. In fact, even knowing accurately the frequency and decay time of just the fundamental $\ell = 2$ f-mode would be enough to eliminate most currently considered equations of state [72].

The f-modes of NSs are promising emitters of GWs that may be excited by glitches or by the nuclear explosions on accreting neutron stars that are thought to produce X-ray flares and soft gamma-ray repeater events. The rise-time of X-ray emission can be as short as a few milliseconds [74], which might be impulsive enough to excite acoustic vibrations. If the rise time of the explosion matches the period of the mode well enough, then a substantial fraction of the energy released could go into mechanical vibrations, and almost all of this fraction would be carried away by GWs, since other mode-damping mechanisms inside NSs tend to be less efficient.

The viability of these scenarios is difficult to quantify, given our general lack of understanding of the detailed dynamics associated with them. Presently, most available models are based on back-of-the-envelope phenomenology. This is well illustrated by the radio-pulsar glitches, enigmatic spin-up events seen in (mainly) relatively young NSs like Crab and Vela. It is easy to estimate that these events are associated with energies of order 10^{42} erg ($10^{-12}\,M_\odot$). This sets a useful benchmark energy level for discussion of GW events associated with NS in our galaxy, but it obviously does not constitute a real estimate of the energy released as GWs. Nevertheless, assuming this level of energy emission through the f-mode at 2 kHz of a star at a distance of 10 kpc it is easy to estimate that these events could create a wave of effective amplitude (see Eq. 12) around 10^{-23}. (The effective amplitude assumes we can do matched filtering, which in this case is not very difficult.) This kind of amplitude should be well within the reach of ET. Observations of these modes would immediately constrain the cold-matter nuclear EoS in significant ways [72, 75].

It is also important to note that NS events seen in X-rays and gamma rays can be much more energetic. In fact, NS oscillations may have already been observed in X-rays [76]. Quasiperiodic oscillations seen in the tails of strongly magnetised NS (magnetar) flares agree well with predicted crustal modes, whose restoring force is the shear strength of the crust. These observations mainly probe the physics of the crust, which represents the low-density region and is not expected to leave a strong imprint on emitted GWs. Nevertheless, the observations allows us to test the astero-seismology paradigm [77], an exercise that has placed (weak) constraints on the EoS. As far as GW astrophysics is concerned, a key question concerns to what extent the more massive NS core takes part in these event. The general expectation is that the magnetic field provides an efficient coupling between the crust and the core. The upshot of this could be that the magnetar events are predominantly due to the interior magnetic dynamics, which may make them associated with detectable GWs. Establishing this requires better theory modelling, but it is still clear that ET will be able to place useful constraints on any such mechanism.

Relativistic instabilities of compact stars The most promising scenarios for detectable NS oscillations involve some kind of instability. Realistic NS may become unstable during different evolutionary stages. A rapidly and differentially rotating proto-NS may be dynamically unstable due to the so-called bar-mode (the l=m=2 f-mode). At less extreme differential rotation, the so-called low T/W instability may operate. Proto-NSs may also be convectively unstable, leading to growing g-modes, due to temperature gradients. The mechanisms connect the birth of a NS with the supernova event, and the level of excitation of the involved oscillations depends to a large extent on how the core-collapse proceeds. Another class of instabilities is powered by with the emission of GWs. First demonstrated by Chandrasekhar [78] in 1971, this instability was shown to be generic in rotating stars by Friedman and Schutz [79] a few years later. They proved that the unstable modes have a very simple signature depending on the pattern speed of the mode, i.e. the angular velocity at which the crests of the pattern passes about the rotation axis of the star. If this velocity is in the same sense as the rotation of the star, but slower than that of rotation, then the mode would be unstable in a perfect fluid star. This instability has come to be known as the CFS instability, after the three authors who discovered and

explained it.

The presence of an instability is, however, not sufficient to make the scenario astrophysically relevant. In order to play a role for real NSs, any instability must overcome a number of damping mechanisms. The problem then becomes exceedingly difficult, especially since we do not have very precise models for the various transport coefficients needed for a model of NS dissipation. Nevertheless, there has been considerable progress on this problem. Focussing on the instability associated with the f-mode, Lindblom and Detweiler [80] showed that the effect of viscosity runs counter to that of radiation reaction, so that the instability is strongest in modes with the longest wavelengths, in principle the quadrupole modes. However, numerical calculations for Newtonian stellar models with realistic viscosity show [81] that the f-modes are not vulnerable to the instability. This would weakens the impact for GW physics significantly. In addition to this, it has been demonstrated that the friction associated with superfluid vortices may suppress the instability entirely [81]. These results do not, however, signal the demise of this mechanism. First of all, the instability is stronger in fully relativistic models [82], especially since the $l = 2$ mode may also be unstable. Secondly, the superfluid friction becomes relevant only after the star has cooled below the relevant transition temperature (below 10^9 K). Hence, there may still be room for the f-mode instability to play a relevant role in very young NSs. Moreover, as the f-mode is an ideal GW emitter (with a short instability growth time, and possible large nonlinear amplitude) the associated signals may well be within reach with ET even for extragalactic sources. This is an interesting possibility that need to be explored by more detailed modelling.

Most recent activity on NS instabilities has concerned a different class of oscillations, namely the Rossby, or r-modes. In contrast to the f-modes, which become unstable above a critical rotation rate, these modes are unstable in a rotating perfect fluid star at all rotation rates. The associated GWs comes from the current-multipoles, rather than from the mass multipoles as in the case of the f-mode. This makes the modelling different, but the main physics issues remain the same. Investigations by a number of authors [83–85] have shown that the r-mode instability could be relevant in hot, rapidly-rotating stars. In particular, it may lead to a nascent NS spinning down significantly, losing angular momentum as GWs. The instability might also operate in mature, accreting NSs, such as those in low mass X-ray binaries (LMXB) (see the next section).

In principle, the fact that the r-mode instability window depends on a balance between GW driving and various dissipation mechanisms makes it a sensitive probe of NS core physics. Observations allow us to test our understanding of exotic physics associated with hyperons [86, 87]. , deconfined quarks and large scale superfluids/superconductors [75]. The signal associated with various r-mode scenarios should be detectable with ET for systems within, and possibly beyond, our galaxy [88] but in order to facilitate such detections we need to make progress on thorny theory issues. Key issues concern the interaction with magnetic fields in the star, the damping due to the vortex mediated mutual friction in a superfluid , the possible role of turbulence, the boundary layer at the crust-core interface and exotic bulk viscosity due to the presence of hyperons or deconfined quarks in the deep neutron star core. These problems are all very challenging. In addition, we need to model the GW signal from an unstable r-mode. This is also difficult because, even though the r-mode growth phase is adequately described by linear theory, nonlinear effects soon become important leading to the evolution, and the associated GW signal, becoming very complex. Future ET observations have the potential to test various proposed r-mode scenarios, improving our understanding of extreme NS physics significantly.

2.3.4 Stochastic background

The superposition of a large number of unresolved sources of GWs produces a stochastic background. We can distinguish between two contributions: a primordial background of cosmological origin, a memory of the early stages of the Universe, and a background of astrophysical origin, a memory of the evolution of the galaxies and star formation. We summarize basic properties of a stochastic GW background in Box 2.6. The strength of the background is characterized by the dimensionless quantity $\Omega_{\rm GW}(f)$, which is the ratio of the energy density in GWs to the critical density of the Universe as a function of frequency.

Primordial background The essential interest of a primordial GW background is the prospect of probing the behaviour of matter and the evolution of the Universe at very high energy scales and densities—potentially even above the energies achievable at current particle colliders. This is feasible thanks to the very large redshift factor (well over ten orders of magnitude) appropriate to times before primordial nucleosynthesis: waves created at extremely short length scales may now be accessible to terrestrial detectors. At such short distance scales and high energies, evidence for new physics may emerge, such as particles beyond the Standard Model, high-temperature phase transitions and topological defects, inflation and reheating, or even extra spatial dimensions.

Box 2.6: The Spectrum of Stochastic GW Background

It is usual to characterize the intensity of a random field of GWs by its energy density as a function of frequency. Since the energy density of a plane wave is the same as its flux (when $c = 1$), we have from Eq. (1) $\rho_{\rm GW} = \pi f^2 h^2/4$. But the wave field in this case is a random variable, so we must replace h^2 by a statistical mean square amplitude per unit frequency (Fourier transform power per unit frequency) called $S_{\rm GW}(f)$, so that the energy density *per unit frequency* is proportional to $f^2 S_{\rm GW}(f)$. It is then conventional to talk about the energy density per unit logarithm of the frequency, which means multiplying by f. The result, after being careful about averaging over all directions of the waves and all independent polarization components, is [89, 90]

$$\frac{{\rm d}\rho_{\rm GW}}{{\rm d}\ln f} = 4\pi^2 f^3 S_{\rm GW}(f). \tag{14}$$

What is of most interest is the energy density as a fraction of the closure or critical cosmological density, given by the Hubble constant H_0 as $\rho_c = 3H_0^2/8\pi$. The resulting ratio is called $\Omega_{\rm GW}(f)$:

$$\Omega_{\rm GW}(f) = \frac{10\pi^2}{3H_0^2} f^3 S_{\rm GW}(f). \tag{15}$$

To evaluate the contributions of various sources to the background we take a fiducial value $H_0 = 70\,{\rm km\,s^{-1}\,Mpc^{-1}}$ for the Hubble parameter and assume a flat Universe with $\Omega_\Lambda = 0.7$.

The ultimate goal of detector development is the observation of the background radiation from the Big Bang. It is expected to be very weak, but it will come to us unhindered from as early as 10^{-30} s, and it could illuminate the nature of the laws of physics at energies far higher than we can hope to reach in the laboratory.

Astrophysical background The astrophysical contribution is important for at least two reasons. On the one hand, it may mask the cosmological background in some frequency windows; on the other hand, its detection would put strong constraints on the physical properties of compact objects and their evolution with redshift, such as the mass of NSs or BHs, the ellipticity and the magnetic field of NSs or the rate of compact binaries.

What is particularly interesting is that using stochastic backgrounds, we are able to put constraints on the mean values and not on the properties of the brightest sources, more likely in the tail of the distributions.

Detecting stochastic backgrounds Random radiation is indistinguishable from instrumental noise in a single detector, at least for short observing times. If the random field is produced by an anisotropically-distributed set of astrophysical sources (the binaries in our galaxy, for example) then over a year, as the detector changes its orientation, the noise from this background should rise and fall in a systematic way, allowing it to be identified. But this is a rather crude way of detecting the radiation, and a better way is to perform a cross-correlation between two detectors, if available.

In cross-correlation, which amounts to multiplying the outputs and integrating, the random signal in one detector essentially acts as a template for the signal in the other detector. If they match, then there will be a stronger-

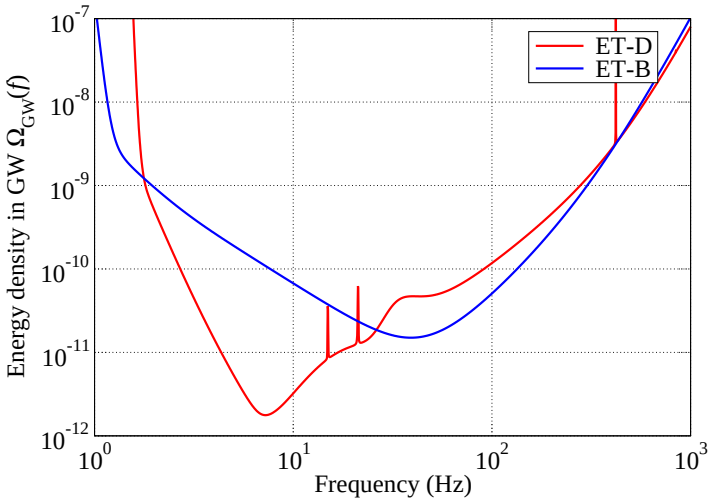

Figure 22: The sensitivity ET-B and ET-D detectors to stochastic background of GW. The curves show the energy density in GW that ET would be sensitive to after a year's integration at 95% confidence level.

than-expected correlation. Notice that they can only match well if the wavelength of the GWs is longer than the separation between the detectors: otherwise time delays for waves reaching one detector before the other degrade the match. In this regard, ET's topology is particularly important. Since it hosts several detectors at the same location there is no time delay involved and hence all frequencies contribute to the cross correlation.

The outcome of cross-correlation is not like standard matched filtering, however, since the "filter" of the first detector has as much noise superimposed on its template as the other detector. As a result, the amplitude SNR of the correlated field grows only with observing time as $T^{1/4}$, rather than the square root growth that characterizes matched filtering [90]; sensitivity to $\Omega_{\rm GW}$, however, grows as $\sqrt{T}$.

ET's sensitivity to stochastic background The only tight constraint on $\Omega_{\rm GW}$ from non-gravitational-wave astronomy is that it must be smaller than 10^{-5}, in order not to disturb the agreement between the standard Big Bang model of nucleosynthesis (of helium and other light elements) and observation. If the Universe contains this much gravitational radiation today, then at the time of nucleosynthesis the (blue-shifted) energy density of this radiation would have been comparable to that of the photons and the three neutrino species. Although the radiation would not have participated in the nuclear reactions, its extra energy density would have required that the expansion rate of the Universe at that time be significantly faster, in order to evolve into the Universe we see today. In turn, this faster expansion would have provided less time for the nuclear reactions to "freeze out", altering the abundances from the values that are observed today [91, 92].

First-generation interferometers have already set direct limits [93] on the cosmological background below the nucleosynthesis limit at $\Omega_{\rm GW} < 6.9 \times 10^{-6}$. Figure 22 plots the sensitivity of Advanced LIGO and ET to stochastic backgrounds assuming cross-correlation of data over a period of one year. The plot is constructed using the formula (15) taking $S_{\rm GW} = 2.56\, S_h(f)/\sqrt{f\, T_{\rm yr}}$, where $S_h(f)$ is the noise power spectral density of the detector in question, $T_{\rm yr}$ is the number of seconds in a year and a factor of 2.56 is inserted to account for the SNR needed for a 95% confidence level. Advanced detectors will probe stochastic backgrounds of strengths $\Omega_{\rm GW} \sim 10^{-9}$ (see Fig. 22) but ET, thanks to its better low-frequency sensitivity, could detect backgrounds at levels approaching $\Omega_{\rm GW} \sim 10^{-12}$ around frequencies of 10 Hz.

Sections 2.6.6 and 2.6.7 discuss possible sources of stochastic backgrounds of primordial and astrophysical origin and the physics we can learn by detecting such backgrounds with ET.

2.4 Fundamental physics and strong field tests of GR

The rich variety of sources and phenomena observed by GW detectors can potentially be used to address outstanding questions in fundamental physics. The sources in question will be in dense environs of ultra-strong gravity and will therefore provide a cosmic laboratory for understanding phenomena and matter in extreme conditions of density, temperature, and/or magnetic fields. Moreover, BBH are fundamentally geometric objects whose interaction close to merger will provide insights into the nature of BH spacetimes and of gravity in ultra-strong fields. Here we will discuss what fundamental physics questions and strong-field tests of gravity could be addressed by ET.

2.4.1 Polarization of gravitational waves

In Einstein's theory of gravity, GWs have only two polarizations, the plus and cross polarizations discussed in Box 2.1. In scalar-tensor theories GWs have four polarizations more than in GR. Observations of gravitational waves could exploit this difference to test GR.

In the long wavelength approximation (i.e. when the wavelength is much longer than the typical distance between test masses), plus and cross polarizations cause quadrupolar deformations in space and the proper distance between test masses changes in a direction transverse to the propagation of the waves (see Fig. 15, Box 2.1). Other polarizations could cause motion of test masses longitudinal to the direction of propagation as well as other patterns in the transverse plane.

ET, with its three interferometers, will be able to resolve the two polarizations, assuming that GR is the correct description of gravity. With a network of other advanced or third generation detectors that might be available at the time one could independently measure the polarization and check if the two measurements are consistent with one another. Conclusively showing (to within experimental uncertainties) the absence of other polarizations could rule out a whole class of alternatives to GR. Advanced detectors could do this to some extent but high SNR events that ET is likely to see will provide compelling evidence.

2.4.2 Bounding graviton mass

In Einstein's theory, gravitational radiation travels at the speed of light. This means that gravitons, the particle counterparts of GWs, are massless particles. Although there is currently no strong motivation to consider massive graviton theories from an experimental point of view, they are natural extensions of Einstein's theory. In a massive graviton theory, GWs would not travel at the speed of light and this can be tested by observation of gravitational-wave sources at very great distances. To do so we would need a source which emits both GW and EM radiation simultaneously. By measuring the difference in their arrival times we could measure or constrain the speed of GWs.

Supernovae and BNS and NSBH systems are sources that are expected to exhibit after-glows in EM radiation soon after they emit a burst of GWs. If the source is near enough (a few Mpc in the case of supernovae, and redshifts of a few in the case of coalescing binaries) and the event is well-localized on the sky (fraction of a degree depending on the distance to the source), then it could be observed in coincidence as a transient EM and GW event.

Current theories of supernovae and coalescing binaries cannot accurately predict how promptly after the collapse (in the case of SN) or merger (in the case of binaries) EM radiation will follow. However, the expected delay is no more than one second. If GWs arrive a time Δt after EM waves, then the fractional difference in their speeds is given by

$$\frac{|\Delta v|}{c} = 3.2 \times 10^{-18} \left(\frac{|\Delta t|}{1\,\mathrm{s}}\right) \left(\frac{3\,\mathrm{Gpc}}{D}\right) \tag{16}$$

where we have assumed that the source is at a distance of $D = 3\,\mathrm{Gpc}$. This can be used to constrain the graviton mass but there is a more robust method that could yield better upper limits.

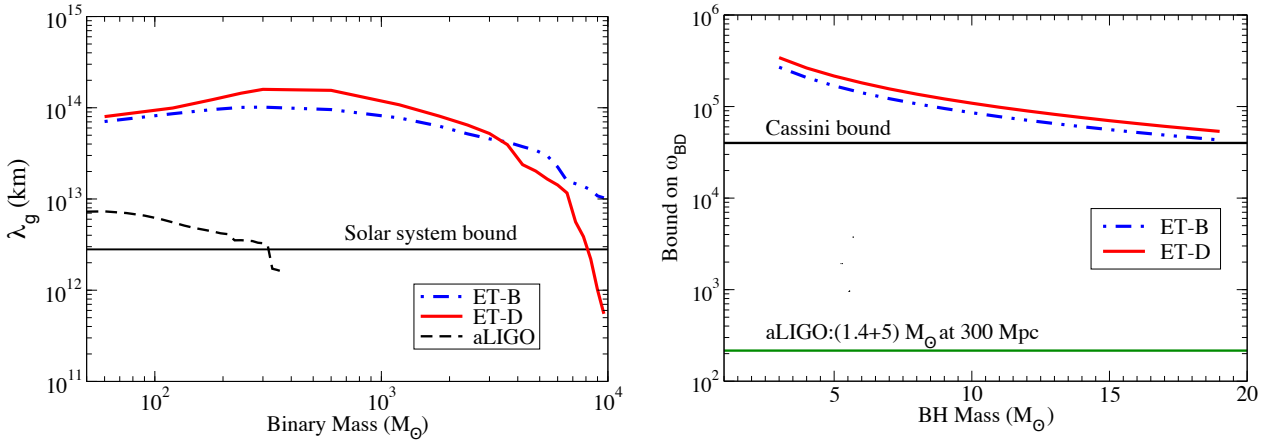

Figure 23: *Left panel:* Bounds on the graviton Compton wavelength that can be deduced with ET-B and ET-D sensitivity curves as function of the total mass of the binary. The mass ratio for all sources is taken to be 2. ET can beat the current solar system bound by up to two orders of magnitude. The limit is independent of the distance to the binary as long as the SNR is large enough for the Fisher matrix calculation to be reliable. *Right:* Bounds on the Brans-Dicke parameter (ω_{BD}) as a function of the total mass of the NSBH binary observed. For all systems, the NS mass is assumed to be $1.4\,M_\odot$. The existing bound from the Cassini experiment and the possible bounds from aLIGO are also shown.

Gravitational waves in a massive graviton theory would suffer disperson and the effect would be greater the farther an observer is from the source. Thus, observations of inspiralling compact binaries at high redshifts can be used to place better bounds on the mass of the graviton, or equivalently the Compton wavelength of the graviton [94], than is possible by comparing the arrival times of GW and EM radiation from a source. Moreover, bounds from GW dispersion do *not* require the detection of an EM counterpart associated with the GW signal.

The basic idea is simple: if there is a mass associated with the propagation of GWs ("a massive graviton"), then the speed of propagation v_g will depend on the wavelength λ as (in units $c = 1$) $v_g \approx 1 - (\lambda/\lambda_g)^2$, where λ_g is the Compton wavelength of the graviton, in the limit where $\lambda \ll \lambda_g$. Irrespective of the nature of the alternative theory that predicts a massive graviton, it is reasonable to expect the differences between such a hypothetical theory and GR in the predictions for the evolution of compact binaries to be of order $(\lambda/\lambda_g)^2$. This quantity will be very small, given that close to merger $\lambda \sim 10^3$ km for stellar mass BBH, BNS and NSBH inspirals and $\lesssim 10^5$ km for binary IMBH inspirals.

As a result, the gravitational waveform seen by an observer near to a source will be very close to that predicted by GR. However, as seen by a detector at a distance D, hundreds of Mpc away, the phasing of the signal will be distorted because of the shifted times-of-arrival, $\Delta t \sim D(\lambda/\lambda_g)^2$, of the waves emitted with different wavelengths during the inspiral. In addition to measuring the astrophysical parameters of the system, such as masses and spins, the matched filtering technique permits one to estimate or bound such effects.

Bounds based on observations of BBH by ET have now been computed [95]. The wavelength-dependent propagation speed changes the arrival time t_a of a wave of a given emitted frequency f_e relative to that for a signal that propagates at the speed of light; that time is given, modulo constants, by

$$t_a = (1+z)\left[t_e + \frac{D}{2\lambda_g^2 f_e^2}\right] . \tag{17}$$

Here f_e and t_e are, respectively, the wave frequency and time of emission as measured at the emitter; z is the cosmological redshift, and

$$D \equiv \frac{(1+z)}{a_0}\int_{t_e}^{t_a} a(t)dt\,, \tag{18}$$

where $a_0 = a(t_a)$ is the present value of the scale factor[1]. This is an ad-hoc procedure because a massive graviton theory will undoubtedly deviate from GR not just in the propagation of GW, but also in the way GW damping affects the phase and the amplitudes of the emitted radiation. However, it turns out that hundreds of Mpc away from the source, the propagation effect will dominate over wave generation effects [95]. In any case, given the fact that there is no generic theory of a massive graviton, there is no choice but to omit these unknown contributions.

Estimates of the bounds on the massive graviton parameter are based on the Fisher matrix formalism, which used a six-dimensional parameter space consisting of the time and phase $(t_c,\, \phi_c)$ of coalescence, the chirp mass $\mathcal{M}$, the mass asymmetry parameter $\delta = |m_1 - m_2|/(m_1 + m_2)$, the massive graviton parameter $\beta_g = \pi^2 D\mathcal{M}/\lambda_g^2(1+z)$, and the luminosity distance $D_{\rm L}$.

Figure 23, left panel, plots the bound on the Compton wavelength as a function of the total mass of the system. The bound plotted is the 1-sigma error in the measurement accuracy of the parameter λ_g. For both choices of sensitivity, ET-B and ET-D, the bound will improve beyond that set by solar system experiments by some two orders-of-magnitude.

The bounds are, in principle, more or less independent of the distance: sources at greater distances will have smaller SNRs but such signals suffer larger dispersion as they propagate greater distances. Hence the overall effect is more or less the same irrespective of the distance to source. However, for very large distances the SNR may not be high enough for the Fisher matrix estimate to be reliable. With the accumulation of sources, the bound can be further improved by $\sqrt{N}$, where N is the number of sources detected. Since ET will observe millions of compact binary coalescences, it has the potential to improve the bounds by several orders of magnitude more than that shown in Fig. 23.

2.4.3 Bounds on Brans-Dicke parameter

The Brans-Dicke (BD) theory [96] is an alternative theory of gravity that has an additional scalar field, which couples to matter, as well as the tensor field of GR. The coupling of the scalar field is described by a dimensionless parameter ω_{BD}; in the limit $\omega_{BD} \to \infty$ the theory goes over to GR. Since scalar-tensor field theories predict dipolar gravitational radiation, this parameter is also a measure of the dipolar GW content.

The best bound on this parameter so far has come from the solar system experiment *Cassini*, by measuring the frequency shift of radio signals to and from the spacecraft as it orbited near the sun [97]. The resulting lower limit on ω_{BD} is about 4×10^4.

Gravitational wave observations can also put interesting bounds on ω_{BD} [98, 99]. This is possible because the GW phasing formula in BD theory is the same as in GR except for an additional dipolar term proportional to ω_{BD}^{-1}. Hence it is possible to measure or bound this quantity from GW observations. The dipolar content in GW also depends on the internal structure of the compact body via a quantity called "sensitivity" s_A (Sec. 3.3 of [100]).

$$\left(\frac{dE}{dt}\right)_{\rm dipole} \propto \frac{(s_1 - s_2)^2}{\omega_{BD}}, \tag{19}$$

where s_1 and s_2 are the sensitivities of the binary constituents. The sensitivity parameter for a BH is $s_{\rm BH} \equiv 0.5$ while that of the NS $s_{\rm NS}$ ranges between $\simeq$ 0.1–0.2 depending on its mass. Thus, for a BNS $|s_1 - s_2| \sim 0.2\delta M/M_\odot$, δM being the difference in mass of the two NS, for NSBH systems $|s_1 - s_2| > 0.3$ and for BBH $|s_1 - s_2| = 0$. Therefore, for bounding BD theories one of the components of the binary should be a NS. The bound is also very sensitive to how asymmetric the binary component masses are. The bound that can be placed on ω_{BD} decreases as the asymmetry increases. Due to these factors, current GW bounds on ω_{BD} are very weak, ~ 5000 at best [98].

However, if ET has very good low-frequency sensitivity it can achieve more stringent limits than the solar system bounds. Figure 23, right panel, shows the bound on ω_{BD} obtained using NSBH systems for ET-D and ET-B.

[1] For $z \ll 1$, D is the same as the luminosity distance $D_{\rm L}$. Hence one can take $D \simeq D_{\rm L}$ in the case of ET for which sources considered are at 100 Mpc.

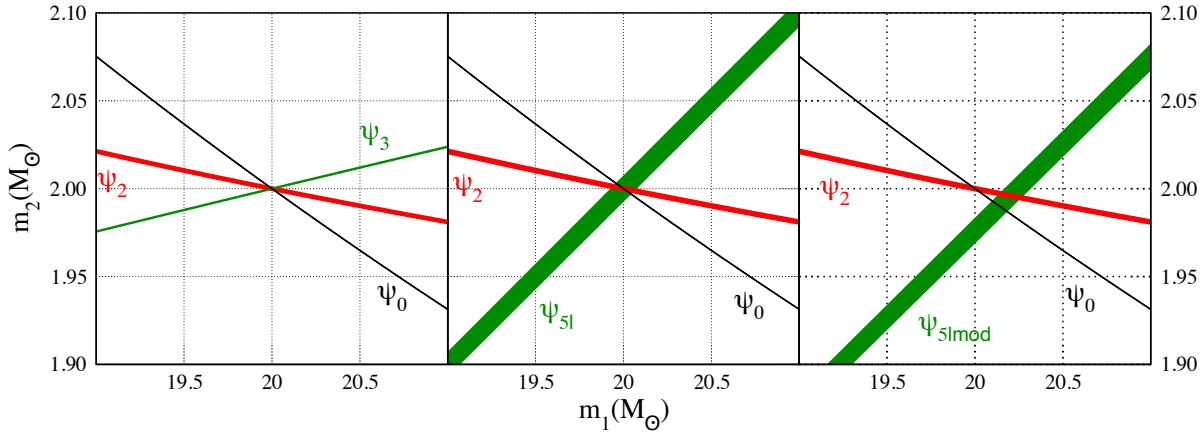

Figure 24: Curves of constant PN coefficients in the (m_1, m_2) plane for a $(2, 20)\,M_\odot$ BBH merger at 300 Mpc observed in ET-B. The left and middle plots correspond to the case when the post-Newtonian coefficients are all as in GR and all three curves intersect at a single point. The plot on the right corresponds to the case when the measured value of ψ_{5l} differs from GR by 1% and in this case the three curves fail to intersect at a common point. The thickness of the lines is the 1-sigma error in the measurement of the corresponding parameter.

The NS mass is assumed to be $1.4\,M_\odot$ and that of the BH is varied from $3\,M_\odot$ to $19\,M_\odot$. The best bounds would come from the observations of NSBH systems with lightest BH mass. Given that ET's sensitivity extends down to 1 Hz, (a basic assumption of these calculations) then the bounds on ω_{BD} could be as high as $\sim 3 \times 10^5$.

2.4.4 Parametrized tests of post-Newtonian theory

It is also possible to test for violations of GR without assuming a particular alternative model. One such test was proposed by Arun et al. [101–103] and is based on the post-Newtonian (PN) expansion of the phase of an inspiral signal in the frequency domain:

$$\Psi(f) = \sum_{j=0}^{7} \left[\psi_j + \psi_{jl} \ln(f)\right] f^{(j-5)/3}, \tag{20}$$

where the PN coefficients ψ_j and ψ_{jl}, $j = 0, \ldots, 7$ can be found in [103]. Under the simplifying assumption that spins are zero, these coefficients only depend on the component masses m_1, m_2 of the binary. Hence only two of these coefficients are independent, and a possible test of PN theory (and hence of GR) is to check for consistency between any three of them. Particular attention has been given to ψ_3 and ψ_{5l}:

- ψ_3 is the lowest-order coefficient which gets contributions from scattering of gravitational waves off the spacetime near the binary, the so-called tail terms: hence it encapsulates the non-linear character of GR.
- ψ_{5l} is the lowest-order coefficient of a logarithmic term in (20). General relativity is not consistent with a simple Taylor expansion.

The basic idea of the test is to measure the PN coefficients by fitting the observed signal to a model in which three of the PN coefficients, instead of two, are treated as independent parameters. As mentioned before, each coefficient depends on the two masses $\psi_j = \psi_j(m_1, m_2)$. Thus, a measured value of one of the PN coefficients can be used to draw a curve in the (m_1, m_2) plane by inverting the relation $\psi_j = \psi_j(m_1, m_2)$, where the left hand side is the measured value and the right-hand side is a function only of m_1, m_2. Intersection of two of the curves, say those corresponding to the measurement of ψ_0 and ψ_2 (ψ_1 is identically zero in GR), gives the component masses. If GR is the correct theory then the curve $\psi_3 = \psi_3(m_1, m_2)$ (left panel of Fig. 24) or $\psi_{5l} = \psi_{5l}(m_1, m_2)$ (middle panel of the figure) will pass through the intersection of the curves corresponding

to ψ_0 and ψ_2. If, however, GR is not the correct theory of gravity and, say, the value of ψ_{5l} is different from that in GR then the curve $\psi_{5l} = \psi_{5l}(m_1, m_2)$ will not pass through the intersection of the other two curves as in the right panel of Fig. 24.

In this way, ET will be able to test the non-linear predictions of GR and confirm whether GR is the correct theory when the gravitational field becomes so strong that orbital speeds get close to the speed of light. No other experiments or observations conceived so far can test GR to such a high order in PN theory.

2.4.5 Measuring the dark energy equation of state and its variation with z

Over the past decade, evidence has emerged suggesting that the expansion of the Universe is accelerating. Possible explanations include a failure of general relativity at large length scales, a cosmological constant in the Einstein equations, or a new contributor to the mass/energy content of the Universe called dark energy (DE) (see [104] for a review). Assuming a homogeneous and isotropic Universe, DE can be characterized by an EoS of the form $p_{\rm DE} = w(z)\rho_{\rm DE}$, where $p_{\rm DE} < 0$ and $\rho_{\rm DE} > 0$ are the pressure and density, respectively. If the EoS parameter $w(z)$ is constant and equal to -1 then this corresponds to having a positive cosmological constant in the gravitational field equations. Current constraints allow for this possibility, but other possibilities are not ruled out. The seven year WMAP data combined with Type Ia supernova measurements and baryon acoustic oscillations in the galaxy distribution lead to the constraint $w = -1.10 \pm 0.14$ at the 68% confidence level [105].

The GW signal from inspiraling compact binaries is particularly "clean" and well-understood. Consequently, as suggested by Schutz, one can think of using inspiral events as "standard sirens", much in the way Type Ia supernovae have been used as standard candles [43]. From the GW signal itself the luminosity distance $D_{\rm L}$ can be inferred, but not the redshift. However, if a particular compact binary coalescence event is accompanied by a sufficiently distinct electromagnetic counterpart, then it will be possible to find its position in the sky, identify the host galaxy, and obtain the redshift z. The relationship $D_{\rm L}(z)$ depends sensitively on cosmological parameters such as the Hubble constant at the current epoch H_0, the normalized matter and DE densities $\Omega_{\rm M}$ and $\Omega_{\rm DE}$, and the DE EoS parameter w. For example, in a spatially flat FLRW Universe and assuming a constant w,

$$D_{\rm L}(H_0, \Omega_{\rm M}, \Omega_{\rm DE}, w; z) = (1+z) \int_0^z \frac{dz'}{H_0 \left[\Omega_{\rm M}(1+z')^3 + \Omega_{\rm DE}(1+z')^{3(1+w)}\right]^{1/2}}. \tag{21}$$

The intrinsic luminosity, and hence the luminosity distance, of an inspiral GW event can be inferred directly from the amplitude of the observed waves and from the component masses, which govern the structure of the signal. Thus, unlike Type Ia supernovae, their calibration does not depend on the brightness of other sources. Thus GW astronomy opens up the possibility of cosmography *without having to rely on the lower rungs of the cosmic distance ladder*.

Compact binary coalescences that involve a NS are assumed to have strong electromagnetic counterparts, mostly in the form of strongly beamed gamma radiation directed perpendicularly to the plane of the inspiral. Such events are believed to be the progenitors of short, hard Gamma Ray Bursts (GRBs): if the beam roughly points towards Earth then a flash of gamma radiation is seen, followed by an afterglow in the lower-frequency electromagnetic spectrum. This would then allow us to identify the host galaxy and obtain a redshift.

The GW signal from a NSBH coalescence will be visible out to $z = 3.5$. Within the corresponding volume, it is reasonable to expect $\sim 10^4$ or more such coalescences per year, but depending on the opening angle of the gamma ray beam only a few percent of these will be visible as a GRB. Hence we should have a few hundred sources at our disposal for which the redshift can be measured. The uncertainty on z will be negligibly small, while $D_{\rm L}$ will be measurable with $\sim 3\%$ inaccuracy at $z = 1$, rising to $\sim 10\%$ at $z = 3.5$. Fitting the measured values of $D_{\rm L}$ against redshift by varying H_0, $\Omega_{\rm M}$, $\Omega_{\rm DE}$, and w in the relationship (21) should then allow for the determination of these cosmological parameters with uncertainties of 5% or better, as discussed further in Section 2.6.1.

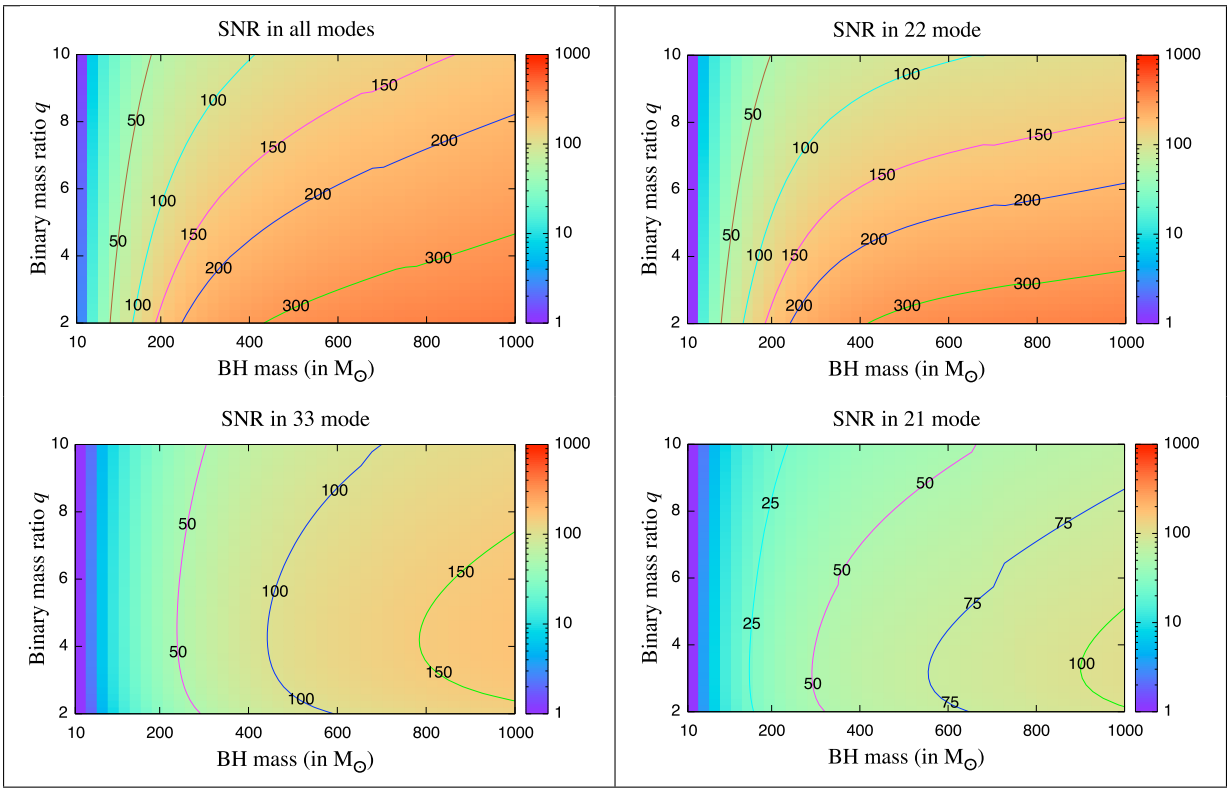

Figure 25: Signal-to-noise ratio of quasi-normal modes in ET as a function of the BH's mass M and progenitor binary's mass ratio q for different modes. Most of the contribution to the SNR comes from the 22 mode but other modes too have significant contributions, 33 being more important than 21.

2.4.6 Testing the uniqueness theorem of black hole spacetimes

It is generally accepted that the compact objects observed in the centres of most galaxies are massive, rotating BHs described by the Kerr metric of GR. This belief comes in part from the uniqueness theorem, which states that the Kerr metric is the unique end state of gravitational collapse [106]. However, this theorem is based on several assumptions – the spacetime is vacuum, axisymmetric and stationary; there is a horizon in the spacetime; and there are no closed timelike curves. If one of these assumptions were violated, then objects that deviate from the Kerr metric could exist.

In BBH systems where one component is much heavier than the other, many GW cycles are emitted while the smaller object is in the strong field region close to the larger object. These GWs encode a map of the spacetime structure in the vicinity of the large BH, which can be used to measure properties of the central object [107]. Using such observations to measure spacetime structure has been explored extensively in the context of extreme-mass-ratio inspirals (binaries of $\sim 10M_\odot$ objects with $\sim 10^6 M_\odot$ objects) for LISA (see [50] and references therein). There is an analogous source for ground based detectors, namely the inspiral of a $\sim 1M_\odot$ object into a $\sim 100M_\odot$ BH. We refer to these as intermediate-mass-ratio inspirals (IMRIs) [108].

ET will be able to detect IMRIs out to redshifts $\sim$ 1–5, depending on the mass and spin of the central IMBH [109]. Assuming that $\sim 10\%$ of globular clusters form IMBHs, ET will detect between a few tens and a few hundreds of events, depending on the mass distribution of the intermediate mass BHs [48]. The biggest uncertainty is in the intrinsic density of IMBHs, which could reduce these numbers by several ordrs of magnitude. Advanced LIGO observations of IMRIs could be used to make very modest measuements of deviations in BH structure from the Kerr metric, e.g., an $\mathcal{O}(1)$ deviation in the quadrupole moment [47, 108]. ET will observe IMRI events for many more cycles, due to its better low-frequency performance, which is very important for the precision of

spacetime mapping measurements. We would therefore expect to obtain constraints that are one or two orders of magnitude better with ET, although explicit estimates of this have not yet been made.

2.4.7 Testing the no-hair theorem using BH quasi-normal modes

Perturbed Kerr BHs emit gravitational radiation which consists of a superposition of damped sinusoids termed quasi-normal modes. The frequencies and time-constants of the modes depend only on the mass and spin of the BH — a consequence of the no-hair theorem. It has been proposed that a measurement of two or more quasi-normal modes could be used to confirm that the source is a BH and to test if GR continues to hold in ultra-strong gravitational fields.

The fundamental mode frequencies and time constants, characterized by two indices (ℓ, m), $\ell = 2, 3, \ldots$ and $m = -\ell, \ldots, \ell$, are given by the general expressions

$$\omega_{\ell m} = \frac{F_{\ell m}(j)}{M}, \quad \tau_{\ell m} = M G_{\ell m}(j), \tag{22}$$

where $F_{\ell m}(j)$ and $G_{\ell m}(j)$ are functions of the dimensionless BH spin magnitude, or Kerr parameter, j. Not all modes are excited equally; when, for instance, two BHs merge to form a single BH the $(\ell, m) = (2, 2)$ mode is the most dominant followed by $(\ell, m) = (3, 3)$ and so on. However, all mode frequencies and time-constants depend only on the mass M and (dimensionless) spin magnitude $j = J/M^2$, where J is the magnitude of the BH's spin angular momentum. Several authors have noted that this aspect of the no-hair theorem could be used to test if massive compact objects at galactic cores are actually rotating BHs described by the Kerr metric of general relativity [110–112]; alternatively, it could be used as a strong field test of GR itself [110].

The key idea behind the proposed tests is the following: If one can reliably decompose the observed gravitational radiation from a ringing BH into a superposition of different modes, then the frequencies and time-constants of each of the modes could be used to infer the mass and spin of the BH. If the object is truly a BH, then the masses and spins obtained from the different modes should all be consistent within the measurement errors. Inconsistencies in the values of the masses and spins inferred from different modes would be an indication of the failure of GR or that the radiation was emitted from an object that is not a BH. If a merging binary does not lead to a BH then the inspiral phase may not result in a superposition of QNMs that can be characterized by just two parameters.

Figure 25 plots the SNR in the ringdown signal (plot titled "SNR in all modes") and contribution from the $(\ell, m) = (2, 2), (2, 1)$ and (3,3) modes as a function of the mass M and mass ratio $q = m_1/m_2$ $(m_1 > m_2)$ of the progenitor binary. Although the (2,2) mode is the most dominant, the other modes are large enough that it should be possible to disentangle the different modes and test the no-hair theorem.

Testing the no-hair theorem by measuring the multipole moments of a source There is an alternative way to test the no-hair theorem. Another consequence of this theorem is that the entire spacetime structure, characterised by "multipole moments", is determined by just two parameters, the BH mass, M, and spin parameter, $S = J/M$, where J is the magnitude of the spin angular momentum. It has been demonstrated that GW observations can measure the mass and spin multipole moments M_l and S_l independently of one another [107]. We can, therefore, directly verify that they satisfy the Kerr relationship $M_l + i\, S_l = M(i\, S/M)^l$. We would only need to measure three multipole moments to rule out an object as a Kerr BH.

It has been shown that IMRI observations with Advanced LIGO could detect an $\mathcal{O}(1)$ deviation in the quadrupole moment of an object [108]. The precision achievable with ET should be at least a factor of 10 better than this due to the improved low-frequency performance. To put this in perspective, one alternative to BHs, boson stars, have quadrupole moments two orders-of-magnitude bigger than BHs of the same mass and spin [113].

Any deviations from the no-hair theorem that are detected will have profound implications for our understanding of relativity and of BHs. Persistent deviations from the theory may lead to important insights in the search for a fundamental theory that unifies all four forces of nature.

Are there naked singularities? One of the assumptions of the uniqueness theorem is that a horizon exists in the spacetime. This arises from a belief embodied by the "Cosmic Censorship Hypothesis" [114] (CCH), which states that any singularity will be enclosed by a horizon. The CCH arises from a desire for predictability in the Universe—when Physics breaks down at a singularity, we do not want information from that to propagate into the rest of the Universe. However, the CCH is unproven and therefore "naked" singularities not enclosed within a horizon may still exist. Gravitational wave observations provide a unique way to look for these exotic objects. Observations may be indirect, via detection of a violation to the "no-hair" theorem. However, they may also be direct—if a horizon is not present in the spacetime, the gravitational waves will not cut off when the object crosses the horizon [115], which will be a clear smoking gun signature for the absence of a clothing horizon in the system.

ET will provide much more stringent constraints on potential violations of the CCH than are possible with Advanced LIGO. ET observations will therefore play an important role in answering the question as to whether naked singularities exist, which could have profound implications for our understanding of various aspects of the theory of relativity.

2.4.8 Limit on the maximum mass of compact stars

It is generally believed that NSs have masses between $\sim 1.3\,M_\odot$ and $\sim 2\,M_\odot$, but such statements rely on guesses regarding the EoS of dense nuclear matter. Above $2\,M_\odot$ a quark star might be created, or some other exotic object. Apart from the existence of such objects and their properties, an interesting question is how massive a star can be while still being stable.

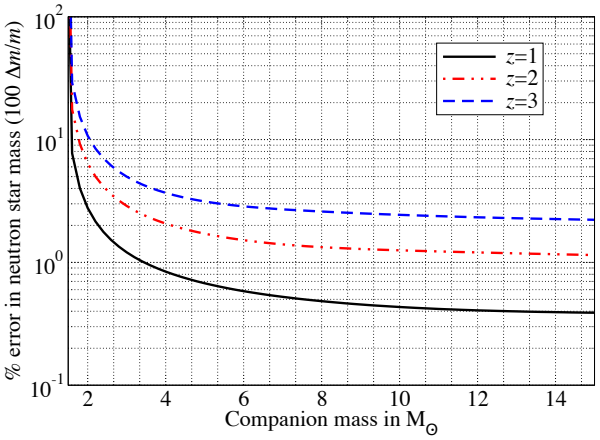

Figure 26: The accuracy with which the mass of a neutron star can be determined, as a function of the mass of the companion object.

Fig. 18 shows the maximum distance to which binary inspirals can be seen in ET for systems with two equal mass companions. The distance reach for a binary with symmetric mass ratio ν would be smaller by a factor[2] of $\sqrt{4\,\nu}$. For a NS of $2\,M_\odot$ and a BH of $5\,M_\odot$, $\nu \sim 0.20$ and so the range would be 90% of that for a binary composed of two $3.5\,M_\odot$ system. Considering NS masses of $1.4\,M_\odot$ and BH masses of $10\,M_\odot$ one gets the distance reach to be 56% of that for a binary of total mass $16.4\,M_\odot$ and composed of two equal mass BHs. The above reasoning shows that ET will have access to NSBH sources out to genuinely cosmological distances, up to redshifts of several, with an expected detection rate in the order of $10^6\,\mathrm{yr}^{-1}$.

Fig. 26 shows how accurately ET will measure the mass of a NS (assumed to be $1.4\,M_\odot$) in an NSBH inspiral process, as a function of the mass of the BH for three different values of the redshift, $z = 1, 2, 3$. We see that for BH masses larger than $2\,M_\odot$ the NS mass is measured to better than 10%. Indeed, most astronomical BH candidates have a minimum mass of $\sim 4\,M_\odot$ and for BH mass $\gtrsim 4\,M_\odot$, the NS's mass can be inferred to a fraction of a percent out to $z = 1$, and up to a few percent out to a redshift of 2 or 3. This would enable us not only to establish the mass distribution of NSs and possible dense exotic objects, but also the evolution of this distribution over cosmological timescales.

[2] A factor of $\sqrt{4\,\nu}$ can be understood in the following manner: The signal-to-noise ratio of an inspiral signal is directly proportional to the product of its amplitude (which goes as ν) and square-root of its duration (which goes as ν^{-1}), or an overall factor of $\sqrt{\nu}$. A factor of 4 is included for normalization as $\nu = 1/4$ for equal mass systems.

2.5 Astrophysics

ET will be a unique observatory in many ways to study neutron stars and black holes. It will be sensitive to relativistic phenomena that efficiently convert energy in non-axisymmetric motion in compact objects into gravitational waves. Examples include quakes in neutron stars, supernovae, proto-neutron stars, inspiralling and colliding binary neutron star and neutron star-black hole systems and gamma-ray burst sources, systems and phenomena where motion ought to be highly relativistic and hence potential sources of GW too. In this Section we will look at what ET can unveil about compact objects and their environs.

2.5.1 Determining the neutron star equation of state from binary coalescences

Several BNS systems have been observed to date, for some of which general-relativistic effects in the binary orbit have been measured to high precision [116]. The inspiral and merger of two NSs in binary orbit is the inevitable fate of close-binary evolution, whose main dissipation mechanism is the emission of GWs. The detection of GWs from NS binaries will provide a wide variety of physical information on the component stars, including their mass, spin, radius and EoS. The central densities of isolated NSs, in fact, can range up to ten times the nuclear saturation density, and during the merger and coalescence of two NSs the maximum density will rise even further, before the remnant object collapses to a BH. The behaviour of bulk matter at these densities is not well understood; measurements of GW signals from NS sources can usefully constrain the EoS at these densities.

Quantum chromodynamics is expected to be a complete description of matter at these energies; the uncertainty in theoretical understanding comes from the many-body problem with strong interactions. The description of bulk neutral matter in terms of hadrons such as protons and neutrons may need to be expanded to accomodate new particles that are formed at these energies, such as hyperons, pions, and kaons. In fact the appropriate degrees of freedom describing cold matter at very high density may no longer be hadrons but the quarks and gluons themselves, in some form of quark matter.

While isolated or inspiralling NSs are well described by the ground state of matter, i.e. with a "cold" EoS, the temperatures reached in the coalescence as a result of the strong shocks will be significant and of the order of $\sim 10^{10}$–10^{12} K. Yet, just as measurements of the hot out-of-equilibrium ion collisions in the Relativistic Heavy Ion Collider constrain the ground state of dense nuclear matter, observed characteristics of NS mergers may be able to constrain the ground state of dense neutral matter. Reviews of the current range of candidate equations of state, and constraints on them from astrophysical observations and heavy ion collision experiments, can be found in [117–119].

The signature of the NS EoS can be found in almost any NS sourced GW: in the peak frequencies of supernova waveforms [120, 121], in the possibility of accretion-induced crust mountains [122, 123], and in the astroseismology of glitches and other oscillation mode excitations. Studies which have specifically explored the effect of varying EoS (or varying compactness for a given mass, which implies variation of EoS) on GW spectra include Refs. [124–128] for binary NS inspiral, Refs. [129–136] for binary NS coalescence, and Refs. [117, 137–139] for mixed NSBH binaries.

Gravitational waves from binary inspiral and merger are expected to be frequently observed in ET and the predicted signals have several interesting EoS-dependent features. This is illustrated in Fig. 27, based on the simulations of [135] where a comparison of GW spectra from BNS mergers is shown together with the noise PSDs of Virgo, aLIGO and ET. The panel on the left plots the spectra for a system with total mass $2.98\,M_\odot$ while the one on the right considers a lighter system of total mass $2.69\,M_\odot$. Both panels show spectra for two different EoS: NSs with the cold EoS give rise to two distinct bumps (blue solid lines), the location and relative heights depending on NS masses. NSs with the hot EoS exhibit a number of spikes (red dashed lines) whose detailed structure depends on the NS masses. The spectrum of a BBH merger (orange solid lines), on the other hand, has no specific feature and is independent of the total mass of the binary. While neither of the two equations of state considered here are realistic, they span in some sense the extremes of the range of possibilities. Most

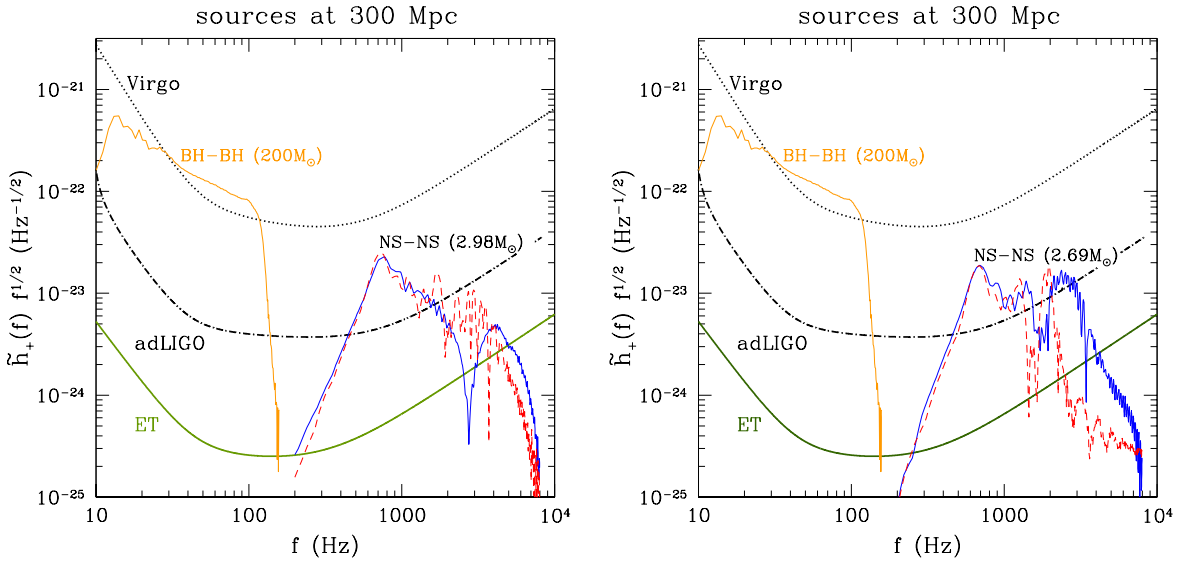

Figure 27: Gravitational wave spectra of merging neutron star binaries compared to sensitivities of Virgo, advanced LIGO (labelled adLIGO) and ET. Left panel shows spectra of high-mass binaries evolved with the cold (blue solid line) or hot (red dashed line) equations of state. Also shown for comparison is the corresponding spectrum of an equal-mass, non-spinning binary black hole with total mass $M = 200\,M_\odot$, which appears in the low-frequency part of the spectrum (orange solid line). Right panel is the same as the left panel but for the low-mass binary. It can be seen that the observed spectra are sensitive to the neutron star EoS.

importantly they show that the GW signal from BNS merger will be very sensitive to the mass of the stars and their EoS.

While this is especially true in the post-merger phase, the inspiral phase will also provide important information on the EoS. Although for most of the inspiral phase, the component stars of a BNS system are well-modeled as point particles, as they approach each other, an EoS-dependent tidal deformation modifies their orbits, changing the late inspiral waveform. The measurability of this effect in GW detectors can be estimated using both PN tidal deformation calculations and full numerical simulations of BNSs with varying EoS. The induced change in the waveform can be used to measure the radius of the NS quite accurately.

Indeed, the set of numerical simulations of Ref. [128] show that for a $1.35\,M_\odot$–$1.35\,M_\odot$ system at 100 Mpc ET can measure the radius to within ± 0.5–1.0 km. This compares favorably to the range in predicted radius of roughly 9–16 km. Parameterizing the variation in the size of a NS by the pressure at a density of $5 \times 10^{14}\,\mathrm{g\,cm^{-3}}$ [127], gives fractional uncertainty in pressure of 5–10%.

The advantage of ET in understanding the NS EoS is not necessarily the larger number of detections possible with increased sensitivity, although information about the mass distribution of NS populations can also be useful for constrainting the EoS. Instead, ET will provide very strong signals at reasonable rates; for example two $1.4\,M_\odot$ NSs inspiralling towards each other within an effective distance of 100 Mpc, which is expected roughly once a year, would give a SNR in ET of over 900. This makes it possible to precisely measure the component masses during the early inspiral phase, to detect small departures from point particle behaviour at moderate frequencies, and discriminate between merger and post-merger signals from different models at high frequencies.

An interesting feature that has emerged from studies of BNS coalescences is the post-merger formation, in some cases, of a hyper-massive remnant object which oscillates and emits GWs on fairly long timescales. The presence or absence of such post merger oscillations, as well as their characteristic frequency and duration, varies with the cold EoS. However, they are additionally sensitive to many physical characteristics such as thermal properties, magnetic fields, particle production, and so forth. The precise details of the signal are not easy to predict.

However, the signal from such a post-merger oscillation should be visible in ET [131], and analysis of the signal following a measured inspiral phase may provide useful constraints on the underlying astrophysics.

Furthermore, magnetic fields are commonly present in NSs and their possible impact on the dynamics of BNSs has only begun to be examined. The effect of magnetic fields on GW emission during the inspiral and merger of magnetized NSs has recently been investigated [140]. It has been shown that while initial fields of strength $B_0 \gtrsim 10^{12}\,\mathrm{G}$ have an impact after the merger, fields of sufficiently strong strength $B_0 \gtrsim 10^{16}\,\mathrm{G}$ will affect the inspiral phase too. ET provides a strong impetus for such theoretical studies. By including more realistic equations of state and realistic radiation transport schemes, it will be possible to considerably increase our level of understanding of these objects.

2.5.2 Neutron star physics from pulsar glitches

Many radio pulsars exhibit *glitches,* events in which a NS is seen to suddenly spin-up, followed by a relaxation period towards stable secular spin-down. Pulsar glitches have a long observational history (beginning shortly after the discovery of the first pulsar) [141]. So far, over a hundred pulsars are known to have glitched at least once (for a recent survey, see, Ref. [142]). Glitches have also been observed in magnetars — highly magnetized NSs. The archetypal glitching pulsar is Vela, which exhibits regular large glitches with an amplitude corresponding to a fractional spin frequency change of the order of 10^{-6} [143].

Despite the wealth of observational data, the glitch remains an enigma from a theoretical point of view [144]. It is widely believed that glitches are related to the existence of superfluids in the interior of mature NSs and that they involve a transfer of angular momentum from a superfluid component to the rest of the star which includes the crust (to which the pulsar mechanism is presumed to be rigidly attached) and the charged matter in the core [141, 144]. Key to this idea is the fact that a superfluid rotates by forming an array of quantized vortices. In essence, the superfluid can spin down only if the vortices can move outwards. If the vortex motion is impeded by 'pinning' to the other component, e.g. the crust nuclei, then the superfluid cannot keep up with the spin-down due to electromagnetic braking. As a result a rotational lag develops between the two components, until some critical level is reached at which the vortices unpin and transfer angular momentum to the rest of the star, and the two components are driven to corotation.

Taking the basic two-component picture at face value, one can estimate the available energy that may be radiated at a glitch event. This suggests that large Vela glitches may release an energy of the order of 10^{42} erg ($10^{-12}\,M_\odot$). This is a useful estimate as it provides an idea of how energetic regular neutron star events in our galaxy may be. Of course, one must keep in mind that this energy may not be associated with GW emission at all. This depends on the detailed glitch mechanism, e.g. the asymmetries involved. From a general point of view, on would expect glitches originating in the star's crust to be associated with very weak GWs (the involved densities are simply too low to be relevant). As the standard glitch scenario is associated with vortex pinning to crust nuclei, this would rule out these events are interesting GW sources. However, there is some evidence that the largest observed glitches may require the fluid core to be involved (e.g. through pinning of vortices to superconducting fluxtubes). This may change the situation dramatically, as the denser regions of the star are now involved. It also hints at the interesting possibility that the observed phenomenon could be the "tip of the iceberg", reflecting more energetic dynamics in the fluid core. This is, of course, speculative but it is relevant to note that the level of sensitive of ET may set strong upper limits on the possible scenarios. Translating the rough energy estimate into a GW amplitude, by assuming that the energy is released through the f-mode (a frequency of 2 kHz lasting for a fraction of a ms at a distance of 10 kpc) we find an effective amplitude around 10^{-23}. (This estimate assumes we can do matched filtering, which is relatively easy for these damped sinusoids.) A signal of this strength should be within the reach of ET. An observed signal would immediately constrain the cold-matter nuclear EoS [72, 75]. A lack of detection would set relevant limits on the asymmetry and fluid dynamics associated with pulsar glitches.

In order to do better than these rough estimates we need to improve our understanding of superfluid hydrodynamics and possible instabilities leading to glitches. There has been some recent progress on this, and it seems reasonable to expect the theory to have developed significantly by the time of ET construction. There has

been particular progress on the issue of the origin of the glitches, e.g. the instability that triggers large-scale vortex unpinning. A recent model suggests that the glitch trigger-mechanism may be the result of a superfluid "two-stream" instability setting in through the inertial modes of the system [145, 146]. However, in this model the unstable modes have very short wavelengths and would not be effective GW emitters. Whether the idea can be developed into a more complete scenario remains to be seen.

Regardless of the theory uncertainties, an instrument like ET would be ideal for detecting a GW signal in the 10–100 Hz band, which would be the relevant for the inertial modes of a Vela-like pulsar. The detection of GW signals from glitching pulsars would provide a tool for probing the interior matter of NSs and supplement EM observations. The realisation of this exciting prospect will require (as in the case of other potential sources of gravitational radiation) the input of theoretical waveform templates. These waveforms need to be computed using detailed multifluid hydrodynamical models for superfluid NSs, accounting for effects like vortex mutual friction and pinning.

2.5.3 GW from the r-mode instability

Neutron stars may suffer a number of instabilities. These instabilities come in different flavours, but they can all be directly associated with unstable modes of oscillation [73]. A study of the stability properties of a relativistic star is thus closely related to an investigation of the star's various pulsation modes. Furthermore, non-axisymmetric stellar oscillations will inevitably lead to the production of gravitational radiation. Detection of these signals would allows us to put constraints on the interior structure of the star and the extreme physics associated with the high-density region.

The most promising instability scenarios concerns rotating stars. Of particular interest are the GW driven instabilities of the f-modes and the r-modes. The action of the former is to deform the star into a bar-shape, which is an ideal GW emitter. Meanwhile, the r-mode radiate predominantly through the current multipoles. The radiation mechanisms are rather different, but the issues involved in studying these instabilities are very much the same. First we need to establish that the modes can become unstable in a realistic neutron star. This means that the GW driven growth must overcome the relevant dissipative damping mechanisms. We need to consider the (standard) shear- and bulk viscosities, and understand how the associated rates depend ion the star's composition. We also need to consider more exotic mechanisms, e.g. strong bulk viscosity associated with hyperon reaction and vortex mediated friction in a superfluid mixture. Significant effort has gone into these problems in the last decades. The current understanding is that the instability of the r-modes is likely to be the most relevant, but scenarios associated with the unstable f-modes should definitely not be ruled out. Basically, the threshold for the r-mode instability to set in in a mature neutron star is a relatively low fraction of the break-up rotation rate. Meanwhile, the f-mode become unstable only near the break-up limit. Moreover, the f-mode instability is thought to be completely suppressed in a superfluid neutron star (due to the vortex mutual friction). This is not the case for the r-modes, which are not dominated by this mechanism.

However, detailed modelling suggests that the r-modes reach nonlinear saturation at relatively low amplitudes. This limits the GW emission. The underlying mechanism, the coupling of the r-mode to a large number of short wavelength inertial modes, also leads to the GW signal being immensely complex (leading to difficulties to carry out matched filtering). Having said that, the best current estimates suggest that the r-mode signals should be detectable from systems in our galaxy (and slightly beyond) [88]. The detectability of the f-modes may be more favourable. In particular, recent work shows that the growth time of the f-mode instability may be extremely short. However, it is not known if the f-mode instability saturates at low amplitudes. If it does not, then the associated signals may be detectable from the Virgo cluster. This would increase the event rate which would counter the fact that we need a very fast spinning neutron star at birth for the mechanism to operate. Further theory progress is needed to make more precise statements. What is undoubtedly clear is that, if these GW signals are at a level that would be detectable by second generation detectors (as suggested) then ET will provide a supreme instrument for extracting the relevant physics information. This is a tremendously exciting prospect, given the dependence on interior neutron star physics that is very difficult to probe by other means.

The strength of gravitational waves from r-modes In order to estimate the GW signal associated with the unstable r-modes, let us make use of a simple phenomenological model. The model accounts for the differential rotation induced by the modes [147], but does not account for much of the complicated core physics considered in other work. Nevertheless, the estimates provide a useful guide to the relevance of these GW signals. Thus detection of such GWs is more difficult than initially supposed. In the model, the amount of differential rotation is described by a parameter K, which encodes the level of differential rotation and which may take values in the range $[-5/4, 10^{13}]$ depending on the initial conditions.

The detectability of GW produced by r-modes depends upon the amount of angular momentum that they carry away. As described in [148], for $K = 0$, the total angular momentum of the star decreases to 65% of its initial value, and part of the initial angular momentum of the star, about 58%, is transferred to the r-mode as a consequence of the rapid increase of the average differential rotation. Therefore the initial angular momentum carried away by gravitational waves is about 35%. This result is strongly dependent on the value of K: for higher K the amount of angular momentum carried away by gravitational waves may even fall below 1%.

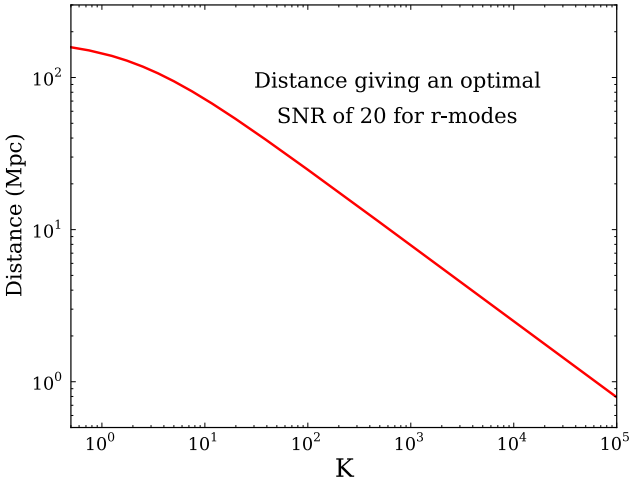

Figure 28: Detectability of r-modes expected in Einstein Telescope (ET-B sensitivity) as a function of the K parameter describing the strength of differential rotation.

In the case of the r-modes, the frequency f of the GWs depends on the NS's angular velocity Ω as $f = 2\Omega/(3\pi)$. The frequency range is estimated as follows: $f_{min} \simeq [77 - 80]$ Hz, depending on the final value of the angular velocity $\Omega(t_f)$ and K; $f_{max} \simeq 1200$ Hz, depending on the initial value of the angular velocity Ω_0. The amplitude in the frequency domain is given by:

$$H(f) = \frac{4.6 \times 10^{-25}}{\sqrt{2+K}} \sqrt{\frac{f_{max}}{f}} \frac{20\,\mathrm{Mpc}}{D}\,\mathrm{Hz}^{-1} \qquad (23)$$

where D is the source distance, f the GW signal frequency and $f_{max} = 1191$ Hz is its maximum frequency.

We may estimate the signal to noise ratio (SNR) at ET by adapting a calculation made for Advanced LIGO in [148][3]. The optimal SNR is given by

$$\frac{S}{N} = \frac{250}{\sqrt{(2+K)}} \frac{20\,\mathrm{Mpc}}{D}. \qquad (24)$$

The strong dependence on the unknown parameter K is clear, as shown in Figure 28 where we consider an SNR of 20, arbitrarily chosen for a confident observation of the signal. This dependence provides a useful illustration of the current uncertainties associated with r-mode signals. On the one hand, it may be that the distance at which a GW signal could be visible with ET is really large. Considering the optimistic case when K approaches zero, we obtain a horizon distance for an optimally oriented source of 175 Mpc. However, in the less optimal case when $K = [10^5 - 10^6]$, the horizon falls to less than 1 Mpc (galactic sources). The latter range agrees quite well with the most realistic models, where the r-mode evolution is determined by nonlinear mode-coupling [88]. Significant uncertainties remain, as all current models are somewhat incomplete, but there is every reason to expect that our understanding of the physics would have improved considerably by the time ET comes into operation. Improvements are certainly necessary if we want to be able to carry out an optimal search for these signals. Still, the current evidence of the astrophysical relevance of the r-modes makes this a very promising target for ET (see Box 2.7).

[3]The sensitivity curve used for our estimation is ET-B.

Box 2.7: R-modes and ET science goals

A significant motivation for studying GWs from the r-mode instability with ET is the opportunity to obtain a unique correlation with the nuclear physics and astrophysical scenarios involving NSs, ranging from their birth following supernovae to the spin evolution of accreting NS in LMXBs. The signal could provide a fundamental probe of NS dynamics. Some possible implications are given below:

- In principle from GW signals and signal models it is possible to trace and quantify the initial conditions of the new-born star such as initial frequency, initial temperature and others. This could lead to the confirmation or exclusion of supernova models, star formation processes and NS models.
- Another implication concerns NS nuclear physics models and the EoS, potentially opening a window on the core and crust physics, especially superfluid aspects.
- The phenomenon of NS cooling due to neutron emission also interacts with the r-mode instability. In this case GWs could provide information about the cooling rate and cooling model, which at the moment is assumed to follow the modified URCA process.
- GWs emitted by accreting NS in LMXBs may limit the attainable rotation rate. Evidence for this would solve a long standing puzzle concerning the absence of extremely fast rotating pulsars.

2.5.4 Solving the enigma of GRB progenitors

Gamma-ray bursts (GRBs) are the most luminous explosions in the universe[4]. Through observations made by satellite-based gamma-ray observatories it was found that the duration of the GRBs follows a bimodal distribution [149]. GRBs are classified either as *short-hard* or *long-soft* bursts depending on their duration and spectra. Through follow-up observations of the x-ray, optical and radio afterglow emission of GRBs it is possible to determine their sky location, redshift and host galaxy.

Long and short GRBs Long GRBs are always associated with late-type star-forming host galaxies [150]. A handful of long GRBs have also been associated with supernovae [65, 151–153]. It is therefore thought that core-collapse supernovae are the progenitor of long GRBs [154, 155].

Short GRBs are observed at lower redshifts than long GRBs and are associated with a variety of galaxy types including early-type elliptical and lenticular galaxies without active star forming regions [156]. Currently, it is widely thought that merger of BNS or NSBH systems are the progenitors of most short-hard GRBs [157]. Some small fraction of short GRBs (less than 15% of known short GRBs) may be caused by soft gamma repeater flares (SGRs) [158, 159]. SGRs are described later in this section.

As discussed in 2.3.1, accurate predictions for the GW emission of the inspiral, merger and ringdown of compact binaries are possible through post-Newtonian approximations to Einstein's equations or through numerical relativity simulations. Therefore, it is possible to employ pattern matching techniques such as matched filtering to extract these signals from noisy data. GWs from inspiralling binaries have been searched using matched-filtering in data from initial interferometers (LIGO, Virgo, GEO) (see, e.g., [160, 161]. A search GW in coincidence with short GRB 070201, whose sky-location error box overlaps the spiral arms of M31, excluded an inspiral progenitor if it was indeed located in M31 with a confidence of 99% [162]. Figure 18 shows the horizon distance for ET, where the figure for BNS with $m_{\rm NS} = 1.4\,M_\odot$ can be read off for a total mass $2.8\,M_\odot$ and spin parameter $\chi = 0$ to be about 17 Gpc. For NSBH systems, the distance reach is $z \sim$ 2-5 depending on the total mass of the system. Since short GRBs are mostly found at lower red-shifts ($z < 1$), ET will observe almost all of them assuming they are indeed progenitors of binary neutron star mergers.

[4] Gravitational waves from merging BHs will be many orders of mangitude more luminous but until they are detected GRBs will remain the most luminous events in the Universe.

Predicting the GW emission of core-collapse supernovae associated with long GRBs is more difficult and involves modelling the complicated internal dynamics of the collapsing star—see *e.g.* [59]. Searches for unmodelled gravitational emission from GRBs on data from initial interferometers (LIGO, Virgo, GEO) have also been carried out [162, 163]. The sensitivity of such searches can be determined as follows: The amplitude of a gravitational-wave burst can be characterized by the root-sum-square amplitude $h_{\rm rss}$ via

$$h_{\rm rss} = \sqrt{\int \left(|h_+(t)|^2 + |h_\times(t)|^2\right) dt}\,. \tag{25}$$

Coherent search analysis techniques [163] can detect generic bursts at 90%-confidence an amplitude $h_{\rm rss}$ of around an ten times the amplitude spectrum of an interferometer, i.e. they can detect a signal if it produces $h_{\rm rss}^{\rm min} \sim 10 \times S_h(f)^{0.5}$. For narrow-band burst signals we can use the following approximation for the energy in GW for a given $h_{\rm rss}$:

$$E_{\rm GW}^{\rm iso} \simeq \frac{\pi^2 c^3}{G} D^2 f_0^2 h_{\rm rss}^2, \tag{26}$$

where $E_{\rm GW}^{\rm iso}$ is the isotropic energy emission in GWs, D is the distance of the source and f_0 is the central frequency. From Eq. 25 we can calculate a lower limit on source distance from the minimum amplitude $h_{\rm rss}^{\rm min}$ for a given value of $E_{\rm GW}^{\rm iso}$. For long GRBs the energy of emission in GWs is not well known but has been estimated to be as high as $0.2\,M_\odot c^2$ in the LIGO-Virgo frequency band of good sensitivity [71] but it could be $0.001\,M_\odot c^2$ [68–70] or even lower. In Fig. 21 we estimate the distance to which various detectors are sensitive to a narrow-band burst of GWs assuming $E_{\rm GW}^{\rm iso} = 0.05 M_\odot c^2$. Clearly, ET has a distance reach of $z > 1$ for long GRBs [57] if the energetics are favourable and could be used as a testbed for different astrophysical models.

Soft Gamma Repeater Flares As described above, a significant fraction, up to 15%, of short, hard GRBs may be associated with flaring activity in soft gamma-repeaters (SGRs). These sources often undergo sporadic periods of activity which last from days to months where they emit short bursts of hard X-rays and soft γ-rays with luminosities $L \sim 10^{41}\,{\rm erg\,s^{-1}}$ and photon energies in the range 10–30 keV. Much more occasionally, they exhibit enormous, giant flares with luminosities as large as $10^{47}\,{\rm erg\,s^{-1}}$. There are 4 known soft γ-repeaters: three in the Galaxy and one in the Large Magellanic Cloud. It is generally believed that SGRs belong to a class of NS, magnetars, with extraordinarily large magnetic fields in the range 10^{14}–10^{15} G where the flaring activity is due to sudden, violent reconfigurations of complex magnetic field topologies.

The hardness of their spectra and the enormous luminosities involved mean that giant flares from nearby SGRs, such as that of SGR 1806-20 [164], represent an intriguing candidate progenitor scenario for some short duration γ-ray bursts. Indeed, in Ref. [165], the authors report a correlation between the positions of some short GRBs with those of low redshift galaxies, suggesting that $10 - 25\%$ of short GRBs occur in the local universe and, therefore, are likely to be associated with giant SGR flares. Furthermore, evidence for the existence of two classes of progenitors for short GRBs is provided in Ref. [159]. Here, it is found that a bimodal luminosity function, representing a dual-population of short GRB progenitors with low and high luminosities, is required to reproduce the observed distributions of short GRB luminosities. As well as statistical evidence, there have been observations of at least three individual short GRBs which present candidates for extragalactic SGR flares.

Optical and infrared observations [166] of GRB 050906 suggest a tentative association with the local, fairly massive ($M \sim 10^{11} M_\odot$) starburst galaxy IC328 which lies at a redshift of $z = 0.031$. If GRB 050906 had indeed originated in IC328, the isotropic equivalent energy would be $E_{\rm ISO} \sim 1.5 \times 10^{46}$ erg in the 15–150 keV range. The giant flare from SGR 1806-20, by comparision, emitted $E_{\rm ISO} \sim 4 \times 10^{46}$ erg with photon energies > 30 keV. As well as the potential similarity in the energetics of this burst, the association with a starburst galaxy, where young, shortly lived magnetars are believed to be most prevalent, corroborates the SGR progenitor scenario.

Two other short GRB-SGR flare candidates, GRB 051103 and GRB 070201, were detected by the Konus-Wind GRB spectrometer [167, 168]. The localisation area of GRB 051103 was found to lie near M81 (3.6 Mpc), suggesting an isotropic equivalent energy $E_{\rm ISO} = 7 \times 10^{46}$ erg. As remarked in [167], if GRB 051103 was *not* related to an SGR flare, we would expect an optical and/or transient in the localisation area, which has not been observed. Finally, the localisation area of GRB 070201 was found to overlap with the spiral arms of M31

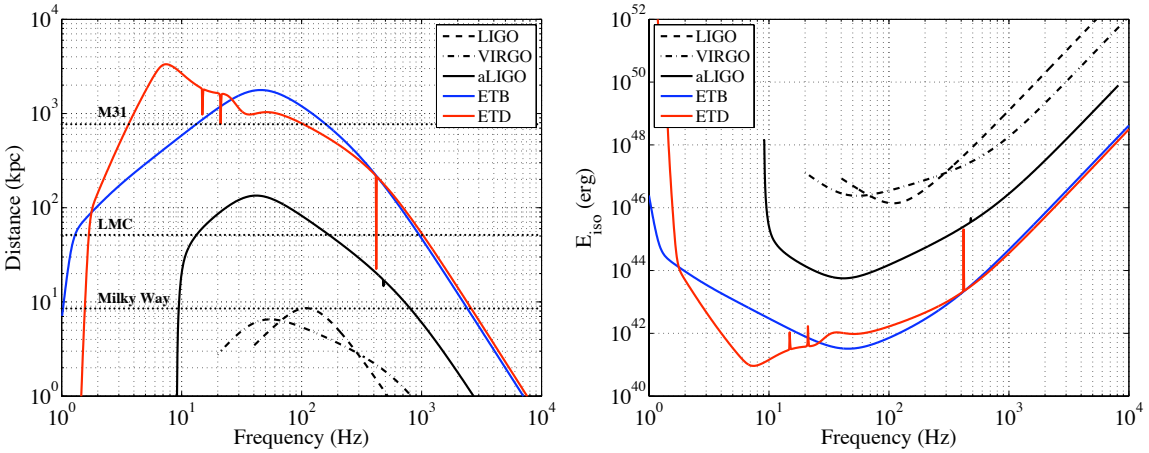

Figure 29: *Left panel*: 90%-confidence lower limit on distance for burst sources assuming $E_{\rm GW}^{\rm iso} = 10^{46}$ ergs for an SGR progenitor scenario. Starting from the lower edge of the figure, the solid horizontal black lines show the distances to the centre of our Galaxy, to the Large Magellanic Cloud and to M31 in Andromeda. *Right panel*: predicted 90% upper limits on isotropically emitted GW energy from a galactic SGR flare (i.e. distance of 10 kpc). The solid black horizontal line shows the expected upper limit of 10^{46} erg from energetic arguments alone.

(0.78 Mpc), leading to an estimate of $E_{\rm ISO} \sim 1.5 \times 10^{45}$ erg under the SGR flare scenario, again comparable to the giant flare from SGR 1806-20.

In addition to these types of arguments related to the energetics of the EM emission, GW observations can provide an extremely powerful tool to identify SGRs as short GRB progenitors. First, we note that the failure to detect the signature of a compact binary coalescence from short GRBs at distances where such a signal is expected can provide compelling evidence for the SGR progenitor scenario alone. Indeed, observations by the initial LIGO instruments recently excluded the coalescence of a binary NS system within M31 at more than 99% confidence as the progenitor for GRB 070201 [162]. Furthermore, a BNS merger is excluded at distances less than 3.5 Mpc with 90% confidence. If, however, the progenitor had been an SGR flare, the LIGO observations imply an upper bound on the isotropic energy released as an unmodeled GW burst of $E_{\rm ISO}^{\rm GW} < 7.5 \times 10^{50}$ erg, within the bounds permitted by existing models.

The non-detection of an expected inspiral GW signature, however, is not the only way that ET could provide evidence for the SGR progenitor scenario. Giant SGR flares are a source of quasi-periodic oscillations, with quadrupolar components in the $\sim$ 10–40 Hz range. Observations of these shear mode oscillations in GWs, with no accompanying inspiral signal, would only be explicable under the SGR scenario. It is also possible that non-radial oscillatory modes would become excited by tectonic activity associated with a giant SGR flare [169]. These modes will then be damped by GW emission, resulting in a characteristic ring-down signal [170]. Various families of oscillatory modes, such as fluid (f), pressure (p) and purely spacetime (w) modes, may be excited and simultaneous GW observations of all three of these families can be used to place tight constraints on the NS EoS [72]. The p- and w-modes, however, tend to have frequencies well above 4 kHz making the f-mode, with frequencies expected in the range 1–3 kHz [171], the most accessible to ET. Again, GW observations of f-mode ring-downs associated with sGRBs, where there is no accompanying inspiral signal, would point directly to an SGR giant flare as the progenitor.

Current models for SGRs [122, 169, 172] indicate that they will emit less than 10^{46} ergs in GWs. In the left panel of Fig. 29 we show 90%-confidence lower limits on the distances to which various GW detectors will be sensitive to GW bursts with this energy. We see that, in their most sensitive frequencies, the current generation of interferometers are just able to probe our own galaxy. While advanced LIGO improves this reach substantially, it is really only with the ET that observations of GWs associated with extra-galactic SGR flares become possible. Figure 29 shows the complementary plot of 90% energy upper limits obtainable by the various instruments for

a galactic SGR (at a typical distance of $\sim 10\,\mathrm{kpc}$). Again, it is only with an instrument like ET that we are able to probe interesting energy regimes across the entire frequency spectrum one might reasonably expect for GW emission associated with SGR flares.

2.5.5 Probing Core-Collapse Supernova Physics

Stellar collapse is one of the most energetic events in the Universe, releasing $\sim 10^{53}$ erg of gravitational energy in the compression of a massive star's iron core to a NS. Most of this energy ($\sim 99\%$) is emitted in neutrinos and only about 10^{51} erg go into energy of the core-collapse supernova (CC-SN) explosion. CC-SNe (SN types II, Ib, Ic) are $\sim$10 times more frequent than thermonuclear type-Ia SNe. A SN explosion pollutes the interstellar medium with the nucleosynthetic products of stellar evolution (CC-SNe are the Universe's primary source of oxygen) and enriches the universe with rare heavy isotopes via the r-process. The perturbation caused by a SN in its vicinity can trigger the formation of stellar systems; CC-SNe are also the birth sites of NS and stellar-mass BH.

The Supernova Problem and GW observations The precise mechanism of explosion operating in CC-SNe is uncertain [59, 173, 174]. When the inner part of the collapsing iron core reaches densities close to those in atomic nuclei, the strong force leads to a stiffening of the nuclear EoS, resulting in *core bounce* of the inner core into the still infalling outer core. A shock wave is formed that propagates outward in mass and radius, but quickly loses energy due to the breakup of heavy nuclei and neutrinos that carry away energy from the postshock layer. The shock stalls, turns into an accretion shock and must be *revived* to drive a CC-SN explosion. If this does not happen, a BH will form on an accretion timescale of $\sim 2\,\mathrm{s}$. *What is the mechanism of shock revival?* This is the fundamental question and primary unsolved problem of CC-SN theory. Indications are strong that the CC-SN mechanism involves a multitude of multi-dimensional processes, including rotation, convection/turbulence, and various hydrodynamic instabilities of the stalled shock and in the proto-NS. This opens up the possibility of probing the supernova mechanism with GWs.

GW, even more so than neutrinos, carry direct dynamical information from the supernova engine deep inside a dying massive star, a region generally inaccessible by the traditional means of observational astronomy. GWs form a core-collapse event have the potential of putting very strong constraints on the CC-SN mechanism [59, 175]. With initial and certainly second-generation interferometric GW detectors, this should be possible for an event in the Milky Way ($D \sim 10$–$15\,\mathrm{kpc}$) and the Magellanic Clouds [59] ($D \sim 50$–$70\,\mathrm{kpc}$), but even optimistic estimates of the CC-SN rate in this region do not predict more than $\sim$ 1–2 events per century. This number roughly doubles if one includes the entire local group ($D \sim 1\,\mathrm{Mpc}$). In the region from 3–5 Mpc a number of starburst galaxies increase the predicted and observed integrated SN rate to $\sim 0.5\,\mathrm{yr}^{-1}$. At $D \sim 10\,\mathrm{Mpc}$ it is $\gtrsim 1\,\mathrm{yr}^{-1}$ [58].

Supernova Science with ET The GW emission processes in a core collapse event give rise to strains h in the range 10^{-24}–10^{-22} ($D/1\,\mathrm{Mpc}$) and most of the emission takes place at frequencies of $\sim$ 200–1000 Hz, but the various explosion scenarios exhibit unique spectral distributions and vary in total emitted energies [59, 175]. In addition, there is likely to be a low-frequency GW-memory-type[5] component with large h up to 10^{-22} ($D/1\,\mathrm{Mpc}$) at 0–20 Hz. ET as currently envisioned is sufficiently sensitive to detect GWs from various CC-SN scenarios out to 2–4 Mpc.

Core-collapse supernovae may lead to the emission of GWs via a variety of multi-dimensional dynamical processes (see e.g. [59] for a review) that are connected to the prominent mechanism driving the explosion. Fig. 30 depicts reach estimates based on the GW burst analysis of simulated ET noise with injected model waveforms using the X-Pipeline [179, 180], assuming a single detector, optimal orientation, one-hour on-source windows, and requiring 90% detection confidence.

[5]The GW non-linear memory effect is a small, non-oscillatory contribution to the GW amplitude [177, 178] The memory effect causes a permanent displacement of the test masses after the waves have passed.

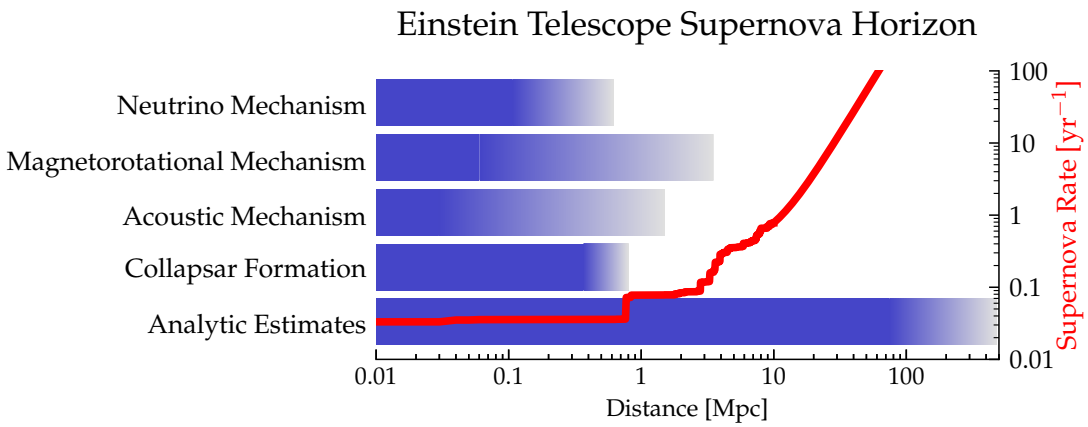

Figure 30: The plot displays ET's distance reach for different mechanisms of supernovae as blue horizontal bars. The plot also shows an estimate of the cumulative event rate (red curve) obtained from the star formation rate computed over a catalogue of nearby galaxies [176].

Model waveforms for GWs from neutrino-driven core-collapse supernovae were drawn from [59, 62, 63, 181], the model waveforms from [61, 64] were used for magnetorotational explosions, and the waveforms of [59] were used to characterize explosions driven by the acoustic mechanism proposed by [182]. In addition, GW emission from failing core-collapse supernovae that form BHs (using the waveforms of [183]) and analytic upper limits on the GW signal in massive star collapse by [70, 184] are included. The reach estimates are contrasted with the supernova rate in the local universe obtained from [58] out to 10 Mpc and assuming a conservative rate of 10^{-4} core-collapse supernovae per Mpc^3 [185] at greater distances.

ET may see multiple CC-SNe during its lifetime and would have the power to provide strong hints for a particular SN mechanism and/or smoking-gun evidence against another – crucial astrophysics information that is unlikely to be attainable in other ways. At the time when ET is implemented, megaton-class neutrino detectors will be operating and, having a range similar to ET, will be able to provide coincident observations, narrowing down the time of the GW emission to ~ 1 ms. In addition, deep high-cadence optical transient surveys will be in progress and targeting near-universe transients, providing additional coincident data as well as additional astrophysical information, for instance on progenitor type/mass and explosion morphology/energy.

Constraining the CC-SN mechanism will mean a breakthrough in our understanding of the large range of phenomena associated with stellar collapse, CC-SNe, BH and NS formation, and gamma-ray bursts (GRBs). However, the astrophysics and physics information provided by GWs observed from a core collapse event with ET goes beyond this. These GWs carry also information on the high-density nuclear EoS, explosion asymmetries and pulsar kicks, the formation of a BH in a failing CC-SN, and can help uncover rare events such as the accretion-induced collapse of a white dwarf to a NS, or weak or failing CC-SNe that have very weak or absent EM signatures.

2.6 Cosmology and Cosmography

ET can observe coalescences of stellar mass BBHs all the way up to the edge of the Universe at redshifts $z > 15$, BNS can be detected from $z \sim$ 1-2 when the star formation rate in the Universe was at its peak and IMBBHs are accessible at a redshift range of $z \sim$ 2-10 depending on the total mass and mass ratio of the binary (see Fig. 18). A large population of such events provides markers distributed throughout the Universe with accurately known luminosity distance and redshift (if the host galaxy could be identified). ET's three interferometers will also be sensitive to stochastic background radiation from primordial process and astronomical populations distributed throughout the Universe. Here we will discuss how ET can be a very powerful tool for cosmography and the early Universe.

2.6.1 Cosmography with a population of standard sirens

The goal of modern cosmology is to measure the geometrical and dynamical properties of the Universe by projecting the observed parameters onto a cosmological model. The Universe has a lot of structure on small scales, but on a scale of about 100 Mpc the distribution of both baryonic (inferred from the electromagnetic radiation it emits) and dark matter (DM) (inferred from large scale streaming motion of galaxies) components is quite smooth. It is, therefore, quite natural to assume that the Universe is homogeneous and isotropic while describing its large-scale properties. In such a model, the scale factor $a(t)$, which essentially gives the proper distance between comoving coordinates, and curvature of spatial sections k, are the only quantities that are needed to fully characterize the properties of the Universe. The metric of a smooth homogeneous and isotropic spacetime is

$$ds^2 = -dt^2 + a^2(t)\frac{d\sigma^2}{1-k\sigma^2} + \sigma^2\left(d\theta^2 + \sin^2\theta\, d\varphi^2\right),$$

where t is the cosmic time-coordinate, $(\sigma, \theta, \varphi)$ are the comoving spatial coordinates, and k is a parameter describing the curvature of the $t =$ const. spatial slices: $k = 0, \pm 1$ for flat, positively and negatively curved slices, respectively. The evolution of $a(t)$, of course, depends on the parameter k as well as the "matter" content of the Universe. The latter could consist of radiation, baryons, DM, DE, and any other possible contributions to the energy-momentum tensor.

The Friedman equation, which is one of two Einstein equations describing the dynamics of an isotropic and homogeneous Universe, relates the cosmic scale factor $a(t)$ to the energy content of the Universe through

$$H(t) = H_0\left[\hat{\Omega}_{\rm M}(t) - \frac{k}{H_0^2 a^2} + \hat{\Omega}_\Lambda(t)\right]^{1/2}, \tag{27}$$

where $H(t) \equiv \dot{a}(t)/a(t)$ is the Hubble parameter ($H_0 = H(t_P)$ being its value at the present epoch t_P), $\hat{\Omega}_{\rm M}(t)$ and $\hat{\Omega}_\Lambda(t)$ are the (dimensionless) energy densities of the DM and DE, respectively. The above equation has to be supplemented with the EoS of DM, assumed to be pressure-less fluid $p = 0$ [$\hat{\Omega}_{\rm M}(t) = \Omega_M(1+z)^3$, $\Omega_{\rm M} = \hat{\Omega}_{\rm M}(t_P)$] and of DE, assumed to be of the form $p = w\rho_\Lambda$ [$\hat{\Omega}_\Lambda(t) = \Omega_\Lambda(1+z)^{3(1+w)}$, where $\Omega_\Lambda = \Omega_\Lambda(t_P)$], with $w = -1$ corresponding to a cosmological constant. The goal of cosmography is to measure (H_0, $\Omega_{\rm M}$, Ω_Λ, w, k, ...), which essentially determine the large-scale geometry and dynamics of the Universe. In the rest of this section we shall assume that the spatial slices are flat (i.e. $k = 0$).

Cosmic distance ladder Astronomers use "standard candles" to measure the geometry of the Universe and the various cosmological parameters. A standard candle is a source whose intrinsic luminosity L can be inferred from the observed properties (such as the spectral content, time-variability of the flux of radiation, etc.). Since the observations also measure the apparent luminosity F, one can deduce the luminosity distance $D_{\rm L}$ to a standard candle from $D_{\rm L} = \sqrt{L/(4\pi F)}$. In addition, if the redshift z to the source is known then by observing a population of such sources it will be possible to measure the various cosmological parameters since the luminosity distance is related, when $k = 0$, to the redshift via Eq. (21). There is no unique standard candle in astronomy that works on all distance scales. An astronomer, therefore, builds the distance scale by using several steps,

each of which works over a limited range of the distance. For instance, the method of parallax can determine distances to a few kpc, Cepheid variables up to 10 Mpc, the Tully-Fisher relation works for several tens of Mpc, the D_n-σ relation up to hundreds of Mpc and Type Ia supernovae up to redshifts of a few. This way of building the distance scale has been referred to as the *cosmic distance ladder*. For cosmography, a proper calibration of the distance to high redshift galaxies is based on the mutual agreement between different rungs of this ladder. It is critical that each of the rungs is calibrated with as little an error as possible.

As discussed in Box 2.4, gravitational waves from inspiralling compact binaries are ideal standard candles. Their dynamics is completely described by Einstein's equations and have been computed in the post-Newtonian theory to a very high order. They are free from complex astrophysical phenomena which normally poses difficulties in treating most sources as standard candles. Moreover, gravitational waves are not subject to attenuation of various kinds that causes EM radiation to be contaminated when travelling over cosmological distances. Gravitational astronomy is, therefore, able to supplement cosmological studies and could provide very valuable information both about the sources as well as the geometry and structure of the Universe.

For sufficiently low-redshift sources ($z \ll 1$), the relationship between the luminosity distance of a source and its redshift is the Hubble law $D_{\rm L} = cz/H_0$, where $v = c\,z$ is the cosmological recession velocity of the source. Therefore, one can measure the Hubble constant with an accurate measurement of the luminosity distance to a soure and its redshift. With only 50 sources up to a redshift of $z = 0.5$, ET would determine H_0 with an accuracy of 0.55% [186].

Cosmology from a population of compact binaries As discussed in Section 2.3.1, the expected rate of mergers within the horizon of ET is $\sim$ several $\times$ $10^5\,{\rm yr}^{-1}$ for BNS and NSBH systems. Such a large population of events with luminosity distances measured to good accuracy would be very useful for measuring cosmological parameters. If, as suspected, BNS and NSBH systems are progenitors of short-hard gamma-ray bursts (GRBs) [158], then it might be possible to make a coincident detection of a significant subset of the events in GW and EM windows and obtain both the luminosity distance and redshift of the source.

Since GRBs are believed to be beamed with beaming angles of order 40°, we assume that only a small fraction ($\sim 10^{-3}$) of binary coalescence events will have GRB or other EM afterglows that will help us to locate the source on the sky and measure its redshift z. Eventually, we will be limited by the number of short-hard GRBs observed by detectors that might be operating at the time. As a conservative estimate, we assume that about $1,000$ BNS and NSBH mergers will have EM counterparts over a three-year period. For definiteness we consider only BNS mergers and take these to have component masses of $(1.4, 1.4)M_\odot$.

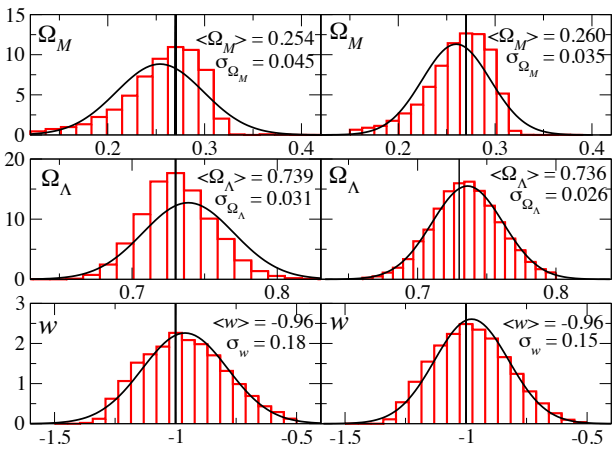

Figure 31: The distribution of errors in $\Omega_{\rm M}$, Ω_Λ and w obtained by fitting 5,190 realizations of a catalogue of BNS merger events to a cosmological model of the type given in Eq. (21), with three free parameters. The fractional 1-σ width of the distributions $\sigma_{\Omega_{\rm M}}/\Omega_{\rm M}$, $\sigma_{\Omega_\Lambda}/\Omega_\Lambda$, and $\sigma_w/|w|$, are 18%, 4.2% and 18% (with weak lensing errors in $D_{\rm L}$, left panels) and 14%, 3.5% and 15% (if weak lensing errors can be corrected, right panels).

How well would we measure cosmological parameters with a catalogue of such sources? The detailed procedure followed to evaluate this is given in Box 2.8.

The distributions $\mathcal{P}$ of the cosmological parameters obtained from a three year catalogue of binary neutron star inspirals is shown in Fig. 31 assuming ($\Omega_{\rm M}$, Ω_Λ, w) are all unknown, in the left panel of Fig. 32 assuming Ω_Λ is unknown (say from other cosmological probes) and that ($\Omega_{\rm M}$, w) are unknown and in the right panel of Fig. 32 assuming that w is the only unknown parameter.

Box 2.8: ET for cosmography

To evaluate how well ET can measure various cosmological parameters we simulated 5,190 realizations of a catalogue of BNS sources that ET is expected to detect. Each catalogue contained 1,000 BNS coalescences with known redshift and sky location. The luminosity distance to the sources is subject to statistical errors from GW observation and weak lensing that the waves suffer when propogating through the clumpy dark matter distribution in the inter-galactic medium.

We assumed that the sources were in the redshift range $0 \leq z \leq 3.5$, distributed uniformly (i.e. with constant comoving number density) throughout this redshift range. The luminosity distance to the source was computed by assuming an FLRW cosmological model with $H_0 = 70\,\mathrm{km\,s^{-1}\,Mpc^{-1}}$, $\Omega_\mathrm{M} = 0.27$, $\Omega_\Lambda = 0.73$, and $w = -1$, but the *measured* distance was drawn from a Gaussian distribution whose width, σ_{D_L}, was determined by the quadrature sum of the errors due to weak lensing and GW observation. The weak lensing error in D_L was assumed to be 5% at $z = 1$ and linearly extrapolated to other redshifts.

The GW observational error was estimated from the covariance matrix C_{km} of the five-dimensional parameter space of the unknown signal parameters $p_k = (M, \nu, t_0, \Phi_0, D_\mathrm{L})$:

$$C_{km} = \Lambda^{-1}_{km}, \quad \Lambda_{km} = \langle h_k,\, h_m \rangle\,, \quad h_k = \frac{\partial h}{\partial p_k}. \tag{28}$$

Here the angular brackets denote the scalar product, which, for any two functions $a(t)$ and $b(t)$, is defined as

$$\langle a,\, b \rangle = 4\Re \int_0^\infty \frac{\mathrm{d}f}{S_h(f)} A(f)\, B^*(f) \tag{29}$$

where $A(f)$ and $B(f)$ are the Fourier transforms of the functions $a(t)$ and $b(t)$, respectively, and $S_h(f)$ is the ET noise power spectral density.

Since GRBs are expected to be strongly beamed, we assumed the angles (ι, ψ) defining the unit normal to the plane of the inspiral to be known. This assumption is well-justified because even if the opening angle of a GRB beam is as large as 40°, the unit normal to the plane of the inspiral would still be confined to only 3% of the area of a unit sphere. Averaging errors over (ι, ψ) with the constraint $\iota < 20°$ would then be little different from taking $\iota = 0°$. We did, however, average the errors over the sky position angles (θ, ϕ).

We fitted each realization of the source catalogue to the cosmological model given in Eq. (21), using the Levenberg-Marquardt algorithm [187, 188], in order to find a set of best fit parameters. Assuming that H_0 is known accurately (see discussion in the text as to how ET will measure H_0 to better than 1% from low redshift sources), the algorithm gave the best fit parameters in $(\Omega_\mathrm{M},\, \Omega_\Lambda,\, w)$ for each of the 5,190 realizations. The distributions $\mathcal{P}$ of the parameters obtained are shown in Fig. 31, where the vertical line is at the true value of the relevant parameter (see text for a discussion of the results).

The relative 1-σ errors in Ω_Λ, Ω_M and w, are 4.2%, 18% and 18% (with weak lensing, left panels) and 3.5%, 14% and 15% (with weak lensing errors corrected, right panels). Although $\mathcal{P}(w)$ is quite symmetric, $\mathcal{P}(\Omega_\mathrm{M})$ and $\mathcal{P}(\Omega_\Lambda)$ are both skewed and their mean values are slightly off the true values. However, the medians are mostly coincident with the true values.

In addition to H_0 if Ω_Λ is also known (or, equivalently, if $\Omega_\mathrm{M} + \Omega_\Lambda = 1$), then one can estimate the pair $(\Omega_\mathrm{M},\, w)$ more accurately, with the distributions as shown in Fig. 31 with greatly reduced skewness and 1-σ errors in Ω_M and w, of 9.4% and 7.6% (with weak lensing) and 8.1% and 6.6% (with lensing errors corrected). Finally, if w is the only parameter unknown, it can be measured to an even greater accuracy as shown in Fig. 32 with 1-σ errors of 1.4% (with weak lensing) and 1.0% (with lensing errors corrected).

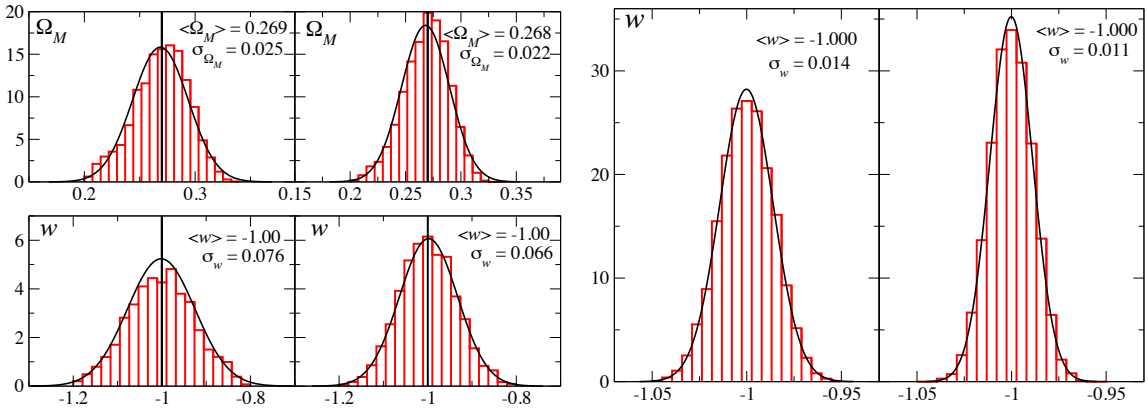

Figure 32: Same as the Fig. 31 except that one or more of the cosmological parameters are assumed to be known. The plot on the left assumes that Ω_Λ is known to be $\Omega_\Lambda = 0.73$, and fits the "data" to the model with two free parameters $\Omega_{\rm M}$ and w. The fractional 1-σ widths in the distribution $\sigma_{\Omega_{\rm M}}/\Omega_{\rm M}$ and $\sigma_w/|w|$, are 9.4% and 7.6% (with weak lensing errors in $D_{\rm L}$, left panels) and 8.1% and 6.6% (if weak lensing errors can be corrected, right panels). The plot on the right is the same but assuming that w is the only unknown parameter. The fractional 1-σ width of the distribution $\sigma_w/|w|$ is 1.4% (with weak lensing errors in $D_{\rm L}$, left panel) and 1.1% (if lensing errors can be corrected, right panel).

Effect of unknown orientation and polarization In the previous section, our study neglected the effect of different inclinations of the orbit to the line-of-sight. Varying the inclination has two distinct effects. On the one hand, as noted in Ref. [189], due to the strong correlation between the luminosity distance and inclination, the estimation of luminosity distance could get corrupted. On the other hand, binaries that are not face-on are, in general, elliptically polarized and have a non-zero polarization angle. Since polarization angle is correlated with the luminosity distance, there could be further degradation in the estimation of the luminosity distance.

In this section we will relax the condition that the inclination of the orbit is precisely known. However, we shall restrict the inclination of the binary's angular momentum with the line-of-sight to be within 20 degrees. We shall also assume that the radiation is described by an arbitrary polarization angle. Since the sky position is still assumed known, this gives us a 7×7 covariance matrix with a revised estimate for the error in the luminosity distance. As before, we construct catalogues of binary coalescence events but with the luminosity distance now drawn from a Gaussian distribution with revised widths. We fit each catalogue to a cosmological model and then repeat the exercise 5,190 times to estimate the accuracy with which the various cosmological parameters can be measured.

As expected, the parameter measurements get worse if we assume two or more parameters to be unknown. For instance, errors in the estimation of $\Omega_{\rm M}$, Ω_Λ and w, are, respectively, $> 100\%$, 24% and 47% with weak lensing and $> 100\%$, 21% and 43%, if weak lensing can be corrected. Similarly, if Ω_Λ is assumed to be known then the errors in the estimation of $\Omega_{\rm M}$ and w are, respectively, 12% and 9.5% if weak lensing is uncorrected for and 11% and 9.2% if weak lensing can be corrected. However, the results are more or less the same if the DE EoS parameter w is the only unknown quantity. Even when the inclination and polarization angles are taken as free parameters, but inclination angle is restricted to within 20 degrees, the error in the estimation of w is 1.4% with weak lensing and 1.3% if weak lensing can be corrected.

Variation of dark energy with redshift We have seen that the Hubble constant H_0 can be measured with high accuracy using low-redshift sources, after which parameters like $\Omega_{\rm M}$, Ω_Λ, and the DE EoS parameter w can be determined, where so far we have assumed that the latter is constant. One could go one step further and use prior information from *e.g.* future Planck CMB measurements to get high-accuracy values for $(\Omega_{\rm M}, \Omega_\Lambda)$, and then measure the variation of w with time (see Box 2.9). Since CMB data would have a very wide prior on w and its first time derivative, this would constitute an independent measurement of the latter variables. Allowing for GRB beaming angles of 40°, following the procedure described in Appendix A.4 one then finds

$\Delta w_0 = 0.096$ and $\Delta w_a = 0.30$, which is comparable to projections from both the SNAP Type Ia supernova and the JDEM Baryon Acoustic Oscillations projects [190]; see Fig. 33. However, we stress that GW standard sirens are *self-calibrating* and have no dependence on a cosmic distance ladder.

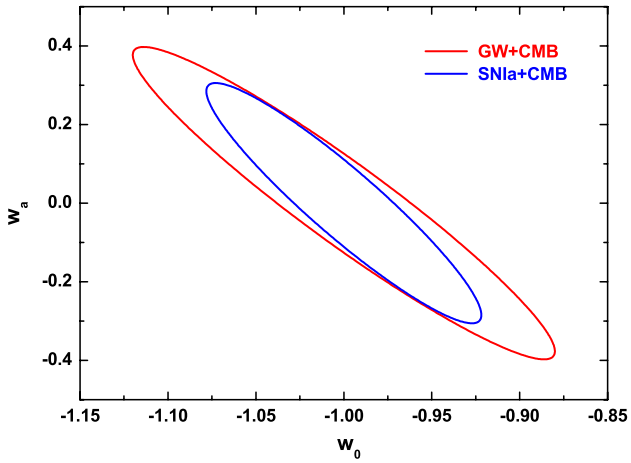

Figure 33: The accuracy in (w_0, w_a) obtained from ET observations of binary neutron stars using projected Planck CMB accuracies as a prior for the other cosmological parameters, compared to the expected accuracies from SN Ia results.

Box 2.9: Variation of w with redshift

Rather than looking at the variation of the dark energy equation of state parameter w with time, it is more convenient to consider variation with the scale factor or redshift:

$$\begin{aligned} w(z) &= w_0 + w_a(1-a) + \mathcal{O}\left[(1-a)^2\right] \\ &\simeq w_0 + w_a \frac{z}{1+z}. \end{aligned} \tag{30}$$

Since here we are mostly interested in the later stages of the universe's evolution, higher order terms will be ignored. With a redshift dependent $w(z)$, the Hubble parameter as a function of redshift becomes

$$H(z) = H_0 \left[\Omega_{\rm M}(1+z)^3 + \Omega_\Lambda (1+z)^{3(1+w_0+w_a)} e^{-3w_a z/(1+z)}\right], \tag{31}$$

and luminosity distance is still related to the Hubble parameter as

$$D_{\rm L}(z) = c(1+z)\int_0^z \frac{dz'}{H(z')}. \tag{32}$$

With a catalogue of sources with accurately measured luminosity distances $D_{\rm L}$ and corresponding redshifts, the above relation can be used to deduce w_0 and w_1. See Appendix A.4 for a discussion of how the errors are computed.

Open problems The results of our simple simulation are quite encouraging but further work is needed to confirm the usefulness of GW standard sirens in precision cosmology. Let us mention some that are currently being purused. Spins of component stars can be legitimately neglected in the case of neutron stars (and hence in BNS) but not for black holes and the modulation in the signal caused by the spin of the black hole can improve parameter accuracies. We assumed, for simplicity, that all our systems are BNS systems with masses $(1.4, 1.4)M_\odot$. In reality, the catalogue will contain a population consisting of a range of NS and BH masses. A

more realistic Monte Carlo simulation would draw binaries from the expected population rather than the same system, some of which (more massive and/or equal-mass systems) would lead to better, but others to worsened, parameter accuracies. The signal contains additional features, such as other harmonics of the orbital frequency than the second harmonic considered in this work and the merger and ringdown signals. Both of these are important for heavier systems and could potentially reduce the errors. These factors are currently being taken into account to get a more reliable estimation of the usefulness of ET in precision cosmography.

2.6.2 Cosmological evolution of compact object populations

The calculation of the coalescence rate as a function of the redshift must take into account the following factors: the star formation rate history $SFR(z)$, the binary fraction $f_b(z)$, the formation efficiency of a given type of binary, i.e. the fraction of number of binaries that lead to formation of coalescing compact object binary, and their distribution of merger times. These quantities may depend on redshift since the stellar populations evolve with cosmic time. Let us examine the effects of evolution of each of these factors.

The star formation rate is known to increase strongly to the redshift $z = 2$, and there is a debate about its behavior for higher redshifts. At redshift $z = 2$, the star formation is estimated to be a factor of 10 larger [191] than the present value at $z = 0$.

The distribution of merger times can be estimated either by analyzing the present population of compact binary objects or by involving the population synthesis. The first approach is limited to dealing with BNSs, and suffers from small number statistics. The second involves several uncertainties due to parametrization of binary evolution. However the two approaches yield similar results. The distribution of merger times for BNSs can be well approximated by a distribution $\propto t^{-1}$. The lower cutoff for the BNS systems lies somewhere between 10 and 100 Myrs. The population synthesis leads to similar conclusions about the distribution of merger times for NSBH and BBH systems, however the low time cutoff may probably lie higher.

The main factor that may affect the evolution of the binaries as a function of redshift are the changes in the distribution of metallicity. Metallicity strongly affects the mass loss rate in stars, and hence has a strong influence on the mass spectrum of compact objects. The lower the metallicity, the higher the maximum mass of a BH that may be formed in the course of stellar evolution. This leads to a stabilization of mass transfers and therefore to an increase in the formation rate of compact object binaries.

Taking together the above factors we see that there are several reasons why the coalescence rate should increase strongly as we go to redshifts of $z = 1$–2. First, the local star formation rate increases and the overall amount of binary formation is larger. Second, the typical delay times for the BNS systems are low therefore their merger rate density will roughly follow that of the SFR. In the case of NSBH or BBH systems the typical delay times between formation and coalescence may be as large as 1–3 Gyrs. This delays the peak of coalescence rate density with respect to the star formation rate. Thus, the delays are significant but not crucial. Third, the metallicity evolution may lead to higher compact object formation rate for high redshifts, and the formation of larger number of massive BBH systems.

This consideration can be put into detailed numerical codes to yield predictions about the rates. However, even without such strong numerical support one can readily estimate with a "back of the envelope calculation" that the ratio of the coalescence rate (per unit volume per unit time) to the local one should be at least a few. The local coalescence rate can only be estimated with observations, since neither the observational not the indirect approach mentioned earlier can yield an estimate of the rate with an accuracy better that an order of magnitude.

The Einstein Telescope will provide a large sample of coalescences with the precisely measured masses and redshifts. This will be an extremely valuable tool for analysis of the cosmic compact object formation history. The measurement of their masses will yield information on the metallicity evolution as well as the evolution of the most massive stars. The Einstein telescope will yield a cosmic compact object census up to redshift $z = 2$, and will yield information about BHs and NSs formed at even earlier epochs because of the delays between formation and coalescence.

There are two distinct routes to form BH binaries. The first, conventional way, is to start with a binary system of two main sequence stars and trace their evolution. There are several big uncertainties in this process. The first one is the initial mass ratio function: what is the distribution of the mass ratio in the binary of two main sequence stars, how does it depend on the metallicity and spectral type. The second, and probably the biggest uncertainty, is related to the "common envelope" evolution, where the NS (or BH) and the helium core are exposed and evolve in the gaseous environment of the star. In this stage the NS or BH could merge with the helium core and not form a binary. The third uncertainty is related to the direction and magnitude of the kick exerted on the newly born BH from the asymmetric supernova explosion. All the above is reflected in the uncertainties on the rate of such binaries [192, 193].

The BH binaries could also be formed in a dense environment such as galactic nuclei. In galaxies with SMBHs ($M < 10^7\,M_\odot$), the relaxation time is less than a Hubble time, and a steep cusp of stars and stellar mass BHs can be formed. BHs, as massive, compact objects, will segregate into the central ≈ 1 pc region. Other dense regions include massive globular clusters and nuclear star clusters in the centres of low-mass galaxies which may not have SMBH. The densities in those regions are high enough to have multiple encounters, with formation and/or hardening of BH binaries.

2.6.3 Reconstruction of the evolution of compact binary coalescence rates by ET

The rate at which NSs and BHs coalesce at different redshifts can provide indirect but extremely valuable insights into the star formation rate (SFR). ET will be able to distinguish between coalescence rate predictions from different SFR models and hence provide indirect evidence for history of star formation at high redshifts. Considering that BNS coalescences are expected to be the most abundant, they are the best "trackers" of SFR, and these are the events we will focus on.

The rate (per unit time and per unit comoving volume) at which BNS systems are observed to coalesce at redshift z in our frame, denoted $\dot{\rho}_c^0(z)$, can be written as [29]

$$\dot{\rho}_c^0(z) = \dot{\rho}_c^0(0)\frac{\dot{\rho}_{*,c}(z)}{\dot{\rho}_{*,c}(0)}. \tag{33}$$

Here $\dot{\rho}_c^0(0)$ is the coalescence rate in our frame at the current epoch, and $\dot{\rho}_{*,c}$ relates the past star formation rate to the rate of coalescence:

$$\dot{\rho}_{*,c}(z) = \int \frac{\dot{\rho}_*(z_f)}{(1+z_f)} P(t_d) dt_d, \tag{34}$$

where $\dot{\rho}_*$ is the SFR itself, z_f is the redshift at which the *progenitor binary forms,* z is the redshift at which the *compact binary coalesces,*. These redshifts are connected by the *delay time* t_d which is the sum of the time from initial binary formation to evolution into compact binary, plus the merging time τ_m by emission of gravitational waves. The delay is also the difference in lookback times between z_f and z:

$$t_d = t_{\rm LB}(z_f) - t_{\rm LB}(z) = \frac{1}{H_0}\int_z^{z_f} \frac{dz'}{(1+z')H(z')} \tag{35}$$

Its probability distribution $P(t_d)$ has been estimated as

$$P(t_d) \propto \frac{1}{t_d} \qquad \text{for} \quad t_d > \tau_0, \tag{36}$$

where τ_0 is some minimum delay time. Thus, the limits in the integral (33) vary from τ_0 to ∞, with no contribution from the upper limit (binaries that take infinitely long to coalesce contribute nothing to the rate). As in Regimbau and Hughes, [29] we assume $\tau_0 \sim 20$ Myr, corresponding roughly to the time it takes for massive binaries to evolve into two neutron stars. The coalescence rate per unit redshift as observed in our local Universe is found by multiplying $\dot{\rho}_c^0$ by the gradient of comoving volume:

$$\frac{dR_c^0}{dz} = \dot{\rho}_c^0(z)\frac{dV_c}{dz}(z). \tag{37}$$

We may now ask how well ET will be able to discriminate between different SFR models $\dot{\rho}_*(z)$ through differences in the resulting observed BNS coalescence rates $\dot{\rho}_c^0(z)$. To this end we consider four different models:

- Hopkins and Beacom [28]: This model is based on an observational compilation, placing lower bounds on SFR using the evolution of stellar mass density, metal mass density, and supernova rate density, and an upper bound using Super-Kamiokande results for the electron antineutrino flux from core-collapse supernovae;
- Nagamine et al. [194]: This is an approach comparing and combining results from direct observations, a model using local fossil evidence at $z \sim 0$, and theoretical *ab initio* models;
- Fardal et al. [195]: Fardal et al. use a model involving a new proposal for the initial mass function with a view on reconciling SFR predictions with the total extragalactic background radiation;
- Wilkins et al. [196]: This model is based on stellar mass density measurements together with a new ansatz for the initial mass function.

The merger rates predicted by these models are plotted in Fig. 34.

Box 2.10: History of star formation rate from binary coalescence rate

To evaluate how well ET can measure the merger rate of compact binaries we start offf with a catalogue of BNS coalescences as described in Box 2.8. The luminosity distances measured from the GW signal, $\hat{D}_{\rm L}$, will be different from the true distance due to (i) the noise in the detector, and (ii) (de)magnification as a result of weak gravitational lensing. Thus, with each source we associate a "measured" luminosity distance

$$\hat{D}_{\rm L}(z) = D_{\rm L}(z) + \delta D_{\rm L}(z), \tag{38}$$

where $\delta D_{\rm L}(z)$ is drawn at random from a Gaussian distribution with a spread given by

$$\Delta D_{\rm L} = (\sigma_{\rm ET}^2 + \sigma_{\rm WL}^2)^{1/2}. \tag{39}$$

We treat the errors $\sigma_{\rm ET}$ and $\sigma_{\rm WL}$ in the same way as in Box 2.8. Using the fiducial cosmological model, the measured luminosity distances $\hat{D}_{\rm L}(z)$ can be inverted to obtain measured redshifts $\hat{z}$ by inverting Eq. (38). In doing so we choose our fiducial cosmological model such that $H_0 = 70\,{\rm kms}^{-1}{\rm Mpc}^{-1}$, $\Omega_{\rm M} = 0.27$, $\Omega_\Lambda = 0.73$, and $w = -1$. The recovered redshifts are then binned to obtain a recovered rate distribution $d\hat{R}_c^0/dz$. By doing this for a large number of different simulated catalogues (say, 1000 catalogues), one can compute an average and a 1-sigma spread for the number of sources in each recovered redshift bin.

To check how well ET will be able to distinguish between different coalescence rate predictions, we can fold in the anticipated efficiency $\epsilon(z)$, i.e. the fraction of coalescences at a given redshift that survive the SNR cut $\rho > 8$. The efficiency is essentially 100% up to $z \simeq 0.7$, after which it starts to drop rather quickly. Beyond $z \simeq 3.5$ no signals can be seen even when optimally positioned and oriented. The efficiency can be folded into the recovered rate distribution:

$$\left[\frac{dR_c^0(z)}{dz}\right]_{\rm recovered} = \epsilon(z)^{-1}\frac{dR_c^0(z)}{dz}, \tag{40}$$

where dR_c'/dz is the distribution inferred from binning the measured redshifts.

Box 2.10 discusses how ET could be used to measure the merger rate as a function of redshift. In a nutshell, simulated BNS sources are placed according to the coalescence rates $\dot{\rho}_c^0(z)$ inferred from the four models using their proposed $\dot{\rho}_*(z)$, with a minimum delay time $\tau_0 = 20$ Myr. Sources are positioned uniformly in the sky; an SNR threshold is imposed such that a source is disregarded unless its SNR is $\rho > 8$. the coalescence rate at the current epoch was (very) conservatively set to be $\dot{\rho}_c^0 = 0.03\,{\rm Mpc}^{-3}{\rm Myr}^{-1}$, in which case between $\sim$ 150,000 and

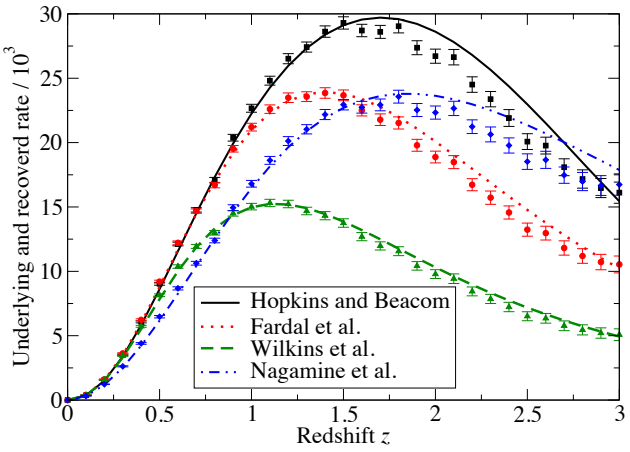

Figure 34: True and recovered coalescence rates (taking into account detection efficiency) for the models of Hopkins and Beacom [28] (solid black line), Fardal et al. [195] (dotted red line), Wilkins et al. [196] (dashed green line), and Nagamine et al. [194] (dot-dot-dashed blue line). The lines are the true rates, the symbols give the number of measured coalescences in a redshift bin, error bars denoting a 2-sigma spread in recovered rates.

$\sim$ 275,000 sources survive the SNR cut, depending on the SFR model. Note that this local coalescence rate will most likely already be measured by Advanced LIGO and Virgo, so that we may consider it a known quantity in the context of ET.

Fig. 34 shows both the underlying rates $dR_c^0(z)/dz$ and the recovered rates, with 2-sigma spreads, for the four SFR models considered. First we note some systematic effects due to uncertainties in the redshift measurements:

- At small redshifts ($z \lesssim 1.5$), the recovered rate distribution is shifted very slightly to the left with respect to the underlying distribution. This is because of higher-redshift events ending up in lower redshift bins due to measurement errors. The effect is not compensated by lower redshift events ending up in higher redshift bins, because at lower redshifts the spread in measured redshift is smaller.
- At intermediate redshifts ($1.5 \lesssim 3$) the true coalescence rate is being underestimated (despite having folded in efficiency loss) because of events ending up in both higher and lower measured redshift bins;
- Beyond $z \simeq 3.5$ the recovered rate diverges, because there are still *measured* redshift values there, but the efficiency $\epsilon(z) \to 0$.

We see that ET can easily distinguish between the four models we took from recent literature. Generally, two models for BNS coalescence rates can be distinguished from each other if over at least one $\Delta z = 0.1$ redshift bin at $z \lesssim 1.5$, the number of sources in the bin differs by more than a few percent.

2.6.4 Intermediate mass black holes

The existence of IMBHs with masses in the range $10^2 - 10^4\, M_\odot$ has not yet been corroborated observationally, but these objects are of high interest for astrophysics. Our understanding of the formation and evolution of supermassive BH, as well as galaxy evolution modeling and cosmography would dramatically change if an IMBH were to be observed. From the point of view of traditional electromagnetic astronomy, which relies on the monitoring of stellar kinematics, the direct detection of an IMBH seems to be rather far in the future. However, the prospect of the detection and characterization of an IMBH has good chances in lower-frequency GW astrophysics, in particular with ET. The detection and characterization of a binary containing an IMBH would corroborate the existence of such systems and provide a robust test of general relativity through tests of the BH uniqueness theorem (see subsection 2.4.6).

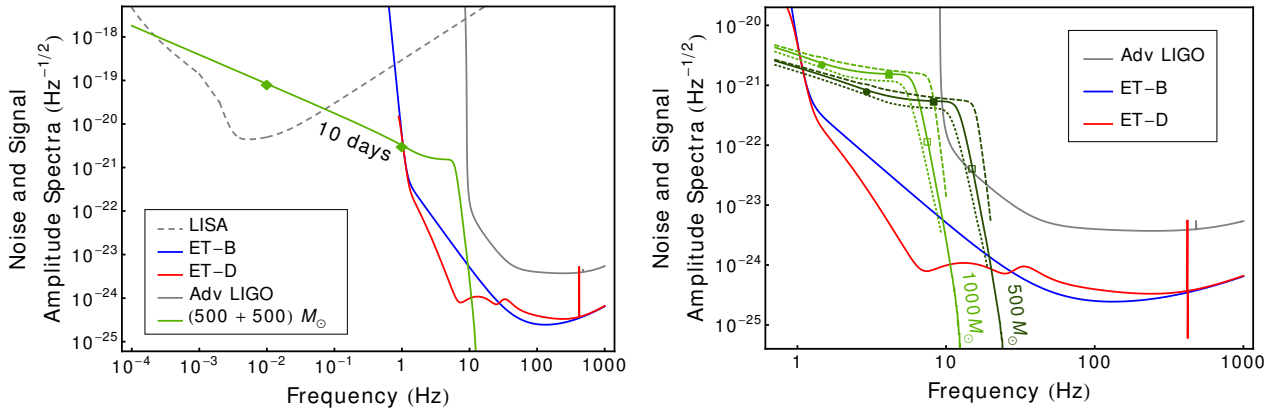

Figure 35: Amplitude spectra of IMBH binaries compared to ET sensitivity curves. Left: Different aspects of the inspiral, merger and ringdown signal from a binary IMBH with *intrinsic* masses $(500, 500)\,M_\odot$ at $z = 2$ can be studied as the system passes in 10 days from the LISA band into the ET band. Observed masses are redshifted by a factor $(1 + z)$ compared to physical masses, so this system would be seen to consist of two IMBHs each of mass $1500\,M_\odot$. Right: Signals from IMBH binaries of intrinsic total mass as labelled by the curves, all at a redshift of $z = 2$ and so have observed total mass that is larger by a factor 3. The solid lines are for equal mass, non-spinning binaries, dashed lines for binaries with equal masses and dimensionless spins $\chi = 0.75$ and the dotted lines for non-spinning binaries with mass ratio $m_1/m_2 = 3$. ET's better low frequency sensitivity is key to observing the intermediate BHs which might have triggered formation of galaxies and large scale structure. ET should be able to see 100-1000 $M_\odot$ binary IMBH mergers at redshifts $z \sim$ 12-3 (see Fig. 18).

Signals from IMBH binaries can start in the band of LISA, and sweep through to the ET band, allowing us to observe different aspects of the coalescence event, as illustrated in Fig. 35. For ET, a lower cut-off frequency of 1 Hz was assumed.

2.6.5 Black hole seeds and galaxy formation

It is widely accepted that the massive black holes (MBHs) found in the centres of many galaxies grow from initial seeds through the processes of accretion and following mergers between their host DM halos. However, little is known about the seeds from which these BHs grow. Open questions include: What are their masses? Where are they? How and when did they form? Current observations are consistent with both *light seed* scenarios, in which $\sim 100 M_\odot$ BH seeds form at redshift $z \approx 20$ from the collapse of Population III stars [197, 198], and *heavy seed* scenarios, in which BH of mass $\sim 10^5\,M_\odot$ form from direct collapse of dust clouds [199, 200]. Mergers between MBHs in merging DM halos will generate GWs. These are a major source for LISA [201], but LISA will only see mergers with total mass $\gtrsim 10^3\,M_\odot$. LISA can therefore probe BH seeds only in the heavy seed scenario and does not have the power to discriminate between the light and heavy scenarios.

ET will have sensitivity in the 1–50 Hz band in which GWs from mergers involving $\sim$ 10–100 $M_\odot$ BHs will lie. It will therefore provide complementary information to LISA and could directly observe the first epoch of mergers between light seeds. Present estimates, based on Monte Carlo simulations of galaxy merger trees [202, 203], suggest ET could detect between a few and a few tens of seed BH merger events over three years of operation [204]. Several of these events will be at high redshift, $z \sim 5$, by which time it is unlikely that $100\,M_\odot$ BHs could have formed by other routes. ET and LISA in conjunction probe the whole merger history of DM halos containing BHs in the 10–$10^6\,M_\odot$ range, which will provide detailed information on the hierarchical assembly of galaxies. ET is able to measure the distance to a GW source, with one additional non-colocated interferometer, to $\sim 40\%$ precision and the redshifted total mass of the system to $\lesssim 1\%$. Using a concordance cosmology, this distance estimate can be used to deduce the redshift with comparable accuracy and so it should be possible to say that the $z \approx 5$ events are of *low mass* and at *high redshift*, and therefore are convincing

candidates as Population III seed mergers.

Just one detection by ET will rule out the heavy seed model. With several detections, we will be able to make statements about Population III seed BH properties, such as their mass distribution, their early accretion history etc. [204]. These observations cannot be made be any other existing or proposed detector — it is science that is unique to ET. Such observations will be vital to our understanding of the assembly of structure in the Universe, and of the close link between BHs residing in the centres of galaxies and their hosts [197].

2.6.6 Primordial gravitational waves

The cosmological stochastic background of GWs [205] is a unique window on the very early Universe, because gravitational radiation propagates uninterrupted to us from cosmic events at the highest temperatures and densities, potentially up to the GUT scale of 10^{16} GeV. The detection of any such background would have huge consequences for fundamental physics, possibly giving us direct indications of inflation, phase transitions or formation of topological defects. A stochastic confusion background of GW from very distant astrophysical sources may also contain significant information on the populations and evolution of the sources. As shown in Figures 36 and 37, many types of cosmological stochastic background are potentially above the ET sensitivity curve. It may also be possible to extract information about the cosmological events that produced GW if an observed spectrum has some characteristic shape.

Primordial GW backgrounds are broadly of two types: wide-band, where $\Omega_{\rm gw}(f)$ is approximately constant over a large range of frequency; and peaked, where $\Omega_{\rm gw}$ varies strongly over f reaching a maximum at $f_{\rm peak}$. Wide-band sources are processes that extend over a large range of the cosmological scale factor $a(t)$, such as inflation and cosmic string evolution. Both these sources depend on unknown fundamental physics, and also have an approximate scaling symmetry. The detectability of a "flat" background spectrum depends only on the value of $\Omega_{\rm gw}$ at a nominal frequency of 10 Hz.

Wide-band sources: inflation and strings There are many models of inflation, but they share a few essential features: exponentially expanding the scale factor in a short time; sourcing primordial density perturbations with amplitude $\mathcal{O}(10^{-5})$ and an approximately Harrison-Zeldovich (scalar spectral index $n_s \simeq 1$) spectrum; and reheating the Universe to at least the temperature required for primordial nucleosynthesis (order of 10 MeV).

Tensor perturbations generated during inflation can be described by an amplitude and spectral index n_t. Since their evolution over cosmological time is similar to scalar perturbations, the *tensor-to-scalar ratio* r is a useful measure. This ratio is sensitive to the "energy scale of inflation" $V^{1/4}$ via an approximate relation $V^{1/4} \simeq (1.8 \times 10^{16}\,\text{GeV})(r/0.07)^{1/4}$ [209]. In single-field models, the value of r also indicates the minimum distance the field travels during inflation in Planck mass units via $\Delta\phi/M_P \simeq 0.46(r/0.07)^{1/2}$.

For a scale-invariant spectrum ($n_s = 1$, $n_t = 0$) the CMB determination of the scalar amplitude $S \sim 10^{-10}$ together with the current bound $r \lesssim 0.2$ translates to a very small value $\Omega_{\rm gw}(f) \lesssim 10^{-15}$ for all frequencies accessible to interferometers [210, 211]. However, since the CMB bounds apply at $f \sim 10^{-18}$ Hz, a positive spectral index n_t could change the picture [212]: we have $\Omega_{\rm gw}(10\,\text{Hz}) = (10^{19})^{\bar{n}_t}\Omega_{\rm gw}(10^{-18}\,\text{Hz})$, where $\bar{n}_t$ is the averaged spectral index between these two frequencies [213]. In Fig. 36 we plot the possible signal for $r = 0.15$, $n_t = 0.2$. It should however be noted that such optimistic values are not typical of field theory models of inflation.

Alternatives to inflation Possible alternatives to exponential inflation as a source of primordial perturbations are the 'pre-big-bang' scenario in string cosmology and the "ekpyrotic" and "cyclic" models involving a contracting phase and subsequent brane collision. For both, it is currently debated whether a realistic spectrum of scalar density perturbations can be achieved. The tensor or GW amplitude is known to be undetectably small in the "cyclic" model [214].

A potentially more interesting case arises from pre-big-bang scenarios in string cosmology [215, 216]. According to these models, the standard radiation-dominated and matter-dominated eras were preceded by phases in which

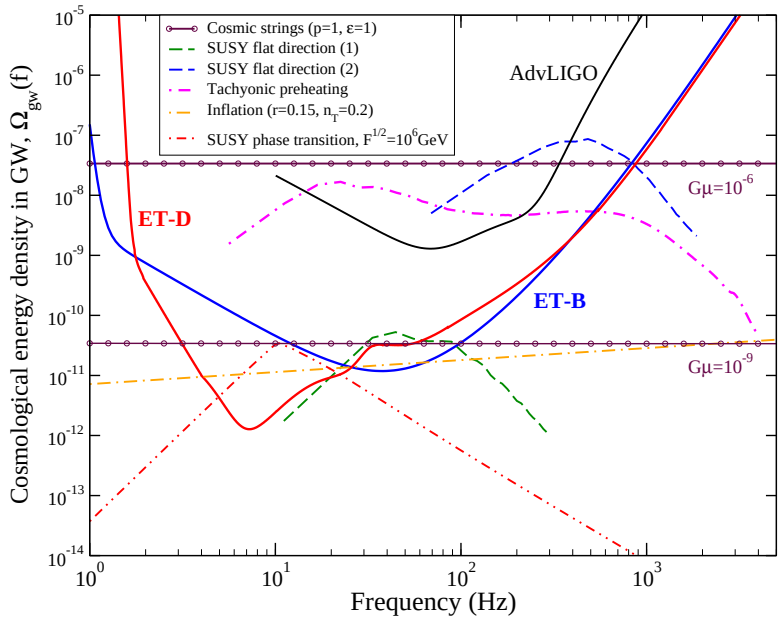

Figure 36: Possible backgrounds of primordial stochastic GW at Advanced LIGO and ET. The sensitivity curves correspond to an observation time of 1 year, S/N of 2.56, and co-located but not necessarily coaligned detectors (see end of Section 2.3.4). Models and parameter values are described in the main text. Data for tachyonic preheating and decay of SUSY flat directions were provided by J.-F. Dufaux; for phase transitions between metastable SUSY vacua, by N. J. Craig; the cosmic string GW spectra are based on a calculation of X. Siemens *et al.* [206].

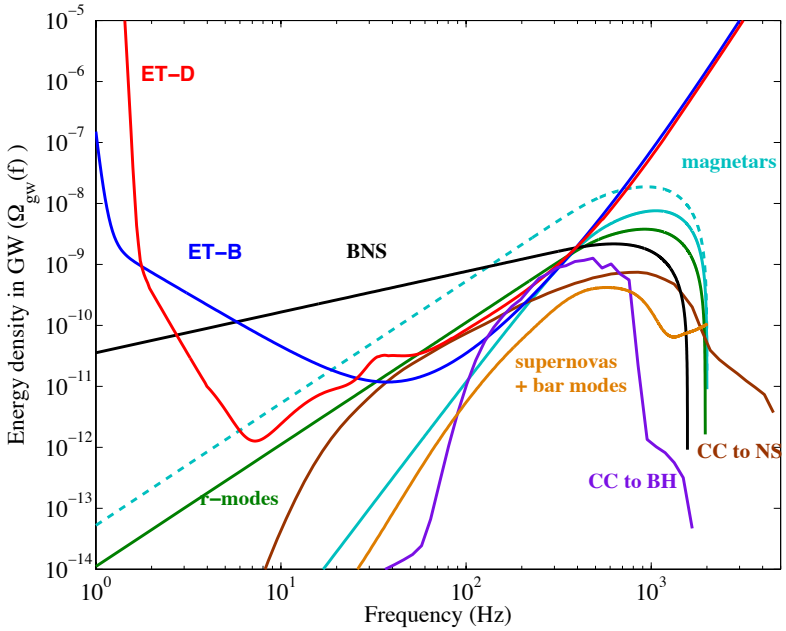

Figure 37: Energy density in GW due to background created by astronomical sources: magnetars (minimal detectable prediction (ET-D) in continuous cyan and model when the spin-down is purely gravitational in dashed cyan), binary neutron stars in black, dynamical bar modes in proto NS in orange, r-modes assuming that 1% of newborn neutron stars cross the instability window in green, Pop II core collapse to NS (model of [207]) in brown and to BH (model D5a of [208]) in purple. ET sensitivity curves are as in Fig. 36.

the Universe was first large and shrinking (inflaton phase) and then characterized by a high curvature (stringy phase). The spectrum of primordial GW from these models is strongly rising at high frequencies, potentially giving a detectable background: see Appendix A.5.1. However, attempts to reach a more realistic spectrum of scalar perturbations by considering specific forms of pre-big-bang cosmological evolution may lead to much smaller values of $\Omega_{\rm gw}$ at frequencies accessible to ground-based detectors [217]. The spectrum and amplitude of primordial GW in such scenarios is strongly model-dependent.

Cosmic string evolution Cosmic strings (see *e.g.* [218]) in field theory are extended topological defects formed in phase transitions. Fundamental strings may also result from cosmological evolution, for instance in "brane inflation" models [219] strings are formed at a brane collision near the end of inflation [220]. After formation, strings evolve by reconnection and oscillation of the resulting loops, which emit gravitational radiation (and possibly other quanta) and gradually shrink. The evolution is believed to have a scaling property and produces an almost flat spectrum in $\Omega_{\rm gw}$ across frequencies accessible to interferometers. The amplitude of such a flat spectrum, if detected, can be related to fundamental properties of the string networks (Appendix A.5.2).

Peaked sources: phase transitions and reheating Peaked sources of stochastic background result from an event localized in cosmic time, typically a phase transition or reheating after inflation. There are many candidate models of high-energy physics in which such events would occur. Their detectability depends on the value of $f_{\rm peak}$ as well as the amplitude $\Omega_{\rm gw}(f_{\rm peak})$; either side of $f_{\rm peak}$ the spectrum will decline as a power law [221]. The present-day frequency f is related to the frequency at the time of production f_* (see *e.g.* [222]) via

$$f = f_* \frac{a_*}{a_0} \approx (6 \times 10^{-8}\,{\rm Hz}) \frac{f_*}{H_*} \frac{T_*}{1\,{\rm GeV}} \left(\frac{g_*}{100}\right), \tag{41}$$

where a is the scale factor, T the temperature, g the number of relativistic degrees of freedom and H the Hubble rate, the suffixes "0" and "$*$" denoting the present time and time of production respectively.

Phase transitions and colliding bubbles Phase transitions are generic events in the evolution of the early Universe in many theories of high energy physics; for instance, the Standard Model of weak and electromagnetic interactions undergoes a phase transition at temperatures of order 100 GeV, when the Higgs field obtains a stable nonzero value. First-order phase transitions proceed by the nucleation of spherical bubbles in a "false vacuum" with latent heat (energy density) ϵ at a temperature T_*. The bubbles grow rapidly and may collide; after collision the bubble walls have a nonzero, rapidly-varying quadrupole moment and radiate GWs. In the latter stages of the transition, GWs may also be sourced by turbulence [223] as the energy difference ϵ is converted into heat. An estimate of the resulting spectrum is given in Appendix A.5.3.

The electroweak phase transition with $T_* \sim 100\,{\rm GeV}$ is likely to produce GW with frequencies at or below the milliHz range [224]. Similarly in the "Randall-Sundrum 1 model" there may be a first-order phase transition in the warped extra-dimensional geometry at temperatures of around 10^3 GeV [225]. A transition temperature of 10^6–10^7 GeV corresponds to the sensitive range of ET [222]: this could be achieved for phase transitions between metastable SUSY-breaking vacua [226]. In Fig. 36 we plot one scenario with a hidden sector SUSY-breaking scale $\sqrt{F} = 10^6$ GeV.

Reheating and related phenomena At the end of inflation, the Universe is reheated by converting the inflationary energy density into radiation. In the "preheating" scenario the fluctuations of fields coupled to the inflaton grow exponentially rapidly via parametric resonance. The stochastic GW spectrum produced from preheating after chaotic inflation has a peak value $\Omega_{\rm gw}(f_{\rm peak}) \gtrsim 10^{-11}$ [227, 228], however the peak frequency is expected to be well above the range of interferometeric detectors, unless coupling constants in the model take fine-tuned (extremely small) values.

Hybrid inflation is a class of models where the exponential expansion ends due to the presence of a *tachyon* or "Higgs" field whose value sits at the top of a hill-shaped potential. At the end of inflation the field decays with

a characteristic spectrum of fluctuations, giving rise to bubble-like regions which collide, fragment and finally thermalize. The resulting stochastic GW spectrum resembles that of a phase transition and, for certain ranges of parameter values, may be accessible to ET [229, 230]: see Appendix A.5.4.

The rapid decay of "flat directions" (scalar degrees of freedom) in supersymmetric models after inflation is a similar potential source of stochastic GW [231]. The characteristic momentum of fluctuations is of order of the SUSY-breaking mass scale $m \sim$ TeV giving a present-day frequency of 10^2–10^3 Hz. We plot in Fig. 36 the spectra for two choices of parameter values. The lower curve is calculated for $m = 100\,\mathrm{GeV}$, reheating temperature $T_R = 10^8\,\mathrm{GeV}$ and an initial field value $\Phi_i = 2 \times 10^{18}\,\mathrm{GeV}$; for the upper curve, $m = 1\,\mathrm{TeV}$, $T_R \geq 10^9\,\mathrm{GeV}$ and $\Phi_i = 10^{18}\,\mathrm{GeV}$.

Conclusion Many diverse and exciting phenomena in the physics and cosmology of the early Universe may be probed by ET via the stochastic GW background, either almost immediately if a signal is well above the detection threshold, or after an extended observation period. Although many potential sources of primordial GW background involve speculative new physics, if a background is measured it may even be possible to estimate the parameters (*e.g.* mass scales and couplings) of the new physics. For example, observational evidence for a cosmological phase transition, or of the temperature of reheating, would be an epoch-defining result.

2.6.7 Confusion background from cosmological sources

In addition to the primordial stochastic background, a gravitational wave stochastic background of astrophysical origin may have resulted from the superposition of a large number of unresolved sources since the beginning of stellar activity. Its detection would put very strong constraints on the physical properties of compact objects, the initial mass function and/or the star formation history. On the other hand, it could be a "noise" that would mask the stochastic background of cosmological origin. In this section, we present the main astrophysical processes able to produce a stochastic background and discuss their detectability with ET (see [232] for a recent review).

Binary Neutron Stars BNS coalescences, which may radiate about $10^{53}\,\mathrm{erg}$ in the last seconds of their inspiral trajectory, up to $1.4 - 1.6\,\mathrm{kHz}$, may be the most important contribution in the ET frequency range [233–236]. In the quadrupolar approximation, the GW energy spectrum emitted by a binary system which inspirals in a quasi-circular orbit is given by

$$dE_{\mathrm{gw}}/d\nu = \frac{(G\pi)^{2/3}}{3} \frac{m_1 m_2}{(m_1+m_2)^{1/3}} \nu^{-1/3}. \tag{42}$$

Assuming $m_1 = m_2 = 1.4\,\mathrm{M}_\odot$ for the star masses, the energy density increases as $\nu_o^{2/3}$ before it reaches a maximum of $\Omega_{\mathrm{gw}} \sim 2 \times 10^{-9} \dot{\rho}_0$ at around 600 Hz, where $\dot{\rho}_0$ is the local rate in $\mathrm{My}^{-3}\,\mathrm{Mpc}^{-3}$ (about 0.01 times the galactic rate). This means that ET should be able to detect the background from binaries even for the most pessimistic predictions of the coalescence rate, down to $\dot{\rho}_0 \sim 0.015$ (ET-B) or 0.02 (ET-D) (roughly equivalent to a galactic rate of $1.5\,\mathrm{My}^{-1}$), for a signal-to-noise ratio of 3, after one year of observation.

Core collapse New estimates of the GW backgrounds generated by Pop III and Pop II sources have been recently published by [237]. These authors use the results of a numerical simulation by [238] which follows the evolution, metal enrichment and energy deposition of both Population III and Population II stars, to predict the redshift dependence of the formation rate of BH remnants of Population III stars with masses 100–500$M_\odot$ and of NSs (BHs) remnant of Population II stars with masses 8–20$M_\odot$ (20–40$M_\odot$). In order to characterize the single source emission, the most appropriate signals available in the literature have been adopted, namely:

- For Pop III stellar collapse, the waveform recently obtained by [239] using a 2D numerical simulation which follows the entire evolution of a zero metallicity 300$M_\odot$ star, taking the effects of General Relativity and neutrino transport into account

- For Pop II progenitors with masses in the range 8–20$M_\odot$ the emission spectrum corresponding to the model labelled as s15r in [240]; as an extreme and promising possibility, the gravitational wave emission produced by the excitation of the g-modes has also been considered using the template spectrum of [207].
- For Pop II progenitors with masses in the range 20–100$M_\odot$, the GW spectra from a set of models (D5a,D5d,A5b) obtained by [208] using numerical simulations in full General Relativity.

The background is out of reach for Pop III stellar collapse, but could be be detected for Pop II progenitors. The authors found that the energy density reaches a maximum of $\Omega_{\rm gw} \sim 10^{-9}$ around 1000 Hz for the collapse to NS model of [207], giving a signal to noise ratio of the order of 10, and of $\Omega_{\rm gw} \sim (4\text{-}7) \times 10^{-10}$ around 500 Hz for the collapse to BH model of [208], giving a SNR of the order of 1–10.

Similarly, [241] estimated the GW signal created by all core collapse supernovae, to NS and BH, using a Gaussian spectrum of the form

$$\frac{dE_{\rm gw}}{d\nu} = A \exp(-(\nu - \nu_*)/2\sigma^2), \tag{43}$$

which was shown to be a good approximation to the models of [242]. Based on simulated spectra of [120] and [208], they considered different models with $\sigma \sim 500$ and $\nu_* = 200$–800 Hz. They found that the signal may be detectable with ET when the fraction of energy converted into GWs (the efficiency) is larger than 10^{-5}–10^{-7}.

The gravitational wave background signal from core collapse supernovae could be enhanced by a number of proposed post-collapse emission mechanisms. One intriguing mechanism is the bar-mode dynamical instability associated with NS formation. These instabilities derive their name from the 'bar-like' deformation they induce, transforming a disk-like body into an elongated bar that tumbles end-over-end. The resulting highly non-axisymmetric structure resulting from a compact astrophysical object encountering this instability makes such an object a potentially strong source of gravitational radiation, and has been the subject of a number of numerical studies [243–247]. Howell (PhD thesis 2010) has calculated the background signal from this emission process using simulated energy spectra data, $dE_{\rm gw}/d\nu$, from [248], who performed the first three dimensional hydrodynamic simulations for stellar core collapse in full general relativity. Assuming a 20% occurrence of this instability, the authors find that the resulting background reaches a maximum of $\Omega_{\rm gw} \sim 4 \times 10^{-10}$ around 2000 Hz which would be detectable with a SNR of about 3 after one year of integration. The optimistic event rate they considered is supported by suggestions that post-collapse neutrino emission by the proto-NSs can induce contraction through cooling. This leads to increased spins through conservation of angular momentum [248] and the instability can begin in tens of milliseconds post-collapse, increasing the rate of occurrence.

Rotating Neutron Stars: Initial Instabilities The stochastic background from r-modes was first investigated by [85] and then reviewed by [249]. These estimates are based on the initial model of [83], which does not account for dissipation mechanisms such as the effect of the solid crust or the magnetic field, which may significantly reduce the gravitational instability. The spectral energy density of a single source is given by:

$$\frac{dE_{\rm gw}}{d\nu} = \frac{2E_o}{\nu_{\rm sup}^2}\nu \text{ with } \nu \in [0 - \nu_{\rm sup}], \tag{44}$$

where $\nu_{\rm sup}$ is 4/3 of the initial rotational frequency and E_0 is the rotational energy lost within the instability window. For NSs with radius $R = 10$ km and mass $M = 1.4\,{\rm M}_\odot$ the spectrum evolves as $\Omega_{\rm gw} \sim 10^{-12}\xi\nu_o^3$, where ξ is the fraction of NS stars born near the keplerian velocity and which enter the instability window, until it reaches a maximum at 900 Hz. ET may be able to detect this signal with a SNR > 3 and $T = 1$ yr if $\xi > 0.2\%$ (ET-B) or 0.36% (ET-D). We obtain similar constraints with the secular bar mode instability at the transition between Maclaurin and Dedekind configurations [250].

Rotating neutron stars: tri-axial emission Rotating NSs with a triaxial shape may have a time varying quadrupole moment and hence radiate GWs at twice the rotational frequency. The total spectral gravitational energy emitted by a NS born with a rotational period P_0, and which decelerates through magnetic dipole torques

and GW emission, is given by:

$$\frac{dE_{\rm gw}}{d\nu} = K\nu^3 \left(1 + \frac{K}{\pi^2 I_{zz}}\nu^2\right)^{-1} \quad \text{with } \nu \in [0 - 2/P_0], \tag{45}$$

where

$$K = \frac{192\pi^4 G I_{zz}^3}{5c^5 R^6} \frac{\varepsilon^2}{B^2 \sin^2\alpha}. \tag{46}$$

Here R is the radius of the star, $\varepsilon = (I_{xx} - I_{yy})/I_{zz}$ is the ellipticity, I_{ij} the principal moment of inertia, B the magnetic field and α the angle between the rotation and the dipole axis.

The majority of NSs are born with magnetic fields of the order of 10^{12}–10^{13} G and rotational periods of the order of tens or hundreds of milliseconds [251–253], and very likely don't contribute very much to the stochastic background. But the population of newborn magnetars in which super-strong crustal magnetic fields ($B \sim 10^{14}$–10^{16} G) may have been formed by dynamo action in a proto-NS with very small rotational period (of the order of 1 ms) [254, 255], may produce a stochastic background detectable by ET [256].

For these highly magnetized NSs, the distortion induced by the magnetic torque becomes significant, overwhelming the deformation due to the fast rotation. When the deformation of the star is small ($K \ll \pi^2 I \nu^{-2}$), the spin-down is dominated by the magnetic torque, but as the ellipticity increases GW emission may become the most important process. Taking $R = 10$ km for the radius, $I_{zz} = 10^{45}\,\mathrm{g\,cm^2}$ for the moment of inertia, and assuming that magnetars represent 10% of the population of NSs, we find that the stochastic signal is detectable with ET after an observation time $T = 1$ yr and with a signal to noise ratio of 3 when $\frac{\varepsilon}{B} > 3.5 \times 10^{-18}$ (ET-B) or $\frac{\varepsilon}{B} > 1.3 \times 10^{-18}$ (ET-D). In the saturation regime where the spin-down is purely gravitational, the energy density increases as ν_o^2 at low frequencies and reaches a maximum of $\Omega_{\rm gw} \sim 1.3 \times 10^{-8}$ around 1600 Hz, giving a signal detectable by ET with a signal-to-noise ratio of 45 (ET-B) or 17 (ET-D).

The sources discussed in this section are summarized in Figure 37. Here, the ET sensitivity curve is estimated for two co-located or minimally separated interferometers with opening angle 60° and relative rotation angle 120°, an integration time of 1 year and a detection SNR of 2.56 [89]. However, a search for stochastic background with co-located detectors could encounter difficulty in separating signal from correlated noise sources: detailed detection strategies are under consideration.

2.7 Computing Challenges

This section deals with the feasibility of the search for GW sources in ET from the computational power point of view. A brief description of examples of existing search methods and parameter estimation tools for different sources is given. For these methods, we provide a preliminary estimation of the computational power needed, which could be used in scaling the requirement for other search techniques. We also evaluate the impact of computing technologies available over the next decade on ET data analysis.

2.7.1 Detection Strategies

Computational resources required to search for gravitational waves depend, quite strongly, on the type of source that is being searched for and the data analysis technique is used. In this Section we will take a look at the search strategies that are currently being pursued for various sources.

Compact Binary Coalescence A search for well-modelled sources whose phase evolution is accurately known, an example of which is the coalescence of compact binaries, is generally performed using matched filtering. As the modelled waveforms depend on a number of parameters, the most optimal way to search for the signal is to filter the data through a bank of templates covering the astrophysically interesting region of the parameter space [257–261]. Matched filtering technique essentially obtains the maximal value of the SNR corresponding to the template that best matches the signal buried in the data. It represents a grid of theoretical waveforms (templates) placed on the space of parameters, each point on the grid being associated with a specific set of parameters. The density of templates is chosen so that one loses no more than a tiny fraction of signals as a result of working with a discrete grid.

The number of templates required to search for coalescing binaries grows as a strong power of the lower frequency cutoff. Thus, matched filtering could be computationally prohibitive in ET since ET aims to push the low frequency sensitivity down to 1 Hz compared to 10-20 Hz in advanced detectors. As shown in Box 2.11, the number of template for an ET-D configuration ranges from 10^9, for binaries with non-spinning stars, to 10^{18}, when the binary is composed of spinning stars but with the spins aligned with the orbital angular momentum.

In Table 3, we summarize the computational time needed for the cases defined in box 2.11, using matched filtering technique[6].

Computers		GPU C2050	E@H	WLCG	Tianhe-1A	Low cost system
Processing power (TFlops DP)		0.25	200	2000	2567	100
Nbr of para	Nbr of templ	Computational time needed				
2	10^9	128 days	4 hrs	24 min	18 min	7 hrs
4	10^{13}	3,520 yrs	5 yrs	182 days	128 days	9 yrs
6	10^{18}	358 10^6 yrs	5 10^5 yrs	5 10^4 yrs	4 10^4 yrs	9 10^5 yrs

Table 3: This table gives the computational time needed for a search with different number of parameters using 1 GPU C2050 A.6.3, E@H, WLCGA.6.4, the supercomputer Tianhe-1A box 2.13 and using the performance of the smallest system in the Top500 list in a couple of years, respectively. The results show that using a matched filtering search with a template bank of six or more parameters is not feasible.

[6]Low cost system in the last column of the Table represents computing power features of the smallest top500 system in a couple of years, Figure 38. Within ten years, it is plausible to expect that such a computing capability will be available at an affordable cost

Box 2.11: Template bank

For an ET-D configuration, we computed the number of templates for three different intrinsic configurations of a binary system: (i) binaries with non-spinning stars treating the two components masses as search parameters, (ii) the same as in case (i) but including sky location angles of the binary, and (iii) binaries with spinning components where in addition to the four parameters in case (ii) the spin magnitudes were treated as free parameters.

In each case, time and phase at coalescence, polarization and inclination angles were also treated as free parameters but they do not add significantly to the computational burden. An optimization over these parameters was perfomed using several techniques: analytically for the coalescence phase at coalescence, numerically for the inclination angle, and by a projection of the metric over the time at coalescence and the polarization angle, respectively. We chose the grid so that

- the loss in the number of events at threshold is no more than 12.5%,
- it covered the range of total mass 1-300 $M_{\odot}$,
- covered the whole sky search in cases (ii) and (iii), and
- the (dimensionless) spin magnitudes were in the range $\in [-1\ 1]$.

The numbers of templates required for the three cases are 10^9, 10^{13} and 10^{18} respectively.

Stochastic Gravitational-Wave Backgrounds Stochastic gravitational waves result from a superposition of a large number of waves. It will not be possible to distinguish each wave separately. The superposition of many different waves forms a background, whose spectrum and spectral power could contain the signature of their origin and the physics behind their production. Stochastic backgrounds could be of cosmological (isotropic distribution, like the cosmic microwave background) or of astrophysical nature (anisotropic distribution following the spatial distribution of the sources, which becomes isotropic if the sources are cosmological in origin). The search method should depend on the angular distribution sources and their properties[262].

The search for isotropic sources, called *isotropic analysis*, is based on the use of a network of detectors [263, 264]. An alternative is the so-called *radiometer search* [265]. In an isotropic search, the bulk of the processing time is taken up by reading and writing the data and finding the frequency dependent cross-correlation spectrum and sensitivity. It is done by splitting the output data from several interferometer pairs into short segments (typically 60 seconds long), separately cross-correlating pairs of segments, and summing the partial results at the end.

Usually the number of cross correlated channels is of the order of some tens, from which it is clear that this kind of analysis is characterized by limitation due to data Input/Output from/to storage; the CPU power seems to be already enough to process data in real-time.

The sky decomposition method is used for anisotropic background, the method provides maximum likelihood estimates of the gravitational wave distribution decomposed with respect to some set of basis functions on the sky. This basis could be pixel basis or spherical harmonic basis defined with respect to the Earth's rotational axis.

For point sources, the best choice is the pixel basis. However, for a diffuse background dominated by dipolar or quadripolar distributions, the best choice is the use of spherical harmonic basis.

The spherical harmonic analysis method can successfully recover simulated signals injected into simulated noise for several different types of stochastic gravitational wave backgrounds, for example, isotropic sources, dipole sources, point sources, diffuse sources, etc. Moreover, applying the spherical harmonic decomposition in the case of an isotropic signal, where only the monopole moment contributes to the stochastic gravitational wave background, allows one to save in computational power and time, compared with the isotropic search method [262].

However, in general, this method is more computationally intensive than isotropic and radiometer methods. The computation time will be proportional to some function of the maximum value $l_{\max}$ of the modes, but roughly estimates show that the spherical harmonic search needs 10 times more CPU time than the isotropic/radiometer searches.

Continuous Waves sources Continuous waves (CW) are signals with duration longer than the typical observation time of a detector. Rapidly spinning non-axisymmetric neutron stars are prime examples of sources that could emit CW over millions of years. The phase of the signal from these sources could be affected by various processes such as intrinsic spin-down, Doppler modulation (in phase and amplitude) due to relative motion of the source and the detector, glitches in frequency caused by internal quakes and pulsar timing noise.

The choice of a search method for CW depends closely on the prior information we have on the signal that we are searching for and on the available computing power. We can distinguish between two cases:

- Targeted search: knowledge about the source parameters (position, frequency, spin-down) are available from electromagnetic observations of the source.
- Blind search: all the source parameters are given within large intervals based on the lack of available theoretical understanding of the astrophysical scenarios.

The targeted search could be implemented as follows: (1) one extracts the band of interest around the emission frequency[7], (2) corrects Doppler and spin-down effects[8], (3) applies matched filtering[9], (4) selects the value of the unknown parameters at maximum of the filter output and, finally, (5) compares it with noise distribution to claim a detection or set an upper limit.

The computational cost for targeted searches relies on the accurate knowledge of the source parameters: position, frequency and spin-down rate. Considering that the frequency is very accurately known within a small bandwidth, one can easily down-sample the data stream around the expected source frequency and the data analysis cost for such sources is, therefore, minimal (few templates)[10].

However, in the case of neutron stars for which no substantial information about the spin-down parameters are known, the computational cost is far higher. The number of templates in this case is esteimated to be in the range $10^2 - 10^{10}$, for a year's worth of integration [267]. It implies that even if we have to perform the search in a narrow frequency band around twice the radio pulsar frequency, the computational task is really tricky. It is apparent that we cannot expect the direct use of matched filtering for a blind search to work as it is necessary to consider in our search the minimal range for the source parameters: the whole sky for angular position and the whole bandwidth for the signal's frequency[11]. In the case of a neutron star on a circular orbit in a binary system, the computational power required is 10^{17} GFlops, far from our actual computational capabilities. Alternative approaches with a small loss in sensitivity but ensure to significantly reduce the computational power are needed.

One of the solutions is the so-called hierarchical search (*stack-slide search* [268]) where coherent and incoherent steps are alternated. In the incoherent step a rough exploration of the parameter space using short data segments is made, with a low threshold that allows for many false alarms from which some candidates are selected. In the coherent step, each candidate is followed up with a more refined search using longer data segments, but searching the parameter space only in the neighborhood of the candidates from the first step.

Both search steps considered above share the following scheme [269]:

[7] The received GW signal is not monochromatic but covers a small frequency band (fraction of a Hz) around twice the electromagnetic frequency, due to Doppler modulation and intrinsic spin-down of the pulsar.

[8] If the spin-down parameters of a source are known with a high accuracy, we can remove both the Doppler and spin-down by multiplying the data by an appropriate function.

[9] Apply matched filter of the slowly varying demodulated signal over the unknown nuisance parameters (amplitude of signal as received on Earth, polarization and inclination angles, initial phase, etc.) and over the uncertainty range of the known parameters (position angles, frequency, spin-down). An alternative to explicitly applying a matched filter for the nuisance parameters is the use of the so-called F-statistics [266].

[10] In a more general case, even for sources observed in the electromagnetic domain, these parameters are known with finite accuracy. This can lead to a loss of sensitivity, especially for very long observation times or an increase in the computational cost.

[11] The computational power is proportional to the maximum observable frequency to the fourth power [267]

- The output data are divided into short segments, called stacks.
- Each segment is phase corrected using an appropriate mesh of correction points to confine an alleged signal in one frequency bin.
- Fourier transform the phase corrected stacks.
- Using finer mesh, the individual power spectras are corrected for residual frequency drift by removing phase modulations over the entire data stream.
- Sum the corrected power spectra.
- Search for candidates exceeding some fixed thresholds.

From the computational point of view, the interesting feature of stack-slide method is the fact that it considers the available computational power as a parameter which fixes the value of the source's parameters that are searched over. In fact, before the search begins, one has to specify the size of the parameter space to be searched (choose maximum frequency, region of the sky, etc.), the available computational power to do the data analysis and an acceptable false alarm probability. From these, one can fix optimal values for the loss in sensitivity and the number and length of stacks. Optimization consists of maximising the sensitivity function over these parameters given the definition of the total computational power as constraint.

The advantages of a hierarchical search are, on the one hand the low threshold in the first step of the search allows detection of low-amplitude signals which would otherwise be rejected, and on the other hand in the second step one can search using longer data slices with a limited computing budget, because of the reduced parameter space being searched, thus excluding false positives from the first step. For given computational resources, this technique achieves the best sensitivity, if the thresholds and mesh points are optimally chosen between the first and second steps of the search.

Another possible alternative is proposed in Ref. [270] where a hierarchical method was developed, allowing a reduction in the computational costs. This method is sub-optimal and the gain processing costs is paid by a small reduction in sensitivity. This method also consists of alternating coherent steps, based on FFT, and incoherent steps based on the *Hough transform*. The Hough transform is a feature extraction technique used typically in image analysis, computer vision, and digital image processing. The purpose of the technique is to find imperfect instances of objects within a certain class of shapes by a voting procedure. This voting procedure is carried out in a parameter space, from which object candidates are obtained as local maxima in a so-called accumulator space that is explicitly constructed by the algorithm for computing the Hough transform. Analyzing the data in roughly real time requires a computational power of 10^8GFlops [271].

Burst Sources Transient gravitational waves whose phase evolution is unknown fall into the class of unmodelled burst sources. Core collapse of a white dwarf is an example where theoretical prediction of the emitted waveforms, both their amplitude and phase evolution, is highly uncertain. There are many different methods to search for unmodeled bursts. Coherent Wave Burst (cWB) is a typical example, wherein the basic idea is to coherently combine time-frequency maps from several detectors [272]. The sky position of the source is encoded in the time delay between different detectors. In the presence of a gravitational wave signal, the excess power in a time-frequency map would be similar (modulo the detector antenna pattern) but with a time delay that depends on the location of the source on the sky. Thus, one can determine the sky location and the strength of the signal from time delay and the antenna pattern and by doing multiple time shifts of the data corresponding to different sky positions [12].

The number of detectors used in cWB does not affect the computational cost since data from different detectors is not analyzed separately, rather only the combined data stream. However, if we do joint analysis with LIGO

[12] In principle, for this type of search only the sky position and strength of the gravitational wave burst could be recovered. However, the likelihood method used in cWB search offers a convenient framework for the introduction of constraints arising from the source models like the different polarization states of the signals [272].

and Virgo detectors, it only makes sense to use the bandwidth where all detectors are reasonably sensitive[13].

Recent implementation of cWB to process two years data from LIGO's fifth science required one week of processing time on the Atlas cluster, whose processing speed is 80 TFlops. During the sixth science run, burst search, using cWB, was run online for H1,L1,V1 producing coherent triggers about 5 minutes behind the real time, doing computation on 1 dedicated computer.

However, in the ET era there might be such a rate of events that it becomes much more computationally intensive. Also if each event is long duration or wide bandwidth, it might consists of millions of pixels. Processing such huge clusters might be quite computationally intensive, but still feasible with the future computational configurations as it will be shown in the next subsection.

Finally, one can emphasize again that the computational cost for cWB search depends on which detectors are used, what frequency band one wants to explore and based on that it could be possible to estimate how many sky locations could or should be considered. But practically, the most important factor is the large false alarm rate that cannot be predicted before the detector is switched on. If a detector is glitchy, it might increase the computational cost a lot, since one would have to process a lot of false positives before rejecting them.

For *modeled bursts* like GRBs from both core collapse, supernovae and binary mergers, the search is based on a matched filtering variant, so-called time sliced matched filtering [273]. The application of matched filtering depends crucially on phase coherence in the true signal, in correlating it to a model template. To circumvent phase incoherence on long time scales created by turbulence in the inner disk or torus of magneto-hydrodynamical systems powered by a Kerr black hole, the template is sliced into several segments on intermediate time scales, for which phase-coherence may be sustained.

Matched filtering is then applied using each slice, by correlating each template slice with the detector output using an arbitrary offset in time. The relevant parameters in this algorithm are: a choice of coarse grained coherence time, fine grained time of onset(s) of the slices of the burst and the mass of the black hole. The mass is equivalent, for all practical purposes, to the duration of the burst. Changing the black hole mass changes the duration and also the strength of the signal, but the latter is automatically absorbed by the algorithm and requires no adjustments [273].

For this kind of search, a computational cost can be estimated as follows: for a single black hole mass parameter, it is about 6 hours of CPU time (core 2 duo) per 1 hour of detector data (sampled at 20 kHz). For a range of black hole parameters with, e.g. , 0.1% partition, a full parameter search amounts to a few thousand hours per 1 hour of detector data.

2.7.2 Computing evolution

Computing has made great strides in recent years in order to provide each year even more fast processors. Since the invention of the integrated circuit in 1958, the number of transistors on a given chip double (roughly) every two years, as predicted by the first Moore's law [274]. This exponential growth has allowed computers to get both cheaper and more powerful at the same time (see Appendix A.6.1 for more details).

Quoting Moore's recent statment issued during an interview "... by about 2020, my law would come up against a rather intractable stumbling block: the laws of physics" [275], we may be led to think that the Moore's Law is at its end. Today the integration scale (the typical size for the CMOS realisation) is about 32-22 nm that is comparable to few hundreds of atomic radii. It is therefore clear that one of the main limitations on continuing to grow the density of processors is imposed by the atomic limit. The difficulty in reducing the integration scale has been evident already during the last 10 years. In fact, major manufacturers introduced several technological innovations and hardware paradigms in order to provide faster processors, limiting the reduction in integration scale and increase in CPU frequencies as described in Appendix A.6.2.

[13] There is no point in combining the data where the sensitivity is very uneven because the weakest detector in a network limits the sensitivity.

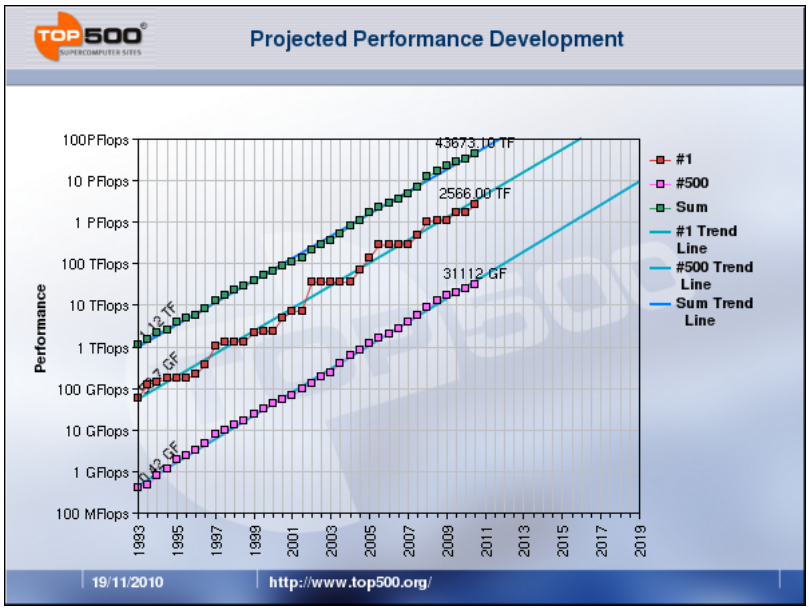

Figure 38: The Top500 past and projected performance (Image credit: Prof. Dr. Hans W. Meuer).

Within computer industry technology's road map one "believes Moore's Law will continue to hold good through 2029", citing Pat Gelsinger, SVP and co-GM of Intel's Digital Enterprise Group (DEG) [276]. Although specialists agree that by 2019 the current strategy of ever-finer photolithography will probably have run its course, it is likely that some new type of technology will be needed to replace the current integrated-circuit production process, like new materials, optical or quantum computers.

In any case it is not a simple exercise to translate transistor growth into practical CPU performances. This is particularly true for recent multi- and many-core systems. Equally, a great stride in software development is also needed to take advantage of the modern multi- and many-core CPUs (cf. Appendix A.6.3). Often it is necessary to substantially think back the software implementation.

There are other factors limiting the possibility of taking full advantage of the modern CPU, such as internal bandwidth and storage speed. In other words memory and disk access speeds have failed to keep up with respect to the CPU. In fact, to reduce the impact due to these problems, different solutions have been introduced in processor and software design, examples of which include out-of-order execution and caching and pre-fetching strategies. This also means that there is still a big optimization margin on other computer components.

The key actions of the next decades can be summarised as follows:

- Chip-Level Multiprocessing (CMP)—increasing parallelism for enhanced performance (many-core architectures),
- Special Purpose Hardware—embed important functions in software and specialised chips inside the microprocessor itself,
- Large Memory Subsystems—Memory access being the main bottleneck in building many high-performing cores, it is important to have a large quantity of memory on-chip and close to the cores,
- Microkernel—Microprocessors will need a sizable integrated intelligence, in order to coordinate all this complexity: assigning tasks to cores, powering up and powering down cores as needed, and, finally,
- Virtualisation—Future microprocessors will need several levels of virtualisation; virtualisation is needed to hide the complexity of the hardware from the overlying software. Kernel and software should not have to deal with the intricacies of many cores, specialised execution hardware, multiple caches, reconfiguration and so on.

Box 2.12: GPU Computing for Coalescing Binaries

Tests carried out with NVIDIA C1060 (i.e. GT200) and NVIDIA C2050 (i.e. the brand new Fermi GPU), are demonstrating how GPU implementation of the pipeline to search for coalescing binaries offers an average gain factor (normalised by price) of about 50 with respect to standard implementation using conventional CPUs [277]. This search involved the use of 30 matched filters per second. The gain factor depends on the size of the data vector, assumed for this search to be 2^{23} samples. Using shorter vectors it is possible to achieve even higher gains. Performing the same test with the new NVIDIA Fermi GPU (i.e. the Tesla C2050), one could increase the number of templates up to 120 templates per second.

A preliminary fully multi-GPU implementation of the pipeline was reported at the E4 Workshop 2010 in Bologna. This software implementation includes specifically an input data conditioning, post-Newtonian signal generator (up to 3.5 PN) [278] and a complete matched filtering procedure with coloured noise. This code offers an efficiency of 95% using 4 GPUs, bringing to an impressive result of proecessing about *400 templates per second* with Tesla C2050 [279].

FFT algorithm is often the core of several data analysis and processing programs. Several benchmarks report a gain factor of 50-80, using GPU as opposed to CPU architecture. This value has been renormalised by device prices. Thus, we can state that using the already available many-core technologies the gain factor with respect to the standard single core architecture is, conservatively speaking, about 100. Obviously an exhaustive analysis of the gain factor needs to deal also with power consumption and other costs.

As for the past 20 years, we can assume that during next decades these innovations will help to keep the Moore's law alive, which we can use to forecast the future computing power. Thus, if we consider the actual computing power of a typical CPU, Moore's law predicts a gain factor of about 200 in 12 years and 700 in 14 years. As general experimental proof of Moore's Law and computing evolution, we refer to *The Top500* project [280]. Its goal is to generate, twice a year, a list of the 500 most powerful computers in the world. The Top500 ranking has always been a good overview of the actual technology trends, and along the last ten to twenty years the list has showed an evident trend towards parallel and massively parallel systems. This trend has been confirmed by the appearance in the home computing system of superscalar and pipilened CPU firstly, and multi-core and many-core CPUs.

Figure 38 shows three different sequences. The first one, labeled *Sum*, represents the combined computing power of all the 500 supercomputers in the list. The second sequence, the one labeled #1, is the power of the first ranked system. The last one, the sequence labeled #500, is the computing power of the 500-th system in the list. If we consider the computing power of the last ranked system in the list ten year ago, it is approximately 100 GFlops. Today, the 500th system, namely a Xeon Cluster, has a power of more the 10 TFlops. This gives a gain factor of about 100, consistent with the prediction of the Moore's first law. Though it may seem incredible, experimental data confirms that in the last ten years we had and increase of a factor 100 in computational speed.

The actual Top500 list emphasises the following evolutionary characteristics:

- Natural evolution from multi-core to many-core era (see Box 2.12),
- Many-core architecture (i.e. GPU), together with multi-core X64 processors is driving the technology,
- Moore's Law is alive and still works well, and
- Development of faster and more integrated interconnects is an obvious consequence of the increase in number nodes and cores.

To reiterate the aforementioned points one can cite the characteristics of the first ranked system on November

2010: the Tianhe-1A (see Box 2.13). This supercomputer is stationed at the National Supercomputer Center in Tianjin, it has achieved a performance level of 2.57 petaflop/s. The system collects together both the trends: fast interconnection and many-cores. It is clear that a new programming paradigms and new algorithms are needed to get top performance from novel computing infrastructures.

As the complexity of a computational architecture grows, it is crucial to design a computational system that is also flexible. Solutions can be worked out only by gathering sufficient computing power and the appropriate know-how. Know-how and computing power must be collected and deployed in an efficient and appropriate manner, so that anyone is able to transparently access any needed information and resources. What we have just pointed out is the general idea of the grid or, perhaps more precisely, of a computational grid environment. This new approach to network computing is known by several names such as: meta computing, scalable computing, global computing, internet computing, and, more recently, peer-to-peer computing as discussed in Appendix A.6.4.

Looking for high performances, one has also to deal with **power consumption**. The power consumption of an HPC resource is a **fundamental aspect** on computing facilities setup. This requires an optimization in terms of efficiency, cost and resources reliability. To achieve greater performance per compute node, vendors have increased not just transistors and speed but consequently also the power density. Thus, a large-scale high-performance computing system requires continual cooling in a large machine room, or even a new building in order to work properly. So to achieve greater performances one has to consider direct and indirect (i.e. cooling system) costs. We have to remember that the increase in failure rate of HPC systems is directly related to their working temperature.

Many-core systems seem to provide good performances also in terms of power consumption. In fact, making the assumption that The Tianhe-1A 2.5 PFlops system was built entirely with CPUs, it would have consumed more than 12 MW. Thanks to the use of GPUs in a heterogeneous computing environment, Tianhe-1A consumes only 4 MW, making it 3 times more power efficient. The most energy efficient supercomputers are based on: IBM BlueGene/Q Prototype with 1680 Mflop/watt, Fujitsu K-Computer at Riken with 829 Mflop/watt, and QPace Clusters based on IBM PowerXCell 8i processor, up to 774 Mflop/watt. Both the BlueGene/Q and the PowerXCell 8i are example of many-core systems. This enforce the evidence that computing hardware architecture is moving towards the era of many-cores.

Box 2.13: Tianhe-1A

This system is equipped with 29376 GB of memory, is based on Nvidia graphics processing units (GPUs) as well as Intel Xeon 5600 series processors. The Tianhe-1A is able to handle data at about twice the speed of InfiniBand, and the system has achieved a performance level of 2.57 petaflop/s essentially thanks to the the acceleration given by Nvidia Fermi GPU processors. It is important to compare the power consumption of Tianhe-1A and Jaguar Cray XT5-HE, that is the second ranked system in top 500. In fact the Jaguar use **5-10 MW** to achieve 1.7 PFlops while Tianhe-1A use **4 MW** to achieve 2.5 PFlops. **This is a success of the many-core architecture providing 3-4 time more computing power per Watt!**

The above discussion, in particular processor speeds, is closely related with computational challenges faced by ET. In the ET era we can try to select some reference core algorithms and use the many-core, Moore's law forecast to predict the realistic computing power in 2025. These results can be used to understand the future capabilities and limitations in ET data analysis. A fundamental point that distinguishes first and second generation gravitational wave detectors with respect to ET is the nature of the experiment. ET has to possess enough sensitivity and computing power to achieve its main goal, namely to develop the field as a tool for obsrevational astronomy and cosmology. This means tha ET has to have the ability to perform real-time or on-time analysis. This will place severe demands on the computing infrastructure, requiring the handling together of two main data processing problems: detection and parameter reconstruction.

2.7.3 Impacts on data analysis

A direct implementation of a matched filter search for coalescing binaries would be obsolete when the number of searched parameters is greater than four, even if we assume that Moore's law will continue to be valid until the ET era. The fact that a great many number of templates are required for a matched filter search would make such a search impossible (see Table-3). This means that we have to evolve other data analysis methods including sampling techniques, hierarchical methods, etc. A promising outcome could be the adaptation of the algorithms developed for the analysis of data from the future space detector LISA, such as MCMC, MHMC or Genetic Algorithms (GA) (see Box 2.14).

For low SNRs, a hierarchical method could be used to recover parameters. Such a search could be implemented by first working with a coarse grid and in the second pass working with a finer grid that filters the data around candidate events from the first pass. However, this could be problematic if we have relatively large SNRs (as expected in ET). Many templates could have approximatively same maximum values of the likelihood even with disparate configuration of parameters. This implies the use of large parameter space intervals for the second step and/or the use of a multi-templates search technique (overlap of many sources). In both cases a huge number of templates and computational power is then needed.

Another possible approach can be a two-step multi-band analysis. In this case the analysis is made first by performing a detection phase with templates starting from higher cut-off frequency and assuming a small SNR-lost, e.g. of about 5%. In fact the template length is reduced exponentially starting from highest frequency. Starting for example from 10 Hz we loose few percent in terms of signal-to-noise but we gain proportionally in terms of computing time. Thus, the first step can be considered similarly to a trigger zero, used for candidates selection. Then, in the second step, the whole template is analyzed for parameters reconstruction and observation, using a finer template bank grid. Another possible optimization could be achieved using the *stationary phase approximation* for template production of the first step and then the PN approximation or the exact waveform from numerical relativity, during the second step.

Box 2.14: Genetic Algorithms

The genetic algorithm (GA) is a search technique that mimics the process of natural evolution based on the positive mutation principle [281].

Initially, a group of organisms (templates) is chosen, each organism is characterized by a different set of genes (parameters). Then, the quality (log of the likelihood) of each organism is evaluated. Based on the value of their quality (templates with higher likelihood), a set of pairs (parents) are selected and their genotypes are combined to produce children (new templates). In the last step, one could, with a controlled probability, allow random mutations in the children's genes (by randomly changing the parameters of the new template to explore a large area of the parameter space). The new children will form the new parent and the procedure is repeated until one reaches a steady state (maximum in the log likelihood).

In the case of coalescing binaries, one should be able to recover the values of the coalescence time and the chirp mass in 1 hour with 1 CPU. For the other parameters, except the direction of the spins, 10 hours would be needed with 100 CPUs. Recovering all the parameters will need a few days of 100 CPUs.

The cost is purely dominated by the computation (time domain generation plus FFT) of the templates (1 to 2 sec with 1 CPU for a waveform lasting 2 years).

For stochastic gravitational wave background, it was shown that the available computational power used by the existing search techniques is already enough. Nevertheless further optimizations could be achieved either by parallelization[14] or, as this type of analysis is limited due to data IO from/to storage, a faster analysis could be

[14] One can reduce the computational time by splitting the data from each detector pair into 'jobs' which contain several segments

performed by realizing high throughput NAS (Network Attached Storage), which gives a faster data access.

CW search is computationally expensive. Even considering a foreseen factor of 200 in the performance of the fastest supercomputers ca. 2010, 2.5×10^6 GFlops, in 2023 the fastest super computer is capable of 5.0×10^8 GFlops. Thus, only the fastest supercomputer in the world will be able to achieve the power computing needs reported in the previous section. We can conclude that with the current type of analysis and knowledge the task will actually not be achievable yet. Nevertheless, the great theoretical and observational efforts which are made to understand these sources would probably make such searches feasible in the near future by narrowing down the uncertainty in the source parameters.

Finally, the burst search should not pose any serious challenges. By about 2023, one could expect a gain factor of 200 in computing speed. Implementing many-core technology, we can consider a conservative gain of a factor of 6. The full parameter search will be roughly 10 times far from the real-time analysis using a CPU model, while trying a many-core implementation, few hours of data will be analyzed in one hour. Thus by about 2014 the real-time analysis of the full parameter space search should be feasible.

2.7.4 Conclusions

The most plausible computing scenario of the near future is a combination of CPU and GPU technologies, an evolution of most recent AMD's APU or Intel's Knight ferry technologies. We already showed that it is possible to exploit GPU power in Coalescing Binaries Detection. That means that many-core programming will not be a choice but rather this will be the state-of-the-art in the ET era. This consideration has permitted to add an extra gain factor to the Moore's law expected performances. In general, we can consider a base gain factor of 200 by 2023 due to Moore's law and an extra factor due to many-core architechture that can fluctuate depending on the analysis, but can be posed conservatively to be 10. This means a potential gain of more than 3 orders of magnitudes.

Given the computing power forecast, we believe that, if we discard a flat search approach with more than 4 parameters and the search for CW with great number of spin-down parameters (where more sophisticated improvements should be done), the combination of existing search methods and the future improvement of computing resources will allow ET to fully take advantage of its technological design and to play its real role as an observatory giving the scientific community the expected information to explore the universe with new eyes.

We should also mention emerging technologies for distributed computing, such as Grid and Cloud computing facilities. Here the Seti@Home, Einstein@Home and LHC@Home experiments are great examples. These will follow the evolutionary trend and will provide important CPU power containers for off-line analysis.

We would like to conclude remarking that, technological breakthroughs are taking place. The computing infrastructure trend is toward many-core solutions, as shown by Top500 and manufacturers' road-maps. The possibility to address future computing power for ET science needs will be proportional on how we will be able to use these new architectures. The doubling of performances each 18 months is no more for free. A change on programming paradigm and coding will be mandatory.

(anything up to a few hundred segments). Then one can run the cross-correlation estimation for all the segments in one job on a single node, and run all these jobs at the same time on several nodes. So, the analysis, which would take about ten days of CPU time, will usually complete within a few hours using the Atlas cluster, for example.

3 Site and infrastructures

3.1 Description

Interferometric gravitational wave detectors are large and complex devices and the selection of their site is an issue of great importance. The selected site should allow the highest possible level of scientific productivity at reasonable cost of construction and operation, and at minimal risk. Of paramount importance are the selection criteria that impact the scientific potential of the observatory. These include natural and anthropogenically generated seismicity and site geological constraints that affect critical parameters such as interferometer arm lengths. The first section provides the requirements for the site and infrastructure of Einstein Telescope. An important aspect within these requirements is the allowed seismic displacement noise, which is addressed according to source frequency. Seismic sources include the ambient seismic background, microseismic noise, meteorologically generated seismic noise, and cultural seismicity from anthropogenic activity.

The second section describes the Newtonian noise which constitutes one of the fundamental infrastructure limitations. Newtonian noise originates from fluctuations in the surrounding geological and atmospheric densities, causing a variation in the gravitational field. Results from new analytical formalisms and finite element models are presented for subterranean detectors. Estimates for Newtonian noise are derived for different geologies. Starting from these models we show that it is possible to deploy seismic sensor arrays that monitor seismic displacements and filter the detector data with Wiener or Kalman filters.

The third section discusses the site selection. As part of the site selection and infrastructure program, a total of 11 European sites were systematically characterised to catalogue regions within Europe that would comply with the site demands. The data that were logged include the local seismic activity, geology, availability of existing infra-structure, population density and local construction costs.

Finally, we discuss the subterranean infrastructure and cost aspects for caverns, shafts, tunnels, vacuum, cryogenic and safety systems for the Einstein Telescope observatory.

3.2 Executive Summary

The design study working group on site selection and infrastructure has carried out detailed site studies at 15 locations in 11 different countries. Furthermore, a comprehensive Infrastructure Reference Design of an underground detector was realised. The site study has revealed several promising EU underground sites that comply with the low seismic background performance requirements. In order to ascertain that all site characterisation procedures were according to the highest standards, measurements and data collection were carried out in collaboration with the Observatories and Research Facilities for European Seismology (ORFEUS) which is maintained by the seismology department of the Royal Dutch Meteorological Institute (KNMI). Site specific issues were discussed with geologists and representative from established underground laboratories (LNGS, LSM, Canfranc, HADES, Dusel and Kamioka) and mines (in Finland, Germany, Hungary, Italy and Romania). In addition, there was close contact with particle physics initiatives (*e.g.* CERN, DESY and ILC).

The infrastructure definition of the reference design contains surface buildings, tunnels, caverns, shafts, vacuum envelope, cryogenic infrastructure and safety systems. With the choice of combining a triple triangular detector topology with a xylophone detector design, Einstein Telescope amalgamates an optimised planned disbursement for a staged construction with a realistic proposal for a robust, highly sensitive, wide-band gravitational wave observatory. Through the design process, the vacuum system, caverns, and tunnel diameter are optimised such that the total infrastructure can be used for decades after its construction. The excavation of underground tunnels, caverns, and shafts will occur over a period of approximately four years. The observatory will be built in stages; the first construction stage containing a single 10 km xylophone detector. Later the second stage will incorporate the second and third 10 km xylophone detectors.

3.3 Infrastructure Reference Design

[Sec:infraref] Einstein Telescope will have excellent sensitivity over a wide frequency range. Within the infrasound observation bandwidth (up to 20 Hz) the scientific potential is affected directly by site location and the observatory infrastructure. Therefore, it is of paramount importance that the infrastructure reference design maximises the scientific potential of the observatory.

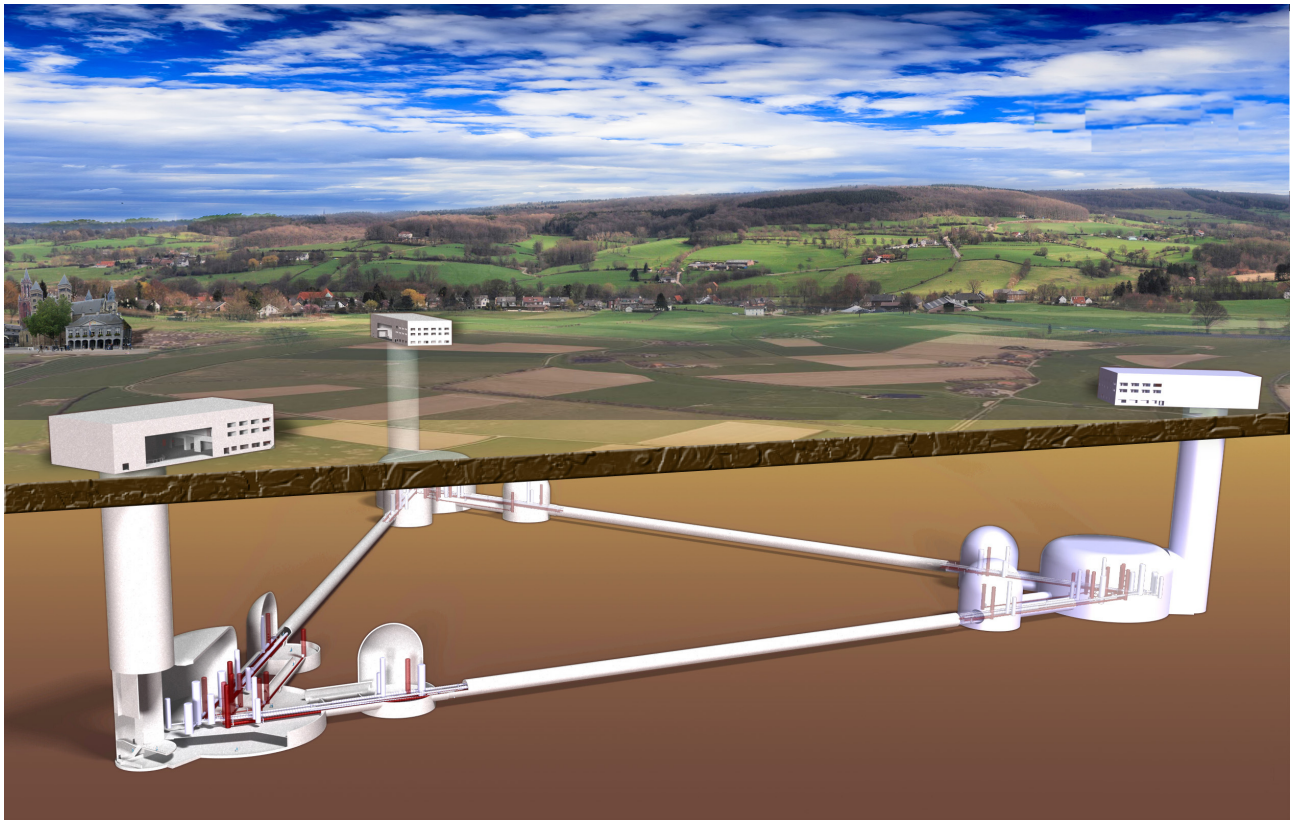

Figure 39: Artistic impression of Einstein Telescope. The observatory has a triangular configuration that can house three xylophone detectors. Each detector is composed of a low-frequency cryogenic interferometer and a high-frequency interferometer operated at room temperature. The corner stations are connected by 10 km long tunnels.

The local seismic activity is one of the most important site specific noise sources that can affect or degrade the interferometer performance. Mitigation of seismic displacement noise is achieved by combining careful siting with advanced suspension systems (outlined in chapter 4). This provides an observation bandwidth down to 1.8 Hz. A prime example of a site that exhibits extremely low seismic background noise, is the site selected for the Large Cryogenic Gravitational Telescope (LCGT) in Japan. LCGT will be located in the Kamioka mine, which currently holds the Super-Kamiokande experiment and the prototype cryogenic gravitational wave detector, CLIO. The Kamioka facility is a former zinc and gold mine and is situated 250 km west of Tokyo. Access to the underground facilities is through a well maintained horizontal road tunnel, allowing for depths down to 1000 m. The performance requirements for Einstein Telescope will surpass those of LCGT and require that the infrastructure reference design advocates for a subterranean observatory. The realisation of substantial underground infrastructure is essential for Einstein Telescope. Various excellent subterranean candidate sites have been identified in Europe. These sites exhibit seismic noise backgrounds that are similar to or below that at Kamioka.

The detector topology for a wide-band gravitational wave observatory must adopt a xylophone detection scheme containing six interferometers housed in triangular configuration. Fig. 39 shows a scaled impression of the underground observatory. Each xylophone detector will be centered around one of the corner stations and is composed of a high and low frequency interferometer pair. The first step in a phased approach towards realisation of Einstein Telescope is the construction of the full underground infrastructure including a single xylophone detector.

Presently, it is not clear whether the observatory will have horizontal or vertical access. When considering sites, the manner in which access to the underground facilities is allowed, requires careful consideration. In traditional mining, access to the underground is via a decline (ramp) or inclined vertical shaft, or adit. Shafts are considered as vertical excavations while adits are horizontal excavations into the side of a hill or mountain.

An important consideration is that the realization of direct vertical access shafts to depths exceeding 200 m (which may be desirable for Einstein Telescope) carries with it construction methods that are significantly more complex than those needed for a more shallow infrastructure. All of these considerations tie in closely to the local geography and geology of a chosen site.

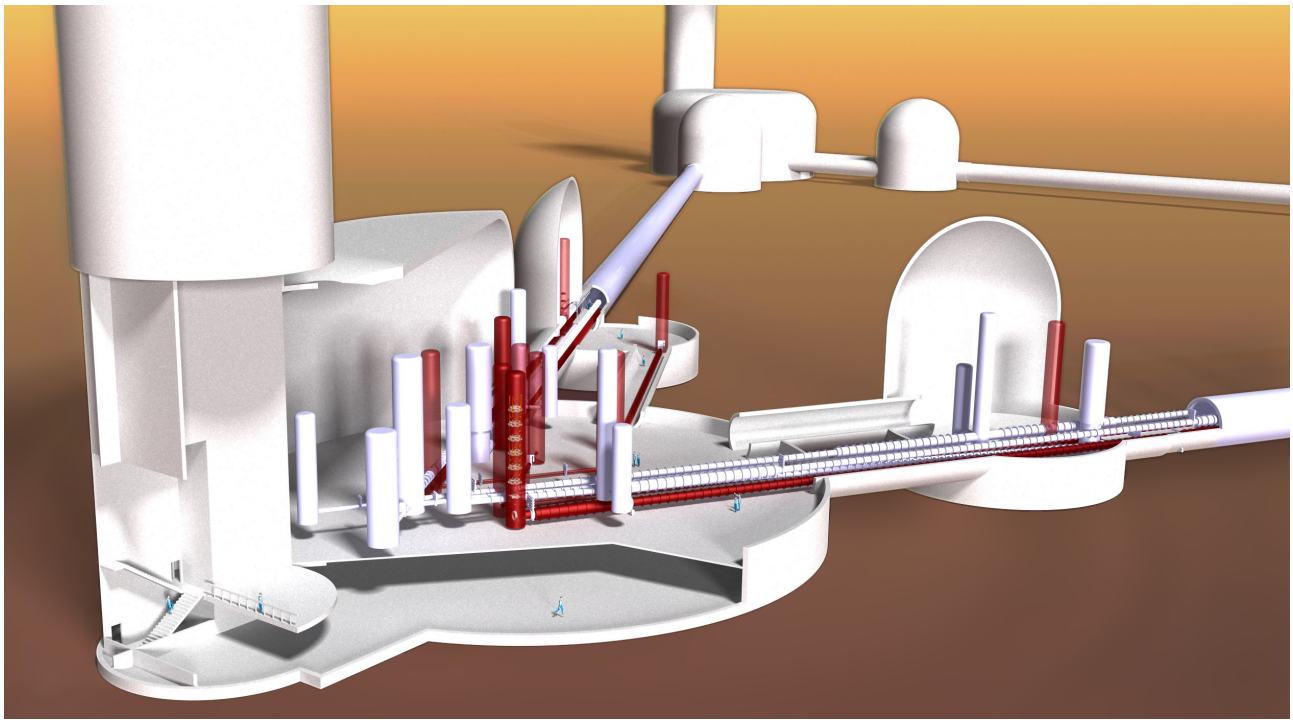

Figure 40: Impression of a corner station. Each station features a large cavern that can be accessed through a 20 m diameter vertical shaft. Two satellite caverns connect via twin tunnels to a main cavern and house input test masses and cryogenic infrastructure.

Figure 40 shows an impression of the observatory in case vertical access shafts are employed. Each corner station is built around a 20 m diameter vertical shaft. If tunnel excavation is accomplished by tunnel boring machines, then these will be lowered through these shafts at the start of construction. After tunnel construction, the shafts will be equipped with concrete elevator modules, staircases and will carry all services (power, water, compressed air, ventilation ducts, *etc.*). Additional shafts with a 10 m diameter are foreseen at the centre of the arms (not shown). The top of the shafts will be integrated in large surface buildings. There the equipment of the various interferometers, such as the vacuum system, will be prepared. Subsequently, the modules will be lowered through the shafts into the caverns by using hoisting devices.

Each of the corner stations has a main cylindrical cavern with a 65 m diameter. These caverns house the laser

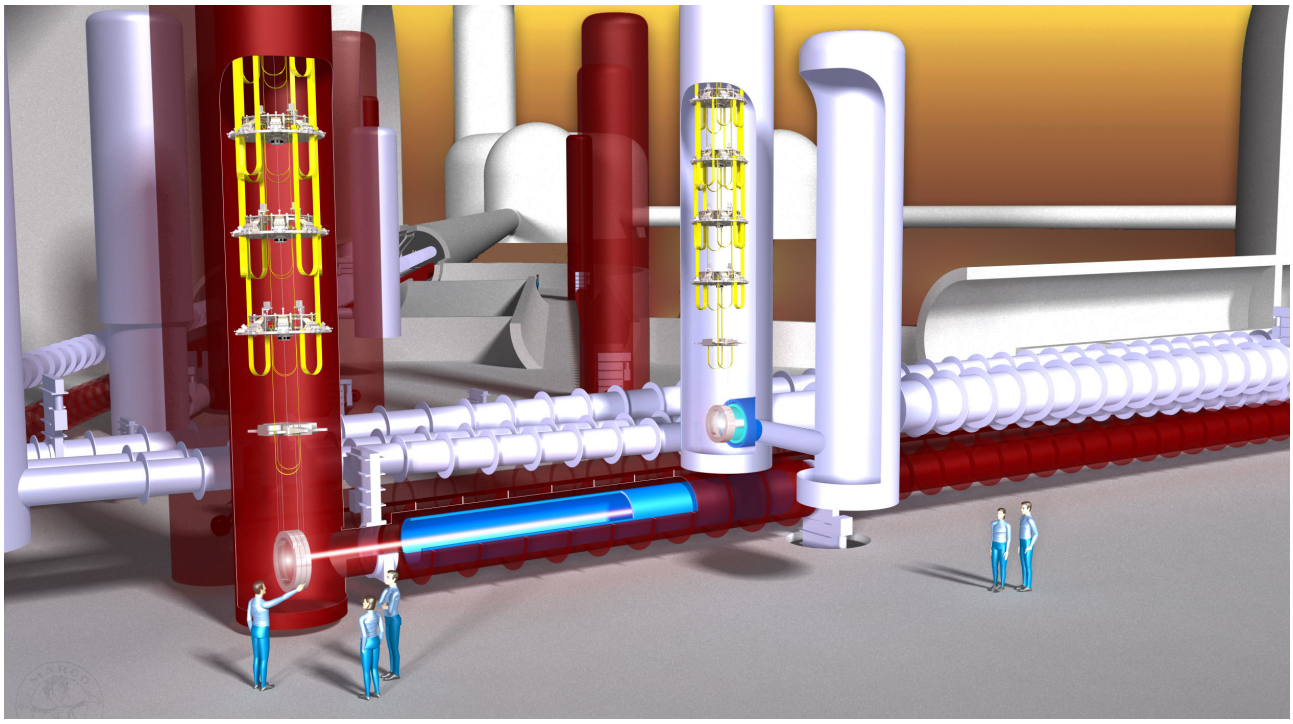

Figure 41: Artistic impression of equipment in a main cavern. Cryogenic and room temperature suspension chains isolate the test-masses located at the bottom of these superattenuators from seismic disturbances. Seismic isolation alone will not suffice and a site with low seismic displacement noise needs to be identified.

injection systems and many of the interferometer seismic isolation systems that suspend the optical components. Each cavern contains two levels. The top level has a height of 30 m, required for housing the main suspension systems and their vacuum envelopes. The basement level contains 3.5 m high passageways that lead to small cleanroom areas below the suspension systems, providing underneath access to the suspended optical components. The vacuum pipes for the low frequency and high frequency interferometer are situated on top of each other. In this way, the interferometer beams propagate horizontally and are housed in separate vacuum pipes. For cryogenic design purposes, the vacuum system of the cryogenic interferometer is situated on top of the high frequency system.

From the detector layout shown in Fig. 41, it becomes clear that each of the corner stations contains detector components from all three xylophone detectors. The main optical components of the interferometers need to be suspended requiring a total of 17 suspension towers in each main cavern. Four of these towers are part of the cryogenic suspension system for the end test masses. A point of interest is that three towers contain double payloads, while another three towers contain triple payloads. Technical difficulties associated with multi-payload suspension systems are dealt with in chapter 4. Finally, the main caverns are occupied by two cryolinks each, that protect the cryogenic end test masses from thermal radiation. The cryogenic infrastructure needed for the operation of these cryolinks is discussed in section 3.9.

An impression of a main- and a single satellite cavern, connected by a tunnel system is shown in Fig. 42. It can be seen that the main cavern is connected to four tunnels. Two of these tunnels accommodate up to six vacuum beam pipes. A third tunnel holds a single vacuum pipe while the fourth tunnel is empty. This parallel tunnel system will be used to allow transportation of equipment between main caverns and auxilliary caverns, while providing parallel escape routes for emergency purposes.

As with the main caverns, the satellite caverns contain two levels with 3.5 m high passageways underneath the 30 m high top level. These caverns are designed with a cylindrical in shape with an inner diameter of 30 m. Although the inner diameter of the cavern could be optimised, the designed cavern provides flexibility and

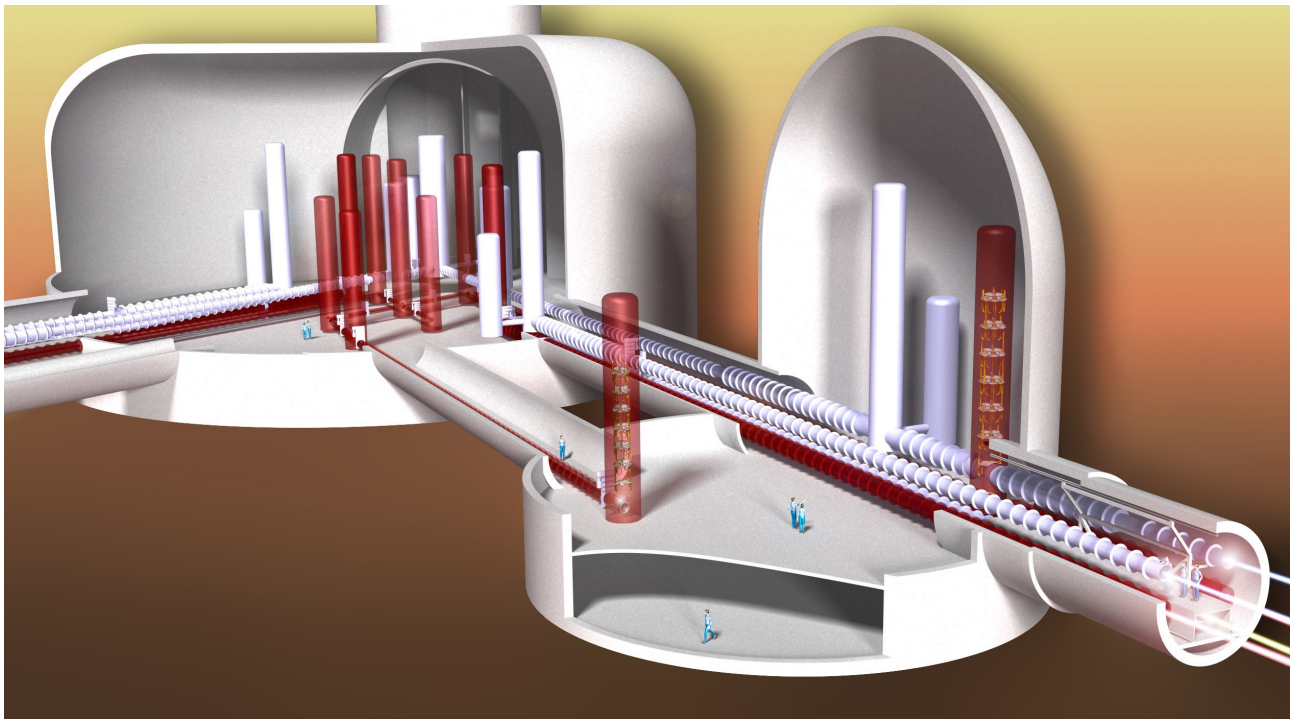

Figure 42: Impression of a corner station of Einstein Telescope. Satellite caverns are connected via double tunnels to the main caverns. Filter cavities for the high frequency interferometer are placed in one of these tunnels. The satellite caverns house the input test masses and the cryogenics infrastructure.

space for possible future infrastructure. In its final configuration, six beam pipes pass through this each of these caverns. The caverns are occupied by the input test masses of both the low frequency and high frequency interferometers. The low frequency input test masses are cryogenic payloads and are protected from thermal radiation by cryolinks. The satellite caverns are equipped with the necessary cryogenic infrastructure.

The corner stations are connected by approximately 10 km long tunnels between the satellite caverns. These tunnels have an inner diameter of 5.5 m over most of their length. The main caverns and the auxilliary caverns are connected by parallel tunnels with a length of 300 m. Consequently, in its final form the observatory will host more than 31 km of total tunnel length. The main interferometer arm tunnels accommodate six vacuum beam pipes: two for the high- and two for the low frequency interferometers, and two for filter cavities. In addition, the tunnel houses the services for electricity, water, compressed air, cryogenics, safety systems and air conditioning. The diameter of the tunnel is sufficiently large to allow transportation of vacuum beam pipes. A sketch of the tunnel is shown in Fig. 43. During the construction of ET, the tunnel will be equipped with a monorail to transport sections of vacuum beam pipes to the welding and installation area. Later, this system is to be converted to a personnel transport system. For safety reasons the tunnel is divided into 500 m sections that are equipped with fire retarding doors, and safety shelters. The tunnel is equipped with an elaborate safety system that allows control of the airflow in order to direct the smoke in case of a fire.

Laser interferometers for gravitational wave detection require ultra-high vacuum systems for housing the optical systems. In order not to be limited by noise due to vacuum fluctuations, requires a base pressure below 10^{-10} mbar. Furthermore, the system must be extremely clean from organic molecules. Einstein Telescope will feature the world's largest ultra high vacuum system and in order to minimise costs, the beam pipes will be fabricated from stainless steel by continuous spiral welding. For this purpose, a dedicated clean factory will be installed on site.

Cryogenic infrastructure is needed for the operation of the various interferometers. Large cryo-traps are foreseen and will be cooled by liquid nitrogen in case of the high frequency interferometers. The cryo-plants required for

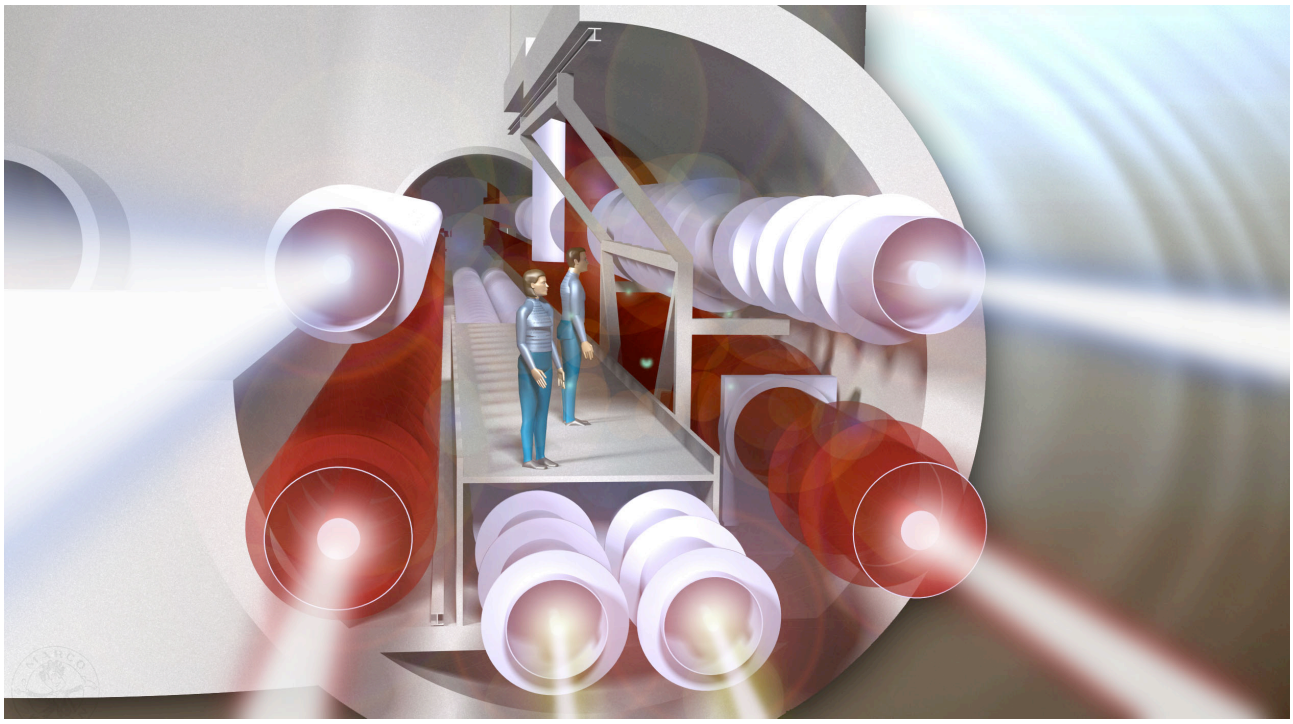

Figure 43: Schematic outline of the tunnel. The tunnel with inner diameter of 5.5 m is occupied by the vacuum vessels that hold the low frequency and high frequency arms of two interferometers. In addition, the vacuum vessels for both filter cavities are housed.

the low frequency interferometer will provide refrigeration power allowing to bring the mirror temperatures to 4 K[15]. This can be accomplished by either a battery of cryo-coolers or by using liquid helium cryostats.

Safety and health will have the highest priority during every stage of the planning, design, construction, and operation of the observatory. Particular attention has to be paid to key areas such as underground communication, ventilation, access, emergency egress and refuge design. During the construction of the subterranean infrastructure, the safety of both engineering and scientific personnel has to be ensured.

3.4 Site specific noise

As was mentioned in the reference design section, it is of great importance to determine if sites contain already existing infrastructure, what the depth of the site is, and what the geologic and seismologic stability is at a given location. This last point is because site specific noise sources, like for instance seismic noise, will most likely influence the final sensitivity of the ET observatory. In order to prevent that the detector sensitivity is affected by seismically induced vibrations, current gravitational wave detectors employ seismic isolation system. Details about the proposed seismic isolation strategies for ET are explained in Chapter 4. For illustrative purposes, figure 41 shows an artist cut-away impression of the 17 m high suspension systems, proposed for the ET test masses.

The seismic isolation requirements for ET scale with the local seismic activity at a given site. Thus, when scaling the seismic isolation requirements from current detectors to those for ET, it becomes clear that sites with a low seismic noise background are required to fulfil the seismic isolation target. Following in the footsteps of LCGT, site studies were therefore aimed at underground environments in Europe. The most significant results of this study are presented in 3.6, showing the variation in local seismic activity in a variety geologies like hard

[15] Although the system allows cooling to 4 K, the system operates at 10 K.

rock (Frejus, Canfranc, Gran Sasso, Sardinia and Hungary in Europe, Homestake in the USA, and Kamioka in Japan), salt (Slanic Salt Mine in Romenia, and Realmonte in Sicily), and in Boom clay (the HADES facility for storage of nuclear waste in Mol, Belgium).

3.4.1 Seismic noise

Noise studies [282–285] often categorise seismic noise sources according to frequency. For Einstein Telescope, critical frequency regions are in the range of 0.1 - 10 Hz, where the seismic noise is variable mainly due to microseismic and human activity. Noise at frequencies below 1 Hz is termed 'microseismic' and its sources are dominantly natural (*i.e.* non cultural and non-local), depending on oceanic and large-scale meteorological conditions (*e.g.* monsoons and cyclones). Around 1 Hz wind effects and local meteorological conditions show up, while for frequencies above 1 Hz additional sources (besides natural) are related mainly due to human activity. Such noise is termed 'cultural noise' or 'anthropogenic noise'. It should be noted that the 1 Hz division is not absolute.

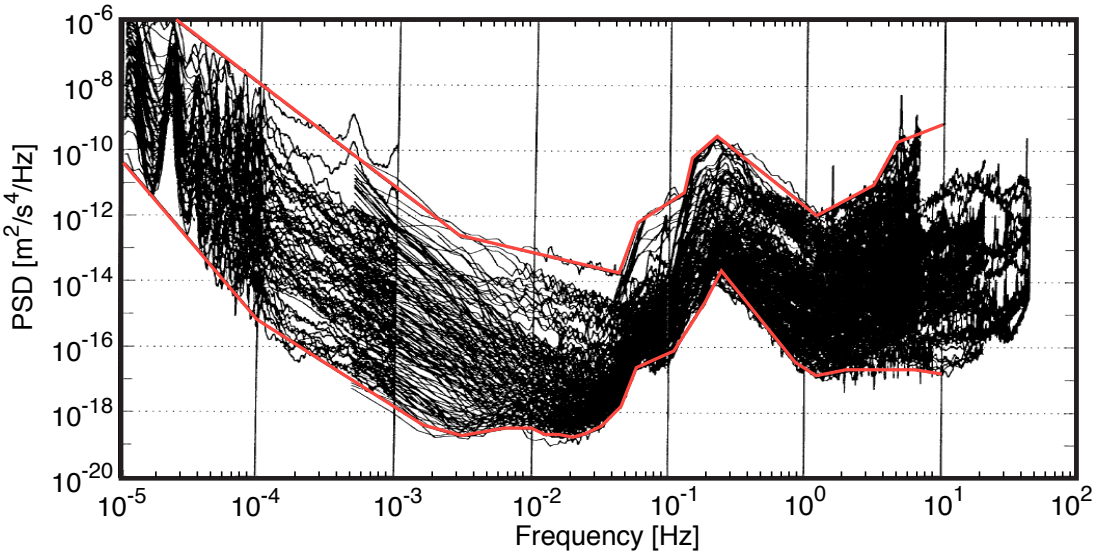

Figure 44: Overlay of network station spectra used in Peterson's background noise study [286] together with straight-line segments fitted to the high-noise and low-noise envelopes of the overlay.

Throughout this section seismic measurements are presented as acceleration power spectral density (PSD)[16] versus Fourier frequency, where PSD values have units of squared acceleration $(\mathrm{m/s^2})^2/\mathrm{Hz}$. The largest PSD values are seen at low frequencies. Here, the surface of the Earth experiences large external forces due to the gravitational attractions of the Moon and Sun. At very low frequencies this causes the surface of the Earth to rise and fall with amplitudes of about 0.5 m with respect to the center of the Earth. This tidal motion can be seen in Fig. 44 at a frequency of 2.3×10^{-5} Hz. Since the motion occurs at very low frequency the interferometer test masses will move *coherently* and differential test mass motion presents no problem. Large PSD values are observed at frequency clustered around 5.5×10^{-2} Hz and 0.2 Hz which correspond to microseisms. Note that a large dynamic range of more than eight orders of magnitude is needed to accommodate signals between 0.01 Hz and 1 Hz.

Peterson [286] catalogued acceleration noise power spectral density plots for frequencies up to 50 Hz from 75 seismic stations distributed worldwide. Several years of data were collected (about 12,000 spectra in total). From the upper and lower bound of the combined data of both surface and borehole sensors (100 - 340 m depth)

[16] In the literature various representations are used, such as the root power spectral density (RPSD), acceleration, velocity and displacement spectral densities.

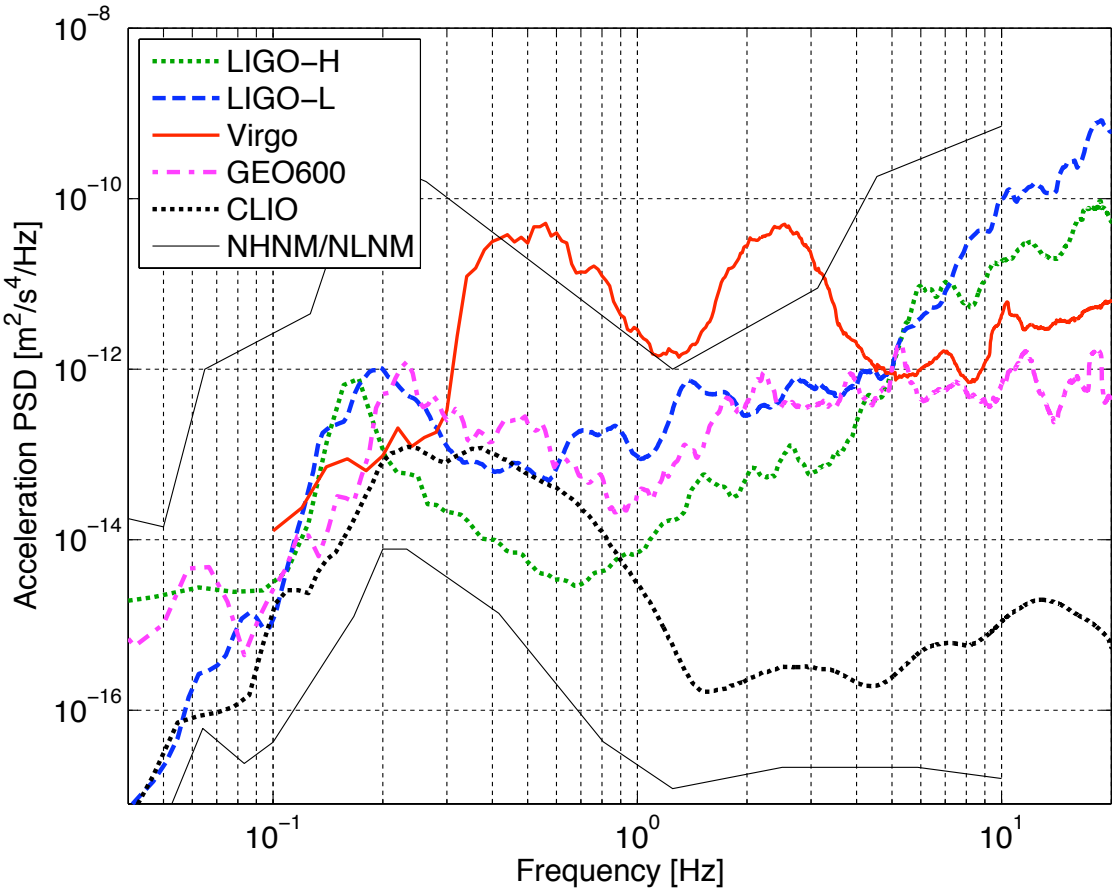

Figure 45: Seismic acceleration PSD at current gravitational wave detector sites. The magenta dotted line represents the most critical seismic performance limits, which are set by gravity gradient noise.

Peterson derived, what is now known as, the new high/low noise model (NHNM/NLNM), which replaced his earlier low noise model [287]. The data including the upper and lower bound fit are shown in Fig. 44.

As can be seen from Fig 44, microseismic ground motion is a prominent feature for frequencies around 0.07 Hz and 0.17 Hz. The small lower-frequency peak (periods of 10 - 16 s) correlates with the frequency of coastal waves, where the ocean wave energy is converted into seismic energy through either vertical pressure variations or from the surf crashing onto the shore. The larger peak, at about twice the frequency (periods of 4 - 8 s), originates from standing ocean waves that couple to the continental shelf. The standing waves are generated by superposition of ocean waves of equal period traveling in opposite directions and have recently been confirmed by satellite observations. Corresponding PSD values change up to 30 dB depending on the storm intensity, while the two frequencies shift upward as storms age.

For Einstein Telescope the critical frequencies f are in the range 0.1 - 10 Hz, where the seismic noise is variable mainly due to microseismic and anthropogenic activity. It is therefore important to chose a site location far from oceans and human activities (both at present and in future). The NLNM yields a PSD of $1.38 \times 10^{-17}\mathrm{m}^2/\mathrm{s}^4/\mathrm{Hz}$ at 1 Hz corresponding to an acceleration of $3.7 \times 10^{-9}\mathrm{m/s}^2$. Like the NLNM many remote sites show an approximately flat PSD response for accelerations in the frequency band of 1 - 10 Hz. Corresponding displacements can be found by double integration of the accelerations yielding a $1/\omega^2$ frequency dependence. The conversion should take the integration bandwidth into account (often 1/3 octave is used corresponding to a range of $\pm 10\%$ about the center value). Note that when a Gaussian signal is passed through a narrow-band filter, the absolute peak signals of the filtered signal envelope will have a Rayleigh distribution (yielding a factor

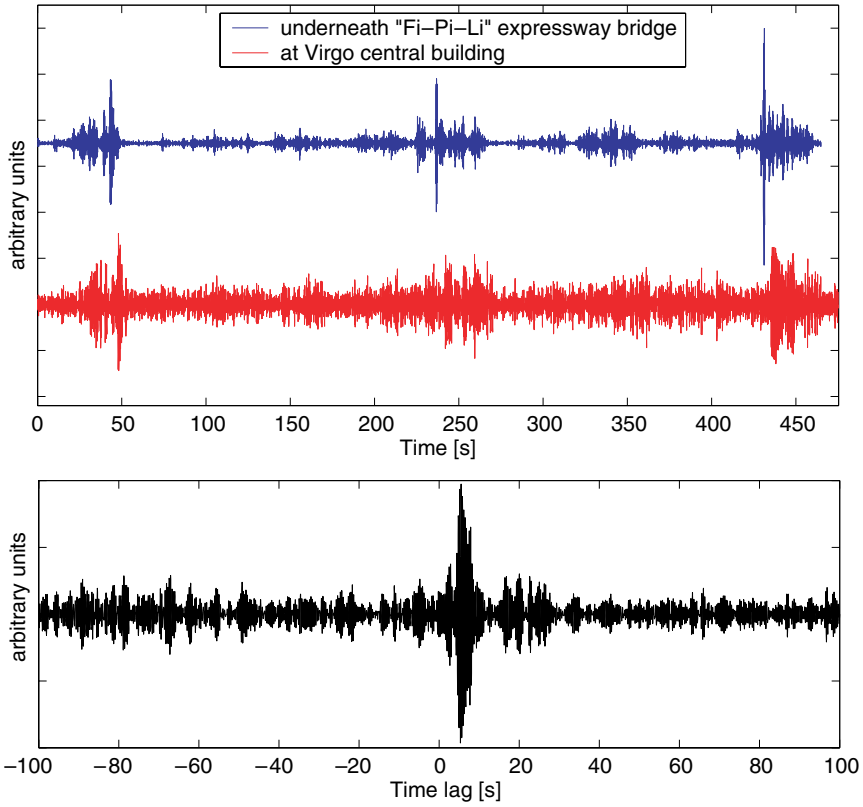

Figure 46: Top: Seismogram recorded on the ground underneath one of the nearby bridges (top signal) and the simultaneous seismogram recorded at Virgo (bottom signal). Three heavy trucks were crossing at approximately 5, 230, and 420s. Both signals have been bandpass filtered between 1 and 4 Hz. Bottom: Cross-correlation of the first 100s between the two seismic channels.

1.253σ for $|\overline{x}_P|$). Using the above, we find that the lowest possible displacements, according to the NLNM, are about 0.1 nm/$\sqrt{\text{Hz}}$ at 1 Hz and decrease with f^{-2}.

Presently, the large interferometric detectors GEO600, LIGO, and Virgo are placed on the surface of the earth and, consequently, are sensitive to seismic disturbances. Virgo has already demonstrated good performance above 40Hz, due to a suitable attenuation scheme. Upgrades to LIGO and Virgo will employ further seismic noise reduction by improving their respective active and passive vibration isolation systems. Fig. 45 shows a comparison of seismic acceleration power spectral densities of the GEO, CLIO (the location for LCGT), Virgo, and LIGO Hanford and Livingston sites. From these ground motion measurements it is clear that the level of seismic noise reduction in the underground environments of CLIO will be less stringent by several orders of magnitude. For Einstein Telescope, the interferometer test masses will be suspended from even more sizeable and complex seismic attenuators, which scheme is discussed in chapter 4. Using these scaled versions of the Virgo super-attenuator at a site that has a low seismic noise background ensures that the ET-D target sensitivity can be reached.

Anthropogenically generated seismic noise

As was discussed above, the NLNM is a composite of many different stations and instruments with different geology and in various geographic regions. Therefore, it is not possible to duplicate its response at one specific location. It has been observed that lowest noise is obtained in continental sites with sensors placed in hard rock. Sensors with low PSD values are often at borehole and subterranean stations operated at remote sites, far

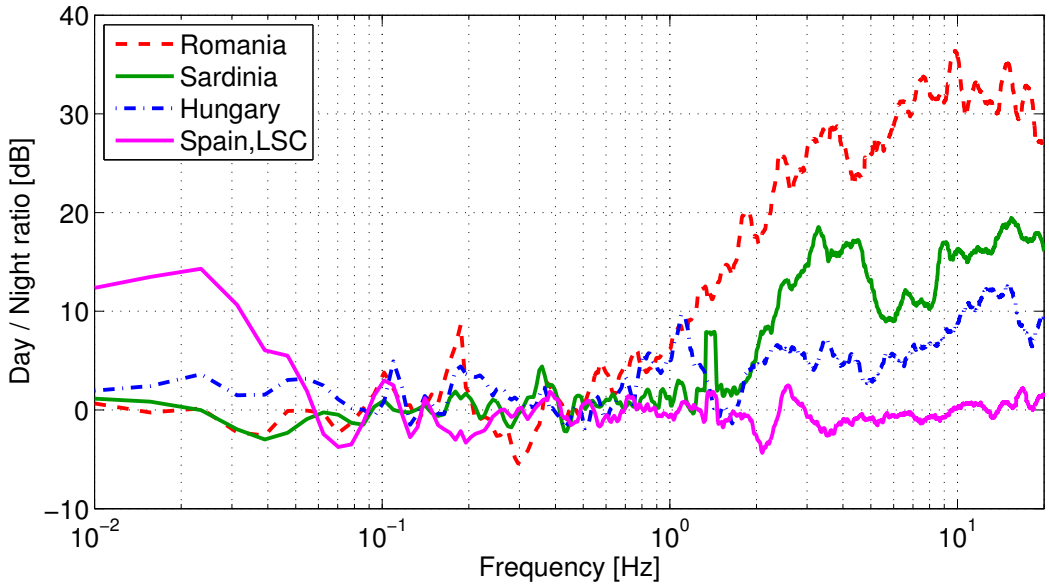

Figure 47: Midday versus midnight noise PSD ratios as a function of frequency at four different measurement sites. Cultural noise is visible for frequencies above 0.7 Hz.

from cultural, oceanic, and meteorologically induced seismic noise. For siting an observatory, this means that the distance to urban areas, highways, railways, and airports, needs be considered.

The influence of traffic induced seismicity on gravitational wave detectors has been studied by various authors. Road noise depends on road structure and materials, traffic density and vehicle type and speed. Schofield *et al*. [288] reported that local traffic, from passenger vehicles to heavy trucks, induced vibrations at the LIGO Hanford, WA, site. Vibrations were measured for frequencies in the 1 - 50 Hz range, with maxima around 4 - 12 Hz. At the Virgo gravitational wave site, road noise was analysed by using recordings of the seismic field at the Virgo site and correlating these recordings with measurements underneath a major high way overpass, 4 km away from the Virgo North arm terminal building [289]. Seismic noise originating from the nearby traffic was found in frequency ranges of 1 - 4 Hz, peaking at 3 Hz. The top plot of Fig. 46 shows the seismic recordings underneath the overpass and at the Virgo end building. The bottom plot of Fig. 46 shows the cross-correlation between the two signals during the first 100 seconds. Coward *et al*. [290] recorded ground vibrations at the AIGO site in Australia for vehicles passing the instrumentation as close as 24 m. Road noise was visible in the 5 - 30 Hz frequency band.

Even in remote areas anthropogenic noise can still be recognised. Spectrograms for frequencies up to 60 Hz have been made by Young *et al*. [291] with seismometers at the surface and within boreholes in the USA for data collected over more than one year. Seismometers were placed in boreholes at Amarillo, TX, at depths of 5, 100, 200, 367, 1219 and 1951 m. The anthropogenic character was present at all depths and exceeded background by about 10 dB. Its source was identified from diurnal patterns and was prominent for frequencies between 1 and 40 Hz. At Datil, NM, seismometers were installed at depths of 0, 5, 43, and 85 m and cultural noise was absent, most probably due to the remoteness of the site. At Pinedale, WY, with seismometers at depths of 3, 13, 30, 122 and 305 m, diurnal patterns in cultural noise were obscured by a pattern of progressive day-time increase of wind noise.

As part of the site characterisation, the presence and spectral PSD values of anthropogenic noise were investigated. Fig. 47 shows an example of the day/night ratio obtained from four different site measurements. Respective high and low frequency disturbances can easily be recognised by comparing the listed day/night ratio values with local population density and the distance to seas and oceans, which are listed in Table 4. Comparing these statistics, and comparing this with the population density map of Europe in Fig. 48 (data from REGIO database of Eurostat) collaborates the day/night ratio's found in Table 4.

Table 4: Population density at four different measurement sites. Population density figures are given in km^{-2}.

Location	Pop. Density [km^{-2}]	Dist. to ocean/sea [km]	Day/Night @ 10 Hz [dB]
Romania	180	300	33
Sardinia	10	10	16
Hungary	75	500	9
Spain	1.38	120	1

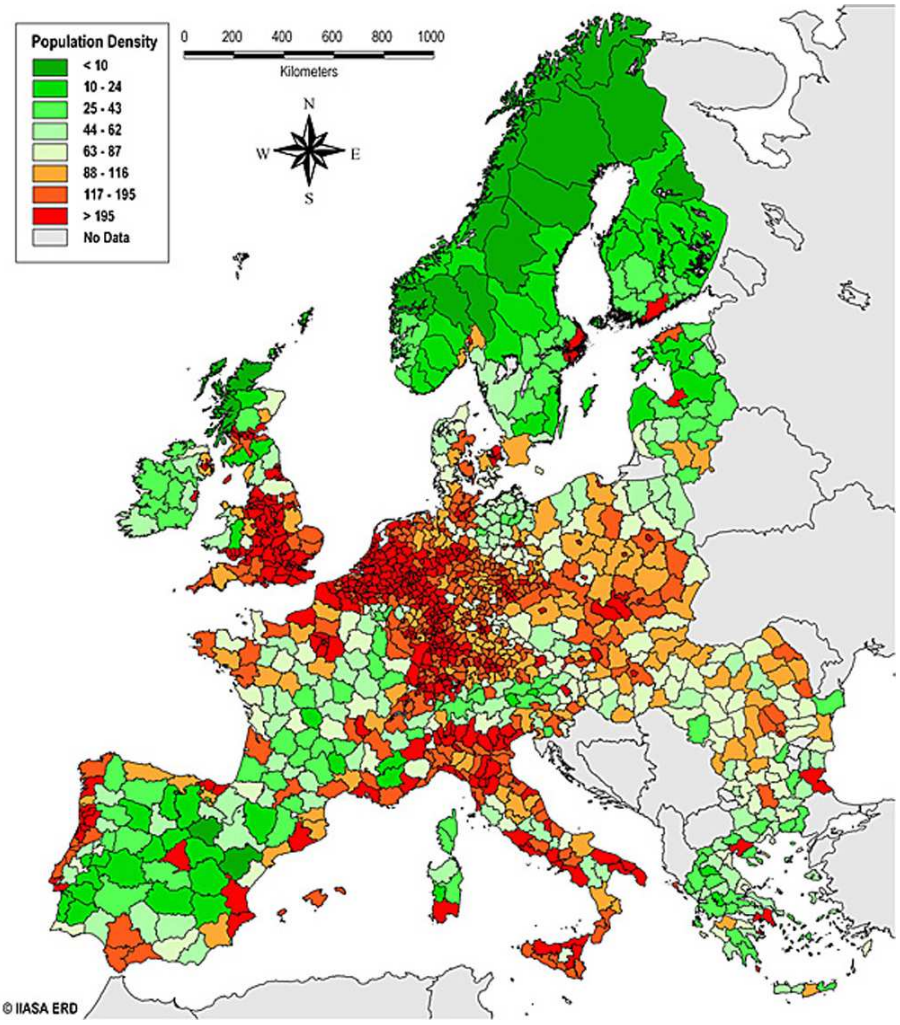

Figure 48: High frequency (1 - 10 Hz) seismic noise is driven by cultural noise. Density of population in Europe from the REGIO database of Eurostat [292].

Wind generated seismic noise

Wind noise has been studied by a number of authors to quantify the conversion of wind energy into ground motion. The presence of wind causes movement of surface objects, such as trees or structures, or directly through turbulent pressures on topographic irregularities. Of particular interest for ET are its frequency range, the wind speed threshold for it to become evident, and its persistence with depth.

Withers *et al.* [293] performed measurements at Datil, New Mexico in the frequency band of 1 - 60Hz. This is a remote site that features sparse vegetation and distances to the nearest road and railroad were 12 and 90 km respectively. Measurements were performed at a depth of 0, 5, 43 and 85 m and the effect of wind noise was evident over the entire observed bandwidth with an ambient background threshold of ∼3 m/s. At a depth of 43 m a reduction of 20 dB was found. Slightly higher reduction factors were found at 85 m.

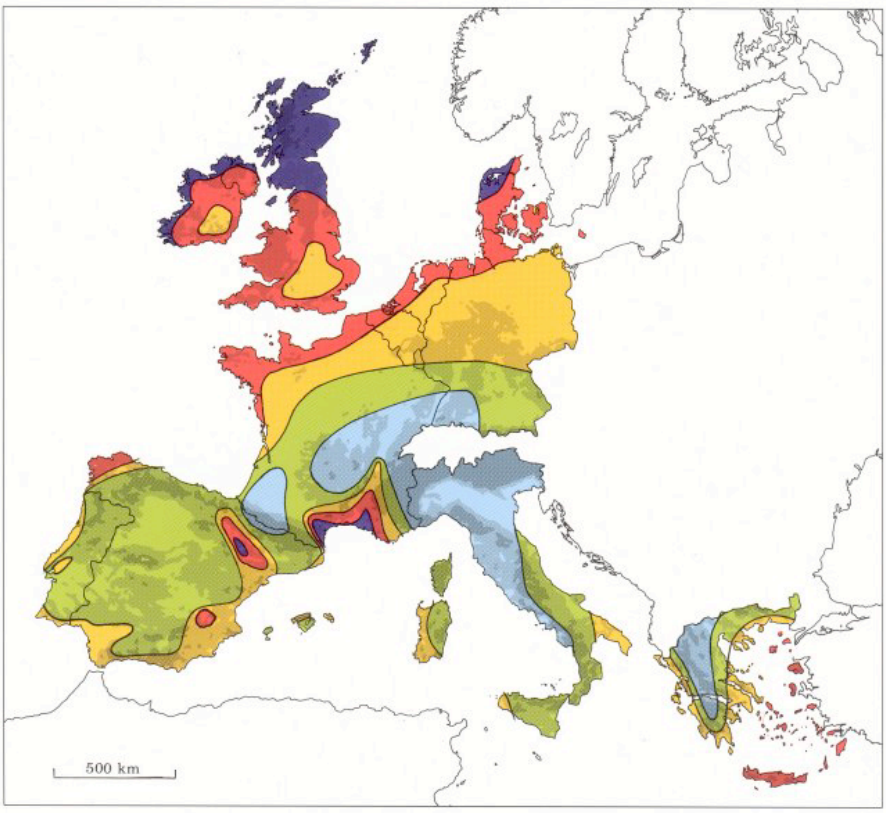

Wind resources[1] at 50 metres above ground level for five different topographic conditions

	Sheltered terrain[2]		Open plain[3]		At a sea coast[4]		Open sea[5]		Hills and ridges[6]	
	$m\,s^{-1}$	Wm^{-2}	$m\,s^{-1}$	Wm^{-2}	$m\,s^{-1}$	Wm^{-2}	$m\,s^{-1}$	Wm^{-2}	$m\,s^{-1}$	Wm^{-2}
	> 6.0	> 250	> 7.5	> 500	> 8.5	> 700	> 9.0	> 800	> 11.5	> 1800
	5.0-6.0	150-250	6.5-7.5	300-500	7.0-8.5	400-700	8.0-9.0	600-800	10.0-11.5	1200-1800
	4.5-5.0	100-150	5.5-6.5	200-300	6.0-7.0	250-400	7.0-8.0	400-600	8.5-10.0	700-1200
	3.5-4.5	50-100	4.5-5.5	100-200	5.0-6.0	150-250	5.5-7.0	200-400	7.0- 8.5	400- 700
	< 3.5	< 50	< 4.5	< 100	< 5.0	< 150	< 5.5	< 200	< 7.0	< 400

Figure 49: European wind resources based on data collected for the European Wind Atlas [294].

Young *et al.* [291] carried out similar measurements. Wind speed thresholds, for the presence of wind induced background noise, were found to be 3-4 m/s at depths of 0-5 m and 8-9 m/s at depths below 100 m. A strong correlation between seismic noise and wind was observed over a broad frequency spectrum range from 1 to 60 Hz. The noise was 34 dB above the NLNM at a depth of 3 m, and decreased to 10 dB above NLNM at a depth of 305 m. Koller *etal.* (2004) determined that many parameters relating to measured ground motion caused the amplitude ratio to vary, but that only wind speed affected the frequency at which the horizontal to vertical ratio curves peaked. Mucciarelli *etal.* (2005) found that, provided the sensor was sheltered from direct wind (inside a concrete box at 1.5 m depth), wind increased the amplitude of all components of seismic noise (vertical, east-west, north-south) in the band 0.1 - 10 Hz similarly, such that ratio was unchanged. This conclusion was valid for wind speeds up to 8 m/s.

The reductions in wind noise are a prime example that surface seismic noise contributions will decay with depth. For ET, the underground environment is expected to improve on all sources of seismic noise since surface seismic

noise is exponentially reduced with depth, $e^{-4d/\lambda}$, where d is the depth and λ is the wavelength of the seismic wave. Fig. 50 shows results from measurements at the Gyöngyösorozi mine by Beker *et. al.* in the Hungary. A factor of ∼10 suppression at 10 Hz at the depth of 400 m, and substantially more at higher frequencies. At Gyöngyösoroszi, the speed of sound at 400 m underground (hardrock) is about 3 km/s, implying that the seismic waves in the 0.1 - 10 Hz band have long wavelengths that at the surface: 300 m - 30 km.

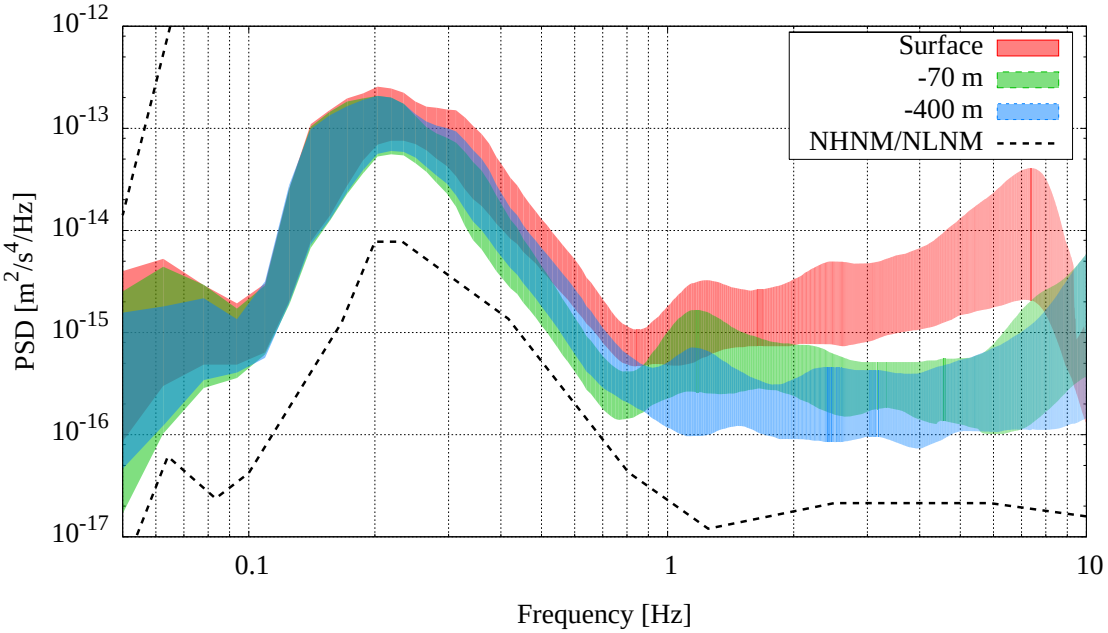

Figure 50: Measured reduction of seismic noise at the Gyöngyösorozi mine in Hungary for three different seismic sensors at depths of 0, 70, and 400 m.

3.4.2 Geological and geographic observations

McNamara and Buland [295] have carried out a study of geographic dependence of ambient seismic noise in the USA. Fig. 51 shows that the strongest geographic dependence is obtained for frequencies above 1 Hz (panel A). Noise levels at the East coast are up to 50 dB above NLNM due to large population centers and represents cultural noise. Microseism shows up in the 0.125 - 0.25 Hz frequency range (panel B) and is dominant is coastal regions. The US continental interior has noise levels about 10 dB above NLNM.

Recently, OneGeology [296], an ambitious online project, under the direction of the British Geological Survey, started the collection of worldwide geological information. Large areas of alluvium can be identified in Europe. Allivium is deposited soft soil composed of silt, clay, sand and gravel. Its material properties vastly differ from hard rock such as granite. This has immediate consequences for the ambient seismic noise levels. The seismic data have been obtained with the ORFEUS (Observatories and Research Facilities for European Seismology) network, a non-profit foundation that aims at co-ordinating and promoting digital, broadband seismology in the European-Mediterranean area. For frequencies around 2 Hz the seismic noise is almost 40 dB higher in alluvium (stationa GE.HLG) than hardrock (station CH.GIMEL). This is caused by the lower velocity of seismic waves in sediments compared to hardrock. Areas dominated by alluvium can be found in the Netherlands, northern Germany and Poland, in the south of Germany, northern Italy (Po area), Toleda area in Spain, and eastern Europe. PSD values about 40 dB larger than hardrock have also been found in alluvium regions near Bejing, China and Santa Barbara, USA. Although for a surface site such regions should be avoided, this is not at all clear for an underground site.

Results of a systematic investigation of ambient noise in Germany [297] were made by Steinwachs. Noise levels

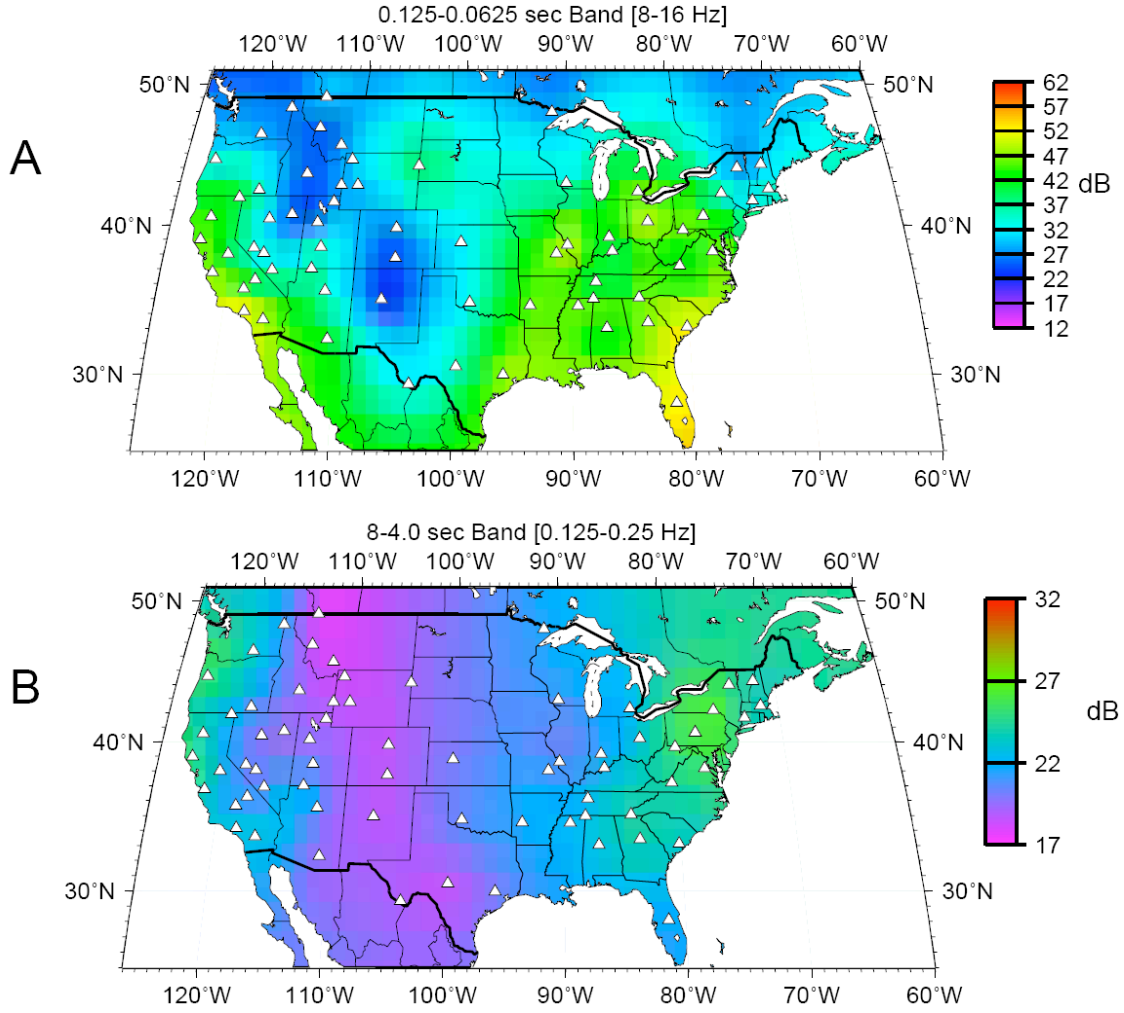

Figure 51: PSD noise levels above the NLNM mapped across the US in two separate frequency bands [295]: panel A or 8 - 16 Hz and panel B for 0.125 - 0.25 Hz.

are lowest for sites in the south of Germany where geology is determined by kristalline granite formations. Highest ambient noise levels are recorded in the north of Germany where the hardrock layers are covered by alluvium (molasse). In between layers of harder Jura formations cover the crystalline granite. Average spectral densities are fitted with exponential functions because of strong oscillations in PSD values. The signal at 2 Hz for the smallest spectral densities has been traced by a directional analysis to Rayleigh waves originating from the coast of Norway. The signal is believed to be due to choppy water waves in the shallow North Sea hitting the shore.

At first sight it may be thought that Scandinavia may provide suitable sites, since it is scarcely populated leading to low cultural noise, while the surface is dominated by old, good crystalline hardrock. However, seismic measurements from the KONO station near Kongsberg, Norway, show PSD values 20 - 30 dB above the NLNM (typically -140 dB around 1 Hz). It should be noted that the KONO sensor is located in a silver mine at 340 m depth. The ambient seismic noise is due to the high frequency tail from the microseismic peak. KONO data show that the microseismic peak show large seasonal variations. Moreover, in the winter months seismic noise can be expected from ice activities in the Baltic Sea.

3.5 Newtonian noise

A source of noise within the gravitational wave detector that originates from the local seismic activity is GGN (gravity gradient noise), also referred to as NN (Newtonian noise). The seismic activity causes perturbations in the local gravity field, which couples directly to the interferometer test masses. Up until now, no experimental methods for NN suppression exist and suppressing this noise source is difficult. As such, it is crucial to identify sites that exhibit low seismicity. It is expected that an underground environment is to improve on all associated sources of seismic noise spectral amplitude, including seismically induced NN. Furthermore, the local environmental conditions underground are usually stable (and controllable) and anthropogenic-induced seismicity is much more controllable underground, where access is limited. The following subsections discuss this issue.

In Subsection 3.5.1 a simple analytical estimations of NN is discussed. The power spectrum of NN is written as a function of a measurable seismic quantity, under the hypothesis of homogeneity for the medium, and neglecting any kind of effects from underground structures. This kind of approach is possible only with simplified models, however it can provide guidelines expecially when detailed informations about the geological structure of the site are not available.

A complimentary approach to analytical estimation, based on finite element models, is presented is Subsection 3.5.2. This is the natural way to give a refined evaluation of aspects that cannot be considered easily in the analytical approach, such as the effect of the infrastructures and of the geological details, for example inhomogeneities.

Finally, two NN subtraction schemes are presented. In Subsection 3.5.3 a subtraction scheme is presented to monitor the NN induced by the ambient seismic background, using a seismic sensor array. This is the approach that must be used when it is not possible to recognise a dominant and localised source of seismic noise.

On the other hand if a strong and coherent source of noise is known (for example a pump), a single accelerometer can be used to monitor the induced seismic field. Using optimal filtering, the NN transfer function is estimated from the source to the interferometer test mass, and can be subtracted from the data. Details about this subtraction procedure are presented in Subsection 3.5.4.

3.5.1 A simplified NN estimate

For a given distribution of masses, which can be described by a mass density function $\rho(\mathbf{x},t)$, the acceleration experienced by a test mass located at $\mathbf{y}$ can be written as

$$\mathbf{a}^{NN}(\mathbf{y},t) = G\int_V \rho(\mathbf{x},t)\frac{\mathbf{x}-\mathbf{y}}{|\mathbf{x}-\mathbf{y}|^3}dV_x \tag{47}$$

where the integration is extended to the volume V of interest.

We are interested in the fluctuating part of this quantity when the medium is an elastic solid. From the expression of mass conservation we get

$$\dot{\rho} + \boldsymbol{\nabla}\cdot\mathbf{J}_m = 0 \tag{48}$$

where the mass density current is given by $\mathbf{J}_m = \rho_0(\mathbf{x})\dot{\boldsymbol{\xi}}(\mathbf{x},t)$, ρ_0 being the density of the medium in the static configuration and $\boldsymbol{\xi}$ its small displacement at a given point.

By inserting Eq. (48) inside Eq. (47) we find

$$\mathbf{a}^{NN}(\mathbf{y},\omega) = G\int_V \boldsymbol{\nabla}\cdot[\rho_0(\mathbf{x})\boldsymbol{\xi}(\mathbf{x},\omega)]\frac{\mathbf{x}-\mathbf{y}}{|\mathbf{x}-\mathbf{y}|^3}dV_x \tag{49}$$

Note that this expression contains two different effects, as can be seen expanding the derivative. The term proportional to $\rho_0\boldsymbol{\nabla}\cdot\boldsymbol{\xi}$ describes the fluctuations of the local density connected to the compression of the medium, while $\boldsymbol{\xi}\cdot\boldsymbol{\nabla}\rho_0$ takes into account the effect of the movement of density inhomogeneities, for example at the surface boundary.

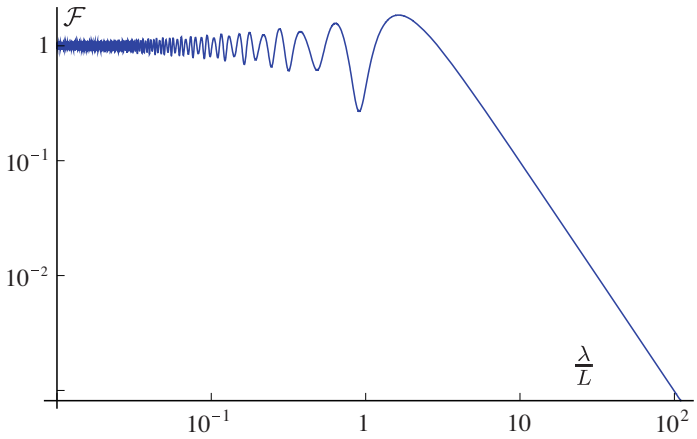

Figure 52: The geometrical suppression factor $\mathcal{F}$ as a function of the ratio between the mode's wavelength and the length L of the interferometer arm. $\mathcal{F}$ suppresses the NN at low frequencies. It is normalized to one in the high frequency region, where the contribution of the motion of each test mass is uncorrelated and adds in quadrature.

Starting from Eq. (49) a general theory about the connection between seismic measurements and NN can be developed. We will not give here the details, which can be found for example in [298]. The general idea is to decompose seismic motion in normal modes, which are supposed to behave as oscillators coupled to unknown stochastic forces. By measuring quantities connected to seismic fluctuations (for example the power spectrum of horizontal and/or vertical displacement, or the correlation between displacements at two different points) we can get information about the excitation of these oscillators. Using Eq. (49) these can be converted to an estimate of NN.

By making some additional assumptions a simple estimate of strain equivalent power spectrum of NN S_h^{NN} can be done. We will present and discuss now this simplified result.

We model the ground as a homogeneous medium of given density ρ_0 and the longitudinal and transverse speeds of sound c_L, and c_T respectively. The mirrors of the interferometer are supposed to be underground, inside a cavity whose effect can be seen to be not important in the low frequency regime we are interested to.

As we said there will be two kind of contributions, connected to surface and bulk fluctuations. The main assumption of the model is that the fluctuations associated to surface Raileigh waves are dominant. In this case both the contributions are exponentially damped with the depth, over a typical scale of $\ell \sim v_s(2\pi f)^{-1}$ where v_s is the speed of sound and f the frequency.

If we assume further that damping effects are negligible, so that each mode is excited essentially only at its natural frequency we can write now the final expression for the NN estimate as

$$\sqrt{\frac{S_h^{NN}(\omega)}{C_{vv}^{seism}(0;\omega)}} = \frac{4\pi G\rho_0}{L\omega^2\sqrt{2}} \times \left(\frac{2(\beta_T^2+1)e^{\beta_L Kz} - (1+2\beta_L+\beta_T^2)e^{Kz}}{\beta_L(\beta_T^2-1)}\right)\mathcal{F}\left(\frac{\omega L}{c_T\sqrt{x}}\right)^{1/2} \tag{50}$$

where we choose to normalise the noise to the power spectrum of vertical surface seismic motion, $C_{vv}^{seism}(0;\omega)$. The function

$$\mathcal{F}(kL) = 1 + 2J_2(kL) - \frac{2}{kL}J_1(kL) - \frac{1}{2}J_2(kL\sqrt{2}) \tag{51}$$

which appears in Eq. (50) describes the coherence between the gravitational accelerations of different test masses. It is apparently real and it goes to zero in the low frequency regime. This is due to the fact that when the wavelength of seismic modes is large compared with the interferometer size each mirror feels the same acceleration, so that the length of the resonant cavities in the arms of the interferometer does not fluctuate. Practically it can be set to one in the frequency range of interest.

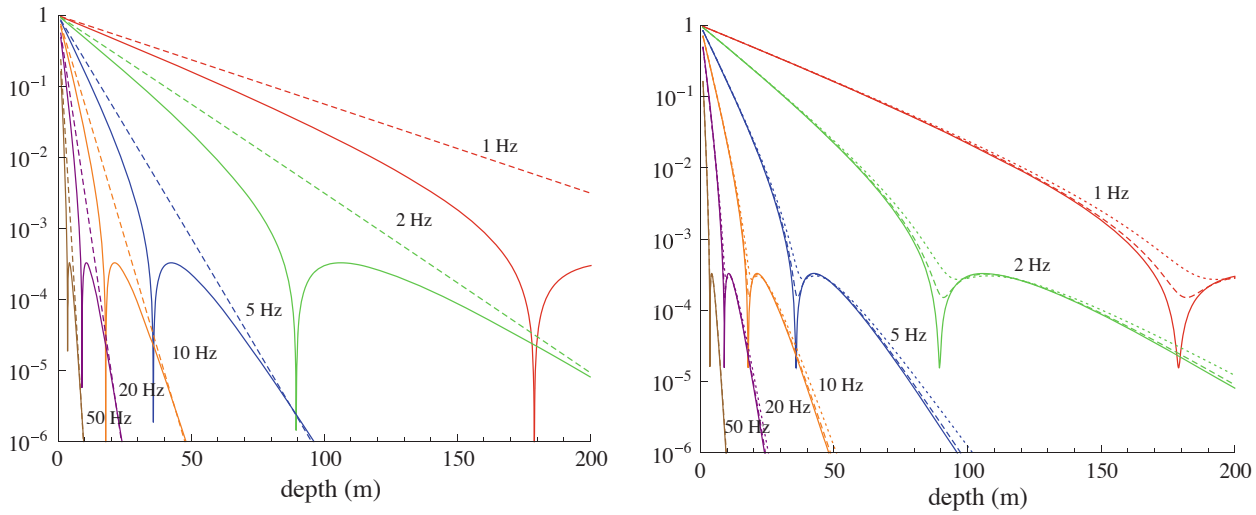

Figure 53: *Left.* The Newtonian noise attenuation factor (vertical axis) predicted by Eq. (51) as a function of depth (horizontal axis) for selected frequencies. The correspondence is red 1Hz, green 2Hz, blue 5Hz, orange 10Hz, purple 20Hz, and brown 50Hz. Here $c_T = 220m/s$ and $c_L = 440m/s$ (continuous curve) or $c_L = 880m/s$ (dashed curve). The zero appears when the two exponentially damped factors in Eq. (51) cancel. Before and after this point the decrease will be dominated by one of the two, therefore the decay constant changes. *Right.* The effect of the soil quality factor (vertical axis) as a function of depth (horizontal axis, in m) for selected frequencies. The quality factor is modeled using Eq. (50) and corresponds roughly to $Q = 10^4$ (continuous curve), $Q = 10^3$ (dashed curve), and $Q = 2 \times 10^3$ (dotted curve)

.

Setting $z = 0$ in Eq. (50) we can directly compare with previous estimates of NN on the surface [299–301], finding essentially an agreement.

The attenuation factor, which is the ratio between the NN amplitude at a depth z and the one on the surface, can be obtained by the middle term in brackets in Eq. (50). It is plotted in Fig. 53 (left) for several selected frequencies, as a function of the depth.

Looking at Fig. 53(left), at a given depth and frequency, the NN contribution can be zero. This in a sense is an artifact of our oversimplified model, and stems from our assumption that a mode contributes to the NN noise only at its resonant frequency. Another consequence of this assumption is that the vertical seismic correlation is proportional to $J_0\left(\frac{\omega r}{c_T\sqrt{x}}\right)$, causing it to decrease quite slowly (as $r^{-1/2}$) at large distances, which is unrealistic. We can take into account coherence effects by add some damping to the seismic modes considered in the model. This is equivalent to give a finite width to its resonant response. Just for illustrative purpose we can choose a Gaussian line shape parameterized by a width parameter Γ and compare the result for the NN estimate. We do not report the analytical details here, instead we present the result comparing the attenuation factor at different values of Γ in Fig. 53 (right).

We see the expected smoothing effect, and also an apparent saturation of the attenuation factor for the smallest soil quality factor Q. This is expected since the soil quality factor is small corresponding to longer wavelength modes, which are excited for a given frequency. The combination of the soil quality factor and coherence effects have also impacts on the estimate of NN, which will not be discussed here.

3.5.2 Finite element models

Complimentary to the presented analytical descriptions of seismic activity, it will be come important, whenever considering a non-homogeneous medium or complex geologies, to have an accurate description of the seismic wave field. Simulations of such systems were accomplished using the FE (Finite Element) software package

Comsol [302]. In the FE framework 3D continuum is subdivided into small hexahedral elements. Within each element the relevant physical parameters, like displacement and stress, are approximated by spline functions of arbitrary order. The following section shows how the FE software can be used to predict the NN contributions from surface and bulk waves in homogeneous media. The analysis provides the basis for simulation in non-homogeneous and/or stratified soils.

The displacement wave field that results from a seismic disturbance, is governed by the elasto-dynamic equations. The wave field in a homogeneous elastic medium can be expressed as a combination of plane body waves [303]. Two types of body waves exist, pressure (P) and shear (S) waves [304]. In the case of P-waves the movement of a ground particles is parallel to the direction of wave propagation. For S-waves the particle motion is perpendicular to the direction of the wave. The characteristics of seismic waves can be described by the ground properties, parametrized by the Young's modulus, E, the density, ρ, and the Poisson ratio, ν, describing the relationship between shear and strain forces. The wave velocities are then given by

$$c_P = \sqrt{\frac{E(1-\nu)}{(1-2\nu)(1+\nu)\rho}}, \text{ and } \quad c_S = \sqrt{\frac{E}{2(1+\nu)\rho}}, \tag{52}$$

for P and S-waves respectively. Typical values for hard-rock range from 3 - 6 km/s for c_P, and 1.5 - 4 km/s for c_S. In a medium that is bounded by another medium, such as air, or is composed of layers, surface and Head waves also exist. Head waves emerge in stratified media where modes propagating along an interface, cause energy to radiate into the low velocity zone. Surface waves are typically referred to as Rayleigh and Love waves. Love waves involve particle motion parallel to the surface and transverse to the direction of propagation. They produce no density variations and therefore have no effect on gravity gradients [301]. Rayleigh waves are polarised perpendicular to the surface and vanish with depth.

Solving the wave equation for harmonic Rayleigh waves results in the following displacement fields [305]

$$\begin{aligned} \xi_x &= iA(k_R e^{-\kappa_P z} - \zeta\kappa_S e^{-\kappa_S z})e^{i(k_R x-\omega t)}, \\ \xi_z &= -A(\kappa_P e^{-\kappa_P z} - \zeta k_R e^{-\kappa_S z})e^{i(k_R x-\omega t)}, \end{aligned} \tag{53}$$

where A is an arbitrary amplitude, t denotes time, ω denotes the angular frequency, z is the depth, k_R the wave number of the Rayleigh wave, and $\kappa_S = \sqrt{k_R^2 - k_S^2}$ and $\kappa_P = \sqrt{k_R^2 - k_P^2}$ decay factors related to the shear and pressure wave numbers. Finally, $\zeta = \sqrt{\kappa_P/\kappa_S}$. The horizontal Rayleigh wave speed, c_R, is slightly lower than the S-wave speed and when expressed in units of c_S is purely a function of ν. It can be found through $c_R/c_S = \chi$ where χ is the real root, in the range $0 < \chi < 1$ of the equation [305]

$$\chi^6 - 8\chi^4 + 8\left(\frac{2-\nu}{1-\nu}\right)\chi^2 - \frac{8}{1-\nu} = 0. \tag{54}$$

The above describes harmonic Rayleigh waves propagating far from the source. In reality, excitation of a medium results in a combination of all the different body and surface wave fields. An important aspect for third generation GW detectors is the influence of cultural seismic noise. It has been shown [306] that the distribution of displacement waves from an excitation with a circular footing on a homogeneous, isotropic half-space largely consists of Rayleigh surface waves: 67 % of the energy, with 26 % and 7 % in shear and compression waves, respectively. One solution to reduce the cultural noise amplitude, is to move away from (sub)urban areas. Their amplitude decays exponentially and is negligible at a depth of a few Rayleigh wavelengths, $\lambda_R = 0.92 c_S/f$. Therefore, it seems natural to consider underground sites for third-generation GW detectors.

As waves propagate through the medium, their amplitude decreases. This attenuation can be attributed to two factors; material and geometric damping. Geometrical damping is a result of energy spreading over an increasing area. The frequency dependent material damping involves energy lost due to friction. Seismic wave attenuation for homogeneous media, can be described by [307]

$$A_2 = A_1\left(\frac{r_1}{r_2}\right)^n e^{-\frac{\pi\eta f}{c}(r_2-r_1)}, \tag{55}$$

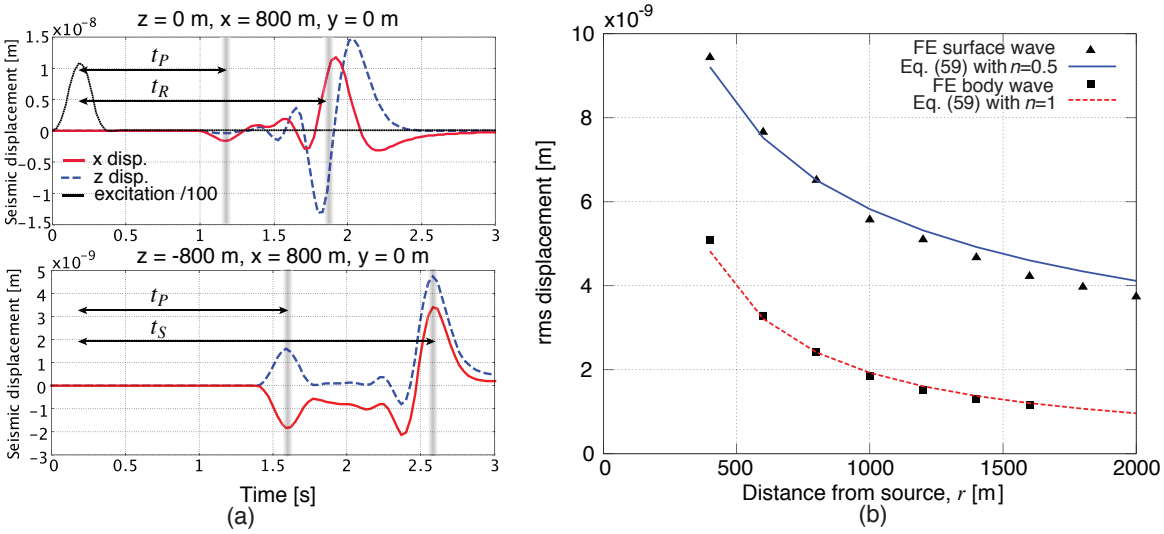

Figure 54: (a) Finite element ground displacement measurements at a surface and subterranean location after a pulse excitation. P, S and Rayleigh wave arrival times are indicated. (b) The finite element results for the rms amplitude of the surface and body waves with increasing distance from the source. The geometric damping contribution to Eq. (55) is plotted for comparison.

where A_1 and A_2 denote the wave amplitudes at distance r_1 and r_2 from the source, n represents the geometric damping coefficient, f is the frequency and c the propagation speed of the wave. The material damping is represented by the loss factor η. The geometric damping coefficient can be determined analytically by assessing the type of wave involved and the source type. For radial surface waves $n = 1/2$ while radial body waves within the medium decay with $n = 1$.

To confirm the ground motion response calculated by a FE model, the arrival times and geometric damping of the wave fields can be studied. A homogenous half-space was simulated by creating a half-sphere model with no reflection of waves incident to the spherical boundary. In view of symmetry the model could be further simplified to a quarter half-space with symmetric boundary conditions on the vertical surfaces. A single vertical excitation force was applied uniformly within a circular area at the origin with a time dependent factor given by $F(t) = A\sin^2(\pi t/T_e)$ for $0 \le t \le T_e$ where T_e is the excitation period. The amplitude scaling factor, A, was adjusted to create a vertical displacement at the excitation point of 1 μm.

The model has parameters $E = 10$ GPa, $\rho = 2.0$ g/cm^3, $\nu = 0.25$ and a radius of 2.2 km. This results in wave speeds of $c_P = 800$ m/s, $c_S = 462$ m/s and $c_R = 424$ m/s. No material damping was implemented in this model.

Fig. 54a shows the FE results of seismic displacements along with expected arrival times at a location on the surface and at a depth of 800 m. Note the phase difference of $\pi/2$ between the x and z displacements of the Rayleigh wave. The rms wave amplitude with increasing distance from the source across the surface and within the medium are plotted in Fig. 54b. As expected from Eq. (55) the wave attenuation is proportional to $1/\sqrt{r}$ along the surface and $1/r$ within the medium.

With the above model, we can calculate the NN for a given distribution of masses, which can be described by the mass density function $\rho(\mathbf{r}, t)$. The resulting acceleration, experienced by a test mass (i.e. an interferometer mirror) located at $\mathbf{y}$, can be written as

$$\mathbf{a}(\mathbf{y}, t) = G \int_V \rho(\mathbf{r}, t) \frac{\mathbf{r}'}{|\mathbf{r}'|^3} dV, \tag{56}$$

where $\mathbf{r}$ is the position of the mass volume dV and $\mathbf{r}' = \mathbf{r} - \mathbf{y}$. In the FE analysis the acceleration is the summation of the contributions from each node i with mass m_i located at $\mathbf{r}_i$. The acceleration at the test mass

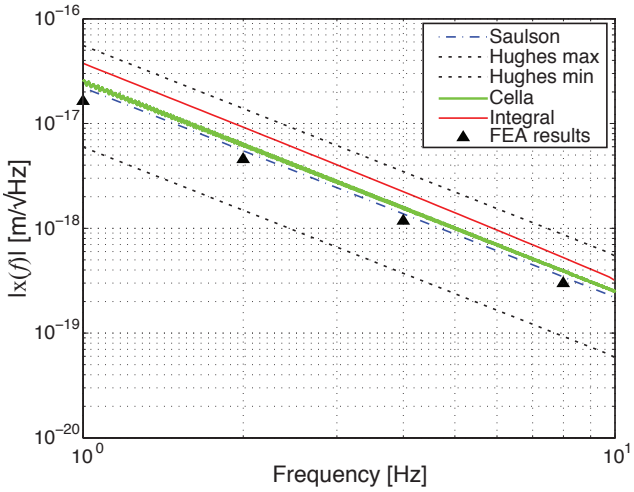

Figure 55: Finite element calculation of the Newtonian displacement noise amplitude for a surface detector. For comparison the results of Saulson, Cella, Hughes and Thorne, and the analytic integral are shown.

is given by

$$\mathbf{a} = \sum_i \mathbf{a}_i = \sum_i G m_i \frac{\mathbf{r}'}{|\mathbf{r}'|^3}, \tag{57}$$

with G the universal gravitational constant. When a seismic disturbance is present, the nodes suffer a displacement denoted by $\xi_i(\mathbf{r}, t)$. The gravity gradient acceleration due to these displacements is given by

$$\mathbf{a}^{NN}(\mathbf{y}, t) = \sum_i (\nabla \otimes \mathbf{a}_i)^T \xi_i(\mathbf{r}, t). \tag{58}$$

Note that in the gravity gradient calculations presented here, the mass associated with each node is assumed to be constant. The corresponding analytical expression can be obtained by substituting $m_i \to \rho dV$ and evaluating the resulting integral.

The calculation of GGN via FE models was validated by creating simple rectangular homogenous half-space models, equivalent to those discussed by Saulson for a surface detector [299]. The isotropic, elastic half-space with $\rho = 1.8$ g/cm^3, $\nu = 0.33$, $c_P = 440$ m/s and $c_S = 220$ m/s was excited on one boundary to yield plane harmonic pressure waves scaled to a flat ambient seismic noise spectrum of 1 nm/$\sqrt{\text{Hz}}$ between 1 and 10 Hz and the subsequent nodal displacements were recorded as a function of time. Boundary conditions were set such that no reflections occurred and seismic waves were continuous. The FE results are compared with the analytic results of Saulson and Hughes and Thorne [299][301]. To facilitate comparison, an integral cut-off radius equal to that used in Saulson's analysis ($r_{\text{cutoff}} = \lambda/4$) was employed in the summation process. Fig. 55 shows that good agreement is obtained. To assess the effect of this cut-off the above model was calculated analytically using Eq. (58). Removing the cut-off leads to an increase of GGN by about a factor 2. The FE results approach those of the analytic expression in the limit that r_{cutoff} decreases to zero.

The pulse excitations and the half-sphere model described earlier, were used to investigate gravity gradients originating from nearby surface excitations (see Fig. 56). The nodal displacements were recorded as a function of time and the GGN was calculated at various depths on a vertical line at a distance $\lambda_P = 800$ m from the z-axis. In order to artificially separate the contributions of the surface and body waves to the GGN acceleration the nodes with a depth less than 200 m were summed separately from those deeper that 200 m. The respective surface and body contributions were combined to give a total acceleration. Note that for times shortly after the excitation, this distinction is not precise. The results for a test mass at the surface and a test mass at a depth of λ_P are shown in Fig. 56. Only the GGN acceleration in the horizontal direction is shown since it has the largest effect on the performance of an interferometer. The expected arrival times of the different waves are indicated in the figures and show that the Rayleigh wave dominates the GGN contribution of a detector on the

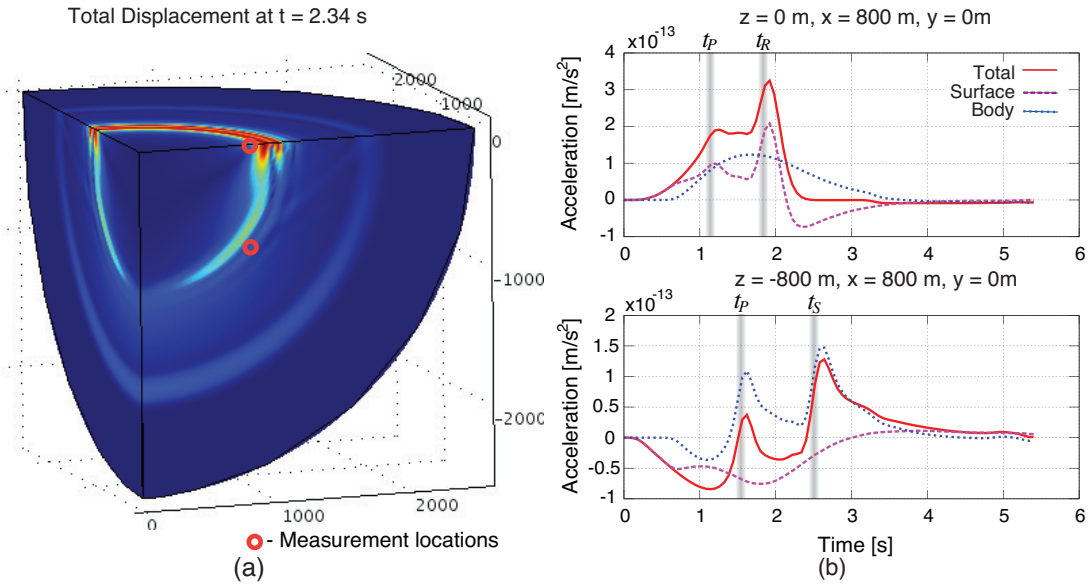

Figure 56: (a) Total displacement for a time domain simulation at 2.34 seconds after a 1 μm pulse excitation at the center of the half-sphere. (b) Time domain evolution of gravity gradient noise acceleration at a surface (z=0 m) and underground (z=-800 m) test mass. Only the horizontal component of the gravity gradient noise acceleration is shown. Arrival times of Rayleigh, S and P-waves are also indicated.

surface. At a depth of λ_P the arrival of the S and P-waves can clearly be distinguished, the S-wave producing a larger contribution, attributed to the larger seismic displacements seen in Fig. 54a. The GGN contribution of a wave is initially negative as the wave approaches then changes sign as the wave passes by the test mass. It is interesting to note that the sign change of the surface contributions between a surface and underground detector. This is due to the sign change of the horizontal component of the Rayleigh wave for depths larger than $0.2\lambda_R \approx 80$ m. The figure also shows that GGN builds up before any seismic disturbance actually reaches the test mass and for short times is only dependent on surface contributions.

3.5.3 Ambient NN subtraction

A possible approach to the problem of NN mitigation is its subtraction. The basic idea is to exploit the expected correlation between NN and a set of auxiliary quantities which are continuously monitored [308]. The natural candidates for these are seismic displacement, and we can imagine a basic scenario where a set of sensors (let's say displacement sensors) record several time series. We will consider here the simplest scenario, namely we suppose that the relevant quantities are stationary in a statistical sense. The time series recorded by the I-th sensor will be $X_I = s_I + \sigma_I$, where s_I is the seismic displacement evaluated at the sensor's position and σ_I its instrumental noise.

We will write the output of the interferometer as $Y = H + N$, where N is the NN and H the remaining part, which we suppose uncorrelated with the seismic motion. The "subtracted" time series Y_s has to be constructed in such a way to satisfy a given optimization criterion. If each of the auxiliary time series X_I are uncorrelated with the gravitational wave's signal in Y and the noise is Gaussian the optimal result can be obtained by

1. applying an appropriate linear and time invariant filter to each of the X_I signals
2. subtracting each filtered signal from Y

The filters will be chosen in such a way to minimise the power spectrum of Y_s, details are given in Box 3.1.

Box 3.1: Stationary noise: optimal subtraction

A simple way to state the problem is asking what is the linear combination of the interferometer's and sensors' time series

$$Y_s = Y(\omega) + \int d\omega' \sum_I \alpha_I(\omega,\omega') X_i(\omega') \tag{59}$$

which we can call subtracted signal which minimise the power spectrum at each frequency. The minimisation variables are the functions $\alpha_I(\omega)$, which clearly represent linear filters that must be applied to the output of the sensors before adding them to the interferometer's data. The power spectrum $S_{Y_sY_s}$ is related to the correlation by

$$\begin{aligned}\langle Y_s(\omega)^* Y_s(\omega)\rangle = \langle Y(\omega)^* Y(\omega)\rangle \quad &+ \quad \int d\omega'' \sum_l \alpha_l(\omega,\omega'')^* \langle Y_l(\omega'')^* Y_l(\omega')\rangle \\ &+ \quad \int d\omega'' d\omega''' \sum_{I,J} \alpha_I(\omega,\omega'')^* \alpha_J(\omega',\omega''') \langle Y_I(\omega'')^* Y_J(\omega''')\rangle \\ &+ \quad \alpha_l(\omega',\omega'')\langle Y(\omega)^* Y_l(\omega'')\rangle \end{aligned} \tag{60}$$

and minimizing this expression with respect to $\alpha_K(\omega',\omega'')^*$ we obtain a set of linear integral equations for the optimal filters

$$\langle X_K(\omega'')^* Y(\omega')\rangle + \sum_J \int d\omega'' \langle X_K(\omega'')^* X_J(\omega''')\rangle \alpha_J(\omega',\omega''') = 0 \tag{61}$$

In principle the expression of α_J's can be obtained by finding the inverse of the kernel $K_{KJ}(\omega,\omega') \equiv \langle X_K(\omega)^* X_J(\omega')\rangle$, formally

$$a_I(\omega',\omega) = -\sum_K \int d\omega'' K^{-1}_{IK}(\omega,\omega'')\langle X_K(\omega'')^* Y(\omega')\rangle \tag{62}$$

If non stationary noise is present, we should define what is the relevant quantity that must be maximised, as the definition of the optimal apparatus sensitivity cannot be given it term of noise spectrum only. In the stationary case we can write

$$\langle X_I(\omega)^* Y(\omega')\rangle = 2\pi\delta(\omega-\omega') C_{SN\,I}(\omega) \tag{63}$$

Here the I, J entry of the array C_{SS} is the cross correlation between the seismic noise measured by the Ith and Jth sensors. Similar $C_{\Sigma\Sigma IJ}$ is the correlation between the intrinsic noises of the Ith and Jth sensors. Finally,

$$\langle Y(\omega)^* Y(\omega')\rangle = 2\pi\delta(\omega-\omega')[C_{NN}(\omega) + C_{HH}(\omega)] \tag{64}$$

is the decomposition of interferometer's power spectrum in a NN contribution plus all which is uncorrelated with it. Putting all this inside Eq. (62) and (60) we get the optimal filters

$$\alpha_I(\omega,\omega') = -\delta(\omega-\omega')[C_{SS}(\omega) + C_{\Sigma\Sigma}(\omega)]^{-1}_{IJ}[C_{SN}(\omega)]_J \tag{65}$$

which in the stationary case considered are time invariant, and the amplitude efficiency $\epsilon(\omega)$ of NN subtraction, which we define in terms of the ration between the power spectra of the subtracted ($S_{Y_S}(\omega)$) and un-subtracted ($S_Y(\omega)$) interferometer's signal spectral amplitude

$$1-\epsilon(\omega) = \sqrt{\frac{S_{Y_S}(\omega)}{S_Y(\omega)}} = \sqrt{1 - \frac{C^+_{SN}(\omega)[C_{SS}(\omega) + C_{\Sigma\Sigma(\omega)}]^{-1} C_{SN}(\omega)}{C_{nn}(\omega)}} \tag{66}$$

Note that $(1-\epsilon)^2$ gives the ratio between the power spectra of the NN contained in the subtracted and un-subtracted signal.

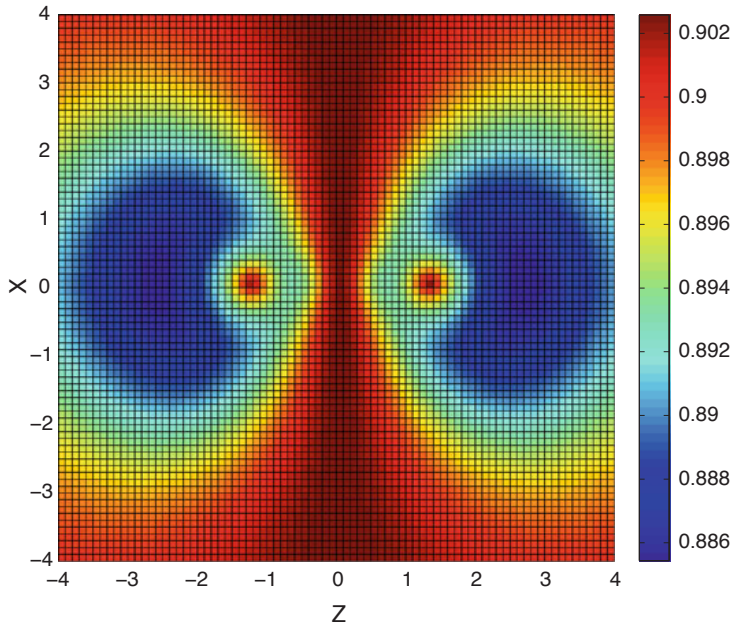

Figure 57: The percentage reduction of NN on a single test mass with three sensors, for the model described by Eq. (60). The test mass is at the origin of the coordinate system, and the sensors measure the local density fluctuations. NN acceleration is sensed along the z axis. Two sensors are fixed at their optimal positions, which are located at the circular spots at $(x, z) = (0, \pm)$. the quantity $1 - \epsilon$ (see Eq. (59)) is plotted as a function of the position of the third sensor. There is axial symmetry around the z axis, so only the $x - z$ plane is displayed.

The ratio between subtracted and unsubtracted spectral noise amplitude, which is given by Equation (66), is a function of

- C_{SS}, an array whose entry in the I-th row and J-th column is the spectral covariance between the I-th and the J-th sensor;
- C_{SN}, a vector whose I-th entry is the spectral covariance between the NN and the output of the I-th sensor;
- C_{NN}, the power spectrum of NN.

This expression tell us that to achieve a good subtraction efficiency three conditions are needed.

- All the sensors should be coupled as much as possible to NN, in other words the correlation C_{SN} between sensor's output and NN must be as large as possible.
- The intrinsic noise of the I-th sensor described by its power spectra $[C_{SS}]_{II}$ should be small.
- The correlation between quantities measured by different sensors, described by C_{SS}, must also be small.

It is important to observe that when the procedure is correctly applied, it will never reduce the sensitivity at each frequency.

Note that only the correlation among auxiliary sensors described by the entries of the matrix C_{SS} can be measured easily, so there is no real hope to fully test the subtraction procedure without building a NN sensitive detector. However Equation (66) can be estimated using a theoretical model. We will use in the following the very simple one described in Box 3.2. This is characterized by a single (frequency dependent) correlation length $\xi(\omega)$.

Box 3.2: Simple subtraction model.

We consider a single test mass inside an infinite medium, and we suppose that each sensor can monitor the mass density fluctuation at its position. The ith sensor is also affected by a intrinsic noise $\sigma_i(f)$, without correlations between $\tilde{\sigma}_i$ and $\tilde{\sigma}_j$ when $i \neq j$. We model the density fluctuations as a Gaussian stochastic field described by an exponential cross correlation function

$$\langle \tilde{\rho}(\omega, \mathbf{x})^* \tilde{\rho}(\omega', \mathbf{x}')^* \rangle = 2\pi\Gamma(\omega)^2 \delta(\omega - \omega') \exp\Big(- \frac{|\mathbf{x} - \mathbf{x}'|}{\xi(\omega)} \Big) \tag{67}$$

The correlation functions relevant for the subtraction are easily evaluated, obtaining

$$\begin{aligned} C_{SS}(\omega)_{IJ} + C_{\Sigma\Sigma}(\omega)_{IJ} &= \Gamma(\omega)^2 \exp(-|\mathbf{u}_i - \mathbf{u}_j|) + \sigma^2(\omega)\delta_{IJ} & (68)\\ C_{SN}(\omega)_I &= 4\pi\xi G\Gamma(\omega)^2 \cos\theta_I \Psi(u_I) & (69)\\ C_{NN}(\omega) &= \frac{16}{3}\pi^2\xi^2 G^2 \Gamma(\omega)^2 & (70) \end{aligned}$$

where $\mathbf{u}_I = \xi^{-1}\mathbf{r}_i$ is the position of the I-th sensor measured in ξ units, θ_I the angle between the axis along which the Newtonian acceleration is measured and the sensor's position vector and

$$\Phi(u) = \frac{1}{u^2}\Big[2 - e^{-u}\Big(2 + 2u + u^2\Big)\Big] \tag{71}$$

For a given arrangement of the sensors Eq. (66) becomes

$$1 - \epsilon = \sqrt{1 - 3\Big(e^{-|\mathbf{u}_I - \mathbf{u}_J|} + \frac{\sigma^2}{\Gamma^2}\delta_{IJ}\Big)^{-1} \Phi(u_I)\Phi(u_J)\cos\theta_I \cos\theta_J} \tag{72}$$

One issue to be investigated is connected with the optimal way in which the set of sensors available must be displaced on the field, by optimizing Eq. (72) over the positions and the orientations.

With two sensors only the optimal positions are on the Newtonian acceleration axis, at a distance $d \simeq \pm 1.281\xi$ from the est mass (we will consider only the $\sigma = 0$ case). The $\cos\theta$ factor is maximised along the axis, while $\Phi(u)$ has a maximum at $u \simeq 1.451$. In this optimal case $1 - \epsilon \simeq 0.902$. If we add a third sensor, we can evaluate $1 - \sigma$ as a function of its position, which the other two fixed. This is represented in figure 57, assuming that the NN is measured along the z axis. We can see how the subtraction efficiency changes with the position of the sensor, measured in unit of the correlation length. There is no improvement if we put the third sensor near the others, due to the complete correlation of the new measurement with the others. We do not gain anything from far from the test mass or at $z = 0$, because in this case the measure is uncorrelated to NN. the best positions are along the z axis, at a distance roughly doubled from the center.

The model is quite crude so these are only indicative results. However, the model does show one particular feature. The separation between the sensors must be optimized accordingly with the typical correlation length ξ of the contributions to NN we want to subtract, which depends on the frequency band where the subtraction is needed.

Another important point to understand is how the subtraction procedure improves with the number of sensors, and how much it is sensitive to a non optimal placement of the sensors. This is important because in a practical implementation the possibility of optimizing the placement will be limited, especially if the number of sensors will be large. It must be remembered that the optimization of the sensors' positions is a global process and all the parameters must be changed at the same time.

Remaining in the framework of the simple model considered we optimized Eq. (72) for a different number of

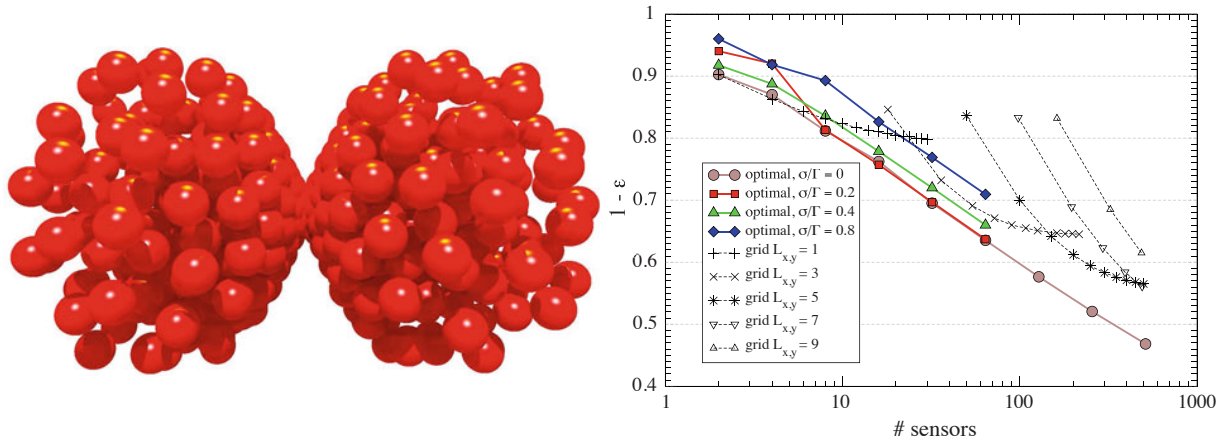

Figure 58: Left). The optimal positions for 512 sensors, evaluated accordingly with the model (60). Each sensor is supposed to measure the local fluctuation of density, and is represented as a sphere with the center on its position and radius ξ. The single test mass considered is at the centre of the two clouds, and the NN is measured along the approximate axis of symmetry of the distribution. Right). The percentage of NN on a single test mass as a function of the number of auxiliary sensors, accordingly with the model (60). The sensors are supposed to measure the local fluctuation of density. Solid lines correspond to optimal configurations, evaluated for different intrinsic noises of the sensors. Dashed curves correspond to regular grids with sizes $L_x = L_y$ and L_z. The grid is centred on the grid and the number of sensors given by L_x, L_y, L_z. The NN is sensed along the z axis, and $\sigma = 0$ in this case.

sensors. We used a simulated annealing procedure to be reasonably sure to find a global minimum. A typical result for the optimal configuration of the sensors is shown in the left illustration of Fig. 58. We considered 512 sensors, adjusting their positions. Each sphere in the plot has a radius length ξ, and is centered on a sensor's position. We see that the spheres attempt to cover the region which is maximally coupled to NN acceleration (the test mass is between the two clouds), but they attempt also not to overlap in order to minimise the correlation between sensors. Fig. 8 correspond to the optimal configuration in the $\sigma = 0$ case. We do not show similar plots for $\sigma > 0$, however in that case we found that the overlap between the spheres increases with σ/Γ. This is expected because in that case a correlation between detectors can be compensated by the average of intrinsic noises.

In the right plot of Fig. 58 we show the relative reduction of NN as a function of the number N of auxiliary sensors. The reference plot is labeled with circles, and it corresponds to the optimal configuration in the $\sigma = 0$ case. We see that the reduction of NN is quite modest, and improves slowly with N. This is partly due to the chosen model, which is quite bad from this point of view, a scan be seen with the following argument. Each sensor can be used at best to subtract the contribution to the NN of a sphere of radius ξ centered on it. The number of non overlapping spheres at distance ξ from the test mass scales as n^2, while the contribution of each of them to NN scales as n^{-2}. We have to sum all the contributions in quadrature, so if all the spheres with $n < N$ are monitored we expect for large n that $1 - \epsilon \sim \sqrt{\sum_k^\infty k^{-2}} \sim n^{-1/2}$ or as the number of sensors N_s scales as n^3, $1 - \epsilon \sim N_s^{-1/6}$.

Different models are expected to allow better subtraction performances, especially when the loss of coherence described by the scale ξ is less relevant. This could be the case in some geological scenarios, while in others the simplified model presented can give an adequate description. It is an important issue, which is currently under careful investigation.

Coming back to the right plot in Fig. (58), the plots labeled with squares, triangles and diamonds gives $1 - \epsilon$ for the optimal configuration in presence of some amount of instrumental noise. As expected there is a reduction of the subtraction performances. Finally, we showed in the same figure for comparison the results which can be obtained with a non optimal configuration, namely a regular grid of detectors with different sizes $L_x = L_x$ and L_z , centered on the test mass. The optimization here is done only on the grid size, and $\sigma = 0$. The best

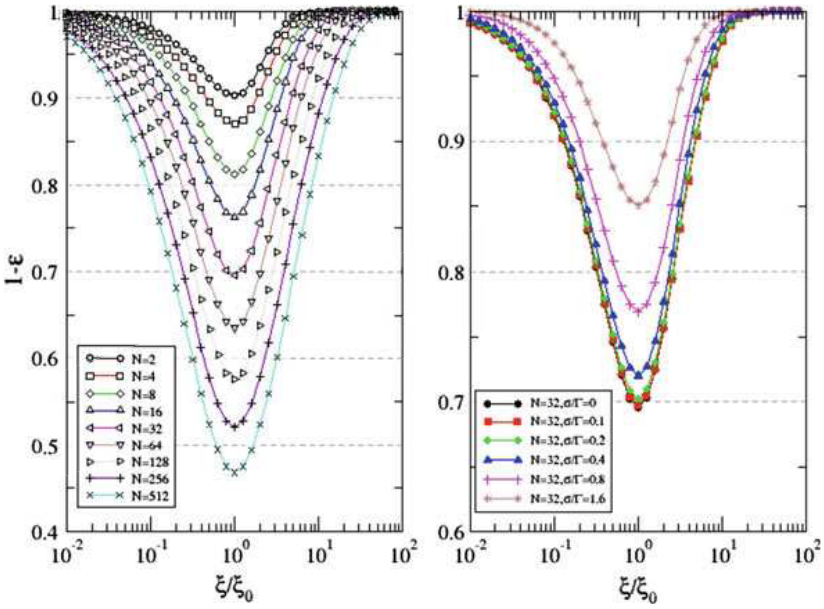

Figure 59: On the left, the reduction of NN for a configuration of the sensors optimized for $\xi = \xi_0$, as a function of the ratio $\xi(\omega)/\xi_0$, where $\xi(\omega)$ correspond to the observed frequency. The different plots correspond to different number of sensors. On the right, for N =32 sensors in the configuration optimized at $\xi = \xi_0$, the reduction of NN is plotted as a function of $\xi(\omega)/\xi_0$. The different plots correspond to different values of the intrinsic noise of the sensors.

regular grids correspond to the shapes which are best overlapped to the region coupled to NN, which means $L_z > 2L_{x,y}$.

The optimization of the positions of sensors can clearly be done at a given coherence length $\xi(\omega)$, while the subtraction procedure will be applied to an entire range of frequencies (we can assume for definiteness ξ proportional to the frequency). This means that the subtraction will be optimal at a chosen frequency only.

In Fig. 59 (left) we plotted the NN reduction as a function of the ratio $\xi(\omega)/\xi_0$ between the coherence length at the observed frequency and the one ξ_0 which correspond to the optimized sensors' configuration. Different plot correspond to a different number of sensors, and $\sigma = 0$. A sensible reduction of the subtraction performance is evident when ξ changes by one order of magnitude. This reduction is somewhat decreased by a large number of sensors.

The effect of noise can be seen in Fig. 59 (right). Here the number of sensors is fixed at 32, and different plots correspond to different values of σ/Γ. The plot suggest (with some extrapolation) that to achieve an hundred fold NN suppression, rock density (and position) fluctuations need to be measured in real time with resolution less than 1% of the actual motion (in quiescent times in a quiet location), i.e. $\sigma/\Gamma < 10^{-2}$. Because the available seismometers have been mainly developed to detect seismic events, their sensitivity is just below the normal rock activity level. A well defined subtraction pipeline has to be tested with models in order to give a precise estimate, however our conservative expectation is that seismic sensors 100 times more sensitive than currently employed must be developed for NN suppression to become useful. Preliminary studies in this direction are being done at Homestake, specifically in the direction of laser strain meters and high sensitivity dilatometers. We expect that these developments, if successful, will also yield important side results in geology.

3.5.4 NN subtraction from periodic sources

Active NN subtraction schemes have been studied both at the LIGO and Virgo laboratories [298, 309, 310]. Methods for active NN subtraction involve placing a witness sensor (seismometer) that monitors the noise source

and estimates the noise transfer function by methods of minimising a cost function J (difference between the measured noise and the estimated transfer function times the seismometer signal). The cost function that is commonly used in filter design optimisation, is the mean-square error (MSE). Minimising the MSE involves only second order statistics (correlations) and stems from the theory of linear filtering, which has many practical applications. In general, the idea is to recover a desired signal $d(n)$ given a noise observation $x(n) = d(n) + v(n)$ by using some linear filter with coefficients $\mathbf{w}$. Minimising the cost function

$$J = E\{e^2(n)\} = E\{(d(n) - \hat{d}(n))^2\} = E\{(d(n) - \mathbf{w}^T\mathbf{x}(n))^2\} \tag{73}$$

with the provisions that the derivative of J with respect to $\mathbf{w}$ and the second derivative to $\mathbf{w}$ are zero and positive respectively, provides the Wiener, or optimal filter solution, which is useful for filter coefficients that are constant in time. If we assume that the seismic spatial distribution, generated by pumps and electricity generators, can be approximated by a Gaussian distributed impulse acting vertically onto the soil, we can use the finite element results to attempt to estimate and subtract the NN from our gravitational wave data channels.

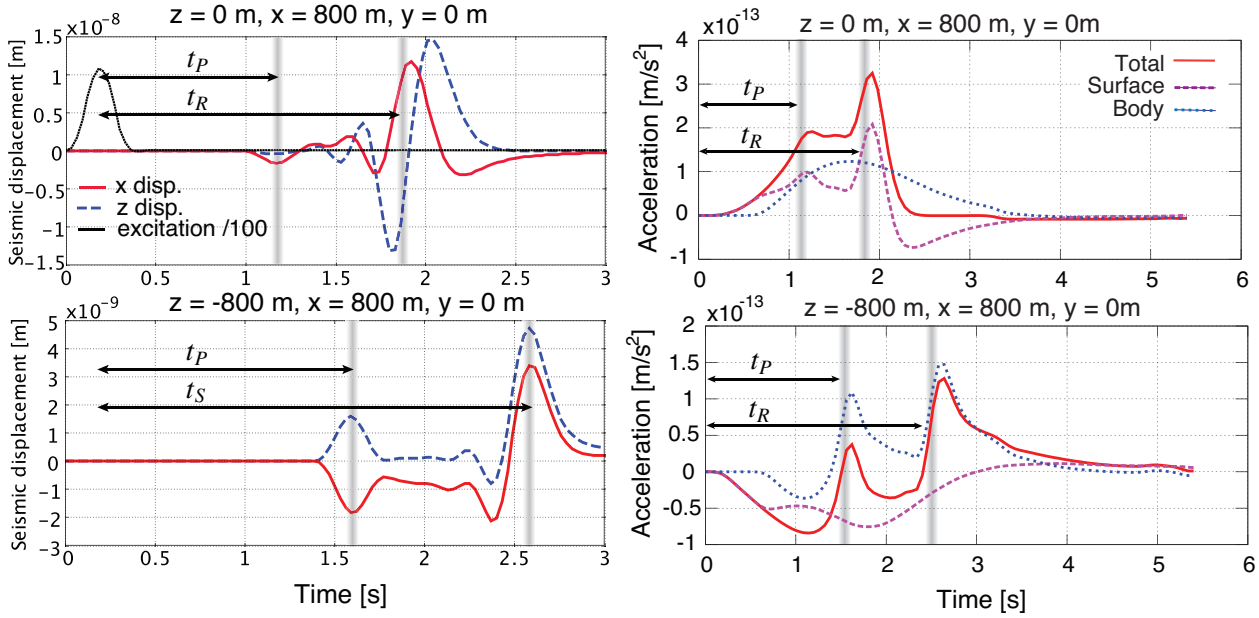

Figure 60: Results of time domain finite element simulations for NN. The grey bars indicate the arrival times and contributions from the pressure and shear wave components. Top left) Element displacement after a 1 μm pulse excitation at the center of the half-sphere. Bottom left). Element displacement at an underground location (x=800 m, z=-800 m) after pulse excitation at the centre of the half-sphere. Top right). Newtonian acceleration at the surface of the half sphere due to a pulse excitation. Bottom right). Newtonian acceleration at an underground location (x=800 m, z=-800 m) due to a pulse excitation.

Figure 60 is a combination of two previous plots (Fig. 54a and Fig. 56b) and shows the FE results of a typical time domain soil displacements and NN response as a function of time. The top and bottom plots on the left show the seismic excitation and the resulting displacement amplitudes at the centre of the homogeneous half space and at a depth of 800m respectively. The top and bottom plots on the right of Fig. 60 show the resulting Newtonian acceleration for a test mass placed on the surface of the half space, 800m from the excitation point and the Newtonian acceleration for a test mass placed at a distance of ∼1130m and a depth of 800m below the surface. Note that, in both cases, as soon as the excitation occurs a Newtonian acceleration is present at the test mass.

The left and right plots in Fig. 60 can be interpreted as individually measured quantities, i.e. a NN signal in our GW detector (right) and a seismic disturbance that is measured at it's source (left). Since the disturbance is impulse like, we can estimate the NN impulse response due this disturbance from this specific source.

After ET becomes operational, it will be of great importance to minimise localised anthropogenically generated seismicity. This does not stop at restricting access to areas close to the interferometer test masses. Thorne *et al.* investigated how the interferometer is affected by NN originating from humans, animals, airplanes, etc. [311]. Within the subterranean environment this extends to placement of electricity generators, pumps, and cryo-coolers to keep the facility operational. These devices will be sources of seismic noise and will therefore generate continuous NN.

3.6 Site selection

As described in the previous sections, ground motion may prove a limiting factor for the low frequency performance of ET. A preliminary site investigation was carried out to make a comparative analysis of various (underground) locations throughout Europe and across the globe. The following paragraphs will discuss the measurement procedures and a list of locations that have undergone investigation. In order to ascertain all site characterisation procedures were carried according to seismologic standards, measurements and data collection was carried out partly in collaboration with the Observatories and Research Facilities for European Seismology (ORFEUS) which is maintained by seismology department of the Royal Netherlands Meteorological Institute (KNMI). Measurements from all locations were obtained over a two month period to ensure minimal seasonal variations.

In order to measure the ambient seismic background low noise broadband seismometers are required. All seismic measurements were carried out using two measurement stations, each station consists of a Trillium 240 (T240) accelerometer and a data acquisition system. The T240 is a broadband low noise seismometer with a flat velocity response from 4 mHz to 35 Hz and a self noise below the low noise model from 0.01 to 10 Hz. The on-site seismic measurements were made over a period of 5 to 6 days. Care was taken to ensure that the measurement time includes at least a weekend and a number of week days.

The following includes an summary and results from selected locations. In all of the following results a fast Fourier transform (FFT) was performed on stretches of 128 seconds of data to obtain an power spectral density (PSD) in $(m^2/s^4)/Hz$. The PSDs are averaged over a period of half an hour. Averaged PSD values are smoothed by taking the average of the PSD values in a constant relative bandwidth of 1/10 decade. (So for low frequencies the averaging is over only a few points, for high frequencies the averaging is over many more points). For comparison the new high and low noise models are also plotted. Spectral variation plots are used here to not only show the amplitude of the seismic signal but also how much time, as a percentage, is spent at a certain level. This is indicated by the color of the plot. The spectral variation plots also contain three solid line plots to indicate the mode and the 90 and 10 % levels. The mode is the most common PSD value in each frequency bin, and 90 and 10 % levels indicate the point under which the PSD will stay for 90 or 10 % of the time, respectively.

3.6.1 Measurement sites

The following section provides a brief description of all locations included within the site characterization and classification program. The selection criteria for these sites was based on the availability of a suitable underground measuring location. Gaining safe access to underground locations with little or no nearby (underground) activity proved very challenging. The majority of the sites are therefore already existing underground laboratories or decommissioned mines that are undergoing environmental rehabilitation or being converted for tourist purposes. Initial selection procedures were based on general suitability for a GW telescope and surface measurement of seismic data. The main purpose of this research was to ear-mark 3 or 4 locations for an extensive seismic and geological study. A followup site selection study would address in more detail the suitability of constructing the Einstein Telescope observatory at or near the location or in similar geological conditions.

A brief description of each location will now be given, followed by a more detailed summary of a selection of sites. The position of each site is displayed on a map given in Fig. 61.

Figure 61: Map displaying position of the seismic measurement sites presented in this report. Red icons with a dot indicate locations where measurements were taken at underground locations, blue icons indicate where data were obtained via the Orfeus network from surface installations.

- *The Netherlands: Heimansgroeve.* The Heimansgroeve is an old quarry situated in the very southern tip of the Netherlands. It contains the oldest rock type found in the Netherlands, Carboniferious, about 360 - 300 million years old. The stone consists of slate and carbonic sandstone. The Royal Netherlands Meteorological Institute has a seismic observatory in a small underground laboratory some 10 meters below the surface. Our seismic stations were placed alongside the institutes permanent seismometers which provided an excellent cross check between instruments and analysis.

- *Hungary: Gyöngyösoroszi.* The Gyöngyösoroszi mine is situated some 107 km North-East from Budapest in the Mátra mountains. This old zinc-lead mine has horizontal access with underground depths ranging from 100 to 350 m at an elevation of about 400 m. Local rock type consists of andezit and andezit tufa. A ecological rehabilitation of the neighourhood and mine was started last year. The mine contains a number of long straight drifts of which the longest is 3 km. The seismic stations were placed 1.4 and 3.8 km from the entrance at depths of 70 and 400 m respectively. There is a permanent Seismological Observatory of the Hungarian Academy of Sciences at Piszkéstetö on the site of the Konkoly Thege Astronomical Observatory. It is situated about 4 km from the mine entrance.

- *Romania: Slanic.* Slanic-Prahova is located, 40 km NE of Ploiesti, or 100 km north of Bucarest in Romania. Very large caverns 30 m wide and 35 m high, dug in salt, are presently existing and a low background laboratory was successfully installed in one of the caverns. The salt exploitation ended in 1971, however another salt mine is still active in the same salt deposit. For the time being the mine is used for tourism and medical purposes. Access into the mine is available via an elevator able to carry up to 10 tons. The network of galleries of Unirea salt mine is very large. The current area is 70 000 m^2 with 2.9 million m^3 having already been excavated. Nearby seismic stations show very low seismic activity in the area. Both seismometers were set-up side by side at a depth of 190 m.

- *France: Frejus.* The underground laboratory LSM 'Laboratoire Souterrain de Modane', is located along the road tunnel between the French Modane and Italy. The overburden at this site is 1700 m of hard-rock or 4800 meters of water equivalent. The LSM, in operation since 1982, already hosts two particle physics experiments requiring an extremely low-background environment to study neutrino properties and to search for dark matter. A seismic station was set-up next to a large neutrino experiment.
- *Spain: Canfranc.* The Canfranc Underground Laboratory (LSC, 'Laboratorio Subterráneo de Canfranc') is located on the Spanish side of the Pyrenees, under the mountain of 'El Tobazo' and has various particle physics programs aimed at very low background experiments for the study of neutrino properties and the search for dark matter. It has 2500 m water equivalent overburden at depths of around 900 m and can be accessed via the roadway or decommissioned railway tunnels.
- *Italy: Gran Sasso.* The Gran Sasso National Laboratory is the largest underground laboratory in the world for experiments in particle physics, particle astrophysics and nuclear astrophysics. It is located between the towns of L'Aquila and Teramo, about 120 km from Rome. The underground facilities are located on one side of the ten kilometer long freeway tunnel through the Gran Sasso Mountain at an average depth of 1400 m. They consist of three large experimental halls, each about 100 m long, 20 m wide and 18 m high and service tunnels, for a total volume of about 180,000 m^3. A seismic station was placed in an escape gallery between the road and railway tunnels at a depth of 800 m.
- *Italy: Sardinia.* The Mediterranean island of Sardinia is seismically quieter than the Italian main land. This is due to its more central position on the European tectonic plate, as opposed to near its boundary. Measurements were performed in a mine near Lula, 50 km south of Olbia on the north-eastern side of the island. This former lead-zinc mine is currently being rehabilitated to allow safe passage into the mine for tourists.
- *Italy: Sicilie.* The Italkali salt mine is situated near the town of Realmonte on the southern coast of Sicily, 10 km east of Agrigento. Salt is excavated by creating huge caverns, some as large as 100 m in length. Measurements were taken at a depth of about 60 m, at an elevation of 30 below sea level. Both stations were installed in a storage cavern about 50 meters apart. One seismic station was on a large concrete pad with the other was placed straight onto the salt floor. The mine was still in active use with a nearby conveyor belt in continuous operation during the measurements.
- *Germany: Black Forest.* The Black forest observatory (BFO) is a geophysical observatory in operation since 1972, owned and operated by Karlsruhe University and Stuttgart University. It is located in an abandoned silver mine and contains gravimeter, seismometers, tiltmeters as well as electromagnetic and weather sensors. The local rock type is granite and the overburden is up to 180 m. The measurements were taken at a depth of 90 m along side of the BFO.
- *Finland: Sumiainen.* The Finish bedrock is amongst the oldest and most stable in Europe, ranging from 3.5 to 2.6 billion years old, making it cheap and relatively trivial to construct underground caverns and tunnels. For this reason much of the infrastructure in Finish cities is built underground. Finland's isolation from major oceans and small population density could prove ideal for a low seismic background environment. No site was visited but data from an already installed surface seismic observatory in central Finland, near Sumiainen, was acquired.
- *Belgium: Mol* Near Mol in northern Belgium an underground laboratory has been constructed to investigate the long-term effects of construction in the "Boomse" clay layer. Clay is impenetrable to water and has self healing properties. For these reasons it has been proposed as an excellent candidate for the long-term storage of highly active nuclear waste. The HADES underground laboratory administered by EURIDICE is situated at a depth of 230 m in a clay layer roughly 150 m thick. In 2002 a new gallery was constructed, in a cylindrical form with a diameter of 4 m and a length of 80 m. A seismic station was setup in the new gallery and measurements were taken during the Christmas break of 2010.
- *Japan: Kamioka* CLIO, a 100 m prototype cryogenic gravitational wave detector has successfully been built in the former Kamioka mine near Toyama, 200 km west of Tokyo. The same mine is also home to the Super-Kamiokande neutrino observatory, and, in the future, will house the 3 km Large Cryogenic

Gravitational Telescope (LCGT). Two seismic stations were installed at the CLIO end stations at depths of around 1000 m.

- *USA: Homestake* The Homestake mine is located in Lead near the western border of the state of South Dakota. Until its closure in 2002 it was the largest and deepest gold mine in North America. It is also famous for the deep underground experiment, set up by Raymond Davis Jr., that was the first to detect solar neutrinos. Since 2007 the mine is being rehabilitated to house the Deep Underground Science and Engineering Laboratory (DUSEL). An array of seismic stations is being installed at depths ranging from 0 to 1500 m and will be the first of its kind in terms of 3D coverage and depth. Two seismometers have been contributed to this array and data were taken for several months in 2010.

  For comparison, data were also taken at Virgo detector in Italy, the GEO detector in Germany, and the Kamioka mine in Japan.

3.6.2 Results from a selection of sites

The following section discusses, in some more detail, three sites that have been selected for further investigation. A complete list of measurements and results is located in Appendix B.1. Seismic measurement results will be presented and discussed, then summarized in the following section.

Sos Enattos mine, Sardinia, Italy

The Sos Enattos mine, Lula, Sardinia, is a former lead and zinc mine of schist rocks composed of sphalerite ([Zn,Fe]S) and galena (PbS). It is situated 50 km south of Olbia on the north-eastern side of the island, 20 km from the coast. A map of the mine is shown in Fig 62, where the yellow circle indicates the experimental area where the measurements were carried out. The seismometers were placed at a depth of 189 m, at an elevation of 206 m above sea level. Data were collected from June 31, to July 5, 2010. The most significant plots, obtained by applying the analysis method described in a previous section, will be presented here.

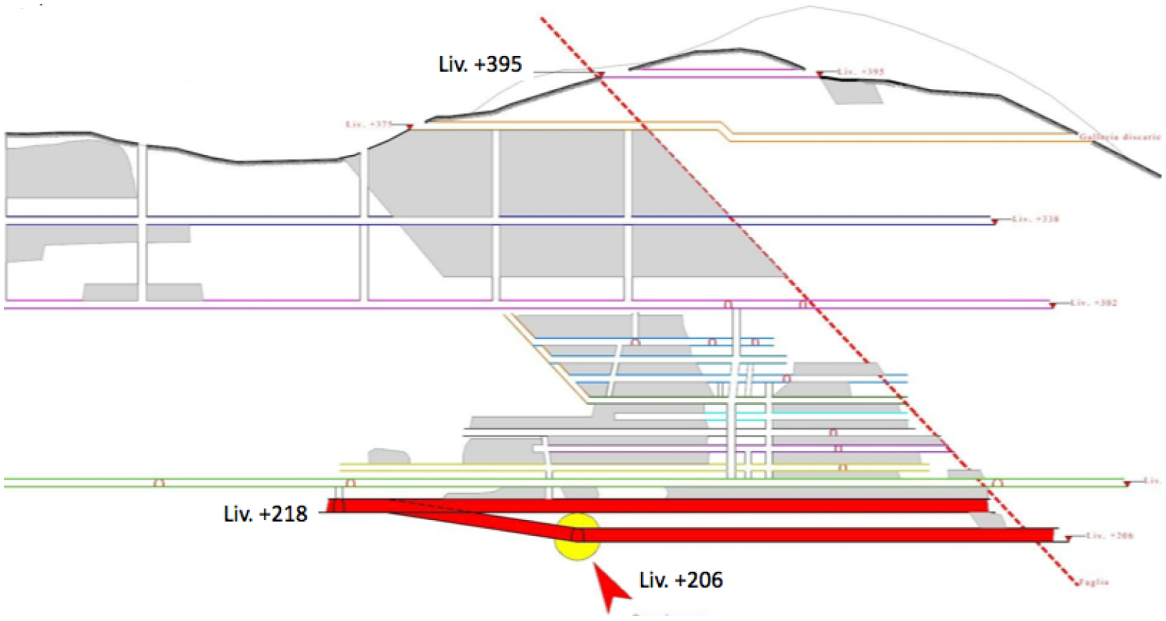

Figure 62: Underground map of the Sos Enattos mine, Sardinia. The yellow spot indicates the measurement location, at an elevation of 206 m and depth of 189 m.

The spectral variation plots from data taken from the Sos Enattos mine are shown in Fig. 63. The primary and secondary microseismic peaks are visible at 0.08 and 0.2 Hz respectively and are within an order of magnitude or touching the low noise model. This is due to the relatively large distance to the Atlantic ocean (1000 km to west coast of France). At higher frequencies, between 0.4 and 0.8 Hz an extra 'tertiary' microseismic peak can be seen. This is due to similar effects that cause the primary and secondary micro-seismics but originate from the Mediterranean sea and are typical of other Italian sites [312].

In the frequency range from 2 to 20 Hz a large variation in the spectral density is evident. Observing the spectrograms in Fig. 64, that plot the spectral density as a function of time it is clear to see that this variation has a daily pattern, indicating that the seismic noise sources at these frequencies originate from anthropogenic sources. More over, in the 2 - 8 Hz range the heightened activity seems to occur during the late morning hours before noon, on all days except Sunday. This coincides with the miners schedule of underground works and tourist activity during these hours.

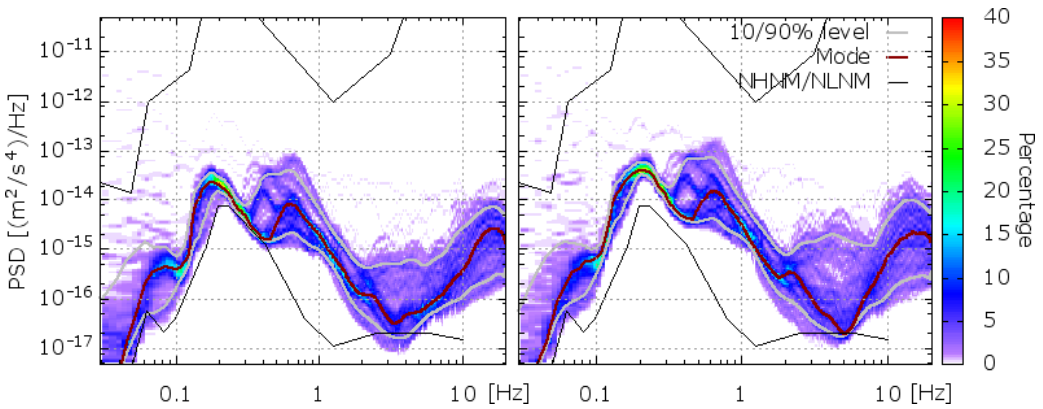

Figure 63: The horizontal component (left) and the vertical component (right) power spectral density plotted as a spectral variation from the Italy - Sardinia site. The 'tertiary' microseismic peak as a result of microseismics from the Mediterranean sea is evident from 0.4 to 0.8 Hz. Large variations at higher frequency are a result of work in the mine and other anthropogenic activity.

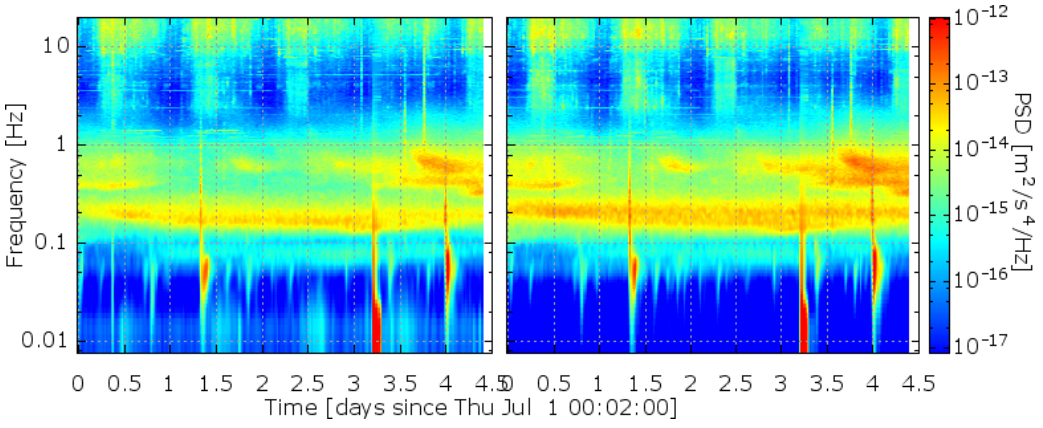

Figure 64: The spectrogram of the horizontal (left) and vertical (right) component from the Italy - Sardinia site. Day and night variation is visible as is the morning underground activity on Thursday, Friday and Saturday.

LSC, Canfranc, Spain

The Canfranc Underground Laboratory is located under the mountain 'El Tobazo' in the Northern Pyrenees, along the 8.5 km road tunnel spanning the French-Spanish border. Situated under 850 m of rock providing

an overburden a 2500 m water equivalent makes it suitable for low background experiments. Access to the laboratory is via either the road tunnel or a parallel decommissioned railway tunnel.

Seismic measurement stations were set up at two separate locations. The first was just behind the access door to a small low background laboratory along the railway tunnel. Due to continuous mechanical activity from pumps and ventilators in the laboratory as well as near-by construction work at the main laboratory, the data from this station were deemed unsuitable for background seismic measurements. A second seismometer was installed in a gallery connecting the road and railway tunnels and acts as an emergency escape route. This location was half way along the tunnel and 1 km away from the laboratory and other human or mechanical activity (besides the traffic in the road tunnel, 50 m away) at a depth of 900 m.

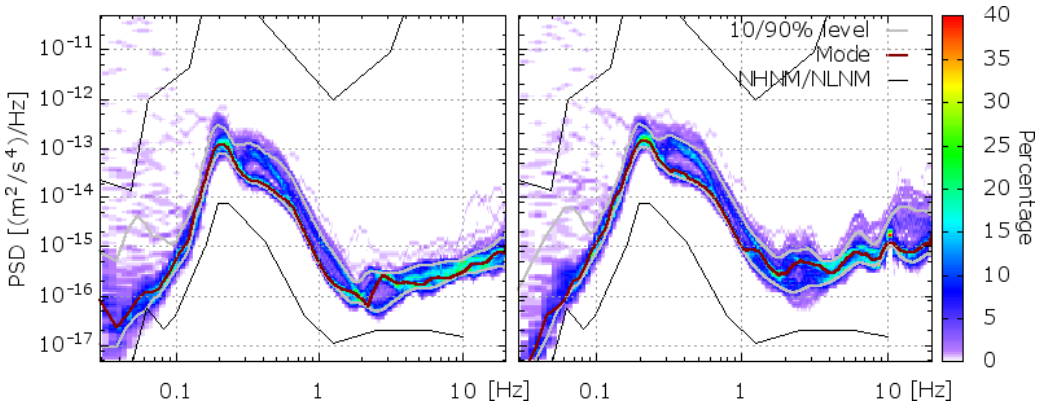

Figure 65: The horizontal component (left) and the vertical component (right) power spectral density plotted as a spectral variation from the Spain - Canfranc Underground Laboratory site. The large microseismic peak is a result of the sites proximity to the Atlantic ocean. The small spectral variation at high frequencies is due to the low population density of the area.

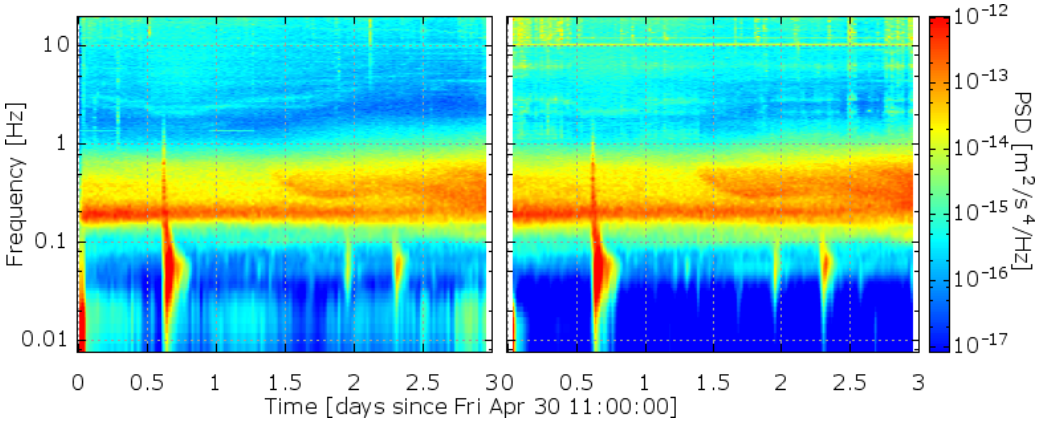

Figure 66: The spectrogram of the horizontal (left) and vertical (right) component from the Spain - Canfranc Underground Laboratory site. No difference in day and night activity is distinguishable indicating there are no anthropogenic sources contributing to seismicity at this site.

The results from the second Canfranc seismic station are shown in Fig. 65 in the form of spectral variation plots. The high microseismic peak around 0.2 Hz is evident consistent with the relatively close proximity of 130 km to the Atlantic ocean. At higher frequencies (2 - 20 Hz), where seismic noise is predominantly a result of anthropogenic noise, the seismicity is low. The variation in the PSD values at these frequencies is low, having just half an order of magnitude between the 10 and 90 % levels. In the spectrograms in Fig. 66, the day and night variation, a measure of anthropogenic activity, is not observed, a result of the very low population density of the area and the considerable depth of the site. This was also evident in day and night ratios, plotted in

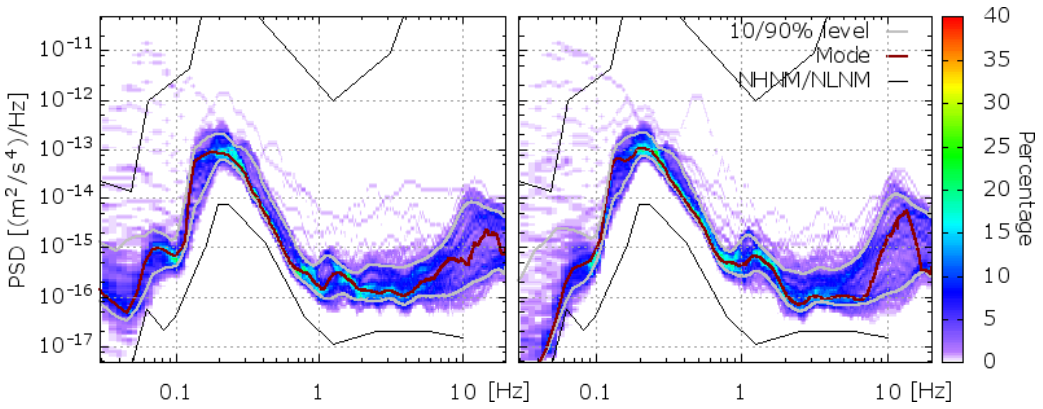

Figure 67: The horizontal component (left) and the vertical component (right) power spectral density plotted as a spectral variation from the Hungary - Gyöngyösoroszi mine site. The microseismic peak drops off quickly providing a low noise at 1 Hz. Large spectral variation at higher frequencies is due to anthropogenic activity.

Fig. 47, of this and the other sites presented in this section.

Gyöngyösoroszi mine, Hungary

The Gyöngyösoroszi mine in Hungary is a former lead and zinc mine that is currently being rehabilitated for environmental reasons. This provided an excellent opportunity to enter safely into the mine without any large scale mining activity nearby. It is situated 107 km north-east of Budapest in the Mátra mountains at an elevation of 400 m above sea level. The surrounding geology is Andezite. Access into the mine was possible on an electric locomotive through a horizontal access tunnel.

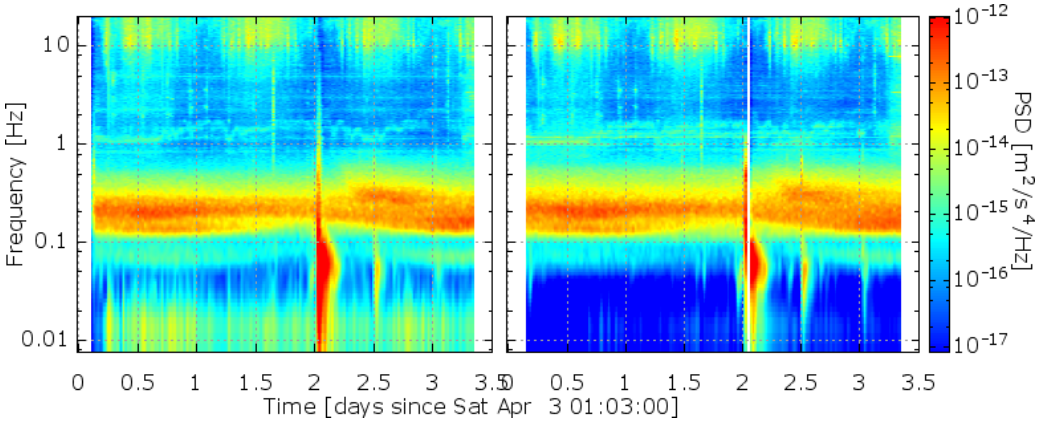

Figure 68: The spectrogram of the horizontal (left) and vertical (right) component from the Hungary - Gyöngyösoroszi mine site. The large event after 2 days is an Earthquake in Mexico with a magnitude of 7.2. Day and night variations due to anthropogenic noise at higher frequencies is still visible.

Two separate seismometer stations were installed at locations along the main drift. At each site the miners had excavated a small hollow into the tunnel wall so that the instruments could be safely installed without being inundated by the small, but steady, flow of water and mud. The first location was 1435 m from the entrance with a rock overburden of 70 m. The second location was 3750 m from the entrance at a depth of 400 m. A permanent seismic station of the Hungarian Academy of Science was situated at the surface, just 2.5 km away from the deepest station. Data were also obtained from this station and compared with the two underground

sites. The results were presented in Fig. 50 and show an order of magnitude decrease in seismic noise between the surface and underground locations at frequencies above 1 Hz.

The spectral variation plot of the Gyöngyösoroszi seismic results are plotted in Fig. 67. The microseismic peak at 0.2 Hz is again obvious and its tail drops off faster than, for example, the Spanish site. From 1 to 8 Hz the acceleration PSD of the horizontal component stays flat and just 1.5 orders of magnitude above the NLNM. At higher frequencies the upper limit of the spectral variation increases by another order of magnitude. This is due to anthropogenic activity that is penetrating down to the measurement site. Evidence of this can be seen in the spectrogram plotted in Fig. 68, where a clear day and night pattern is visible.

Box 3.3: Site selection summary

The preliminary site investigation set out to explore the possibilities of finding a suitably seismically quiet environment for ET. Seismic measurements were taken at several sites throughout Europe and data were also analyzed from a number of existing seismic observatories. A complete list of measurement results is located in Appendix B.1. It has been shown that at a number of sites visited the seismic background environments is comparable to that for LCGT. The spectral variations were taken over periods of a week. Three sites where selected according to their seismic suitability and presented here. The results of these underground sites, the near surface site in the Netherlands and from the site of the existing GW detector Virgo, are plotted for comparison in Fig. 69. It is clear to see that moving to a quiet location can improve seismic noise effects by several orders of magnitude. In the case of the underground sites by comparison to the Virgo site, up to 5 orders of magnitude improvement in terms of seismic acceleration power can be obtained. A follow-on study is proposed at, or in similar geographical conditions to, these sites to investigate long-term seismic and geological characteristics and investigate the possibility of housing large underground facilities.

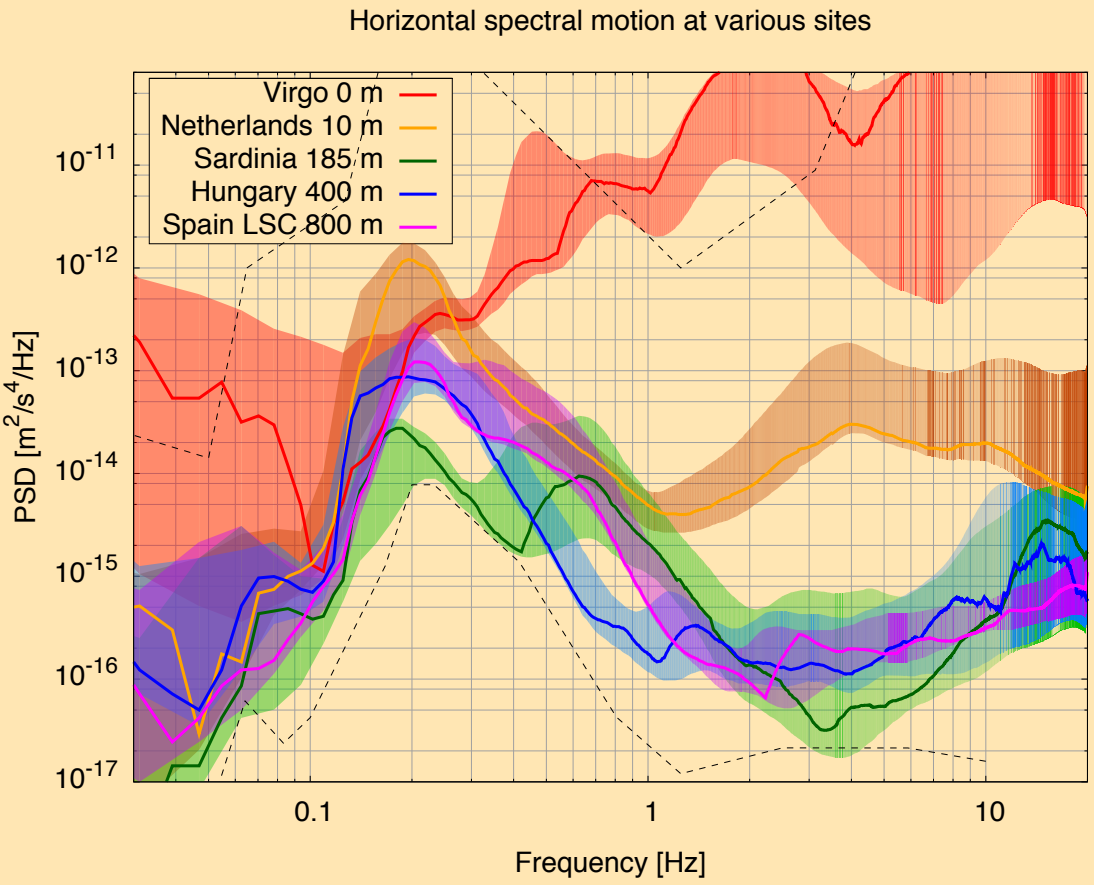

Figure 69: One-week spectral variation results of the three European sites. Plotted for comparison is the site of the current GW detector Virgo. The solid lines correspond to the mode, while the upper and lower limits of the transparent regions are the PSD levels that weren't exceeded for 90 and 10 % of the time respectively.

3.7 Infrastructure realization

3.7.1 Infrastructure overview

Einstein Telescope will have excellent sensitivity of about $10^{-22}/\sqrt{\text{Hz}}$ at low frequency (2 Hz). This is achieved by employing advanced suspension systems, discussed in Chapter 4, with a frequency cut-off below 1.8 Hz at a site that features low seismic noise. Fig. 69 shows that various excellent candidate sites for Einstein Telescope have been identified in Europe. Einstein Telescope will be constructed underground in order to benefit from low seismic and gravity gradient noise. It is well known that the major part of the seismic noise in the frequency range 1 to 10 Hz is generated at the surface. The corresponding gravity gradient noise is then partly suppressed at underground locations due to surface averaging effects. The gravity gradient noise attenuation factor has been shown in Fig. 53. It is seen that gravity gradient noise effects from surface waves can be attenuated by more than 2 orders of magnitude for frequencies $f > 2$ Hz for underground detectors at moderate depth (> 100 m) for soft-soil and homogeneous conditions. Dedicated studies [300] show that in general it will be a challenge to obtain sites with low gravity gradient noise properties. Finite element analysis calculations reveal large differences in attenuation between 1 and 2 Hz. The required depth is driven partly by the wavelength of the seismic waves. Roughly $\lambda/4$ is required for about a factor of 100 suppression. The wavelength scales with the seismic velocity. While for soft soil typical values of 440 m/s are found for the longitudinal velocity c_L, these values increase to 6000 m/s for stressed hard rock such as granite at great depth. Consequently, while the depth of Einstein Telescope could be limited to a few hundred meters when constructed in soft soil, significantly larger depths may be required when considering siting in hard rock.

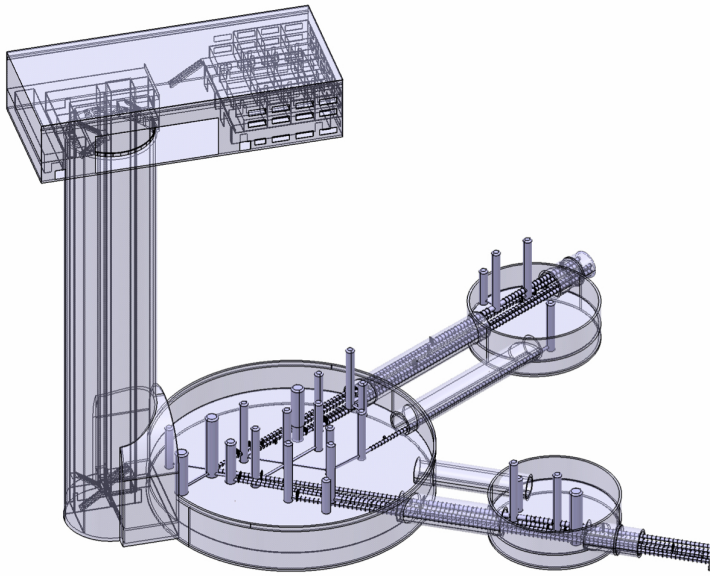

Figure 70: Impression of one of the corner stations for Einstein Telescope. Surface buildings connect via a vertical shaft to the underground facilities that feature one main cavern and two satellite caverns. The observatory has a triangular configuration that can house three xylophone detectors. Each detector is composed of a low-frequency cryogenic interferometer and a high-frequency interferometer operated at room temperature. The three corner stations are connected by 10 km long tunnels.

The Einstein Telescope site studies were performed at various underground locations in hard rock (Frejus, Canfranc, Gran Sasso, Sardinia and Hungary in Europe, Homestake in the USA, and Kamioka in Japan), in salt (Slanic Salt Mine in Romenia, and Realmonte in Sicily), and in Boom clay (the HADES facility for storage of nuclear waste in Mol, Belgium). The lowest seismic noise was obtained in hardrock. Note that homogeneity and

seismic correlation length of the medium are expected to be important parameters for future gravity gradient noise subtraction schemes.

The realization of Einstein Telescope requires the construction of substantial underground infrastructure. Fig. 70 shows an impression of the one of the corner stations of the observatory.

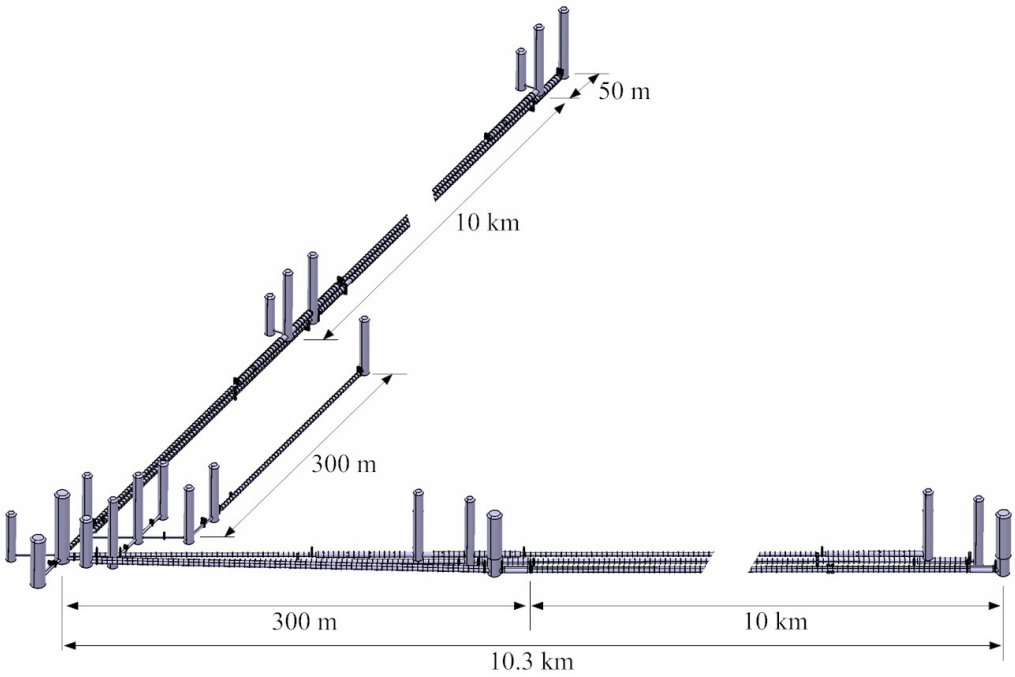

Figure 71: Global view of a single xylophone detector showing the vacuum system and suspension towers needed to house the various optical components. Note that distances are not to scale.

The Einstein Telescope observatory has a triangular topology that houses up to three xylophone detectors. The first phase of the project features a single xylophone configuration that consists of a cryogenic low-frequency interferometer and a room-temperature high-frequency interferometer (see Fig. 72).

The three corner stations are connected by 10 km long tunnels. Each corner station consists of a collection of surface buildings. The main assembly building gives access to a 20 m diameter shaft that leads to the underground infrastructure. At each corner there are three large experimental caverns, the main cavern houses the laser injection systems and the beam splitters, while both the end-test masses of the filter cavities for the high frequency beams (ETM-FC-HF) and the input test masses of the filter cavities for the low frequency beams (ITM-FC-LF) occupy the auxilliary caverns. Tunnels house the interferometer arms and have an inner diameter of 5.5 m. In the following we discuss infrastructure aspects of the tunnels, underground caverns, and the vertical shafts and their construction. In addition, we discuss issues encountered at other underground projects and that may be of relevance for Einstein Telescope.

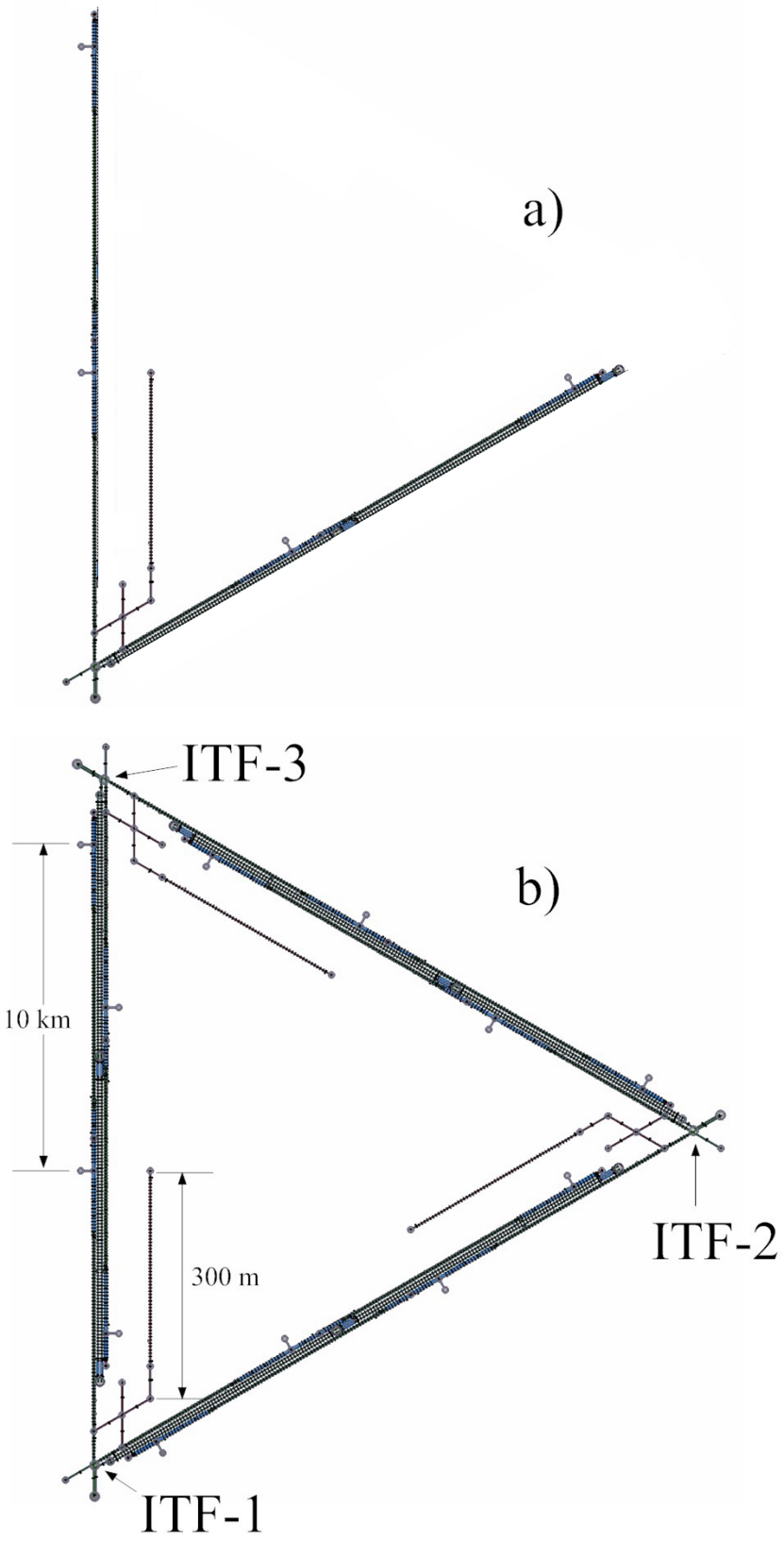

Figure 72: Global layout of Einstein Telescope. Upper panel: during phase I the observatory will house a single xylophone detector. Lower panel: in phase II a triple xyolophone detector system will be implemented. Note that distances are not to scale.

3.7.2 Caverns

Main caverns

An outline of the detector system in one of the large underground caverns is shown in Fig. 73. The cavern has a cylindrical shape with 65 m diameter and 30 m height. It contains detector components from all three xylophones (denoted by the last number on the labels). The laser of the low-frequency interferometer for xylophone 1 is denoted LLF-1. It injects into the power-recyling mirror PRM-LF-1 and is directed onto beamsplitter BS-LF-1. Arrows indicate the directions of the two beams towards the 10 km long interferometer arms. In the same manner the laser of the high-frequency beam of xylophone detector 1 is denoted LHF-1. It injects the beam into PRM-HF-1 and then onto beamsplitter BS-HF-1. Again arrows indicate the directions of the two beams. Steering mirrors, SM-HF-1, are used to direct both HF beams towards the long interferometer arms. Steering mirrors are used solely in the HF beams, since the requirements for low-frequency seismic noise isolation are less stringent for HF beams than for the LF beams. Both LF and HF beams use separate beam pipes. The LF beam is on top (in the vertical direction) of the HF beam as this approach simplifies the cryogenic superattenuator design (see section 3.8).

The LF beam at the dark port ends on signal-recycling mirror SRM-LF-1. The light is bounced off three steering mirrors, indicated in Fig. 73 by SM-SR-LF-1, and is directed towards a beamsplitter at the entrance of filter cavity 1, BS-FC-LF1. Part of the light now enters the beam tube of filter cavity 1, FC-1-LF-1, and falls on the injection test mass ITM-FC2-LF-1 located in the auxilliary cavern. FC-1-LF-1 is 10 km long and ends on the end test mass ETM-FC-LF-1 located in the main underground cavern at the other side of the interferometer arm. The other part of the light enters a second filter cavity, FC-2-LF-1, and via ITM-FC-2-LF-1 in the satellite cavern it enters the 10 km long filter cavity. Again a test mass is located in the corner station at the other end. Both filter cavities use separate beam pipes. The low frequency interferometer allows injection of squeezed light (indicated in Fig. 73 with label SLI).

Also the HF beam at the dark port implements a filter cavity. Light from signal recycling mirror SRM-HF-1 is reflected via steering mirror SM-R-HF-1 into the injection test mass ITM-FC-HF-1 of the filter cavity. The cavity is 300 m long and the end test mass ETM-FC-HF-1 is located in an satellite cavern.

Each main underground cavern houses two end test masses of both other interferometers. In Fig. 73 this is indicated by ETM-LF-2 and ETM-LF-3 for the two other low-frequency interferometers, and by ETM-HF-2 and ETM-HF-3 for the other high-frequency interferometers. In addition, the main cavern houses the two end test masses of the filter cavities for one of the other low-frequency interferometers. In Fig. 73 this is indicated with ETM-FC-LF-3.

The main optical components of the interferometers need to be suspended. Each main cavern houses 17 suspension towers; 4 of these towers are part of the cryogenic suspension system needed for the suspension of the end test masses of the two other LF interferometers. Three towers are used to suspend double payloads, while three towers are used to suspend triple payloads. In two cases the low frequency beam passes through the suspension system of the high frequency beam.

The main cavern is occupied by two cryolinks that protect the cryogenic end test masses of both other interferometers from thermal radiation. In addition, cryolinks are employed near the end test masses of the filter cavity of one of the other interferometers. The cavern must accommodate the cryogenic infrastructure needed for the operation of the four cryolinks.

It can be seen in Fig. 73 that each main cavern is connected to four tunnels. Two of these tunnels accommodate six vacuum beam pipes, a third tunnel holds the filter cavity for the high frequency interferometer, and the fourth tunnel is empty. The latter is used to allow transportation xof equipment between main cavern and satellite cavern.

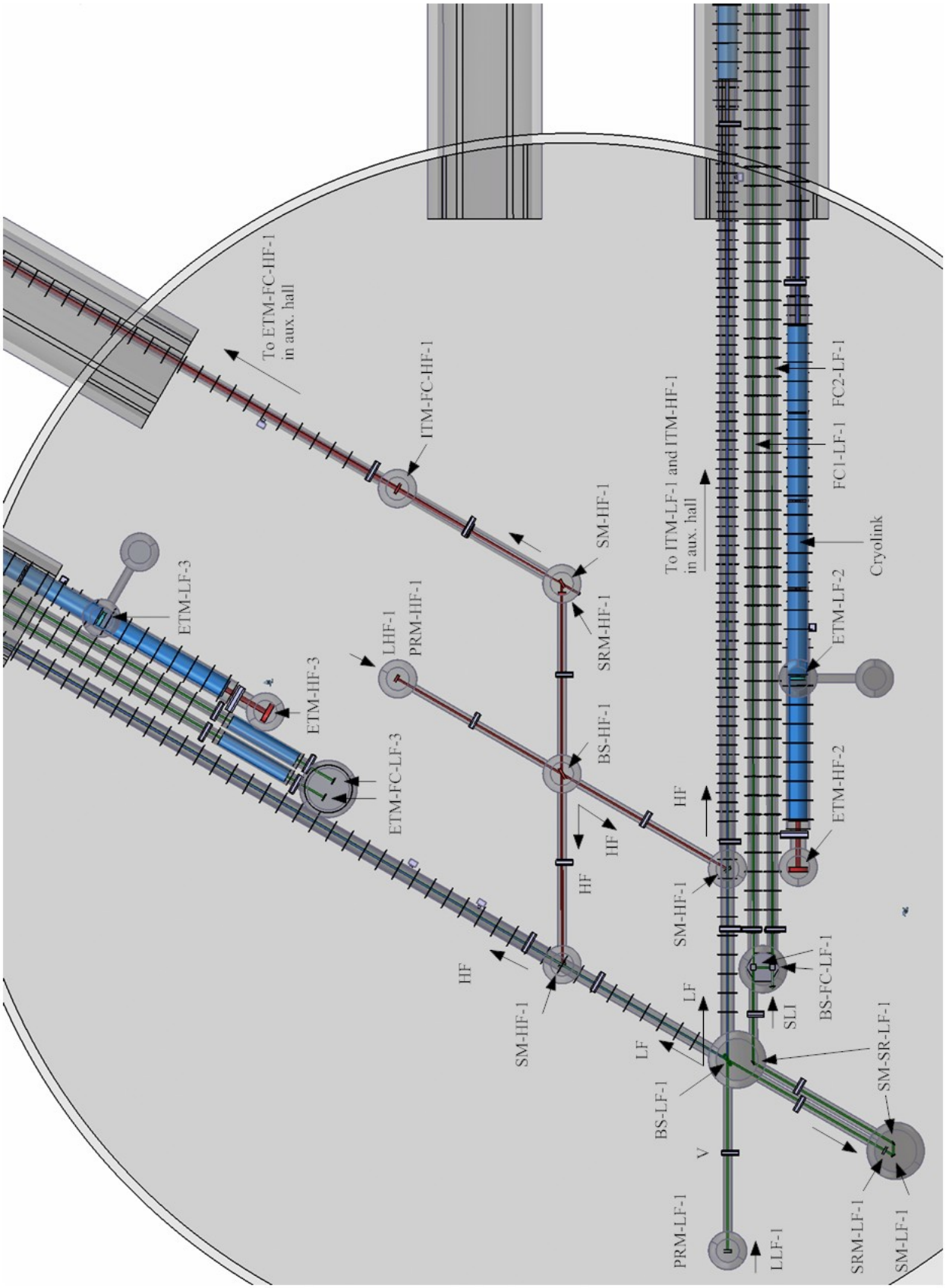

Figure 73: Schematic outline of the main infrastructure in one of the large underground caverns. The labels are explained in the text.

Satellite caverns

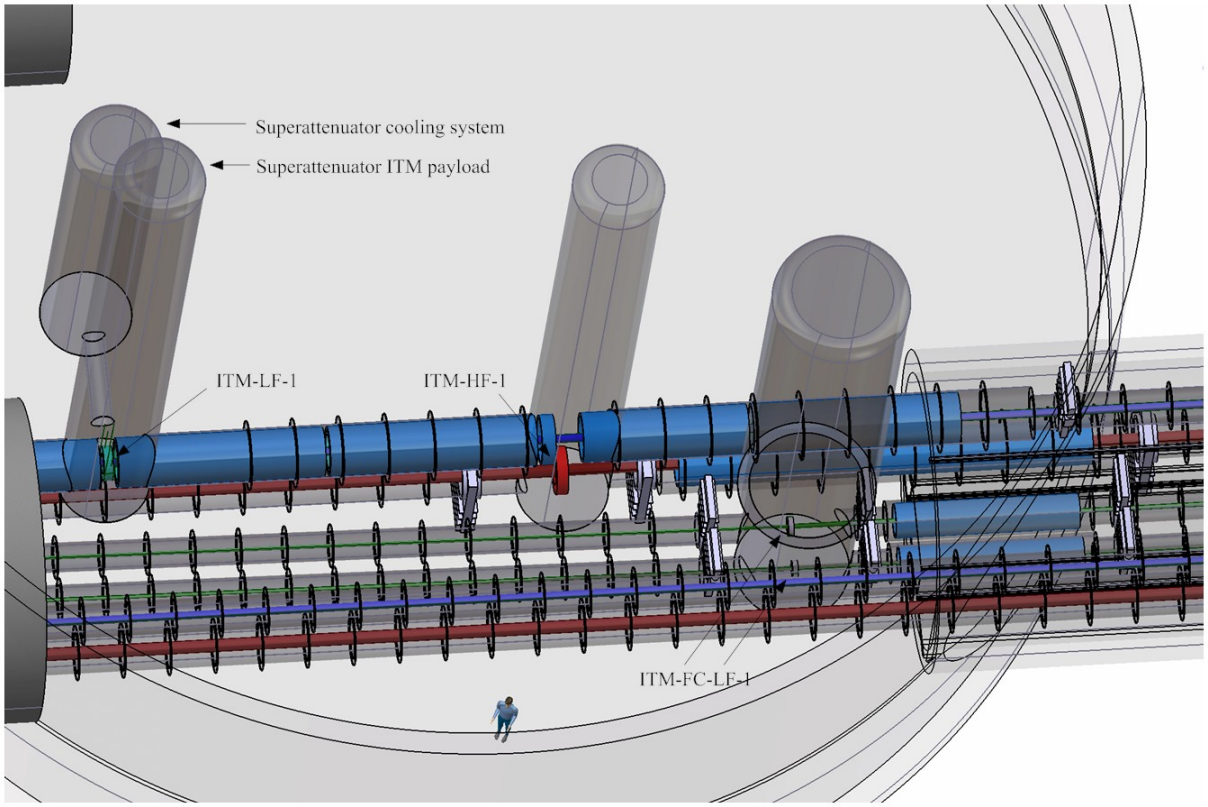

Figure 74: Schematic outline of the main infrastructure in one of the satellite underground caverns. The labels are explained in the text.

An impression of the infrastructure of one of the satellite caverns is shown in Fig. 74. The necessity of having these satellite caverns is explained in Chapter 5. These caverns are cylindrical in shape with a diameter of 30 m and a height of 30 m. In its final configuration, six beam pipes pass through this cavern. The cavern is occupied by the input test masses of both the low frequency and high frequency interferometer. The low frequency ITM is a cryogenic payload and is surrounded with a cryolink. The cavern is equipped with the necessary cryogenic infrastructure. It can be seen in Fig. 73 that each satellite cavern provides the entrance to a main interferometer arm tunnel.

Cavern construction issues

Einstein Telescope will have a total of 9 underground caverns. Each corner station will have a large cylindrical underground cavern with a diameter of about 65 m and a height of 30 m. Each corner station will have two smaller satellite caverns with diameter and height of 30 m.

Einstein Telescope's caverns will be constructed by the drill and blast (D&B) technique. Worldwide various such large underground structures have been constructed. Fig. 75 shows the underground hydropower station in Quebec (Canada).

Einstein Telescope can profit from the large body of experience in underground cavern construction for physics experiments. In particle physics there are LHC (previously LEP) at CERN in Geneva, HERA at Desy in Hamburg, SLAC in Palo Alto and Fermilab in Chicago. In addition, there are non-particle physics facilities

Figure 75: The construction of the Robert Bourassa hydropower station in Quebec, Canada. Drill and blast was used to excavate the powerhouse with dimensions 296 m by 25 m by 47 m. More than 11,000 rock bolts were used.

Figure 76: The construction of the CMS cavern for the LHC project at CERN, Geneva.

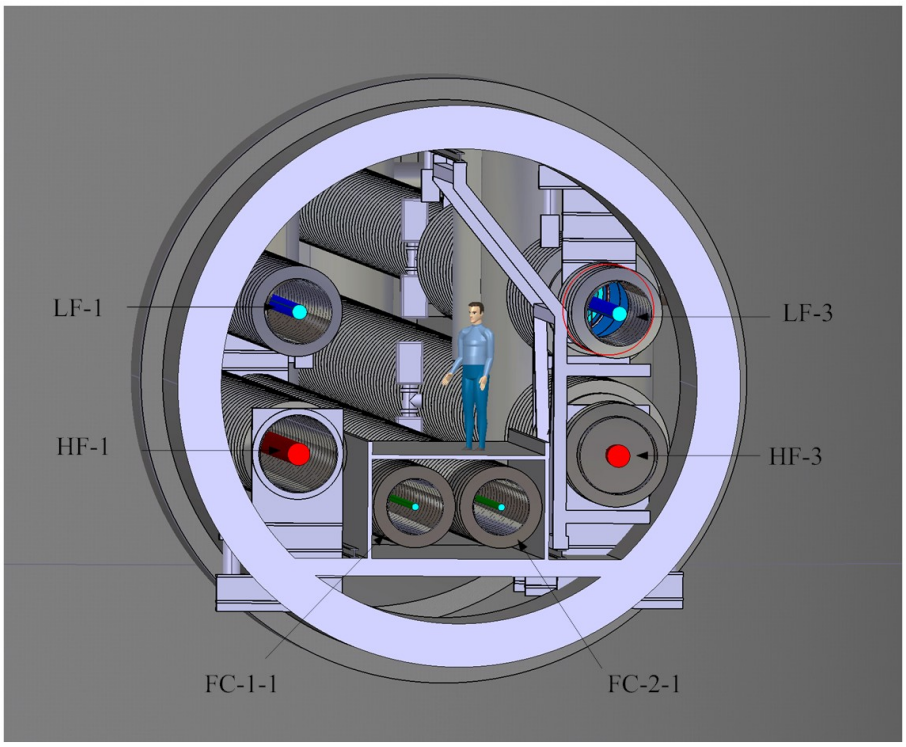

Figure 77: Schematic outline of the tunnel. The tunnel is occupied by the vacuum vessels that hold the low frequency (LF-1 and LF-2) and high frequency (HF-1 and HF-2) arms of two interferometers. In addition, the vacuum vessels for both filter (FC-1-1 and FC-2-1) cavities are housed. The inner diameter is 5.5 m and the tunnel wall has a thickness of 50 cm.

as LNGS in Gran Sasso, LSM in Frejus, LSC in Canfranc, Kamioka in Japan and Dusel in South Dakota. Furthermore, there is experience from the mining industry.

As an example we show some of the experience in realizing large underground caverns for the LHC project at CERN. These caverns host the Atlas and CMS experiments and have been constructed by D&B. The left photo in Fig. 76 shows the waterproofing foil used in the CMS cavern at CERN. The right photo shows the completed cavern. The Atlas cavern is located at a depth of 92 m and has a length of 55 m, a width of 32 m, and a height of 35 m. The CMS cavern is located at a depth of 20 m and has a length, width and height of 53, 27, and 25 m, respectively.

The construction of the Atlas cavern took 4.5 years and that of the CMS cavern 6.5 years. It is clear that for Einstein Telescope the various caverns must be constructed in parallel in order to avoid excessive construction times.

3.7.3 Tunnels

The corner stations are connected by 10 km long tunnels. These tunnels have an inner diameter of 5.5 m and an outer diameter of 6.5 m (depending on geology and construction method). At the location of the cryolinks, the inner diameter will be increased to 6.0 m. The main caverns and the auxilliary caverns are connected by a double tunnel structure with a length of 300 m. Consequently, the observatory hosts more than 31 km of tunnel.

The main interferometer arm tunnels accommodate six vacuum beam pipes. In addition, the tunnel houses the services for electricity, water, compressed air, cryogenics, safety systems and air conditioning. The diameter

of the tunnel is sufficiently large to allow transportation of vacuum beam pipes. An impression of the tunnel was shown in Fig. 77. During installation the tunnel will be equipped with a monorail system. This is used to transport the vacuum beam pipes. Provisions are made to accommodate the large vacuum valves in the tunnel walls, and to allow welding of the beam sections. For safety reasons the tunnel is divided into 500 m sections that are equipped with fire retarding doors, and safety shelters. The tunnel is equipped with an elaborate safety system that allows control of the airflow in order to direct the smoke in case of a fire.

Tunnel construction

At present there is a vast body of experience in tunnel construction. This is to a large extent driven by the increasing worldwide demand for the creation of underground tunnels. For the construction of high speed trains alone, in 2010 about 1000 km of lines is taken in operation, while the current demand for 2020 is estimated at 3500 km [313].

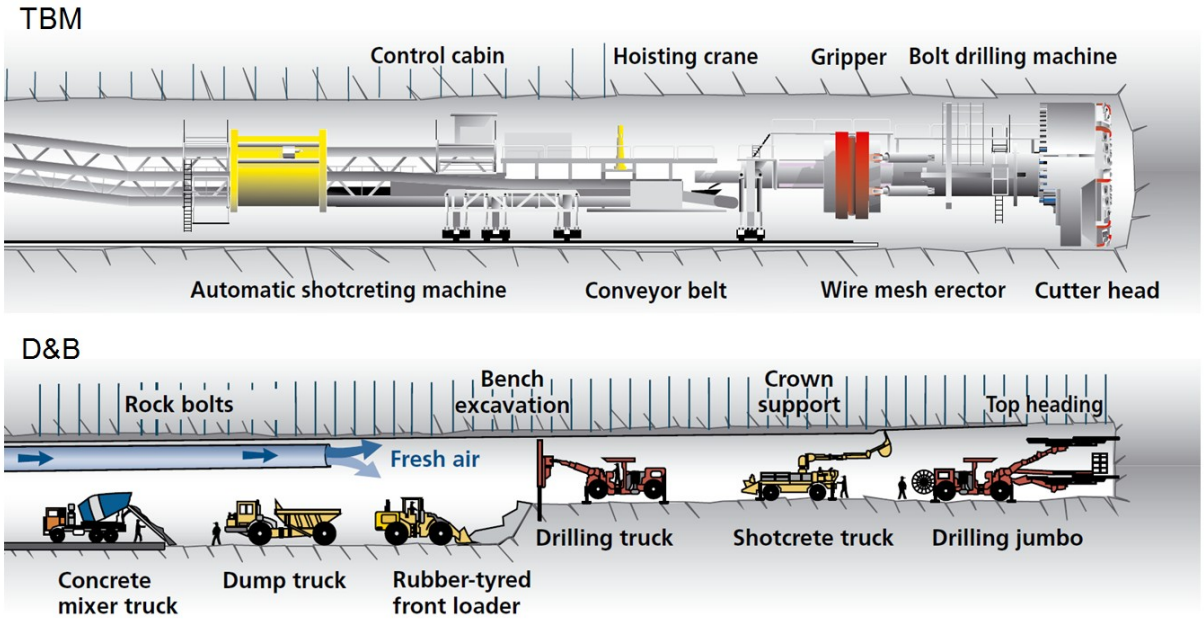

Figure 78: Underground tunnels can be constructed with tunnel boring machines (TBM), or by using the conventional drill and blast method (D&B).

For the construction of underground tunnels, two major technical approaches can be distinguished: tunnel boring machines and drill and blast. Fig. 78 schematically shows the two techniques.

Tunnel construction with TBMs

The TBM technique is state of the art, and excavation rates of 20–25 m per day are routinely obtained. The geology must be well understood through site surveys and one must realize that given the large size of the machine (typically 400 m for the TBM and train combination) it is difficult to adapt to changes (for example in geology).

Fig. 79 shows an outline of a gripper TBM from Herrenknecht [314]. This TBM has a 9.58 m diameter and a length of 441 m. A power of 7.8 MW is required to drive the machine. The TBMs needed for Einstein Telescope would have a diameter of 6.5 m.

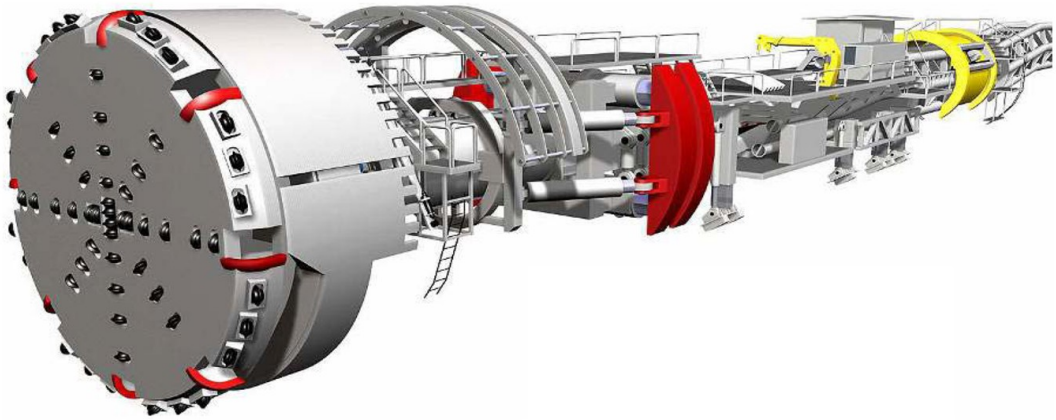

Figure 79: Schematic representation of a gripper tunnel boring machine from Ref. [314].

The investment costs are large (*e.g.* about 20 M€for the TBM shown in Fig. 79) and set-up times are long. In the case of Einstein Telescope several TBMs would be required in order to keep the construction time limited to 2 years. Sizeable diameters are needed for the vertical shafts in order to lower the equipment. A typical TBM cycle would involve boring 2 m of tunnel, followed by clearing out the rock. The tunnel wall support with anchors, shotcrete and steel arches is then implemented next. Tunnel construction would Per day shifts 1 and 2 would involve the above cycle, while shift 3 would be dedicated to the service and repair of the TBMs.

Tunnel construction with D&B

The drill and blast technique is highly adaptable, but excavation rates are limited to 6 - 10 m per day. A cycle consists of drill, charge, and detonate. After ventilation, various tasks as support and muck removal take place. In good rock conditions 1 cycle can be accomplished in an 8 hour shift.

Figure 80: Special tooling has been developed for the D&B technique for tunneling.

In order to cope with the relatively low advance rate, various teams have to work in parallel. Advanced multi-head drilling tools have been developed (see Fig. 80) in order to increase the advance rate. Fig. 81 shows that support of the tunnel walls can be provided in parallel with the multi-head drilling activities.

Figure 81: Support of the tunnel walls can be erected in parallel to the drilling process.

Practical experience with tunnel construction

There is a vast amount of experience available with tunnel construction in various soil types and under various conditions. When long tunnels (typically with lengths exceeding 6 km) are considered and smooth walls are needed (*e.g.* for high speed trains) then TBMs are often selected. Underground infrastructure such as train tunnels are designed for a lifetime of about 100 years. Thus, special wall treatment is needed to ensure such a long lifetime.

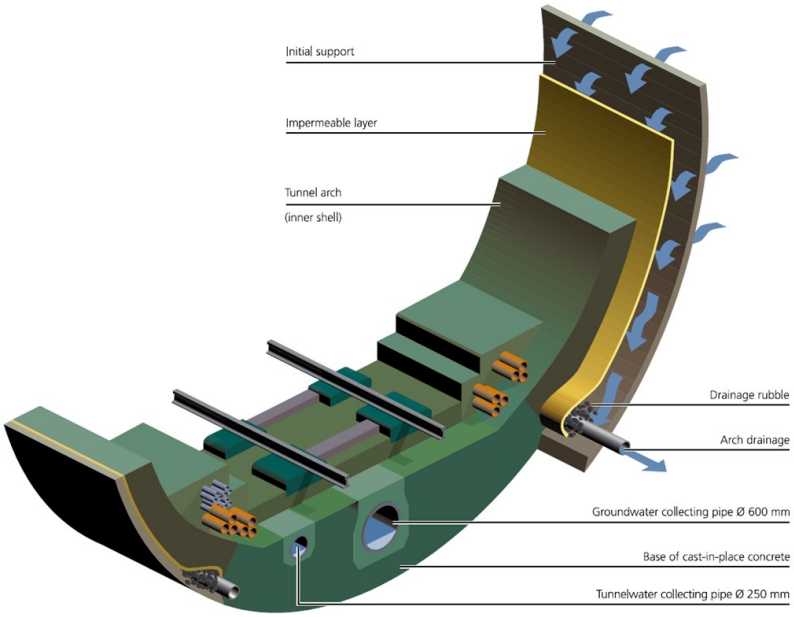

Figure 82: Wall segments used in the construction of the Gotthard-Basistunnel. This project represents the world's largest underground construction.

Fig. 82 shows a wall segment that has been used in the construction of the Gotthard-Basistunnel. The Gotthard-Basistunnel represents the longest tunnel project in the world: a total tunnel length of 98.135 km has been constructed with TBM and 53.705 km with D&B. The lining is designed to handle corrosive water containing chloride, sulphates, *etc.* The impermeable layer avoids swelling of the concrete, corrosion of the anchors, and sintering in the drainage system. The drainage system is designed to prevent groundwater pressure buildup.

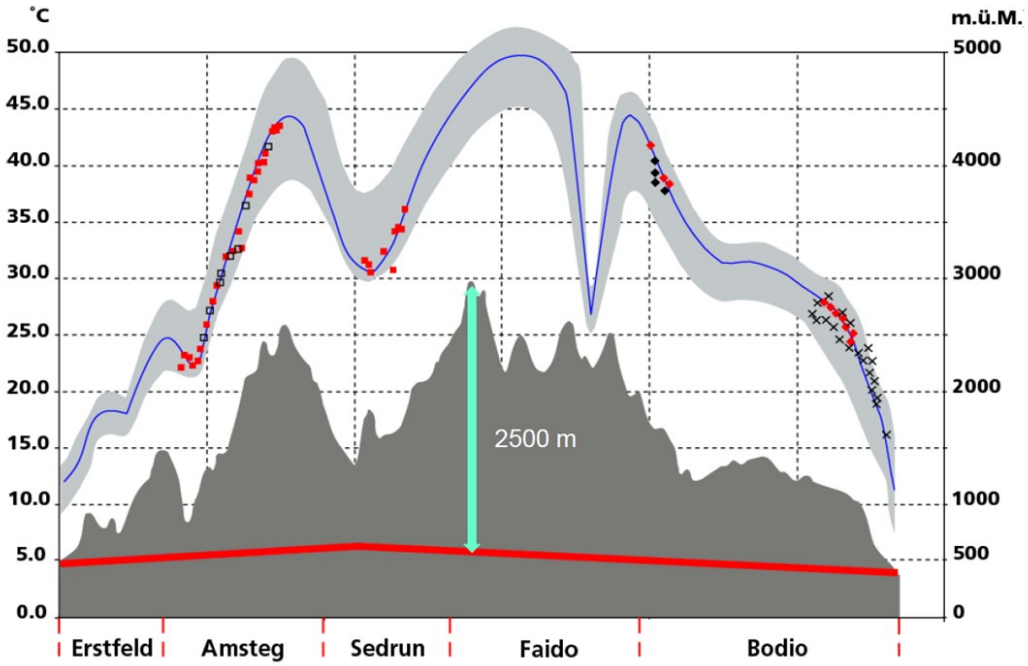

Figure 83: Rock temperature distribution in the Gotthard-Basistunnel. Temperature is shown on the left vertical axis and depth on the right axis (m.ü.M = meters above sea level). Erstfeld, Amsteg, *etc.* are locations along the tunnels.

Construction of tunnels at large depth has various implications. Fig. 83 shows that in general rock temperature increases with depth. For train tunnels these temperatures can be handled (since the trains act as pistons), but it may cause troubles for Einstein Telescope. Sizeable and costly ventilation systems must be installed. These systems also dilute dust and remove methane and radon (detection systems for these gases must be installed). Other problems encountered in construction at large depth include rockfall, rockbusts and possibly large deformations.

For Einstein Telescope the issue of micro tremors may be significant. In the context of the Gotthard-Basistunnel project, the Swiss Seismological Service, SED, recorded an accumulation of seismic activity in the area of the MFS Faido (see Fig. 84). Events were recorded in the period between March 2004 and June 2005. Normally, this is a region with very low seismicity. A local seismic network was set-up at the multi-purpose station, MFS Faido, consisting of 9 stations at the surface, including one station from the SDSNet. The stations were installed in a circular arrangement 10 to 15 km around the MFS Faido. In addition, 2 seismic stations were placed in the tunnel. The hypocenters of the micro tremors were reconstruction in 3D. It was clear that this seismicity was related to the underground tunnel construction. The tremors were observed over at least a 2 year period.

Several water dams are located in the vicinity of the Gotthard-Basistunnel. TPS and GPS measuring systems were installed around these dams in order to monitor surface ground motion. Fig. 85 shows that several mm displacements have been measured at these dams. The movements are correlated with the TBM activity at Nalps North and were first observed in December 2005. It is believed that although these dams are several km away from the underground construction, the movements are due to changes induced in the ground-water levels.

In general the construction of the Gotthard-Basistunnel went according to expectations. However, a major

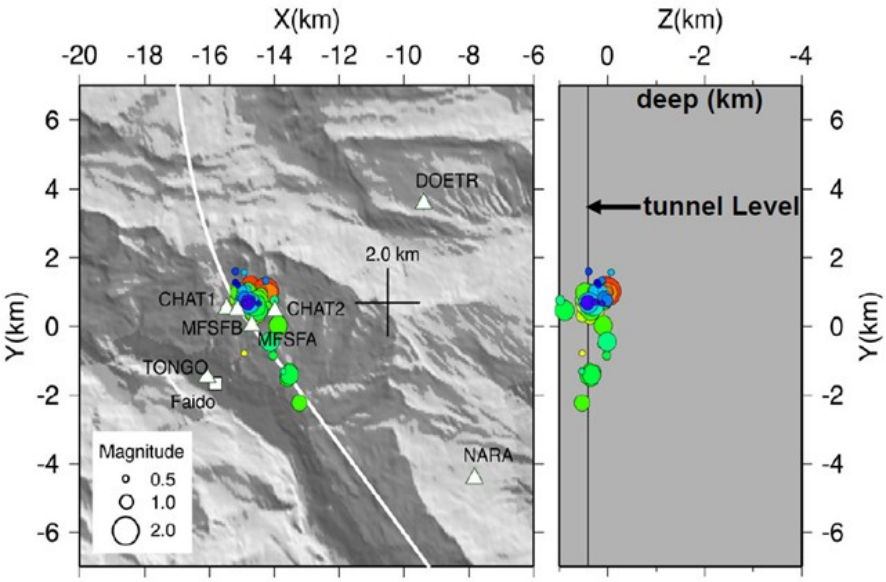

Figure 84: A seismic network set-up near Faido for the Gotthard-Basistunnel project measured various micro tremors over a 2-year period.

problem occured in 2003 when crossing the horizontal fault zone at Bodio. The TBM got stuck for more than 6 months and had to be excavated. This was possible since the project features 2 tunnels (an East and a West railway tube).

TBMs can also be used to drill tunnels in soft soil. In that case special types of TBMs (*e.g.* mixshield) must be used that have a submerged wall, a working chamber, air cushion and pressure bulkhead. The tunnel walls require advanced lining, while the TBM servicing requires special manpower (divers). In general, tunnel construction in soft soil is considerably more expensive than in hardrock.

The tunnel for the HERA ring (6.6 km circumference) at DESY in Hamburg, Germany and the LHC (the LEP) tunnel (26.7 km circumference) at CERN in Geneva, Switzerland have been constructed with TBMs. The 6 km tunnel for the LCGT project in the Kamioka mountain in Japan will be constructed by D&B. The Einstein Telescope team is in close contact with LCGT and will more this project in detail over the next years.

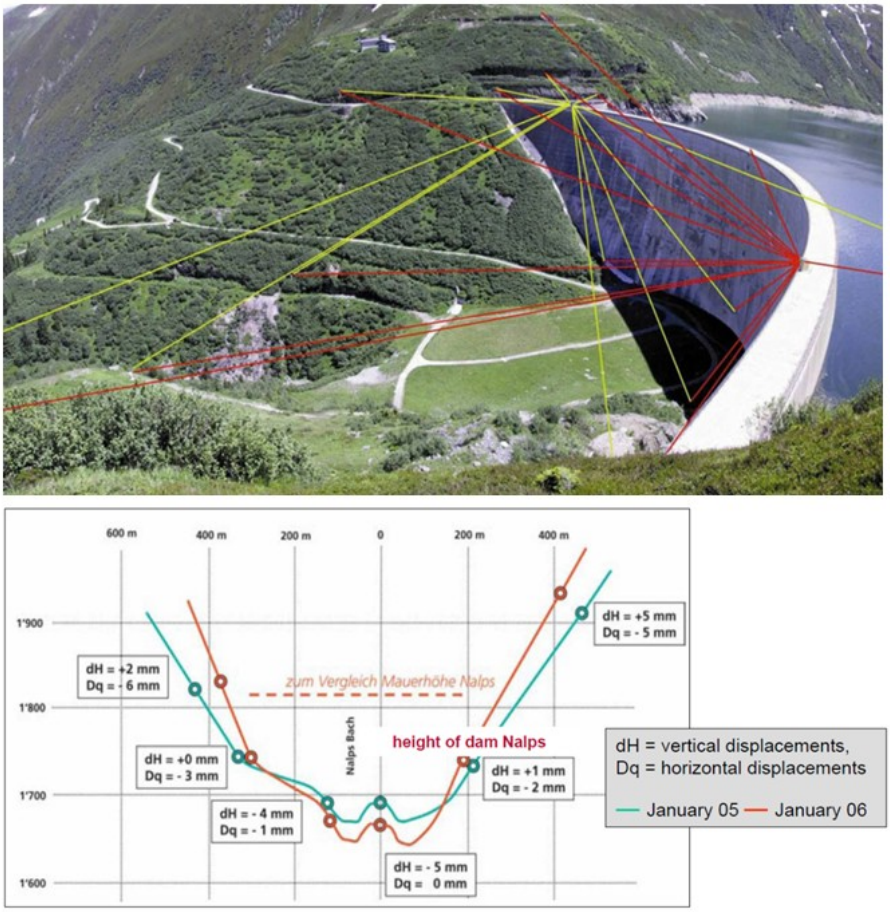

Figure 85: Horizontal and vertical displacements measured at the water dam Nalps are related to the Gotthard-Basistunnel project.

3.7.4 Shafts

Presently, it is not clear whether Einstein Telescope will have horizontal or vertical access. In the case of vertical access, there is a significant increase in complexity of the construction methods needed for shafts with depths exceeding 200 m.

In the following, we present a discussion that is based on vertical access, similar to for example the LHC experiment at CERN (see Fig. 86).

Figure 86: The construction of the CMS access shaft for the LHC project at CERN, Geneva. This shaft has an 18 m diameter and the entire CMS experiment was lowered through it. To facility its construction, the ground at the shaft walls was frozen.

Each corner station will be accessed through a 20 m diameter vertical shaft. For excavation of the tunnels, the TBMs (in case this technique is adopted) will be lowered through these shafts. After tunnel construction, the shafts will be equipped with concrete elevator modules, staircases and will carry all services (power, water, compressed air, ventilation ducts, *etc.*). Additional shafts with a 10 m diameter are foreseen at the center of the arms.

The top of the shafts will be integrated in large suface buildings. There the equipment of the Einstein Telescope interferometers, such as the vacuum system, will be prepared. Subsequently, the various modules will be lowered through the shafts into the caverns using hoisting devices.

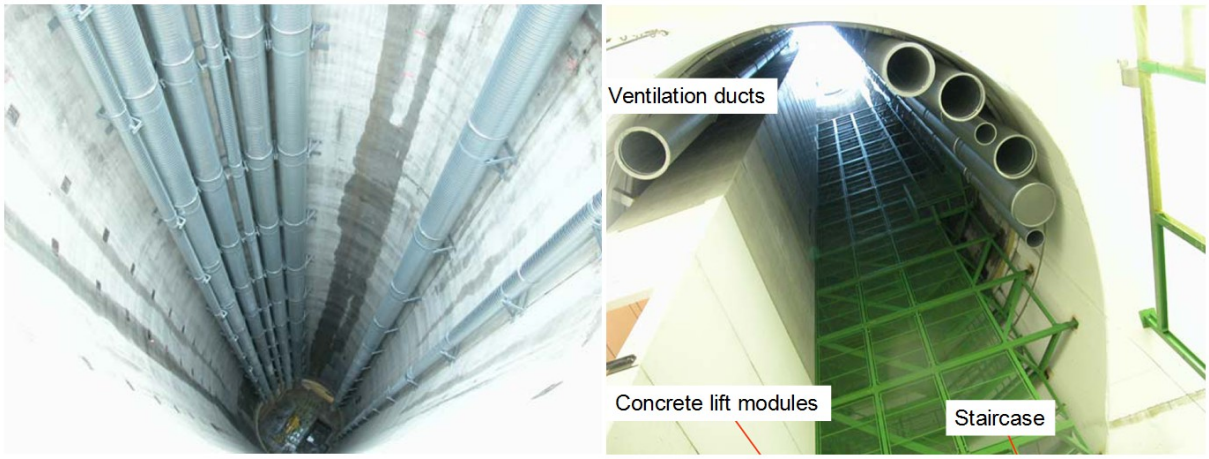

Figure 87: Completed access shafts for the LHC project at CERN, Geneva.

3.7.5 Final remarks

Cost analysis shows that tunnels, shafts and caverns constitute the main cost drivers for the Einstein Telescope project. It is obvious that the cost of underground construction is site dependent and contains large uncertainties at this stage of the project.

In follow up studies it is imperative that risk management of the project is assessed. Worldwide many problems occured during underground construction. Furthermore, in our discussions with insurance companies it became clear that part of the risk cannot be insured (*e.g.* water leaks in tunnels). The Technical Committee on Geotechnical Reports of the Underground Technology Research Council has established guidelines for a so-called geotechnical baseline report (GBR) for construction. It is customary that a project starts by defining such a GBR in order to establish a baseline on risks (*e.g.* from geology) for industry and client. After site selection such a GBR must be realized. It contains as much as possible detailed site information based on geophysical surveys, lidar surveys, drilling samples, probabilistic assessment of rock mass behavior, *etc.* and requires close collaboration between the client, industry, and geophysicists.

3.8 Vacuum systems

3.8.1 Introduction

In laser interferometers for GW detection most of the instrument has to be kept under High-Vacuum or Ultra-High-Vacuum (HV, UHV) for several reasons:

- reduce the noise due to vacuum fluctuations along the beam path to an acceptable level
- isolate test masses and other optical elements from acoustic noise
- reduce test mass motion excitation due to residual gas fluctuations
- reduce friction losses in the mirror suspensions
- contribute to thermal isolation of test masses and of their support structures
- contribute to preserve the cleanliness of optical elements.

A vacuum system of this kind (Fig. 88) is composed of several UHV pipes with kilometric length and several cylindrical vertical HV/UHV tanks (towers) containing the optical elements and their support structures (Fig. 89). In general it is necessary to have the whole vacuum system constituting one single volume, without physical

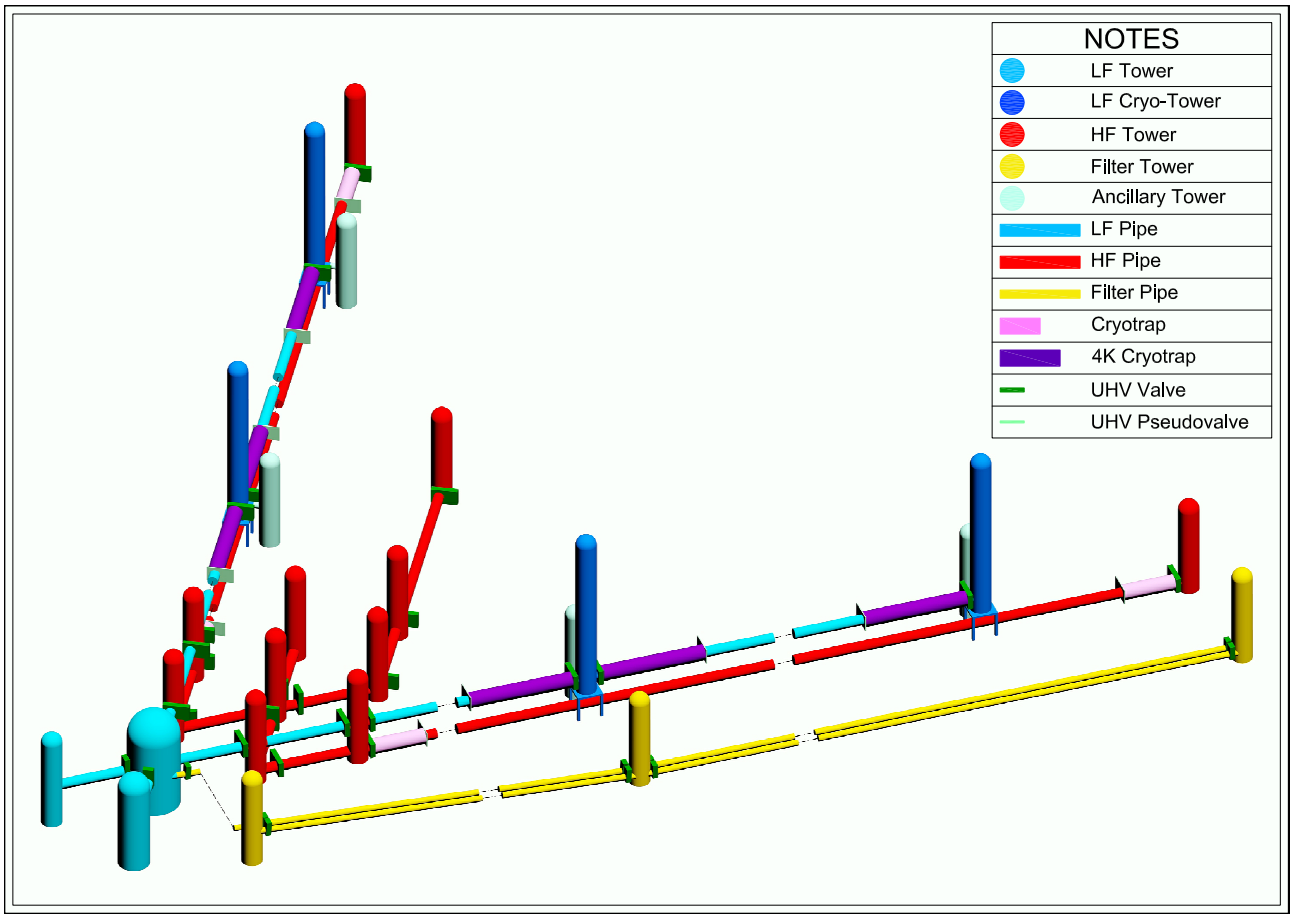

Figure 88: Schematic of the ET vacuum system lay-out, out of scale. Only one xylophone detector is shown, out of three.

separations (windows) on the laser beam path. HV volumes (the towers) contain parts of the apparatus not easily compatible with UHV pipes where, on the contrary, the large majority of the laser beam has to travel. The separation between HV and UHV is obtained by differential pumping or by cryogenic traps, stopping the migration of water and other high vapor pressure components.

The vacuum enclosure will be built of stainless steel (304L); this material is preferred for its easy availability, its price, the large experience in machining and welding, the mechanical properties (ductility), the chemical properties and the achievable outgassing rate. The same choice has been made in the past for Virgo and LIGO. The vacuum system parameters are summarized in table 17, in the appendices.

3.8.2 Average base pressure in the arm pipes

The noise due to vacuum fluctuations (index instabilities due to statistical fluctuations of the number of molecules in the volume occupied by the laser beam in the arms cavities) has been calculated by several people for Virgo and LIGO [315]. It is (at first approximation) inversely proportional to the square root of the beam volume (or to the beam average radius or to the square root of the arm length or to the square root of the average pressure). Conservative beam shape parameters have been used to compute the residual gas noise shown in the figure (Fig. 90).

As it is common practice in matter of vacuum, we will take a safety factor of at least 10 with respect to the pressure producing a phase noise at the limit of the best sensitivity. The residual gas composition will be

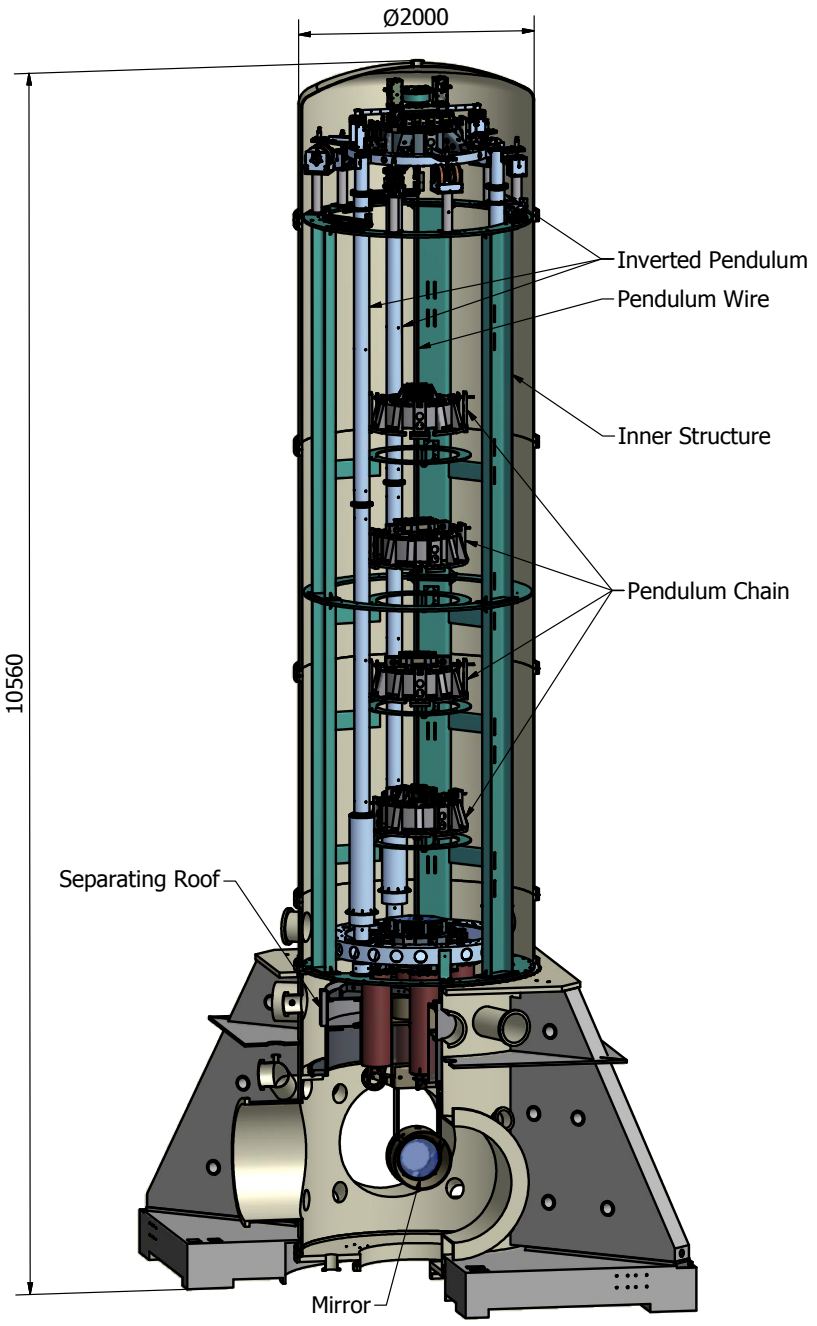

Figure 89: As an example the cross-section of a Virgo a mirror tower is shown.

dominated by hydrogen with presence of water and other gases; we will aim to keep the total residual pressure at about $1\,10^{-10}$ mbar, corresponding to a noise level below $1\,10^{-25}$ $Hz^{-1/2}$ (see Fig. 90). The vacuum system will be extremely clean from heavy organic molecules, both to limit the phase noise and to prevent pollution of the optical components. Hydrocarbon partial pressure shall be at the level of 10^{-14} mbar.

To reach these conditions it will be necessary:

- to fire (one week in an air oven at 450°C) the stainless steel vacuum enclosure elements (or the raw material sheets) in order to reduce the H_2 outgassing rate at the level of 10^{-14} mbar l /cm^2 s
- to bake for one week at 150°C the pipes already assembled and under vacuum in order to eliminate the water molecule layers sticking to the pipe inner wall.

Cryotraps will be necessary to separate the baked UHV pipes from the water dominated unbaked mirror towers, in HV regime. Concerning the phase noise, the path length of the beams in HV will be kept short, that is a negligible noise contribution, when compared to the kilometers in the UHV arm pipes. Large gate valves will be put at each end of the arm pipes, in order to preserve vacuum when venting a tower. For the same reason each tower will be separable from the rest of the vacuum enclosure by suitable gate valves. The filter cavities being less sensitive to vacuum noise require a residual pressure at the level of 10^{-7} mbar. Their pipes will not be fired at 450°C nor baked at 150°C.

3.8.3 The arm pipes

Due to the multi interferometer/xylophone choice for ET, several beams will run along each side of the triangular tunnel, we assume four main beams and two filter cavity beams, taking into account all the three detectors (six interferometers) composing the full ET.

The chosen baseline configuration includes four pipes, one for each main beam: two with a 0.9 m diameter for the HF interferometers and two 0.75 m diameter pipes, for the LF interferometers. In addition, two 0.69 m pipes for the two filter cavity beams belonging to each LF interferometer. HF interferometers will be equipped also with a 300 m long filter cavity, running in a dedicated tunnel, inside a 0.6 m diameter pipe. Also solutions with larger pipes (up to 2 m diameter) to contain several beams along the same arm have been considered. They have not been retained due to the difficulty of connecting one pipe to the several towers containing mirrors of different interferometers. Additional problems would arise from the combination of cryogenic and room temperature towers and from cross-talk between interferometers due to diffused light. Some flexibility in flattening the budget time distribution would also be lost.

The pipes will be arranged inside the tunnel cross-section as shown in Fig. 91: the filter cavities at the bottom, under a movable floor, the two HF beams on the floor at the tunnel sides and the two LF beams on top of them (see below the "Tower" subsection).

The pipe construction procedure merges Virgo and LIGO experience, even if the final choice will be performed in due time, with the appointed company. The pipes will have stainless steel thin walls (3 – 4 mm) with external stiffening rings, every 1 – 2 meters. Two rings will be larger, serving as attachment for the supports (see below).

20 m long pipe elements will be fabricated by continuous spiral welding in a suitable clean factory installed on site. At one end of each element a suitable bellows will be added to accommodate thermal expansion, during bake-out; winter/summer temperature excursion should be negligible under ground. At both ends 2 mm thick lips will be added, to allow UHV compatible welding of adjacent elements, without inert gas protection on the inner side of the weld (this technique has been successfully applied in Virgo).

The possibility to build the ET pipes as 10 km long thin wall bellows has been discarded to avoid the heavy risks of damages during the second and third detector installation nearby already operating interferometers. From the cost point of view, the choice has been judged neutral: the increase of raw material for a straight wall pipe being compensated by a much simpler fabrication.

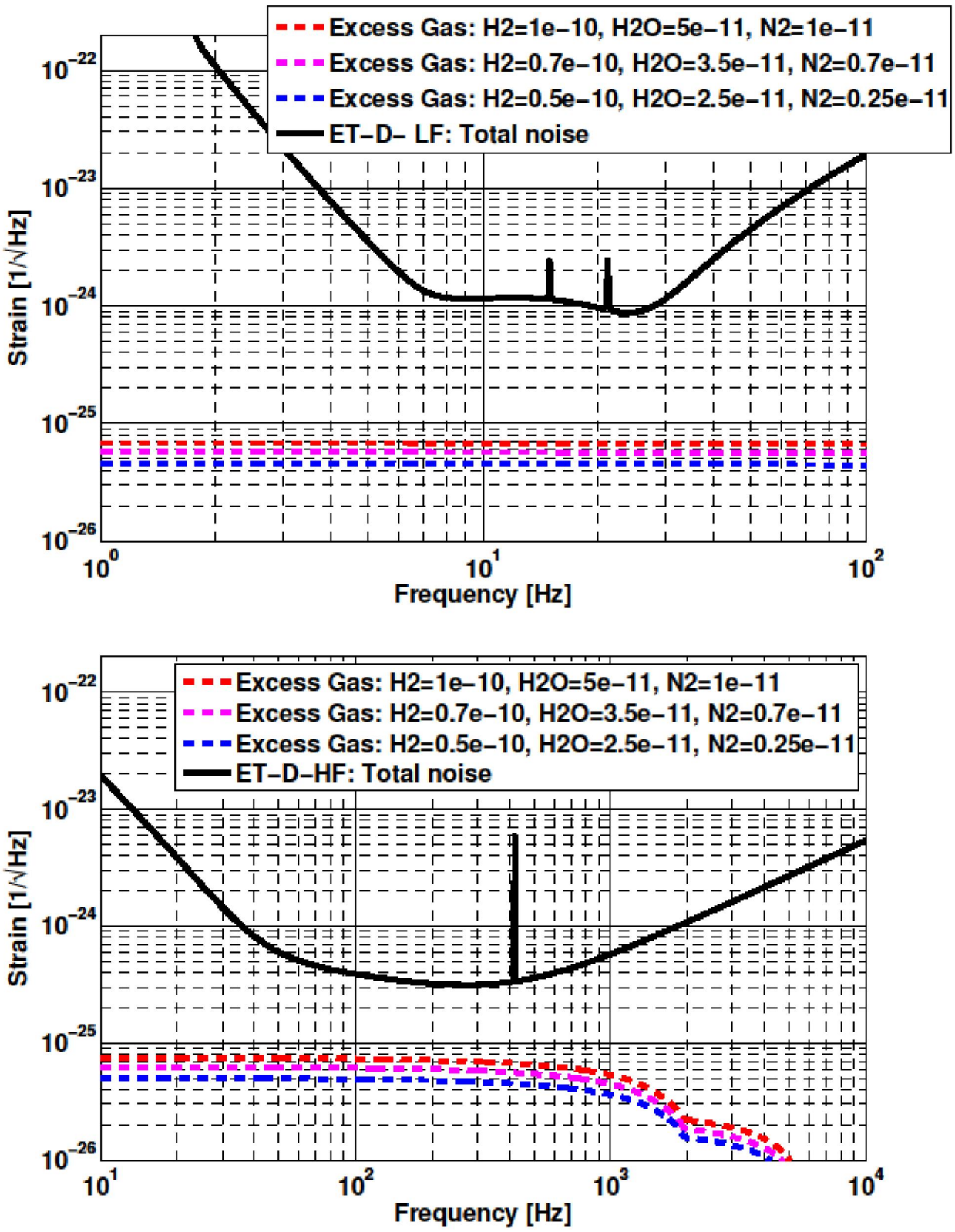

Figure 90: Phase noise given by the residual gases compared to the expected sensitivity, computed for the appropriate beam profile for different gas compositions. (Goal gas composition: Hydrogen [$1\,10^{-10}$ mbar], Water [$5\,10^{-11}$ mbar], Nitrogen [$1\,10^{-11}$ mbar])

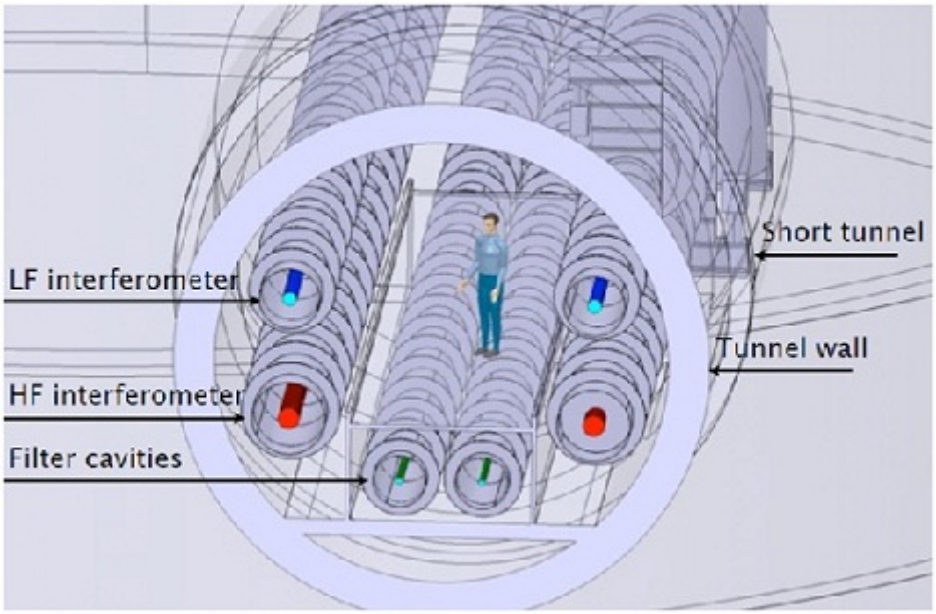

Figure 91: Arrangement of the vacuum pipes in the tunnel cross-section.

Simple supports "a la LIGO", using steel cables and adjustable stretching screws will be sufficient, coping with the expected stability of the tunnel.

The pipes will be aligned in the tunnel using optical instruments and laser beams, since GPS will not be applicable under ground. The requested straightness error for the arms is of the order of 10 mm. Periodical surveys will be necessary every few years, in order to detect dangerous pipe displacements due to ground movements.

Each 10 km pipe will contain a few hundreds of metallic baffles for diffused light mitigation. They shall be made out of stainless steel with a suitable conical shape and serrated inner edge (Fig. 92) against diffraction. The radial width of the baffles, between 50 and 100 mm, and their position will be determined by a suitable simulation [316] [317].

3.8.4 Pipe Assembly

The 20 m pipe elements will be lowered to the corner caverns with the ends sealed by suitable end-caps and equipped with thermal insulation; each element will weight about 1.5 t. The element will be put on and bolted to a simple carriage made of two parallel 20 m long beams supported by small train wheels. In this way pipe elements can be pushed to their position one after the other by an electric tractor running on 5 km long rails reaching up to mid arm. The rails, two for each pipe, are supported by frames extending to the whole tunnel cross-section. These same frames have the function, as said before, of supporting the pipes.

In alternative the element could be suspended to a 20 m long beam running, as a bridge crane carriage, on a 5 km long rail. The rail, one per pipe, is supported by the already mentioned frames. Also in this case pipe elements can be pushed to their position one after the other by an electric tractor or by a traction line.

Every 500 m, along the tunnel, there is an enlarged room ("pump room", Fig.93) foreseen to host pumping, bake-out and control equipment; those rooms are used also to weld the pipe elements at ease in a wide area, under a mobile clean tent. A pump room is an enlargement of the tunnel for a width of 12 m and a length of 10 m, allowing the installation of the pumps, which are hold in their position by a metallic frame not shown in the figure. Three cabinets housing the electronics of the vacuum equipment are included, together with an electrical

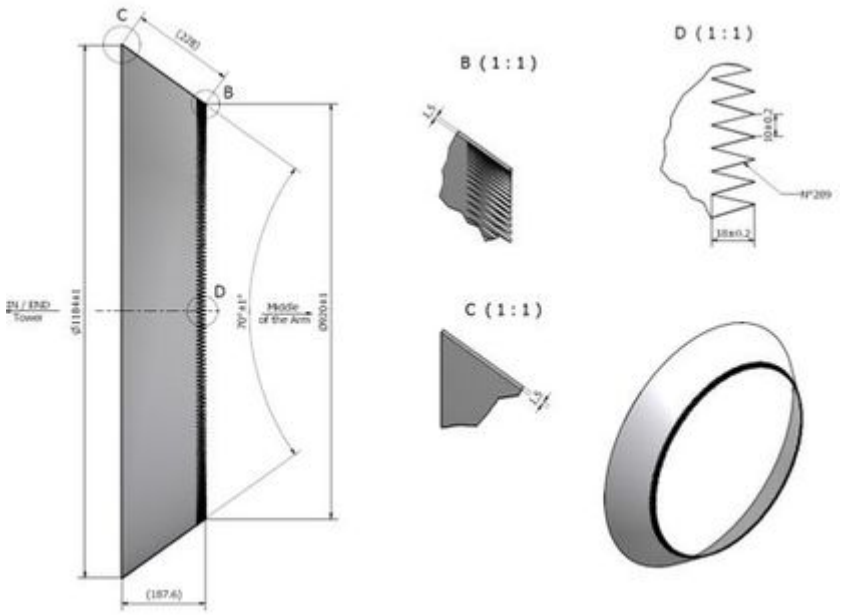

Figure 92: As an example the Virgo pipe conical baffles are shown.

power supply for baking (60 VDC 300 kW). A bridge crane shall be present, and the room shall probably need a conditioned humidity and temperature, to allow electronics efficiency.

The assembly sequence of a vacuum pipe is described below and is graphically shown in Fig. 94.

The first pipe element is stopped with the rear end under the tent prepared in the 9^{th} pump room, counting from the corner cavern; when the front end of the second element is close, the sealing lids are removed, after starting appropriate clean air flows. The corresponding end lips of the adjacent elements are precisely adjusted and welded. The beams of the two carriages (under or above the pipe, according to the chosen option) are rigidly bolted together, taking care of appropriate compression/extension of the bellows.

The two modules are shifted forward until the rear end of the second module is at the welding position; now the front end of the third module is adjusted and welded as before. This procedure is continued until the 25^{th} module is welded and the 500 m long section of pipe is completed.

The 500 m long section will be then shifted by 20 m to its final position.

Every pair of upper support cables (as said, in the LIGO style) are attached to the corresponding support ring, the cables are tightened, the bolts of the pipe elements to the carriages are removed, the elements are lifted (lowered, in the case of suspended transportation) by 10 mm in 1 mm steps. The 500 m long train composed by 25 carriages is sent back to the end cavern, to start the assembly of the second 500 m pipe section. The lower support cables are attached to the pipe support rings and suitably tightened.

The ends of the assembled pipe section are closed with vacuum tight lids, the section is evacuated and tightness tests are performed. The closing lids will be strongly fastened to the tunnel wall, in order to keep the 6.4 t axial load due to atmospheric pressure.

The clean tent and the welding equipment are transferred to the next (8^{th} from the corner cavern) pump room and the assembly of the second 500 m pipe section is started. Once completed and vacuum tested, taking advantage of the bellows and of the support cables, the front lip of the new 500 m section and the rear lip of the previous section are connected welding-in a 1 m long junction piece. These final welds are the last to be performed in that particular pump room.

The procedure continues contemporarily extending the installed pipe from mid arm to both arm ends.

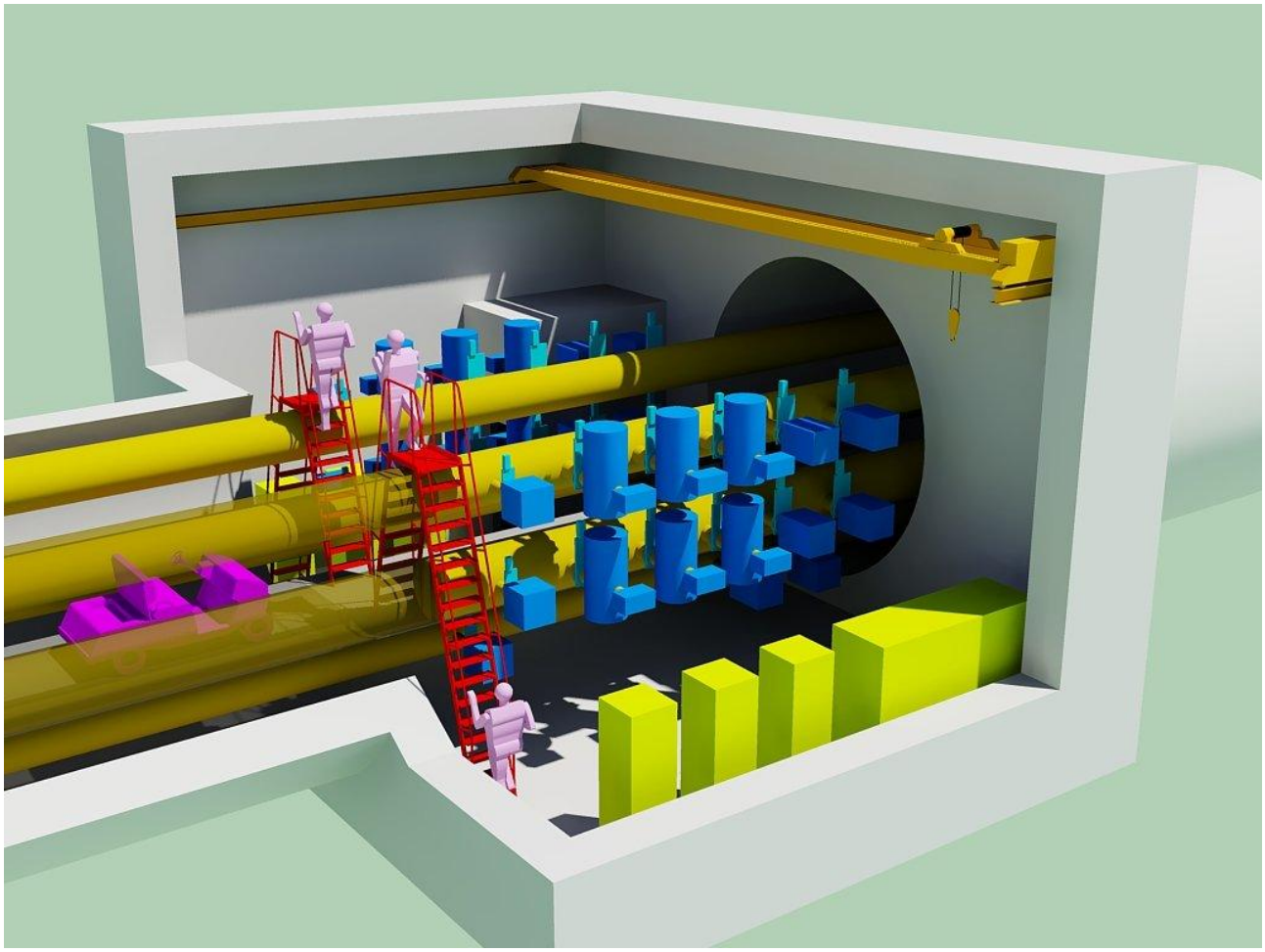

Figure 93: 3D view of a pumping station: the blue objects represent the pumps and sensors, the yellow ones the cabinets for pumps control and baking power supply (1 cabinet for all). A separate small room is reserved for the high voltage electrical transformer.

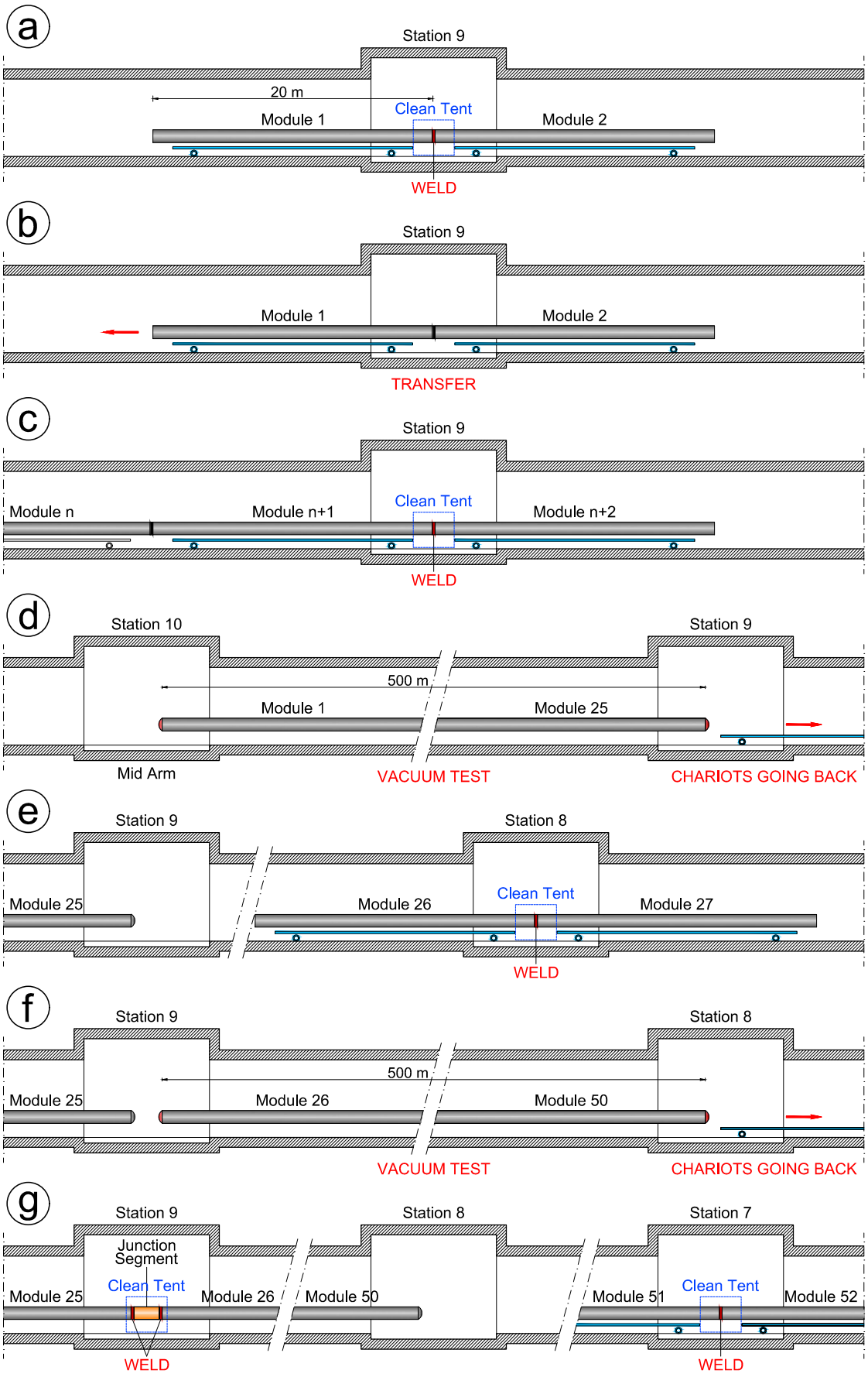

Figure 94: The assembly sequence of one vacuum pipe.

Concerning the pipes arrangement in the tunnel, it is necessary to have the possibility to inspect and repair the welds between pipe elements. This could be achieved leaving a minimum clearance of about 0.5 m between the "nude" pipes and the tunnel wall (at least every 20 m). This will be barely sufficient also in the case of small maintenance interventions on the tunnel wall lining.

3.8.5 Pipe pumping system

The pipe pumping system has been conceived to be composed of standard modules, grouped together, in order to limit the number of pumping stations along the arms.

The goal total residual pressure (hydrogen and other gases) of $1\,10^{-10}$ mbar can be obtained, after firing and bake-out (see a previous subsection), with one 5000 l/s pumping group, every 500 m, both in a 0.9 m and in a 0.7 m diameter pipe, the smaller gas load due to the smaller diameter being compensated by the relatively reduced conductance.

Below is described the pumping system for one single pipe.

Each permanent pumping group will consist of three identical modules, each made of one 2500 l/s Ti sublimation pump (TSP), connected to the pipe through a 250 mm gate valve (the Ti will be sublimated not in the tube but in a separated chamber), coupled to a 300 l/s ion pump. The former to pump active gases, the latter to pump inert gases. At such a low pressure TSPs are expected to require not more than one yearly regeneration. NEG (Non Evaporable Getter) pumps are being considered as a possible alternative to TSPs. Some redundancy is necessary to cover the Ti pumps regeneration periods.

Besides the permanent pumping group, every pumping station will include suitable vacuum gauges and two 2000 l/s turbo, backed by a scroll pump, for initial evacuation and bake-out.

The filter cavity pipes, requiring a 10^{-7} mbar residual pressure, will be equipped only with the turbo/scroll groups, possibly reinforced with 77 K cryo-pumps. To meet these specifications, the bake-out will not be necessary, hence filter pipes will not be equipped with thermal insulation.

Every 10 km pipe will have three residual gas analysers (RGA), at each end and in the middle, to monitor the vacuum quality and for easier diagnosis in case of problems.

3.8.6 Pipe bake-out system

In order to perform the 10 days bake-out under vacuum at 150°C, the pipe could be heated by electrical current flowing in its walls, closing the circuit by a suitable Al bar or cable. Closing the circuit with the pipe of the adjacent twin interferometer would save the Al conductor cost, but does not seem practical. The use of DC will assure a uniform current and temperature distribution on the pipe walls and improve human safety. Typical arrangement of the circuit could be, similar to Virgo, a series of double ring circuits with one DC source every 500 m delivering 1000 A at 50 V along 250 m in each direction. Such a system will deliver 200 W per meter of pipe, which has been experimentally demonstrated to be sufficient to reach 150°C, if the pipe is wrapped in a suitable 10-20 cm thick thermal insulation layer. Each DC source will consist of a transformer/rectifier supplied by medium voltage AC (15 kV). This choice is dictated to reduce the cross section of cables to distribute 2 MW along 10 km. 15 kV equipment will be confined in dedicated rooms.

In this configuration, delivering 300 W per meter of tunnel, in absence of ventilation, a very crude estimate considering a 6 m aperture tunnel, drilled in isotropic rocks (assumed $\rho = 2500$ kg/m^3, k = 2.0 watt/m K, C = 800 joule/kg K) gives an increase of room and wall temperature by about +13°C after a 10 days bake-out. This situation, being at the limit of what could be tolerable, suggests to exploit several remedies like baking at a lower temperature for more days and improving the thermal insulation properties, in order to reduce the temperature increase of the tunnel walls. A suitable air cooling system will be designed to reduce further the ambient temperature (possibly renewing once per hour the tunnel air volume). The overall power release

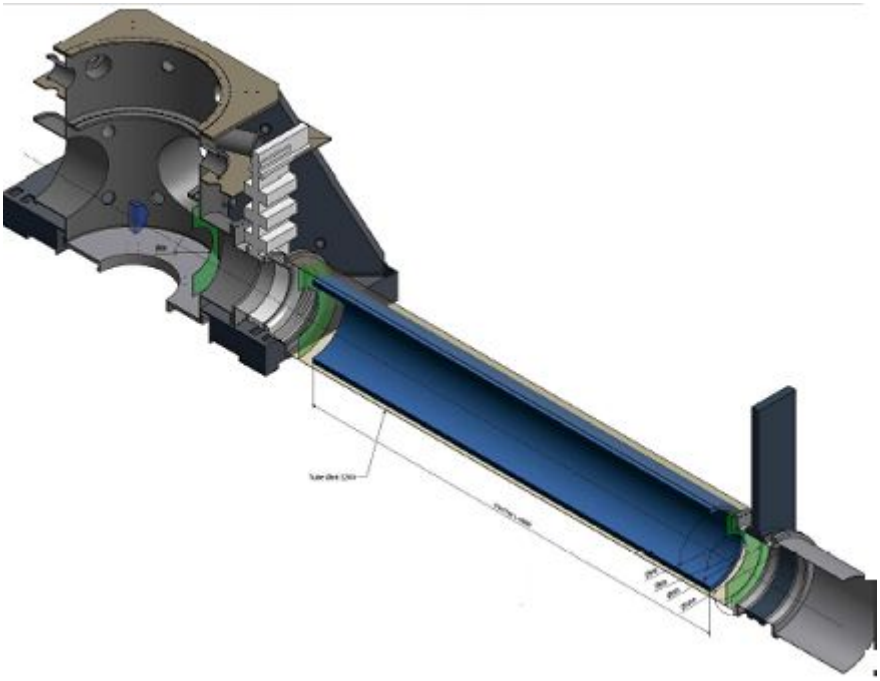

Figure 95: A liquid nitrogen cryotrap.

inside the tunnel could be reduced also performing bake-out in sequence on shorter pipe sections, separated by "pseudo-valves", vacuum tight, but able to sustain null pressure difference.

3.8.7 Cryotraps

HV volumes (e.g. the towers) will communicate with the UHV pipe through liquid nitrogen cryotraps, to prevent migration of water and other high vapor pressure contaminants. In order to allow the beam passage the cryotraps will consist of a large hollow muff, containing liquid nitrogen, suspended inside an increased diameter pipe section, with a design very similar to the one adopted for LIGO, Virgo and Advanced Virgo (Fig. 95). The lateral surface will be thermally isolated by a few cylindrical metal screens; the heat exchange at both ends will be limited by suitable circular baffles, leaving passage for the beam. The propagation of mechanical noise due to liquid nitrogen bubbling will be limited installing cryotraps at least 20 m away from the mirror towers; this will help to avoid excessive cooling of the mirrors (to avoid condensation, in no circumstance a mirror should be the coldest point in the environment). Cryotraps will have valves at each end, in order to be confined during warming-up for regeneration (not more than once per year). The traps will be 7–10 m long for pipes with diameters of 0.6 – 1.0 m. The liquid nitrogen consumption has been evaluated to be about 10 liters per hour per trap. In correspondence of the cryogenic towers for the 10 K mirrors of the LF interferometer, the cryotraps will be much longer (50 m) and will include liquid helium sections to strongly limit the mirror heat exchange as described in the following section. We refer to the same section for a description of the supply plant for cryogenic liquids.

3.8.8 Towers

Mirror towers upper part will have a 2–3 m diameter to contain easily the pendulum chains of Superattenuators and the inverted pendulum legs; the structure will be an evolution of the Virgo towers (Fig. 89). The lower chamber of the towers will have a diameter up to 3 m, to contain large payloads. The HF interferometer towers will have a large bottom lid to allow installation of payloads from a clean basement, under a filtered air shower.

The height will be 10 m for the main mirrors of the warm HF interferometer. Auxiliary mirrors or benches requiring lower isolation, will be located in shorter towers. The towers containing the cryogenic mirrors of the LF interferometer, to achieve full seismic isolation performance down to 2 Hz, will be up to 20 m tall. In these towers, sitting on top of the HF interferometer, the payload installation will be performed through a lateral port. This order of superposition has been chosen to have the low power LF beam passing through the HF mirror suspensions (at room temperature) and not the high power HF beam passing through the low temperature LF mirror suspensions. The lower part of the cryogenic towers will be described in the next section. Each cryo-tower will be coupled to an ancillary tower to support the heat extraction chain preventing seismic noise propagation.

3.8.9 Tower pumping system

Mirror towers will be made of two or three vacuum compartments in order to separate by differential vacuum the lower mirror chamber from the less clean suspension mechanics in the upper chamber. The horizontal separating walls will have a low conductance hole for the passage of the pendulum chain support wire. The mirror chamber will be equipped with a permanent pumping group consisting of one 2500 l/s Ti sublimation pump coupled to a 300 l/s ion pump. In addition one 2000 l/s turbo, backed by a scroll pump, will be operated for initial evacuation. The tower upper chamber(s) will be pumped by suitable turbo/scroll groups.

An effort will be performed to build the suspension mechanics and electronics with ultra clean and low outgassing components, in order to pump permanently also the upper chamber with ion pumps. The use of large cryo-pumps is being considered to increase pumping power and to eliminate moving parts from the vicinity of mirrors.

3.8.10 Valves

A great number of UHV gate valves with large aperture, up to 1 m will be necessary. They will be all metal with only the gate gasket out of vacuum outgassed Viton. Every tower will be separable from the rest of the vacuum system by such valves. Every cryotrap will also be separable for regeneration; the HV side will be equipped with a Viton gasket valve, while the UHV side will be equipped with a totally metallic “pseudo valve”, vacuum tight, but tolerating only a few mbar pressure difference.

3.9 Cryogenic service infrastructures

We present two possible approaches for the cryo-plants to be set up mainly for the LF- Interferometer. In fact the HF- interferometer includes just cryo-traps installed at the tube ends for fulfilling the ultra high vacuum requirements. These traps already present in the LIGO detector and now planned also for Advanced Virgo, are based on the use of liquid nitrogen. Similar cryotraps for the ET HF- interferometer have been already presented in a previous section and from here after we focus on the cryogenic requirement of the LF - interferometer. The cryo-plant for the LF-interferometer will provide the refrigeration power needed to bring the mirror temperature in the 4 K range. This porpoise can be pursued either by setting up a system based on a battery of cryo-coolers or in alternative using the classic approach of liquid helium cryostats. In the next we sketch the main characteristics of ET cryostats. Then we present and compare the two alternative cryo-plants.

3.9.1 The ET cryostats

In order to reduce the thermal noise impact on the ET sensitivity curve its is sufficient to cool at cryogenic temperature the four test masses of the LF- detector. The heat is extracted from the mirror via the suspension fibres attached at the other end to the marionette. Moreover the marionette is suspended to the super attenuator which attenuates the seismic noise up to few hertz. Thus, it is extremely important to preserve the mechanical isolation between the mirror and the cooler system. On the other hand an efficient thermal link between the payload and the cooling system plays is crucial for the design optimization: we have to design links as short as

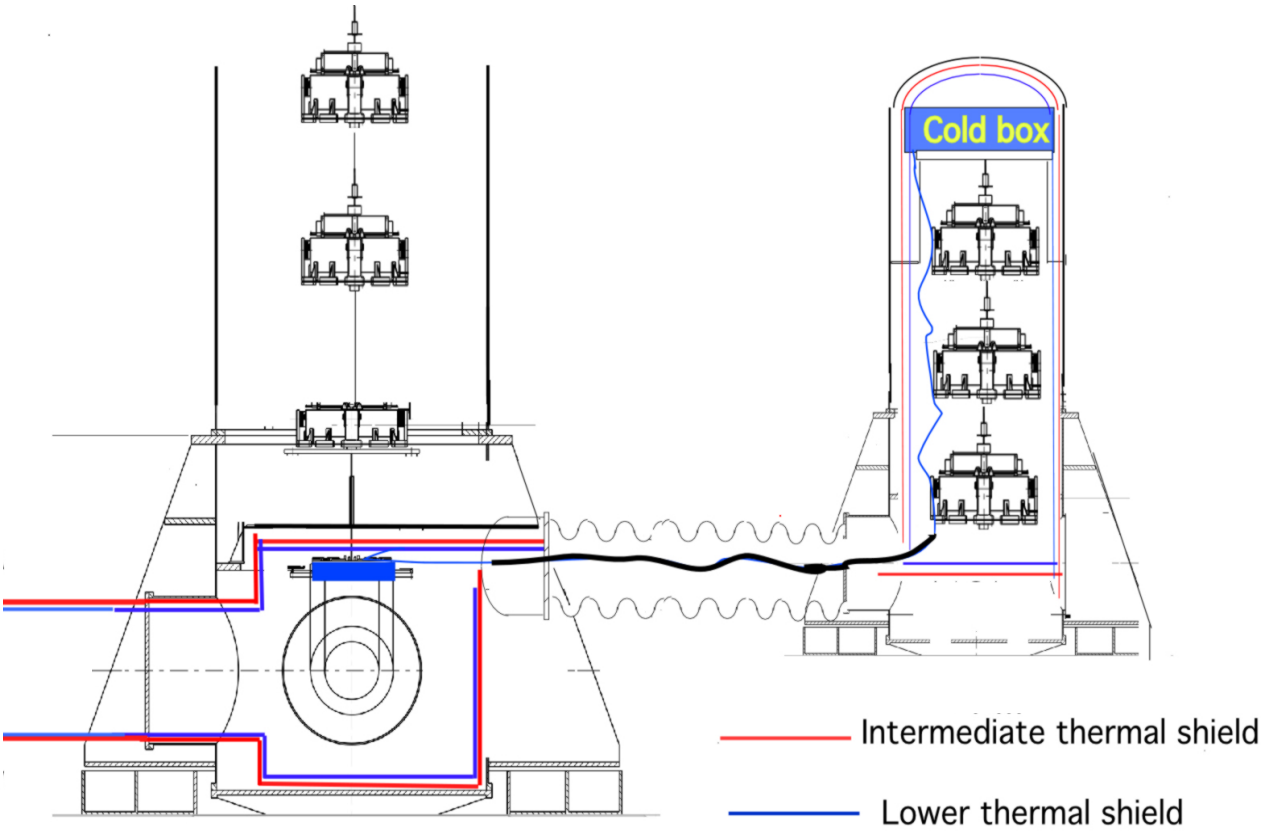

Figure 96: Scheme of the cryostats needed for cooling a test-mass of the LF-interferometer.

possible and optimize the thermal contacts, in order to avoid refrigeration power loss. In figure 96 we report a sketch of the cryo-mechanical system to be adopted for ET-LF.

The whole payload that we will describe in the suspension chapter is hosted in the lower part of the vacuum tower hosting the 17-m long super-attenuator chain. The vacuum tower basement is a cryostat with two thermal screens: the blue line schematizes a surface at $\sim 4\,\mathrm{K}$, while the red one is the shield at intermediate temperature ($\sim 80\,\mathrm{K}$). The upper part and lower part of the tower are separated by a roof crossed by the Ti-6Al-4V thin rod which holds the whole payload[17]. The blue line define a volume that has to be vacuum tight. It will permit to cool and warm up faster the whole payload by adding pure Helium gas in this experimental volume. Few mbars of helium will provide an efficient heat exchange during the cooling phase of the payload from room to cryogenic temperature. Once the equilibrium temperature is achieved, the helium gas is pumped out before the laser light injection. The basement of the main tower hosting the mirror is connected to an ancillary tower shown in the figure. The ancillary tower is hosting the cold box, which will keep the mirror at cryogenic temperature. The box can be either a simple liquid helium container in the case of a cryoplant based on cryofluids or the cold head of a cryo-refrigerator in the case of a cryocooler plant.

A thermal line of 20 m maximum length connects the cold box to the last stage of the mirror suspension. It can be made of a braid of a high purity material as the electrolytic copper or the grade 6 aluminum (99.9999 % purity). Both of them are metals characterized by thermal conductivity value of 2 kW/m/K in the range 1-10 K. In fact a braid of 20 m length, made of 8 wires 1 mm diameter can support an heat flow of 200 mW for a temperature difference of$\sim$ 1K at the link ends.

To damp the vibration associated to the cooling system, the soft braid is mechanically coupled to the auxiliary

[17]The interface between the upper and lower suspension is described in section (4.3.3.

super attenuator chain, hosted in the ancillary tower and fully complaint with the cryogenic environment.

In order to define the requirement of the cryo plant we have to estimate the cryostat thermal inputs, which depend on the cryostat dimension and the quality of the thermal insulation.

Assuming that the inner vacuum chamber has to host a mirror with a half meter diameter, we derived the order of magnitude of the thermal input for the cylindrical cryostats whose dimensions are reported in the following table:

Table 5: Cryostat dimensions

Container	Diameter [m]	Height [m]
Payload vacuum chamber	1.5	3
Auxiliary tower	1	2

The thermal super insulation is a standard technique used in the modern cryostats. The thermal shield is formed by highly heat reflective thin layers, set under vacuum for increasing radiation reflection and decreasing radiation heat transfer through the insulation. The most known implementation is based on layers of porous (self-vented) mylar sheets, which are aluminized on one side. The sheets are wrapped around the surface to be insulated and form a multilayer blanket. The mylar is an hydroscopic material incompatible with the HUV requirements of ET. As a consequence the proposed solution implies to separate the chamber hosting the mirror to the insulation vacuum of the cryostat. A dedicated pumping system (rotary-roots-turbo-molecular group) will provide the vacuum insulation.

Wrapping 25 and 75 layers of self vented aluminized mylar around the two thermal shield, we achieve the condition to limit the thermal input below 1 W for the 4 K shields and around 50 W for the intermediate ones. We assume in this evaluation that the thermal input due to laser light absorbed by the mirror and the thermal radiation emitted by the the km tube is in the range of few tens of milliwatts thanks to low silicon absorption at the laser wavelength and to the helium cryotraps described in 3.9.2.

It is forth-worth to evaluate in more details these data in the context of the ET technical design study.

3.9.2 The LF-interferometer cryotraps

Motivations.

Box 3.4: Thermal radiation

All substances continuously emit electromagnetic radiation by virtue of the molecular and atomic agitation associated with the internal energy of the material. The emitted radiant energy can range from radio waves, which can have wavelengths of tens of meters, to cosmic rays with wavelengths less than 10^{-14} m. In this paragraph we will consider only radiation that is detected as heat. Such radiation is termed *thermal radiation*; it occupies the intermediate frequency range between approximately 10^{-6} m and 10^{-3} m. Radiation from the warm surfaces to the cold surfaces is the dominating mode of heat transfer in vacuum.

The main heat inputs into the cold mirror of the LF interferometer are the thermal radiation coming from the warm surface of the vacuum tube, and the heat load due to the absorption of a small fraction of the laser light into the mirror surface. The latter can be estimated considering that the laser power circulating in the optical cavity is 18 kW, and that a reference value for the absorption coefficient of the mirror optical coating at the working wavelength is around 1 ppm. This gives an approximate value of 20 mW of absorbed laser power.

The radiation from the warm surface of the vacuum tube to the mirror can be estimated by the modified Stefan-Boltzmann equation:

$$\dot{Q}_r/A_1 = \sigma F_e F_{1-2}(T_2^4 - T_1^4) \tag{74}$$

where $\dot{Q}_r/A_1$ is the heat transfer rate by radiation per unit area of the mirror surface, $\sigma = 5.67\,10^{-8}\,\mathrm{W/m^2/K^4}$ is the Stefan-Boltzmann constant, F_e is the emissivity factor, and F_{1-2} is a geometric configuration factor relating the two surfaces, whose temperatures are T_2 (warm) and T_1 (cold). From Eq. 74 the heat flux on the mirror at $T_1 = 10\,\mathrm{K}$, coming from the vacuum tube at $T_2 = 300\,\mathrm{K}$ can be as high as $\dot{Q}_r/A_1 \sim 460\,\mathrm{W/m^2}$. This huge heat flux is not compatible with the cryogenic environment and needs to be reduced by several orders of magnitude.

In order to reduce the thermal radiation from the beam duct into the cold mirror, two strategies are viable, as shown by Eq. 74: the reduction of the emissivity factor and/or the reduction of the geometric configuration factor, i.e. the reduction of the solid angle under which the warm surface is seen by the cold surface.

The emissivity factor can be reduced by an appropriate choice of material for the wall of the tube, or trough the deposition on the warm surface of a low-emissivity coating. The reduction of the geometric configuration factor, on the other hand, can be obtained by building in the region adjacent to the mirror cold sections of the vacuum tube (thermal shields or cryotraps), that "move away" the warm section of the tube from the mirror, and in this way reduce the solid angle under which the warm surface is seen by the cold mirror. The temperature(s) and length(s) of these sections must be chosen in order to minimize the ration heat transfer to the mirror, and, at the same time, the overall cost of the cryogenic plant. Moreover, they will also serve as cryogenic pumps. In particular, in the region immediately adjacent to the mirror, a zone *colder* than the mirror itself is needed to avoid the condensation of the residual gas on the surface of the mirror, that could lead to the growth of a layer of contaminants and spoil its optical characteristics.

Maximum heat load on cryogenic mirror.

The equilibrium temperature of the mirror is reached when the power extracted by the cooling system is equal to the power absorbed by the mirror ($\dot{Q}_{abs} = \dot{Q}_{coolsys}$). The power extracted by the cooling system mostly flows through the four silicon suspension wires (a small fraction is exchanged with the surroundings through thermal radiation) to the penultimate mass (the marionette) and then is removed by the heat sink directly connected to the cooling system. The equilibrium temperature of the mirror T_{mir} can be calculated by a simple analytical model if we assume that the temperature of the penultimate mass is kept fixed at the design value of 5 K:

$$\dot{Q}_{abs} = \frac{4S_w}{L} < k_{Si} > (T_{mir} - T_{mario}) \tag{75}$$

$$< k_{si} > = \frac{1}{\Delta T} \int_{T_{mir}}^{T_{mario}} k_{si}(T)\,dT \tag{76}$$

where S_w is the section of the silicon suspension wire, L is its length and $k_{si}(T)$ is the thermal conductivity of silicon. In the following calculations we shall use the thermal conductivity shown in Fig. 97 [318]. From this figure we see that $< k_{si} > \sim 1.4\,10^3\,\mathrm{W/m/K}$ in the temperature range of interest (5–10 K). We also take the design values for the silicon suspension wires (diameter: 3 mm, length: 2 m). The maximum power that can be extracted from the mirror, keeping its temperature at the design value of 10 K, is approximately 100 mW. Since the laser power absorbed by the mirror is approximately 20 mW, we can conclude that the thermal radiation heat load must not exceed $\sim 80\,\mathrm{mW}$.

The above back-of-the-envelope calculation was checked by a finite element model of the mirror and its suspension system, as shown in Fig. 98 The parameters used in the model are summarized in table 6.

The calculation was done setting on the front surface of the mirror a fixed heat source, representing the power coming from the laser and absorbed by the mirror, of 20 mW, with superimposed a variable heat source, representing the additional heat load due to thermal radiation. For the sake of simplicity the temperature of the penultimate mass was set at the fixed value of 5 K. The thermal conductivity of silicon shown in Fig. 97 was used in the model [318].

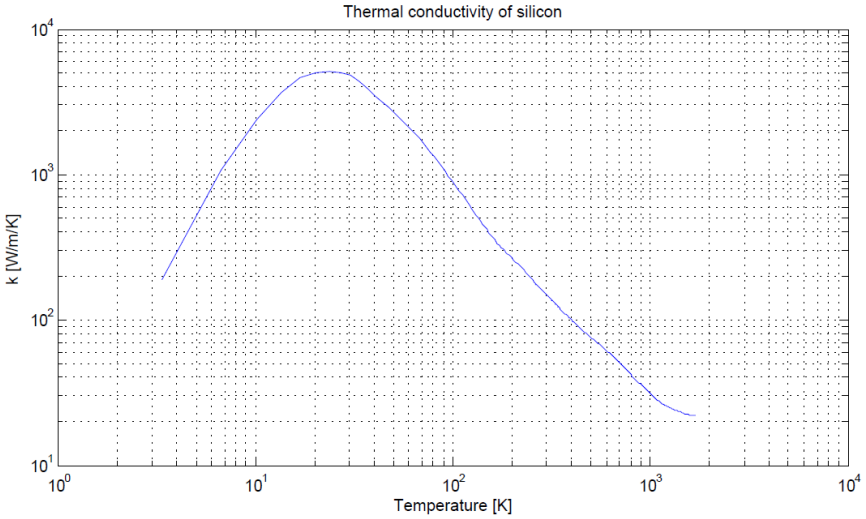

Figure 97: Thermal conductivity of silicon (from [318])

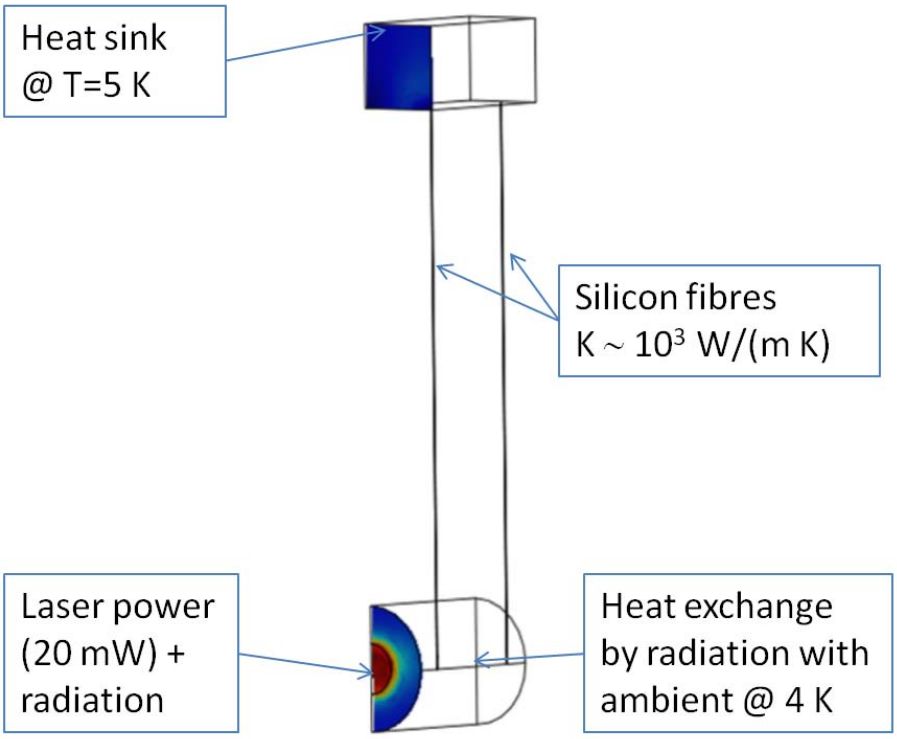

Figure 98: Finite element model and boundary conditions

Table 6: Finite element model parameters

Mirror temperature	10 K
Mirror diameter	45 cm
Mirror mass	211 Kg
Silicon fibers length	2 m
Silicon fibers diameter	3 mm
Marionette temperature	5 K
Power in cavity	18 kW
Absorbed power	20 mW
Beam radius	9 cm

The solution of the problem was calculated sweeping the variable heat source in the 0–0.1 W range, with steps of 10 mW, and looking at the temperature in the central area of the mirror. The results are shown in Fig. 99. They confirm the order-of-magnitude values found in the previous section. The temperature of the central area of the mirror does not exceed 10 K when the thermal radiation is lower than 70 mW, corresponding to 90 mW of total power absorbed by the mirror.

Box 3.5: Maximum thermal radiation power on cold mirror

The maximum power that the mirror can absorb, keeping its temperature at the fixed value of 10 K is approximately 90 mW. Since the power absorbed from the laser is 20 mW, the thermal radiation power must not exceed 70 mW. In order to reduce the thermal radiation from the beam duct into the cold mirror, two strategies are viable: the reduction of the emissivity factor and/or the reduction of the geometric configuration factor, i.e. the reduction of the solid angle under which the warm surface is seen by the cold surface. The reduction of the geometric configuration factor can be obtained by building in the region adjacent to the mirror cold sections of the vacuum tube, that "move away" the warm section of the tube from the mirror, and in this way reduce the solid angle under which the warm surface is seen by the cold mirror.

In the following paragraph we shall find out how to design the thermal shields in the region adjacent to the mirror to keep the thermal radiation from the warm surface of the vacuum tube at a value not greater than few tens of milliwatts.

Thermal radiation from vacuum tubes - Direct exchange.

Radiative transfer of heat from one area to another depends, among other things, upon the fraction of the radiant energy emitted by one area which is intercepted by a second area. This fraction is identified by several names, such as the configuration factor, the interchange factor, the angle factor, or the geometric view factor, and is a function of the geometrical relation of the areas involved. The configuration factor is defined as the fraction of diffusely radiated energy leaving surface A that is incident on surface B, and it is represented by the F_{1-2} factor that appears in Eq. 74.

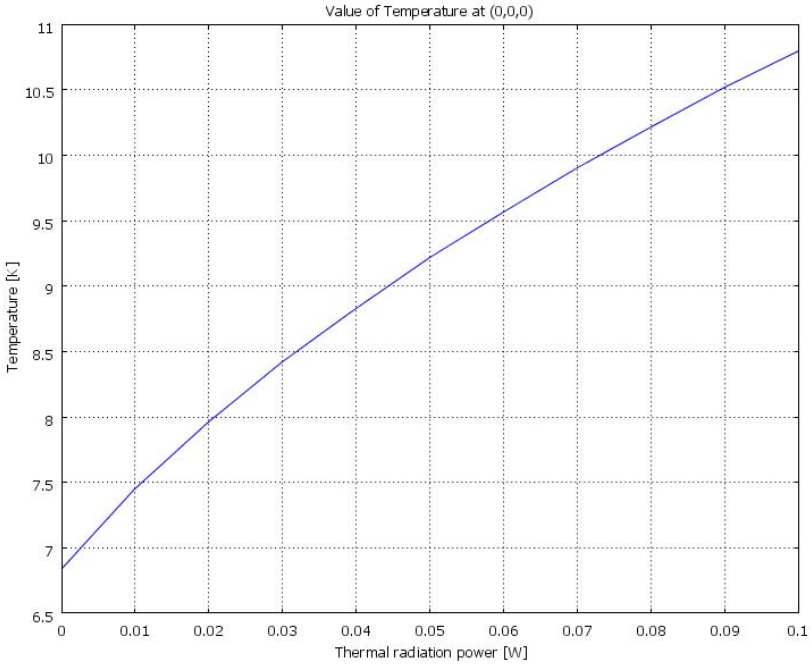

Figure 99: Temperature at the center of the mirror vs. thermal radiation power

We have to explicitly calculate the configuration factor for the geometry schematically shown in Fig. 100

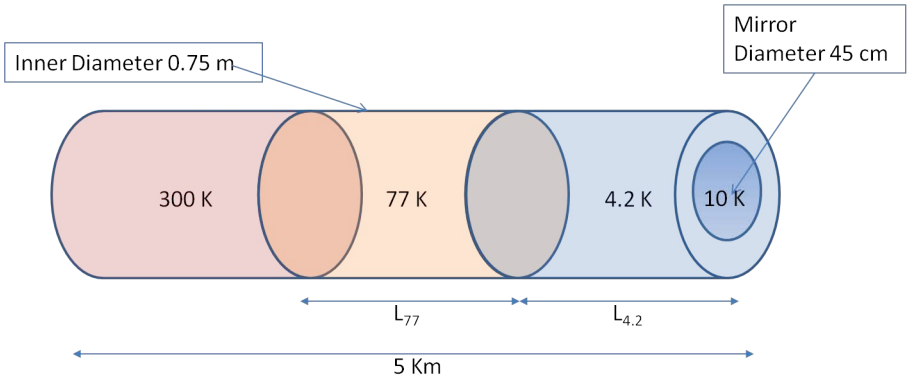

Figure 100: Conceptual scheme of the vacuum tube with cryotraps

The details of the calculation are presented in Appendix B.3. Making use of Eq. 74 we can calculate the thermal radiation power on the mirror as a function of the lengths of the two cold sections, at 4.2 K and 77 K. The result is shown in Fig. 101

Box 3.6: Lenghts of the cryotraps

We see that to keep the thermal radiation power in the range $\sim 10\,\mathrm{mW}$, we need a 4.2 K section of few meters and a 77 K section of few tens of meters. For example, with $L_{4.2} = 10\,\mathrm{m}$ and $L_{77} = 50\,\mathrm{m}$, we are in a situation were the *direct* transfer of thermal energy from the warm tube to the mirror is approximately 3 mW, well below the maximum allowed value.

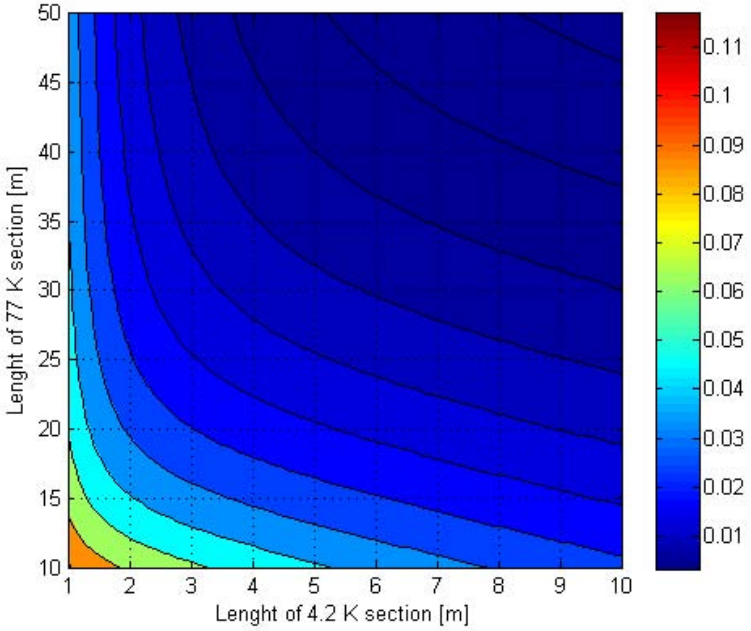

Figure 101: Thermal radiation on the mirror vs. lengths of 4.2 K and 77 K sections.

Thermal radiation from vacuum tubes - specular and diffuse reflection.

Box 3.7: Specularly and diffusely reflecting surfaces

The calculation of the thermal energy *directly* transferred from the warm surface to the cold mirror is not sufficient. For the correct evaluation of the thermal radiation on the cold mirror reflections along the cryo-shields including the reflective properties of the surfaces must be taken into account. These are rather difficult to specify as the reflected energy depends not only on the angle at which the incident energy impinges on the surface but also on the direction being considered for the reflected energy. Two important, and relatively simple, limiting cases can be used for calculating heat exchange: *diffuse* surfaces and *specular* surfaces. In specular reflection, also called mirror like reflection, the propagation direction of the radiation is not significantly changed, whereas in the case of diffuse reflection the reflected radiation is reflected into all directions. An ideally diffusely reflecting surface will have will equal luminance for all directions.

For a diffuse surface the incident energy from the direction (θ, ϕ) that is reflected produces a reflected intensity that is uniform over all (θ_r, ϕ_r) directions. When a diffuse surface element irradiated by an incident beam is viewed, the element appears equally bright from all viewing directions. In the previous paragraphs, all the surfaces involved in the calculation of the configuration factors—in particular the inner surface of the vacuum tube—were assumed to be diffuse emitters.

Mirror-like, or specular, surfaces obey well-known laws of reflection. For an incident beam from a single direction, in a specular reflector, the reflected beam is at the same angle away from the surface normal as the incident beam, and is in the same plane as that formed by the incident beam and surface normal. When reflection is diffuse, the directional history of the incident radiation is lost upon reflection. With specular reflection the directional history of the incident radiation is not lost upon reflection. Consequently, when dealing with specular

surfaces, it is necessary to account for the specific directional paths that the reflected radiation follows between surfaces.

An important parameter for deciding whether a surface falls in the diffuse or specular limit is the surface roughness, or more precisely the ratio of the root-mean-square roughness to the wavelength of the radiation. For long-wavelength radiation a smooth surface tends toward being optically smooth, and the reflections tend to become more specular. Thus, although a surface may not appear mirror-like to the eye (i.e. for the short wavelengths of the visible spectrum), it may be specular for longer wavelengths in the infrared.

The contribution to the thermal radiation heat transfer coming from *diffuse* reflectivity was calculated for the geometry given in Fig. 100 by a finite-element model (for the details see Appendix B.4). The geometric dimensions of the system were the same as in table 6, with the lengths of the cold sections $L_{77} = 50\,\mathrm{m}$ and $L_{4.2} = 10\,\mathrm{m}$. The results are shown in Fig. 102:

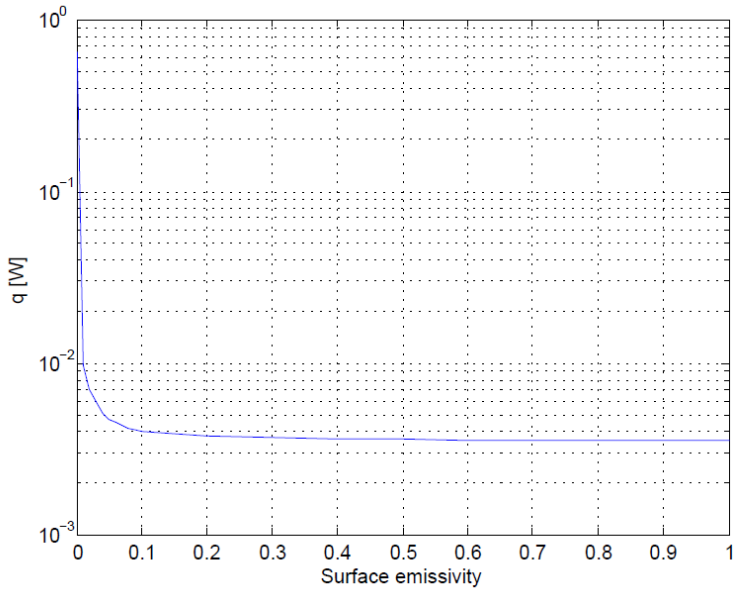

Figure 102: Thermal radiation heat transfer in the diffuse reflection limit

The case when the pipe walls are specularly reflecting was discussed in [319, 320]. A large heat load caused by thermal radiation through a metal shield pipe was observed in a cooling test of a cryostat for a prototype of the cryogenic interferometric gravitational wave detector (CLIO) in Japan. The heat load was approximately three orders of magnitude larger than the value calculated by the Stefan-Boltzmann law. The phenomenon was studied both by simulation and by experiment and it was found that found that it was caused by the conduction of thermal radiation in a metal shield pipe due to multiple specular reflections in the pipe.

A simple model for the evaluation is illustrated in Fig. 103 [321].

In the case we are considering the aspect ratio of the pipe is sufficiently large to make the number of reflections

$$N \sim \frac{L}{d} \tan\theta \tag{77}$$

a number large compared to unity. At each reflection the radiation intensity is reduced by an amount $\rho(\theta) = 1-\epsilon$ the specular reflection coefficient of the wall. The total reduction in intensity due to reflections at a given angle of incidence in the tube is determined by ρ^N.

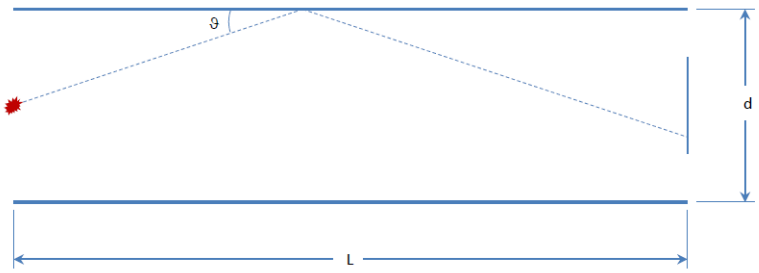

Figure 103: Thermal radiation "light-pipe" geometry for an on-axis source

The efficiency of transfer of radiation, η emitted by an on-axis point source is then

$$\eta = \int_0^{\frac{\pi}{2}} \rho^N \sin\theta \, d\theta \tag{78}$$

The plot of the radiation heat transferred to the mirror by specular radiation is shown in Fig. 104.

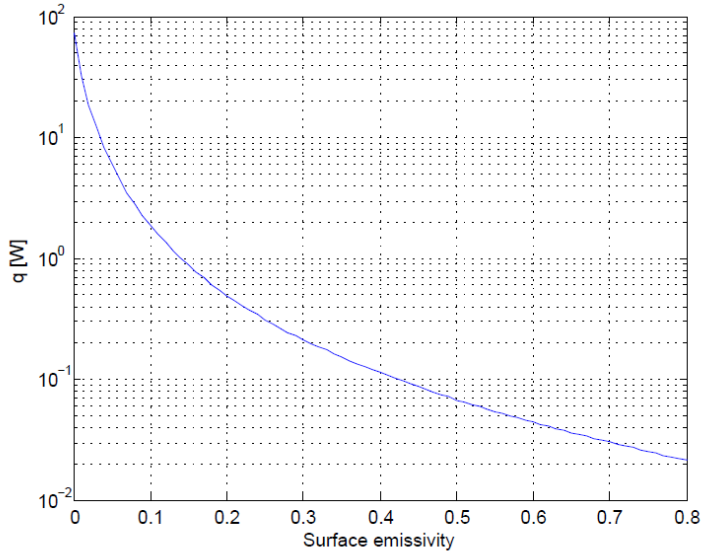

Figure 104: Thermal radiation heat transfer in the specular reflection limit

Box 3.8: Heat transfer from diffusely and specularly reflecting surfaces

We see that for $\epsilon \geq 0.1$ the heat transferred to the mirror is essentially the direct contribution from the warm tube. Only for small values of $\epsilon < 0.1$ (high reflectivity $\delta > 0.9$) the contribution to the heat transfer from the surface reflectivity increases dramatically. On the other hand, we see that for specularly reflecting surfaces a huge amount of heat reaches the mirror for almost all the values of the emissivity. Specular reflections inside the vacuum pipe must be strongly suppressed.

Mitigation strategies.

- The *direct* radiation heat from the tube at 300 K to the cold mirror is strongly suppressed with cold sections (cryogenic shields, or cryotraps) near the mirror. With a section 10 m long, cooled at liquid helium temperature, and a section 50 m long, cooled at liquid nitrogen temperature, the direct heat transfer can be reduced in the milliwatt range.
- For the given cold pipe aspect ratio $L/d \sim 80$, the contribution of *diffuse* reflectivity of the surface of the cold sections becomes important only for reflectivity $\delta > 0.9$ ($\epsilon < 0.1$).
- Specular reflection in the cryogenic shields can increase the radiation heat transfer by two or three orders of magnitude. The effect can be controlled by placing absorbing baffles on the radiation paths inside the cold pipe; by coating the inner surface of the cold pipe with an high emissivity layer ($\epsilon > 0.9$); increasing the surface roughness of the cold pipe to suppress the mirror-like reflections

Box 3.9: The Pulse Tube cryocooler

The Pulse Tube cryocooler (PT) is based on the displacement and the expansion of a gas, usually helium (He^4). A piston compressor and a rotary valve are used to create the pressure oscillations (the typical average pressure in a PT is 25 bar, and the oscillation amplitude is ranging between 2 and 7 bar). Let us refer to the figure 105 for explaining the thermal process.

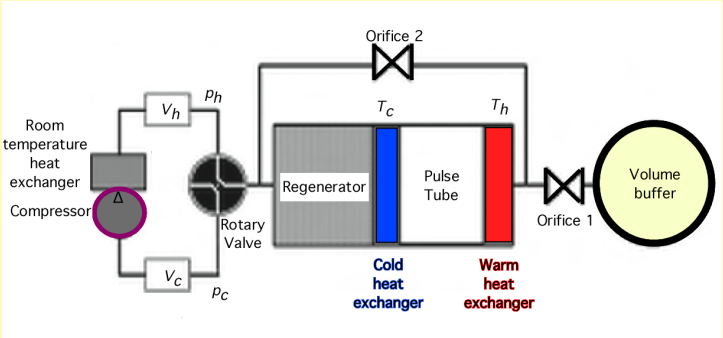

Figure 105: Scheme of a Pulse Tube cryocooler.

We note that a crucial element of the cryocooler is the PT regenerator, a heat exchanger acting as *cold storage* systems for the pulsed flow process. In practice, the regenerator stores the energy from one stream and later transfer the energy to a second stream, for example between the out-of-phase pulses of gas.
The orifice 1 is connecting the warm end to a buffer volume, ten times larger than the volume of the pulse tube so that its pressure is almost constant and close to the average pressure in the pulse tube. The combination of the orifice and the buffer provides a phase difference between the flow of the gas in the tube and the pressure oscillation; such phase difference is necessary for optimizing the PT performance [322]. The function of the second orifice is to reduce losses allowing some gas to bypass the regenerator [323] .

- When the pressure rises, the gas element moves through the regenerator in the direction of the cold heat exchanger. At the regenerator output the temperature of the gas element is T_c and enters the tube. There, the gas element is compressed adiabatically, while it moves towards the orifice and Its temperature rises together with the pressure.
- Now, the orifice 1 is open and the gas at pressure p_h flows from the tube to the buffer since the buffer pressure is lower than that of the tube.
- The orifice 1 is closed and the rotary valve is set to connect the system to the low-pressure side of the compressor (p_c). The gas moves back to the cold heat exchanger and the expansion takes place. At the end of the expansion step, the pressure of the gas element is equal to p_c and theits temperature is below T_c.
- The expansion stops, and the orifice is open again. The gas continues to flow in the direction of cold heat exchanger and when it is crossing it , the gas warms up to the temperature T_c. The amount of heat, which the gas takes away from the heat exchanger, is the cooling power.

To obtain temperatures below 20 K, the system is operated at low frequency (~ 1 Hz). The frequency defines the diffusion depth δ in the working gas and the regenerator material:

$$d = \sqrt{\frac{k}{\pi \nu C}}$$

where k is the heat conductivity, ν is the frequency and C is the volumetric heat capacity of the regenerator material. Thus, it follows that when the frequency is increased, the diffusion depth decreases, and the heat storage in the regenerator degrades. Moreover, a high operating frequency leans to a large pressure drop in the regenerator, i.e. a poor performance of a system.

3.9.3 The cryogenic infrastructure based on pulse tube cryo-coolers

A simple approach to cool down the mirrors is based on the use of cryocoolers [324]. In particular, Gifford-McMahon (GM) refrigerators have been developed since a long time and are widely used in various fields of science and industries because of their convenient handling. However, their cooling power is provided by the motion of a displacer which causes large vibrations at the cold head, an aspect which makes them not suitable for all applications where a low acoustic noise level is necessary.

In more recent times, the pulse tube (PT) cryocoolers have been developed. The particular thermal cycle of PT refrigerators gives them a two or three times higher efficiency than GM cryocoolers for loads temperatures between 55 and 120 K, and requires no moving elements at low temperature. This latter characteristic is quite important: because of it, we expect PT refrigerators to be intrinsically more reliable and less noisy than classic GM coolers [325]. Thus, a pulse tube cryocooler seems to be an interesting option for our purposes. However, because of the gas pulse flowing in its cold head, also this kind of refrigerator injects mechanical noise in the cooled sample, at a level which is still far too high for the elements of a gravitational antenna. Indeed, in order to detect gravitational waves, current detectors have reached displacement sensitivities of the order of $10^{-18} m/\sqrt{(Hz)}$ and an increase by at least two orders of magnitude is foreseen for ET, where we have to implement the use of low temperatures.

The starting point of the system design is the choice of the pulse tube refrigerator model. We compared two different models of cryo-coolers, the Cryomech PT 407 and the Sumitomo SRP-052A. For both systems, we measured the acceleration of the 4 K cold head.

Our data show that the vibration noise level generated by the Sumitomo is lower by a factor $\sim$ 10 than that by the Cryomech. Moreover, our model of Sumitomo has the additional advantage of having the room temperature throttle valve separated from the main body of the refrigerator, with the possibility to keep it far from the cryostat obtaining a further attenuation of the noise produced by this element. However, the first harmonic generated by the pulse tube is around 1 Hz and it is not attenuated efficiently by the super attenuator chain. In order to overcome this difficulty, the plan is to apply the technologies developed for gravitational interferometers and to reduce the vibrations of the cold finger of a PT cryocooler by an active control system. In the past we designed a vibration free cryostat [326] for limiting the cryocooler vibration, according to the issues discussed above. The cryostat scheme is sketched in figure 107. It is based on the idea to attenuate the cryocooler vibrations by directly acting on it. The cold head vibration is monitored by an optic bundle fibre, a displacement sensor acting as low temperature, while the actuation is based on three piezoelectric stacks set at room temperature outside the cryostat vacuum. The cryocooler cold head is clamped to a platform placed on dampers and it is connected to the cryostat by a soft bellow designed to mechanically decouple it from the cryostat. The feedback correction signal is sent to the three piezo-actuators which are loaded by the platform and can push the cold head platform elastically coupled to cryostat mechanical structure.

At present the attenuation achieved controlling just the vertical degree of freedom is of the order of $3 \cdot 10^{-3}$. A further improvement is expected by controlling the horizontal degrees of freedom and by reducing the recoil effect on the structure holding the monitor sensor of the 4 K stage. However this active attenuation system is not sufficient and in parallel to this R&D effort industrial studies are under way [327] . In particular we cite the new cryo-cooler of the AttoCube System [328] providing a refrigeration power higher than 1.5 W at 4.2 K and very low mechanical vibrations ($<$ 4.2 nm peak-to-peak vibration amplitude) measured on a cold platform decoupled to the pulse-tube cold head. Moreover new proposals have been presented [329] to reduce the the cryo-cooler vibration. We discuss some new ideas in the R&D section 3.9.7.

The cryo-plants based on PT cryo-coolers implies to install for each tower hosting a test mass a doublet of one stage and two stage PT cryocoolers. A similar solution is used to cool the ancillary tower. It will permit to speed up the cooling process providing a redundancy during the data taking phase. Each PT cold head is driven by a helium compressor via a couple of high pressure flexible line of a maximum length of 30 m. A larger number of cryocoolers ($\sim$ 10) are needed for the helium cryotraps (see 3.9.2). Each compressor operates at a pressure $\sim$ 22 bar, it requires 5 l/min of refrigerated water and it absorbs an electrical power drawn at 50 Hz between 5–8 kW depending on the model. Although they are classified as silent models the typical acoustic

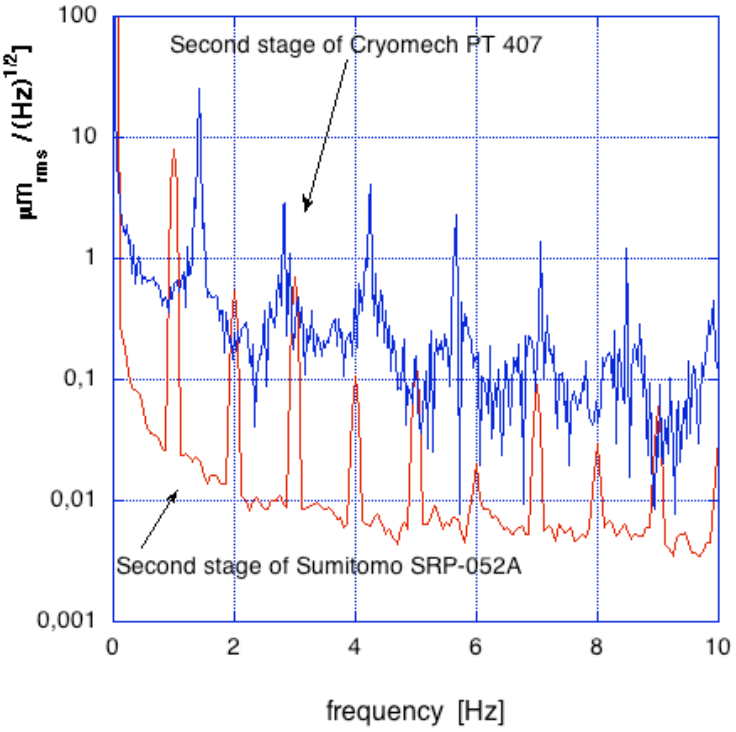

Figure 106: The displacement noise spectrum of the second stage cold point of the CRYOMECH PT407 and of the Sumitomo SRP-052A as function of the frequency.

noise level at 1 m distance is ~ 53 dB(A). To reduce the noise trouble, due to the presence of compressors, an underground hall must be created as a separated part of the main cavern hosting the super attenuator towers. The wall of this hall has to be treated by a sound insulation system, to avoid noise transmission between the compressor hall and the test mass area (see fig. 108). Seen the number of compressors for each tower and the requested amount of water flow and electric power great emphasis must be put on the safety issues concerning this auxiliary hall of $\sim 100\,\mathrm{m}^2$ surface. We have to notice also that the gas pulse vibration is transmitted also along the high pressure helium flexible lines. Thus, the line require a specialized design and construction: it will include an acoustic sheath covering the flexible tube and massive concrete slabs to anchor several sectors of the gas lines.

Although this solution has been adopted in LCGT, we stress that the vibration issue is one of the most limiting factors of a low temperature GW experiment and it requires a R&D activity to be carried on in collaboration with the specialized industries. We conclude noting that recently a new model of cryo-cooler has been developed by the AttoCube System [328] providing a refrigeration power higher than 1.5 W at 4.2 K and very low mechanical vibrations ($<$ 4.2 nm peak-to-peak vibration amplitude) measured on a cold platform decoupled to the pulse-tube cold head.

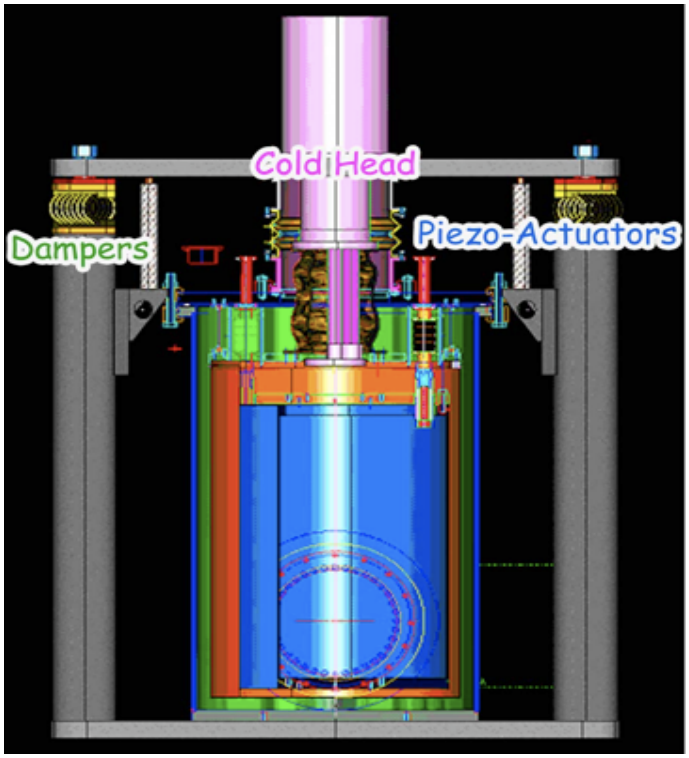

Figure 107: A simplified scheme of the vibration free cryostat.

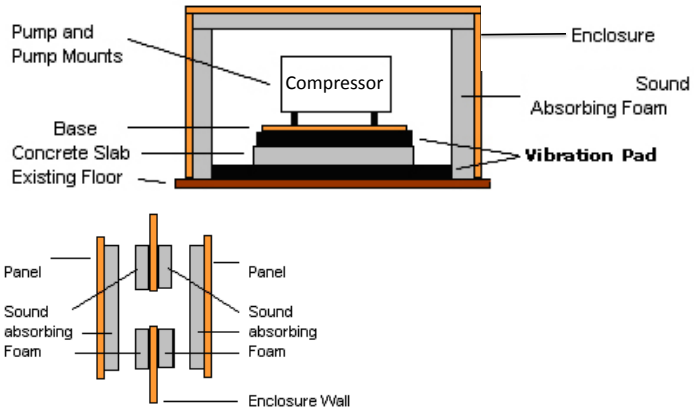

Figure 108: The standard mounting of a compressor to damp the vibrations.

Box 3.10: Summary of pro and contra of the cryocooler approach

In favor
Higher duty cycle
Limited manpower
Against
High level of vibration
High electric power consumption in the underground environment
Infrastructure requirements
Distribution of high pressure lines
Compressors hosted in auxiliary caverns
Efficient water refrigeration system

3.9.4 The cryogenic fluid approach

Cryogenic fluids in the form of liquid helium and liquid nitrogen are required to circulate for cooling the cryostats of the test masses and the associated cryotraps. The heat load requirement at a particular temperature is a prime important factor to select a helium refrigerator/liquefier and to define the dimensions of the nitrogen plant. The cryogenic systems of ET should operate in different modes cool down, steady state and warm up for each test mass tower, The cooling time is a trade off between the need to limit the detector down time and the stress due to the thermal gradients During cool down the recommended flow rate of helium gas will be approximately ~ 1 g/s. The heat load requirement of cryogenic systems including the transfer loss at steady state is approximately ~ 20 W at 4 K helium refrigerator/liquefier. A helium refrigerator/liquefier having refrigeration capacity of 160 W at 4 K in refrigerator mode and 50 L/h in liquefier mode without LN2 pre-cooling and 200 W at 4.5 K in refrigerator mode and 100 L/h in liquefier mode with LN2 pre-cooling, is sufficient to guaranty the cooling in the vertex area of the triangular interferometer. In this evaluation a redundancy factor has been included so that the system will satisfactorily cater the refrigeration load at different state.

As we anticipated before, to reach a full flexibility of the system, the possibility of performing the cool-down and the regeneration with the main refrigerator has been foreseen too. The cryogenic system will include a distribution valve box and the cryogenic piping up to the interface of the ET cryostat. The distribution valve box contains a 1000 L liquid helium control dewar, a heat exchanger, an electrical heater, a Joule-Thompson cryogenic valve and relevant instrumentation for pressure, temperature and flow rate measurements. The cryogenic system has to deliver, in a controlled way, the cooling helium from the refrigerators to the client. It includes mainly a 80 K gas helium circuit and a 4.5 K helium circuit, that can be interconnected through bypass valves; both shut-off valves and control valves are used. The 1000 L liquid helium dewar is used as buffer to stabilize the thermal loads and as re-cooler of the helium coming from the main refrigerator. An electrical heater and a cooling system are planned to make the system appropriate to operate an high temperature regeneration (470 K) and to cool it down again to room temperature.

The redundancy of several elements is added to improve the reliability and the effectiveness of the cryoplant during the experimental conditions and to make it more flexible.

The European industries have demonstrated there ability to construct complete refrigeration systems both for the needs of the huge accelerator and the associated detectors. Thus, the main refrigerators for ET will be realized with proven industrial technologies and tailored on the GW detector needs. It will be based on Claude cycle and it will provide the coolant helium at the required temperature for cooling the mirror. For the liquid helium distribution, we recall here that long and low thermal loss lines were developed at CERN already in

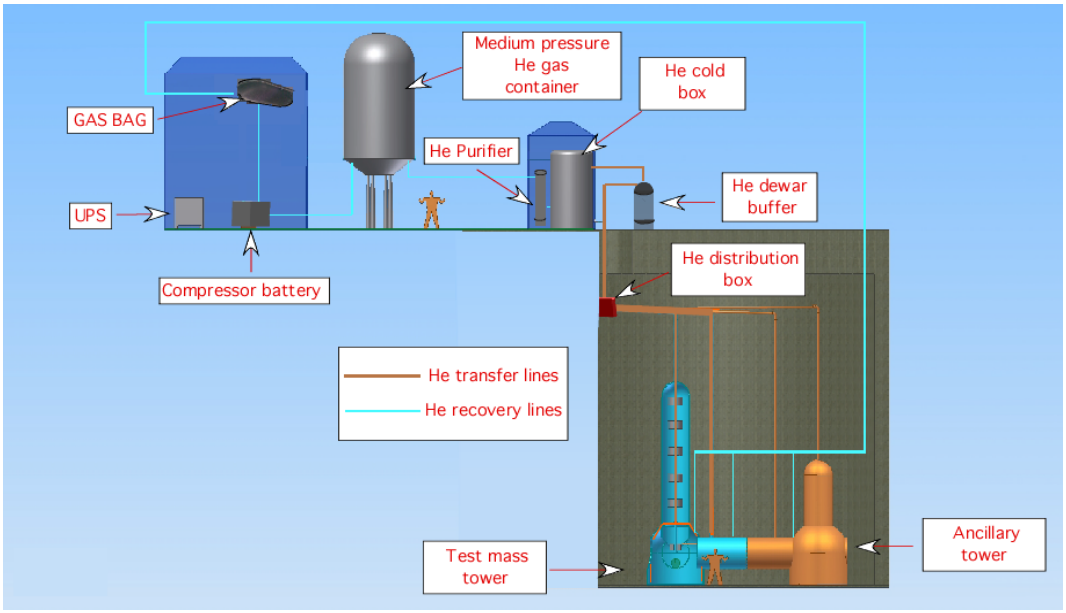

Figure 109: A simplified scheme of the cryogenic plant based on the use of cryofluids.

the context of the LEP project. Since this time several improvements in design with respect to earlier lines of similar construction, made it possible to achieve reproducibly linear heat in-leaks of $\sim 30\,\mathrm{mW/m}$. At present the LHC refrigeration system is connected to the 27 km long accelerator thanks to high performances helium transfer lines, which exhibit a variety of types, sizes, design choices and layouts.

In the ET case the refrigerator will be installed on the surface building and the liquid helium has to be sent by long transfer lines to the underground detector, like the case of the LHC cryoplant. The transfer lines are based on the four-fold coaxial corrugated tube design Each line is made of austenitic stainless steel and the coaxial assembly provides an inner channel for the supply of liquid or gaseous helium an annular channel acting as a shield for the return of cold vapor, and a common vacuum enclosure for thermal insulation. Low thermal conductivity spacers, made of teflon PTFE are set between the outer tube, return channel and supply pipe. The outer corrugated tube of the return channel is also super-insulated by several layer of aluminized mylar (see figure 110).

In order to reduce the quantity of impurities in the helium and to recover the gas, a Purification and Recovery System is implemented in the cryogenic plant. It is composed by a helium vaporizer, a high pressure recovery compressor and a helium cryogenic purifier system. An atmospheric gas bag (100 m^3), high pressure containers (20 bottles at 20 MPa, 10 N m^3 each) for impure gas helium, 3 medium pressure tanks (30 m^3 at 2 MPa) for pure gas helium, a liquid nitrogen container (50,000 L) and dedicated transfer stainless steel pipe lines are provided for the fluids storage. The helium to be recovered is collected in the gas bag; if its temperature is too low to enter in the gas bag, the cold helium is sent to a vaporizer where it is heated to the ambient temperature before entering the helium gas bag. The helium coming from the gas bag is sent to the recovery compressor and stored in the high pressure (20 MPa) bottles from which is delivered to the impure gas storage. The impure gas helium flows to the purifier and then it is stored in medium pressure (up to 2 MPa) pure helium buffers connected to the cycle compressors.

The cryoplant will be installed in a building close to the main experiment building on surface. To reduce the noise trouble, due to the presence of compressors, a cryogenics compressor hall will be created as a separated part of the technical supplies building. The wall of this hall will be treated by a sound insulation system, to avoid noise transmission between the compressor hall and the other building.

Figure 110: A cross section of a flexible transfer line developed at CERN in collaboration with Kabel Metalelectro [330]

3.9.5 Cryogenic plant control

The cryoplant design and the technical solutions to be adopted are focused on the optimization of the system performances and it will be conceived to implement all the required operative scenarios in a fully automatic mode.

The facility control system, based on a master/slave architecture, will be split into three plants (each for interferometer vertex) and three distinct supervisory systems will be provided with engineer and operator workstations. The three control systems will be independent, but inter communication signals will be exchanged among the station units. The internal structure of the cryogenic control system will be based on PLCs (Programmable Logic Controllers), equipment of proven reliability in the industrial environment. A PLC will act as master of the local unit PLCs, with the purpose to coordinate the cryoplant activities and interface the logic unit with the upper subsystem level. Feedback control will be necessary to control for example the speed of the turbines or other parameters like temperature and pressure of the helium in different part of the cryogenic system; since the time constraints are not strict (response times of the order of seconds), the control routines will be executed without problems by PID (Proportional-Integral-Derivative) controllers inside the PLCs. A commercial off-the-shelf Supervisory Control and Data Acquisition system will be employed to monitor the plants, for operator intervention, commissioning, test purposes and data storage.

3.9.6 A future development: lowering the temperature with Helium II

In order to increase the cooling efficiency and to get a further reduction of the thermal noise contribution, in the ET future we can plan to cool down to the λ point the thermal bath used for cooling the mirror. In principle the use of the liquid helium II (He II) has great advantages: it limits the vibration noise associated to the other cryogenic fluids [331] and it provides a powerful way for extracting the heat from the mirrors. Modern large engineering projects for high-energy physics require thermostatic control of working components at the level of 1.8 - 2 K and are constructed with lengths of channels containing He II. The uniqueness of He II is that it contains a superfluid component with zero entropy, which moves through other liquids and solids with zero friction to an extent dependent on the temperature of the liquid. He II is a liquid of extremely low viscosity and very high heat capacity, which prevents small transient temperature fluctuations. Moreover, thanks to its very high thermal conductivity is able to conduct away heat a thousand times better than any metallic conductor like copper.

In He II, the heat from a hot surface is carried away by the superfluid component, so in any design with complicated geometry and helium flows, the entire heat load acts on the phase interface. The boiling mechanism involves evaporation from surfaces ad in a flow of ordinary boiling liquid, the heat influx is uniformly distributed in unit volume of the two-phase mixture. In stratified He II, the heat influx is associated with the interface between the phases, so the He II evaporation rate is increased by a substantial factor. A major feature of boiling in He II is that the evaporation of the superfluid component predominates. The heat load is transported by convection in the superfluid component, and this consequently evaporates more rapidly than does the normal component.

When a two-phase flow of He II moves in a heated channel, a droplet structure or mist is formed in the vapor space as the amount of liquid in the stratified flow decreases. In a stratified flow of an ordinary liquid in a large-diameter tube, an increase in the bulk vapor content leads to the vapor becoming superheated and the liquid evaporating completely. In He II one prevents the vapor becoming superheated by encouraging the spontaneous formation of a droplet structure with a large heat-transfer surface, which provides a constant temperature over the channel cross section.

An efficient and quiet configuration for cooling the mirror by He II is the *bain de Claudet*. Here the idea is to provide superfluid helium at atmospheric pressure and to insure continuous refilling from the container of the helium in the normal state. In this way the He II bath is kept in a quiet hydrodynamic status well far from the boiling point . In this case the cold box on top of the super attenuator of the ancillary tower is an heat exchanger filled by superfluid helium at atmospheric pressure and operating in the stationary condition of zero mass flow, which implies $\rho_s v_s = -\rho_n v_n$ in absence of the vapor phase, where ρ and v are the density and the velocity of the normal (n) and superfluid (s) components[332].

The He II mirror cooling approach requires also a deeper analysis of the impact of the acoustic losses of the fluid to the dynamic behavior of the suspended test masses. This effect should depend on the hydrodynamic regime of the helium II. In particular we need to consider the interaction mechanism between the two liquids (normal and superfluid), which determines the heat transport. In the case of a superfluid helium vortex formation this is described by the Gorter-Mellink force per unit length, which results a function of the velocity difference $|\vec{v}_n - \vec{v}_s|$. For a one dimensional helium flow f can be written as

$$f = \frac{\rho_n \rho_s}{(\rho_+ \rho_s)^2} \eta_n |\vec{v}_n - \vec{v}_s| \tag{79}$$

where η_n the viscosity of the normal fluid.

Moreover the design of the heat exchanger providing a sufficient refrigeration power is not straightforward. In fact the velocity difference of the two fluids depends strongly on the geometry of the heat exchanger, the nature of the material in contact with the fluid and the status of the contact surfaces. In conclusion in order to assess the validity of the cooling approach for the cryogenic design of the ET detector, we need to develop a complete hydrodynamic model including vapor phase and extra interaction terms as well as a deep R& D activity and prototyping.

3.9.7 R&D in Cryo-coolers

As we pointed out in the previous section the focus of the R&D activity for cryo-cooler will be on the reduction of the vibration generated by the pulse tube. The pulsed force due to the gas deforms the tube of the cold head displacing the cold plate of several microns. These effect has been simulated via finite element software showing that in function of the the cold geometry the longitudinal expansion of the tube can be of the same order the horizontal displacement. Thus, there is a large margin of improvement on the active attenuation damping of the harmonics associated to the gas pulse.

Moreover it has been proposed to modify the mechanical design of the cold head to reduce the displacement vibration. Several attempt have been done already by several groups in the world, using different tube material, adding glass fibre support or using coaxial geometry [333].

An interesting idea has been proposed by Suzuki to utilize the vibration as counter force to compensate the pulse tube expansion with the constraint to adopt a compact configuration. In practice adding to the same cold head a couple of tubes pressurized by a gas wave with opposite phase to the other couples we can obtained a cancellation effect. In figure 111 we show a first test carried on at KeK they tied improved the cancellation by adding more than one couple of tubes with suitable phase difference.

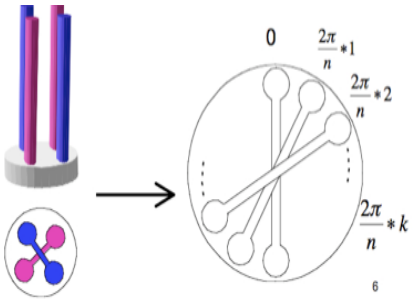

Figure 111: The pulse tube scheme proposed and tested by T. Suzuki at Kek [329]

As we discussed in the previous section 3.9.6, there are significant advantages to lower the temperature below the λ point and we can succeed to lower the temperature by modifying the cryoplant based on cryogenic liquids. However, the same temperature can be achieved using cryo-coolers. The standard two-stage PT operate with ^{4}He as working fluid. Consequently the minimum no-load temperature of these PTs was above 2 K, because the thermodynamic properties of ^{4}He near the superfluid phase transition prevent cooling to lower temperatures. A regenerative cryocooler can cool below 2 K when ^{3}He is used as working fluid instead of ^{4}He. This approach was pursued and a minimum stationary temperature of 1.27 K was achieved and at 4.2 K the cooling power was found to be larger than with ^{4}He [334]. This result has to be regarded as the starting point of a possible evolution of the ET cryo-cooler plants, which requires higher refrigeration power and less vibration. To succeed in getting a significant improvement without spoiling the refrigerator performance a strong interaction with the PT experts and specialized cryogenic industry has to e set up.

3.10 Cost estimate for the Intrastructure Reference Design

Preliminary cost analyses have been performed in order to optimize the cost-to-performance ratio for the Infrastructure Reference Design for Einstein Telescope. Various component costs were estimated, options compared and significant cost-driven changes were implemented will maintaining the scientific performance goals. The estimates were based in some cases on European-wide tenders and by using the lowest reasonable price for the dedicated specifications. In addition, estimates were made of the explicit work force needed to support the respective activity.

The total estimated value for the Infrastructure Reference Design is 775 MEuro (in 2011 €). The cost is determined for a single xylophone detector mode. This configuration constitutes the phase I instrumentation of the project. Phase II will be realized later and features a triple xylophone interferometer configuration.

The site specific costs are related to the direct costs for providing the infrastructure to site the observatory and are estimated at 592 MEuro (2011 value level). These costs include the underground civil facilities, services (electricity and water distribution), buildings and surface construction. The actual site-specific costs will depend on the location where the observatory is constructed, and the facilities that already exist at that location. For the estimates we have used 260 €/m^3 for the excavation costs. This includes digging cost, soil transportation and deposit, and finishing the floor and cavern walls with concrete. In addition, construction machines, running cost, maintenance, preparation and management costs are included. Several underground sites in Europe have been identified that comply with such costs, although a significant bandwidth applies. The number is also compliant with the site costs for LCGT in Japan.

The infrastructure costs include the direct costs for the safety and security systems, cooling and ventilation systems, the vacuum system and the cryogenic infrastructure. These costs are based on both the experience at GEO, Virgo and worldwide tenders. In order to realize the vacuum system at the estimated cost, it will be needed to set-up three vessel construction facilities at the observatory site.

3.11 Technologies to be developed

3.11.1 Introduction

The optimal site for a European third generation gravitational wave observatory should ideally provide the following characteristics [300]:

- The level of seismic and gravity gradient noise should be compatible with the anticipated sensitivity requirements for Einstein Telescope.
- The local geology should be able to support the required infrastructure and potentially allowing the application of gravity gradient subtraction techniques.
- An active involvement of a team of local scientists as well as the funding body of the corresponding country.

Research and development is needed to achieve the sensitivity foreseen for the third generation of underground and cryogenic interferometric detectors. The fundamental noise sources that limit the design sensitivity at very low frequency (1 - 10 Hz) are seismic displacement noise and gravity gradient noise (GGN). While the first can be handled by advanced superattenuators, the latter affects the detector sensitivity since the vibrating soil can directly couple to the suspended optics. Furthermore, seismic noise complicates the control of the seismic filter chain (so-called control noise).

The R&D program includes studies at candidate sites, the development of suitable sensor networks, and techniques to quantify and understand the low frequency noise contributions. The studies encompass the development of GGN subtraction schemes.

Initial steps along these directions have been taken in de Einstein Telescope design study [335]. A first round of seismic measurements at various European underground sites has been completed. In addition, analytical calculations were carried out to address GGN. These calculations assume infinite and completely uniform bedrock around the caverns. They do not take into account the effects of the surface above, and consider uniform and frequency-independent seismic excitation. In an attempt to go beyond these limitations, numerical, finite-element modeling of the site, including effects of stratification, seismic noise reduction as a function of depth, varying speed of sound, varying coherence levels and the effects of the surface above, has been implemented to achieve more accurate GNN reduction estimates. At present, these models are not yet supported by suitable experimental measurements that must provide all the necessary preliminary information to make these evaluations reliable.

The R&D program envisions extensive field studies of candidate sites for the Einstein Telescope observatory. These studies will be performed by local scientific teams with arrays of high quality commercial seismic sensors. In addition, the development and integration of prototypes of both unidirectional opto-mechanical monolithic and MEMS-based sensors is foreseen. These sensors will be optimized to be used standalone for both seismic noise monitoring and geophysics applications, with particular attention in their design to the necessary immunity to environmental noise. The arrays will be upgraded as soon as new improved sensors are available. Data from these arrays will provide information about attenuation of seismic noise with depth, dependence on geology, *e.g.* sediments, hardrock and salt, and coherence length of signals between various sensors. We will attempt to decompose seismic noise according to surface waves, such as Rayleigh and Love waves, and body waves. Furthermore, daily variations will be exploited in order to estimate contributions from cultural noise. Although limited seismic information is available from a variety of sites, the proposed studies will include long-term observations. These studies will aid to identify a possible R&D path towards seismic isolation systems, while the data will be used as input to the underground-surface site decision making process. It will allow identifying time-dependent contributions in Newtonian background from surface seismic compression waves, weather activity

(variations in atmospheric pressure), ground-water dynamics, slow gravity drifts of geophysical origin, cultural noise (moving object: humans, machines, *etc.*). The proposed studies will quantify these various contributions and identify approaches to limiting gravity gradient noise with active correction systems with data from seismic sensors, accelerometers, strainmeters, rock thermometers and piezometers.

3.11.2 Research and development program

The R&D program integrates theoretical and experimental activities: characterization of possible underground sites, and development of sensors and networks to be optimized for the specific site studies.

The main experimental activities will be

- Acquisition of seismic data at various underground sites in Europe. The data provide information about attenuation of seismic noise with depth, dependence on geology, *e.g.* sediments, hardrock and salt, and coherence length of signals among different sensors.
- Development of seismic sensors and sensor networks, and their application in GGN monitoring and subtraction schemes.
- Data analysis of the acquired data for geophysical applications and modeling of the underground sites.

Theoretical studies will be carried out in parallel with the experimental activities:

- Validation of seismic background noise models for specific sites. This work will be done in collaboration with geophysicists. Evaluation of geophysical applications of Einstein Telescope.
- Analytical modeling of seismic and atmospheric systems, and extraction of estimates for GGN in an underground environment. A set of simplified models, which can be analyzed analytically, will be used.
- Validation of analytical and numerical (finite element) models by using data acquired at underground sites. Analytical estimates will be compared with predictions from finite element models. The finite element approach is the only possible approach for the detailed modeling of a realistic environment.
- Studies of the GGN subtraction problem. The idea here is to subtract the Newtonian noise contributions from the data by using auxiliary measurements. The activity will consist in obtaining estimates about subtraction efficiency, and in the optimization of auxiliary sensors placement configuration. Several scenarios must be taken into account. Firstly, subtraction of stationary noise generated by far away sources. Secondly, GGN subtraction of nearby sources typically associated with non stationary contributions. Wiener and Kalman filtering schemes will be evaluated.

3.11.3 Coordination of activities

It is imperative to coordinate the activities of the Einstein Telescope science team members addressed to the identification of the optimal site for the observatory and the consolidation of the infrastructure design. The following activities are planned.

Coordination of site studies and assessment

- A site assessment process will be instituted. Required site studies will be defined. Particular emphasis will be given to the seismic noise and gravity gradient noise measurements and the local geology. Scientists of candidate countries will be involved in long term site characterization measurement activities. Results will be compared by means of dedicated workshops.
- A database will be set up and administered to consolidate geo-physical and technical information on possible sites in Europe.

- Based on the information collected in the site database a refinement process of the list of site candidates to host the Einstein Telescope observatory will be organized. Technical validation will be separated from political selection criteria.
- A scheme will be implemented to extract site ranking information including cost evaluation. The development of tools that enable trade off processes between infrastructure cost and site parameters versus achievable science will be coordinated. The primary goal of the above listed activities is the realization of comprehensive investigations of the geo-physical properties of potential candidate sites as well as the evaluation of the scientific and financial interests of the countries hosting the candidate sites, aiming for a down-selection of the site candidates.

3.11.4 Consolidation of infrastructure requirements

It is important to coordinate the consolidation of the vacuum, cryogenics, safety and infrastructure requirements for a third generation gravitational observatory. Most infrastructure aspects of Einstein Telescope will differ significantly from currently operating gravitational wave detectors. We plan to maintain and extend the currently available expertise. This will be achieved by making use not only of the activities within the GEO and Virgo collaborations, but also by networking with various relevant projects within Europe and worldwide. It is of importance that Einstein Telescope continues to monitor and strengthen its connections to the following activities:

- The realization of second-generation detectors such as Advanced Virgo, Advanced LIGO and GEO-HF and the experience gained from their commissioning will feed directly into the consolidation of the Einstein Telescope infrastructure requirements.
- Cryogenics are a crucial component for any third generation detector. R&D from small-scale prototypes in Europe and especially the knowledge gained from the commissioning of the Japanese CLIO and LCGT projects are of high value for Einstein Telescope and will be closely monitored.
- The infrastructure will be the largest cost factor for a third generation observatory and therefore special emphasis is required for the infra-structure costing. Several large-scale underground projects outside the gravitational wave community such as the Large Hadron Collider at CERN, International Linear Collider, and the Sanford Deep Underground Science and Engineering Laboratory collaborations will be consulted and used as reference to update and improve the cost planning.

Consolidation of vacuum, cryogenics, safety and infrastructure requirements

- In regular intervals the general requirements for vacuum, cryogenics, safety and infrastructure of the Einstein Telescope observatory will be assessed and updated, according to any new knowledge evolving.
- The activity of consolidation of the Einstein Telescope design, optimized for each site, will be coordinated. Stimulus will be provided for setting up committees with local scientists and engineers in order to adapt the infrastructure reference design to each individual site and its geological properties.

Modeling of seismic and gravity-gradient noise

- Evaluation of gravity gradient noise models and subtraction techniques (based on both analytical and finite-element) will be stimulated.
- Results will be collected and compared by means of dedicated workshops.

In summary, the sensitivity requirements at low frequencies for third generation interferometers imply the need to extend the candidate site studies, to develop suitable tools (sensors and techniques) for the measurements, analysis and compensation of seismic and Newtonian noise, aimed to define the physical and geological characteristics of candidate underground sites in Europe to host the Einstein Telescope.

4 Suspension systems

4.1 Description

The suspension system of a gravitational wave detector is conceived to isolate the test masses from ground seismic vibrations and local disturbances so that they are considered nearly in a free fall state in the frequency bandwidth of interest. A typical suspension chain is obtained cascading a set of passive mechanical filters providing a suited attenuation from seismic and acoustic noise above a certain cut-off frequency. Below this frequency value an active feed-back control strategy is developed by using sensors and actuators disseminated along the suspension chain and keeping the interferometer at its working point.

The upper part of the suspension chain, called *Superattenuator* (SA), is essentially a N-stage pendulum supported by a three-leg elastic structure, called Inverted Pendulum (IP). In an N-stage pendulum the horizontal displacement of the suspension point, at a frequency f much higher than its normal modes $(f_1, f_2, ..., f_N)$, is transmitted to the last stage with an attenuation proportional to f^{-2N}. In order to attenuate the vertical vibrations, each mass of the multi-stage pendulum is replaced by a cylindrical mechanical filter with a set of concentric cantilever blade springs with low stiffness. The blades support, through a long metallic wire, the next mechanical filter, forming a chain of low frequency oscillators also in the vertical direction. In Virgo the blades work in parallel with a magnetic anti-spring system, assembled on each filter and designed to reduce its vertical mode from about 1.5 Hz down to 0.5 Hz. Thanks to the anti-springs the vertical modes of the chain are all below 3 Hz. Starting from a few Hz, the mirror is thus well isolated from vertical seismic noise too.

The last suspension stage (LSS), called *optical payload* or simply *payload*, is the system designed to couple the test mass to the SA chain, to compensate the residual seismic noise and to steer the mirror through internal forces exerted from the last SA element. The main components of a Virgo-like LSS are: the Marionette, the Recoil Mass (RM) and the Mirror. The marionette is the first stage used to control the mirror position by means of coil-magnet actuators acting between the last stage upper part suspension and the marionette arms, while the recoil mass is used to protect and to steer the mirror. On its mechanical structure, indeed, the coils of the electro-magnetic actuators acting on the mirror back side are mounted.

LSS plays also another important role: all the mechanical elements which are connected to the mirror are designed not to degrade the intrinsic mechanical losses of the mirror itself. This is necessary because of the well known relation between mechanical dissipations and thermal motion in macroscopic systems. The thermal noise contribution is reduced by developing sophisticated suspension systems with materials having low mechanical dissipation and low friction mechanical clamps. However, to achieve the goal sensitivity of the ET Project at low and intermediate frequency, a further reduction of thermal noise contribution is obtained by cooling the mirror and its last stage at cryogenic temperature[336]. Cryogenic operation introduces additional difficulties, but the benefits in thermal noise reduction is also enhanced by the materials selection with improved properties at low temperatures.

A major challenge for cooling the mirror is to provide an efficient path for heat conduction while still maintaining good thermal noise and mechanical isolation performance. The cooling system needs to provide adequate heat extraction from the test masses, for both steady state operation and for cooling from room temperature in a reasonable time, without adding noise or short-circuiting the mechanical isolation. This constraint has an important impact on the design of a last stage of cryogenic suspension.

In the next sections we analyze in sequence all these aspects and we will try to summarize a perspective solution for each of them presenting also possible alternative approaches. Finally, an overview of the related technologies to be developed is presentsd in section 4.6.

4.2 Executive summary

We organized the design study of the ET suspension focusing the activity on four main arguments:

- The upper part of the suspension, the *superattenuator* (SA), providing the needed seismic and acoustic isolation. This issue is discussed and the solution is presented in the Upper Stage section 4.3;
- The last stage (payload), crucial for the defining the thermal noise performances and the mirror control are presented in paragraph 4.4;
- The local control strategy and the related instrumentation, analyzed in sections 4.4.7, 4.4.8, 4.4.9;
- An overview of the main technologies to be developed for achieving the ET scientific goal (see sec. 4.5.1, 4.5.2, 4.5.4).

We notice that to clarify some of the open problems, several R&D programs have been carried out with limited resources. In particular, a bigger effort should be done in the domain of the material studies and of the low temperature sensing devices. Nevertheless we succeed in preparing a reference solution and a set of alternative scenarios for driving the ET technical design. However the solution selection requires intensive experimental activity and the coordination efforts will be significantly effective only if continuous activity in the laboratories is sustained and coordinated in collaboration with the Japanese project LCGT.

The preliminary activity of the ET working group, devoted to the conceptual design of the suspensions, was centered on the definition of ET suspension requirement. In particular we collected and compared the mechanical and thermal properties of the materials at room and low temperature. Both silicon and sapphire potentially offer superior performance at cryogenic temperatures. In particular silicon samples can be obtained in large cylindrical blocks of mass higher than 100 kg. Its attractive thermal and thermo-mechanical properties makes it a strong candidate for the mirror and the suspension fibre in the future detector operating at cryogenic temperatures.

The low and high frequency interferometers (ET-LF and ET-HF) proposed in the ET design study require different suspension systems. In the following we will show that the SA as it is operating within the Virgo interferometer is already compliant with the HF interferometer requirements. On the other hand for ET-LF a dedicated effort is required. In fact, to extend the detection bandwidth of the Einstein Telescope in the low-frequency region starting from a couple of Hz, a better seismic attenuation in the ultra-low frequency range is needed. The *Superattenuator* dynamics in the low frequency range, where the inner normal modes of the mechanical filter chain are confined, has been simulated by using the electro-magnetic equivalent circuit and a detailed simulation campaign devoted to this design study has been performed. On this base we concluded that we can fix to six the number of filters because a better attenuation performance in the high frequency range is not necessary anymore since the safety margin is large enough in Advanced Virgo and even larger in an underground environment. Then, a SA 17-m high with six magnetic anti-spring filters ("equal-spaced" configuration) tuned with a vertical cut-off frequency around 300 mHz, represents the reference solution for ET-LF interferometer.

As we anticipated above, the last stage of the suspension system is crucial in defining the suspension thermal noise performances. In particular for the ET-LF case we deal with a system of coupled oscillators with masses at different temperature. For this reason, the thermal noise evaluation required to develop a specific model,where the interacting masses are at different temperature in steady state condition. The study of the thermal noise of this system has been carried on by using two different methods and the suspension thermal noise curves have been compared with the ET-D goal sensitivity curve driving the design of the last stage of the mirror suspension.

Thus, the conceptual design of the payload for LF and ET-HF has been completed. It includes for ET-LF the analysis of the heat flow, the definition of the fibre material and geometry and the heat path from the mirror to the cold box via the marionette trough the suspension fibres and the dedicated heat sinks.

The ET-LF payload will be installed in the lower part of the vacuum tower hosting the 17-m long super-attenuator chain. The vacuum tower basement is a cryostat separated to the upper part by a roof crossed by the Ti-6Al-4V thin rod, which holds the whole payload. The cold box is set on top of a cryo compatible attenuator chain hosted in an ancillary cryostat. The box will keep the mirror at cryogenic temperature: it can be either a simple liquid helium container in the case of a cryoplant based on cryofluids or the cold head of a

cryo refrigerator in the case of a cryocooler plant. Both solutions are discussed and compared in more details in the infrastructure section. The final choice will depend on the outcome of a dedicated R&D effort.

A sophisticated control systems will be implemented in order to hierarchically control test mass positions to bring the interferometer to operation. The actuation system is needed to align the interferometer mirrors and to automatically maintain the operation point. It is based on the signals derived from the circulating light to apply internal forces exerted through the last stages of the suspension. The actuation based on a coil-magnet system for ET is reviewed in details and its limit associated to the $1/f$ potential noise is assessed; the alternative electrostatic approach is also discussed.

For the coarse mirror control optical conduits and bundle fibre served as position sensors have been tested at low temperature [326]. They can be used together with short-arm optical levers and small interferometric systems for fine position control to achieve an alignment accuracy within 10 nrad RMS. Hence low frequency cryogenic accelerometers have being developed for this purpose.

Finally, it should be underlined that the complex study on the ET suspension system is not limited to a definition of a reference solution. Some crucial technologies to be developed in the domain of the slicon fibre and cryo-device construction have been identified. These are issues of potential interest for industrial world too.

4.3 Mechanics of the suspension upper stages

4.3.1 LF interferometer

In this paragraph we discuss in details the problem of the attenuation of the seismic noise and we present a possible solution for both ET-LF and ET-Hf interferometers. The focus is set on a Virgo *Superattenuator* solution. In fact, it has been experimentally demonstrated [337] that this solution provides already a seismic noise attenuation of more than ten order of magnitude starting from a few Hertz. Alternative approaches are cited in the Appendix, where the geometric anti-spring and the active filter developed in LIGO, GEO, TAMA and at the NIKHEF laboratory are described. The material compatibility of the *Superattenuator* with a cryogenic environment is discussed also there. In the following we will present in sequence

- The ET attenuation requirements
- The Virgo Superattenuator
- Seismic isolation measurements with the Superattenuator (SA)
- SA modifications for Low Frequency ET
- Noise from SA mechanical micro-glitches
- SA control strategy and improvements for ET

a) Attenuation Requirements As shown in figure 112, Virgo is operating close to its design sensitivity also in the low frequency range. Looking at the detector noise budget, it turns out that its response is not limited by the mirror seismic noise passing through the anti-seismic suspension (*Superattenuators*). A set of measurements aimed to check if the present *Superattenuator* performance is compliant with the higher sensitivity of the next generation antennae, in particular with the Einstein Telescope, has been performed. The mechanical transfer function requirements for seismic noise isolation of the mirror in future detectors can be obtained starting from their design sensitivity curve expressed in terms of the mirror displacement. To this purpose, in figure 113, the design sensitivity curves of Advanced Virgo [7], the upgraded 3 km-long interferometer expected to enter in action in 2014 at the Virgo site, and those ones for the two reference solutions of the Einstein Telescope, are compared. The maximum acceptable transfer function amplitude of the seismic isolation system in different antennas is plotted as a function of the frequency in figure 114. This is given by the ratio between the detector displacement sensitivity curves reported in figure 113 and the linear spectral density of seismic noise measured

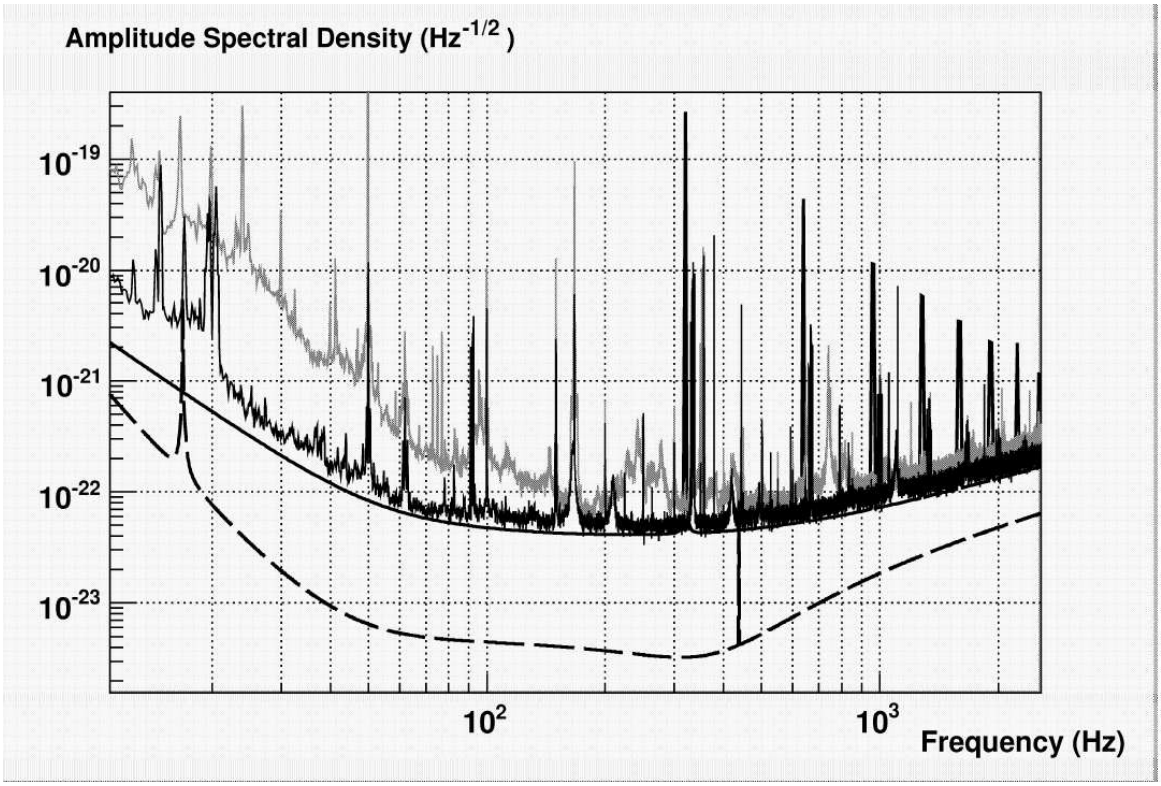

Figure 112: Virgo sensitivity achieved after a few months of the second scientific run (*VSR2* - black experimental curve), compared with the sensitivity reached in 2007 during the first scientific run (*VSR1* - grey curve). The continuous curve is the Virgo design sensitivity, discussed in [338], while the dotted curve is the design sensitivity of Advanced Virgo, the next generation detector.

on site at ground level. At the Advanced Virgo site (the same of Virgo) the linear spectral density of the ground seismic displacement has been measured to be roughly isotropic and well approximated, between a fraction of Hz and a few tens of Hz, by the function A/f^2, where f indicates the spectral frequency and A is around $10^{-7}\,\mathrm{m}\cdot\mathrm{Hz}^{3/2}$ [339]. A conservative value of A around $5\times10^{-7}\,\mathrm{m}\cdot\mathrm{Hz}^{3/2}$ has been considered to take into account possible fluctuations in some spectral regions, and the fact that the residual displacement due to seismic noise affects all four mirrors of the two Fabry-Perot cavities. Since the Einstein Telescope site has not yet been chosen, the requirement has to be considered as provisional. The linear spectral density seismic noise of $5\times10^{-9}/f^2$, measured in the Kamioka mine, where the new cryogenic Japanese interferometric detector is planned to be installed [340], is taken as a reference value. The recent progresses of Einstein Telescope working group for site selection are promising [341]. In particular, a measurements campaign of seismic noise for different underground sites in Germany provides seismic spectra smaller by a few units or comparable with that one measured in Kamioka mine. This makes the chosen reference seismic floor conservative for our goals (the requirements are likely more stringent than necessary).

It is important to stress that the transfer function requirements are valid both for vertical and horizontal seismic

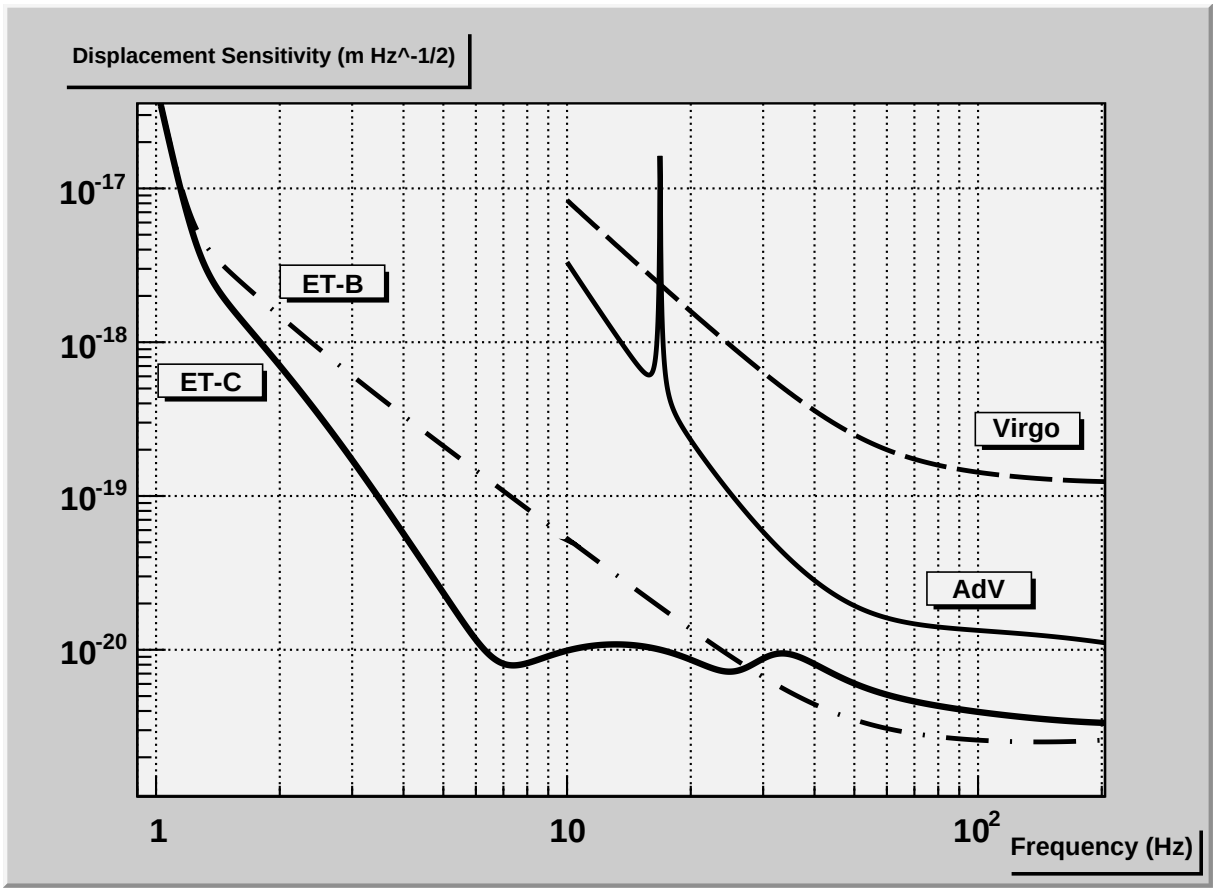

Figure 113: Displacement design sensitivities of Virgo, Advanced Virgo (AdV), and of the two reference configurations of the Einstein Telescope: the high-frequency interferometer (ET-B) and the 'xylophone' design (ET-C), optimized for the low frequency detection. While the detection bandwidth of Virgo and AdV starts from 10 Hz, Einstein Telescope aims to extend the detection bandwidth in the low frequency region starting from a few Hz.

noise, that have a similar magnitudes. While for horizontal direction the argument is straightforward, in the vertical case the plot represents the maximum fraction of vertical seismic noise that can be transferred to the mirror along the beam direction without affecting the antenna sensitivity. As shown in the following section, only a fraction of the mirror vertical motion is transmitted along the beam because of unavoidable mechanical coupling and Earth curvature (making 10 km far plumb lines [18] not parallel each other).

b) The Virgo Superattenuator (SA) Since it will be shown that the *Superattenuator* as it is operating within the Virgo interferometer is already compliant with the ET project requirements above 3 Hz, it is important to provide a detailed description of the apparatus. The *Superattenuator* working principle is based on a simple idea. Exciting in horizontal direction the suspension point of a simple pendulum at frequency f higher than the pendulum normal mode f_0, it is easy to prove that the oscillation is transmitted to the suspended mass with an attenuation proportional to $(f_0/f)^2$. Therefore a device suspending a mirror based on the working principle of a simple pendulum, represents a good isolation system for seismic noise at frequency $f > f_0$. A better attenuation performance is achievable considering a *n-stage* pendulum. With this system an oscillation at a frequency f higher than the frequencies of the chain normal modes ($f > f_0 > f_1 > \ldots > f_n$), is transmitted to the suspended mass with attenuation proportional to f^{-2n}. In particular, the ratio between the linear spectral

[18] A plumb line is regarded as directed exactly toward the earth's center of gravity.

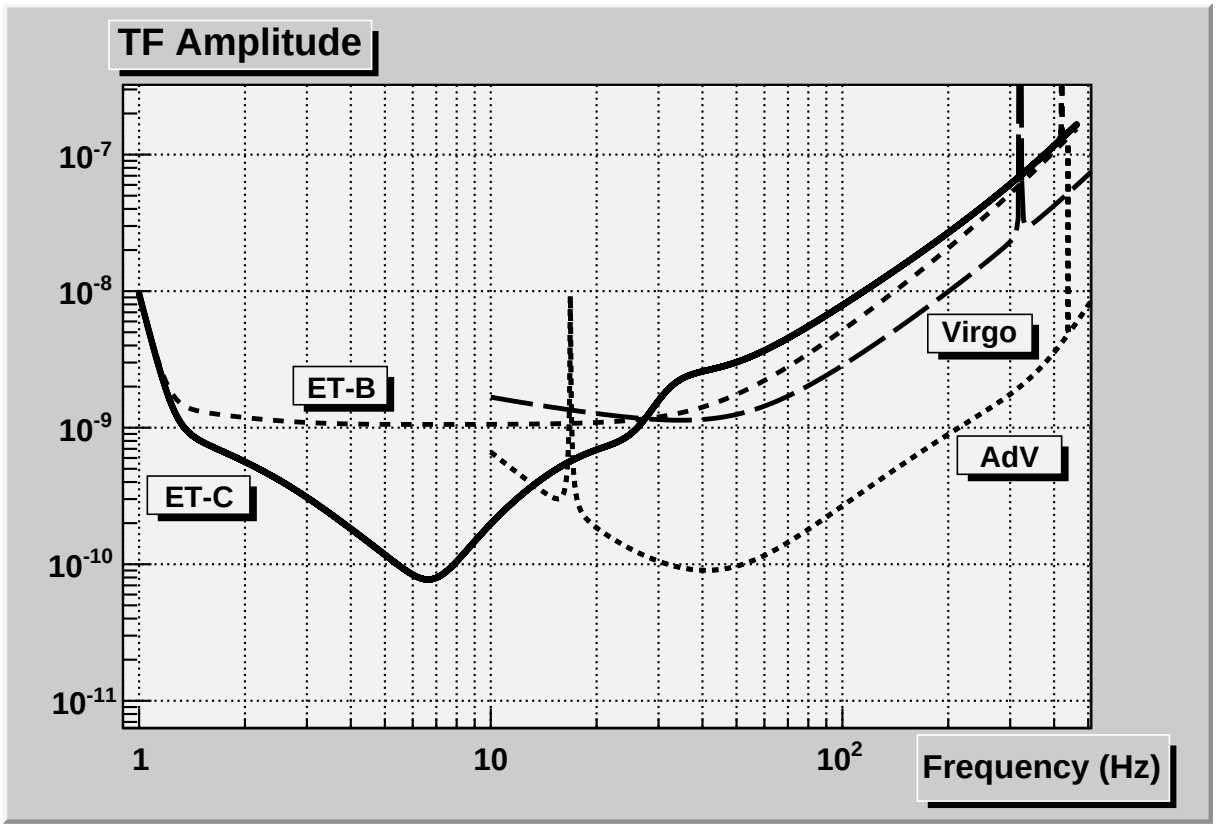

Figure 114: Seismic vibration transfer function requirements for different antennas. The curves represent the ratio between the displacement sensitivities reported in figure 113 and the conservative linear spectral density of seismic noise at the level where the interferometer is located. Since seismic noise will be at least a couple of orders of magnitude smaller in underground environment, Einstein Telescope, despite its better sensitivity, is less demanding in terms of seismic attenuation at high frequency.

density of the last mass displacement (the optical component) and the linear spectral density of the suspension point displacement (where the excitation is applied), decreases as A/f^{2n} where $A = f_0^2 \cdot f_1^2 \cdot f_2^2 \cdots f_n^2$ and n is the number of stages. In this way a very large attenuation of seismic noise horizontal component can be obtained in the frequency range above the highest pendulum resonance, simply increasing the number of stages. The longer are the pendulums, the lower are the resonant frequencies of the system and higher is the attenuation response at a given frequency.

Unfortunately, due to different directions of the plumb line on the curved Earth surface, the end mirrors, suspended 3 km away in the Virgo interferometer and 10 km in Einstein Telescope, are misaligned (each with respect to the other) by about 3×10^{-4} rad and 10×10^{-4} rad respectively. For this reason it is necessary to tilt one mirror with respect to the other by the same amount, making at least one mirror misaligned with respect to the local plumb line. With this setting up the mirrors are not perfectly perpendicular to the laser beam and then any vertical vibration will be partially transmitted to the interferometer horizontal axis (laser beam direction). In addition any vertical vibration will be partially transmitted to the interferometer horizontal axis because of an unavoidable coupling among different degrees of freedom. Thus vertical motion will cause a phase change of the laser beam. It is thus clear that a vertical attenuation of seismic noise comparable with the horizontal one is fundamental to reduce the observation frequency threshold. With a multistage pendulum this goal can be achieved by replacing each suspension wire with a spring to form a cascade of oscillators also along the vertical direction. The spring should support a heavy load and, at the same time, it should be soft enough to exhibit a low resonant frequency. With this technical solution it is possible to confine the vertical resonances of the chain in a low frequency range obtaining a strong attenuation starting from a few Hz.

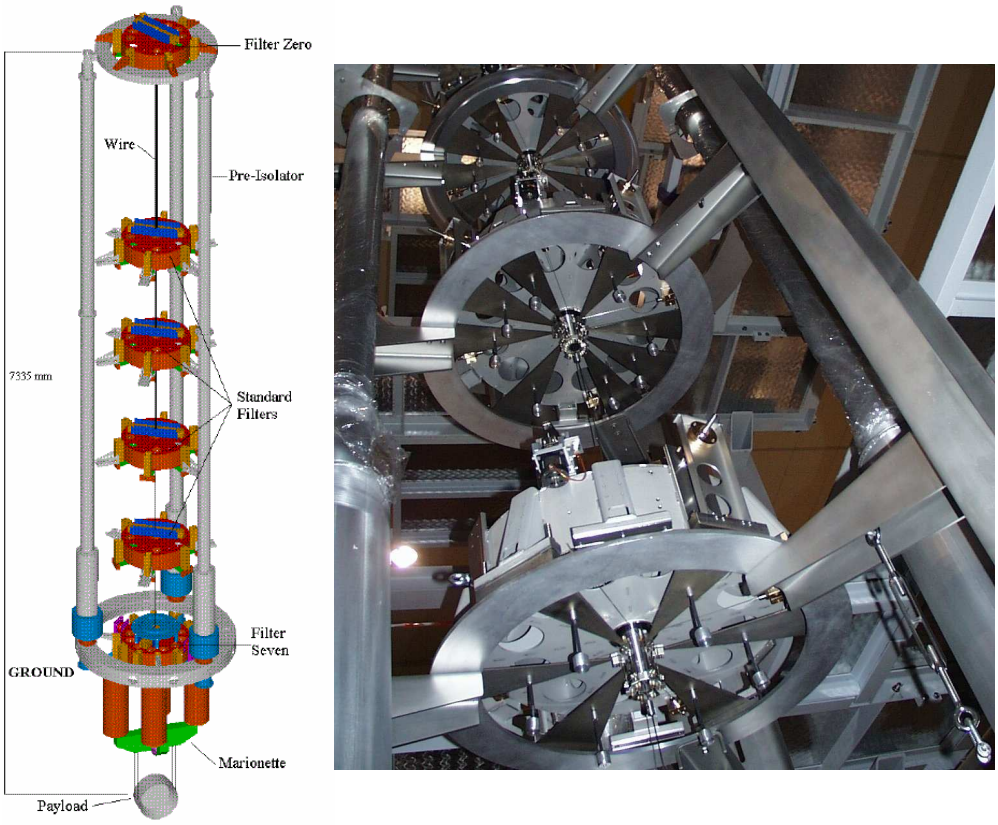

Figure 115: The Virgo *Superattenuator* suppresses the transmission of ground seismic vibrations to the suspended mirror. The mechanical filter chain and the three legs of the inverted pendulum are visible. In our attenuation measurements the excitation is applied to the filter chain suspension point.

Even the unavoidable mechanical couplings between rotations and horizontal beam direction can cause a phase change on the interferometer laser beam. In order to confine these rotational mode frequencies well below the detection band, each pendulum mass has to be replaced by a structure having a high momentum of inertia. In addition, the diameter of the suspension wire, connecting two consecutive stages, has to be small enough to reduce its restoring torque which opposes the rotation of the chain and determining its rotational frequencies. An interconnection of the stages at small distance and as close as possible to their centres of mass, guarantees low frequency tilt modes (i.e. rotational modes around the two horizontal axes) and a negligible coupling effects on the horizontal displacement of the suspended mass.

Keeping in mind all the considerations reported above, the Virgo *Superattenuator* has been conceived having a mechanical structure based on the working principle of a multistage pendulum [342]. Each mirror, indeed, is suspended to a 8 m-long SA chain with 6 mechanical filters (see Fig. 115). The system consists of three fundamental elements: the Inverted Pendulum (*IP*), the mechanical seismic Filters (*SF*) connected each other by metallic suspension wires and the Last Stage (*LS*) or optical payload. The suspension system is described here below, while more detailed information of each single chain element can be found in reference [343].

The Inverted Pendulum top stage The top stage of the *Superattenuator* is designed to fulfil three main functions:

- to introduce a very low frequency (about 40 mHz) horizontal filtering stage, limiting the amount of seismic

energy feeding into the SA and thus reducing the SA excitation resonant modes and improving its overall attenuation performance;

- to provide the SA with a suspension point positioning system: the amplitude of the slow tidal drifts over three km is far beyond the dynamic range of the actuators exerting the locking forces upon the mirror. Therefore tidal drifts are compensated by moving softly the SA suspension point: the tidal strain over 3 km can be as large as a few hundred microns in 6 hours;
- to provide a soft suspension stage on the top of the chain to allow active mode damping of the chain resonant modes and seismic noise depression by means of inertial sensors, positioning sensors and electromagnetic actuators. The main goal is to reduce the *swing* of the optical payload down to a fraction of micron allowing a low-noise control of the mirror in the interferometer.

To fulfil all the above requirements in the horizontal plane a device based on the working principle of an Inverted Pendulum (*IP*) has been built. An IP is a suitable device for several reasons. An ideal Inverted Pendulum can be conceived as a mass-less vertical bar of length l connected to ground by means of an elastic joint with stiffness k and supporting a mass M on its top. In such a pendulum the gravity acts as an anti-spring and the resonant frequency can be tuned to have a very low resonant frequency (about 40 mHz in Virgo). The required force to displace the suspended chain from an IP resonating at 40 mHz is very low: the needed force, in DC mode, for moving a 1 ton SA chain by 1 cm is less than 1 N. Therefore soft electromagnetic actuators can be used to control the mirror position. For this reason the IP is a good platform to act upon for the active damping of the SA normal modes.

The present Virgo Inverted Pendulum (see Fig. 115 left side) is a three-leg metallic structure interconnected on their top with a steel ring (the Top Ring). The Top Ring surrounds the first filter of the chain (hereafter called Filter Zero) to which is rigidly connected. The Filter Zero together with the Top Ring form a platform suspended by three thin wires (31 mm long) accommodated on top of the legs. The elasticity of the structure is due to three flexible metallic joints. They are screwed onto the legs to form an interconnection element between the upper part and the bottom one of the aluminium pipes. A bottom steel ring, on which the Inverted Pendulum is anchored, completes this metallic frame. Each leg is essentially a light hollow cylinder made of aluminium with an inner diameter of 125 mm and an outer diameter of 130 mm. The total length of the leg, from the bottom of the flexible joint to the suspension point of the SA is about 6.2 m. The leg is composed by two sections flanged together and reinforced with titanium inserts.

The three legs are made in Aluminium to minimize their weight. Nevertheless the leg mass is about 26 kg. An extension below the flex joint is necessary to tune the *percussion point* avoiding an isolation performance spoiling. The flex joint is therefore mounted on top of a 0.8 m high rigid support. A proper counterweight is attached to a high bell-shaped 0.9 m long skirt bolted to the bottom of the leg.

The Inverted Pendulum structure is surrounded by a rigid metallic frame (called Ground Reference Structure—visible in Fig. 115 right side), holding the parts of sensors and actuators that needs to stay "on ground". It is provided with [344, 345]:

- three motorized sleds set on the external structure in front of the legs top. Each sled is connected to the corresponding leg top through a soft spring. The motors are used to set the IP roughly in its working point, so that to minimize the correction signals in the closed loop operation;
- 3 horizontal *LVDT* position sensors set in pin wheel configuration. The secondary windings stay on the ground reference structure, while the primary ones are rigidly connected to the top stage;
- 3 horizontal coil-magnet actuators, set in pin wheel configuration. The coils, arranged as a Maxwell pair, stay on the ground reference structure, while the magnets are rigidly connected to the top stage;
- 3 horizontal accelerometers, set on the top stage;
- 2 vertical accelerometer, set on the Filter Zero crossbar;
- 1 vertical *LVDT*, measuring the position of the Filter Zero crossbar with respect to the top stage;
- 2 vertical coil-magnet actuators, acting between the Filter Zero body and its crossbar.

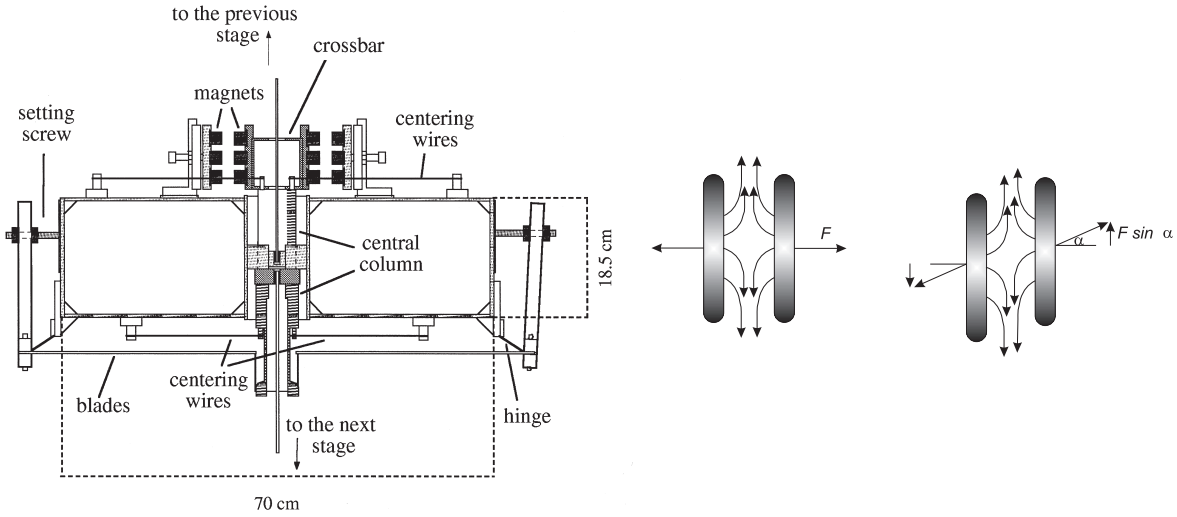

Figure 116: The Virgo seismic filter: a technical drawing (*left side*). The working principle of the magnetic anti-spring system accommodated on the seismic filter crossbar (*right side*).

The Seismic Filters In the Virgo *Superattenuator* each pendulum mass has been replaced by a rigid metallic structure drum shaped acting as an oscillator in vertical direction too. A sequence of six mechanical filters is able to isolate the optical components from seismic noise in accordance with the working principle of a multistage pendulum (see Fig. 115). A detailed description of the design and performance of a single filter can be found in reference [346]. A seismic filter is a rigid steel cylinder (70 cm diameter, 18.5 cm high for a total weight of about 100 kg) suspended as close as possible to its centre of mass (see Fig. 116 left side). On the outer circumference of its body bottom part, a set of triangular cantilever spring blades is clamped. Each blade (3.5 mm thick and 385.5 mm long) is bent at a constant curvature radius and with different base width according to the load to be supported. A nominal load, ranging between 48 kg and 96 kg hung on the blade tip, forces it in flat and horizontal position. The blade tip is connected by a 1 mm diameter wire to a central column, inserted through a hole in the centre of the filter body. Any movement of the central column, apart from the vertical direction, is prevented by two sets of four centreing wires accommodated on the top and on the bottom of the filter body.

A crossbar, bolted on the upper part of the central column, is used as a mechanical support for the magnetic anti-spring system described in the next sub-paragraph. The central column and the crossbar, connected to the blade spring, represent the moving part of the mechanical filter from which the load of the lower stages is suspended by a steel suspension wire. By connecting each filter to the next one, a chain of mechanical oscillators in vertical direction is obtained.

According to the previous description of our filtering system it is clear that the total load of the chain is suspended by the triangular steel blades. The base width of the triangle ranges from 180 to 110 mm in accordance with the load to be supported. For the same reason the top filter is equipped with 12 blades while the last one needs only four blades.Once properly loaded the main vertical resonant frequency of each filter is about 1.5 Hz.

Maraging steel has been used in place of standard steel for blade construction in order to minimize micro-creep effects [347, 348] due to the high load applied. The same material has been used to machine the suspension wires with nail-head at both ends [349]. Since the suspended load decreases going from the top to the bottom of the chain, the wire and the nail-head diameters change along the chain in the ranges 4–1.85 mm and 8–6 mm, respectively. In this way it has been possible to confine the violin vibration mode within the high frequency

band and to reduce its angular stiffness which determines the rotational frequency around the vertical axis.

The two nail-heads of the wires connecting a filter on the chain to the previous and to the next one are screwed in the central part of its body at a relative distance of 5 mm, very close to the filter centre of mass. As mentioned above, this guarantees a small return torque to rotations of the filter around the horizontal axis and thus a low tilt frequency.

The magnetic anti-spring The suspension wire length of 1.15 m in the Virgo *Superattenuator* sets the pendulum resonant frequency of each stage at about 0.5 Hz. In the vertical direction the stiffness of the triangular blade springs fixes the natural resonant frequency at about 1.5 Hz. In order to reduce the vertical stiffness of the blades, and then to confine the main vertical resonant frequency of each filter below the pendulum one, a system of magnetic anti-springs [346, 350] has been adopted (see Fig. 116 left side). It consists of two sets of permanent magnets (the first assembled on the crossbar and the second one on the filter body), facing each other with opposite horizontal magnetic moment (namely in a repulsive configuration). In this way the two matrices screwed on the crossbar are forced to move in vertical direction only.

When the magnets are perfectly faced the repulsive force has a null vertical component, but as soon as a matrix is moved in the vertical direction, a vertical component of the magnetic force appears. Considering a small relative displacement (Δy), compared with the distance (d) between two matrices of magnets and with their transverse dimension, the vertical component of the repulsive force (F_y) is proportional to Δy:

$$F_y \approx F_0 \cdot (\Delta y / d) \tag{80}$$

where F_0 is the modulus of the repulsive force (see its working principle in Fig. 116 right side). Such device is equivalent to a vertical spring with a negative elastic constant (anti-spring) whose modulus is F_0/d. Thus, its rest position is that of the two couple of matrices perfectly faced. On a seismic filter the magnetic anti-springs act on the crossbar in parallel with the blade springs, so that the vertical modes frequency of the chain are confined below the highest frequency of the horizontal ones. The advantages of this system are the vacuum compatibility and the contact-less action performed on the filter, for this reasons it represents the reference solution for the third generation detector.

An evolution of the Virgo mechanical filter to be used as vertical seismic noise suppression system, is the Geometric Anti Spring (GAS) filter described in the appendix C.2. It was proposed by R. De Salvo et al. [351] few years ago and it has been tested in TAMA. The GAS filter is used as seismic isolation system for the 10 m long interferometer at AEI Hannover and the same technology is developed by the NIKHEF group for the optical bench of the light injection in the interferometer for Advanced Virgo.

The Steering Filter The last mechanical filter of the Virgo seismic attenuation chain is the Steering Filter [342]. It has been designed to suspend and orientate the payload, a multi-body mechanical system whose core is a test-mas of the gravitational-wave detector, by means of forces exerted within the suspension. The payload plays a crucial role in the overall dynamics of the system and its presence has been included in all the projections shown in this section of the report, assuming a basic design similar to that one actually developed for Virgo (Fig. 115). However a dedicated section 4.4 will be devoted to the issues related to this system provided its crucial role in dealing with test-masses as mirrors of the interferometer. In the Virgo experimental apparatus the steering filter has been equipped with four Aluminium legs (about 900 mm long and 250 mm in diameter) bolted on the filter body bottom part. These legs are the mechanical support of the coils mounted in front of the permanent magnets screwed on the marionette wings and used to control the payload position.

In addition the Steering Filter is equipped with different vacuum compatible stepping motors. Two of them are dedicated to the filter alignment around its vertical axis. The first one is accommodated on top of the filter body and it is used to move the filter and the payload with respect to the upper part of the *Superattenuator* while the second one is mounted at the bottom of it to change the relative position of the filter with respect to the payload. This last one is used to optimize the coil-magnet distance for the actuation on payload. A

second pair of vacuum compatible stepping motors completes a set of remote controlled devices mounted on this mechanical filter. By moving some small masses attached to a mechanical trolley on top of the filter body, a fine adjustment of the tilt (rotations around the two horizontal axes) can be performed.

c) Seismic isolation measurements with the Superattenuator (SA) The attenuation performance of the *Superattenuator* has been measured by using the Virgo interferometer. In particular, a direct measurement of the mechanical transfer function has been obtained exciting with sinusoidal forces the top stage of the mechanical filter chain. The measurement consists in detecting the presence of a spectral line with the same excitation frequency at the level of the mirror, i.e. at the interferometer dark port. The ratio between the linear spectral density at the excitation frequency of the mirror and that one of the top stage displacement (measured by means of the accelerometers) provides a measurement of the *Superattenuator* mechanical transfer function magnitude. When the line is not detected at the level of the interferometer, only an experimental upper limit of the transfer function amplitude can be given. We remind that the linear spectral density of the noise floor of the top stage sensors or of the interferometer dark port, does not depend on the time length of the measurement while the amplitude of a spectral line increases with square root of the time interval. The longer is the integration time, the higher is the capability to distinguish a spectral line from the interferometer noise floor. Moreover, in those measurements where the peak is not distinguished at the level of the mirror, the upper limit of the transfer function, given by the ratio between the noise spectral floor and the top stage peak at the excitation frequency, improves (i.e. becomes smaller) increasing the integration time. In this case, the linear spectral density of the excitation line (denominator) becomes larger, while the interferometer noise floor (numerator) does not change.

A campaign of measurements has been performed exciting the suspension top stage both in horizontal laser beam direction and in vertical direction. The excitation is applied to the suspension point through the coil-magnet actuators used in the Inertial Damping of the chain resonance modes. The experimental results have been compared with the requirements of the future generation detectors (as reported also in Fig. 114) and plotted in Fig. 117.

Above 3 Hz all the measured transfer functions (upper limits or direct measurements) turn out to be within the requirements of Einstein Telescope. Changes to the *Superattenuator* structure (such as a length extension of the filter chain) will be needed in Einstein Telescope only in the case the detection threshold frequency will be moved below 3 Hz. In reference [342], where a stage by stage (indirect) measurement of the *Superattenuator* total transfer function (valid at any frequency) has been provided (and compared with simulation), a very steep behavior around 3 Hz is well visible. Considering this as a reference result, it is clear that even changing by a couple of orders of magnitude the input seismic noise as well as the attenuation requirements, the crossing frequency between the transfer function and the requirement curve should remain around 3 Hz.

In addition, around 30 Hz and in the 7-9 Hz region, our measurements put in evidence some peaks above the interferometer noise floor while excitation is applied on the top stage. This is an indication of noise transmission a couple of orders of magnitude larger than expected from simulation and indirect measurements (stage by stage). However, also in these cases, the transfer function has been measured to not exceed the detector requirements. Other mechanisms could cause the detected tiny motion of the mirror by-passing the extremely high mechanical attenuation, as discussed in [337, 352]. The extension of the multistage pendulum length, linked to the need of moving down below 2 Hz the cross-over between the horizontal seismic noise and the antenna sensitivity (see next section), is welcome for a better separation of the top-stage control and the optical payload control preventing cross-talks.

It is important to stress that, during our measurements campaign, the pre-isolator stage (described above) has been excluded from the transfer functions measurements. So that an additional attenuation factor, of the order of 20–40 dB, has to be considered as safety margin. With this additional attenuation factor, one can conclude that the cross-over for the Einstein Telescope requirements is expected to be around 2.8 Hz by using the present *Superattenuator* scheme. The cross-over is dominated by horizontal seismic noise.

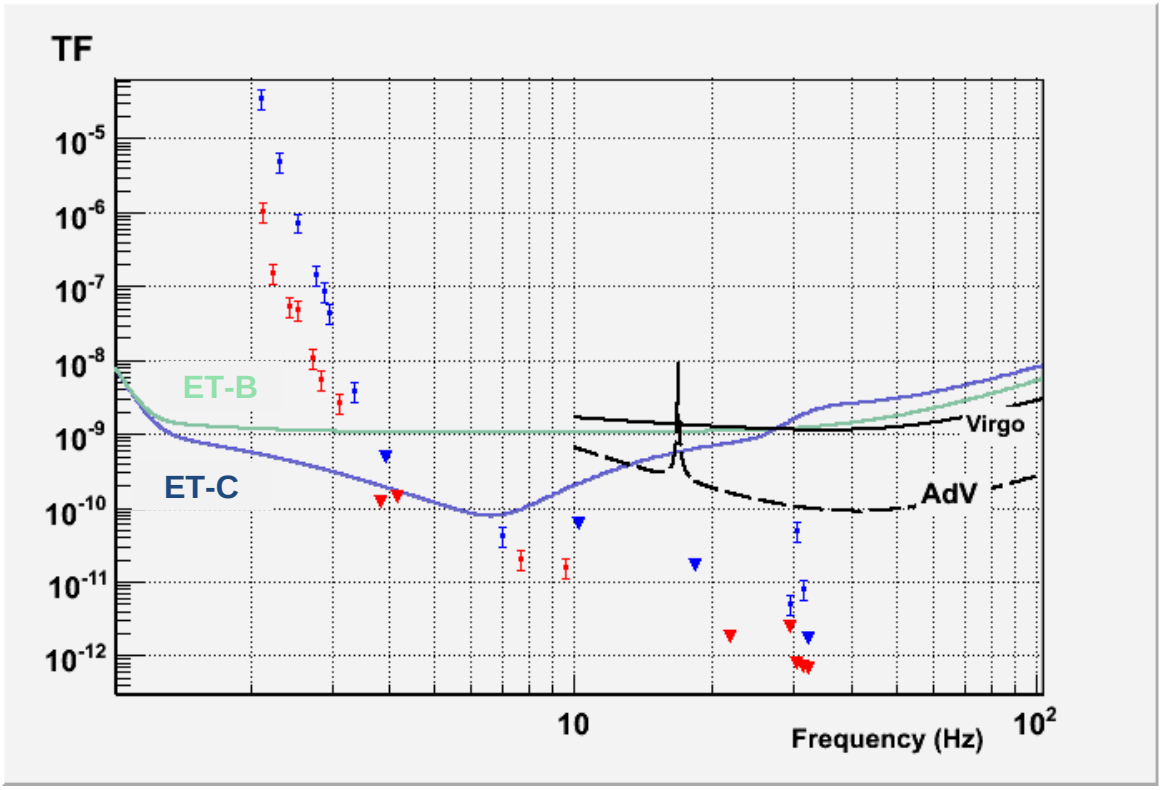

Figure 117: The measurement of the transfer functions at different frequencies. In red are reported the measurements where a vertical excitation of the top stage is applied. In blue are the measurements with the excitation in horizontal direction. The upper limits are indicated by triangles, while the direct measurements (when a signal is detected at the level of the mirror) are indicated with the bars. For the discussion of the error bars see reference [337].

d) SA modifications for Low Frequency ET In order to extend the detection bandwidth of the Einstein Telescope in the low-frequency region starting from a couple of Hz, a better seismic attenuation in the ultra-low frequency range is needed. To this purpose a detailed simulation campaign devoted to this design study has been performed. The SA dynamics in the low frequency range, where the inner normal modes of the mechanical filter chain are confined, can be well simulated by using the electro-magnetic equivalent circuit (a series of oscillators). A maximization algorithm, called *Simplex* [353], based on the possibility to change the masses and the mechanical filter chain lengths, has been developed. It searches for a maximum attenuation performance at a fixed frequency that, in our case, was 2 Hz. Since the transfer function has a smooth shape, it turns out that to get a higher attenuation at 2 Hz, we should have a lower "cross-over frequency" with the requirements curves (see Fig. 118). As showed in the direct measurement performed with the Virgo interferometer (see section 4.1.1.c), the cross-over between seismic noise at the mirror level and the requirements is dominated by the residual horizontal seismic vibrations. For this reason to move the cross-over at lower frequency, we need to improve the attenuation performance of the horizontal seismic vibration in the low frequency range. An important preliminary conclusion of our design study is that, fixing the length and the number of mechanical filters, the optimal configuration (i.e. that one minimizing the cross-over frequency or maximizing the attenuation performance at 2 Hz) is that one where the filters are separated along the chain by the same distance. This "equal-spaced" configuration represents the optimal one even because the vertical transfer function is not influenced by the filter positioning along the chain. Moreover it has been proved that increasing / decreasing the number of filters or changing their masses do not play a fundamental role in determining the cross-over frequency between the horizontal

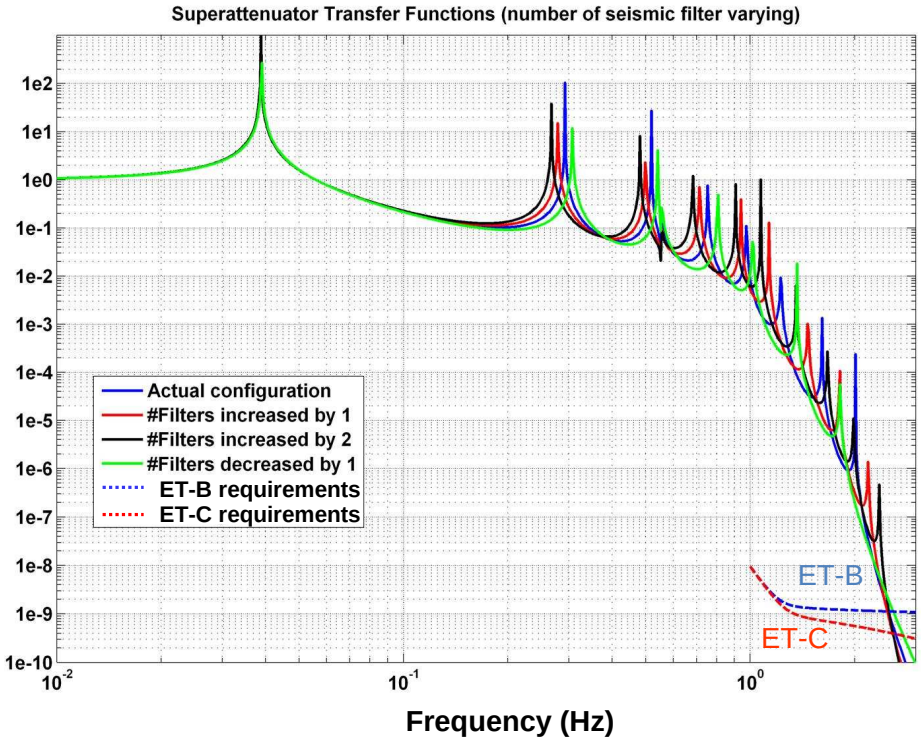

Figure 118: Simulation results of the SA horizontal transfer function with the present chain length (9 m). Changing the number of ("equal-spaced") filters the resulting horizontal transfer function is compared with the ET requirements (for High Frequency—*ET-B*—and low frequency or "xylophone" configuration—*ET-C*). Adding or removing filters along the chain length do not have remarkable role in the positioning of the cross-over frequency with the requirements.

transfer function and the requirements. The results obtained are plotted in Fig. 118 and Fig. 119 while in the corresponding captions complementary information is available. The only way to move in the low frequency region the cross-over frequency extending the Einstein Telescope bandwidth below 3 Hz, is to increase the SA chain total length. The simulation results for different configurations can be found in figure 120 and described in [352], while the best solution seems to be represented by a SA with 6 filters and a total length of 17 m (identical the Virgo configuration, where 5 mechanical filters suspended from an horizontal pre-isolator stage plus the marionette are assembled forming a filter chain about 9 m long). As shown in Fig. 122, with this solution the cross-over frequency has been placed around 1.7–1.8 Hz, that is considered enough for our purpose. Indeed, Newtonian noise and other technical noise are assumed to prevent an effective detection above a couple of Hz. With this configuration, the vertical cut-off frequency of the whole system is set below 1.8 Hz by tuning each mechanical filter having the main vertical frequency around 300 mHz (see Fig. 121). The corresponding vertical transfer function is plotted in Fig. 122. Since the residual seismic noise along the vertical direction, at the level of the mirror, is expected to limit the Einstein Telescope sensitivity again around 1.7–1.8 Hz, a coupling factor of 10^{-3} has been considered. This is due to the fact that the Earth curvature makes plumb lines at a 10 km distance not parallel each other. At least one mirror has to be inclined with respect to the local plumb line performing the alignment of the cavities. This transmits the residual vertical mirror motion along the beam with the mentioned coupling factor (10^{-3}). Since years in Virgo many mechanical filters with a cut-off frequency of around 300 mHz *Superattenuators* are in operation with an excellent stability. By using the Virgo interferometer data, it has been observed that the long-term change of the chain main resonant frequencies induced by the

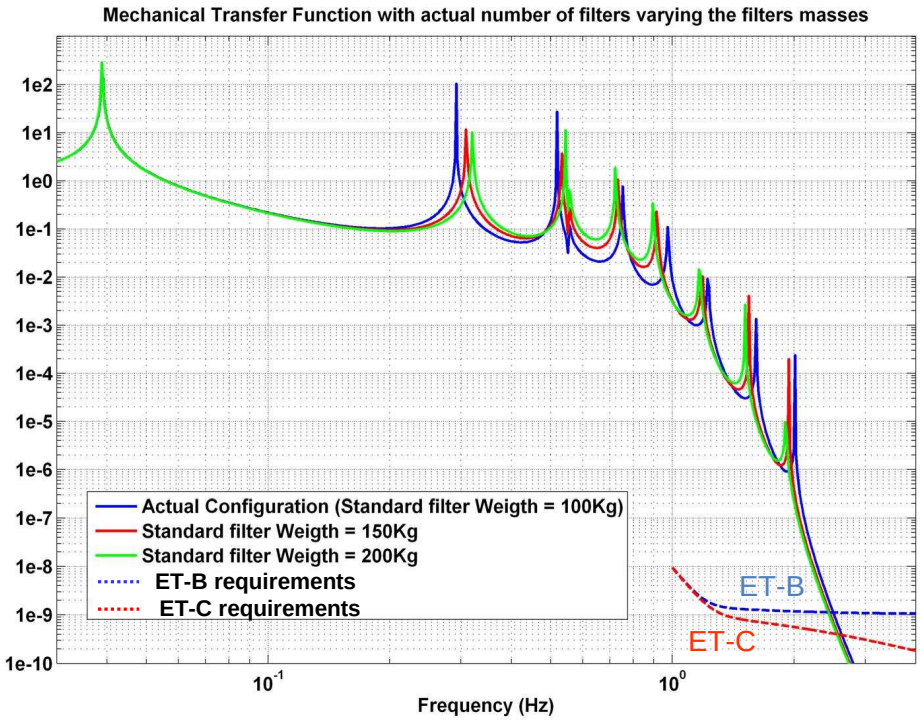

Figure 119: The horizontal transfer function of the present *SA* (6 filters weighting 100 kg each one for a total length of about 9 m) is compared with the same transfer function changing the mass of each filter (150 kg and 200 kg). Also in this case the cross-over frequency with the ET requirements is not remarkably affected by the change of the filter mass.

temperature variation under vacuum are well inside the line-width of the chain vertical resonances. No effect on the interferometer control is due to this potential disturbance. Moreover, even if the temperature variations induce a motion of the suspension chain and then a slow vertical displacement (*breath*) of the mirror (a few mm per $^{\circ}C$ is the measured value for the Virgo *Superattenuator*), this effect is well within the specifications of any interferometer (vacuum tank provides an excellent temperature stability - fraction of $^{\circ}C$ peak to peak). The standard SA, presently in operation on the Virgo interferometer, is already well inside the third generation specifications from this point of view too.

In addition, it is important to remind that the requirements in the tens of Hz range are less stringent in Einstein Telescope than in Advanced Virgo (see section 4.1.1.a) and thus, fixing to six (a choice lead by the reduction of the cross-over frequency) the number of filters, a better attenuation performance in the high frequency range is not necessary anymore since the safety margin is large enough in Advanced Virgo and even larger in an underground environment. In conclusion, a SA 17 m high with 6 magnetic anti-spring filters ("equal-spaced" configuration) tuned with a vertical cut-off frequency around 300 mHz, represents the reference solution for the Einstein Telescope.

In the Appendix C.3 we briefly describe the Advanced LIGO approach to suppress seismic noise. It includes a large two-stages platform fully active controlled, that, in principle, could improve the compactness of the ET-LF chain. However a dedicated R&D study is required for assessing the technical feasibility of this approach in the ET-LF case.

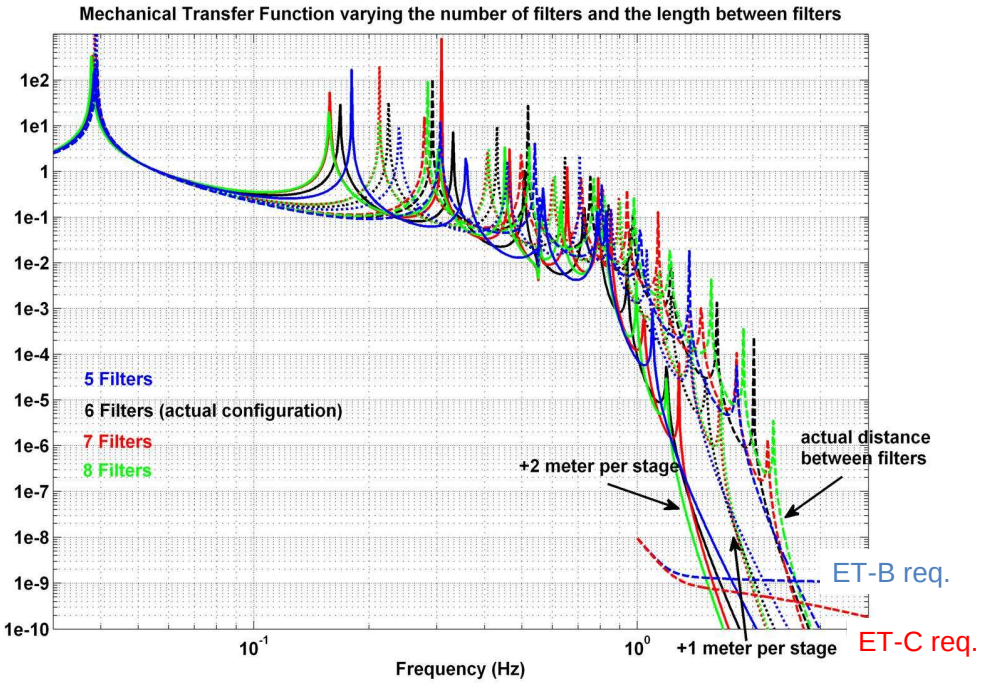

Figure 120: Simulation results for different configurations. The horizontal transfer function of the *SA* is plotted changing the number of filters and keeping fixed their relative distances ("equal-spaced" geometry) along the chain (changing, as a consequence, the full length of the SA).

e) Noise from SA mechanical micro-glitches The dislocation motion in the elastic elements of the anti-seismic filter under stress follow a "self-organized criticality dynamics" [354] causing a mechanical noise force along the vertical direction. This force due to micro-glitches exhibits an "$1/f$-spectrum", and it is sometime called "creep noise". This noise mechanism could affect the interferometer sensitivity. For this reason the Virgo interferometer has been used to set upper limits on the noise floor induced by this spurious mechanism. As sketched in Fig. 123, the dynamics of the optical payload along the vertical axis can be seen as the motion of three rigid bodies (mirror, reference mass and marionette) connected by three constraints (suspension wires). As a consequence, the payload vertical motion attached to the elastic blade spring of the last filter of the chain exhibits three fundamental modes along the vertical direction involving mainly (but not only) the vertical displacement of the reference mass, mirror and marionette respectively (see Fig. 123). These vertical modes are well visible on the Virgo interferometer output port, namely they appear as peaks on the output photodiode placed in front of the detector dark fringe (see Fig. 124). This means that the modes are excited by some spurious vertical force of unknown origin. The micro-creep, such as thermal noise or the electro-mechanical noise floor coming from the coil-magnet actuators are only possible excitation mechanisms. Using the coil-magnet actuators steering the marionette it is possible to excite the three vertical normal modes of the payload. More in general, it is possible to measure the transfer function between the vertical force acting on the marionette and the mirror longitudinal displacement (measured with very high accuracy by the Virgo interferometer). The measured transfer function (mirror displacement along the beam, expressed in m over the vertical force applied on the marionette, expressed in N) is plotted in Fig. 125. In order to set an upper limit on the vertical force presently acting on the marionette, one can make the ultra-conservative hypothesis (likely not realistic) that the vertical spurious force is dominant in all the band, namely it is responsible of the present sensitivity of the detector. With this assumption, dividing the present sensitivity (expressed in displacement along the

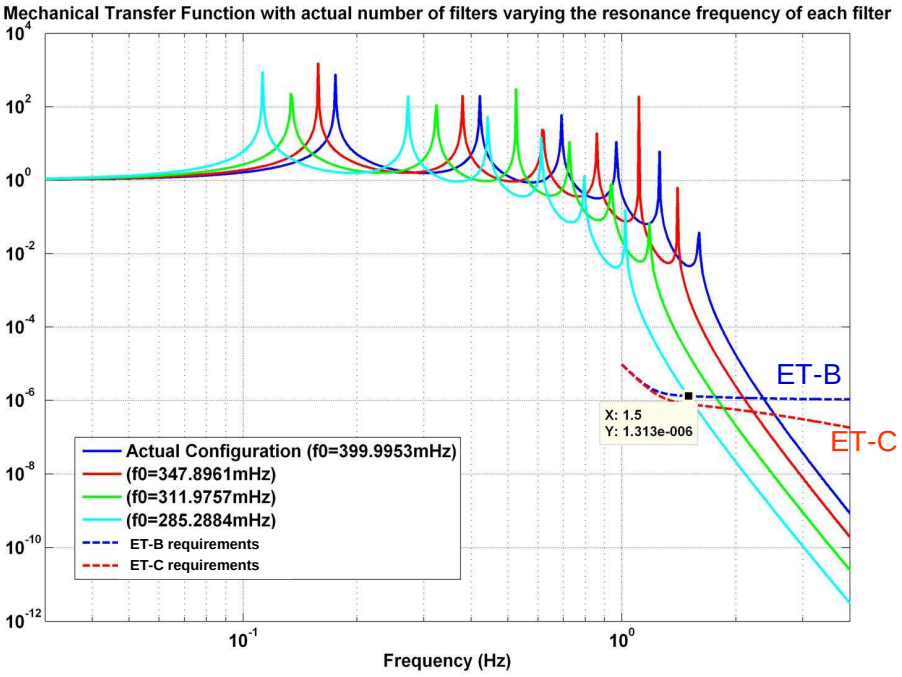

Figure 121: Vertical Transfer Function of the SA considering the six stages (as it is now, i.e. with the pre-isolator or "Filter Zero" plus other five mechanical filters). The different curves have been obtained changing the filter vertical resonant frequency. With filters working around 300 mHz it is possible to move the cross-over below 2 Hz.

beam) by the mentioned transfer function (mirror displacement vs. vertical force) the linear spectral density of the maximum vertical force acting on the marionette compatible with the measured sensitivity can be plotted (see Fig. 126). The deeps due to the three vertical modes of the payload (where the denominator - the transfer function - is large because of the resonant frequencies) are well visible. As mentioned above, the micro-glitches are expected to induce a shot-noise, namely a "$1/f$-colored force" thus one can set also the maximum "$1/f$-like force" compatible with the present sensitivity (see line at Fig. 126). By multiplying the plotted $1/f$-force by the measured transfer function (mirror displacement divided by vertical force on the marionette) one can thus obtain the linear spectral density of the maximum displacement induced by the micro-glitches on the mirror. This upper limit is compared in Fig. 127 with the sensitivity of the Virgo and AdV. From this figure, one can see that the upper limit just set is sufficient to exclude a dominant contribution in AdV. An important remark is that the micro-glitches are expected to increase when the operation vertical frequency of the anti-seismic filters is reduced. On the other hand, as described in section 4.1.1d, we know that working with seismic filters tuned around 300 mHz is a must to achieve the required vertical attenuation in the Einstein Telescope. However, several last filters of the *Superattenuator* chains are already working around 300 mHz and thus our result, excluding a dominant effect due to micro-glitches in Advanced detectors at the level of last filter blades , is valid also at this tuning frequency. The present upper limit is thus surely valid also in Einstein Telescope. On the other hand this upper limit is far (several orders of magnitude) from the third generation sensitivity, especially in the ultra-low frequency range. Since the micro-glitches of the elastic blades taking place on the upper stages of the chain are strongly filtered by the anti-seismic filter underneath, it is obvious that possible problems coming from micro-glitches (if present) can affect the sensitivity of the third generation antenna only if they take place at

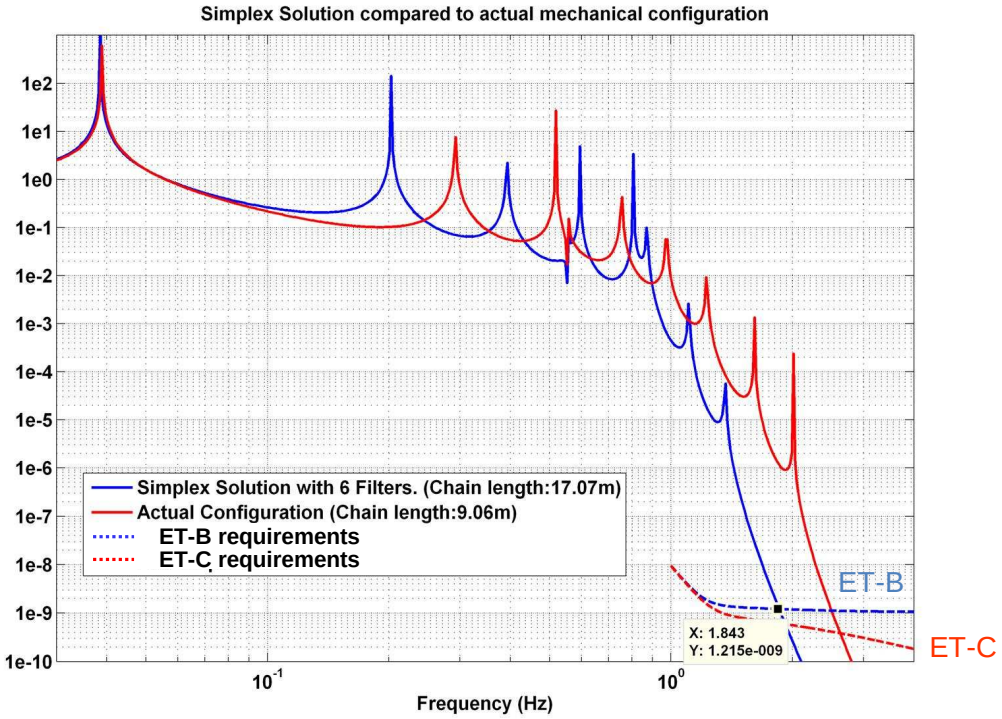

Figure 122: The proposed reference solution for the *SA* configuration of the Einstein Telescope. Other slightly different configurations are discussed in [352].

the level of the last filter(s) of the chain. A dedicated R&D programme to minimize micro-glitch effects on the cryogenic payload (see Appendix) and, if necessary, on the last stage(s) of the *Superattenuator*, is mandatory. In any case this is not expected to affect our anti-seismic isolation strategy, at least on the upper isolation chains.

f) SA control strategy and improvements for ET The Suspension Control System plays a crucial role in the interferometer operation. At the top level, it provides DC positioning control and damping of chain normal modes along horizontal, vertical and yaw degrees of freedom. At the bottom it provides the handle to apply residual correction from ground onto the horizontal and yaw degrees of freedom through the steering filter usually left actuation-free. Given the payload suspension point controlled with suitable accuracy, another section of the control is devoted to apply internal forces to the payload and to the interferometer control. The overall structure, described by more than 80 vibrational modes model, is presently (Virgo/Virgo+) controlled by 18 coil-magnet pairs actuators while its status is monitored by using about 20 sensors.

Such controls make use of two main classes of error signals: *local controls* and *global controls*. Local controls use error signals generated by local sensors, accommodated on or close to the suspension structure. Global controls are those whose input signal is generated by sensors located "far" from the suspension mechanics or traced by the interferometer signal. Typical local control sensors are accelerometer located on suspension and position sensors measuring displacement between suspension and suspension enclosure like linear variable differential transformers (*LVDT*). For the payload local control CCD cameras and PSD optical levers are used. Usual global control sensors are photo-diodes or quadrant photo-diodes providing information on suspended optical elements along three directions related to the interferometer beam (longitudinal displacement and two transverse

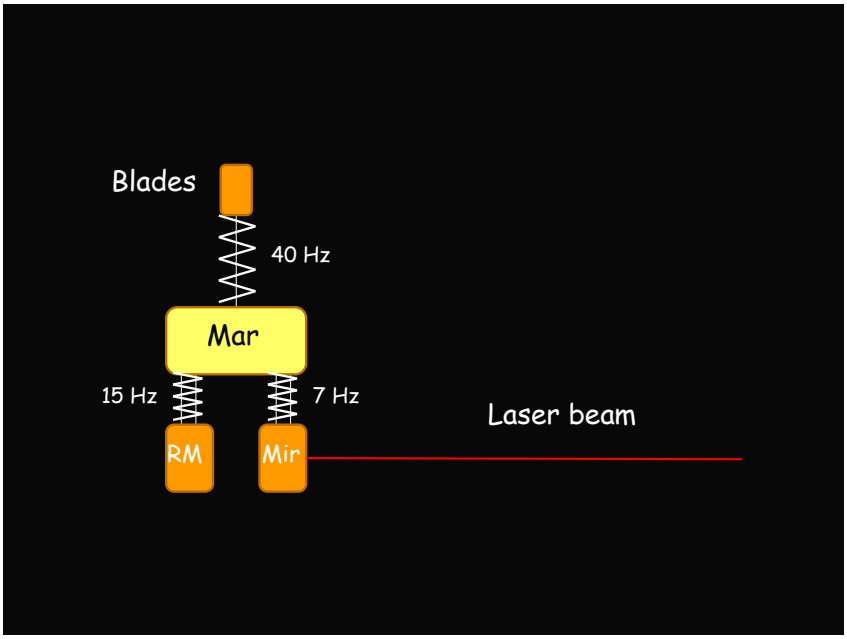

Figure 123: The three vertical modes of the optical payload suspended from the blades of last filter of the chain. For the vertical dynamics the two thin wires in a cradle configuration suspending the reference mass and the mirror can be thought as single vertical springs. As mentioned in the text, the vertical normal modes involve mainly (but not only) displacements of each payload element suspended from the blades: Marionette (*Mar* – 40 Hz), Reference Mass (*RM* – 15 Hz) and Mirror (*Mir* – 7 Hz).

tilts).

In order to ensure drift-less control and to provide suitable response of the system during far earthquakes, with the Virgo set-up, remote sensors and interferometer signals are combined with local sensors. Significant examples are the drift-less local control of mirrors alignment and the Global Inverted-Pendulum Control (*GIPC*). Long suspensions in their *rest* position, without any applied force, are usually up to a several millimetres far from their nominal working point. For this reason the control system has a large dynamics, i.e. it is able to control over several order of magnitude, and this task is accomplished by using suitable large dynamics sensors and actuators. Once the RMS accuracy of the suspension point (at the top of the mechanical structure) is brought to $\sim 0.1\,\mu$m, large angular oscillations or DC misalignment can still be present at the level of the payload and local controls are engaged to slow down mirror motion to $\sim 1\,\mu$m/s while aligning it from $50\,\mu$rad down to 10 nrad accuracy. In section 4.4 some specific issues involving local controls of the payload will be further commented. In fact for ET the role played by the payload and its controls will be crucial in the overall suspension performance even more critically than for Virgo.

In Virgo we successfully tested multi-dynamical range actuators, to apply locking force through the payloads, which are capable of switching between operational modes without introducing discontinuities in the feedback. Meeting injected noise requirements should not be an issue using such devices. To cover the whole huge dynamical range actuation forces are distributed along the chain. In the case of the ET suspension, whatever will be its final mechanical design, it seems that we cannot use less than four actuation points (presently inverted pendulum, steering filter, marionette and mirror).

Digital controllers used in suspension control system are quite complex: about 250 poles for each suspension requiring about 150 *MFLOPS* computation capabilities (sustained). One of the key points for a second generation system will be providing tools to ease control engineers life. Today control loops performances are a function of who actually implements the control algorithm. In the past this approach showed to slowly con-

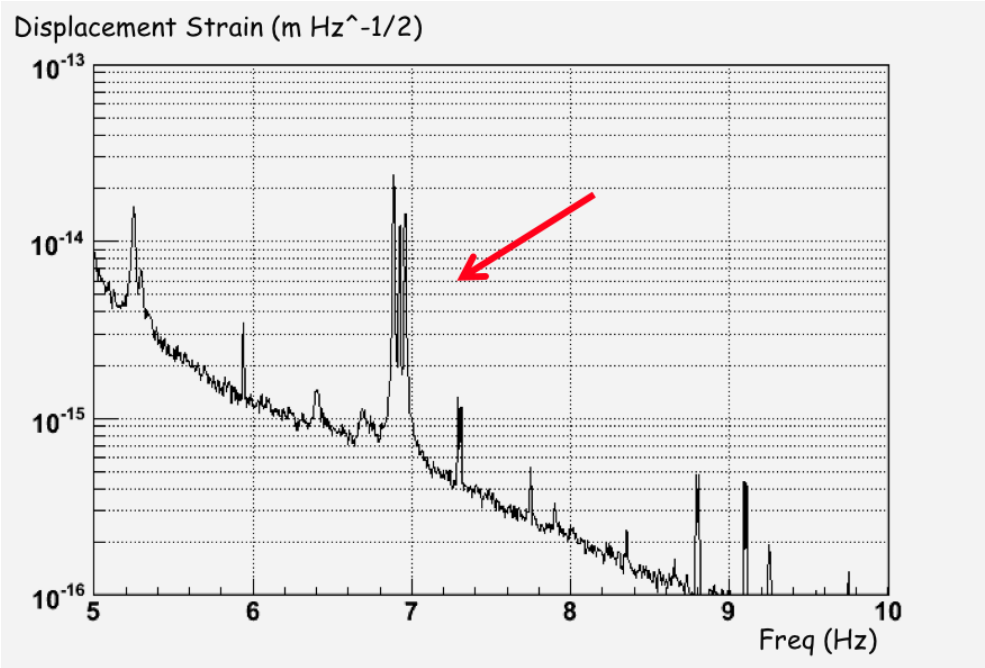

Figure 124: The photo-diode signal at the dark port of the Virgo antenna expressed in strain sensitivity. The four peaks around 7 Hz correspond to the vertical modes where the mirror displacement is mainly involved. A peak for each one of the four mirrors accommodated along the two Fabry-Perot cavities appears in the dark port (each at a slight different frequency around 7 Hz).

verge to a nearly optimal control. The present evolution of this techniques allows optimal control using almost automated procedures much more human independent than *Nyquist* like approach used so far.

4.3.2 HF interferometer

As detailed in section 4.1.1.c, the measurements campaign performed with the Virgo interferometer and devoted to evaluate the attenuation performance of the *Superattenuator*, demonstrated that, above 3 Hz, a multistage pendulum suspended to a three legs mechanical structure, as pre-isolator stage, is compliant with the ET requirements. The results reported in figure 117 have been obtained by using a *Superattenuator* with *six* seismic filters (for a total length of about 9 m) hung to a platform accommodated on top of the Inverted Pendulum which has been by-passed during the suspension point excitation phase of the measurements. This represents a good safety margin from attenuation point of view, because passing the seismic noise through the mechanical structure of the Inverted Pendulum, it will be additionally attenuated by a factor around 20–40 dB.

Starting from the long experience acquired in operating a similar mechanical system for seismic noise suppression, a base line for the LF and HF Detectors of the ET Project has been tracked. It is based a seismic attenuation system designed for the Virgo interferometer with common peculiarities: the first one can be conceived extending the detection bandwidth below 3 Hz by improving the chain total length up to 17 m , while for the second a Virgo-like *Superattenuator* can be built. The advantages of this choice are different:

- even considering a conservative cut-off frequency of the whole system around 5 Hz, it turns out that there will be a wide overlap between the HF Interferometer bandwidth the LF Interferometer one (following our indication starting around 2 Hz);
- the construction technology, mainly based on the use of magnetic anti-spring, has been deeply tested in vacuum for a very long time period (about ten years);

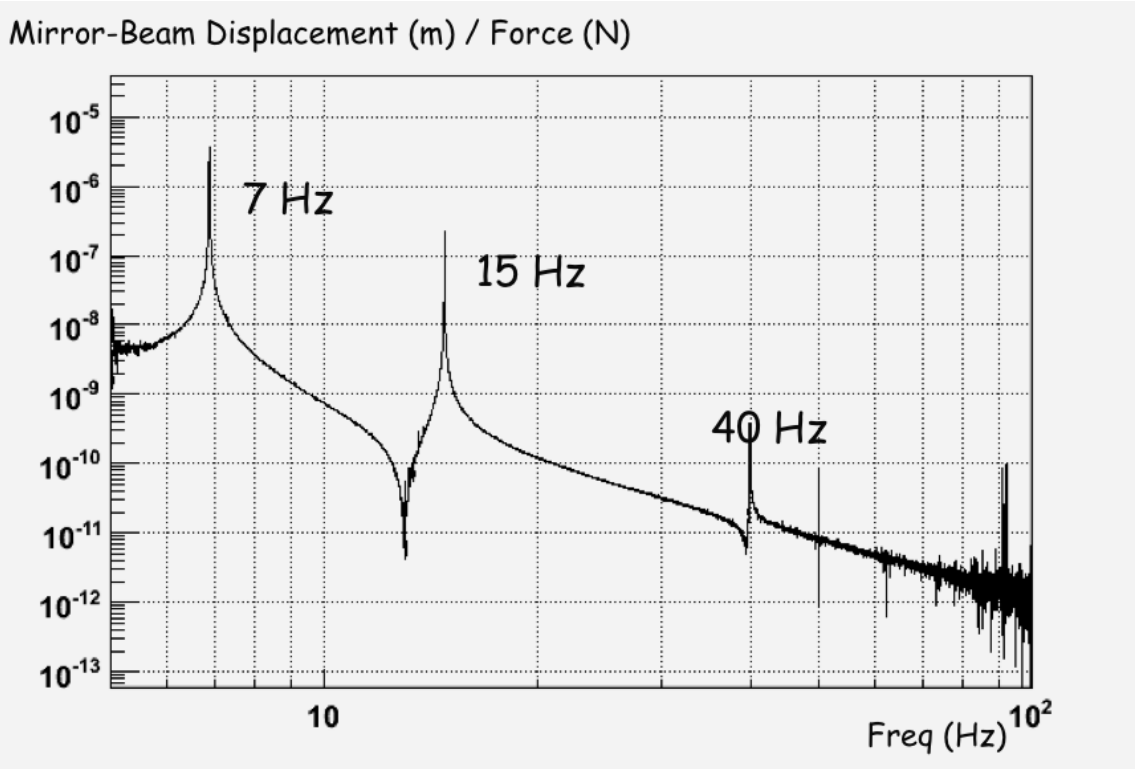

Figure 125: The transfer function between the mirror displacement along the beam (expressed in m) and the vertical force acting on the marionette (expressed in N). The vertical to horizontal coupling-factor (i.e. how much the mirror displacement in vertical is transmitted horizontally along the beam) is obviously already included in our measured transfer function and does not require any additional evaluation.

- the behavior of high stressed elastic elements (blades and wires) has been studied;
- many mechanical and electro-mechanical elements are compatible with cryogenic environment (see the Appendix C.1);
- the upgrades, presently in progress for the Virgo *Superattenuator*, can be used for this application too.

In this context and considering the ET requirements the choice of the Virgo *Superattenuator* as seismic isolation system for the third generation of gravitational wave detector,seems to be the natural one.

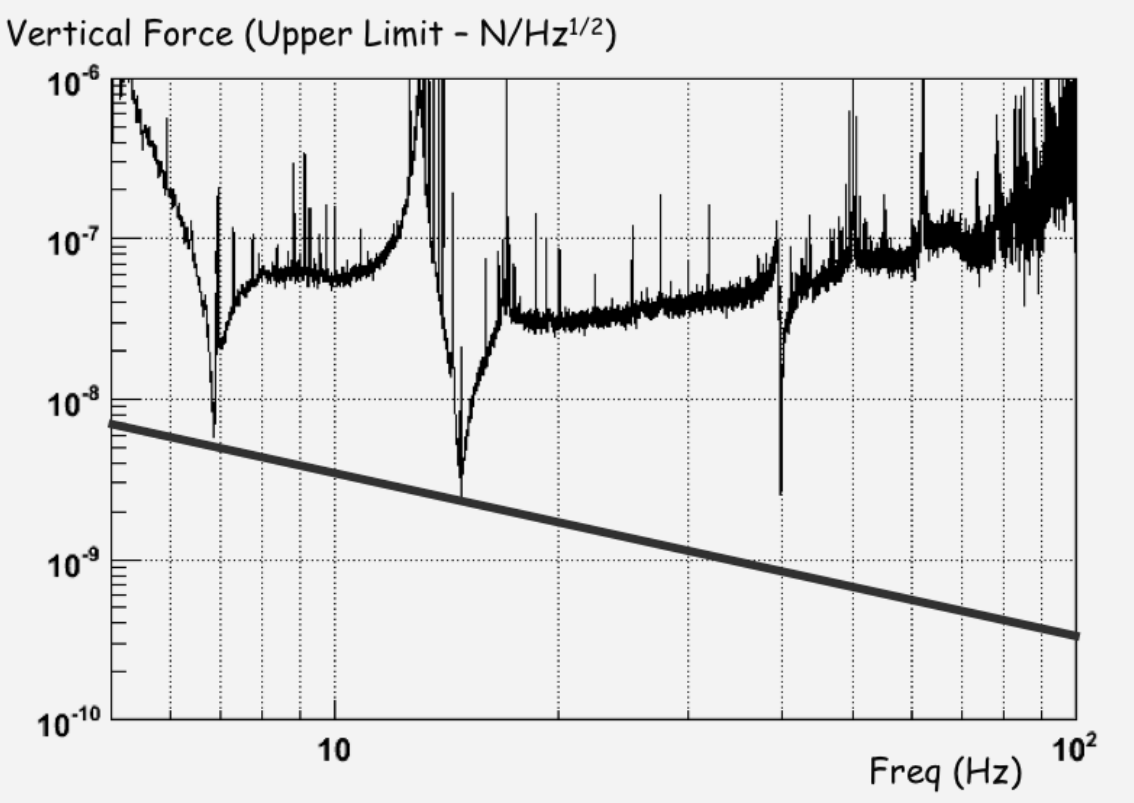

Figure 126: The linear spectral density of the maximum possible vertical force acting on the marionette compatible with the Virgo sensitivity. This is given by the simple procedure described in the text. Since the "$1/f$-behavior" of the micro-glitches force is assumed, one can find what is the maximum force having an "$1/f$-profile" at the level of the marionette compatible with the Virgo sensitivity. This is given by the minimal "$1/f$-shape" line touching the curve that gives the general upper limit on the vertical force just plotted.

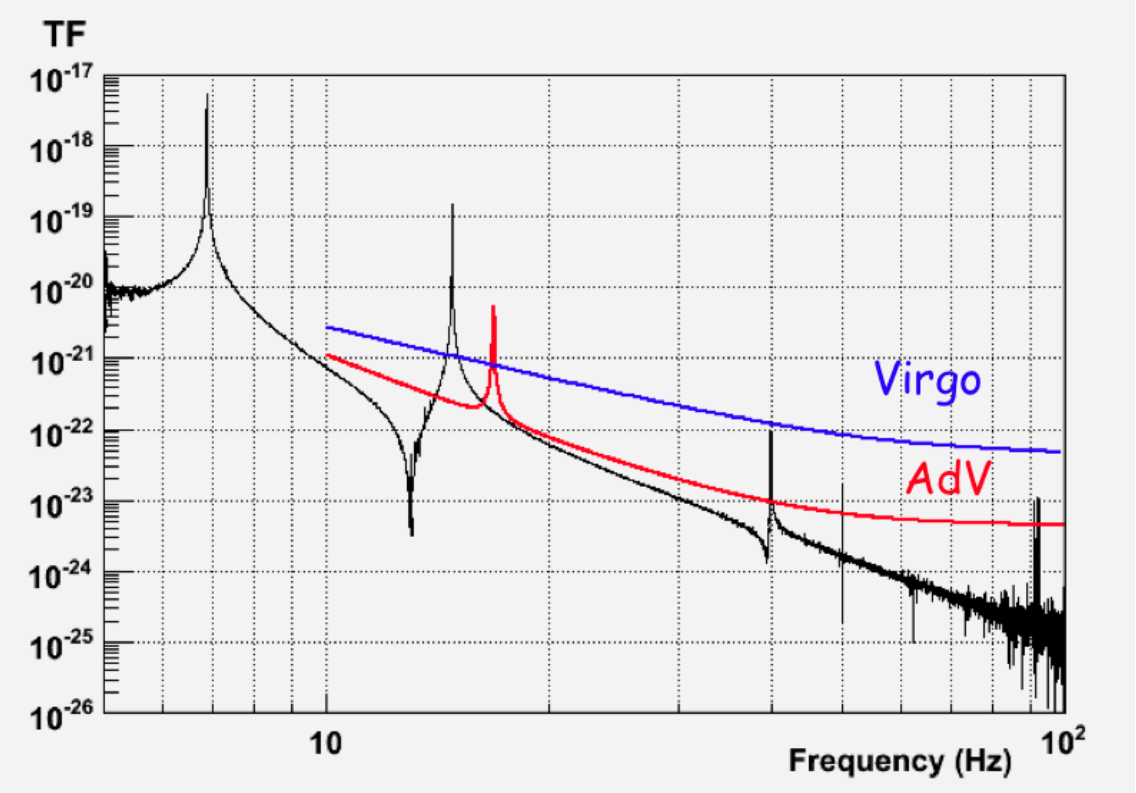

Figure 127: The upper limit of the micro-creep noise floor taking place in vertical on the blades of the last stage is given by the "$1/f$-force" upper limit plotted in the previous figure and the mentioned transfer function (stating how this force is transmitted along the beam). The upper limit of this noise floor is compared with the design sensitivity curves of Virgo and AdV. The upper limit, except around the resonant peaks, is enough to state that AdV will not be affected by this source of noise.

Box 4.1: Final considerations on Suspension for ET-LF and ET-HF

- Above 3 Hz the present Virgo *Superattenuator* is compliant with the ET requirements. Minor changes are needed to extend the detection bandwidth in the low frequency region (below 3Hz). The *Superattenuator* is a very good candidate to be installed in the *LF Interferometer* for the following reasons:
  - it has well tested behavior over 10 years activity;
  - it has well tested technology;
  - vacuum compatibility of crucial elements (under vacuum for many years);
  - many mechanical and electro-mechanical elements compatible with cryogenic environment.
- A *Superattenuator* 17 m tall with six stages (filters) in "equal-spaced" configuration and filter tuning (using the magnetic anti-spring) with a vertical cut-off around 300 mHz represents the reference solution for the ET Project. With this set-up a suspension system with a conservative cross-over frequency around 1.8 Hz (compliant with ET requirements) can be built.
- The Virgo *Superattenuator* could be used as seismic isolation system of the *HF Interferometer* for the following reasons:
  - the attenuation performance is compliant with the ET requirements;
  - the cross-over frequency (around 5 Hz) is good for this purpose;
  - the technology used (magnetic anti-spring filters) for its construction is well tested ;
  - all the upgrades of the system, presently in progress, are available also for this application.
- Ten years of activity on the control system of the *Superattenuator* represents a clear demonstration that a feed-back control at low-noise can be used to improve its performance in the low frequency region (below 5 Hz). The acquired experience on this subject is a valuable starting point for the commissioning of next generation detectors.
- The construction of the seismic isolation systems for Einstein Telescope could start immediately after a slight refinement of the project. Thanks to the Virgo experience the *Superattenuator*, developed to filter seismic noise at the mirror level, is the reference solution for the project.

4.3.3 Upper-lower suspension interface

As described all along this document, the ET Project is based on two different detectors. The first one aimed to the detection of gravitational wave signals in the low frequency range (*LF Interferometer*) and the second one for the detection of high frequency signals (*HF Interferometer*). The LF experimental apparatus will have a detection bandwidth as wide as possible in this specific region adopting, as seismic isolation system, the Virgo *Superattenuator*. The main difference is represented by the length of the multistage pendulum (for details see section 4.1.1.d), an important parameter to move the cut-off frequency of the whole system to the best value in accordance with the ET requirements (around 2 Hz for a total chain length of about 17 m). The main characteristic of the LF Detector is that the suspension upper part will be at room temperature while the payload is maintained at cryogenic temperature for beating the thermal noise limit. These working conditions will not be present in the HF Detector where a seismic isolation system based on the Virgo *Superattenuator* 9 m high will be operated at room temperature thanks to its attenuation performance above 3 Hz compliant with the ET requirements.

For this project a complex vacuum system has been studied with both interferometers within the same tunnel

and in particular with the pipes for LF Interferometer running on top of those ones of the HF Detector. This configuration will include a cooling shield containing the payload within the vacuum tower basement of the LF Interferometer. While the test mass and the penultimate stage of the suspension will be accommodated within the cryostat, a suspension wire made of Ti-6Al-4V will be used to suspend the payload from the *Superattenuator* upper part at room temperature (see section 3.4). This interconnection element has a key role in preserving the thermal isolation between the payload and the suspension upper part. Moreover, the cryostat structure will have a hole through which this suspension wire will pass. This hole should be large enough to avoid possible wire friction during standard working condition, but it should not create an important and undesirable thermal input for the cryostat operation. The penultimate stage, indeed, will be directly connected through a thermal link to an ancillary suspension where a *cold box* will be installed. In this way the heat extraction from the mirror is obtained via the suspension fibres attached to the penultimate stage, and then through the thermal link toward the ancillary suspension.

Since the hole in the cryostat structure will be also used for pure helium gas exchange during the cooling down process (pure helium gas will be injected within the experimental volume to speed up the cooling down/warming up procedure), it will be equipped with a mechanical shutter (vacuum tight) driven by a stepping motor (remotely controlled for opening/closing procedure) to be installed in the roof structure separating the tower upper part from the bottom one. This mechanical solution together with an adequate pumping system and a well defined evacuation procedure will be important steps to reach the needed vacuum level.

4.4 Mirror last stage suspension

The Last Stage Suspension (LSS) is the system designed to couple the test mass to the *Superattenuator* chain, to compensate the residual seismic noise and to steer the mirror through internal forces exerted from the last Superattenuator element (4.3.1) [355].

The main components of a Virgo-like LSS are the Marionette, the Recoil Mass (RM) and the Mirror as shown in figure 128. The marionette (M_1) is the first stage used to control the mirror position with coil-magnet actuators operating between the upper suspension stage and marionette arms; the recoil mass (M_3) is used for the Mirror (M_2) steering and its protection, it carries the coils of the e.m. actuators acting on the mirror rear side.

Using the last stage we have to perform the alignment of the test masses and compensate the residual seismic noise below 1 Hz. LSS includes a dedicated set up for controlling the position and orientation of the suspended masses to the respect of the local reference frame It is useful also for dumping large oscillation eventually excited during the adjustment phase.

The last stage has to operate in an ultra high vacuum environment. Moreover, to avoid extra dumping mechanisms and spurious couplings the use of magnetic and electrostatic materials must be limited as much as possible. In particular the choice of the suspension material and its shape is crucial for limiting the thermal noise contribution of the interferometer sensitivity.

The mechanical and electromagnetic design is conceived following specific requirements:

- The mechanical resonance frequencies of the last stage elements must be as high as possible to avoid spurious thermal noise contributions to the interferometer output
- The steering of the optical elements needs to be performed in an ultra-high vacuum (UHV) space.
- The payload components (marionette, reaction mass and e.m. actuators) has to be conceived in such a way to limit the dust contamination of the optical element during the assembly phase and in operation (class 1 clean-room compatibility)
- It is necessary to limit the cross-talk effects among the various degrees of freedom to be controlled. This implies an accurate design of the electromagnetic actuators and a careful design of the suspension point of the mechanical elements.

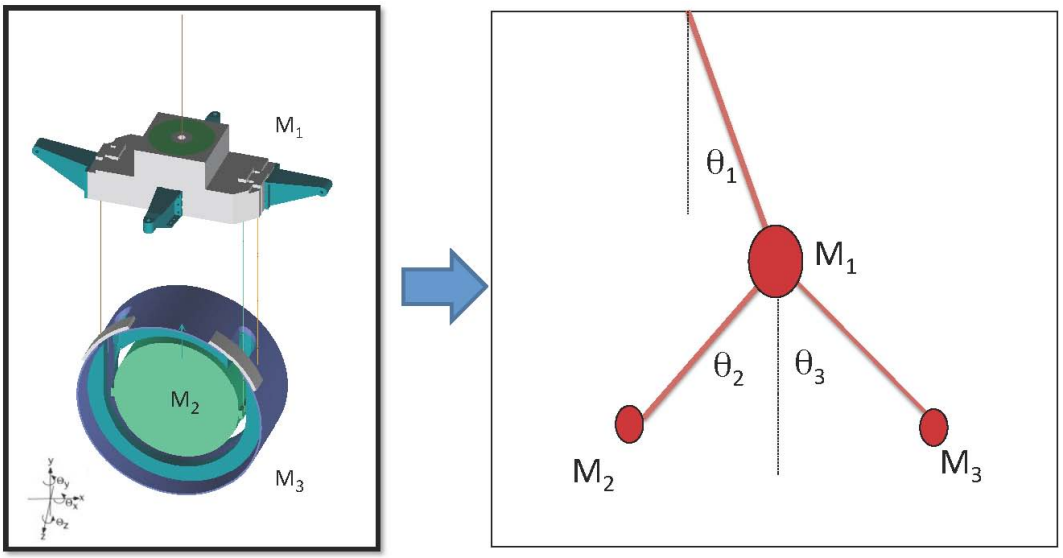

Figure 128: Left: Sketch of the Virgo-like Last Stage suspension. Right: Scheme using the point-like masses M_1: Marionette, M_2: Mirror, M_3 : RecoilMass

In particular, to fulfill the last requirement to simplify the Multi Input Multi Output (MIMO) control, we have to keep

- the center of masses alined along the Superattenuator axis
- the three principal axis of the ellipsoid of inertia of each suspended body parallel to the gravity line, the interferometer optical axis and its transversal direction.

Finally, we add a couple of constraints derived from our past experience of controlling the Virgo mirrors:

- we need to limit the recoil effect by optimising the mass values of the suspended elements,
- we should avoid the insert of composite bodies (as for example a mirror clamped to an external frame) along the main beam path, which can cause the presence of spurious resonance in the control bandwidth of he instrument.

In the next sections, we model the thermal noise of the mirror suspension and we describe the mechanical designs for LF- and HF-ET. Then we focus on the control issues and the related actuators and sensors. Finally we discuss the technologies to be developed.

4.4.1 Material selection for the last stage suspension

The last stage suspension is the most critical point of the whole suspension chain. It determines the thermal noise of the suspension elements. Thus, low mechanical loss materials in combination with a monolithic suspension technique as used in GEO600 [356, 357] and the Advanced Detectors [6, 358, 359] is preferred. Here the material of choice is fused silica which fulfills these requirements and has been studies in great detail in the past.

In the low temperature detector the suspension elements have to fulfill a second crucial duty - they have to extract the thermal load that is put into the optical component by the laser beam. This additionally demand rules out fused silica as a suspension element due to its very small thermal conductivity at low temperatures as an amorphous material (see figure 129). In contrast, crystalline materials have a very high thermal conductivity at low temperatures.

Both materials—silicon and sapphire—show a large thermal conductivity in the temperature region of interest

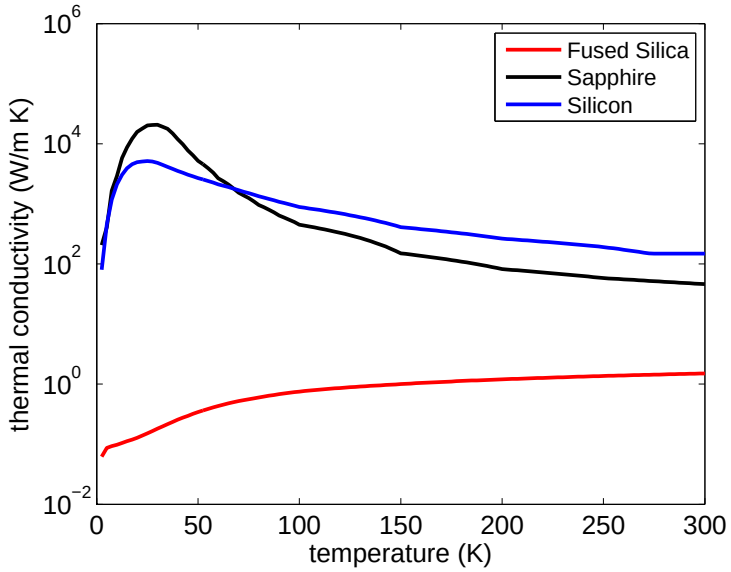

Figure 129: Thermal conductivity of bulk fused silica, sapphire and silicon. The plotted values are obtained from Touloukian [360, 361] as 'recommended' curves.

(typically below 20 K which will be shown later by means of thermal noise considerations in section 5.6.5). Sapphire has a higher thermal conductivity as silicon below 20 K. Sapphire fibres for heat extraction have been investigated in detail by Japanese groups for CLIO and LCGT [362–364].

A third point for the selection of the suspension material is the possibility to bond the suspension element to the test mass. As will be shown later the most likely substrate material will be silicon for the Einstein Telescope due to its availability in large pieces. Sapphire samples are not available in large enough pieces which are needed for the LF detector (see section 5.6.1). The bond strength of sapphire-silicon [365] bonds is smaller than silicon-silicon [365, 366] bonds based on hydroxid-catalysis-bonding. The reason for the weaker bonds in a sapphire-silicon configuration is so far unknown—beside direct chemical effects during the bonding process imperfections in the polished surfaces of the bonded samples are very likely to be the origin of this effect. Besides the weaker bonds the different coefficients of thermal expansion might cause stress during operation at low temperatures which might reduce the reliability of the sapphire-silicon bonds.

All these considerations lead to a preferred design based solely on silicon. Silicon suspension elements are currently under investigation in the form of fibres [367] and ribbon-like structures [368]. Details about the ongoing work can be found in section 4.5.

The thermal conductivity of crystalline materials is dependent on different effect:

- the concentration of impurities,
- the sample dimension,
- the phonon density at the given temperature.

These properties define the shape of the thermal conductivity curve in dependence on temperature. At higher temperatures thermal phonons collide with other phonons or impurities which leads to a finite thermal conductivity. At lower temperatures the effect of phonon-phonon collision becomes weaker due to the reduced density of phonons. The impurities dominate this region. At sufficient low impurity concentrations the thermal phonons begin to collide with the sample boundaries before other collisions. The phonons propagate now ballistically and the thermal conductivity becomes geometry dependent. At even lower temperatures the thermal conductivity decreases due to a lack of available phonons for carrying heat. This general behaviour of a crystalline material

can be seen from figure 129.

A very high impurity density is present in polycrystalline samples. Here, the grain boundary act as very efficient scattering surfaceimpurity and reduce the thermal conductivity of the sample (see figure 130). In order to get high thermal conductivity suspension elements polycrystalline samples need to be avoided.

The effect of impurities and phonon-phonon scattering by means of N- and U-processes on thermal conductivity has been studied in detail in the past [369, 370]. For very pure silicon samples it was observed that the natural composition of isotopes acts as scattering centers as well. If these scattering centers are removed by enriching the silicon with one isotope the thermal conductivity can be even further increased (see figure 130).

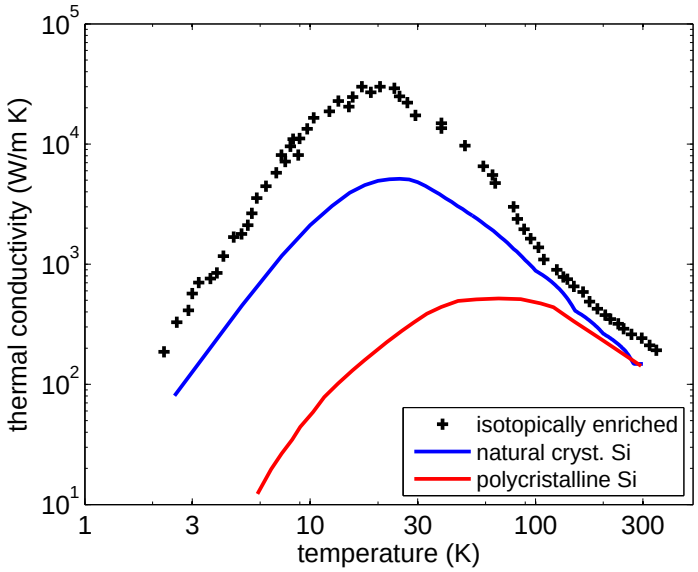

Figure 130: Thermal conductivity of silicon. The results for natural and the polycrystalline silicon are obtained from [360] for the isotopically enriched sample from [371].

The impact of the sample geometry on the thermal conductivity will become important for the design of suspension elements. These elements are naturally thin in at leas one dimension. If one dimension of the suspension element gets into the region of the mean free path of the phonons the thermal conductivity becomes size limited.

A detailed theoretical model of thermal conductivity in semiconductors including scattering of phonons at other phonons, impurities and boundaries can be found in [372].

It is clear from this observation that for all calculations that include the thermal conductivity of small samples great care must be taken. A conservative value of 1000 W/m K at 10 K for the total thermal conductivity was assumed in the following calculations, which incorporates already phonon-boundary and impurity scattering.

Besides thermal conductivity the specific heat capacity as well as the coefficient of thermal expansion (CTE) play an important role in order to build a low noise suspension. The heat capacity of crystalline materials follows Debye's T^3-law. Thus, at very low temperature we expect very small values for the heat capacity (see fig. 131(a)).

The CTE determines the level of thermo-elastic loss and thus thermo-elastic noise of the suspension elements. Here, fluctuations of the local temperature is directly transferred into a position fluctuation by means of the CTE. In order to get a low level of thermo-elastic noise it is necessary to choose an operational temperature that provides a low CTE. Fig. 131(b) summarises the temperature dependence of the CTE for sapphire and silicon. The general trend shows that lower temperatures lead to smaller CTE. Silicon has a special behaviour where

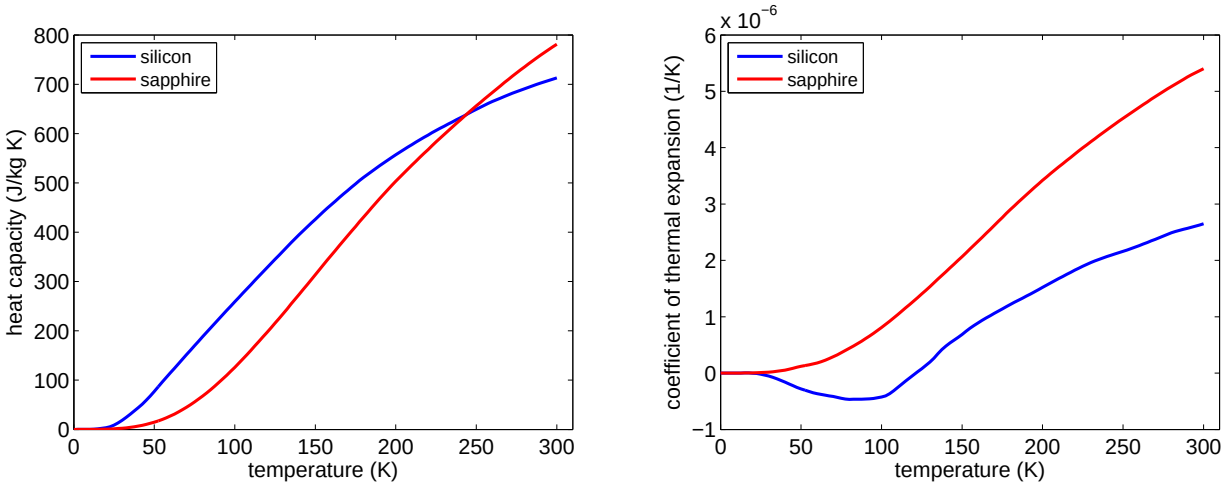

(a) Heat capacity ([373, 374]).

(b) Coefficient of thermal expansion ([375, 376]).

Figure 131: Heat capacity and coefficient of thermal expansion for silicon and sapphire as a function of temperature. The heat capacity of both materials follows the predictions of the Debye-law that states a T^3 behaviour. The coefficient of thermal expansion also decreases with decreasing temperature. Silicon shows a special behaviour having two distinct temperatures (around 18 K and 125 K) where the coefficient of thermal expansion vanishes.

the CTE changes its sign at 125 K and at around 18 K. Thus, at these two point the CTE is zero and thus the contribution of the thermo-elastic noise in theory zero. However, due to the demand that the suspension element has to extract the residual heat from the optical absorption in the test masses they will not be in a thermal equilibrium and thus a homogeneous temperature distribution along the fibre/ribbon cannot be expected. The lower the overall temperature of the suspension element is the smaller the total thermo-elastic noise contribution.

Brownian thermal noise of the suspension is strongly dependent on the mechanical loss of the suspension element. The mechanical loss is usually studied by means of a ring-down experiment. For different materials this parameter has been studied in the past in detail (see e.g. [368, 377–381]) both for bulk materials (see section 5.6.1) and suspension elements made from fused silica (see e.g. [382–386]). There is only little known about the intrinsic loss of silicon or sapphire samples with dimensions close to the ones used in suspension elements. Silicon studies have revealed that thin silicon flexures can reach a mechanical loss as low as 4.4×10^{-7} at about 80 K [368] and even 3.5×10^{-8} at around 10 K [381]. The mechanical loss of a thin silicon flexure studied down to 10 K is presented in figure 132(a). The mechanical loss drops by around 3 orders of magnitude during cooling from room temperature to below 10 K. The behaviour of the mechanical loss is dominated by the thermo-elastic damping at higher temperatures. At around 125 K the vanishing CTE causes a dip in the mechanical loss curve.

Compared to the mechanical loss of bulk silicon this value is slightly higher. The reason for this higher mechanical loss is currently assumed to be associated with surface losses. The investigation of the origin of these surface losses is within the focus of the current R&D (see section 4.5). Losses of about 10^{-8} are believed to be within the range of achievable values by the time ET will be built.

Figure 133 summarises the different loss contributions of a fibre suspension element typically needed for ET. While at room temperature thermo-elastic loss contributions dominate the low temperature suspension element is limited by intrinsic mechanical loss and surface loss which is assumed to be frequency independent as a first approximation. Both, the mechanical loss as well as the surface loss of silicon structures are within ongoing investigations (see Sec. 4.5.3). For the ET design a conservative estimate fof 1×10^{-8} was assumed for typical suspension elements. However, each improvement in the mechanical loss or the surface loss of the suspension elements leads to further lowering of suspension thermal noise.

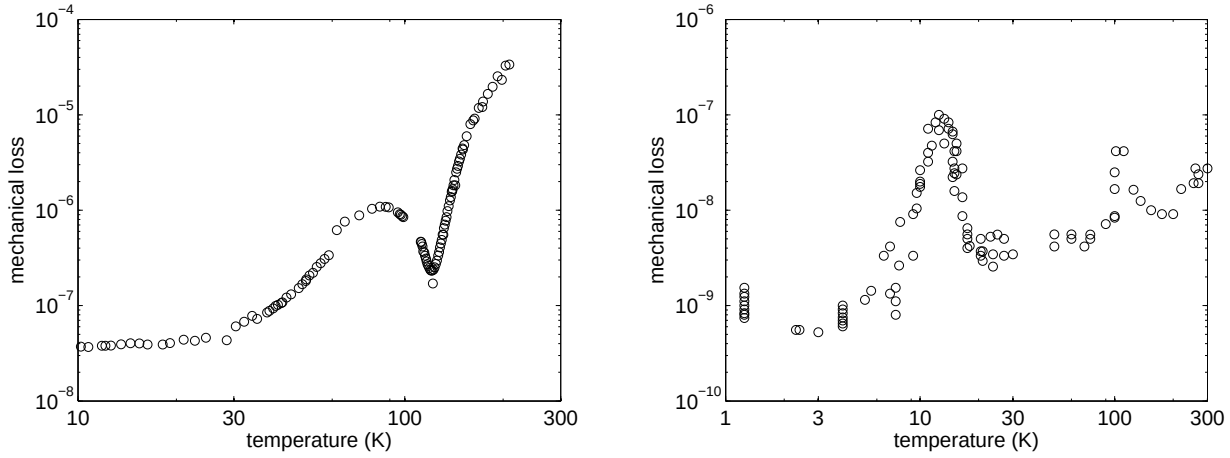

(a) (b)

Figure 132: Comparison of the mechanical loss of silicon. (a) – silicon flexures [381] at 19.6 kHz, (b) – bulk silicon [377]. Loss peaks in the bulk material measurement are associated with impurity induced losses that can be avoided.

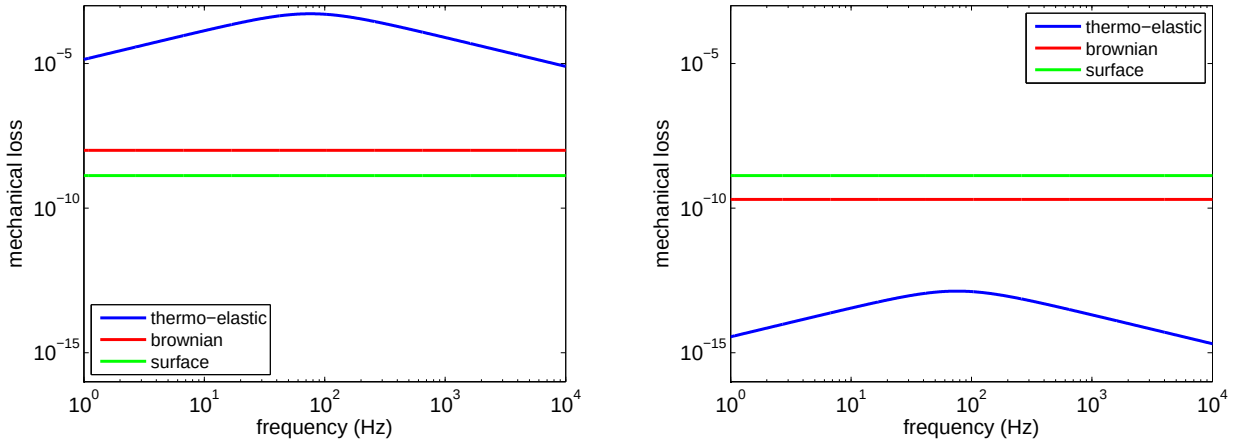

(a) 300 K. (b) 10 K.

Figure 133: Comparison of the loss contributions of a suspension fibre with a diameter of 3 mm that has been proposed to be used for the low frequency detector of ET.

Currently, there are two possible techniques under investigation for the fabrication of silicon suspension elements. The first technique is the so-called micro-pulling technique [367]. Here, a thin fibre with typical diameters in the lower millimetre range is drawn from a silicon melt. The fabricated fibres are not perfectly single crystalline - but recent work has improved the crystallinity of the fibres. Currently, these fibres are produces with a length of 30 cm for the initial investigations. In principle there is no limit for the maximum achievable length and thus this technique is promising to be used for the low temperature suspensions for ET. For technical details of the fibre pulling technique see the section 4.5.1.

The second attempt is to use suspension structures etched out of single crystals or wafers. This technique provides suspension elements with a rectangular or quadratic cross section due to selective etching of the

crystalline silicon in different directions. This technique utilises different well established processes from the fabrications of MEMS (micro-electro mechanical systems). A very well known and accurate silicon processing exists to fabricate structures out of crystalline silicon. Figure 134(a) shows such a typical element. A thin silicon flexure was fabricated from Si-wafers with a rectangular cross-section. The thickness of the flexure is in the range of a few 10 microns while the width and the length are in the range from 5 to 70 mm. The selective etching technique is just limited by the wafer size and in principle it is possible to create much longer elements. These structures have been used to investigate the intrinsic losses of silicon flexures [368] as well as intrinsic losses of coating materials applied to them [387–389].

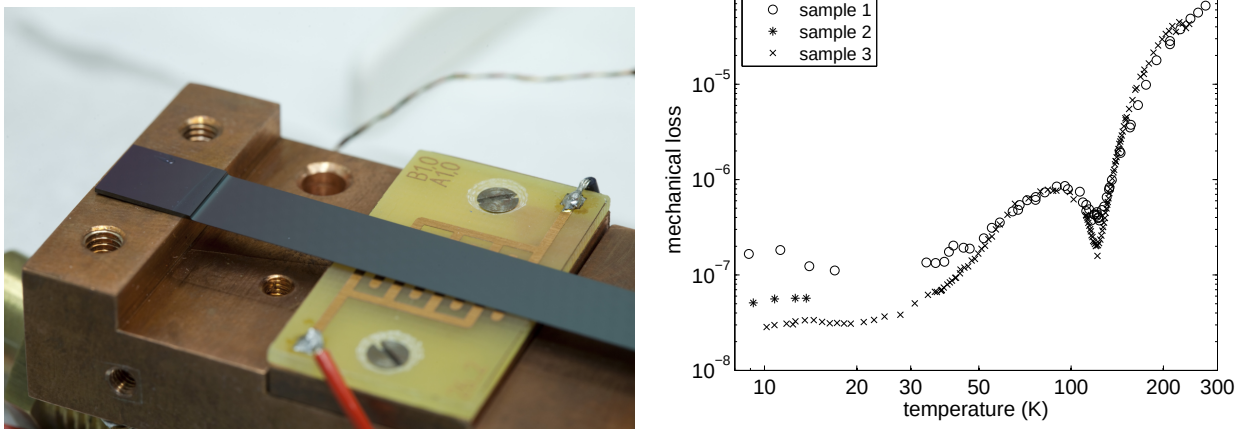

(a) (b)

Figure 134: (a) Silicon flexure etched out of a silicon wafer. (b) - Mechanical loss obtained from different surface qualities. Depending on the surface preparation different roughnesses have been obtained (sample 1 - 330 nm, sample 2 - 33 nm, sample 3 - 6 nm; RMS roughness over 100 μm).

There exist different etching techniques to fabricate such structures. The most frequently used ones are selective wet chemical etching and dry etching. These two technique provide different surface qualities strongly depending on the exact process parameters. Fig. 134(b) indicates that the minimum obtainable loss from these devices at low temperatures is strongly surface dependent. The origin of the surface losses in silicon are so far not fully understood and within the focus of the research carried out by several institutions involved in this design study (see section 4.5.3).

The promising flexure structures that are currently available and that are showing very low mechanical losses have an anisotropic stiffness due to their geometry. While in one direction the suspension element is soft (e.g. in beam direction) it is very hard in the perpendicular direction. This might lead to problems in the control of the interferometer (see section 4.4.7). Therefore, the investigation of the fabrication of crystalline fibres as well as novel control strategies including anisotropic properties need to be done. A summary of ongoing R&D activities regarding the suspension elements can be found in section 4.5.

4.4.2 Suspension thermal noise model

Box 4.2: Thermal noise

Thermal noise is due to the brownian motion of the molecules of a system continuously exchanging thermal energy with the environment at thermal equilibrium, via the dissipation mechanisms. As a result the thermal noise of a macroscopic body is a fluctuation of its position which can be formally described as a displacement spectrum using the fluctuation dissipation theorem (FDT). For this reason temperature and mechanical losses are important parameters for the entity of such a noise.

Thermal noise of the mirror suspensions is one of the intrinsic limits to the detector sensitivity in the low frequency range below 10 Hz. To calculate the thermal noise curve of this system along the horizontal and vertical degrees of freedom, we can write the Lagrangian by supposing the 3 elements as point-like masses so that the Virgo-like last stage suspension is a cascade of three pendula: to the first pendulum (the marionette, M_1) the mirror M_2 and the recoil mass M_3 are hung as branches (see figure 128). As a consequence the rotations about the coordinate axes are not included. This choice can be reasonable if we suppose a negligible coupling of such degrees of freedom with the interferometer output coordinate.

The study of the thermal noise of this system can be carried on by using two different methods: the Fluctuation Dissipation Theorem (FDT) and the modal expansion methods [390, 391]. For both these methods we write the motion equations from the Lagrangian and the dissipation functions.

The FDT approach uses the mechanical impedance matrix $\hat{Z}$. The spectral density of the thermal displacement noise of the i_{th} mass of the system, is given by the formula:

$$S^i_{therm}(\omega) = \frac{4k_bT}{\omega^2}\mathcal{R}e\left\{(\hat{Z}^{-1})_{ii}(\omega)\right\} \tag{81}$$

where k_b is the Boltzmann constant and T is the temperature of the system. In the modal expansion method, the motion equations are diagonalised and the normal modes frequencies and coordinates are found in function of the free oscillators ones. In this way it is possible to infer the frequencies, the displacements and the losses of each pendulum from the measured ones on the system modes. The main difference between this model and the FDT treatment, is that it allows us to insert the Langevin stochastic thermal forces independently acting on each pendulum. In this way we can study it even in a steady thermal state in which every oscillator has a different stationary temperature.

This behaviour can be schematised by setting each mass of the i_{th} pendulum at steady thermal state T_i as if it has a constant heat exchange with a thermal bath at the same temperature. In this case each pendulum is subject to a different thermal stochastic force:

$$< F^2_{thi} >= \frac{k_bT_iM_i}{\tau_i}; i = 1, 2, 3 \tag{82}$$

Using the modal expansion model it can be shown that the thermal displacement noise of the i_{th} mass is also affected by the thermal noise of the other masses of the pendulum chain, mainly by the marionette's stage via its dissipation mechanisms. The FDT and the modal study of the thermal noise lead to the same result if the temperature of the whole suspension is homogeneous. A complete study of both the models can be found in the reference [390], here we will illustrate the main calculation lines of this method.

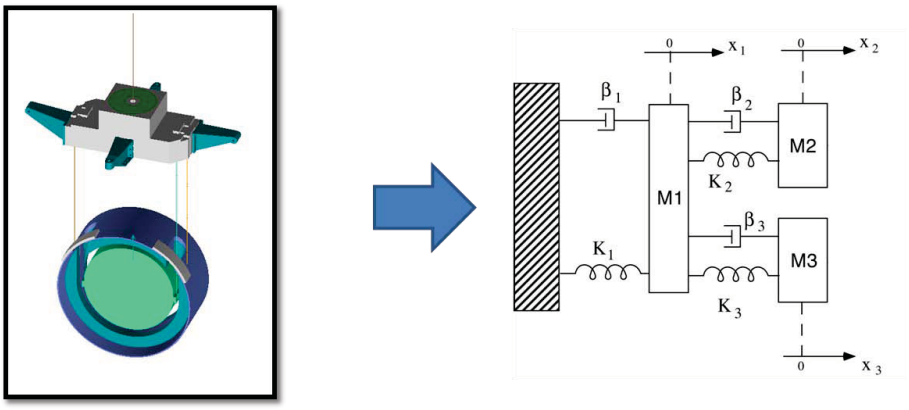

Figure 135: A Virgo-like last stage suspension is a cascade of three pendula. To the first pendulum (the marionette, M_1) the mirror M_2 and the recoil mass M_3 are hung as branches.

4.4.3 Normal mode formalism

In the mode expansion, the eigenvectors of the characteristic matrix of the system are the coordinates Y_-, Y_0, Y_+ of the modes and its eigenvalues are the modal frequencies $\omega_-, \omega_0, \omega_+$, thus every normal quantity is a function of the uncoupled ones. Moreover, the stochastic normal forces F_-, F_0, F_+, acting on each mode, are found in function of the uncoupled ones [390].

Within this formalism, the mirror coordinate X_2 is expressed in terms of the normal eigenvectors and its thermal noise is calculated with its power spectrum. We find:

$$\left\langle X_{th2}(\omega)^2 \right\rangle = \left\langle {F_{th1}}^2 \right\rangle |T_{n1}(\omega)|^2 + \left\langle {F_{th2}}^2 \right\rangle |T_{n2}(\omega)|^2 + \left\langle {F_{th3}}^2 \right\rangle |T_{n3}(\omega)|^2 \tag{83}$$

where $T_{ni}(\omega)$ are generalized transfer functions depending on the uncoupled mechanical parameters of the pendula [390].

This result is fully equivalent to the FDT calculation shown in equation (81) at homogenous temperature, however the explicit dependance on the temperatures T_i (in the $\left\langle {F_{thi}}^2 \right\rangle$ given by the equation 82) is the new result which permits to calculate the thermal noise of a suspension at a thermal steady state but with the stages at different temperatures.

4.4.4 Thermal noise computation of LSS for the LF interferometer

Using equation 83, we have studied the thermal noise of a Virgo-like last stage suspension for the LF cryogenic interferometer characterised by the parameters summarised in table 7. The working temperature at the mirror level is 10 K, corresponding to the minimum mechanical losses of the coatings ($Ti : Ta_2O_5$, see section 5.6). The material for the mirror bulk and its suspension wires is silicon with a loss angle of 10^{-8} (see sections 4.4.1 and 5.6). The marionette and the RM masses have been chosen in order to reduce the marionette recoil effects as much as possible. For this reason the marionette mass must be the sum of the masses of the mirror and the RM at least. The materials used for making the suspension wires are silicon for the RM and Ti6Al4V alloy for the marionette with a loss angle of 10^{-5} [392]; their length is 2 m. The diameter of the silicon wire has been chosen to be 3 mm: with this value the temperatures of the marionette and the mirror in the steady state are 2 K and 10 K respectively with a silicon wire having an thermal conductivity which is more than an order of magnitude worst than that one of the highly pure material (with 1000 W/K/m mean value see section 4.4.1). These value can take into account the presence of the thermal resistances due to the contacts between the mirror wire and the suspension system.

	Marionetta	Recoil Mass	Mirror
Masses for ETDLF (kg)	422	211	211
Wire Diameter (mm)	3	3	3
Wire length (m)	2	2	2
Wire Material	Ti6Al4V	Silicon	Silicon
Loss Angle	10^{-5}	10^{-8}	10^{-8}
Temperature (K)	2	10	10

Table 7: Parameters used in the design of the mirror last stage suspension for the LF interferometer.

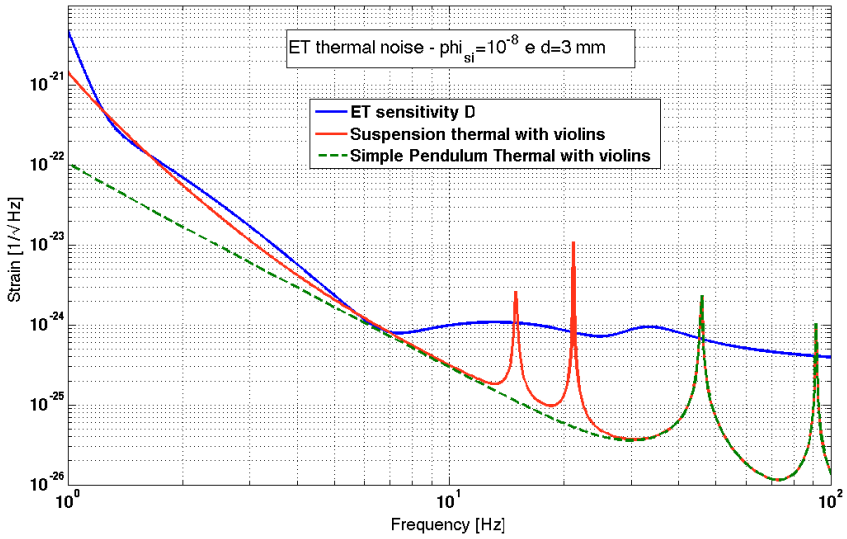

Figure 136: ET-D-LF sensitivity curve (blue) compared with the suspension thermal noise calculated with the parameters of the table 7 (red) and with the simple pendulum thermal noise (dashed green).

The obtained thermal noise curves have been compared with the ET-D goal sensitivity curve where the power stored in the cavities of the cryogenic interferometer 18 kW. The results are sketched in figure 136 where the obtained suspension thermal noise is also compared with the simple pendulum one. It can be noticed that, below 10 Hz, the overall contribution of the whole last stage suspension system is higher than that one of the simple pendulum, and it must be taken into account for a correct optimisation of the sensitivity curve in this range of frequency.

4.4.5 The payload of the HF interferometer

The LSS design of ET-HF is greatly based on the experience on Virgo and Advanced Virgo. The marionette will be almost the same as in Advanced Virgo, while the recoil mass design of can be adapted to different mirrors lengths. We will accommodate in it the thermo compensation plate (CP), an other optical element s essential for compensating the thermal lensing induced in the test mass mirror by the huge laser power stored in the HF Fabry-Perot cavities. A Marionette Recoil Mass is being developed: facilitates installation and operation for large diameter mirrors, could improve thermal noise matching for Test Mass Mirrors, it is necessary for larger mirrors (i.e. the BS).

The materials with low acoustic loss for the mirror and for the suspension is crucial to reduce the thermal nose contribution to the sensitivity of ET-HF. In the marionette design the requirements for cleanliness, vacuum compatibility, mechanical precision, magnetic and electrical properties apply. Moreover several new aspects must be considered: the use of the fused silica fibres and the change of geometry of the mirror.

Moreover, monolithic suspensions currently being tested in GEO and with a 21 kg mirrors in Virgo should be developed for a 200 kg test mass (4.5.2). In the case of the monolithic suspensions, the silica wires must be attached to the marionette by a new kind of clamps which must not introduce further mechanical losses in the interface between the silica and the marionette surface. These new clamps have to be placed in such a way the fibre bending point lays on the horizontal plane passing through the centre of mass of the marionette to minimise the coupling between different degrees of freedom. As the wire bending section is different by the clamping section, because of the tapered fibre tip (see section 4.5.2), this is carefully taken into account in the new design. The coupling between the marionette and the fibre also influences the mounting procedure of the payload and consequently the new assembly tool design. Moreover the change of the position of suspension wires of the new reference mass, and, in case of need, of the balancing motor, are taken into account.

In the new reference mass (RM) design the requirements for cleanliness, vacuum compatibility, mechanical precision and magnetic and electrical properties apply. The new design takes into account the bigger thickness and mass of the mirrors, the implementation of the mirror control and the thermal compensation system.

The actuators have to be designed to fulfil the displacement requirements for the locking purposes and consequently are related to the optical configuration. There are two different options for the mirror actuation by the reaction mass: the coil-magnet actuators and the electrostatic actuators. We present them in the sections 4.4.8, 4.4.9.

The RM surrounds the mirror in order to protect it by accidents and hosts its actuators. It is equipped with safety stops designed taking into account the different shape and increased mass of the mirrors suspended with a monolithic structure. The design is conceived to host the ring heater and compensation plate foreseen in the thermal compensation system. To this aim, the dielectric parts of the RM must work at high temperature because of the possible contact with the heaters. The presence of a compensation plate could deeply affect the dynamical behaviour of the last stage suspension: the centres of mass of mirror and RM must coincide to reduce the coupling among the various degrees of freedom. The structure required to carry the compensation plate will make more difficult to satisfy this requirement.

In the case of the coil-magnet actuation (see section 4.4.8), here assumed as the reference solution, it is necessary to design RM as made of a dielectric material to avoid eddy current dissipation and magnetisation effects. The mechanical strength of the new insulating material must allow to use the reaction mass also as a safety structure for the mirror.

The dielectric material must be chosen to be UHV and cleanliness compatible. However, it could produce electrostatic charge on the mirror by friction with the RM. A solution can be the use of dielectric materials having also a resistivity value sufficient to avoid the formation of stray currents but reduces the presence of static charges. A possible choice is the TecaPeek CF30, a kind of polymeric plastic, loaded by carbon and grafite particles to increase its density and have a slight electrical conductivity which is useful to avoid the static charges formation.

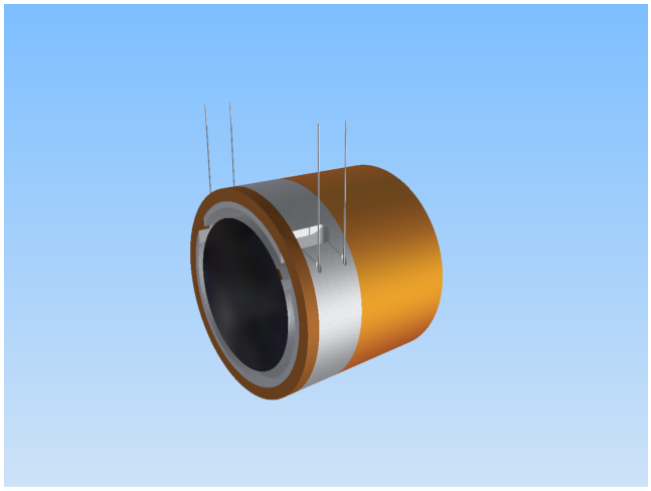

Figure 137: Schematic picture of the new mirror reaction mass. The various colors indicate the different materials used.

The ET configuration for the last stage suspension system can include a new element: the Marionette Reference Mass (MRM). The new element will permit

- to suspend a larger diameter mirror avoiding any mechanical interference between the marionette and the pots installed on the separating roof of the Ultra High Vacuum (UHV) chamber;
- to simplify the payload installation and its preliminary alignment procedure;
- to guarantee a high level of mirror cleanness without spoiling mechanical performance of the suspension system.

The MRM will be suspended within the UHV chamber between the marionette and the last filter of the *Superattenuator* chain. It will host the actuator coils for steering the marionette. In this way a more compact design of the payload will be conceived and the IVC structure could be revised to accommodate a mechanical filtering system for the air flow entering within the UHV chamber. Following these project guidelines, the payload integration on the suspension system will benefit of:

- a wider clearance for the monolithic payload assembly, including the possibility to install a larger diameter mirrors;
- a compact payload, which is pre-aligned before the final installation in the vacuum chamber. In this way it is possible to reduce the time spent by the operators for the installation and positioning;, which is the main cause of environmental pollution;
- a quasi-laminar flow of clean air within the UHV chamber volume to be used during the assembly phase (TBC).

Monolithic fused silica (FS) suspension of the four 200 kg Fabry-Perot cavity mirrors will be realised for ET HF, exploiting the experience achieved developing the Virgo+ payload. The optimal geometry and technology is being pursued with the objectives of minimising the pendulum thermal noise, fulfilling the requirements for an optimal control of the test mass, ensuring safety and reliability. For Virgo+ a large amount of work has

been made to reduce the risk in the welding procedure. The fibres (once welded directly to the mirror) are now welded to intermediate components (called ears) silicate bonded to the lateral flats of the test mass (see figure 138). The former procedure induced a lot of thermal stress on the bonded surfaces that could damage the silicate bonding and eventually break it. Another problem is that the fibres pass through a dangerous manipulation procedure that can open cracks on their surface decreasing their breaking strength. To recover these problems a new technique has been developed: two lateral supports with vertical grooves are attached using silicate bonding to the mirror lateral flats. In parallel, a fused silica bar is previously welded to an upper clamp and a lower anchor and then the fibre is produced. The fibres are then placed in position clamping the upper part to the marionette and inserting the lower anchor below the lateral supports bonded to the mirror. In the end the anchor and the supports are bonded together through silicate bonding or *water glass*. Although this solution has been successfully implemented for Virgo it would be easier (and with lower mechanical dissipation) to avoid the lateral bonding of the supports to the mirror.

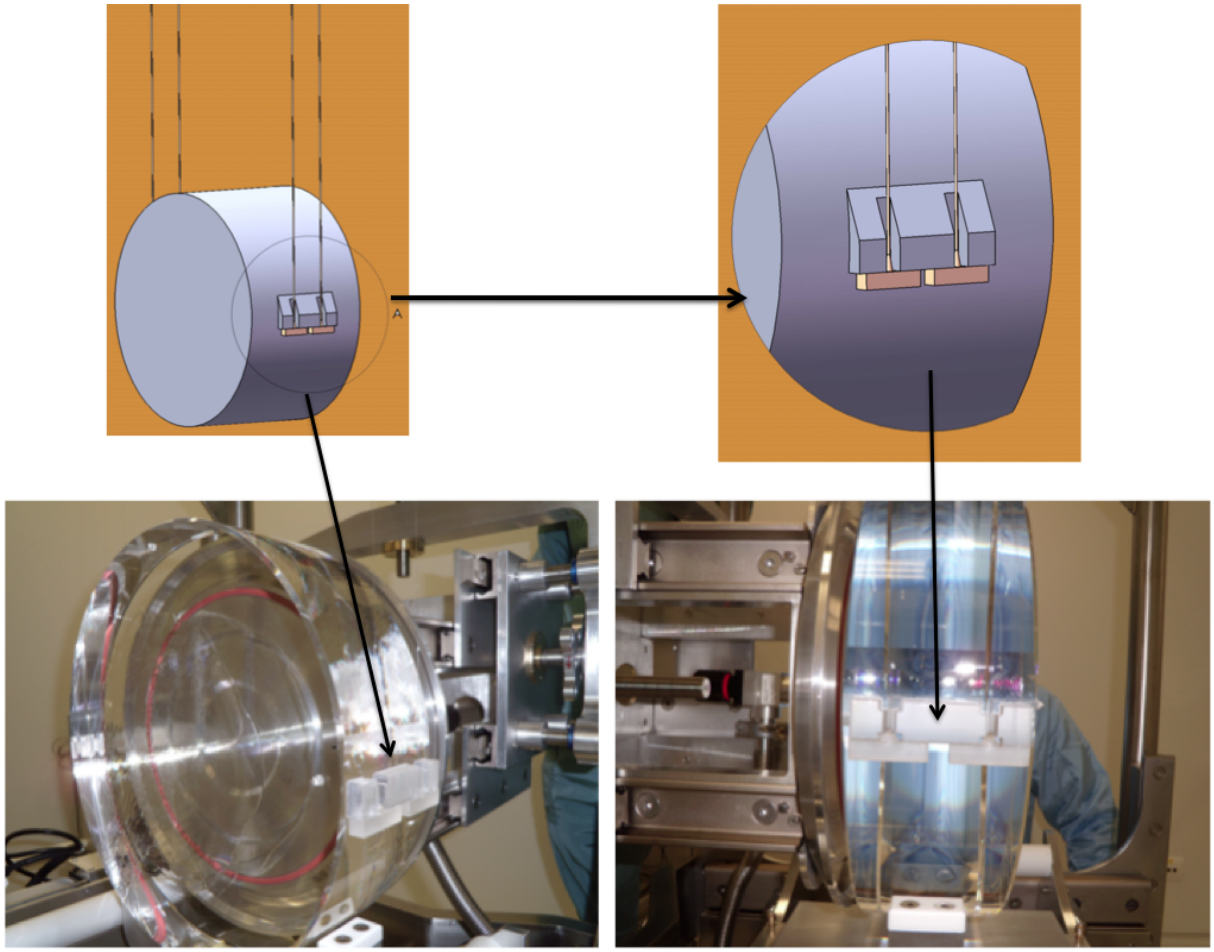

Figure 138: On the upper part of the figure we show a scheme of the silica anchor attached by the silica bonding. The various colors indicate the different pieces bonded each other. In the lower part we show the frontal and lateral views of a Virgo mirror with the silica anchors already bonded.

The suspension scheme, already tested inVirgo, will reduce the most critical part induced by silicate bonding the lateral supports on the lateral mirror flats. The supports can be machined out from the mirror , the lower surface of the support is polished to perform a silicate bonding which will be discussed in the following section 4.5.2. The suspension scheme proposed is the following: one fused silica part called "anchor" will be welded to a $\sim 7\,\mathrm{mm}$ fused silica bar and to an upper clamp. Using the CO_2 laser machine the fibre will be produced from the bar welded to the clamps, the whole clamp-fibre will be placed in position on top to the

marionette and on the bottom under the mirror support. The contacting surfaces of the two parts (both with a polishing) will be bonded onsite using the silicate bonding or *water glass* procedure as for Virgo. To this aim it is necessary to find a geometry of the lateral supports easy to machine, and to demonstrate that the surface quality is sufficiently good for thermal noise performances.

The role of the upper clamps coupling with the marionette in order not introduce further frictions and recoil losses is very important. For this purpose a stainless steel box has been carefully designed with the aim to host the silica upper clamp and to attach it to the marionette without introducing further losses. The steel box is formed by two pieces. An external one fastened to the marionette by four screws. An internal one in direct contact with the fused silica and fastened by lateral screws to the external one. The silica core is kept fixed in its box by an upper lid fastened by screws. The steel inner box is also designed as the support of the upper clamp during the fibre pulling (see section 4.5.2) and then is coupled to the tool used to insert the fibre on the marionette lateral side, as foreseen by the assembly procedure.

4.4.6 The payload of the LF interferometer

Assuming for ET an optic configuration with mirror losses of the order of 10^{-6} and a stored light power of $\sim 18\,\mathrm{kW}$, we deal with the need to implement a cryogenic system able to extract tens of milliwatts of heat from the mirror during the working steady state. This requirement is compatible both by defining a cooling strategy based on closed loop cryo-coolers or by setting up a dedicated liquid helium plant.

Moreover for the employment at low temperature in a GW detector we need to design the suspension system in such a way

- to transmit the refrigeration power to the mirror without spoiling the control procedure of the mirror degrees of freedom
- to extract the heating power coming from the laser light in the more efficient and quicker way.

The materials used for building a cryogenic payload must follow these requirements, thus those materials with a very high thermal conductivity, good mechanical and optical properties at low temperature can be taken into account. Silicon is one of the best candidates both for the mirror and its suspensions in this case, indeed it has a very high thermal conductivity and very low thermal expansion rate. On the other hand the silicon material has very low mechanical losses at cryogenic temperatures.

For this reason in our analysis we have considered a last stage suspension designed as it is in the Virgo interferometer with a silicon mirror suspended to silicon fibres in a monolithic way.

The choice of the materials for building the marionette and the recoil mass must fulfil the requirements given by the work at cryogenic temperatures. In figure 139 it is shown how a cryogenic suspension should work during the interferometer operation, i.e. when the payload has been cooled down and the laser is turned on. The fraction of the laser power, which is absorbed by the mirror ($\dot{Q}_{\mathrm{laser}}$), flows through suspension wires; then it crosses the marionette clamps and reaches the refrigerating system. To this aim the marionette is directly connected with very efficient, soft heat links to the cooling power.

In a similar way as for the mirror the reaction mass is cooled down via its suspension wires and, if there is not extra thermal input on that, it reaches the thermal equilibrium and acts as a thermal shield for the mirror. The choice of the wires for the recoil mass must fulfil the request of having a good mechanical and thermal performance. For this reason, the use of a silicon suspension also for this part is a possible option.

In the scheme there is also the reaction mass of the marionette (MRM), absent in the present Virgo-like payloads. This part is an intermediate element between the marionette and last filter of the higher suspension which can act as a mechanic and thermal decoupler and as a thermal shield. In our study the MRM is not included because it has a negligible contribution to the thermal noise of the mirror [390].

The thermal equilibrium is reached when the power extracted by the cooling system is equivalent to that one absorbed by the mirror ($\dot{Q}_{\mathrm{abs}} = \dot{Q}_{\mathrm{coolsys}}$). At this condition most part of the power absorbed by the mirror

flows through its suspension wires (a small fraction is lost in radiation), and then it is removed by the heat link directly connected to the cooling system. The equilibrium temperature of the mirror $T_{\rm mir}$ can be calculated by the simple analytical model relating it to the temperature of the thermal bath $T_{\rm bath}$ of the cooler via the power flow through the mirror wires:

$$\dot{Q}_{abs} = \frac{4\Sigma_w}{L} < K_{si} > (T_{\rm bath} - T_{\rm mir}) \equiv \frac{1}{Z_{\rm therm}} \Delta T \tag{84}$$

where we have

$$< K_{si} >= \frac{1}{\Delta T} \int_{T_{\rm bath}}^{T_{\rm mir}} K_{\rm si}(T)\, dT \tag{85}$$

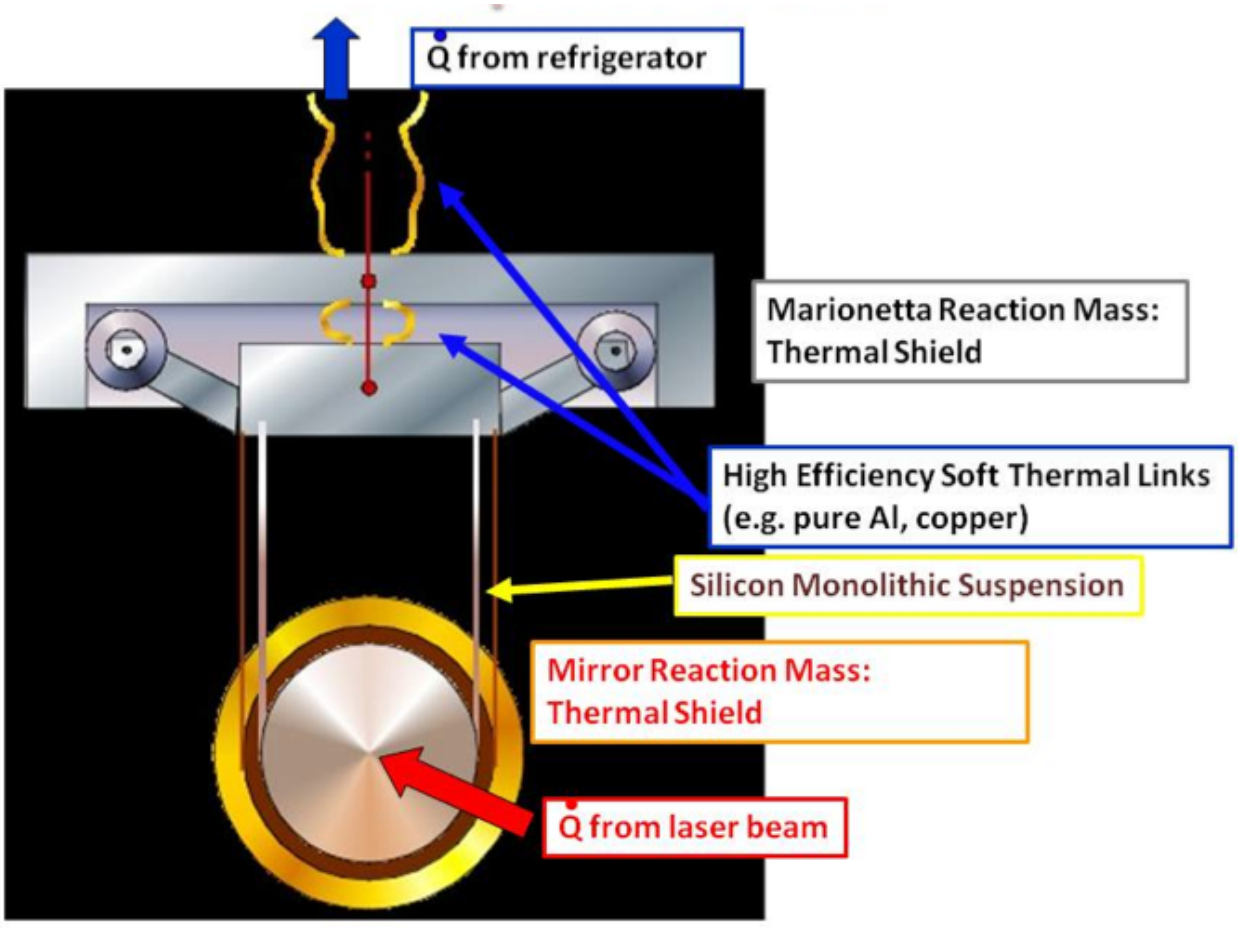

Figure 139: The conceptual scheme for a cryogenic suspension

where Σ_w is the wire section, L its length and $K_{si}(T)$ is the thermal conductivity of silicon. For a given thermal input $\dot{Q}_{abs}$, the thermal impedance Z_{therm} is important to yield the final temperature of the mirror: this is the quantity which sets up the performance of our system and influences the choice of the material and of the geometry of the mirror suspension wire.

On the other hand, also the transient phase to reach the steady state must be taken into account, because we do not want too much long cooling times. For this reason the thermal capacity of the whole system plays also a role. Thus the presence of all the masses of the system is important for determining its thermal behaviour.

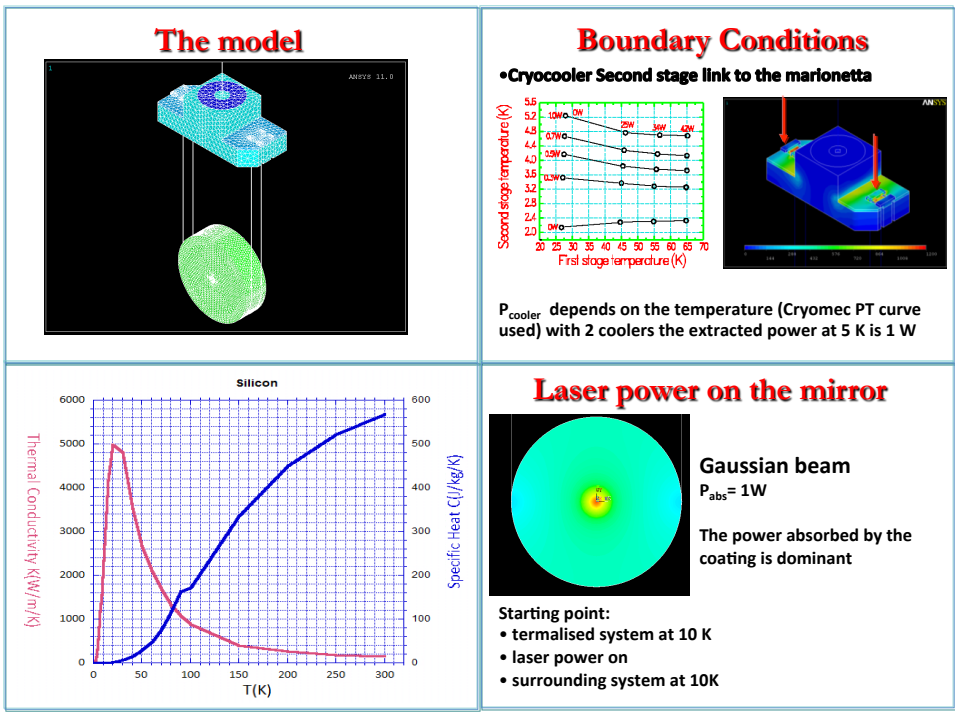

Figure 140: The reaction masses are not present in the simulation, their screen effect is simulated by the surround system at 10K. The marionette arms are not present, silicon thermal properties vs temperature are included in the simulation.

To this aim some studies with a finite element simulation have been helpful. In figure 140 it is shown the FEM model developed to perform such a study. The reaction masses are not present, for reasons of computing time, and their screen effect is simulated by the surrounding system at 10 K. For similar reasons as for the reaction masses, the marionette arms are not present. The mirror is suspended with a silicon fibre of 1 mm diameter. The silicon thermal properties vs temperature are included in the model. The mirror is heated with a power of 1 W distributed around its centre with a gaussian shape to simulate the laser mode. The cooling power, directly linked to the marionette, comes from 2 pulse tube cryocoolers with a cooling capacity (W) depending on the temperature: when the last stage of the cryocooler (cold finger) is at 4.5 K the power is 1 W, while at 20 K the cooling power is about 10 W. At the thermal equilibrium the cold finger temperature is 4.5 K. A similar behaviour is obtained using the liquid helium with a temperature of the thermal bath of 1.8 K. The simulation results agree with the formula (84) when $T_{\rm bath} = T_{\rm cold\ finger}$ and give the thermal distribution on the whole payload, as shown in figure 141 where it is evident that the final temperatures of each payload elements are not the same.

This result cannot be neglected when the thermal noise of the last stage suspension system is calculated for two main reasons: the thermal properties of the suspension wires change as the second equation in (84) shows; a different temperature upper stage can differently influence,depending on its temperature and mechanical losses, the thermal noise of the mirror. For these main reasons we presented in the previous paragraph 4.4.2 the thermal noise model generalised to the case of the stages at different temperatures.

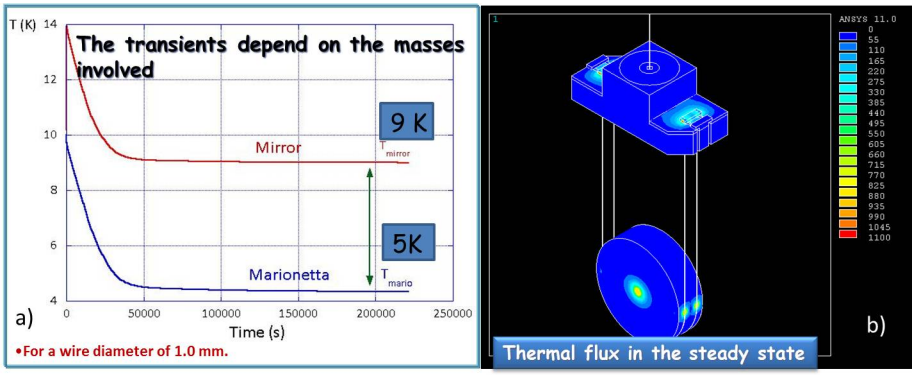

Figure 141: FEM results: a) time evolution of the mirror's and marionette's temperatures, b) thermal distribution on the whole payload.

4.4.7 The payload local control for ET

The local control of test masses plays a crucial role in gravitational wave detectors with independent test masses. Payload local control system is meant to slow-down and align the test masses as interferometer's mirrors, driving their dynamics within the gain range of automatic error signals (wavefront sensing for angles and locking for longitudinal position). As said, in order to preserve the quasi-inertial state guaranteed at the level of payload suspension point by the Superattenuator, only internal forces should be used. The procedure developed in Virgo should be easily tuneable towards the advanced detector performances; on the other hand the ET digital/analogic chain (Fig. 142) needs to be improved, namely by reducing by more than one order of magnitude the overall low frequency noise re-injection during locking force reallocation to payload stages. The related R&D will naturally follow the developments of advanced detector implementations.

However, the ET system will be complicated by the presence of cryostats surrounding the vacuum chambers hosting the payloads (Fig. 142), whose design will not be trivial.

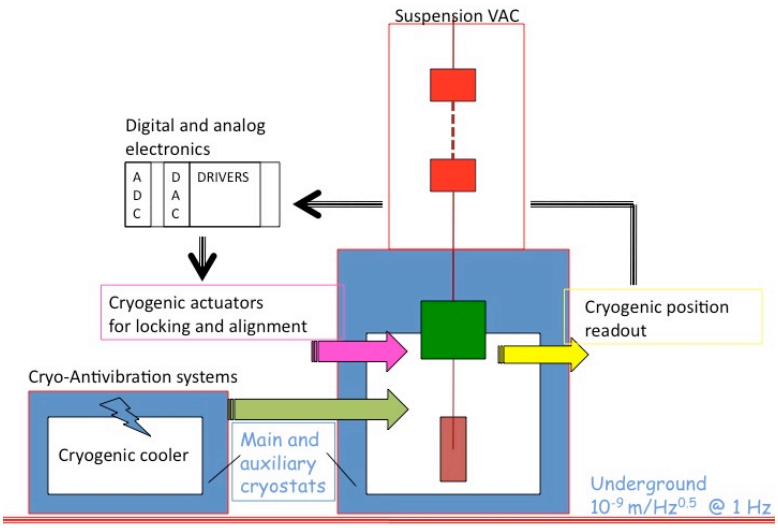

Figure 142: Schematic picture of ET suspension assembly concerning local control role.

The main issues that drive ET-related R&Ds concerning local controls leading to the identification of final solutions are listed below.

- Sensing access to the mirror position without significant perturbation of cryostat performance in mirror cooling.
- Non-perturbing or reliably reproducible effect of cryogenics onto mirror position-sensing apparatus.
- Compliance with cryostat links and its vibration control system.

For a cryogenic detector the viewports are sources of thermal input, a safe engineering approach is to limit the number of viewports to be installed.

The fibre-optic lever technique is the simplest method for non-contact and high-precision displacement detection. Its principle was originally recognised by Frank and Kissinger, then analysed by Cook and Hamm. The sensor utilises the internal reflection properties of step-index fibres that have significant motion sensitivity as a displacement transducer.

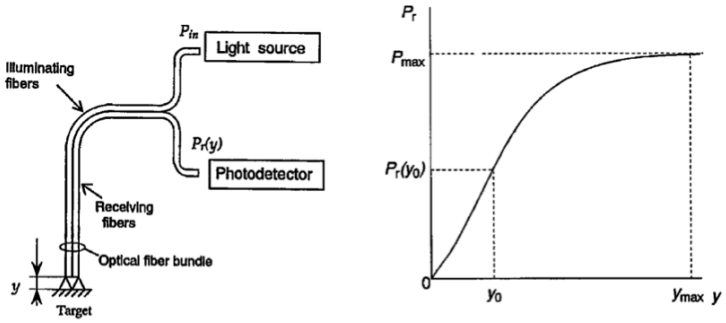

Figure 143: On the left sensor we show a schematic illustration of a basic optical fibre displacement. On the right we plot a typical curve of the receiving light power versus the gap y between the fibre bundle end and the target surface.

The system consists of a light source, a bifurcated optical fibre bundle, and a photosensor. The light radiated from the light source enters the illuminating fibres and then radiates to a target. It forms a diverging cone or annular ring on the target surface. The reflected cone is differentially subtended as a function of the target distance, by receiving fibres and is transmitted to a photosensor. Consequently, the target distance is sensed by the photosensor as the subtended power. The device has been used successfully at low temperature during the cryogenic payload test carried on at the Virgo site.

To that extent, imaging systems (e.g. CMOS or CCD cameras), the use of optical conduits and bundle-fibre-served position sensor devices have also been considered for *coarse* mirror control together with short-arm optical levers and small interferometric systems for *fine* in order to provide the required dynamics of error signals (from several mrad's to nrad's). The scheme of payload local control will be studied in compliance/integration with the spurious low-frequency vibration injection arising from cryogenic system. Hence low frequency cryogenic sensors (accelerometers) are being developed for this purpose.

Normally, as done in Virgo, the centres of mass of the suspension bodies are close to bending points of suspension wires. That is a condition which is particularly relevant for the marionette. For ET the payload will necessarily be controlled also transversally to the beam direction in order to prevent the mirror roll through the transmission of residual transversal disturbance reaching the marionette suspension point. Hence dedicated actuators and sensors will be added to the simple scheme of Virgo. In must be remarked that given the delicate balance demanded to payload marionettes further balancing counterweights (transversal) will be also needed.

Even though the thermal contacts allowing the cooling down of the payload will transmit a vibration that can be made smaller than ground seismic vibration by using passive or active systems, from the point of view of the dynamical state of marionette's suspension point, isolated by the ground through the Superattenuator that

will appear as a mechanical short-cut and expectedly dedicated inertial sensing/control system will be needed at the level of Superattenuator/payload interface.

4.4.8 The coil–magnet actuators

The actuators acting on the marionette and the reaction mass are designed to allow active control of the locking and alignment during operation.

Small and fast corrections of the mirror position can be obtained, through the marionette, if the mechanical transfer function of the system is taken into account. For example, due to the response of pendulum mechanical filters, the displacement amplitude of the mirror face with respect to that applied to the marionette arms decreases with the frequency. Then, in order to avoid self-oscillations at higher frequencies, a significant increase of the feedback gain, at the edge of the dynamics of the electronics, is needed. Furthermore, when forces are applied to the marionette, the spectral components of the feedback energy can be absorbed at the mechanical resonant frequencies of the SA, making the desired control more complex. Then, the need of direct actuation of the mirror for fast position control has motivated the use of a reaction mass.

In the present Virgo configuration two magnets are placed on the marionette x oriented arm and have the axis in the direction z. The other two, attached on the marionette z arm, are oriented along y. Through these two pairs of actuators, and choosing properly the sign of the currents flowing into the coils, it is possible to steer, around θ_x and θ_y , and displace, along y and z, the mirror and the reaction mass as a whole. Longitudinal and angular forces can be applied to the mirror by coil-magnet actuators, which are attached to the reaction mass and the mirror respectively.

In order to design the coil - magnet actuators for the marionette and the mirror of the LF interferometer, several constraints must be taken into account.

Here we considered only the effect of the magnetic noise produced by the magnet at 4.2 K and its magnetisation change due to the cooling, the current noise of the coil and the power dissipated by the current flowing in the coil.

The force exerted onto the magnet by the coil is $F = \alpha\mu I$ where μ is the magnetic moment of the magnet, I the current in the coil and α depends on geometrical factors. It can be shown that the interaction force has a maximum at an optimal distance between coil and magnet and can be considered constant for small displacements around this position and for small misalignment of the magnet axis with respect to that of the coil [355]. As μ and I play the same role in determining the actuator force, similar considerations hold for both the quantities.

As regards the magnetisation, measurements have been carried out on a cylindrical SmCo magnet [393], 10 mm diameter and 4 mm height, axially magnetized, of the same type used in the Virgo marionette. The magnetic field at room temperature at the top surface of the magnet is 0.36 T. For convenience, all the low temperature data have been taken at 4.2 K, in liquid helium at atmospheric pressure. The measurements of magnetisation change have been performed with a fluxgate magnetometer with cryogenic probe and the magnetic noise measurements with a commercial SQUID system coupled to a superconducting pick-up coil fixed coaxially on the magnet 144. A detailed description of the experiment is reported in [394] and here we summarise just the results having an impact on the ET design study.

Figure 145 shows a typical flux noise spectrum (calculated at the SQUID loop and expressed in units of $\Phi_0/\sqrt{Hz}$, $\Phi_0 = 2.07 \times 10^{-15}$ Wb), produced by the magnet in the niobium shield and obtained by combining two spectra taken with different frequency range and averages.

In order to determine the different noise contributions, several noise measurements have been realised in different configurations. The analysis of these measurements has suggested the following interpretation of the noise spectrum of figure 145.

At frequencies higher than 200-300 Hz the noise is dominated by thermal magnetic noise that is magnetic field fluctuations arising from the thermally agitated motion of electric charges of the conductor (SmCo in this case).

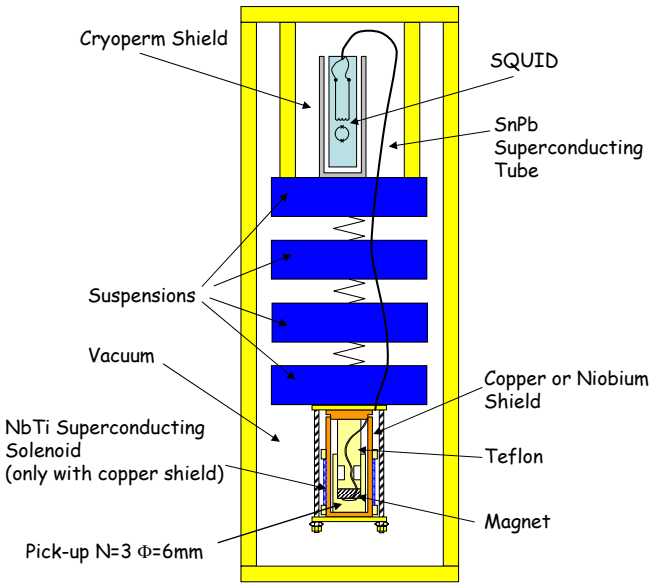

Figure 144: Experimental set for the magnetization noise measurements at 4.2 K.

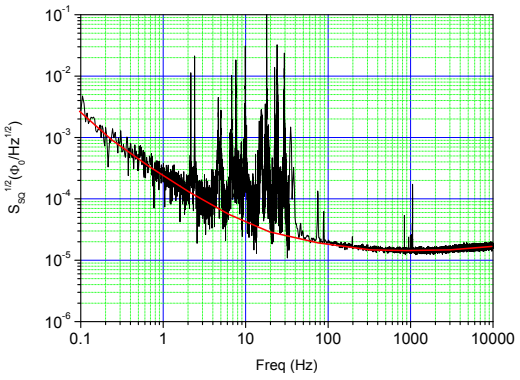

Figure 145: The magnetic flux noise spectrum produced by the SmCo magnet and referred at the SQUID loop. The spectrum is obtained by combining two spectra taken with different frequency range and averages.

This noise can be related to the temperature of the metal via a Nyquist type relation. A similar noise level has been obtained with the stainless steel cylinder. Vibrational peaks are present between 2 e 100 Hz (as expected, suspensions are effective between 100 and 1000 Hz). Between 0.1 and 4 Hz the noise, of the $1/f$-type, is due to the magnet and tends to decrease with time.

We have also measured the noise produced by the magnet when it is subjected to a dc or low frequency (0.1 Hz) magnetic field with magnitude comparable to that needed to produce a force of the order of 1 mN. All the tests have shown that the application of magnetic field does not change the noise of the magnet.

The frequency range 2–100 Hz is dominated by vibrational peaks but the shape of the magnet intrinsic noise can be easily guessed and is described by the red curve in figure 145 that we consider as reference noise level for the following calculation of the force noise acting on the mirror.

As the force of the actuator is proportional to the magnetic moment of the magnet and this is proportional to the magnetic flux picked-up by the pick-up coil connected to the SQUID, we have

$$\frac{{S_{\Phi p}}^{1/2}}{\Phi_p} = \frac{{S_F}^{1/2}}{F} \tag{86}$$

where ${S_{\Phi p}}^{1/2}$ is the flux noise at the pick-up in Wb/$\sqrt{\text{Hz}}$, Φ_p is the DC flux at the pick-up in Wb, ${S_F}^{1/2}$ is the maximum force noise of the actuator in N/$\sqrt{\text{Hz}}$ when the maximum force F is generated.

Then, from the noise spectrum of figure 145 expressed as the equivalent flux noise at the pick-up ${S_{\Phi p}}^{1/2}$, the dc flux that crosses the pick-up Φ_p, and the maximum force F needed, the force noise that the actuator exerts on the mirror (or the marionette) can be estimated.

For example, considering one of the mirror actuators with a maximum force needed of 0.1 mN and the mirror (200 kg) as a free mass one can calculate, from the force noise, the displacement noise spectrum and then the equivalent strain noise spectrum on the basis of the 10 km arm length ET-D LF model. The comparison with the ET-D LF total noise is shown in figure 146.

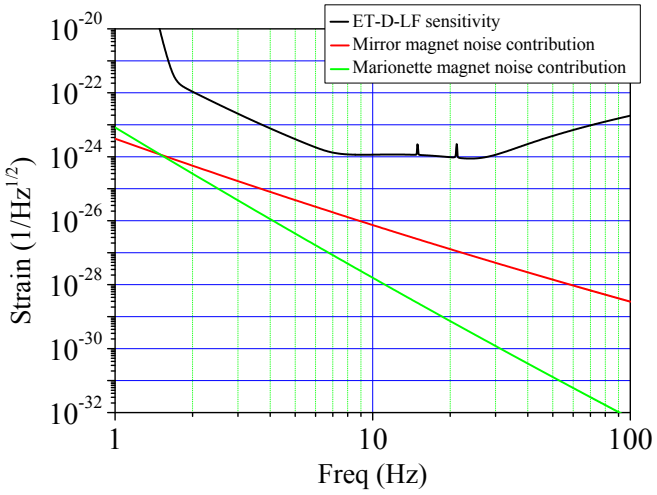

Figure 146: Magnetic noise contribution to the strain sensitivity in the case of maximum force of 0.1 and 0.5 mN compared to the ET D sensitivity curve.

In the same figure it is also shown the strain noise contribution considering one of the marionette actuators with a maximum force needed of 5 mN. This rough estimation has been obtained by assuming the marionette as a free mass and the resonance frequency of the mirror pendulum (about 0.3 Hz) much less than the considered noise frequencies.

As is evident from this figure we can conclude that the displacement noise at the mirror level, induced by the coil-magnet actuators of the marionette and mirror, is negligible.

To design the actuators acting directly on the mirror a further constraint, related to the thermal noise of the mirror pendulum mode, has to be considered. The random magnetic force exerted by the actuators has to be kept below the intrinsic noise limit of the system, i.e. the mirror thermal noise force S_{f_T} :

$$S_{f_T} = 4k_B T Re\Big[Z(\omega)\Big] = 4k_B T \frac{\Phi M {\omega_o}^2}{\omega} \tag{87}$$

where $Z(\omega)$ is the mechanical impedance of the suspended mass and Φ is the loss angle of the mechanical system assumed to be frequency independent. Here, the second equality holds in the simplified case of a simple pendulum.

The e.m. actuators are used in the digital control loop to keep the interferometer locked. During the operation, these kinds of actuators have to adjust the mirror position along a 1 μm range. As the force acting on the mirror is a linear function of the current I flowing in the coils, we have introduced the actuation factor $\alpha_m = F^{(m)}/I$. The control loop, which concerns these magnetic actuators, is conceived to compensate the fast changes in the mirror position and orientation. The quantised electronic noise of the digital feedback loop drives the random motion of the mirror. The noise spectral density of the current driving the reaction mass coils is intrinsically related to the noise injected into the control loop by the readout. The simplest readout scheme is a system of two components: a photodiode and a mixer. This second element is needed to demodulate the signal of the interferometer. To characterise the noise figure of the photodiode we can introduce the parameter D^2 defined as

$$D^2 = \frac{\langle i_d \rangle^2}{S_{in}} \tag{88}$$

where $\rangle i_d \langle$ is the mean current flowing into the mixer which follows the photodiode readout and the current noise spectral density of the photodiode:

$$S_{in} = 4e^2 D^2 \tag{89}$$

Using the two previous equations (87), (89) and imposing the inequality $4e^2 D^2 {\alpha_m}^2 \ll S_{f_T}$, we get the upper limit for the actuation factor

$$\alpha_m \ll \frac{1}{e\ D} \sqrt{k_B T M \frac{{\omega_o}^2 \Phi}{\omega}} \tag{90}$$

A typical figure of the ET parameters is: $\Phi \sim 10^{-8}$, $M \sim 200\,\mathrm{kg}$, $\omega_0/2\pi \sim 0.3\,\mathrm{Hz}$, $D \sim 10^8\ \sqrt{\mathrm{Hz}}$, and $T \sim 10\,\mathrm{K}$. Then, from equation (90) we derive the upper limit at $\omega/2\pi \sim 1\,\mathrm{Hz}$:

$${\alpha_m}^{(max)} \simeq 4 \times 10^{-4}\,\mathrm{N/A} \tag{91}$$

The typical driving current of the actuators compatible with the low noise regime of the electronic drivers is in the range of few mA. It follows that the maximum force exerted on the mirror will be in the range of 10 μN providing to use magnets of small magnetic moment in order to limit the viscous dissipation effect due to the eddy currents on marionette and reaction mass. However, in order to achieve the condition in which, at low frequency, the ET sensitivity is limited by the internal friction of the mirror pendulum mode, we must use a dielectric material both for the reaction mass and the marionette arms.

Box 4.3: The need of low dissipative actuators for ET-LF payload

We have to point out that in a cryogenic apparatus we need to limit the power dissipated in vacuum by the current flowing into the actuator coil. It useful to report here the observation done on a prototype of cryogenic payload cooled at 10 K. The payload has the typical dimensions of the Virgo and it holds a fake 20 kg mirror made of silicon. It is equipped with actuator coils made of copper, by means of which we measured the electro-mechanical transfer function of system at low temperature. To do that we need to drive the actuators with an electric current of few mA. Despite of the significant decrease of the copper resistivity with temperature, the heat radiated in vacuum cause a large drift of the temperature of silicon mass as it is shown in figure 147. These measurements suggested us to design the ET coils made of NbTi with the core made of copper. In this way at cryogenic temperatures we will take advantage of the superconducting transition of the metallic alloy.

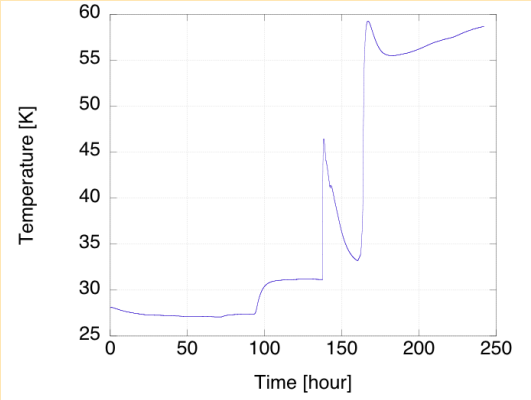

Figure 147: The temperature drift of the 20 kg silicon mirror hold in a prototype of cryogenic payload during the mechanical transfer measurements.

4.4.9 The electrostatic actuators

Electrostatic Actuators (EA) are an interesting alternative for the control of the test masses, respect to the widely used coil-magnet pairs.

Such solution was already applied for the GEO 600 detector [395] and it is under study also for other detectors, currently adopting coil-magnet pair actuators. The use of EA offers several advantages. The first one is the possibility to keep the mirrors under control without the need of gluing the magnets on the mirror bulk, saving, in this way, the mechanical quality of the test masses and, as a consequence, reducing the final thermal noise [396]. Another advantage is the strong reduction of the coupling with external magnetic fields, that is an important issue for magnetic actuators, since no direct coupling is anymore possible in the case of EA. Another possible advantage, mainly for third generation detectors, is linked to the possibility to control the suspended test mass, in science mode, only from the previous suspension stage, avoiding the need of a reference mass. In this case an electrostatic actuator, fixed on ground, represents the simplest way for the lock acquisition without adding any extra noise when the control is transferred to the upper stage.

The working principle of an electrostatic actuator is simply described by standard electrostatic, giving, for a device of capacitance C, polarized at fixed voltage V, a resulting force along the x axis equal to:

$$F_x = -\frac{1}{2}\left|\frac{\mathrm{d}C}{\mathrm{d}x}\right| V^2 = -\alpha V^2 \tag{92}$$

where the capacitance is supposed to vary by changing the system characteristics along the x axis while the minus sign is due to the characteristic of such forces, that are always attractive. In the case of actuator for suspended dielectric mirrors, such devices mainly consist in a set of close conductive strips, arranged in a suitable geometry, alternately polarised at two different voltages. The strips, together with the dielectric suspended test mass, placed at distance a x with respect to the actuator plane, constitute a capacitor, with a capacitance variable by changing the distance of the test mass with respect to the actuator.

The deduction of the theoretical expression of the capacitance, for such system, is described in [397]. It can be written as: For the simplest geometry, i.e. a set of N parallel conductive strips with period b, rectangular in shape, of length L and width a, laying on a substrate with relative dielectric constant ϵ_s, placed at distance x from the test mass having a relative dielectric constant ϵ_m, the capacitance can be written as:

$$C(x) = C_\infty \alpha_m \left(\tilde{a}, \tilde{x}, \epsilon_m\right) \tag{93}$$

where $\tilde{a} = a/b$ is the normalised strip width, $\tilde{x} = x/b$ is the normalised distance, α_m is a function of the listed parameters describing the effect of the mirror at distance x, and C_∞ is the capacitance of the isolated actuator (i.e. with $x \to +\infty$). This expression is calculated in the approximation of infinitely long strips and taking into account only the contribution of the first image charges, both for the substrate and for the mirror. As a consequence the capacitance of real devices become different from the this value for small values of x with respect to b due to the increasing weight of border effects and image charges as the distance decreases [397].

The force expression (92) has to be modified to consider also the presence of a stray electric charge q on the dielectric mass. In this case, by making the simple approximation that the electric field is proportional to the polarisation voltage applied to the actuator, it is possible to write:

$$F_x = -\alpha V^2 + \beta V \tag{94}$$

where the factor β is, in general, a function of the charge q, the distance x and the geometry of the actuator. The effects of this term were already observed on a similar set-up [398], and some techniques for its mitigation were already developed [399]. To reduce the effect of the stray charges, it is also possible to modulate the driving signal, to obtain a zero averaged contribution of the linear term of the actuation force even in presence of charges on the test masses [400]. This driving technique was already successfully experimented in the control of a bench top Michelson interferometer with a suspended mirror controlled by a such EA [401].

To clarify this approach, let $A(t)$ be the driving signal we want to apply on the test mass, A_{DC} the voltage bias and $f_M = \omega_M/2\pi$ the modulation frequency of the full driving signal. The square root is computed and sent, with the modulation, to the actuator driver. In this way the voltage applied to the actuator is:

$$V = G\sqrt{A_{DC} + A(t)}\cos\omega_M t \tag{95}$$

where G is the gain of the EA driver. With this voltage, the force exerted on the test mass becomes:

$$F = -\frac{1}{2}\alpha G^2 \left(A_{DC} + A(t)\right)\left(1 + \cos 2\omega_M t\right) + \beta G\sqrt{A_{DC} + A(t)}\cos\omega_M t \tag{96}$$

If the modulation frequency is chosen at enough high frequency to have negligible effects on the test mass motion and the frequency content of the driving signal is much smaller with respect to f_M, the main contribution of the force (96) only consists of a DC bias term plus a term proportional to the driving signal $A(t)$. This is the required behaviour for such actuator.

The characterization of an EA with such driving technique is described in [400]. The most interesting results are related to some observed deviation from the theoretical model. The measurements are shown in figure 148. The filled dots represent the force measured in AC bias, both with positive or negative G, while the open circles are the force measured in DC bias with different sign of G. The deviation from the foreseen behaviour, clearly visible for all the points in DC bias, in particular in the case of negative G, is due to the presence of spurious charges on the dielectric suspended mass. In fact in this case, equation (96) becomes:

$$F = -\alpha G^2 \left(A_{DC} + A_{AC}\cos\omega t\right) + \beta G\sqrt{A_{DC} + A_{AC}\cos\omega t} \tag{97}$$

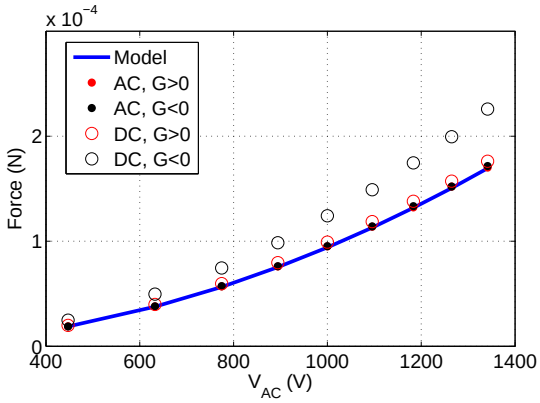

Figure 148: Comparison between the model and the force measured, in different bias conditions, for a excitation with $f = 0.1$ Hz.

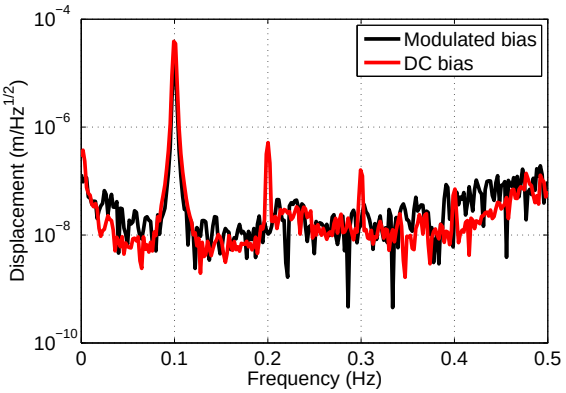

Figure 149: Spectra of the test mass displacement with the same actuation force, at $f = 0.1$ Hz in two different bias conditions.

and a not negligible contribution could arise from the last term. Moreover this contribution depends on G as confirmed by the results. The two opposite polarisation, for the AC bias, give instead the same results, as the experimental measurements are practically overlapped. This confirms the effectiveness of the alternate bias technique that is insensitive to any static stray charge present on the test mass.

Following the (97) a larger disagreement would be expected also for the case of DC bias with positive G, but one should consider that the description of the electrical field between the EA and the test mass is very roughly approximated in the model; moreover a slight dependence of β from the sing of G is expected. More investigations are need in this direction which also require some upgrade in the experimental set-up, as the possibility to change the distance between the EA and the test mass without opening the chamber and changing, in this way, the amount of charges on the mass. The displacement spectra, in case of measurements in DC bias conditions, also show additional lines placed at multiple frequency respect to the one injected by the signal. These lines disappear if the measurement is performed in AC bias as shown in figure 149.

Starting from theoretical model, and on the basis of the previous results, it not too difficult to effectively design the electrostatic actuation system for ET. By assuming a mirror mass of 200 Kg (it is slightly higher for LF-ET, but the difference is not very relevant), a wire length of the last stage of 2 m and a conservative residual motion of the test mass $x \sim 10\,\mu$m, the minimum force required for damping the mirror motion is:

$$F \sim m\omega_0^2 x = 250\,\mu\text{N} \tag{98}$$

Since the beam radius is about 9 cm and the mirror diameter is 45 cm (in the worst case) the maximum reasonable residual space useful for the EA is about 10 cm. Moreover the distance between the test mass and the actuator has to be at least 5 mm, in order to reduce the damping from the residual pressure, and this also fix the period of the electrodes strip, that has to be close to the mirror-actuator distance to enhance the field fringes. From these figures it results that each actuator can be composed by 5 strips large 4 mm arranged in concentric arches. For such pattern the model provide $\alpha = 1.8 \cdot 10^{-10}$ N/V^2. By using equation (92) it results that the required force, using 4 pattern, can be achieved with a maximum voltage of about 600 V, that is a good value for voltage amplifiers with low electronic noise and large bandwidth. After the lock acquisition the actuation noise can be easily reduced by reducing the voltage bias of the actuator, hence by reducing the noise of two order of magnitude. Of course, in case of full locking reallocation at the marionette level the electrostatic actuator can even be switched off and no actuation noise is introduced.

4.5 Technologies to be developed

4.5.1 R&D on the production of high purity silicon crystal fibre for the LF interferometer

In designing the ET low frequency cryogenic interferometer, fused silica monolithic suspensions are no longer suitable, due to a broad dissipation peak in silica around 40 K which spoils its performances. Among the suggested materials, silicon is very promising due to its very low intrinsic mechanical loss [402] [377] and thanks to the high thermal conductivity, suitable to remove the heat deposited into mirrors by the laser.

Suspension elements must therefore be realised starting from pure silicon material. A study [367] has been carried out on crystalline silicon fibres grown starting from a melt of pure silicon and using the μ-pulling down technique, to investigate the possibility of employing this technique in the realisation of silicon suspension elements in a cryogenic interferometer. The interest in this technique is manyfold. Besides of mechanical applications, silicon is a very important material for many technological fields, such as electronics, photovoltaic industry, and integrated photonics. Let see some aspects in more details. The photovoltaic industry for solar cell production is a rapidly expanding market. Many efforts are spent worldwide in order to increase the efficiency of solar cells or to diminish the production costs. In both respects the production of silicon fibres can play an important role because new geometrical schemes can be tested and the silicon fibres are produced directly in a ready-to-use shape, thus cutting the processing costs and loss of material. Another important potential application of Silicon fibres is for the transmission and processing of signals in integrated photonic circuits. Silicon has important optoelectronic properties, such as its high thermal conductivity, high optical damage threshold, and low losses in a wide spectral range from 1.2 to 6.6 μm. Recently Stimulated Raman Scattering (SRS) has been used to demonstrate Raman laser in integrated wave-guides in the near infrared (NIR) or for image amplifiers in the mid infrared (MWIR). The production of optical fibres with a silicon core would be an important complement to this emerging research field, but up to now silicon fibres have had a limited success due to the low crystal quality of the fibres. In fact a new production technique that has recently been presented is not capable to produce single crystal silicon-core fibres [403] and the presence of several domains and interfaces increase the transmission losses of the optical device. The availability of single-crystal Silicon fibres would be a great advance in this field, too.

The method of production consists in placing the melt in a vitreous carbon crucible, heated with a radio frequency generator. A seed of crystalline silicon is then inserted in an orifice at the bottom of the crucible and pulled downward. The melt cools down in a controlled way passing through the nozzle and a fibre is grown (figure 150). About 15 crystalline silicon fibres have been grown with thickness ranging from 0.3 to 3 mm and length up to 310 mm (figure 151). Produced fibres showed a good diameter regularity for most of their length, except for some abrupt change in thickness probably due to instabilities in the RF generator. The crystalline orientation was determined using the Laue X-ray diffraction method: as a result, the fibres were not single crystals, but are composed of several single crystal parts.

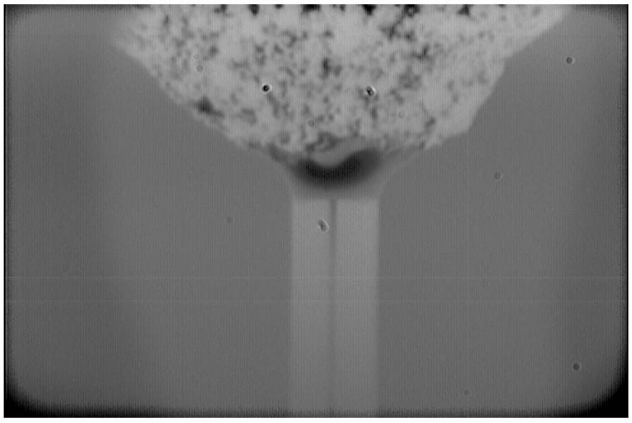

Figure 150: A closeup view of the crucible nozzle during the production of a fibre.

Table 8: Measured room temperature parameters for two crystalline Si fibres. Values are pretty close to the ones reported in literature for silicon.

length [mm]	E [GPa]	α [K^{-1}]	κ [W m^{-1} K^{-1}]
111.5 ± 0.5	150 ± 11	$(2.54 \pm 0.13) \times 10^{-6}$	146 ± 13
308.0 ± 0.5	174 ± 12	$(2.56 \pm 0.11) \times 10^{-6}$	138 ± 11

The loss angle of the fibres was evaluated at room temperature using a ring-down technique, and was dominated by the thermoelastic contribution. The thermoelastic loss peak allowed to experimentally measure the thermomechanical parameters of the realised fibres (see table 8). In order to get rid of surface contaminants (mainly SiC) the produced fibres were superficially etched before the measurements, using a HNA isotropic etching (in a 75%HNO_3, 20%HF, 5%CH_3COOH solution).

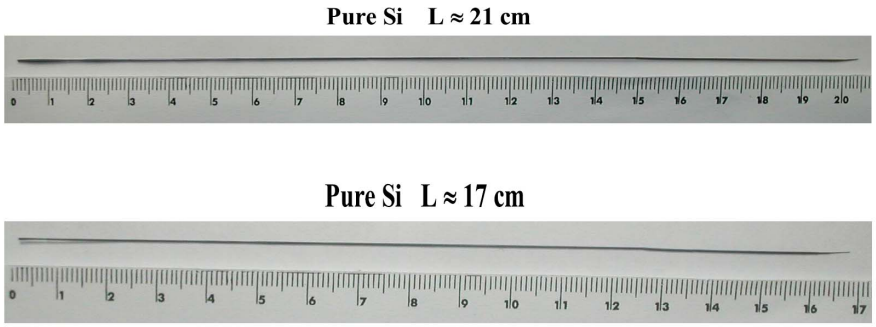

Figure 151: Two silicon crystalline fibres produced using the μ-pulling down technique.

The longest fibre among the produced ones was 310 mm long. After this study, the technique has been improved and new unpublished results have been obtained [404]. They recently succeeded in growing single-crystal Silicon fibres up to 10 cm long. In all cases the diameter is around 3 mm with small fluctuations (around 0.1 mm) along the whole length of the fibre. A successive X-ray analysis confirmed the single-crystal character of the fibres, and the only crystal phase detected is that of pure Si. Moreover a SEM analysis did not detect the presence of any impurity in the crystal material within the sensitivity of the instrument. It is presumably feasible to grow Si fibres with diameter from 0.5 mm up to 5-10 mm and virtually unlimited length. In the used facility the maximum length possible is limited to 40 cm by the dimensions of the pulling machine.

A problem was highlighted in the cited study, concerning the welding of the produced fibres to other parts. Due to the very high thermal conductivity, it turned out to be very hard to weld the fibres tip to silicon pieces. The alternative to the welding consists in using the parts to be welded as seeds for the growth of the fibre. Similarly, the crucible can be removed at the end of the pulling, leaving intact the contained material: in this way, a fibre with a thick head can be obtained. This procedure seems to be promising to realise a monolithic silicon suspension and needs to be investigated experimentally.

This study proved the feasibility of thin silicon crystalline fibres suitable to be employed as suspensions for a cryogenic silicon mirror. The investigation of the loss and thermomechanical behaviour of these fibres is an important step in the technical development of the optimal suspension design. More studies are needed to evaluate the fibres parameters in cryogenic conditions.

4.5.2 R&D on the bonding of silicon for the production of quasi-monolithic silicon suspensions

It will be necessary to identify the optimum method by which the silicon suspension elements may be attached to the silicon mirrors, whilst maintaining high thermal conductivity (for cryogenic operation) and low mechanical loss (to minimise thermal noise). The technique of hydroxide-catalysis bonding [ref Gwo patent] was implemented in the GEO600 gravitational wave detector in order to create quasi-monolithic suspensions of the

fused silica mirrors and is being used in the upgrades for Advanced LIGO and Advanced Virgo. The resultant bonding material has been demonstrated to have very low mechanical losses [ref Sneddon, Smith, Cunningham] in addition to mechanical strength (shear) being reported being > 27 MPa. Studies also suggest that hydroxide catalysis bonding is unaffected by temperature cycling [ref Elliffe], which will also be crucial for the long-term operation of ET-LF, where the use of cryogenics is required to achieve the desired displacement sensitivity at low frequency.

Various studies have already been carried out to investigate the use of hydroxide catalysis bonding for jointing silicon components [366, 405]. This includes a detailed study of the mechanical strength of bonds at both room temperature and cryogenic temperature (77 K) [405], which is summarised in Figure 152. The average bond strength at cryogenic temperature is similar to that at room temperature, albeit with a slightly larger dispersion. No correlation was observed between oxide layer thickness and bond strength above ~ 50 nm, therefore the oxide layer thickness should be minimised to this level to minimise potential thermal noise.

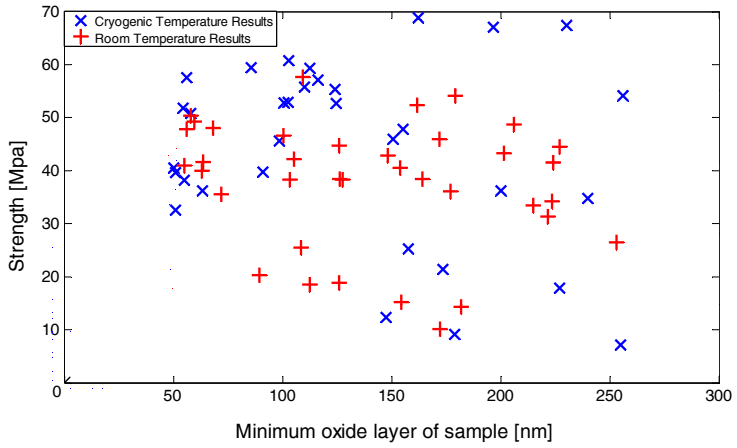

Figure 152: Plotted strength results for various silicon-silicon bonds at room and cryogenic (77 K) temperatures.

Studies are also ongoing into quantifying the thermal conductivity of bonded silicon components at low temperatures. Measurements of the thermal conductivity suggest that bonded silicon components at low temperature can be modelled as pure silicon with an thin (~ 700 nm) interfacing glass-like layer. These results, as shown in Figure 153, suggest that hydroxide catalysis bonding can facilitate the necessary extraction of heat, deposited on the mirrors by the incident laser beam, through to the silicon suspensions elements and towards the cooled upper-stage.

[we need to choose a bond area and calculate actual heat flow expected - and compare to heat flow through typical fibre geometry as a function of temperature]

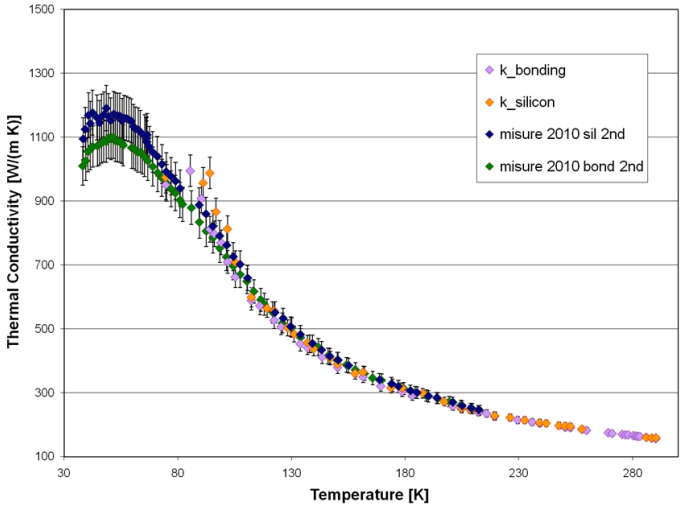

Figure 153: Measured thermal conductivity through silicon rods (1" diameter, 28 and 48 mm lengths) carried out in Florence. Bonded samples fabricated in Glasgow.

4.5.3 R&D on surface losses in silicon

At cryogenic temperatures the performance of the fibres or ribbons used as suspension elements will be limited by surface loss (see Fig. 133). Thus, the study of the surface loss mechanism is of great interest to minimise the suspension thermal noise. The wide field of micro-mechanical systems investigated surfaces losses in silicon (see e.g. [406–408]). However, a systematic and general modelling of surface losses has not been made. The origin of surface losses is still unclear and needs to be investigated.

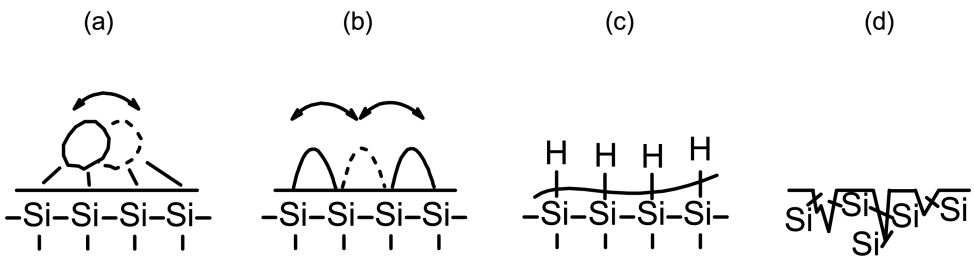

Figure 154: Possible sources of surface losses in silicon (explanation see text).

So far, possible sources of surface losses in silicon have been identified to be (see Fig. 154):

- (a) particles on the surface,
- (b) un-terminated (dangling) bonds,
- (c) surface layers,
- (d) micro-cracks in the surface layer due to mechanical treatments.

Different treatments of the surfaces lead to different levels of mechanical losses at low temperatures (see Fig. 134(b)). A possible correlation with the residual micro-roughness and/or the treatment method is currently under investigation [381]. Different treatment techniques like wet chemical etching or dry-etching (ion etching) is under investigation and the surface loss parameters are extracted.

For the ET design study a very conservative value of the surface loss has been used. However, any further improvement of surface losses will lead to a lower suspension thermal noise and thus will improve the performance

of the detector.

4.5.4 R&D on a new generation of monolithic accelerometer for the suspension control.

The development of inertial sensors, with high sensitivity and large measurement band is a key point for the inertial damping to perform on the suspension system of third generation interferometric detectors.

In particular we developed a low noise high resolution horizontal monolithic folded pendulum (FP) sensor [409, 410]. The design is based on the use of micro-machining techniques (to reduce the sensor size to dimensions suitable for placing it in sea floors or in boreholes) and the application of laser optics techniques for the implementation of the sensor readout system (to improve the sensitivity and the immunity to environmental noises) [411, 412].

An accurate description of the dynamics of a Folded Pendulum (FP) is given by the simplified Lagrangian model developed by J.Liu et al. [409], based on the mechanical scheme shown in Figure 155. The FP model consists of two vertical beams of lengths l_1 and l_2 and masses m_{a_1} and m_{a_2}, respectively. The central mass is modelled with two equivalent masses, m_{p_1} and m_{p_2}, located near the hinge points at distances l_{p_1} and l_{p_2} with respect to the pivot points of the pendulum arm and of the hinging point of the oscillating mass.

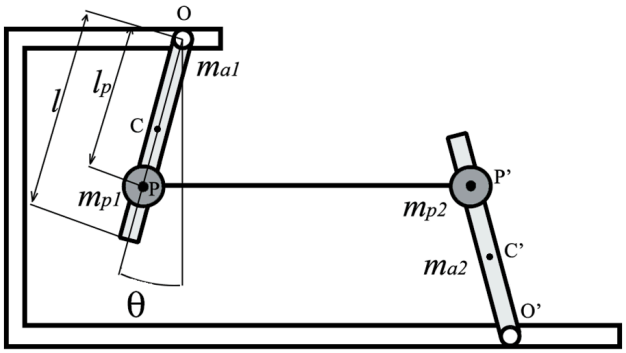

Figure 155: Folded Pendulum Mechanical Model

Assuming that the centre of mass of the pendula is in $l_i/2$ and using the approximation of small deflection angles, then the FP Transfer Function can be easily obtained by solving the Lagrange Equations. Defining the coordinate of the pendulum frame (fixed to the ground) as x_s and the coordinate of the FP central mass as x_p (see Figure 155), then the FP transfer function is

$$\frac{x_p(\omega)}{x_s(\omega)} = \frac{\omega_0^2 - A_c\omega^2}{\omega_0^2 - \omega^2} = 1 + \frac{(1 - A_c)\omega^2}{\omega_0^2 - \omega^2} \tag{99}$$

where

$$\omega_0^2 = \left(\frac{g}{l_p}\right) \cdot \frac{(m_{a_1} - m_{a_2})\frac{l}{2l_p} + (m_{p_1} - m_{p_2}) + \frac{k}{gl_p}}{(m_{a_1} + m_{a_2})\frac{l^2}{3l_p^2} + (m_{p_1} + m_{p_2})} \tag{100}$$

is the square of FP resonant angular frequency and

$$A_c = \frac{\left(\frac{l}{3l_p} - \frac{1}{2}\right)(m_{a_1} - m_{a_2})}{(m_{a_1} + m_{a_2})\frac{l^2}{3l_p^2} + (m_{p_1} + m_{p_2})} \tag{101}$$

is the parameter related to the center of percussion effects [409].

The tuning can be obtained changing the values of the masses m_{p_1} and m_{p_2}, adding a tuning mass, M_l, at a distance D from the pendulum suspension point.

A better physical interpretation of the dependence of the FP resonant frequency from its physical and geometrical parameters, can be obtained if Equation 100 is rewritten as

$$\omega_0^2 = \frac{(m_{a_1} - m_{a_2})\frac{gl}{2l_p^2} + (m_{p_1} - m_{p_2})\frac{g}{l_p} + \frac{k}{l_p^2}}{(m_{a_1} + m_{a_2})\frac{l^2}{3l_p^2} + (m_{p_1} + m_{p_2})} \tag{102}$$

Defining the equivalent gravitational constant, K_g, as

$$K_g = (m_{a_1} - m_{a_2})\frac{gl}{2l_p^2} + (m_{p_1} - m_{p_2})\frac{g}{l_p} \tag{103}$$

the equivalent elastic constant, K_e, as

$$K_e = \frac{k}{l_p^2} \tag{104}$$

and the equivalent mass, M_e, as

$$M_e = (m_{a_1} + m_{a_2})\frac{l^2}{3l_p^2} + (m_{p_1} + m_{p_2}) \tag{105}$$

then the FP resonant frequency, $f_o = \frac{\omega_o}{2\pi}$, can be rewritten as

$$f_0 = \frac{1}{2\pi}\sqrt{\frac{K_g + K_e}{M_e}} \tag{106}$$

It is easy to recognize in Equation 106 the classic expression of the resonant frequency of a spring-mass oscillator with an equivalent elastic constant $K = K_g + K_e$.

The FP mechanical prototype is a monolithic system, shaped with precision machining and electric discharge machining (EDM) [411, 412]. In fact, the monolithic mechanical design has the great advantage of avoiding the shear effects at the contact surface among mechanical parts that can generate hysteresis and dissipation in a non monolithic structure [409]. The result is a very compact sensor, with a high Q-factor (the Q factor of the material) and a good thermal sensitivity that guarantees a very good sensor directivity: coupling factors of less than 10^{-4} among the different degrees of freedom have been obtained in monolithic structures [410].

The four torsional flexures, connecting the pendulum arms to the central mass and to the frame, have an elliptical profile with $100\,\mu m$ minimum thickness with ellipticity ratio of $\epsilon = 16/5$. The pendula arms are designed to minimise the mass and the moment of inertia without reducing rigidity and symmetry. The values of the masses of the pendulum arm, of the inverted pendulum arm and of the central mass are $m_{a_1} \approx 40\,g$, $m_{a_2} \approx 50\,g$ and $(m_{p_1} + m_{p_2}) \approx 600\,g$, respectively.

The tunability of the monolithic FP natural frequency was obtained machining several drilled holes for fixing suitable shaped and positioned tuning masses, as predicted by Equation 100. In fact, tuning the FP at its lowest possible natural frequency maximises the sensor measurement band at low frequencies. But, the lower is the natural resonance frequency, the lower is the restoring force of the pendulum to external perturbations. Furthermore, a lower natural resonant frequency permits to relax the specifications of the control system for force feedback sensor configuration. The drawback of soft restoring forces is that the test mass easily touches the frame, saturating the sensor. Therefore, the gaps between the central mass-arms and arms-frame was set at 2 mm. In this way the dynamics of the monolithic FP sensor is quite large, but still far from the elastic limit of the material. These large gaps have another vantage when the FP works in air. In fact, the Q of the instrument in air is strongly influenced by the damping effect of the air present in these gaps, that largely reduces its value. This effect reduced the value of Q from $Q = 3000$ in vacuum to values of $Q = 3$ in air [410]. Our technical choice allowed us to obtaining a measured value of $Q = 140$ in air, perfectly acceptable for an use of monolithic FP as sensor.

The measurement of the transfer function was made using a standard measurement procedure used in control theory to obtain the transfer function of a linear system using white noise. For this task the central mass, m_p, was excited with white noise (input signal) through the coil-magnet actuator while the output signal, that quantifies the central mass motion, was read with the optical lever readout. Then the transfer function of the monolithic FP is obtained by simply dividing the output spectrum by the input one. The results of this first test are shown in Figure 156, where both the theoretical model and the experimental points are reported. We notice the very good agreement between the data and the predictions, which supports our confidence in the theoretical model. The analysis of these data show the natural *design* resonance frequency of the monolithic FP is 720 ± 5 mHz with a $Q \approx 140$ in air.

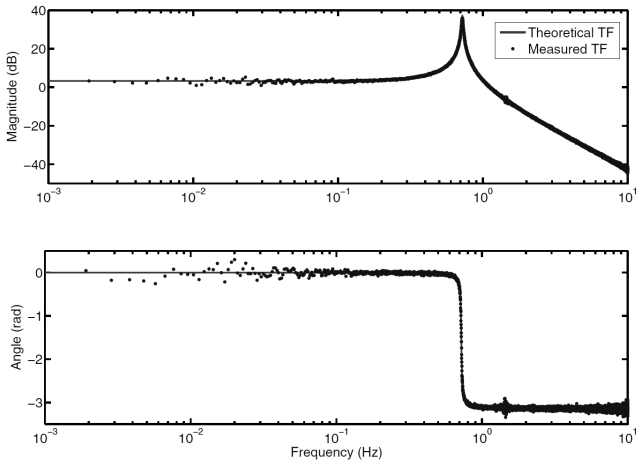

Figure 156: Theoretical and experimental Transfer Function of the horizontal monolithic FP.

To test the tuning procedure, we used tuning masses of different weights, in order to implement a rough or fine calibration, positioned in the opening of the test mass. The FP sensor was positioned on a platform for levelling. The tuning masses were moved in small steps, of less than 1 mm.

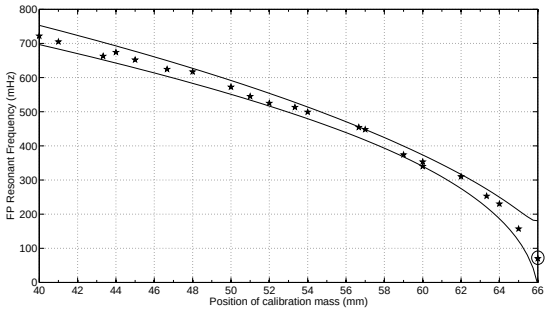

Figure 157: Measured resonance frequencies of the horizontal monolithic Folded Pendulum sensor. The best measured frequency, $f_r = 70$ mHz, is circled.

We made different sets of measurement to evaluate the stability of the measurement procedure. In Figure 157 the measured frequency versus the tuning mass position is shown. The data were interpolated using Equation 100 with adaptive parameters $(m_{p_1} + m_{p_2})$ and k. Figure 157 shows the very good agreement between the experimental data and the 3σ error bars of the theoretical model. The three sets of measurements performed over 10 days fall on the same curve within errors. The interpolation parameters with an error bar with a level of significance $\alpha = 0.05$ are in good agreement with the experimental ones, such as the distributed masses and the angular stiffness interpolated are in good agreement with the measured ones in this case, too.

The second step was a direct measurement of the Q of the monolithic FP sensor. For this task we performed a set of measurements in air in order to obtain an experimental curve expressing Q as function of the monolithic FP resonance frequency, f_o. We are well aware that these measurements are largely dependent also on the environmental conditions, but they are important to obtain an empirical physical law for our prototype, useful to predict the values of Q at different resonance frequencies. For this task we used a tuning mass of $M_l = 120\,g$. The results of this set of measurement are reported in Figure 158, where it appears evident that all the measurements follow a linear law. In fact fitting the data we obtained a confidence factor equal to $R = 0,95$.

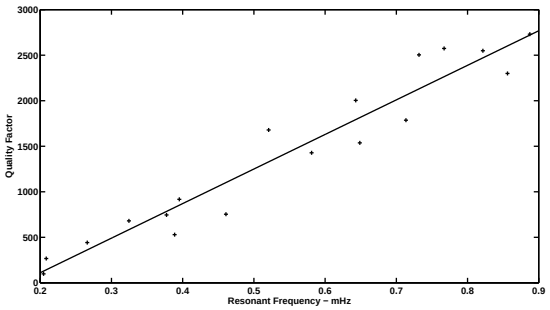

Figure 158: Mechanical quality factor versus resonant frequency for FP sensor in air.

4.6 The cost evaluation of the suspension system

The cost of the various items are reported in the final chapter of this book. Here we summarize just the guidelines for its evaluation. The suspensions system has a relevant impact on infrastructure: it constraints the cavern dimensions and requires auxiliary installation on site for the assembly. Items listed below have to be included in the infrastructure budget.

- Clean rooms for payload assembly
- Payload washing machine
- Facility for the construction of the silica fibres
- Facility for the construction of the silicon fibres
- Low vibration electric vehicle for payload transport
- Vacuum oven for thermal treatments

The evaluation of the suspension cost for the ET-HF interferometer is based on the Virgo investment updated for the Euro currency inflation. It concerns:

- Superattenuator filters
- Inverted pendulum
- Cables and wires
- Suspension electronics
- Safety structure
- Payload mechanics
- Assembly tools
- Sensors and actuators
- Local system control

The ET-LF case includes extra cost to the respect of the ET-HF case. In particular we have to consider

- The mechanics for the interface separating the upper and lower suspension system
- The reviewed cost estimation for the longer Superattenuator
- The Superattenuators hosted in the ancillary towers
- The active vibration dumping included in the cryogenic solution based on the pulse tube
- The reviewed cost estimation for the cryogenic payload
- Temperature monitor and control
- The reviewed cost of the local system control for the mirror at low temperature

For the cryogenic payload cost we based the evaluation on the experience gained on the system set up for the R & D FP6 - ILIAS- STREGA project [413].

5 Optical design

5.1 Executive Summary

The optical design of the Einstein Telescope refers to the design of the laser interferometer, the core instrument in which the effect of a passing gravitational wave is transformed into a read-out signal, measuring the changes in the distance between suspended mirrors using ultra-stable laser beams. The amplitude of this signal scales at first linearly with the light power stored in the interferometer arms. This led to the development of long-baseline detectors utilising high-power lasers. The interferometers of first generation GW detectors were already extremely sensitive to arm length changes (and thus to gravitational waves). Their sensitivity over a wide frequency range was limited not by technical inaccuracies but by intrinsic noise of their fundamental parts, such as the quantum fluctuation of the laser light. The optical design efforts since then have focused on developing and implementing advanced optical technologies to reduce the impact of these noise sources on the read-out signal.

Gravitational waves exist in two distinct polarisations. To capture the full signal a GW observatory should be able to detect both polarisations at all times. This can be achieved by employing multiple co-located detectors. The optimal footprint of the observatory will depend on the geographical details of the yet unknown location. It is possible to position three detectors in a triangle as shown in Figure 159. Such a triangular shape represents the minimal topological solution and has been chosen as the baseline geometry for ET.

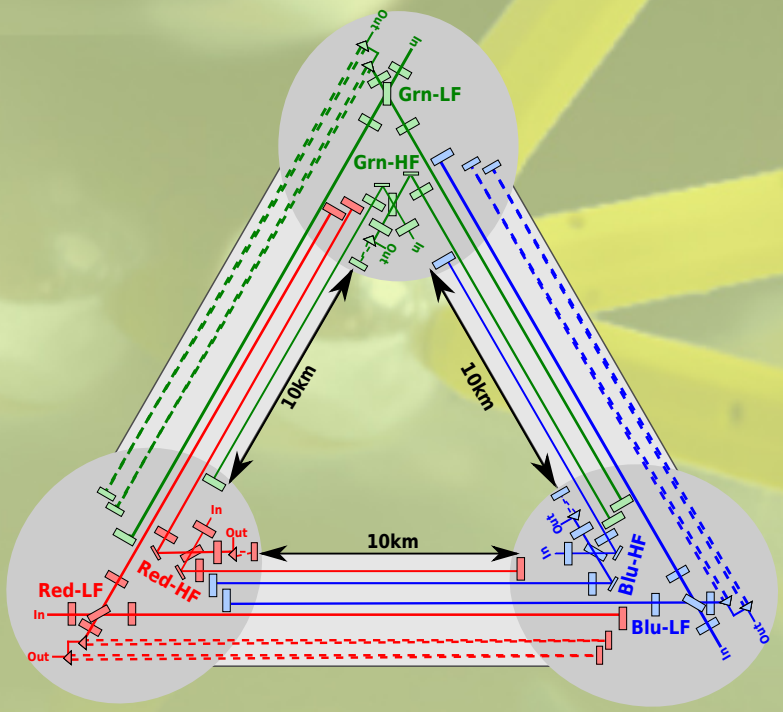

Figure 159: Schematic full view of the optical layout of the ET Observatory. the full instrument consists of 3 pairs of km-scale interferometers positioned such that they form a triangular shape. Each interferometer pair represents one wide-band detector, in which one interferometer is optimised for gravitational waves at low frequencies (LF) and the other for high frequencies (HF). Please note that this graphic is not too scale and does not show the exact position of the optical components. Instead, it provides an overview of the general shape and complexity of the optical layout of the main interferometers.

The core interferometers of the Einstein Telescope will be advanced Michelson interferometers with an arm length of 10 km, a length which was a given input parameters for the optical design. Some technologies for

noise reduction are not necessarily compatible with each other. Therefore the optical design includes two parallel, 10 km long interferometers per detector, one interferometer being optimised for low-frequency (LF) gravitational waves, the other covering the high frequency (HF) part of the spectrum; this approach has been called 'xylophone' design. The main characteristics of the two interferometer types are:

- the **HF** interferometer is a room temperature interferometer with very high laser power and fused silica test masses similar to Advanced detectors, but using an alternative laser beam shape, the Laguerre-Gauss LG33 mode.
- the **LF** interferometer is a cryogenic interferometer with medium laser power, using silicon test masses and a laser system with a 1550 nm wavelength.

One of the main noise sources to suppress by means of optical design is the quantum noise of the light. A detailed study of newly proposed schemes for quantum noise reduction, such as speed meters or optical bars has been undertaken and two interesting candidates have been identified: the ET baseline design will make use of dual-recycled Michelson interferometers, very similar to those planned for Advanced LIGO, with the additional injection of frequency-dependent squeezed light into the dark port. In parallel, we will continue to study speed-meter like configurations, in particular those based on the Sagnac topology.

The choice of using Michelson interferometers (with recycling techniques) has the great advantage that much of the research and development towards the Advanced detectors can be applied directly. In particular, for the conceptual designs of auxiliary systems such as input-output optics, the interferometer control or the thermal control of the interferometer mirrors, we can adapt the current state of the art with only small envisaged changes.

A summary of all the optical parameters of the Einstein Telescope baseline design is given in the table below:

	ET-HF	**ET-LF**
Approximate frequency range	10–10^4 Hz	1–250 Hz
Detection scheme	DC readout	DC readout
Input power (after IMC)	500 W	3 W
Laser wavelength	1064 nm	1550 nm
Beam shape	LG_{33}	TEM_{00}
ARM CAVITIES		
Arm length	10 km	10 km
Opening angle	60 °	60 °
Arm power	3 MW	18 kW
Temperature	290 K	10 K
Mirror material	fused silica	silicon
Mirror diameter	62 cm	>45 cm
Mirror thickness	30 cm	about 50 cm
Mirror mass	200 kg	211 kg
Beam radius (at mirror)	7.2 cm	9.0 cm
Beam waist (symmetric cavity)	2.51 cm	2.9 cm
RoC (symmetric cavity)	5690 m	5580 m
Scatter loss per surface	37.5 ppm	37.5 ppm
Finesse	880	880
Reflective coating ITM	tantala/silica 8 $\lambda/4$ doublets	tantala/silica 9 $\lambda/4$ doublets
Reflective coating ETM	tantala/silica 17 $\lambda/4$ doublets	tantala/silica 18 $\lambda/4$ doublets
Transmission ITM	7000 ppm	7000 ppm
Transmission ETM	6 ppm	6 ppm

	ET-HF	**ET-LF**
	CENTRAL INTERFEROMETER	
SR-phase	tuned (0.0)	detuned (0.6)
Focussing element	in or near the ITM focal length = 303 m	in or near the ITM focal length = 303 m
Distance ITM–BS	300 m	300 m
Distance BS–MPR	10 m	10 m
Recycling cavity length	310 m	310 m
Beam size on BS	4.7 mm	6 mm
Beam size on MPR	2.7 mm	3.4 mm
Recycling gain	21.6	21.6
Recycling cavity free spectral range	484 kHz	484 kHz
Round-trip Guoy phase	10.5 °	9.6 °
mode separation frequency	28 kHz	26 kHz
Recycling cavity temperature	room temperature	room temperature
Beam splitter material	fused silica	fused silica
Transmission PRM	4.6 %	4.6 %
Transmission SRM	10 %	20 %
	FILTER CAVITIES	
Quantum noise suppression	frequency-dependent squeezing	frequency-dependent squeezing
Filter cavities	1×300 m	2×10 km
Half-bandwidth	5.7 Hz	5.7 Hz and 1.5 Hz
Detuning	25.4 Hz	25.4 Hz and 6.6 Hz
Round-trip loss	75 ppm	75 ppm

5.2 Description

Modern gravitational wave detectors are based on km-scale laser interferometers. Also the Einstein Telescope is using a sophisticated laser interferometer to convert the signal of a passing gravitational wave into a readout signal that can be processed electronically. The basic interferometer design is still similar to that of the original interferometer by Michelson (used more than 100 years ago in the famous Michelson and Morley experiment to disprove the existence of a so-called aether). However, to achieve better sensitivities the interferometry has been refined and extended continuously, especially during the last two decades, driven by the gravitational wave community. As a result, modern interferometers are now able to reach unprecedented sensitives beyond the Standard Quantum Limit of interferometry. At the same time the optical design has become a more challenging task. Modern interferometers couple all involved optical systems into one closely coupled, complex machine.

The focus of the optical design was to identify and develop an optical layout for the core interferometer of a third generation detector which includes advanced optical technologies required to reach the target sensitivity of the ET detector. The term 'optical layout' includes a number of layers of complexity in optical design: first of all, the core interferometer is the part of the detector which converts the gravitational wave signal into a measurable optical signal. Second, the core interferometer by design couples all auxiliary subsystems together. Thus part of the effort in this design study was dedicated to how the signal and all possible noises couple into the detector output. And third the optical layout largely defines the type of instrument, i.e. it defines the shape of the detector, the type of interferometry used, as well as which advanced optical technologies are included.

In order to achieve the envisaged sensitivity of the Einstein Telescope, once again the interferometry must be pushed beyond the state-of the art. For the first time a number of advanced technologies such as cryogenic mirrors, squeezed light and alternative beam shapes are to be combined in one system. This section describes in detail the design process towards the optical layout of ET which forms the baseline for the design of the

infrastructure, as well as the mirror suspension systems. All the currently active GW detectors are L-shaped, with orthogonal arms; although this geometry maximises the sensitivity of the single detector with respect to the arm length, other geometries are possible. In particular, triangular-shaped detectors have been proposed in the past; the LISA geometry is also triangular. Two L-shaped detectors, forming a 45 degrees angle, could fully resolve the two polarisation amplitudes of the incoming wave. Obviously in an underground site, the realization of this geometry is difficult, due to the high cost of the infrastructure. If the angle between the two arms of each detector is reduced to 60 degrees, three detectors can be accommodated in a triangular-shaped underground site, minimizing the required number of caverns. An analysis of a triangular-shaped third generation GW observatory is described in sections 5.3 with the conclusion that if a site that can accommodate a triangular observatory is found, the triple co-located interferometers will be the best choice and the triangular shape has been adopted as the baseline for the current ET design.

Each detector within a triangular observatory can in principle be composed of one or several interferometers of different topology. It can be shown that one interferometer per detector is not ideal. Spanning the wide detection band envisaged for ET is technically extremely challenging: Different noise types dominate the various frequency bands and often these noises show opposite response for changing the involved design parameters. Sometimes the reduction techniques for different noise types are incompatible. A well-known example for a parameter that affects different frequency regions differently is the correlation of the two quantum noise components: photon shot noise and photon radiation pressure noise. In order to improve the shotnoise-limited sensitivity at high frequencies one needs to increase circulating optical power, which at the same time increases the radiation pressure noise and therefore worsens the low frequency sensitivity. Alternatively, lowering the circulating power reduces the radiation pressure effects and improves the low frequency sensitivity, while the shotnoise contribution will rise and reduce the high frequency sensitivity. This dilemma can be resolved by following the path of electromagnetic astronomy, where telescopes are being built for a specific, rather narrow-banded detection window (visible, infrared etc) and later on the data from different frequency bands are combined to cover the desired bandwidth. Building two interferometers, each optimised for reducing the noise sources at one specific frequency band, can form a xylophone observatory providing substantially improved broadband sensitivity. We have developed a 2-band xylophone detector configuration to resolve the high-power low-temperature problem of a single band ET observatory as described in section 5.4. Based on this design envelope of three xylophone detectors in a triangular setup, a more detailed design of the optical layout can be performed. This formed the basis for the investigation into the required cavern size and associated infrastructure impact, see section 3.

Currently the Michelson interferometer topology is used in laser-interferometric gravitational wave detectors. However, alternative topologies, such as the Sagnac interferometer or so-called 'optical bars', have been suggested and would also fit into a triangular, xylophone based detector. The main attraction of alternative interferometer topologies is that they allow the implementation of different quantum noise reduction schemes. While classical interferometers are limited by the Standard Quantum Limit, a noise floor composed of photon shotnoise and radiation pressure effects, clever interferometer designs and the use of squeezed light allow us to push beyond that limit. A detailed study of a wide range of possible quantum noise reduction schemes has been undertaken and is reported in sections 5.5 and D.2. As the outcome of this study, taking into account technical considerations, a Michelson-based topology with Signal Recycling and squeezed light injection has been selected for the Einstein Telescope baseline. The study also showed that Sagnac-based speedmeter topologies are an appealing alternative and should be studied further. The chosen design implements so-called filter cavities to generate the frequency-dependent squeezed light. During the course of the design study a lot of original research has been undertaken to derive requirements for such cavities and their implementation, details are reported in appendix D.3.

With the baseline of the optical layout selected, the design progressed into essential subsystems. The core element of these laser interferometers are the large principal mirrors of the arm cavities. The thermal noise of these mirrors represents one of the main limits to the achievable sensitivity. Towards the realisation of second-generation interferometric detectors, a major research effort is underway to study and improve all aspects of these mirrors, especially the quality of the dielectric coatings. This work has been extended here to determine the requirements for the Einstein Telescope. A further challenge is to identify the best material and design choices for the cryogenic mirrors to be used in the low-frequency interferometer. Two solution based on Sapphire and silicon as mirror bulk material have been identified and carefully studied in section 5.6 alongside fused-silica mirrors for the high temperature interferometer. This work is complemented by tables stating the optical,

mechanical and thermal properties in appendix E.

The following sections 5.7.1, 5.7.2, 5.7.3 and 5.7.4 provide details about auxiliary optics system, such as the injection optics, providing the laser beam to the main interferometer, the detection system, responsible for converting optical into electrical signals and the control systems required to maintain a stable operating position of the entire interferometer. The design of these systems is a direct application and extension of the work done and experience gained with the first and second generation of detectors and we expect future changes to these systems based on the experience gained when the advanced detectors start operating.

Building on the detailed baseline design of the optical layout as well as the main subsystems, section 5.8 provides a cost evaluation of the optical system for the Einstein Telescope. We also provide a guide to future R&D activities by outlining in section 5.9 which of the technologies require major R&D efforts before they could be incorporated in a technical design of the Einstein Telescope.

During the course of the design study we have also investigated a number of new and hypothetical effects or technologies. One hypothesis that gained popularity for a while proposes a new kind of noise originating from the holographic principle of unification physics, which can arise in the high-precision interferometry [414]. We investigated this so-called holographic noise (cf. Appendix D.6) and came to the conclusion that it is so far insufficiently developed and verified from both theoretical and experimental sides, and we do not expect it to have any impact of the design of ET. Further, a technique proposed to eliminate all types of noise associated with the motion of test masses is the so-called *displacement-noise free interferometry*. Also this has been investigated in Appendix D.7, but dismissed as it currently provides no route towards a realistic experimental implementation.

5.3 Review on the geometry of the observatory

This section briefly reviews the reasoning behind the shape of current gravitational wave detectors and then discusses alternative geometries which can be of interest for third-generation detectors. We will use the terminology introduced in the review of a triangular configuration [415] and discriminate between the *geometry*, *topology* and *configuration* of a detector as follows:

- The *geometry* describes the position information of one or several interferometers, defined by the number of interferometers, their location and relative orientation.
- The *topology* describes the optical system formed by its core elements. The most common examples are the Michelson, Sagnac and Mach–Zehnder topologies.
- The *configuration* describes the detail of the optical layout and the set of parameters that can be changed for a given topology, ranging from the specifications of the optical core elements to the control systems, including the operation point of the main interferometer. Also the addition of optical components to a given topology is often referred to as a change in configuration.

5.3.1 The L-shape

Current gravitational wave detectors represent the most precise instruments for measuring length changes. They are laser interferometers with km-long arms and are operated differently from many precision instruments built for measuring an absolute length. Viewed from above they resemble an L-shape with equal arm length. This geometric form follows directly from the nature of gravitational waves: gravitational waves are transverse, quadrupole waves, thus a length change measured along any axis occurs with opposite sign along the axis orthogonal to the previous one and the direction of propagation. This key feature allows us to make a differential measurement between two orthogonal interferometer arms, yielding twice the amplitude of a single arm. More importantly, a differential measurement allows us to potentially discriminate between gravitational wave signals and those types of noise common to both arms, such as, for example, laser amplitude noise. To achieve this the interferometer arms generally have to have approximately the same length. The most simple L-shaped

interferometer capable of doing this type of measurement is the symmetric Michelson interferometer, on whose topology all current interferometric detectors are based.

The long arm length of the detectors represents the simplest way to increase the signal-to-noise ratio in the detector because for wavelength larger than the detector dimensions, the 'tidal' effect of the gravitational wave increases with the base length over which the measurement is taken. In contrast the fundamental noises are connected to the interaction of light with the optical components or the photo detection and thus do not scale with the length of the interferometer arms. We can summarise that for typical ground-based detectors with sufficiently good vacuum and mirror position control systems, an increase in arm length will increase the sensitivity of the detector proportionally.

Using the framework developed in [52] we can compute the sensitivity of a laser interferometer with two arms to gravitational waves, taking into account the geometry of the detector, the location of the source and the changes of both over time. The equations show directly that the arms of the detector do not have to be perpendicular. A right angle, however, provides the maximum response of an ideal detector to gravitational waves, which more generally can be written as

$$h(t) = F_+(t)h_+(t) + F_\times(t)h_\times(t) = \sin\zeta\, f(t, \psi, \dots) \tag{107}$$

with ζ the opening angle of the interferometer arms, F_+ and $F_\times$ the beam pattern functions and $f(t, \psi, \dots)$ a function of the remaining parameters describing the geometry (the location of the detector and of the source in space and time and the wave polarisation angle).

In summary we can say that for a gravitational wave of given direction and polarisation, a properly aligned symmetric L-shape is an ideal optical layout for an interferometric detector; the arms should be as long as possible and the sensitivity is maximised for an opening angle of 90°. It should be noted that this does not put severe constraints on the type of interferometer topology used. In fact, most common interferometer types can be used in a form that features two large symmetric arms in an L-shape while potential other interferometer arms or sections are shortened such that they can be considered as part of one corner of the detector.

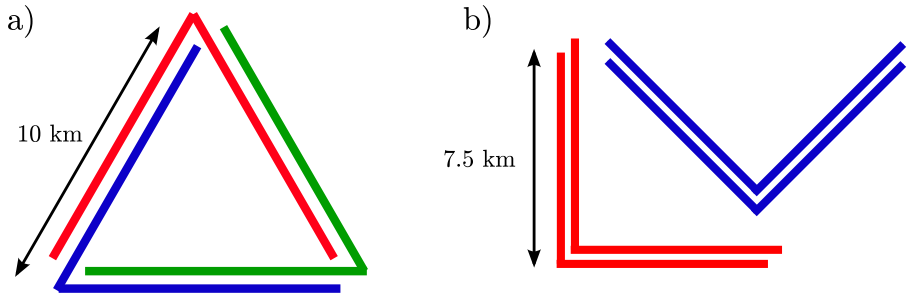

Figure 160: **a)** Triangle geometry: three L-shaped detectors with 10 km arm length are positioned in a equilateral triangle. **b)** Four L-shaped detectors at 0° and 45°. The integrated length of all interferometer arms in both configurations is 60 km and two interferometer arms can share the same structure. Note that for avoiding noise correlations between two detectors the neighbouring interferometer arms would probably be housed in a separate vacuum tubes.

5.3.2 The triangle

At any given moment an L-shaped detector can only detect one linear combination of polarisations of a gravitational wave. However, for estimation of source parameters from the measured signal, the full polarisation information is essential. Thus it is of considerable interest to design a detector that is able to detect both polarisations (and thus the full content) of a gravitational wave at all times. This can be achieved by combining two co-located L-shaped detectors which are positioned at 45° to each other. More than 20 years ago it was recognised that a triangular geometry would provide the same sensitivity to both polarisations as detectors at 45° whilst requiring less enclosed space and fewer end stations [416]. In particular, the sensitivity of the two

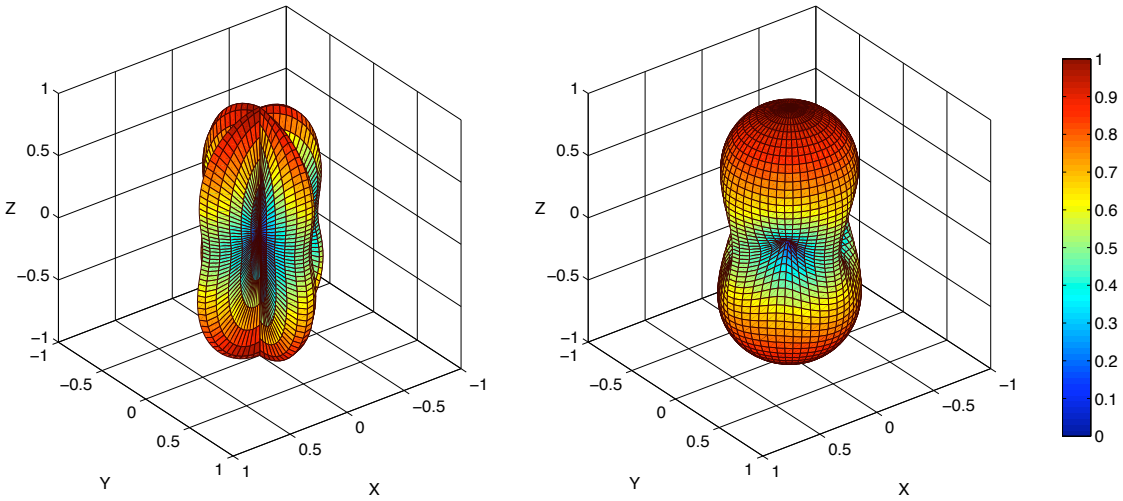

Figure 161: The response of a detector to a linear polarised gravitational wave as a function of the detector orientation. Both plots show the normalised sensitivity to a wave travelling along the z-axis. Each data point represents the sensitivity of the detector for a specific detector orientation defined by the detector normal passing the respective data point and the origin. The colour of the data point as well as its distance from the origin indicate the magnitude of the sensitivity. The left plot depicts the response of a single Michelson, while the right plot gives the response of a set of three interferometers in a triangular geometry.

geometries shown in Figure 160 differs only by 6% [415]. The difference in the sensitivity to different polarisations between a single L-shape and a triangular geometry can be best illustrated with a plot of the so-called antenna pattern as shown in Figure 161.

Using co-located detectors yields another advantage. Both layouts shown in Figure 160 represent detectors with redundancy. Redundancy here can be understood in relation to the continuous operation of the detector as an observatory, or as a feature of the data streams generated by the full system. Redundancy in operation is achieved by having multiple detectors which generate an equal or similar response to gravitational waves. This is desirable in observatories which are expected to produce a quasi-continuous stream of astrophysically meaningful data over a substantial amount of time. Typically laser interferometers cannot produce science data during upgrades and maintenance work. Thus only alternating upgrades and data taking of redundant detectors can avoid long down-times, for example during detector upgrades.

Such redundancy is obviously provided in the case of the 4 L-shaped detectors, where two detectors are always identical but can be operated independently. However, one can easily show that the triangular geometry provides exactly the same redundancy [415]. For example, for three equal L-shaped interferometers oriented at 0°, 120° and 240°, one obtains:

$$-h_{0^\circ} = h_{240^\circ} + h_{120^\circ}\,, \tag{108}$$

where the sign of the operation is defined by which ports of the interferometers are used to inject the laser light. Thus the two interferometers at 120° and 240° create exactly the same response as the one at 0°. This allows us to construct so-called null-streams (or null-data streams) [417]. Null-streams are a powerful data analysis method that allows one to identify noise that is uncorrelated between the detectors. Even though this does not increase the strain sensitivity of a detector, it can add significantly to the robustness of the data processing pipelines and thus to a larger number of detected events. The triangular geometry represents the minimal setup in one plane that can resolve both polarisations and provides redundancy for the generation of null-streams.

To date no laser interferometer topology other than the Michelson has been used for gravitational wave detection. However, some very advanced noise reduction techniques proposed for future detectors are based on topologies of the Sagnac interferometer, the Fox-Smith cavity or the Mach-Zehnder interferometer [418–420].

It is worth noting that a triangular geometry as discussed above is compatible with different interferometer

topologies. In particular it is possible to use different topologies while maintaining the L-shape of the single interferometers as displayed in figure 162. Therefore, for example, three Sagnac interferometers or three cavities could be used to form a triangle. Such detector designs can provide similar benefits as described above for the triple Michelson geometry so that the triangular geometry is largely independent of the topology of the individual interferometers.

Box 5.1: Different topology options

In this box we will list the different main interferometer topologies that can be used for gravitational-wave detection and describe their basic optical systems. A full gravitational-wave detector could actually consist of more than one of those main interferometers and could also be equipped with additional techniques in order to achieve a specific susceptibility to the quantum noise as will be described in Sec. 5.5. Note that in principle, all of the mentioned interferometer topologies can be fitted into

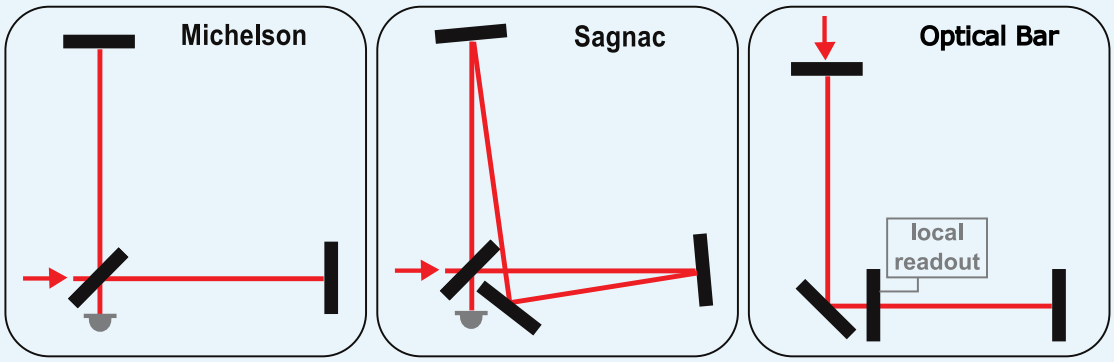

Figure 162: Different (basic) topology options: simple Michelson interferometer topology (left panel); zero-area Sagnac interferometer topology (midd3le panel); optical bar topology (right panel)

an L-shape or into another two-arm shape under an arbitrary angle, as shown in Fig. 162.

- **Michelson interferometer** (basic): a laser beam is split at a beam splitter and sent along two perpendicular interferometer arms (cf. left panel of Fig. 162). The ends of these arms (north and east) are marked by highly reflective identical end mirrors, which reflect the beams back into themselves so that they can be recombined at the beam splitter. Generally, the Michelson interferometer has two outputs, the south port and the west port (which is also the input port). Both output ports can be used to obtain interferometer signals, however, most setups are designed in such a way that the signals are detected at the south port. For the detection of gravitational waves, the Michelson interferometer has to be sensitive to small perturbations in the difference of the two arm lengths and the phase relation is chosen in such a way that this signal interferes constructively at the south port. Usually the south port is kept nearly dark, with all light reflected back to the west input port, then also called the bright port of the interferometer. A power-recycling mirror can be positioned at the bright port in such a way that it forms a resonant cavity for the carrier light together with the mirrors of the two interferometer arms. Furthermore, each interferometer arm can be replaced by equal Fabry-Perot cavities, formed by an input mirror and an end mirror. An additional mirror can also be placed at the interferometer's south port, known as the signal-recycling mirror. Another possibility is to send the output signal at the west port into an additional resonator, a so-called sloshing cavity. Furthermore, polarizing optics can be used in order to send the beam back into

the interferometer. The Michelson interferometer is the standard topology for interferometric gravitational-wave detectors. The great advantage of this configuration is that there is a lot of experience gathered.

- **Sagnac interferometer** (basic): a laser beam is split into two beams at the beam splitter which both travel through the whole interferometer but in opposite directions. The two beams are recombined at the beam splitter. The interferometer has only one output port, namely the south port. A Sagnac interferometer is by construction always operated at a dark port, i.e. all carrier light is reflected back to the input port. The arms can be folded in such a way that both beams circulate around a zero area (cf. middle panel of Fig. 162) in order to make the interferometer insensitive to rotations and forming two perpendicular interferometer arms. Those arms can be replaced by ring resonators, either of rectangular or triangular shape. For the Sagnac interferometer topology, an additional mirror at the input port can realize power-recycling and an additional mirror at the output port can realize signal-recycling. Up to now a Sagnac interferometer has never been adopted as a large-scale interferometric gravitational-wave detector. Only some features have been tested in table-top experiments and a theoretical study has started to explore noise couplings in a Sagnac interferometer [421].
- **Optical bar**: The optical bar topology is an optical realization of a mechanical resonant bar gravitational-wave detector. It essentially consists of two coupled optical resonators, which are shaped as a L and coupled through a light, partially transmissive mirror as shown in the right panel of Fig. 162. An additional local meter is applied to the central mirror, reading out its motion. The local meter could in principle be any device but its sensitivity is essentially determining the sensitivity of the optical bar detector. It is even not obligatory for the local meter to be an optical device, for instance it could be a SQUID-based microwave meter as a speed meter, or some other high precision superconductive sensor. The optical bar topology can be transformed into an optical lever topology by inserting an additional mirror into each arm of the L, forming a resonant cavity together with the corresponding end mirror.

The case for alternative topologies is largely based on ideas for the reduction of quantum noise. In general, the signal-to-noise ratio of a single interferometer is different for each topology, with the actual difference depending also on the type of noise under investigation. However, it is not possible to identify a topology with a meaningful signal-to-noise ratio or sensitivity since these vary dramatically with the interferometer *configuration*.

During the design and construction of the first generation of detectors the Sagnac topology has been investigated and prototypes have been built [422] but it did not show significant advantages over the Michelson topology [423]. More recently it has been proposed to use the Sagnac topology as a *speed meter* [418] to reduce the quantum noise. The Sagnac topology can be hosted in different ways in a triangular geometry: each Sagnac as an equilateral triangle, or as an L-shaped zero-area Sagnac. Noise couplings due to the Sagnac effect favor the zero-area Sagnac topology: it can be shown that for a typical choice of optical parameters the extra noise couplings do not impose stringent new requirements in the case of a zero-area Sagnac interferometer [415].

We note that Michelson-based detectors currently offer the advantage of using the experience as well as the advanced optical technologies of the first two detector generations.

5.4 Optical layout

This section describes the details of the ET optical layout, such as the laser beam sizes, beam shapes and distances between optical components inside the arm cavities and central interferometer including the power and signal recycling cavities. A schematic sketch of the optical layout of all core optical of the interferometers is shown in figure 163. Constraints imposed onto the optical layout are briefly discussed in section 5.4.1, while

section 5.4.2 lays out the motivation for choosing a dual-tone xylophone detector. The optical layout of the arm cavities is discussed in detail in section 5.4.3. Finally section 5.4.4 describes the layout of the recycling cavities.

5.4.1 Constraints on the optical layout from classical noise sources

Apart from the quantum noise there are many other noise sources, usually called classical or technical noise sources, degenerating the sensitivity of a laser interferometric gravitational-wave detector. In the third generation of detectors these classical noise sources have to be addressed with different techniques which impose additional constraints onto the optical layout of the ET interferometers.

The suspension thermal noise of the low frequency interferometers will be one of the limiting noise sources at the low-frequency end of the ET detection band (for more details refer to Sec. 4.4.2). In order to guarantee optimal thermal noise performance, the fibers of the suspended optics—especially those in a cryogenic environment—have to be be kept at their designed operating temperature. Since each detector consists of two interferometers, the question arises how to arrange the collinear interferometer arms in the tunnel. One of the interferometer arm could be placed above the other. In that case it is unavoidable that the laser beam of the interferometer on top intersects at some point with the suspension fibers of the other interferometer. Therefore, we chose to arrange the individual interferometer beams in a way that the beams of the low-frequency interferometers sit on top of the beams of the high-frequency interferometers. This configuration ensures, that no high power laser beams comes close to any cryogenic suspension fibres and only the low power beams of the low frequency interferometers have to pass the between the rather uncritical fibres of the room temperature suspensions of the high frequency interferometers (see Figure 163).

The noise coming from thermal effects influencing the test-mass mirrors is dominating the noise spectrum in the mid frequency regime. There exist several different contributions to the total thermal noise of which the coating Brownian thermal noise is the largest in current interferometer topologies utilizing arm cavities. The obvious way of lowering the thermal noise contributions is cooling the mirrors down to cryogenic temperatures. However, such cryogenic test-masses allow only for a limited amount of optical power passed through the mirror substrates and coatings, which is the reason why we consider cryogenic mirrors only for the low frequency interferometers.

Another branch of techniques to lower the thermal noise is to increase the beam size on the test masses and change the mode of the laser beam inside the interferometer (cf. Sec. 5.9.1). The maximal practical beam sizes for the ET interferometers is given by the the maximal available substrate size on one hand and the required cavity stability one the other hand (see Sec 5.4.3). In order to obtain an optimal noise performance of the high-frequency interferometers we consider them to operate with laser beams of the Laguerre-Gauss (3,3)-mode (LG_{33}) [424, 425]. The limitation in using LG modes[19] is that they can resonate only in cavities with an even number of mirrors. Therefore, no triangular cavity may be used.

Box 5.2: The Laguerre Gauss LG_{33} mode

To reach the envisaged sensitivity for ET, the thermal noise has to be reduced significantly with respect to Advanced detectors. So far, no single technique or technology can achieve this but a combination of methods needs to be employed. The current design includes the use of the higher-order Laguerre Gauss mode LG_{33} instead of the standard, fundamental Gaussian TEM_{00} beam for the high-power, high-frequency interferometer. Laguerre-Gauss modes are commonly given in their orthonormal form, see for example [426]:

$$\begin{aligned} u_{p,l}(r,\phi,z) &= \frac{1}{w(z)}\sqrt{\frac{2p!}{\pi(|l|+p)!}}\exp(\mathrm{i}\,(2p+|l|+1)\theta(z)) \\ &\times \left(\frac{\sqrt{2}r}{w(z)}\right)^{|l|} L_p^{(|l|)}\left(\frac{2r^2}{w(z)^2}\right)\exp\left(-\mathrm{i}\,k\frac{r^2}{2q(z)}+\mathrm{i}\,l\phi\right), \end{aligned} \tag{109}$$

[19] All throughout this document, we refer to the so-called 'helical' Laguerre-Gauss modes, whose intensity pattern is circularly symmetric. See e.g. definition in [424].

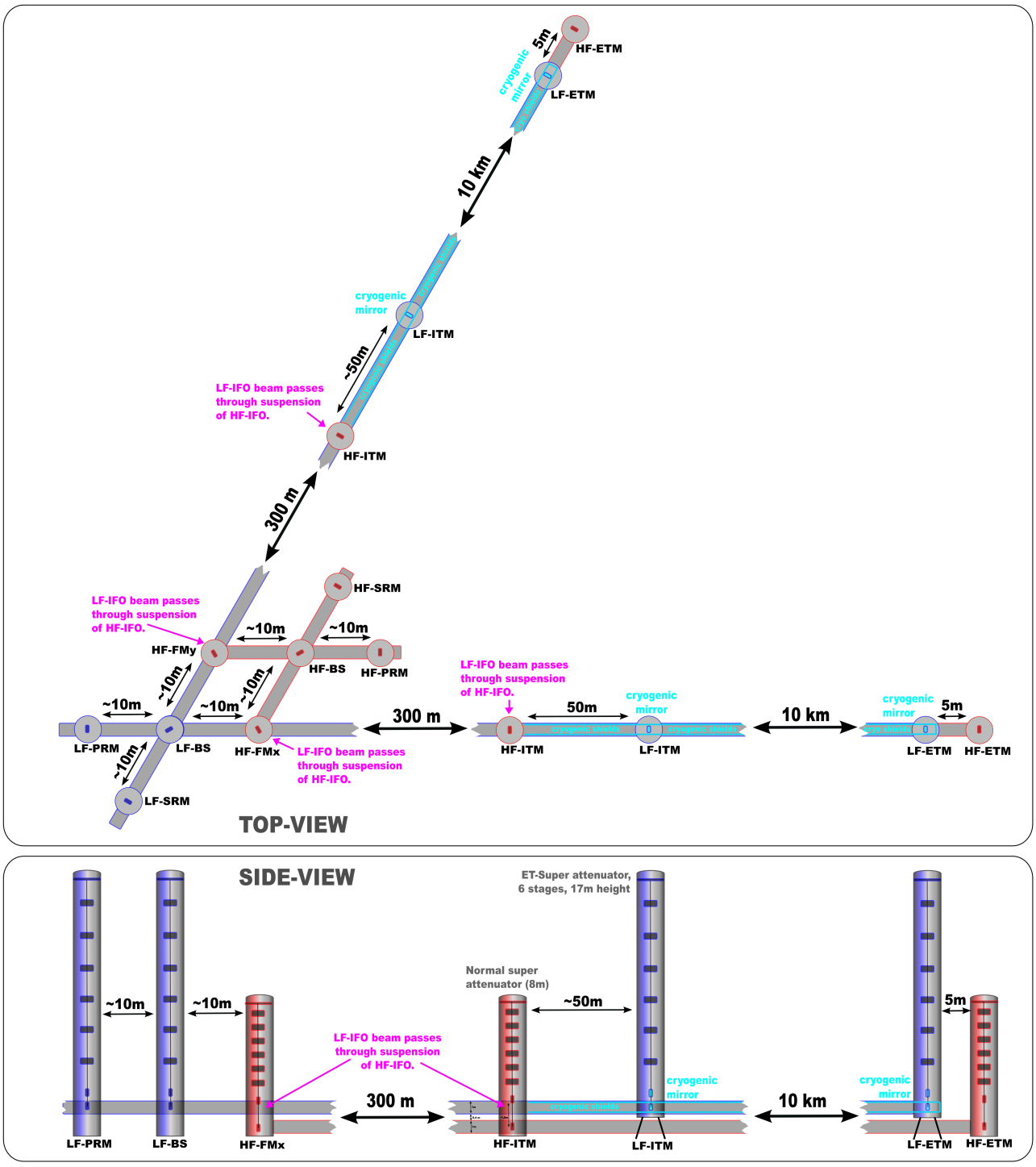

Figure 163: Simplified drawing of the low and high frequency core interferometers of a single ET-detector. Injection and detection optics as well as filter cavities have been omitted for clarity. Please not that the complete ET observatory consists of three such detectors.

with r, ϕ and z as the cylindrical coordinates around the optical axis. The letter p is the radial mode index, l the azimuthal mode index and $L_p^{(l)}(x)$ are the associated Laguerre polynomials. The other parameters used in equation 109 are defined as follows: w_0 is the beam radius at the *beam waist* and z_0 the position of the beam waist along the z-axis. w is the beam radius, q is called the *Gaussian beam parameter* and θ is the Gouy phase. The LG_{33} is shown in Fig. 164, it provides wider intensity pattern which directly reduces the impact of thermal noise as well as thermal lensing. The spherical phase front makes it possible to use this mode with spherical mirrors.

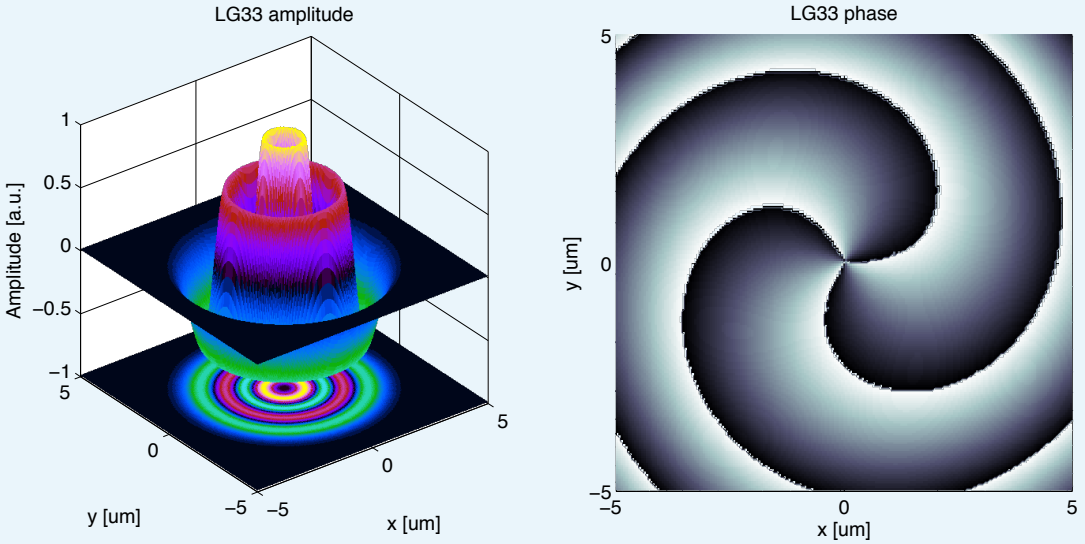

Figure 164: The amplitude distribution of a LG_{33} mode (left panel) shows a ring structure with 3 dark rings. The phase front of such a mode (right panel) is basically spherical with an additional helical structure superimposed.

The use of such a Laguerre-Gauss mode has been selected for the ET design because it is directly compatible with other advanced technologies for the suppression of thermal or quantum noise and does not requires a larger envelope or additional interferometer hardware. Wherever possible optical design options have been analysed for the fundamental Gauss beam as well as the LG_{33} mode. LG modes so far are untested in high-precision interferometry. Several other alternatives are also under active development, for example, Khalili cavities or wave guide coatings, see Appendix D. These techniques can be used as a drop-in replacement for LG modes without substantial changes to the rest of the optical design.

5.4.2 A xylophone design for ET

Spanning the detection band over four orders of magnitude in frequency, as is asked for third generation GW observatories such as ET, is technically extremely challenging: different noise types dominate the various frequency bands and often show opposite responses for different tuning of the same design parameter.

In the following we give some examples of fundamental issues of a broadband third generation interferometer that could be resolved by using a set of xylophone detectors:

- **High Power vs Cryogenic Temperature**: Using a single broadband ET observatory as described in [427] features the challenge of the simultaneous use of high optical power (a few megawatts) to achieve the required high frequency sensitivity and test masses at cryogenic temperatures in order to provide the

required suppression of thermal noise. Even though tiny, the residual absorption of the dielectric mirror coatings deposits heat in the mirrors which is difficult to extract, without spoiling the performance of the seismic isolation systems. A possible solution for this problem would be to build a xylophone observatory consisiting of a high frequency detector featuring high power and high temperature and a low frequency detector featuring low power and cryogenic temperatures.

- **Shot Noise vs Radiation Pressure Noise**: Due to the fact that the shot noise contribution scales inverse with optical power, but the photon radiation pressure noise contribution on the other hand scales proportional to the optical power, it will be hard to obtain the desired bandwidth with a single detector. Therefore, again it might be useful to split ET into a low-power low-frequency and a high-power high-frequency companion.
- **Mixing Interferometer Topologies**: Xylophone configurations would also allow us to mix alternative interferometer topologies, such as Sagnac interferometer [418] and optical levers [428], with the standard Michelson interferometer. For example one could imagine that ET upgrades would feature a standard high-frequency Michelson interferometer with a low-frequency optical lever as companion.

The xylophone concept was first suggested for Advanced LIGO, proposing to complement the standard broadband interferometers with an interferometer optimized for lower frequency, thus enhancing the detection of high-mass binary systems [429, 430].

One may think that a xylophone might significantly increase the required hardware and its cost by the need to build more than one broadband instrument. However, such an argument does not take the technical simplifications that it would allow, the better reliability of simpler instruments, and the more extensive scientific reach allowable into account.

For example splitting a third generation observatory into a low-power, low-frequency and a high-power high-frequency interferometer, has not only the potential to resolve the above mentioned conflict of photon shot noise and photon radiation pressure noise, but also allows to avoid the combination of high optical power and cryogenic test masses. To reduce thermal noise to an acceptable level in the low frequency band, it is expected that cryogenic suspensions and test masses are required. Even though tiny, the residual absorption of the dielectric mirror coatings deposits a significant amount of heat in the mirrors. Since this heat is difficult to extract, without spoiling the performance of the seismic isolation systems, it imposes a limit on the maximum circulating power of a cryogenic interferometer.

The baseline for ET is a 2-band xylophone detector configuration, composed of a low-frequency (ET-LF) and a high-frequency (ET-HF) detector. Both interferometers are Michelson interferometers featuring 10 km arm-length and an opening angle of 60 degrees. Due to their similar geometry both detectors will share a single facility. Table 10 gives a brief overview of the main parameters of the analysed low-frequency (ET-LF) and high-frequency (ET-HF) detector. Figure 165 shows sketches of the corresponding core interferometers and the filter cavities. The full layout of the two core interferometers of a single ET detector is depicted in Figure 163.

5.4.3 Arm cavity design

The size and shape of the laser beam inside the interferometer is defined by the surface shape of the cavity mirrors; the beam sizes at the arm cavity input mirrors (IM) and arm cavity end mirrors (EM) as well as the position of the cavity waist are determined by only two parameters, the radii of curvature (ROC) of IM and EM. Since inside the two Fabry-Perot cavities of the Michelson interferometer the GW interacts with the laser light, creating signal sidebands, the two arm cavities can be seen as the heart of the ET interferometers. The characteristics of the arm cavities have not only a high impact on the detector sensitivity and bandwidth, but also on the overall detector performance.

The choice of the beam size on the arm cavity mirrors is a trade-off process taking the following considerations into account:

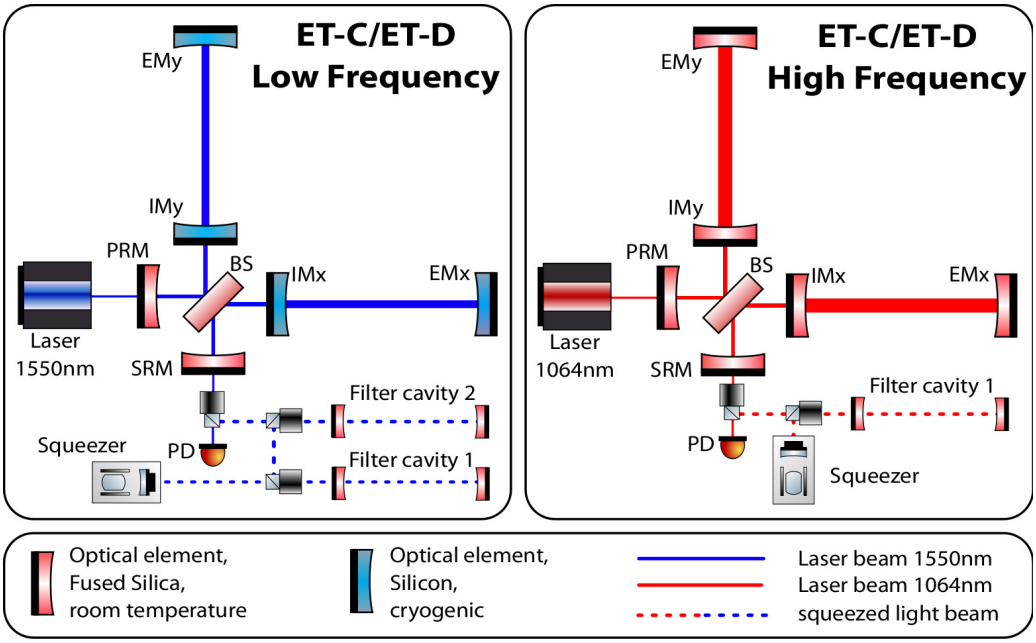

Figure 165: Simplified sketch of the ET low and high frequency core interferometers of a single ET-detector.

Parameter	ET-D-HF	ET-D-LF
Arm length	10 km	10 km
Input power (after IMC)	500 W	3 W
Arm power	3 MW	18 kW
Temperature	290 K	10 K
Mirror material	fused silica	silicon
Mirror diameter / thickness	62 cm / 30 cm	min 45 cm/ T
Mirror masses	200 kg	211 kg
Laser wavelength	1064 nm	1550 nm
SR-phase	tuned (0.0)	detuned (0.6)
SR transmittance	10 %	20 %
Quantum noise suppression	freq. dep. squeez.	freq. dep. squeez.
Filter cavities	1×10 km	2×10 km
Squeezing level	10 dB (effective)	10 dB (effective)
Beam shape	LG_{33}	TEM_{00}
Beam radius	7.25 cm	9 cm
Scatter loss per surface	37.5 ppm	37.5 ppm
Seismic isolation	SA, 8 m tall	mod SA, 17 m tall
Seismic (for $f > 1$ Hz)	$5 \cdot 10^{-10}\,\mathrm{m}/f^2$	$5 \cdot 10^{-10}\,\mathrm{m}/f^2$
Gravity gradient subtraction	none	none

Table 10: Summary of the most important parameters of the ET-D high and low frequency interferometers. SA = super attenuator, freq. dep. squeez. = squeezing with frequency dependent angle.

- For a given cavity length there is a minimal achievable beam size, which is determined by the divergence of the beam.
- Above this minimal beam size, any further increase in beam size leads to and additional reduction of the various thermal noise contributions.
- Finally the upper limit for the manageable beam size is given firstly by the maximum available mirror substrate size and secondly by the approaching of the cavity instability.

Box 5.3: Beam waist of the arm cavity beam eigenmode

In the case of a two-mirror cavity the size of the beam can be computed conveniently from the stability parameters g_1, g_2 defined as:

$$g_{1,2} = 1 - \frac{L}{R_{C\,1,2}} \tag{110}$$

with L the length of the cavity and $R_{C\,1,2}$ the radius of curvature of the input and end mirror respectively.
The waist size w_0 of the cavity eigenmode can then be computed as :

$$w_0^2 = \frac{L\lambda}{\pi}\sqrt{\frac{g_1 g_2(1-g_1 g_2)}{(g_1+g_2-2g_1 g_2)^2}} \tag{111}$$

In many cases a symmetric or near-symmetric cavity layout will be used (or can be used to estimate design options). In that case we set $g = g_1 = g_2$ which leads to a much simpler equation:

$$w_0^2 = \frac{L\lambda}{2\pi}\sqrt{\frac{1+g}{1-g}} = \frac{L\lambda}{2\pi}\sqrt{\frac{2R_C}{L}-1} \tag{112}$$

Typically we are interested in the size of the beam on the mirror, rather than the waist size directly. The beam size can be computed similarly as the waists; for the input mirror we get:

$$w_1^2 = \frac{L\lambda}{\pi}\sqrt{\frac{g_2}{g_1(1-g_1 g_2)}} \tag{113}$$

And in the case of a symmetric cavity we obtain:

$$w^2 = \frac{L\lambda}{\pi}\sqrt{\frac{1}{1-g^2}} = \frac{\lambda}{\pi}\sqrt{\frac{RL}{2-\frac{L}{R}}} \tag{114}$$

Arm cavity mirror size

A common method to define the mirror size is to demand the optical power loss due to clipping (light being lost because it 'falls over the edge of the mirror') to be less than 1 ppm. The computation of the scaling factors is described in [431] and results in:

mode	TEM_{00}	LG_{33}
mirror radius to beam radius	2.63	4.31

Minimal mirror sizes for ET

Using the currently discussed options for ET we can compute minimal mirror sizes for various options, by using $L = R_C$ resulting in $w_{\min} = \sqrt{\frac{L\lambda}{\pi}}$.

setup	min beam radius [cm]	min mirror diameter [cm]
LG_{33}, 1064 nm	5.8	50.2
TEM_{00}, 1550 nm	7.0	37.0

Realistic mirror sizes for ET

Using the minimal beam sizes is obviously not optimal in terms of thermal noise. Therefore we intend to push the beam sizes for ET towards the maximum feasible size, which corresponds to about 60 cm substrate diameter for fused silica mirrors and 50 cm for the silicon mirrors. Assuming 10 km long arm cavities, we can derive the following arm cavity characteristics.

IFO	λ	beam shape	mirror diameter	R_C	w_0	z_0	w	z_R
ET-HF	1064 nm	LG_{33}	62 cm	5691 m	2.51 cm	5000 m	7.2 cm	1859 m
ET-LF	1550 nm	TEM_{00}	45 cm	5577 m	2.9 cm	5000 m	9.0 cm	1698 m

5.4.4 Central interferometer design

The central interferometer consists of the two recycling cavities and the central Michelson interferometer formed by the beam splitter and the arm cavity input mirrors. The design of the central interferometer is mainly determined by two constraints. First of all it should allow for the implementation of non-degenerate recycling cavities. Second, the central interferometer has to serve as mode-matching telescope for the arm cavities.

The non-degenerate recycling cavity design used by the advanced detectors (see Figure 197) can probably not be directly adapted for ET, because no beam splitter substrates of the required dimensions would be available. For example the high frequency interferometer featuring an opening angle of 60 degree would require a beam splitter with a diameter of 115 cm.

Therefore we plan to investigate design options making use of input mirror substrates including a focussing lens with a focal length of 0.2 to 1 km and shifting the input mirrors away from the beam splitter. Figure 163 illustrates how such a configuration would look like. Please note that the arm cavity mirrors are the only full sized optical elements and that beam splitter and recycling mirrors can be significantly smaller. In addition in this scenario no additional folding mirrors are necessary in the recycling cavities.

Layout option for TEM_{00}, 1550 nm

The optical parameters of a possible solution based on a arm cavity length of $L = 10$ km and a TEM_{00} mode at 1550 nm are provided below:

- focussing element in or near the ITM with a focal length of $f = 303$ m
- distance ITM–BS: 300 m
- distance BS–MPR: 10 m
- beam size on BS: 6 mm
- beam size on MPR: 3.4 mm

The recycling cavity formed by MPR and ITM has a length of 310 m and a free spectral range of 484 kHz. The round-trip Gouy phase is given by ≈ 9.6 deg which corresponds to a mode separation frequency of 25.8 kHz.

Layout option for LG_{33}, 1064 nm

Using the same distances and focussing elements for the interferometer with a LG_{33}, 1064 nm beam, we also obtain reasonable numbers:

- beam size on BS: 4.7 mm
- beam size on MPR: 2.7 mm

- Gouy phase: 10.5 deg
- mode separation frequency: 28.1 kHz

These layout options are not yet optimised but they show that a separation between beam splitter and input optics in the order of 300 m represents a useful baseline. The numbers for the beam sizes at the beam splitter and recycling mirrors in both cases need to be checked against a detailed thermal noise computation.

Furthermore, the design needs to be evaluated for losses originating from astigmatisms inside the recycling cavities as well as for scattered noise issues.

5.5 Quantum noise reduction techniques

In a laser-interferometric gravitational-wave detector, there are different types of noise sources, which are usually categorized into quantum noise sources and classical noise sources (cf. Sec. 5.4). In terms of the noise, the main difference in the sensitivity of the different topologies comes from the spectral distribution of the quantum noise, even though there could also arise differences in the susceptibility to the classical noise, due to the fact that there are e.g. a different number of mirrors or different shapes of cavities. Therefore, the choice of topology is mainly defined by the choice of quantum noise reduction techniques used.

Quantum noise The so-called free-mass standard quantum limit (SQL) [432, 433] on high-precision measurements is imposed by the Heisenberg uncertainty principle, when it is applied to free-falling test masses. The spectral representation of this quantity, which falls off with one over frequency in amplitude and only depends on the test-mass weight and arm length of the detector, has become a standard reference for the quantum noise of interferometric gravitational-wave detectors. With the help of this reference one is able to compare the quantum noise of different topologies and configurations having the same test-mass weight and arm length. The quantum noise of a gravitation-wave detector consists of two parts: the quantum measurement noise, i.e. the direct imprecision of the measurement, and the quantum back-action noise. For interferometric gravitational-wave detectors, the direct measurement process consists of counting the number of photons by recording the photo current of a photo diode. The photons of a coherent beam arrive according to a Poissonian distribution. The photon counting error represents the direct measurement noise, which is usually called photon shot noise. The power of this noise source is inversely proportional to the circulating laser power. The measurement back action is clearly given by the laser light fluctuating radiation pressure which imposes a force onto the mirror and causes the radiation-pressure noise in the measurement output. The power of this noise source is, in contrast to the photon shot noise, directly proportional to the circulating laser power. Since the suspended mirrors in a gravitational-wave detector can be approximated as free falling test masses in the direction of the incident laser beam—due to a very low eigenfrequency of the pendulum created by the mirror's suspension—and since the two quantum noise sources are uncorrelated, they result in the free mass standard quantum limit. In this case, the radiation-pressure noise dominates the spectral density of the quantum noise at lower frequencies while the shot noise dominates at higher frequencies. Therefore, one in general needs to compromise between high optical power for a low shot noise and not too high optical power in order to cope with the radiation-pressure noise.

Box 5.4: Xylophone configuration

Based on the requirements on the quantum noise sources (and technical ones, cf. Sec. 5.4), we have chosen a xylophone configuration [434] as an optimal design of ET (cf. Sec. 5.4.2). Each detector in a xylophone configuration is split into two interferometers, one optimized for low frequencies, operating at low light power and the other optimized for high frequencies operating at high light power. A xylophone configuration resolves two major problems:

- The simultaneous usage of high circulating light power for increasing the high-frequency sensitivity and cryogenic mirrors for decreasing thermal noise. In a xylophone configuration the low-frequency interferometer utilizes relatively low optical power which does not pose a problem of heating the cryogenic mirrors, while the mirrors at room temperature in the high-frequency interferometer allow use of much higher light power.
- Simultaneous decrease of photon shot noise and radiation pressure noise. The sensitivity of the radiation pressure noise-dominated low-frequency interferometer benefits from low light power, while the sensitivity of the shot noise-dominated high-frequency interferometer benefits from the high light power.

On the other hand, the SQL is actually not a real limitation on the quantum noise strength of a gravitational-wave detector. Several methods for overcoming the SQL, which are suitable for laser interferometric gravitational-wave detectors, have been proposed. They have different, and often very special, requirements on the optical topology. The quantum-noise reduction techniques can be divided into two main groups, where the classification is not chosen in terms of the topology, but by the technique of how the quantum noise is reduced: the first one is based on the principle, that the goal of the gravitational-wave detectors is not the measurement of the test-mass position, which is a quantum variable and thus cannot be measured continuously with a precision better than the SQL, but rather the detection of a gravitational-wave strain as a signal, which can be treated as a classical (tidal) force acting on the test mass mirrors [435]. It was shown that by introducing cross-correlation between the quantum measurement noise and the quantum back-action noise, arbitrary high sensitivity (in terms of the quantum noise) can be achieved [436]—assuming the absence of optical losses. The correlations are actually used here to quantum-mechanically cancel the back-action noise in the measurement output. Thus, this method relies clearly on **noise-cancellation techniques**. The second group of methods is based on the idea that the spectral distribution of the SQL itself is not a fixed constant, but depends on the test object dynamics, i.e. on the (mechanical) susceptibility of the test mass, which relates the test-mass motion to all forces acting on it. Therefore, the free-mass SQL can be beaten by using a more responsive object and thus increasing its signal displacement—the harmonic oscillator as an example has much stronger response to near-resonance forces and therefore a better sensitivity than the free-mass SQL around the resonance frequency. Therefore, the sensitivity gain is obtained not by delicate cancelation of the quantum noise, but by a classical **signal amplification**. More details about quantum-noise-reduction techniques are given in Sec. 5.5.1. In that section we will also see that with those topologies there are different detector options for the main interferometer: the position meter, the optical spring interferometer, the speed meter, the optical transducer. Furthermore, all these main interferometer detectors can then be additionally equipped with the input-squeezing technique (for details cf. Sec. 5.5.3) and the variational readout technique (cf. Sec. 5.5.1).

5.5.1 Review of quantum non-demolition topology options

Already the second generation of laser-interferometric gravitational-wave detectors (such as the Advanced LIGO detector [5] and the the Advanced VIRGO detector [7]) are expected to be limited by the quantum noise—the shot and the back-action noise—nearly within the full detection band. Within the context of the third generation of detectors this aspect becomes even more important, since there is an enormous effort in increasing the quality of the technical components of the interferometer—such as the mirror and beam splitter materials as described in Sec. 5.6; the suspension systems (see Sec. 4); the stability of the laser source (Sec. 5.7.1)—in order to decrease

the strength of all the technical noise sources by a large amount. Beside parameters such as the circulating optical power and the test-mass weight, the spectral distribution of the quantum noise mainly depends on the topology of the detector, including the injection strategy at the bright port as well as the detection strategy at the dark port of the interferometer. Therefore, the choice of the topology and configuration of the detector are severe for the design of future gravitational-wave detectors. Especially, because parameters as the optical power and the test-mass weight will always be limited due to technical reasons, the design of future gravitational-wave detectors requires quantum-noise-reduction techniques. As we have seen in Sec. 5.3.1, there are different topology options available which can all be fitted into an L-shaped geometry. With the different topologies one can build up different types of detectors, having specific quantum noise features, as we have reviewed within this design study. Many of them have actually great potential in reducing the quantum noise, but there is a big discrepancy in terms of readiness: some are far away from being ready to be implemented into gravitational-wave detectors, others have been already demonstrated experimentally as a proof of principle or have been even already implemented into gravitational-wave detectors. We have investigated and reported the potential sensitivities of the following topology options (see details in Appendix D.2).

- **Optical-spring interferometer**. Optomechanical coupling in the arm cavities of a Michelson interferometer with detuned signal-recycling can induce a restoring force onto the differential motion of the arm-cavities mirrors—the optical spring effect, which can up-shift the mechanical resonance frequency into the detection band. The sensitivity of the detector is enhanced around an additional resonance, the optical spring resonance.
- **Speed-meter interferometer**. A speed meter is able to surpass the standard quantum limit broadbandly by removing the (frequency-independent) radiation-pressure noise from the measurement output. Speed-meters can be realized in different ways, for instance by using a sloshing cavity or polarizing optics in a Michelson interferometer, using the Sagnac interferometer with the ring cavities, etc.
- **Optical-inertia interferometer**. A detuned signal-recycling cavity turns a speed meter interferometer into an optical inertia interferometer: the optomechanical coupling influences the dynamics of the test-masses—it modifies their dynamical mass by introducing an optical inertia. The hope is that in this way one can create a test object which has a high resonance-type mechanical susceptibility in a broad frequency band.
- **Optical transducer with local readout**. The idea of such schemes is not to measure the phase shift of the laser field via monitoring the outgoing modulations fields at the dark port of an interferometer but to measure the redistribution of optical energy directly inside an interferometer by converting the gravitational-wave strain via radiation pressure into real mirror motion. This motion should then be sensed by an additional highly sensitive local meter.
- **(Frequency-dependent) input-squeezing interferometer**. The squeezed field injection with frequency dependent squeezing angle allows an overall quantum noise reduction including the radiation pressure noise (details in Sec. 5.5.3). Frequency-dependent squeezing can be achieved with special filter cavities. The filters allow the preparation of squeezed states providing a frequency-dependent squeezed quadrature which is adapted to the interferometers quadrature rotation (details in Sec. 5.5.4). The injection of such a prepared squeezed state leads to a quantum noise reduction over the entire detection band.
- **Variational-output interferometer**. Interferometer detectors can be equipped with a balanced homodyne detection and with the variational-output technique. Here filter cavities are used to make the quadrature angle of the detected output field frequency dependent and therefore realize a broadband evasion of the radiation-pressure noise.

Our analysis shows that one of these techniques alone is probably not able to reduce the quantum noise in the required broadband way, but certain combinations among these techniques are possible. Due to the technical readiness issues of the reviewed topology options, we propose to split the detector into two dual-recycled, squeezed light-injected Michelson/Fabry-Perot interferometers, the low- and high-power ones, as a conceptual design of the 3rd generation GW detector for the means of reduction of quantum noise (see details about xylophone configuration in Sec. 5.4.2). However, the study of speed-meter topology of the low-power interferometer

as a potential method of improving the low-frequency sensitivity should be included into the R&D phase.

5.5.2 Alternative topologies and interferometry types

We investigated the possibility of implementation of displacement noise reduction techniques in ET (see Appendix D.7). The class of so-called displacement noise free interferometers allows complete cancelation of all the information about the displacement noises from the output signal of the interferometer at the cost of significant reduction of the GW susceptibility. This is possible due to the distributed nature of the GWs as opposed to the localized nature of displacement noises. Another class of schemes allow partial displacement noise cancelation of some of the optical elements (cavity mirrors, beamsplitters, etc) in the linear combination of the interferometer's output signals. However, both types of noise reduction schemes suffer from either very weak GW susceptibility or very impractical requirements (rigid platforms, etc) and uncanceled noises (like laser noise) thus making them barely advantageous over the conventional topologies.

We also investigated the alternative to laser interferometry—atomic interferometry (see Appendix D.8). Light pulse atom interferometry can be thought of as a comparison of time kept by internal atom clocks and optical wave of the laser. The incoming gravitational wave changes the rate of time which can be seen in an interferometer phase shift. The major advantage of the atom-light interferometry over conventional optical interferometry is that the atoms, playing the role of inertial sensors, are not subjected to the external fluctuations in comparison with the mirrors, and thus do not require sophisticated vibration isolation techniques. Although light pulse atom interferometry has already found applications in atomic clocks, metrology, gyroscopes, gradiometers and gravimeters, its implementation in gravitational-wave detection requires detailed and comprehensive study and further development of the noise-lowering techniques. With the current available technologies atomic interferometers cannot provide the same level of sensitivity as the well-developed optical interferometers.

5.5.3 Quantum noise reduction with squeezed states of light

The following description of squeezed light usage in gravitational wave detectors is an excerpt of the article [437]. At first glance, quantum physics imposes a fundamental limit on metrology—the science of measurement—and thus imposes a corresponding limit on the sensitivity of GW detectors. A fundamental problem in optical interferometry is the random distribution of photons arriving at the photodiodes. This statistical fluctuations obscure the tiny power variations caused by GW signals. Fortunately, quantum physics also provides a solution to this problem via the concept of quantum entanglement.

Box 5.5: Quantum metrology with squeezed states of light

"Quantum metrology" uses quantum entanglement to improve the measurement precision beyond the limit set by measurement counting noise. The first such proposal was made by C.M. Caves in 1981 [438]. He showed that the quantum noise limited sensitivity in a shot noise dominated interferometer can be enhanced by the injection of a broadband (frequency independent) squeezed field into the interferometers signal port. Furthermore he stated that "[...]the greatest potential usefulness of squeezed states lies in its ability to increase the sensitivity without increasing the circulating laser light power[...]". Accordingly at a point, where the interferometer performance will be limited by the available laser power or thermal load in its optics, squeezed light injection can be used to either relax the high power requirement or to increase the sensitivity further. Fig. 166 illustrates the principle of squeezed light enhanced metrology.

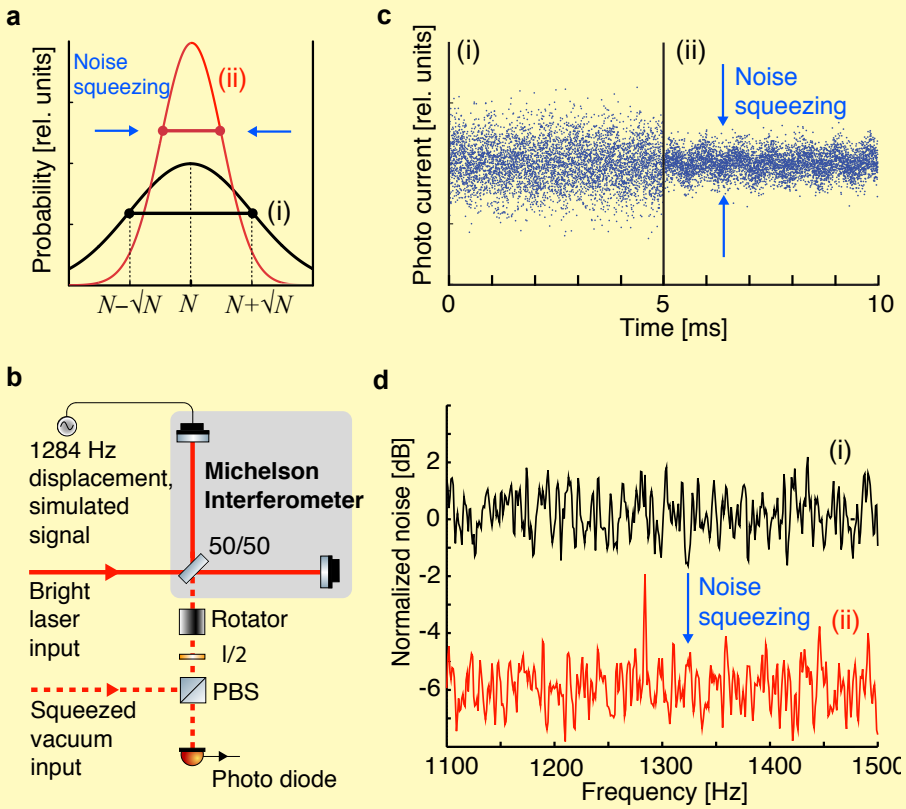

Figure 166: Squeezed light enhanced metrology (a) For large photon numbers N, squeezed light shows a photon counting statistic with a standard deviation smaller than $\pm\sqrt{N}$. In all panels, (i) correspond to shot-noise and (ii) to 6 dB squeezed noise. (b) A squeezed vacuum beam is injected into the dark signal port of a Michelson interferometer, in addition to the conventional bright laser input. The squeezed beam leads to path entanglement of the light fields in the two arms and to an improved signal to noise ratio, as shown on the right. Without squeezing, the optical path length modulation at 1284 Hz is neither visible in the time series of the photo-electron current (c, simulation by B. Hage, AEI) nor in its noise power spectrum (d, measurement, courtesy of H. Vahlbruch, AEI [439]). In (c) as well as in (d), the signal is clearly visible when squeezing is applied (ii).

Squeezed states [440–443] belong to the class of so-called *nonclassical* states of light. Generally, nonclassical states are those that cannot be described by a classical (positive valued) probability distribution using the coherent states as a basis (the P-representation) [444]. Let us first consider the coherent states. If light in a coherent state is absorbed by a photodiode, mutually independent photon 'clicks' (in terms of photo-electrons) are recorded, a process that is described by Poissonian counting statistics. Due to quantum mechanics, every individual 'click' is not predictable, but rather the result of a truly random process. If the number of photons per time interval is large ($N \gg 1$), its standard deviation is given by $\sqrt{N}$, see Fig. 166 a (i). This uncertainty gives rise to *shot-noise*. For a *squeezed* light beam, the detection of photons is not time-independent but instead contains quantum correlations. Nevertheless, the photon statistics still cannot be predicted by some external clock. It instead shows auto-correlations that give rise to a reduced standard deviation, as shown in Fig. 166 a (ii). The correlations might be described in the following way. Whenever the quantum statistics might drive the actual photon number above the average value N, a similar number of photons destructively interfere with the main body of photons providing a (partial) compensation of the fluctuation. These quantum

correlations *squeeze* the interferometer's shot-noise below its natural value. Another complementary way of describing the properties of squeezed states is based on the phase space quasi-probability distribution using the amplitude and phase quadratures of a light wave (the Wigner function) [441, 444].

A squeezed state that contains only quantum-correlated photons with no coherent amplitude is called a *squeezed vacuum state* [444]. If such a state is overlapped with a coherent laser beam on a semi-transparent beam splitter, two beam splitter outputs are generated which are quantum correlated. As a consequence, the overall (bi-partite) quantum state cannot be written in terms of products of the two beam splitter output states. Such a quantum state is called non-separable or *entangled*. This is exactly what happens if a squeezed state is injected into the signal output port of a laser interferometer for GW detection (Fig. 166 b). The two *high-power* light fields in the interferometer arms get entangled and the light's quantum fluctuations in the two arms are correlated with each other. Although the fluctuations are not predictable from the outside, they provide an improved signal-to-noise ratio in the interferometer. Recall that an interferometer measures the optical path length change in one interferometer arm with respect to the other arm. If the quantum noise in the two arms is correlated it will cancel out. This entanglement interpretation was not discussed in the initial proposal by Caves. Nevertheless, it shows that the application of squeezed states in interferometers is a real application of quantum metrology by its very own definition. The entanglement produced by splitting a squeezed state at a semi-transparent beam splitter was tomographically characterized and quantified in [445]. Fig. 166 c shows a simulated signal from a photodiode, without (i) and with (ii) *squeezing*. The tiny modulation in the interferometer's output light due to the (simulated) passing GW is visible only with the improved signal-to-noise ratio. Fig. 166 d shows the analogue in frequency space, i.e. after a Fourier transform of the photo current was applied.

The above paragraph shows that squeezed states can be conveniently combined with the extremely high photon numbers of coherent light to improve a laser interferometer, as proposed in [438] and shown in Fig. 166 b. In fact, the stronger the squeezing factor [441, 444] the greater the path entanglement and the signal-to-noise improvement.

Shortly after Caves proposed squeezed states of light for laser interferometers in 1981, the first experimental demonstration of squeezed light [446] and proof of principle demonstrations of quantum metrology were achieved [447, 448]. In parallel, it was theoretically discovered that squeezed states offer even more advances in metrology than 'just' reducing the quantum shot-noise. From the early days of quantum physics, when fundamental aspects of the measurement process were discussed, it was clear that, in general, a measurement disturbs the system to be measured [433]. The measurement of quantity A (say a position of a mirror) increases the uncertainty of the non-commuting quantity B (say the mirror's momentum). Both observables are linked by a Heisenberg Uncertainty relation. For repeated measurements of A, the increased uncertainty in B disturbs the measurement of A at later times. This is referred to as *quantum back-action noise*. Here, the back-action arises from the fluctuating radiation pressure due to the reflected light [449]. It is significant if the mirror's mass is low and a large photon number is reflected. In the 1970s, ideas were developed that showed how, in principle, back-action noise for continuous measurements can be avoided. Such schemes were called quantum-non-demolition (QND) measurements [450, 451]. However, for laser interferometric GW detectors using *quasi-free* falling mirrors it remained unclear if QND schemes exist. In [438, 449] it was concluded that back-action noise of a free mass position measurement can in principle not be avoided and, together with photon counting noise, defines a *standard quantum limit* (SQL). In [452, 453] it was argued, however, that measurements below the SQL of a free mass are indeed possible. The discussion remained controversial [454] until Jaekel and Reynaud [455] were able to convincingly show that the cleverly arranged squeezed states in a GW detector can simultaneously reduce the shot-noise and the radiation pressure noise, by almost arbitrary amounts (as long as most of the photons belong to the light's coherent displacement).

So far no experiment has achieved a position measurement with sensitivity even at, let alone below, its standard quantum limit. Eventually this will be achieved, possibly first in future gravitational wave detectors. Advanced detectors are in fact designed to have a sensitivity at or just below their SQLs. Once the SQL is reached, a new level of quantum metrology is achieved, because the position-momentum uncertainty of the mirror becomes correlated with the quadrature uncertainty of the reflected optical field. In this way, entanglement between the mechanical and the optical system can be observed [456]. This is all the more remarkable from the perspective of GW detectors since we are talking about mirrors with masses of 40 kg, planned for the upcoming Advanced LIGO

[6], and even in the order of a 100 kg concerning the envisaged LF-detector of ET. Eventually, even two such mirrors might be projected via entanglement swapping [457] into an entangled state [458]. Obviously quantum metrology opens the possibility for further studies of the peculiarities of quantum physics at a macroscopic scale.

Squeezed light for Gravitational wave astronomy Laser interferometers for GW astronomy are facing extreme sensitivity requirements that can only be achieved if all available tools, inclusive of quantum metrology, are combined in an elaborate measurement device. Squeezed light must be generated in a non-linear interaction. Squeezed light was first produced in 1985 by Slusher et al. using four-wave-mixing in Na atoms in an optical cavity [446]. Shortly after, squeezed light was also generated by four-wave-mixing in an optical fibre [459] and by parametric down-conversion in an optical cavity containing a second order non-linear material [460]. In these early day experiments, squeezing of a few percent to 2 to 3 dB were routinely observed (For an overview of earlier experiments and squeezed light generation in the continuous-wave as well as pulsed regime please refer to Ref. [461]).

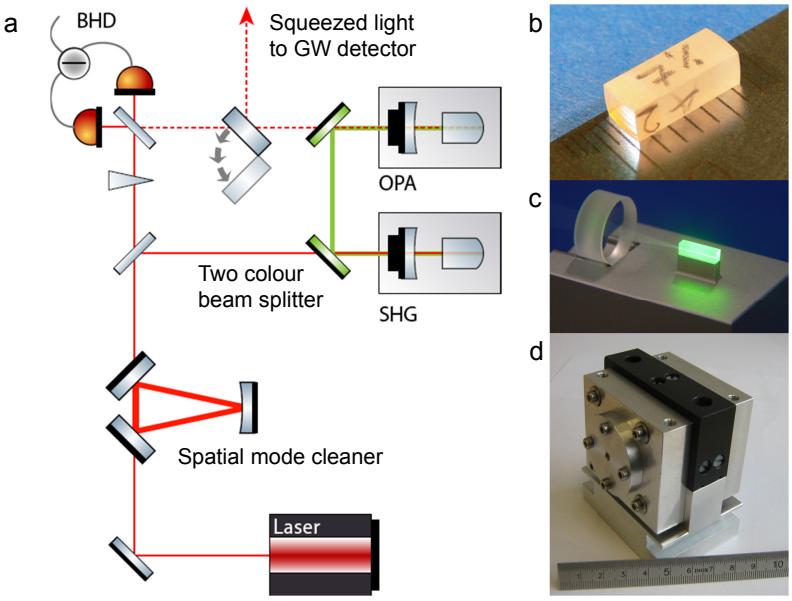

Figure 167: Generation of squeezed light (a) A continuous-wave laser beam at the GW detector wavelength is first spatially filtered and then up-converted to a field at half the wavelength (second harmonic generation, SHG). That beam is then mode-matched into the 'squeezing resonator' in which a tiny fraction of the up-converted photons are spontaneously down-converted by optical parametric amplification (OPA) producing a squeezed vacuum state. The squeezing factor is validated by a balanced homodyne detector (BHD). SHG as well as OPA are realized by a non-linear crystal (b), here a 6 mm long MgO:$LiNbO_3$ crystal, inside an optical resonator (c) formed by an external cavity mirror and the dielectrically coated crystal back surface. The two non-linear resonators may be constructed in an identical way and are put into temperature stabilized housings (d).

GW detectors are operated with high-power, quasi-monochromatic continuous-wave laser light with an almost Fourier-limited spatial distribution of a Gaussian TEM_{00} mode. For a non-classical sensitivity improvement, squeezed light in exactly the same spatio-temporal mode must be generated and mode-matched into the output port of the interferometer [438], providing interference with the high-power coherent laser beam at the interferometer's central beam splitter. High-power lasers for GW astronomy are based on optically pumped solid-state crystals in resonators [462], suggestive of a similar configuration for a "squeezed light resonator". Fig. 167 (a) shows a schematic setup for generation of squeezed light that is built upon one of the very first squeezing experiments [460], a setup that has been used in many experiments thereafter [463–466]. The setup uses a solid state laser similar to those used as master lasers in high-power systems. After spatial mode filtering, second harmonic generation (SHG) in an optical cavity containing a second-order non-linear crystal is applied

to produce laser light at twice the optical frequency. The second harmonic light is then mode-matched into the squeezing resonator to pump a degenerate optical parametric amplifier.

Fig. 167 (b-d) show photographs of the non-linear crystal, the optical arrangement and the housing of a squeezing resonator. The crystal is temperature-stabilized at its phase-matching temperature. At this temperature the first-order dielectric polarization of the birefringent crystal material with respect to the pump is optimally overlapped with the second-order dielectric polarization of the resonator mode at the fundamental laser frequency. This ensures a high energy transfer from the pump field to the fundamental Gaussian TEM_{00} resonator mode, i.e. efficient parametric down conversion.

Initially, the resonator mode is not excited by photons around the fundamental frequency, i.e. it is in its ground state, characterized by vacuum fluctuations due to the zero point energy [444]. Note that the process is typically operated *below* oscillation threshold in order to reduce phase noise coupling from the pump [467]. This setup produces a squeezed vacuum state [444]. The down-converted photon pairs leaving the squeezing resonator exhibit quantum correlations which give rise to a squeezed photon counting noise when overlapped with a bright coherent local oscillator beam. The squeezed field is detected by interfering it with a coherent local oscillator beam, either in a balanced homodyne detector (BHD), see Fig. 167 (a), or when injected into a GW detector and detected with a local oscillator from the GW detector along with an interferometric phase signal, see Fig. 166. The closer the squeezing resonator is operated to its oscillation threshold, and the lower the optical loss[20] on down-converted photon pairs, the greater the squeeze factor is. For instance, the observation of a squeezing factor of 2 is only possible if the overall optical loss is less than 50% [461]. A 90% nonclassical noise reduction, i.e. a squeezing factor of 10, or 10 dB, already limits the allowed optical loss to less than 10%.

Although squeezed light was demonstrated in the 1980s shortly after the first applications were proposed [446, 459, 460], several important challenges pertaining to the application of squeezed states to GW detectors remained unsolved until recently.

First, squeezing has always been demonstrated at megahertz frequencies, where the technical noise of the laser light sources is not present. At these frequencies, the laser operates at or near the shot-noise limit. In the 10 Hz to 10 kHz band where terrestrial GW detectors operate, technical noise masked and overwhelmed the observation of squeezing. For example, thermal and mechanical fluctuations can be many orders of magnitude larger than shot noise. Until recently, it was not certain that a laser field could even be squeezed and matched to the slow oscillation period of GWs. Second, it was previously not known whether squeezed light was fully compatible with other extremely sophisticated technologies employed in GW detectors, such as signal-recycling. Third, the technology to reliably produce stable and strong squeezing with large squeeze factors was lacking. Long term observation of strong squeezing was a technical challenge until recently.

These challenges have all been overcome in the past decade. All the open questions have now been satisfactorily addressed. This development is very timely since many known advanced classical interferometric techniques have almost been exhausted. Many remaining classical improvements are becoming increasingly difficult and expensive to implement.

Generation of squeezing in the audio-band A major breakthrough in achieving squeezing in the audio band was the insight that the dominant noise at audio frequencies that degrades squeezed light generation couples via the coherent laser field that was used to control the length of the squeezed light laser resonator, whereas noise coupling via the second harmonic pump field is insignificant [469, 470]. This led to the first demonstration of audio-band squeezing at frequencies down to 200 Hz [471], see Fig. 168 a. There the length of the squeezing resonator was stabilized without a bright control beam by using the phase sensitivity of the squeezing itself—a technique known as quantum noise locking [472]. Subsequently a coherent beam control scheme was invented [473] for simultaneous control of both the squeezing resonator length and the squeezing angle [444]. Shortly thereafter another noise source was identified and mitigated, which allowed for squeezing of more than 6 dB throughout the audio-band down to 1 Hz [474]. This noise source arose due to tiny numbers of

[20] In this context the term optical loss refers to the total power loss experienced by the squeezed light from the squeezed light source to the photo detector.

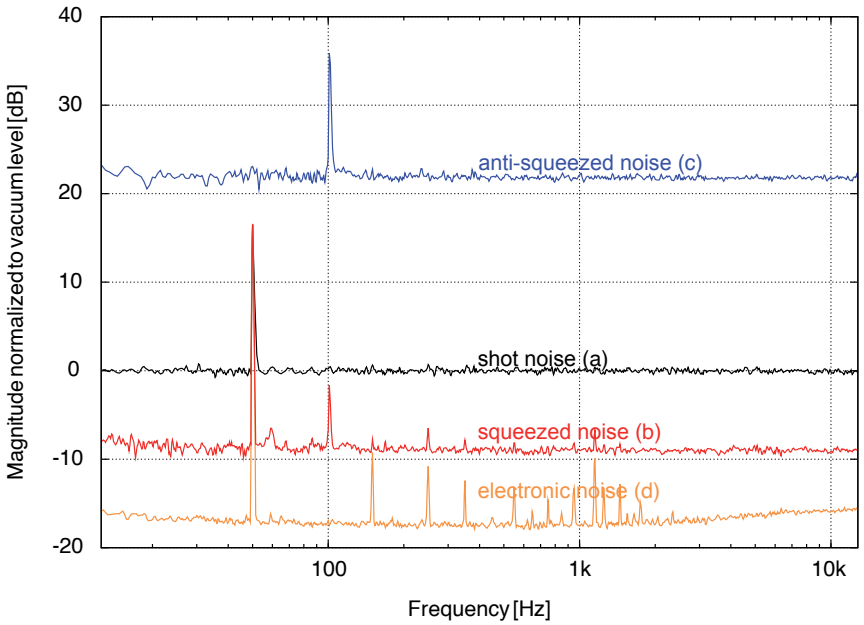

Figure 168: Quantum noise squeezing The spectral analysis of measured noise powers without (a) and with 'squeezing' (b). Trace (a) is the 'non-squeezed' shot-noise, serving as reference level (0 dB). The corresponding noise in the orthogonal quadrature, 'anti-squeezed', is shown in trace (c). Trace (d) shows the electronic dark noise level. Current best performance of a squeezed light laser for GW detection shows an up to 9 dB squeezed noise over the complete detection band of ground-based GW detectors [468].

photons that were scattered from the main laser beam and rescattered into the audio band squeezing mode after having experienced a frequency shift due to vibrations and thermal expansions of potential scattering surfaces, an effect known as *parasitic interferences*. Since bright laser beams cannot be completely avoided, the recipe for the generation of audio-band squeezing turned out to be fourfold: avoiding scattering by using ultra-clean super-polished optics, avoiding rescattering by carefully blocking all residual faint beams caused by imperfect anti-reflecting surfaces, reduce the vibrationally and thermally excited motion of all mechanical parts that could potentially act as a re-scattering surface and avoid pointing fluctuations [475].

Compatibility of squeezing with other interferometer techniques Current detectors achieve their exquisite sensitivity to GWs due to their kilometre-scale arm lengths, the enormous light powers circulating in the enhancement resonators (arm, power- and signal-recycling cavities), and sophisticated pendulum suspensions that isolate the test mass mirrors from the environment When these techniques were developed, squeezing was not envisioned to become an integrated part of such a system. Building on existing theoretical work [476, 477], a series of experimental demonstrations of squeezed state injection into GW detectors were carried out. These included compatibility with power recycling, with signal recycling [478, 479], and with the dynamical system of suspended, quasi-free mirrors [480, 481].

Generation of strong squeezing Squeezing has significant impact in quantum metrology if large squeezing factors can be produced. Squeezing of 3 dB improves the signal-to-noise ratio by a factor of $\sqrt{2}$, equivalent to doubling the power of the coherent laser input. Squeezing of 10 dB corresponds to a ten-fold power increase. Remarkably, the experimentally demonstrated squeezing factors have virtually exploded in recent years [482–484], culminating in values as large as 12.7 dB [8]. All the squeezing factors above 10 dB were observed with monolithic resonators and at MHz frequencies. However, reduced optical loss in non-monolithic resonators and a careful elimination of parasitic interferences should in principle enable such factors also in the GW band. An

8 to 10 dB improvement based on strong squeezing seems realistic for future GW detectors in their shot-noise limited band [8].

So far, strong squeezing values have been reported for a wavelength of 1064 nm. However, the procedure of squeezed light generation is also applicable for the wavelength of 1550 nm that will be required for future, cryogenic GW detectors. Recently, the generation of squeezing at a wavelength of 1550 nm was reported in a first proof-of-principle experiment [485].

The first squeezed light laser for GW detection Based on the previous achievements reviewed here, very recently the first squeezed light laser for continuous operation in GW detectors was designed and completed [439, 468]. Up to 9 dB of squeezing over the entire GW detection band have been demonstrated (Fig. 168b). This laser produces squeezed vacuum states and is fully controlled via co-propagating frequency-shifted bright control beams. This 9 dB squeezing factor is limited by technical effects: the squeezing resonator has to have an adjustable air gap to allow for an easy way to apply length control. The anti-reflection coated surface in the resonator introduces additional loss and reduces the escape efficiency. Moreover, a Faraday isolator has to be used in the squeezed beam path in order to eliminate parasitic interferences. This rotator produces a single pass photon loss of about 2%. This squeezed light source is designated for continuous operation in the GEO600 GW detector. A squeezed light source based on a design that should have less sensitivity to retro-scattered light [486] is being prepared for deployment on one of the most sensitive detectors, the 4 km LIGO detector in Hanford, Washington.

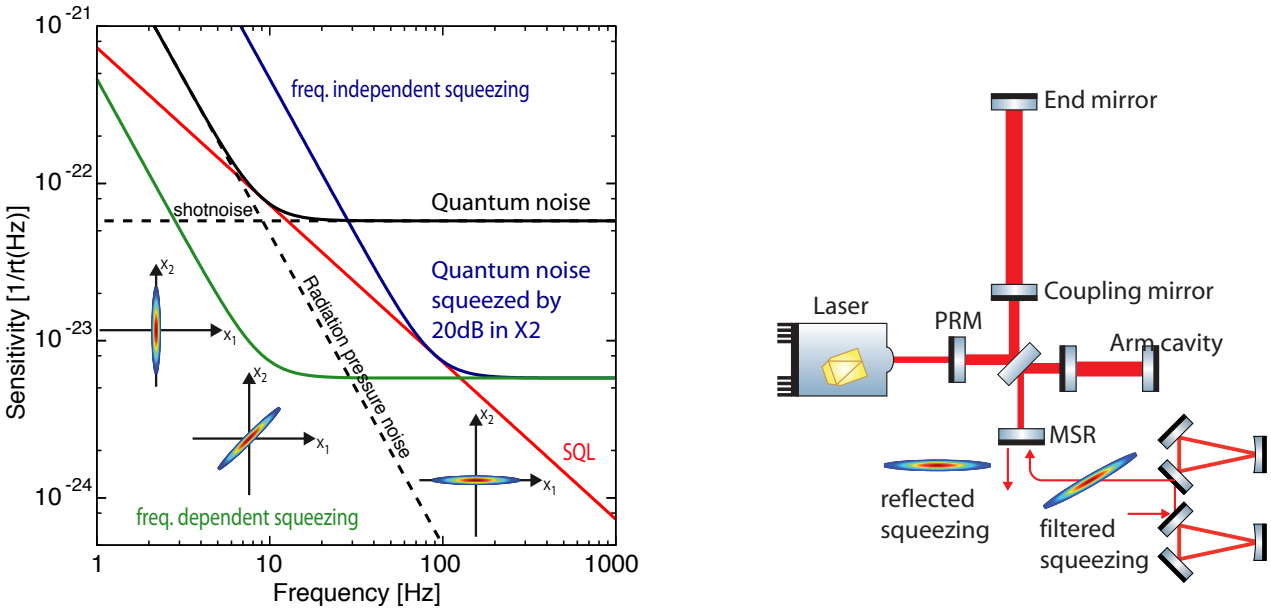

Figure 169: Beating the SQL in position meter with frequency dependent light (left). Injection of frequency dependent squeezed light injection in an optical spring interferometer (right).

5.5.4 Filter cavities

At first view the enhancement of an interferometer's sensitivity with frequency independent squeezing (squeezed light with a fixed quadrature angle) can only be achieved in a certain frequency range. This is a direct consequence of the Heisenberg uncertainty principle. Considering a simple Michelson interferometer the quantum noise in its phase quadrature (shot noise) can be reduced by the amount of squeezing. Unfortunately, the quantum noise in the amplitude quadrature (radiation pressure noise) will be increased by the same amount enhancing the noise at low frequencies.

It was revealed by Unruh [487] and others [452, 488] that squeezed field injection with frequency dependent squeezing angle allows an overall quantum noise reduction including the radiation pressure noise thereby beating the standard quantum limit (SQL). This is demonstrated in Fig. 169 (left). Figure 169 (right) illustrates squeezed light injection in an optical spring interferometer. Here, an additional rotation of the squeezing ellipse is caused first by the phase-space rotation of a detuned cavity and second due to the optical spring resonance. In this case at least two filter cavities are necessary to achieve a broadband reduction of quantum noise with squeezed states of light. This is what we propose for the low-frequency ET-LF interferometer (cf. Sec. 5.4.2). For the high-frequency ET-HF interferometer one filter cavity is enough (cf. Sec. 5.4.2 and [489]). Details about the derivation of the filter cavities design parameters are given in Appendix D.3.2.

Figure 170 shows the Wigner representation of a coherent vacuum state and a 20 dB squeezed state for different squeezing angles.

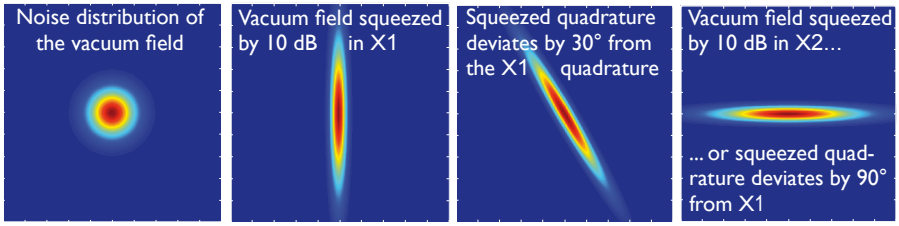

Figure 170: From left to right: Wigner representation of a vacuum state (left), a pure 10 dB amplitude squeezed state, a 10 dB squeezed state rotated in phase-space by 30 degrees and an amplitude squeezed state rotated by 90 degrees, i.e. a phase squeezed state.

Restrictions for the baseline length of the filter cavity According to the laws of quantum mechanics, whenever the optical losses (like scattering, absorbtion, etc) are encountered in the optical train, the light in the vacuum state is introduced. This generally unsqueezed light mixes up with the squeezed light thus lowering the squeezing factor of the latter. This is usually referred to as the degradation of the squeezed state which leads to the decrease of sensitivity. We demonstrate this degradation schematically in Fig. 171 and show dependence of the squeezing factor on the losses in Fig. 172.

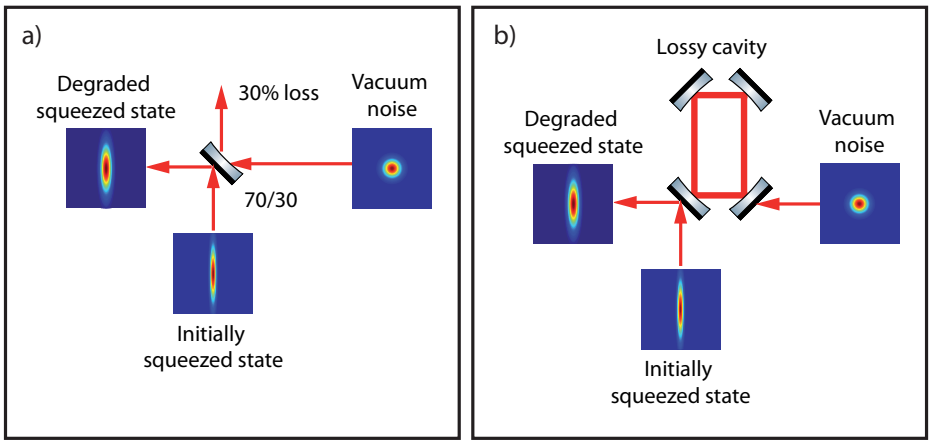

Figure 171: The figure illustrates the intermixture of vacuum noise to a squeezed field at lossy (open) ports. a) Consideration of a beam splitter with $R_{\rm bs} = \rho_{\rm bs}^2 = 0.7$ and $T_{\rm bs} = \tau_{\rm bs}^2 = 0.3$. In reflection of the beam splitter the initially squeezed state gets attenuated by the factor $\rho_{\rm bs}$. The vacuum noise couples to the reflected squeezed field with an efficiency of $\tau_{\rm bs}$ leading to a degradation of the squeezing level. b) Consideration of a lossy cavity. In this case, the intermixture of vacuum noise is frequency dependent, since the transfer function of the cavity comes into play. The degradation is maximum at the resonance frequency of the cavity. At frequencies far away from resonance the cavity behaves like an almost perfect mirror, i.e. the squeezing is preserved.

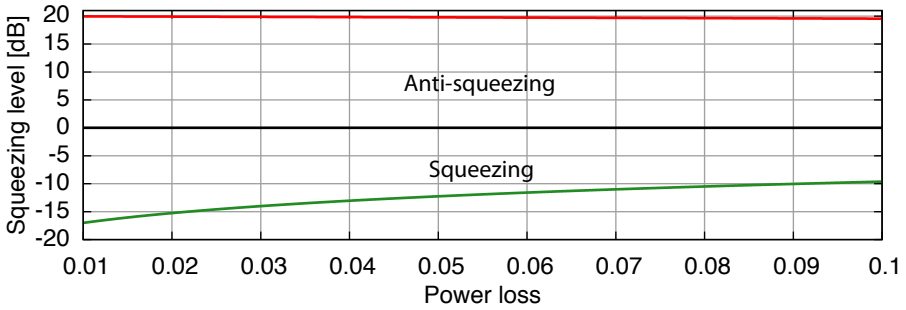

Figure 172: The figure shows the degradation of a 20 dB squeezed state due to optical loss. It can be seen that in contrast to the anti-squeezing level, the squeezing degrades rapidly with increasing loss. At a power loss of about 9 % the squeezing level is reduced from 20 dB to 10 dB whereas the anti-squeezing level is still about 19.6 dB.

Generally, any round-trip loss will degrade the squeezing level at sideband frequencies being resonant in the filter cavity. For a given power round-trip loss (mainly caused by scattering) the resulting loss in reflection of the filter cavity increases with a decreasing baseline length of the filter. As well, for a certain length and a certain round-trip loss the loss imposed on the squeezed field increases with a decreasing half-bandwidth that needs to be realized. The details about determination of the baseline length are given in Appendix D.3.1. Figure 173 shows the filter cavity performance as a function of its baseline length.

Our investigation demonstrated that the round-trip loss ultimately restricts the minimal allowed baseline length and consistently the performance of the filter cavities. As it is expected that the round-trip loss of the filters will be dominated by scattering at imperfect mirror surfaces, the optical layout needs to be designed such that the amount of scattering is reduced as much as possible. The scattering in different optical layouts is treated in below. Figure 174 demonstrates the sensitivity of the ET-D-HF interferometer at various lengths of the filter cavities. Note that the high-frequency sensitivity is mostly independent of the cavity length while the low-frequency one decreases with the decrease of length.

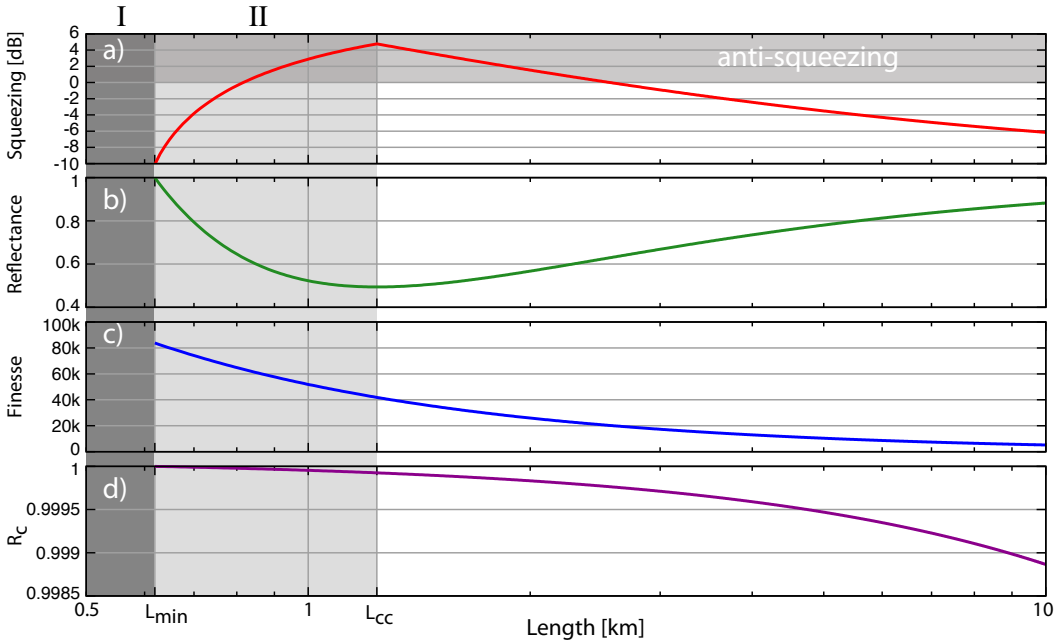

Figure 173: The figure shows the filter cavity performance as a function of its baseline length L_{fc} (details in Appendix D.3.1). Graph a) shows the remaining squeezing level in reflection of the filter cavity at its resonance frequency. Graph b) shows the according reflectance of the filter cavity. Graph c) and d) show the filter cavity finesse and coupling mirror reflectance R_{c}, respectively. The two grey shaded areas in the left highlight the region where $L_{\mathrm{fc}} < L_{\mathrm{cc}}$ (area II) and where $L_{\mathrm{fc}} < L_{\mathrm{min}}$ (area I). In the considered example ($\gamma_{\mathrm{fc}} = 2\pi \cdot 1.4\,\mathrm{Hz}$, $\Phi_{\mathrm{fc}_1} = 2\pi \cdot 6.6\,\mathrm{Hz} \cdot L_{\mathrm{fc}_1}/c$, $l^2_{\mathrm{rt,fc}} = 75\,\mathrm{ppm}$) the critical length L_{cc} is about 1239 m. The top grey shaded area in graph a) highlights the anti-squeezed region. Due to the unbalanced loss for upper and lower squeezing sidebands in the detuned filter cavity, for high resulting loss (i.e. for a cavity reflectance much smaller than one) the detected noise can be enhanced even when compared to the vacuum noise (refer to Fig. 261). In the considered example the detected noise is already enhanced (anti-squeezed) for filter cavity baseline lengths smaller than approximately 2.5 km.

Robustness of filter cavity design parameters The most obvious quantities, that will potentially change the properties of the filter are: the reflectance factors of the used mirrors, the round-trip loss, the macroscopic length, and the resonance frequency.

The first three quantities affect the bandwidth of the filter cavity and thus the required phase-space rotation around the targeted resonance frequency. A deviation from the design values of these quantities could not be compensated if the filter cavity is realised as a single resonator. An adaption of the filters bandwidth would be possible if coupled resonators—e.g. a linearly coupled three-mirror cavity—are utilised. Although it should be always possible to tune the filter cavity to the required resonance frequency, for the sake of completeness we treat a potential mismatch (see details in Appendix D.3.3). From the results, the requirements for the length stabilisation with regard to displacement noise could be determined. If a tolerable degradation of the squeezing by less than 2 dB (related to the squeezing levels achievable with the design parameters) is targeted, a deviation of the bandwidth less than 5 % is acceptable. From this value, the tolerances for the design parameters can be deduced.

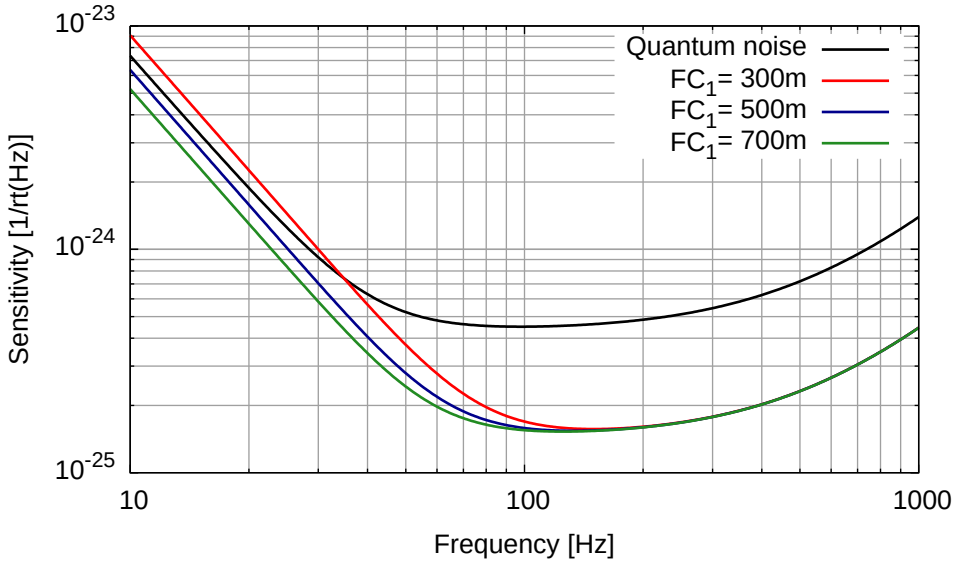

Figure 174: Sensitivity curves for ET-D-HF assuming various lengths for the filter cavity. Parameters used: round-trip loss 75ppm, 9% frequency independent propagation loss, pure 20dB squeezing injected.

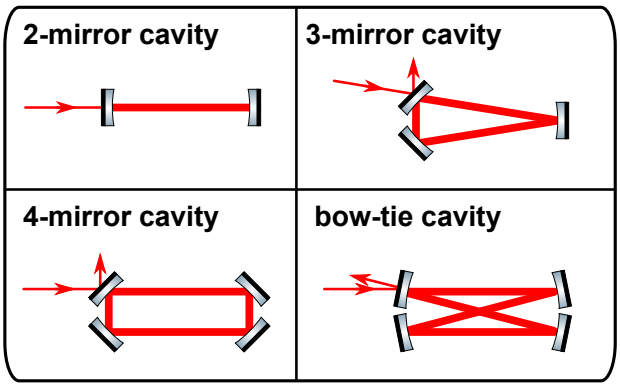

Figure 175: Four geometries were analysed from the scattering point of view.

Choosing the optical layout of the filter cavity The Einstein Telescope required two 10 km long and one comparatively short (several hundred meters long) filter cavities per detector. Such filter cavities provide the correct frequency dependence for the injected squeezing state in order to obtain broad band quantum noise suppression in the main interferometer. The light reflected off these cavities needs to be injected into the interferometer dark ports. In principle any cavity geometry can provide the correct filtering, however, practical concerns will put constraints on the geometry. The four cavity geometries depicted in Fig. 175 are possible candidates; the following advantages and disadvantages follow directly from the geometry (given a long baseline):

- the 2-mirror cavity has the advantage of using only two mirrors but in order to extract the reflected beam, polarising optics are required which introduce additional optical losses and phase noise
- the 3-mirror cavity provides the reflected beam without the need for extra optics. However, the small angle between the beams at the far right mirror means that the setup is more sensitive to small angle scattering, a problem which has been seen for example in the triangular input mode cleaner cavity of

VIRGO. Another problem is that the large angle of incidence on the two left mirrors requires the mirrors to be significant larger compared to the 2-mirror setup. of the 10 km long linear arm cavities. Since the ET optical design is assuming the largest available mirrors being used for the linear arm cavity, this filter cavity geometry can be excluded.

- the rectangular 4-mirror setup also has the problem of requiring larger mirrors due to the angle of incidence.
- The bow-tie cavity can separate the reflected beam from the injected one and does not feature large angles of incidence so that the mirror sizes are similar to those of a linear cavity. However, it is sensitive to small angle scattering.

A detailed study of scattering in the main interferometer and the filter cavities has not been done yet. In Appendix D.3.4 we provide a first analysis of the amount of scattering between the suspended optics itself and conclude that this effect can be ignored in the selection of the cavity geometry.

5.6 Main interferometer optical components

The materials for the optical components for the ET HF and LF detector have to be chosen taking different factors into account: the optical properties, mechanical properties as well as thermal properties. The ET HF interferometer will be based on the first and second generation of GW detectors and will use fused silica for all optical components. This material is currently state of the art in precision optics. The ET HF detector will be operated at room temperature.

The ET LF interferometer has to be built from crystalline materials due to thermal noise requirements which will be described in this section. Possible materials that fulfill the mentioned demands are silicon and sapphire. These materials will be operated at cryogenic temperatures. The following sections contain detailed discussions of the material properties, their mechanical and thermal properties and the detailed description of the thermal noise arising from the different materials. The material properties are summarised in Appendix E. The final outcome of this section will be the definition of the geometry of the test masses - as summarised in Appendix D.1 - due to thermal noise requirements. Additionally, we describe the optimum operational temperature of ET LF which was found to be 10 K.

5.6.1 Bulk material selection

Different materials have been proposed in order to reduce the thermal noise of the optics of future gravitational wave detectors. Three main candidate materials are the most promising ones to construct a 3rd generation detector: fused silica, sapphire and silicon.

Fused silica is the favorite substrate material for an interferometer that operates at room temperature. It is the substrate material of advanced detectors like Advanced LIGO and Advanced Virgo. Due to the extensive use of fused silica for first and second generation gravitational wave detectors, this material has been extensively characterised at room temperature. Fused silica exhibits very low optical absorption (as low as 1 ppm/cm at 1064 nm and below) with high homogeneity and low birefringence. Driven by the research effort for the advanced detectors, polishing and coating techniques exist that provide excellent performances. Micro-roughness of better than 0.05 nm RMS and flatness of better than 8 nm RMS over a surface of dia. 150 mm have been achieved [490].

Moreover, fused silica is available in large pieces with an extremely high purity. Additionally, there exist techniques to fabricate quasi-monolithic suspensions based on pulled fused silica fibres and silicate bonding. These techniques have demonstrated their reliability for years in the GEO600 detector [356, 357]. This convincing result triggered the implementation of this technique in Advanced LIGO [6, 358, 359] as well as Advanced Virgo [491, 492]. Fused silica has a very low mechanical loss at room temperature, exceeding 4×10^{-10} at 100 Hz [386]. The coefficient of thermal expansion is extraordinarily low at room temperature, providing a small thermo-elastic noise of the bulk material. However, the mechanical loss increases as the temperature is decreased (see

e.g. [493, 494]), reaching values as high as 10^{-3} at 10 K. This would result in a high substrate Brownian noise and makes fused silica unsuitable for optics operated at low temperatures. Additionally, the thermal conductivity of fused silica decreases to 0.4 W/mK at 10 K [495] which is more than 1000 times smaller than for typical crystalline materials.

The second candidate material is **sapphire**. This material is under consideration as a test mass material for LCGT (Large-scale Cryogenic Gravitational-wave Telescope) in Japan [496]. Hence, sapphire mirrors have been investigated with respect to their performance at cryogenic temperatures. Sapphire has a small coefficient of thermal expansion: below 20 K it can be approximated by $\alpha = 7.5 \times 10^{-13}\, T^3\, [\mathrm{K}^{-1}]$ [497]. This leads to a very small thermo-elastic noise at the low temperature regime. The mechanical loss of sapphire has been determined from Q-factor measurements. At 4.2 K losses of 4×10^{-9}, and at 20 K of 10^{-8}, have been observed [498]. The measured sample was a CSI (Crystal System) Hemlite grade. Additional excellent properties like the high thermal conductivity at low temperatures make sapphire a good candidate as a bulk material for cryogenic optics. The optical absorption at 1064 nm has been measured by the LCGT group to be about 90 at 5 K [496]. They report that the absorption is temperature-dependent reaching 168 ± 24 ppm/cm at room temperature. The value of the absorption is an important property influencing effects like thermal lensing and cooling of the mirror. In both cases—at room temperature and cryogenics—the sapphire substrate has about ten to a hundred times higher absorption than that of typical fused silica. This may cause thermal lensing effects in a cryogenic interferometer based on sapphire because the strain due to the thermal lens effect is proportional to the absorption, thermal coefficient of refraction, and input power. However, this does not completely exclude the sapphire option, as there are investigations aimed at decreasing the sapphire absorption by annealing [499].

As artificial sapphire crystals are broadly used in industries (e.g. as laser rods, heat sinks, etc.) there are many sapphire manufacturers available. The biggest currently available crystal is dia. 330×200 mm, 65 kg, manufactured by the US company Crystal System (CSI) [500]. This size is not enough for a potential use in the ET LF interferometer. Here, a mirror with a minimum mass of 211 kg is proposed in view of the suppression of the radiation pressure noise. This corresponds to a mirror of about dia. 620×180 mm which is far away from current availabilities. Additionally, the quality of such a large crystal is not believed to be good enough yet. When the c-axis of the crystal and the beam axis are different, optical losses occur. Therefore the cylinder shape of the mirror must be produced precisely along the c-axis. Also, the deviation between the beam axis and the c-axis increases the birefringence. The currently measured birefringence of sapphire with 250 mm diameter indicates that the birefringence level exceeds the LCGT requirement of the fringe contrast by three times [501]. As another current technical issue, there is no known way to bond sapphire wires onto the sapphire substrate with sufficient strength, which would be important for the fabrication of a low thermal noise quasi-monolithic suspension [365]. To suspend the mirror and to extract the heat from the substrate, the bonding should be done with enough strength while conserving the thermal conductivity. Despite all the issues, it is still anticipated to have large crystals. A possible technique would be using smaller high-quality crystals as a seed crystal and growing this to a bigger crystal while keeping the high quality [500].

Sapphire mirrors will be used in the cryogenic phase of the LCGT interferometer within the next years.

Box 5.6: Q-factor vs. mechanical loss

The mechanical loss ϕ of a material is a crucial parameter that determines Brownian thermal noise. In general, the lower the mechanical loss of the component is the lower the Brownian thermal noise is. Thus, low loss materials are preferred for designing low thermal noise components.
The mechanical loss angle is defined as the phase angle between stress and strain. It can be shown [502] that this corresponds directly to the phase angle between the imaginary and the real part of the complex Young's modulus of the material. Typical values are well below 10^{-2} even for very lossy materials like glass. Therefore, a direct measurement of the mechanical loss is very complicated and cannot be done for most of the interesting materials.
However, the phase lag between stress and strain goes along with energy dissipation in the system.

Thus, a straightforward way to investigate these mechanical losses would be the measurement of the energy dissipation in the device under testing. This is typically done in ring-down experiments. Here, the test sample is excited to resonant vibrations. After a sufficiently large amplitude is reached the excitation is switched off and the subsequent free ring-down of the vibrational amplitude is recorded. The amplitude follows an exponential behavior. The characteristic ring-down time τ where the amplitude decays to $1/e$ of the initial amplitude is directly connected to the internal losses – the longer the ring-down takes the lower the losses become. In resonant systems these losses are often characterized by the Q-factor. The Q-factor determines the quality of the resonance - the larger the Q-factor is the narrower the resonance is and hence the mechanical loss is lower.
The Q-factor is given by

$$Q = \pi \tau f_0,$$

with the resonant frequency f_0. In the case that the intrinsic loss of the test object only consists of one loss mechanism the mechanical loss ϕ and the Q-factor are linked by means of $\phi = Q^{-1}$. In reality the mechanical loss of a test sample originates from different factors: Usually a thin surface layer has a different loss to the intrinsic bulk material. Another example are coated samples where two different materials are combined. Here, the ring-down experiment reveals only the total Q-factor and a total mechanical loss. In such a case different experiments with different samples combine with the modeling of the influence of the different loss sources allows the determination of the intrinsic losses of bulk, surface or coating.

The third candidate material that has been proposed as a future detector material is **silicon** [379, 503]. Silicon has excellent mechanical and thermal properties and is available in high quality due to the large market of the semiconductor industry. The coefficient of thermal expansion is zero at two special temperatures around 18 and 125 K [504]. At these temperatures the contribution of thermo-elastic noise will therefore vanish. The mechanical loss of silicon has been studied by Q-factor measurements. It was experimentally shown that silicon bulk samples can reach mechanical losses as low as 5×10^{-10} at 2 K, 1×10^{-9} at 10 K, 4×10^{-9} at 20 K and 5×10^{-9} at 30 K [377]. Intensive studies are in progress to link the mechanical loss of the bulk samples with purity, surface preparation, or the crystal orientation of the sample.

Due to the huge demand of high purity silicon wafers for the semiconductor industry silicon bulk samples are available in relative large pieces. The available sample diameter is dependent on the fabrication process. The two main growing processes for single crystal silicon used in semiconductor industry are the Czochralski (CZ) and the Float Zone (FZ) method. CZ silicon is grown from a silicon melt in a silica crucible. It results in relative large samples with a reasonable purity. The most dominant impurities in undoped CZ-grown silicon are carbon (typically $10^{18}\,\mathrm{cm}^{-3}$) and oxygen (typically up to $10^{19}\,\mathrm{cm}^{-3}$). In contrast, FZ silicon contains these impurities typically with much smaller concentrations (up to 10^3 times smaller). Single or poly-crystalline silicon is remelt by means of inductive heating in vacuum or under an inert atmosphere during the FZ process. Impurities dissolve better in the melt than in the solid part. The re-crystallised material has therefore a higher purity than the initial one. By slowly sweeping the melt from one end to the other it is possible to purify in steps. The mechanism of inductive heating sets limits to the currently available setups and leads to smaller currently available samples[21]. Well established polishing methods exist for silicon due to the wafer fabrication. Micro roughness and flatness needed for optical applications can be achieved. Additionally, silicon provides the possibility of jointing pieces by means of bonding techniques (see also section 4.5). Two possible techniques under discussion are anodic bonding and the well establish hydroxide catalysis bonding [365, 366] currently in use in 1st and 2nd generation detectors.

Using silicon as a test mass material demands a change in operational wavelength. Silicon is not transparent at 1064 nm (optical absorption is approximately $10^{-1}\,cm^{-1}$ at 1064 nm [505]), and has a smaller optical absorption at longer wavelengths. Erbium-fibre lasers provide a reliable light source in the IR spectrum. At 1550 nm silicon

[21] There is still no technical limit reached for the float zone process. The maximum diameter currently available is set by the demands of the semiconductor market.

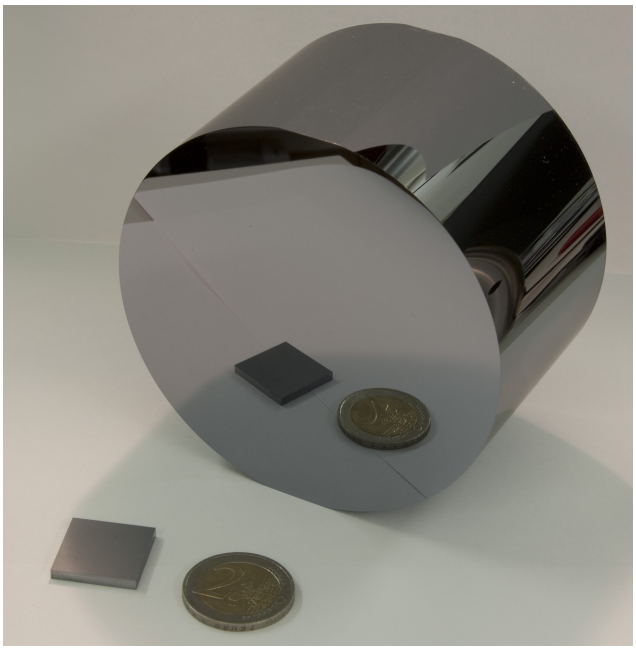

Figure 176: Silicon sample as being used for cryogenic mechanical loss measurements [380]. The single crystalline material is cut in a cylindrical shape and polished at the front and back side as well as the barrel.

is transparent and can be used as an standard optical material in reflection and transmission applications. Optical absorption measurements based on the creation of electron-hole-pairs suggests a minimum absorption of $3.2 \times 10^{-2}\, cm^{-1}$ at 1450 nm at room temperature [506]. However, a detailed analysis of the absorption processes and the total optical absorption of silicon at 1550 nm and low temperatures does not exist so far. A similar lack of parameters exists for other optical properties like the refraction index n or the thermo-refractive coefficient dn/dT [507]. Currently, several institutions wor ldwide are investigating these optical properties. Several institutions involved in this design study play a key role in this research.

A collection of the mechanical and thermal properties of fused silica, sapphire and silicon can be found in appendix E.2 and appendix E.3. Selected literature values at 10, 20, 30 and 300 K have been summarized in table 11 and 12. These values have been used for all thermal noise estimates presented within this document.

Parameter	T	Fused silica		Sapphire		Silicon	
		Value	Ref.	Value	Ref.	Value	Ref.
heat capacity (J/kg K)	10 K	6.3	[374]	0.085	[508]	0.276	[509]
	20 K	25.2	[374]	0.72	[508]	3.41	[509]
	30 K	54.6	[374]	2.6	[508]	18.55	[509]
	300 K	738	[374]	781	[508]	713	[509]
thermal conductivity (W/m K)	10 K	0.098	[361]	2900	[361]	2110	[360]
	20 K	0.13	[361]	15700	[361]	4940	[360]
	30 K	0.18	[361]	20700	[361]	4810	[360]
	300 K	1.5	[361]	46	[361]	148	[360]
thermal expansion coefficient (1/K)	10 K	-2.2×10^{-7}	[376]	1.0×10^{-9}	[508]	8.8×10^{-10}	[509]
	20 K	-5.8×10^{-7}	[376]	4.0×10^{-9}	[508]	-2.5×10^{-9}	[509]
	30 K	-8.0×10^{-7}	[376]	1.6×10^{-8}	[508]	-5.3×10^{-8}	[509]
	300 K	5.0×10^{-10}	[376]	5.6×10^{-6}	[508]	2.7×10^{-6}	[509]
mechanical loss	10 K	7.9×10^{-4}	[494]	5×10^{-9}	[498]	1×10^{-9}	[377]
	20 K	1.0×10^{-3}	[494]	5.6×10^{-9}	[498]	4×10^{-9}	[380]
	30 K	1.0×10^{-3}	[494]	1.4×10^{-8}	[498]	5×10^{-9}	[377]
	300 K	4×10^{-10}	[386]	3.8×10^{-9}	[378]	1×10^{-8}	[380]
dn/dT (1/K)	10 K	–	–	$< 9 \times 10^{-8}$	[510]	$< 1 \times 10^{-6}$	–
	20 K	–	–	$< 9 \times 10^{-8}$	[510]	1×10^{-6}	–
	30 K	1×10^{-6}	[511]	$< 9 \times 10^{-8}$	[510]	3.3×10^{-6}	[507]
	300 K	8×10^{-6}	[511]	1.3×10^{-5}	[512]	1.9×10^{-4}	[507]

Table 11: Temperature dependent thermal parameters for fused silica, sapphire and silicon bulk material used for thermal noise estimates at selected temperatures. dn/dT is given at 1064 nm for fused silica and sapphire and at 1550 nm for silicon.

Parameter	Fused silica		Sapphire		Silicon	
	Value	Ref.	Value	Ref.	Value	Ref.
density ρ (kg/m^3)	2202	[513]	3980	[513]	2330	[513]
Young's modulus Y (GPa)	72	[513]	400	[513]	188	[513]
Poisson's ratio ν	0.17	[513]	0.24	[504]	0.22	[513]
refractive index n	1.45	[495]	1.75	[495]	3.453	[495]

Table 12: Parameters of bulk materials that are assumed to be temperature independent for the thermal noise calculations. The refractive index of fused silica and sapphire is given at 1064 nm whereas this parameter is listed at 1550 nm for silicon.

5.6.2 Coating material selection

The construction of the 3rd generation of GW detectors has specific constraints on the thermal noise level. Several studies have already demonstrated that the coating is the most important noise source in the frequency range around 10 to 100 Hz. To avoid coating materials generating a noise level larger than the expected sensitivity, very high quality coatings are needed. First, the absorption has to be less than 5 ppm and the loss angle of the material has to be as low as possible in order to obtain a minimum coating Brownian noise level. To produce coatings with such quality, an ion beam sputtering is needed. Mirrors for GW detectors involve several parameters: the nature of the substrate (polishing, operational temperature), the characteristic of the sputtering source in the coater (temperature and emission law) and the pressure in the coater. To get a coating that follows the GW detector specifications, sputtering deposition is required because the energy lies in the range of 10 to 50 eV and the impact velocity is in the range of km/s [490]. This causes a dense coating with a high optical and mechanical quality.

Driven by the research performed for the 1st and 2nd generation of GW detectors, a state-of-the-art deposition

technique - ion-beam-sputtering (see box 5.7) exists that provides high performances coatings.

Box 5.7: Ion Beam Sputtering

Coatings for the current GW detectors are made by an ion-beam-sputtering (IBS) technique. The target material is hit by accelerated ions (typically argon ions) coming from an ion source. This source consists of a heated cathode and an anode which are arranged along a common axis. Applying a high voltage between the anode and cathode creates an electrical field inside the ion source, confining electrons from the heated cathode in the center of the source. When argon is injected into the source the high electric field causes the gas to ionize - a plasma is created inside the source. The positively charged argon ions are accelerated by means of the high electric field inside the source towards the cathode forming a collimated ion beam. This ion beam is pointed towards the sputtering target where it sputters the target material onto the sample.

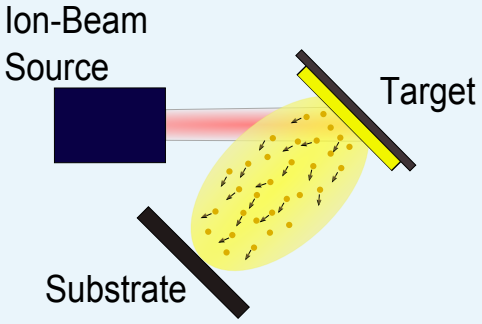

Figure 177: Schematic view of an ion-beam-sputtering process. Ions are created and accelerated inside the ion source. The ion beam is pointed towards the target where it releases the sputtering material. This material is deposit on the substrate forming a dense coating.

The high energy of the argon ions allows a good transfer of energy and momentum on the target particles. Thus, the coating material particles arrive with a high energy and momentum at the substrate forming a very dense and homogeneous coating. It has been shown in the past that IBS creates coatings with the lowest mechanical loss among all other coating techniques (e.g. magnetron sputtering, electron beam vapour deposition, etc.). Thus, IBS is currently the best technology to create high performance optical coatings.

(a) (b)

Figure 178: IBS coating machines operated at the Laboratoire des Matériaux Avancés (LMA) in Lyon.

The world largest IBS coater is currently operated at the Laboratoire des Matériaux Avancés (LMA) in Lyon. The vacuum chamber has a size of 2.4 x 2.4 x 2.2 m^3 which allows the fabrication of coatings for current and future GW detectors. The coating machine is operated in a class 1 clean room to fulfill the requirements of high performance optics. This coating machine would be capable of fabrication the mirrors for the proposed Einstein Telescope based on silica and tantala.

Typically, $\lambda/4$ layers of alternating low and high refractive index materials are used to form a high-reflectivity coating. Commonly used materials are tantala (Ta_2O_5) as the high refractive index material and silica (SiO_2) as the low refractive index material.

At first, the design study considered silica (refractive index n=1.45) and tantala (refractive index n=2.03). These two materials' oxide layers have the best optical and mechanical properties in the 1st and 2nd generation of GW detectors. The measurements made on the Ta_2O_5/SiO_2 coatings have shown that the lossier material is the Ta_2O_5. Thus, the material improvement has been focused on tantala. Several doped materials were tested to improve the mechanical losses of Ta_2O_5. By doping Ta_2O_5 with Ti and with an optimization of the deposition process, it is possible to decrease the losses of high refractive index material from 3.8×10^{-4} to 2×10^{-4}. To date, other materials have been considered for doping the Ta_2O_5 layers. New materials should also be considered to replace the Ta_2O_5 layers with another high refractive index material. In this context, table 13 presents the parameters values needed for thermal noise calculation for different coating materials. A summary of the thermal noise estimates can be found in [495, 513].

Extensive studies of the temperature dependence of the mechanical loss of tantala (Ta_2O_5) have been undertaken and the effects of post-deposition heat-treatment and of doping with titania (TiO_2) have been investigated [387–389]. In general the loss increases at low temperature, with three loss peaks observed to occur at different heat-treatment temperatures. Tantala heat-treated at 300°C and 400°C exhibits a loss peak at approximately 35 K. A larger and narrower loss peak was observed at 20 K in tantala coatings heat-treated at 600°C. There is some evidence that the 35 K peak may also be present in tantala heat-treated at 600°C, underlying the peak at 20 K. It is known that ion-beam sputtered tantala crystallises when heated above approximately 650°C. A large and very broad loss peak has been observed in tantala heat-treated at 800°C. While of interest for studies of the loss mechanisms in tantala, crystallised tantala is not suitable for use in an high-reflective coating due to its poor optical properties.

Further work may be required to establish the optimum heat-treatment temperature for a silica/tantala multilayer coating for use at cryogenic temperature. High heat-treatment temperatures are generally desirable for

	SiO_2	Al_2O_3	$Ti:Ta_2O_5$	Ta_2O_5	TiO_2	Nb_2O_5	ZrO_2
Loss angle	0.5×10^{-4}	2.4×10^{-4}	2×10^{-4}	3.8×10^{-4}	6.3×10^{-3}	6.7×10^{-4}	2.85×10^{-4}
Density ($kg\,m^{-3}$)	2200	3700	6425	6850	4230	4590	6000
Thermal conductivity ($W\,m^{-1}\,K^{-1}$)	0.5	3.3	0.6	0.6	0.45	1	1.09
Specific heat ($J\,K^{-1}\,kg^{-1}$)	746	310	269	306	130	590	26
Thermal expansion coefficient (K^{-1})	0.51×10^{-6}	8.4×10^{-6}	3.6×10^{-6}	3.6×10^{-6}	5×10^{-5}	5.8×10^{-6}	10.3×10^{-6}
Thermo-optic coefficient (K^{-1})	8×10^{-6}	1.3×10^{-5}	14×10^{-6}	2.3×10^{-6}	-1.8×10^{-4}	1.43×10^{-5}	10×10^{-5}
Young's modulus (GPa)	60	210	140	140	290	60	200
Poisson's ratio	0.17	0.22	0.23	0.23	0.28	0.2	0.27
Refractive index	1.45	1.63	2.06	2.03	2.3	2.21	2.15

Table 13: List of the optical and mechanical values of different coating materials at 300 K.

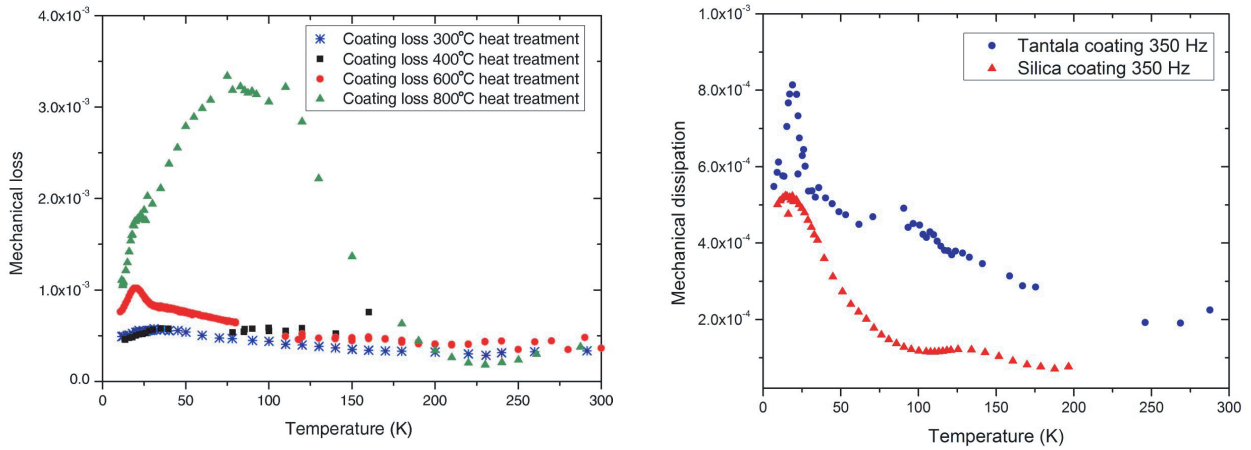

(a) (b)

Figure 179: (a) – Measured values of the coating loss of tantala annealed at different temperatures. (b) – Comparison of 600°C heat treated tantala and silica coatings at low temperatures and 350 Hz.

optimal optical properties. Furthermore, studies of the mechanical loss of ion-beam sputtered silica coatings have shown a systematic reduction in the loss at room temperature with increasing heat-treatment temperatures. Thus carrying out heat-treatment at the maximum temperature which can be achieved without inducing crystallisation in the tantala layers may be desirable. However, as shown in Figure 179(a), tantala has a significantly lower loss at temperatures below 100 K when heat-treated at lower temperatures (300 or 400°C) than when heat-treated at 600°C. While the loss of the tantala layers dominate the loss of a multilayer silica/tantala coating at room temperature, the loss of ion-beam sputtered silica has a similar magnitude as the loss of tantala at temperatures below 50 K. Thus further studies of the effect of heat-treatment on the temperature dependence of the mechanical loss of ion-beam sputtered silica are also required to allow the optimal heat-treatment temperature to be chosen. In addition, measurements of the temperature dependence of the optical properties of the coating may be required.

A comprehensive summary of R&D activites needed for understanding and characterising the coating properties can be found in section 5.9.3.

5.6.3 Thermal noise estimates for reflective components

The thermal noise of a fully reflective mirror comprises thermal noise arising from the bulk material and the coating. The bulk material thermal noise consists of Brownian thermal noise and thermo-elastic noise. Brownian noise represents the thermal fluctuations ('Brownian motion') of the atoms within the bulk material and is dependent on the sample temperature T and the mechanical loss of the bulk material ϕ [514, 515]:

$$S_{\mathrm{x}}^{\mathrm{bulk}}(f,T) = 2k_{\mathrm{B}}T\frac{1-\nu}{\pi^{3/2}fYw}\phi \tag{115}$$

with the Boltzmann constant k_{B}, the frequency f, the beam radius w, the substrate Poisson's ratio ν and Young's modulus Y. It is obvious that the Brownian thermal noise is only dependent on mechanical properties of the material.

Box 5.8: Thermal noise in optical components

There are two fundamental origins of thermal noise in optical components: The first is driven by the thermal energy $k_B T$ that is present as soon as the component is operated at non-zero temperatures. Here, the thermal energy causes thermal fluctuations of the atoms of the optical component, which causes a thermally driven fluctuation of the reflective surface of the element. This type of noise is probably closest to the process that to mind when talking about thermal noise. In many different field this type of noise—Brownian noise—is present. Throughout this document this type of noise is called Brownian thermal noise.
However, there is a second type of noise that arises from temperature fluctuations. When operating a macroscopic object at non-zero temperatures the local (microscopic) temperature is not a constant value but fluctuates around the average temperature T. Due to the fact that many material properties are temperature dependent this opens a channel to introduce the second type of noise. Here, the temperature fluctuation causes a phase or position fluctuation by means of the temperature dependence of a property, e.g. the coefficient of thermal expansion α or the refractive index n. The process that is associated with α is called thermo-elastic noise whereas the other process is referred to as thermo-refractive noise.
Although in both cases the temperature is the fundamental driving force one distinguishes between then strictly due to the different coupling mechanisms of the fluctuation to the read-out noise.

The thermo-elastic noise of the bulk material is created by statistical temperature fluctuations. By means of the coefficient of thermal expansion α these fluctuations are translated into displacement noise. The thermo-elastic spectral noise density is given by [516]:

$$S_{\mathrm{TE}}^{\mathrm{bulk}}(f,T) = \frac{4k_B T^2 \alpha^2 (1+\nu)^2 \kappa}{\sqrt{\pi^5}\rho^2 C^2 f^2 w^3} \tag{116}$$

with the coefficient of thermal expansion α, the thermal conductivity κ, the heat capacity C, and the mass density ρ. This equation is valid if the thermal diffusion length

$$l_{\mathrm{th}} = \sqrt{\frac{a^2}{f}} \tag{117}$$

of the material is smaller than the beam diameter. The parameter $a^2 = \kappa/(\rho C)$. This assumption is called the adiabatic case. During one period of oscillation all temperature fluctuations that are present at the observation volume stay inside this volume. If the thermal diffusion length gets larger (e.g. by means of high thermal conductivity or low frequencies) the thermo-elastic effect gets weaker. Especially, for low temperature applications this non-adiabatic correction becomes important and reduces the contribution of thermo-elastic noise further. This correction has been taken into account for all calculations presented in this document. Details of the calculation can be found in [513, 517].

Figure 180 compares the Brownian and thermo-elastic noise of one single mirror made of fused silica, sapphire or silicon at 10 and 300 K. The parameters used for the calculation are listed in tables 11 and 12.

At room temperature fused silica provides the lowest level of thermal noise due to its low mechanical loss and small coefficient of thermal expansion (see figure 180(a)). All crystalline materials show a high coefficient of thermal expansion and thus a large thermo-elastic noise. Therefore, crystalline materials should be avoided in room temperature detectors in order to achieve the minimum thermal noise level of a mirror substrate.

In contrast, at low temperatures fused silica has a large mechanical loss reaching values of 10^{-3} around 10 K. Crystalline materials behave differently resulting in a low mechanical loss of better than 10^{-8} at low temperatures

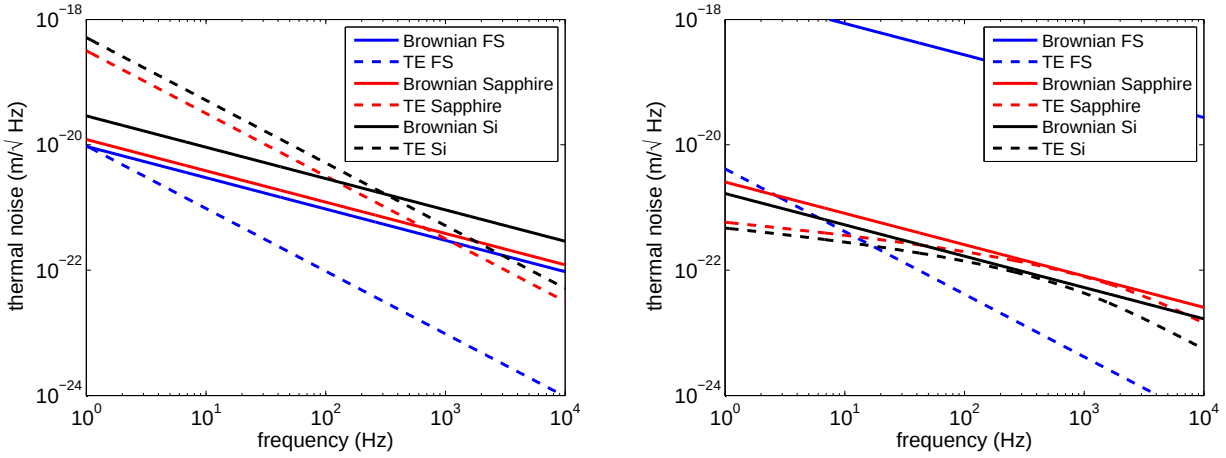

(a) (b)

Figure 180: Comparison of the Brownian and thermo-elastic noise for fused silica, sapphire and silicon at 300 K (a) and 10 K (b) (TE – thermo-elastic noise, FS – fused silica). At room temperature the crystalline substrate materials show a large thermo-elastic noise. In contrast, at cryogenic temperatures fused silica has a large Brownian thermal noise due to its large mechanical loss.

(see Tab. 11). Additionally, the coefficient of thermal expansion is very small at low temperatures. This reduces dramatically the thermo-elastic noise contribution compared to room temperature operation (see figure 180(b)). Thus, using cryogenic temperatures and crystalline materials will result in a low total bulk thermal noise.

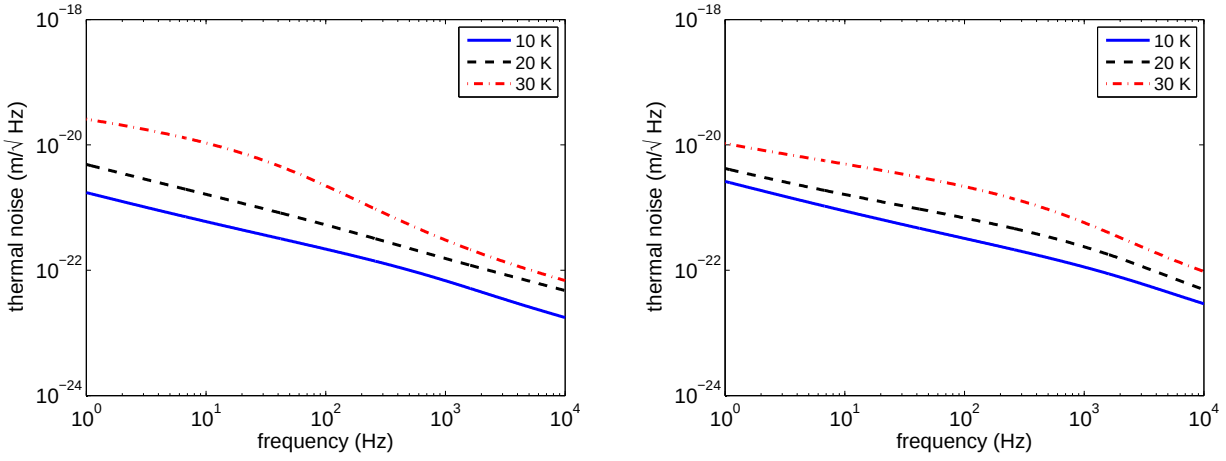

(a) (b)

Figure 181: Comparison of the total bulk thermal noise of a mirror substrate made of silicon (a) and sapphire (b) at different temperatures. The parameters used for this calculation are summarised in tables 11 and 12.

Figure 181 compares the total bulk thermal-noise consisting of thermo-elastic and Brownian thermal noise for sapphire and silicon at selected temperatures. Due to the small mechanical loss and coefficient of thermal expansion, a low thermal noise level is achieved. At 20 K both materials show a comparable thermal noise level. At higher temperatures thermo-elastic noise becomes dominant. Here, sapphire has a slightly lower level of thermo-elastic noise due to the combination of its thermal properties (mainly the high thermal conductivity).

At 10 K silicon has a slightly lower total thermal noise than a sapphire mirror substrate.

All calculations so far are based on semi-infinite mirror substrates. This assumption is true for a first comparison of the materials and in cases where the beam radius compared to the mirror radius is small. However, for application in gravitational wave detectors it is preferable to increase the beam diameter to the maximum possible size that is in agreement with the optical clipping losses. The corrections for finite size test masses have been made by different authors for the different noise contributions. The calculations are quite long and thus only the results are shown here. The detailed discussion can be found in the literature [518, 519].

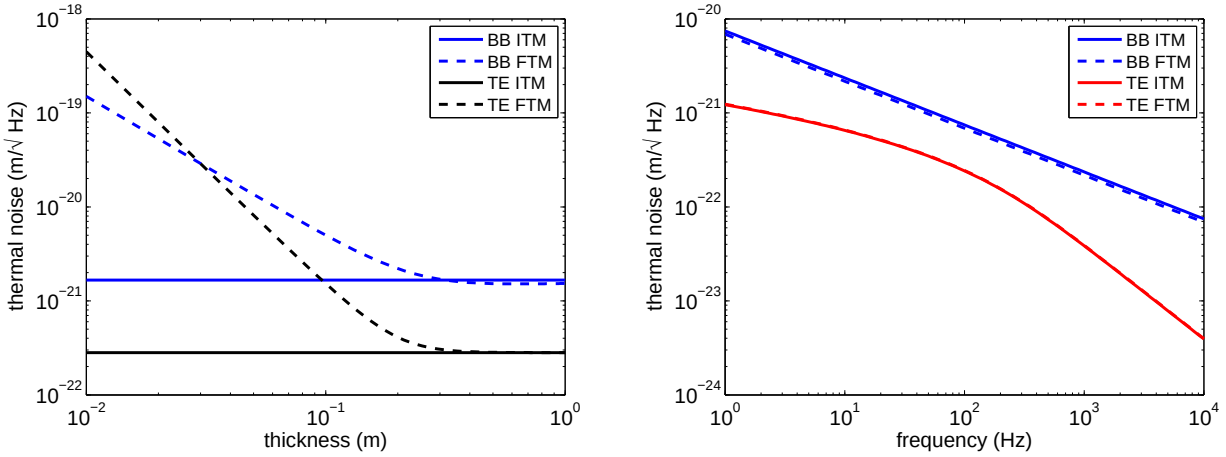

Figure 182: Finite size test mass mirror thermal noise. (a) – Dependence of the mirror Brownian and thermo-elastic thermal noise of the thickness of the substrate (silicon, 10 K, diameter: 0.5 m, frequency 10 Hz). (b) – Effect of the finite size correction for a typical ET end mirror geometry (silicon, 10 K). BB – bulk Brownian, TE – thermo-elastic, ITM – inner test mass, ETM – end test mass.

Figure 182 gives the dependence of the substrate thermal noise. It is obvious that for reasonable thicknesses of the substrate the correction is small. Only for very thin substrates does a strong deviation from the simplified infinite half space model appear. At larger thicknesses the finite sample correction leads to a small decrease in thermal noise (approx. 5 . . . 10% for bulk Brownian and less than 1% for bulk thermo-elastic noise).

Optical components being used in GW detectors consist of a bulk material and a coating. The coating usually comprises several alternating dielectric layers formed by high and low refractive index materials. Typically, these layers are formed by amorphous tantala and silica layers with an optical thickness of $\lambda/4$. The circulating laser beam of the interferometer interacts mainly with the coating (point of first contact between light and mirrors). Thus, it can be expected that the optical coating contributes strongly to the total thermal noise of a mirror.

Similar to the thermal noise of the bulk materials, the coatings also show Brownian thermal noise. It is again dependent on the temperature T and the effective mechanical loss ϕ_{eff} of the coating [514, 515]:

$$S_x^{\text{coating}}(f,T) = 2k_{\text{B}}T\frac{1-\nu}{\pi^{3/2}fYw}\phi_{\text{eff}} \tag{118}$$

with the Boltzmann constant k_{B}, the frequency f, the beam radius w, the Poisson's ratio ν and the Young's modulus Y of the substrate bulk material. The effective mechanical loss contains all coating relevant parameters and is given by:

$$\phi_{\text{eff}} = \frac{t}{\sqrt{\pi} w} \left(\frac{Y}{Y_\perp} \phi_\perp + \frac{Y_{||}}{Y} \phi_{||} \right). \tag{119}$$

This description of the effective mechanical loss assumes small Poisson's ratios of the coating materials, which is usually fulfilled. t is the total thickness of the coating layer. The Young's moduli Y_i, the thicknesses t_i and the mechanical losses ϕ_i are combined as follows ($i = 1, 2$ to indicate the different coating layer properties):

$$Y_\perp = \frac{t_1 + t_2}{\frac{t_1}{Y_1} + \frac{t_2}{Y_2}}, \tag{120}$$

$$Y_{||} = \frac{Y_1 t_1 + Y_2 t_2}{t_1 + t_2}, \tag{121}$$

$$\phi_\perp = \frac{Y_\perp}{t_1 + t_2} \left(\frac{t_1}{Y_1} \phi_1 + \frac{t_2}{Y_2} \phi_2 \right) \tag{122}$$

$$\phi_{||} = \frac{Y_1 t_1 \phi_1 + Y_2 t_2 \phi_2}{Y_{||} (t_1 + t_2)} \tag{123}$$

Light penetrates the first dielectric layers of a high-reflective mirror and thus interacts not only with the front surface. Here, a fluctuating local temperature causes a change in the thickness of the layer by means of the coefficient of thermal expansion α and additionally a change of the refractive index n of the materials. In total, these two effects sum up and change the optical path of the light being reflected. This statistical process combining effects of thermo-elastic (due to α) and thermo-refractive (due to the change of n) is called thermo-optical noise. Depending on the sign of α and dn/dT these two effects can result in a smaller noise than the two terms predict separately.

Thermo-optical noise can be calculated following the approach by Evans et al. in 2008. The calculation is too complex to be presented here—see [520] for the full description of it.

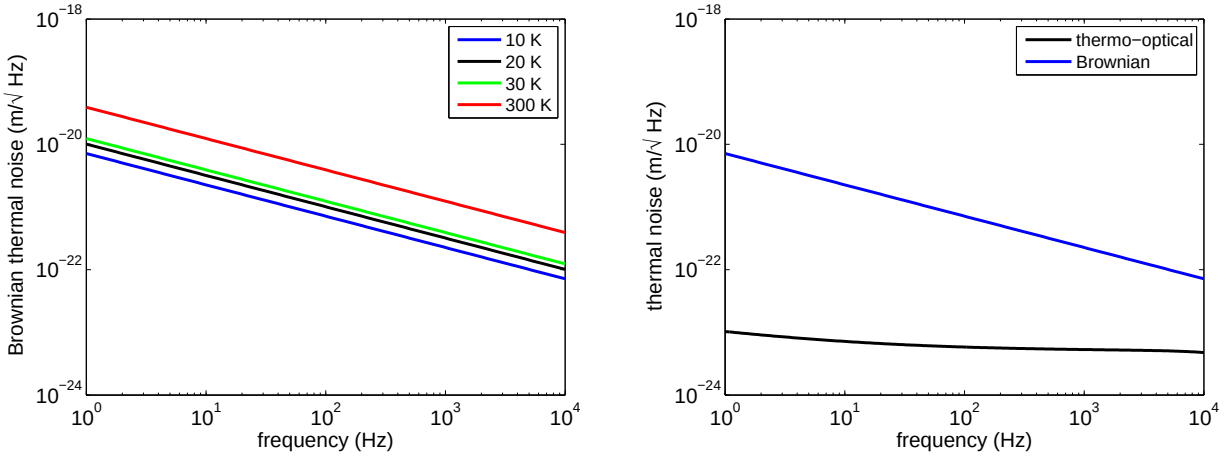

(a) (b)

Figure 183: (a) – Comparison of coating Brownian noise at different temperatures. (b) – Comparison of coating thermo-optical and Brownian noise at room temperature. Both calculations assume a 18 doublet alternating silica-tantala quarter wavelength layer with a $\lambda/2$-endcap. The coating is assumed to be put on a silicon substrate. A wavelength of 1550 nm was used for the estimates.

Figure 183 compares the Brownian and thermo-optical noise levels of different coatings at low temperatures and room temperature. Parameters are used from tables 10, 11, 12 and 13. A direct comparison at 10 K reveals

that the thermo-optical noise is much smaller than the coating Brownian noise. This statement is also true for higher temperatures which makes thermo-optical noise not a dominating source of total thermal noise of a reflective component for a gravitational wave detector.

Box 5.9: Operational Temperature of ET-LF

The design temperature of the low frequency interferometer of ET was chosen to be 10 K. This value arises directly from different restrictions. From a thermal noise point of view the lowest possible temperature would be desirable. However, this collides with the necessary heat removal through the suspension as given in section 4.4.1. At very low temperatures (well below 10 K) the thermal conductivity of the suspension materials will be very low and it is impossible to remove the deposit heat from the laser beam through the fibres. The maximum tolerable temperature from a point of view of thermal noise is around 24 K (see Fig. 265). However, as can be seen from Fig. 179 the currently proposed coating material tantala shows a large loss peak around 18 K when it is annealed to 600 degrees to improve the optical quality. Thus the final decision has been made to go as low as possible in operational temperature to stay below that dissipation peak that would cause an increased level of coating Brownian noise. A summary of the total mirror thermal noise at different temperatures can be found in the appendix D.4.

The level of coating Brownian noise is additionally larger than the total noise level of the bulk material presented in figure 181. Thus, coating Brownian noise is the most important type of thermal noise of a high reflective mirror and great care must be taken in choosing the optimum operational temperature and the appropriate material combination. Avoiding the mechanical loss peak in amorphous dielectric coatings at around 15 to 30 K (depending on the actual material, see figure 179) was one of the strongest reasons for the 10 K target temperature of the cooled mirrors of the ET-LF detector.

Details of the ongoing and future research in the field of mechanical losses of bulk and coating materials as well as other thermal noise issues are given in section 5.9.

5.6.4 Thermal noise estimates for transmittive components

The total thermal noise of a transmittive component considers the noise contribution described in the previous subsection and additionally the thermo-refractive noise that occurs from statistical fluctuations of the refractive index n due to its temperature dependence dn/dT. A temperature fluctuation produces a small change of n which leads to phase changes detected by the interferometer. The thermo-refractive noise has been calculated by equations given by Braginsky [521] in addition with correction terms developed by Benthem and Levin [522].

Taking into account the configuration of Einstein Telescope given in figure 165 and table 10 results in the following equation for the thermo-refractive noise (power spectral density) in an interferometer with arm cavities of finesse F:

$$S_h(f,T) = \frac{4}{L^2}\left(\frac{\lambda}{8F}\right)^2 (kl\beta)^2 \frac{4k_B T^2 \kappa}{(C\rho)^2 l}\left(1+\frac{(kn)^2 w^2}{\left(1+\left(2kn\sqrt{\frac{\kappa}{C\rho\omega}}\right)^4\right)}\right)\int_0^\infty \frac{k_i dk_i}{2\pi}\exp\left(\frac{-w^2k_i^2}{4}\right)\frac{k_i^2}{\omega^2+a^4k^4}, \tag{124}$$

where

$$k = \frac{2\pi}{\lambda} \tag{125}$$

and

$$a^2 = \frac{\kappa}{C\rho}. \tag{126}$$

l is the thickness of the input mirror, β the thermo-optic coefficient of the substrate material, T is the temperature, k_B the Boltzmanns constant, κ the thermal conductivity, C the specific heat, ρ the density of the substrate material, w is the beam radius, L the arm length of the interferometer, and n the refractive index of the substrate material. Details of this equation can be found in [523].

At 300 K the silica substrate provides the lowest thermo-refractive noise (see figure 184). Substrate materials with a low thermo-optic coefficient show a low thermo-refractive noise. As a numerical result, for silica, sapphire and silicon, it is respectively 8×10^{-6}, 1.3×10^{-5} and 5.15×10^{-5}.

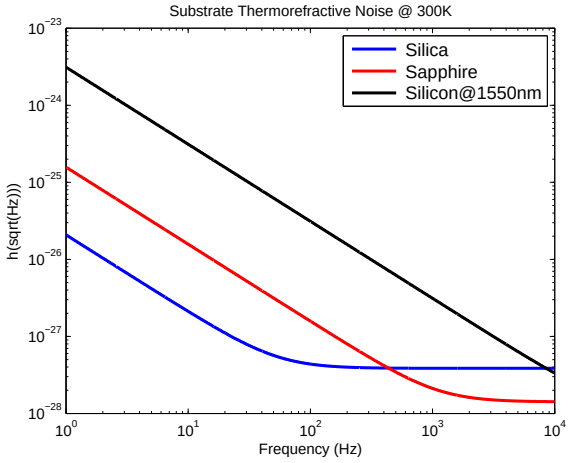

Figure 184: Substrate thermo-refractive noises for silica, sapphire and silicon at room temperature.

Then, the thermo-refractive noise is compared for silicon and sapphire as the most promising test mass materials at cryogenic temperatures. The substrate thermo-refractive noise is largely dependent on the thermo-optic coefficient. This value has been measured for sapphire at low temperatures and reaches $9 \times 10^{-8}\,\mathrm{K}^{-1}$ below 4 K [510]. For silicon the parameter is not very well known. The only currently literature source available reports values of n and dn/dT down to 30 K [507]. However, the values reported for dn/dT do not agree with the slope of the $n(T)$ curve of the same reference. Thus, the knowledge of the parameter is strongly limited. At temperatures around 20 K a value of $1 \times 10^{-6}\,\mathrm{K}^{-1}$ can be assumed as an upper limit of dn/dT based on the experimental values given in [507]. At even lower temperatures it is reasonable to assume a further decrease of the value due to thermodynamical assumptions: at 0 K all temperature dependent properties have to become constant—thus the temperature derivative has to vanish.

Figure 185(a) shows the thermo-refractive noise of silicon and sapphire at 10 K based on equation (124) given above. The dn/dT for silicon is assumed as $1 \times 10^{-6}\,\mathrm{K}^{-1}$ and the dn/dT for sapphire is $9 \times 10^{-8}\,\mathrm{K}^{-1}$.

Sapphire shows a very small thermo-refractive noise due to its small thermo-refractive coefficient β. Although it is higher, the thermo-refractive noise of a silicon substrate is also very low and should not affect the total thermal noise of the system. The operational frequency of the LF detector is between 1 and 250 Hz. Above this frequency the HF detector takes over and limits the sensitivity of the Einstein Telescope. It is expected that experimental values for the thermo-refractive coefficient of silicon is even lower than the one given here (see section 5.9).

Figure 185(b) shows the evolution of the thermo-refractive noise for different temperatures (10 K, 20 K, 30 K). It shows that the thermo-refractive noise decreases with the temperature. Thus, operating at the highest possible temperature that allows a low thermal noise operation is preferred. This leads to a possible optimization process.

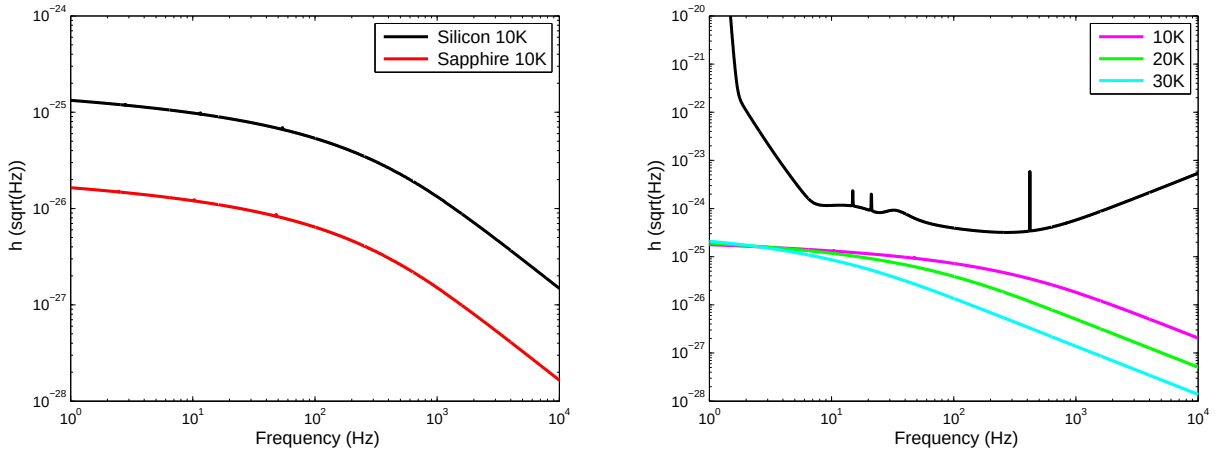

(a) (b)

Figure 185: (a) – Substrate thermo-refractive noise of silicon and sapphire at 10 K (beam size: 9 cm). (b) – Substrate thermo-refractive noise of silicon at 10 K, 20 K, 30 K (dn/dT unchanged: $1 \times 10^{-6}\,\mathrm{K}^{-1}$).

5.6.5 LF interferometer large mirror definition

The Einstein Telescope detector is split into two interferometers (ET-LF and ET-HF) due to thermal noise and heating reasons. The ET-LF detector assumes a beam radius size of 9 cm, corresponding to an effective test mass diameter of 45-50 cm, but at the same time keeps the overall test mass weight at about 210 kg [489] with sufficient thickness. This mass leads to a thickness for a future silicon test mass of approximately 46-50 cm. The thickness would drop to about 30 cm for sapphire due to the higher material density. For the substrate, the thermo-refractive noise is dependent on the thickness of the mirror.

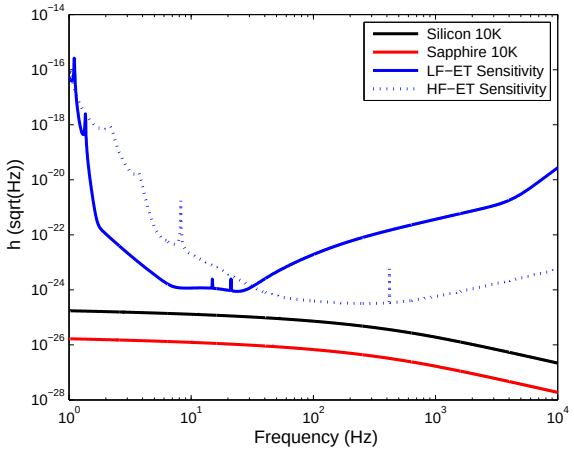

Figure 186: Substrate thermo-refractive noise of silicon (w = 9 cm, thickness 50 cm) and sapphire (w = 9 cm, thickness 50 cm) substrate compared to the ET-D sensitivity.

Figure 186 shows that the thermo-refractive noise of silicon and sapphire is well below the ET sensitivity target. Therefore, we can foresee that the assumed dimensions are possible and promising. A plot of all the thermal noises for silicon and sapphire is shown in Figure 187.

For a silicon mirror, thermal noise is dominated by the coating Brownian noise and the substrate thermo-

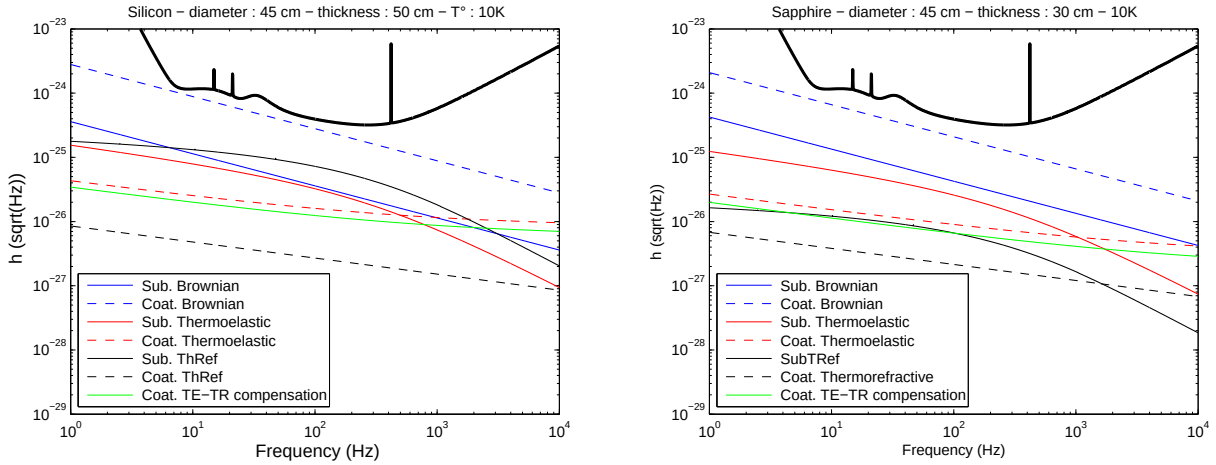

(a) (b)

Figure 187: (a) – Thermal noise contribution for a silicon mirror ($w = 9\,\mathrm{cm}$, thickness 50 cm, $T = 10\,\mathrm{K}$). (b) – Thermal noise contribution for a sapphire mirror ($w = 9\,\mathrm{cm}$, thickness 30 cm, $T = 10\,\mathrm{K}$).

refractive noise. Coating Brownian noise is, in reality, higher than all other noises considered but still below the ET-LF sensitivity target. For a sapphire substrate, coating Brownian noise is also the highest thermal noise. Therefore, a cooled silicon (or sapphire) mirror provides a low enough thermo-refractive noise in the frequency band covered by the LF detector.

In conclusion, both materials—sapphire and silicon—provide low thermo-refractive noise levels that are compatible with the requirements for the Einstein Telescope. An exact estimate of the thermo-refractive noise level of silicon will not be possible until the thermo-refractive coefficient is measured for different types of silicon. It can be expected that this parameter strongly depends on the level of doping. Several institutions are currently working on experiments to extend the existing parameters to temperatures below 30 K.

Based on the calculations presented in sections 5.6.3 and 5.6.4 it is now possible to give an overall estimate of the expected thermal noise from the optical components of the ET-LF detector. The total estimate is based on the simplified sketch of the ET-LF detector in figure 165. The input coupler of the cavity as well as the end test mass are cooled to cryogenic temperatures around 10 K. The beam splitter is operated at room temperature.

In order to achieve a good thermal noise performance of the optical components a large beam radius w as large as 90 mm is needed. This requires the use of large diameter bulk samples to avoid large clipping losses. This requirement lead to a typical substrate diameter of 50 cm. In addition the suppression of radiation pressure noise requires large masses—for the ET-D design a mass of 211 kg is needed. In combination with the maximum available diameter of a potential silicon test mass material this leads to a required minimum thickness of 46 cm for the optical components involved in the arm cavities (end test mass and input coupler). A further increase of the thickness will reduce radiation pressure noise further—however, it will increase the thermo-refractive noise of the input test mass.

The option to use sapphire as a test mass material seems to be strongly limited by the availability of the materials. So far, it is not expected that by the time ET will be built sapphire test masses with a required diameter of 50 cm will be available on the market. Thus, all estimates in this section are based on the choice of silicon as a test mass material—although sapphire will totally satisfy all noise demands if operated at the same temperature and if it is available in the same geometry.

Figure 188(a) shows the total thermal noise of an end test mass cavity mirror for ET. The calculations are based on the properties presented in tables 10, 11, 12, and 13. A silicon test mass with a diameter of 50 cm and a thickness of 46 cm was assumed to be operated at 10 K. The ETM uses 18 $\lambda/4$-doublets of tantala/silica layers

and the ITM 9 $\lambda/4$-doublets of tantala/silica to form the cavity. While the laser beam reads out the surfaces of the cavity mirrors

$$N = 2/\pi F \tag{127}$$

times (F – finesse of the cavity) it only senses the thermo-refractive noise of the ITM twice (input and output of the cavity). This reduction factor is included for the ITM and the thermo-refractive noise recalculated as an effective displacement noise for comparison.

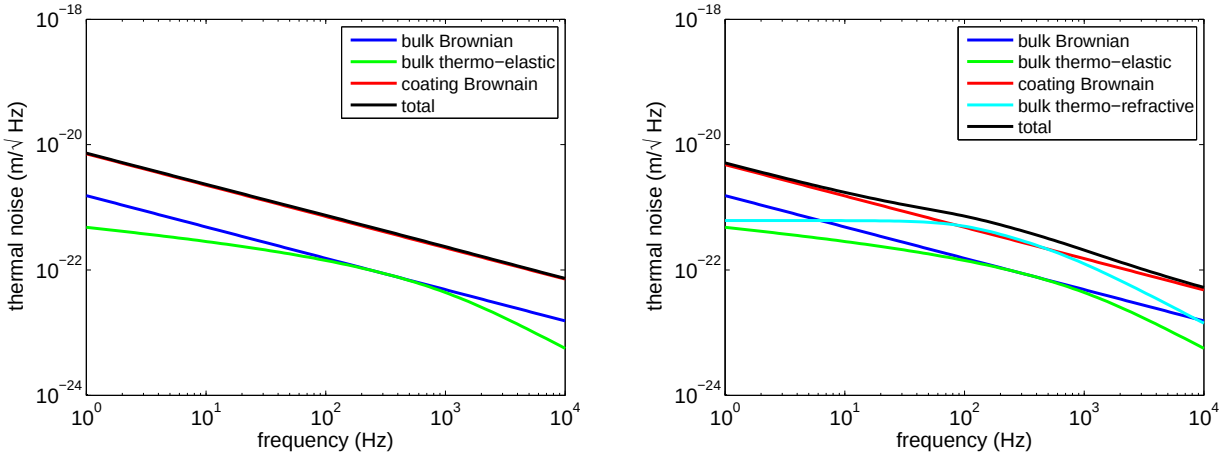

(a) (b)

Figure 188: Total thermal noise of an end test mass (a) and an input test mass (b) of the arm cavity of ET-LF. Both substrates are assumed to be made of silicon with a diameter of 50 cm and a thickness of 46 cm. The operational temperature is 10 K. The ETM is equipped with 18 $\lambda/4$-doublets of a tantala/silica high-reflective stack while the ITM is coated with 9 $\lambda/4$-doublets to achieve a transmission of about 7000 ppm.

For both—the ETM and the ITM—the coating Brownian noise dominates over all frequencies. For the input test mass the required 46 cm thickness leads already to significant contributions from the thermo-refractive noise. The uncorrelated sum of the different noise contributions in the ETM and the ITM can be used as a good estimate for the total thermal noise contribution of one arm cavity.

An additional noise source in the interferometer is the beam-splitter. Due to the fact that this element is situated outside the arm cavities its thermal noise contribution to the overall thermal noise of the detector is again reduced by the factor given in eq. (127). Thus, cooling might not be needed for this component. The beam splitter is assumed to be made of fused silica and operated at room temperature. The different thermal noise contributions based on the equations given in the previous sections are summarised in figure 189(a). The beam splitter is assumed to be coated with 3 $\lambda/4$-doublets of tantala/silica as an upper limit calculation. The thickness of the beam splitter is 10 cm and the aspect ratio is kept similar to the end test masses.

The thermo-refractive contribution from the beam-splitter is based on the calculation by Benthem and Levin for GEO600 [522]. Thermo-refractive noise is the most dominating noise source of the beam splitter due to the very low mechanical loss of fused silica at room temperature and the small number of coating layers. If the beam radius of the laser beam at the beam splitter is further reduced, thermo-refractive noise increases as shown in fig. 189(b). This reduction of the beam radius might be beneficial to reduce the necessary size of the beam splitter. Due to the fact that the beam splitter is operated under an angle the necessary size is increased compared to an end mirror. These mirrors are currently already designed to be at or close to the edge of what is and will be available by the time ET will be built. Thus, a reduction of the dimensions of the beam splitter is needed.

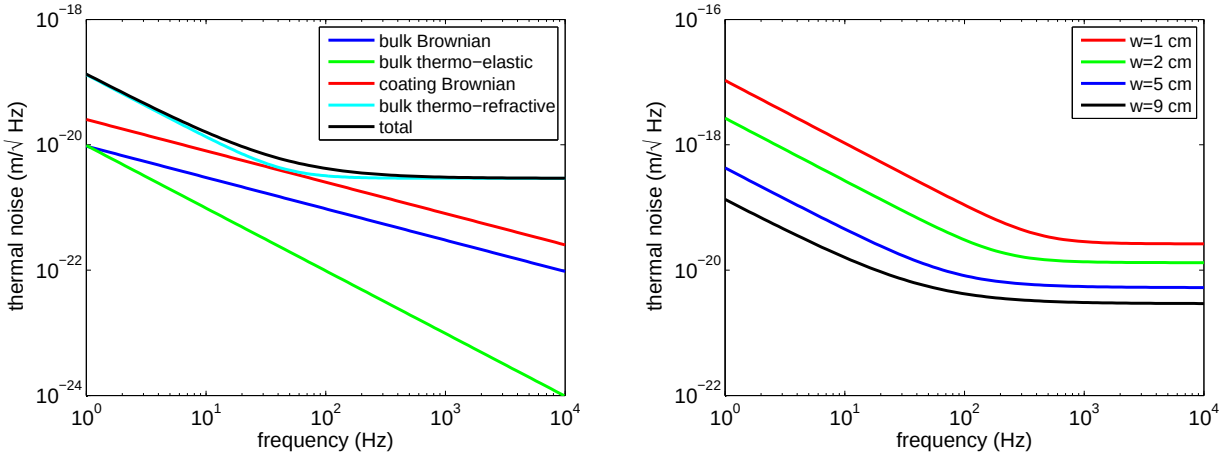

(a) (b)

Figure 189: (a) – Summary of the different thermal noise sources in a potential ET-LF beam splitter made of fused silica and operated at room temperature. (b) – Evolution of the total thermal noise of the beam splitter with different beam radii at the beam splitter.

Combining all noise contributions from the two arm cavities and the beam splitter (incoherent sum) leads to an estimate of the total thermal noise contribution for ET-LF, which is given in figure 190 for different beam radii at the beam splitter.

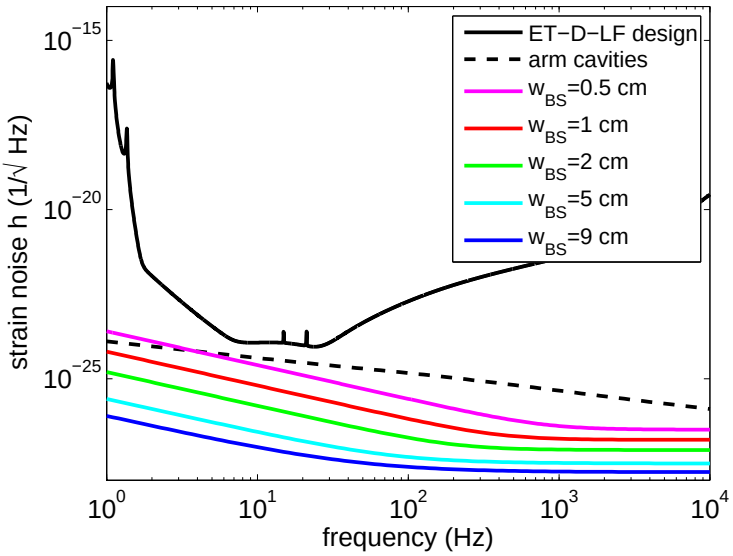

Figure 190: Total thermal noise arising from the optical components of ET-LF for different beam radii at the beam splitter.

It is obvious that the main thermal noise contribution comes from the arm cavities. Even if the beam radius at the beam splitter is chosen to be as small as 0.5 cm the noise contribution from the beam splitter is smaller than the contribution from the arm cavities. This relaxes the demands for the size of the beam splitter and the thermal noise contribution of the beam splitter is in agreement with the proposed beam diameter at the beam

splitter of 6 mm.

5.6.6 HF interferometer large mirror definition

Fused silica is the material of choice for the high frequency detector operating at room temperature. Fused silica is one of the most commonly used materials in optics and has been improved during many decades. Appropriate polishing methods exist to obtain a very high surface quality. Fused silica has remarkable properties at room temperature: low mechanical loss (see section E.2) which leads to a small substrate Brownian noise, and an exceptional low coefficient of thermal expansion (see section E.3) which results in a small thermo-elastic noise.

Parameter	ET-HF
temperature	290 K
arm length	10 km
mirror material	Fused silica
mirror diameter	62 cm
mirror thickness	30 cm
mirror mass	200 kg
laser wavelength	1064 nm
beam shape	TEM_{00}
beam radius	12 cm
coating high index	$Ti : Ta_2O_5$
coating low index	SiO_2

Table 14: Summary of the parameters used for the thermal noise estimate of the HF interferometer.

The assumed parameters for the ET-HF interferometer are listed in Table 14. The mirror geometry was chosen so that the mass reaches 200 kg to suppress radiation pressure noise and that the mirror geometry causes only 1 ppm diffraction loss at its boundaries [425]. For the sake of simplicity, in this estimates a TEM_{00} beam has been taken into account, considering the use of LG_{33} as an option for the HF interferometer. Using LG_{33} modes will further reduce thermal noise. However, it will be shown that the currently assumed geometry is already compliant with the ET-HF sensitivity curve if a TEM_{00} mode is assumed.

In order to compare the behaviour of different substrate materials the thermal noise of a high reflectivity mirror was calculated using the same 'standard' coating and different substrate materials. The 'standard' coating is a multilayer $(HL)_{17}HLL$ coating made of $Ti : Ta_2O_5$ and SiO_2 quarter wavelength layers. On a fused silica substrate this coating corresponds to a transmission of 6 ppm. The lowest mechanical loss experimentally observed has been considered for the coating materials (see section E.2). The result of this comparison is shown in Figure 191. The graph plots different noise sources in the substrate materials as well as their coatings.

At 300 K, the total thermal noise for silicon is limited by two substrate thermal noises: substrate Brownian noise at high frequencies and substrate thermo-elastic noise at low frequencies. Sapphire must also be discarded due to its large thermo-elastic noise at low frequencies. Therefore, the most adapted substrate at room temperature is fused silica. In this case, coating limits the sensitivity of the future detectors only through its Brownian thermal noise.

Mirror coating As explained above, the total thermal noise of the test masses is a combination of coating Brownian, substrate Brownian, substrate thermo-elastic, substrate thermo-refractive, and thermo-optic noise. Taking into account these five noise sources, the coating Brownian noise is the most important one and can limit the sensitivity target. A state-of-the-art of different coating material have been realized in order to compare different combination of multilayer stacks.

Figure 192 shows the total thermal noise for different coatings on a silica substrate at room temperature. The calculations are based on the currently best available data of the materials (table 13). Each coating corresponds

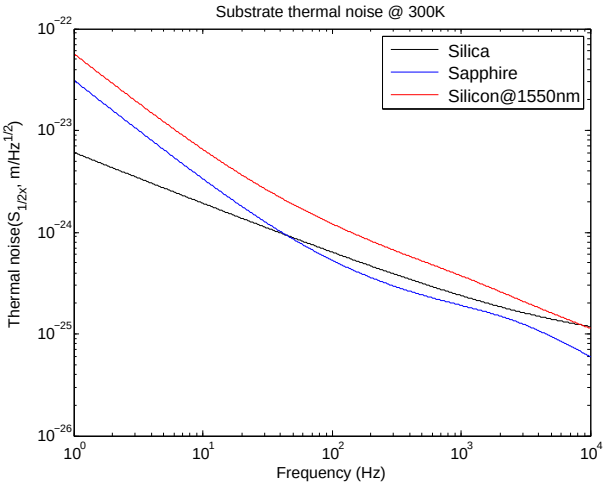

Figure 191: Total thermal noise of three different substrates at 300 K: silica, sapphire, and silicon at 1550 nm.

to a transmission of 6 ppm on a fused silica mirror. Therefore, all multilayers are different according to materials taken into account.

We need:

- $(HL)_{17}HLL$ for a coating made of $Ti : Ta_2O_5$ and SiO_2 quarter wavelength layers,
- $(HL)_{13}HLL$ for a coating made of TiO_2 and SiO_2,
- $(HL)_{13}HLL$ for a coating made of Nb_2O_5 and SiO_2,
- $(HL)_{16}HLL$ for a coating made of ZrO_2 and SiO_2,
- $(HL)_{24}HLL$ for a coating made of $Ti : Ta_2O_5$ and Al_2O_3, and
- $(HL)_{22}HLL$ for a coating made of ZrO_2 and Al_2O_3.

According to the refractive index of the material the number of layers can vary by a factor of two.

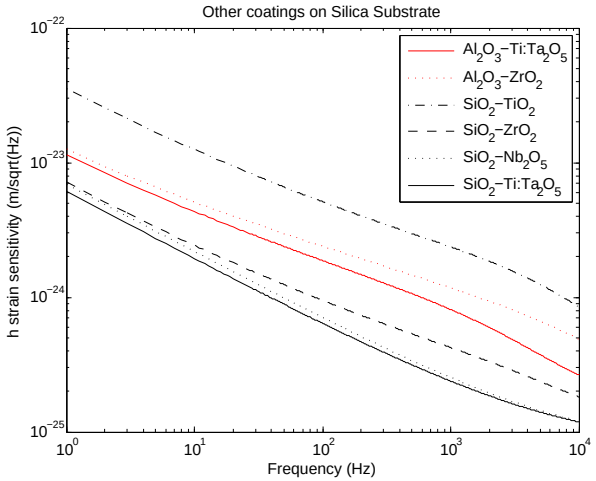

Figure 192: Comparison of the thermal noise of different coating materials on a fused silica substrate at room temperature.

There is a clear advantage for the $SiO_2 - Ti : Ta_2O_5$ coating showing the lowest coating thermal noise. The

results obtained for $SiO_2 - Nb_2O_5$ and $SiO_2 - ZrO_2$ are encouraging as well. However, if we include the optical absorption of the coatings, the use of the standard coating is even more strongly supported. So far, there is no better coating to be used at room temperature than the $Ti : Ta_2O_5 - SiO_2$.

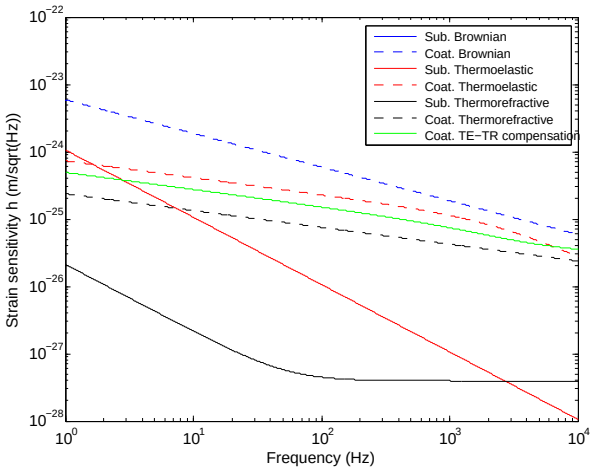

Figure 193: Contribution of the different thermal noises for a fused silica mirror at room temperature.

In conclusion, we have evaluated the total mirror thermal noise at room temperatures by implementing a model that includes Brownian, thermo-elastic and thermo-refractive noise. From the different calculations we have presented based on the parameters listed above we draw the conclusion that fused silica is the best test mass material for the high frequency detector of the 3rd generation GWD. The optimized mirror for the HF interferometer is, at present, a fused silica test mass with a diameter of 62 cm and a thickness of 30 cm.

5.6.7 Mirror surface defects

Here we discuss investigations of mirror surface defects in order to understand their effects on cavity resonance and losses, and to define requirements for surface polishing. For convenience, the mirror surface deviations from the perfect surface can be classified into two categories, depending on their spatial frequencies. Defects in the high frequency range (above a few hundred m^{-1}) will scatter light outside the cavity and thus generate cavity losses and scattering noise. Defects in the spatial low frequency range (between 1 and 100 m^{-1}) may induce resonance of unwanted modes in the cavity, and thus degrade the mode purity inside the cavity.

The ET arm cavities were simulated by FFT propagation using the simulation software *SIESTA* [524]. Artificial mirror maps were applied to both mirrors of the cavity. The artificial maps were randomly generated in order to reproduce a defect distribution similar to that found in actual VIRGO and LIGO mirrors [525–527].

Table 15 shows the cavity gain and round-trip losses for the fundamental mode resonating in the cavity (wavelength of 1064 or 1550 nm), with varying RMS flatness of the surface defects. The distribution of defects considered here goes as f^{-2}, where f is the spatial frequency. It has been shown in [527] that such a distribution, with a RMS of 1.0 nm, overestimates the low-frequency defects with respect to what has already been obtained for the Advanced LIGO mirrors. Therefore the surfaces obtained by current polishing techniques seem already good enough to obtain reasonably small round-trip losses for the fundamental mode. Using a wavelength of 1550 nm is particularly favourable from this point of view (smaller losses).

The situation for LG_{33} is more delicate. It has been shown [527] that LG_{33} is significantly more sensitive than the fundamental mode to surface defects in the low spatial frequency range. Essentially, since a cavity tuned for LG_{33} is degenerate for all modes of order 9, the low-frequency defects may induce the coupling between the injected LG_{33} and the other modes of the same order. Polishing techniques such as corrective coating or ion beam polishing are able to reduce the amount of defects in the low-frequency region, approximately below

RMS flatness	TEM_{00} 1064 nm		TEM_{00} 1550 nm	
	cavity gain	r.t. losses [ppm]	cavity gain	r.t. losses [ppm]
0 nm	567.4	2	567.4	3
0.5 nm	564.5 ± 0.9	20 ± 6	566.7 ± 0.3	7 ± 2
1.0 nm	555.9 ± 3.7	73 ± 24	564.4 ± 0.9	21 ± 6

Table 15: Cavity gain and round-trip losses for the arm cavities, computed from FFT simulations, as a function of surface defects RMS. The fundamental TEM_{00} mode is considered, for the wavelengths 1064 and 1550 nm. Data are expressed as mean $\pm$ standard deviation on an ensemble of 10 different cavities. For each cavity, random surface maps with a given RMS amount of defects are applied to both mirrors. The random surface maps are generated from a f^{-2} spectral distribution.

$100\,\mathrm{m}^{-1}$ ($1\,\mathrm{cm}^{-1}$). Ion beam polishing has currently been used for Advanced LIGO, whereas corrective coating is under evaluation for Advanced VIRGO [528, 529]. Preliminary results indicate that a further improvement is required for LG_{33} with respect to the state of the art of such techniques [527]. More work is planned to verify the agreement of FFT simulations with experiments on LG_{33} (see section 5.9.1).

In addition to the above work, the coupling between higher-order modes due to mirror surface defects was investigated using a frequency domain simulation tool, *Finesse* [530]. In this work, similarly to the simulation mentioned above, a Fabry-Perot cavity with imperfect mirrors was simulated. Real surface maps of VIRGO mirrors were reconstructed by fitting with Zernike polynomials, and an artificial map was built by a sum of Zernike polynomials. A LG_{33} beam was injected into a cavity where a surface map was applied on one of the two cavity mirrors. The light field inside the cavity was analyzed and found not only the couplings between the same order, but also the frequency split of the resonant frequency which will result in quasi-degenerate modes.

The next step is to expand the optical configuration to a realistic topology such as a RSE interferometer in order to obtain practical requirements for the mirror surface. Also, the effects of advanced polishing techniques such as corrective coating or ion beam polishing need to be better understood.

5.7 Standard Optical Technologies

This section describes several optical technologies, such as for instance laser and signal detection systems, required for the realisation of any interferometric gravitational wave detector. In the following we refer to these techniques as 'standard optical technologies' because when building ET we will be able to rely on ample experience in these technologies collected from commissioning and operating the first and second generation of gravitational wave detectors.

In section 5.7.1 we describe the ET injection system consisting of the pre-stabilised lasers and the input mode cleaners. The readout of the gravitational wave signal and the design options for output mode cleaners are discussed in section 5.7.2. Section 5.7.3 gives an general overview on how to control the main optical components of ET for their longitudinal and angular degrees of freedom. Finally section 5.7.4 describes strategies to mitigate the effects of thermal lensing by means of thermal compensation.

5.7.1 Injection system

Box 5.10: Laser beams required at the input of the main interferometers

	ET-HF	ET-LF
Wavelength	1064 nm	1550 nm
Beam shape	Laguerre Gauss 3,3	TEM_{00}
Optical power in front of PRM	500 W	3 W

Pre-stabilized laser At the development time of second generation GWDs, Neodymium doped Yttrium Aluminium garnet (Nd:YAG) was the best choice as the gain material for 100 W class lasers. However, in the last years, particularly thin disc lasers based on Ytterbium doped crystals have been undergoing a rapid development. The pure power scaling of these systems into the multi-kW range was mainly driven either by material processing or defense applications [531, 532], which do neither require single-frequency nor fundamental mode output. Nevertheless, good progress has also been achieved in the power scaling of high beam quality laser systems. In particular, near fundamental mode operation with more than 200 W of output power and up to 98 W of single-frequency output power has been demonstrated [533]. Further possible advantages are that the 940 nm pump diodes used for e.g. Yb:YAG have potentially longer lifetimes than their 808 nm Nd:YAG counterparts and that the lower quantum defect of Yb:YAG causes less thermal effects. However, Yb:YAG is a quasi-3-level system and thus its main disadvantage is that it is more sensitive to increased temperatures within the gain medium.

In order to produce lasers with power levels of several 100 W and to amplify these systems into the kW region, different design concepts are proposed. The main concerns are the thermal management in the gain material and to reduce beam aberrations. In particular, Nd:YAG suffers from a significantly higher quantum defect compared to Yb:YAG making the thermal management even more important. One way to reduce the thermal effects is to use a zig-zag beam path to average over the thermal gradient in the laser crystal. Edge-pumped slab geometries can be combined with conduction-cooling techniques, which avoid vibrations introduced by cooling fluids in conventional layouts. However, one of the main challenges in using slabs is to avoid parasitic oscillations within the high gain regions.

Problems caused by depolarisation and by defocusing can be addressed in different ways. In principle, an efficient birefringence compensation can be implemented [534]. However, better than compensating effects is to reduce these. For this, there are in principle two different options. Firstly, Koechner and Rice [535] and Soms et al. [536] have shown that the amount of depolarisation depends on the Nd:YAG crystal orientation. Therefore, crystal orientations other than the standard [111]-cut could be an option to reduce the depolarisation intrinsically. Shoji and Taira [537] suggested the use of [110]-cut crystals in combination with small beam size in the high pumping regime to reduce depolarisation. In recent experiments [538], the [100]-, [110]- and [111]-crystal orientations were compared in a single pass configuration in the pump power regime relevant for 2nd generation GWD. Although these results are very promising in terms of intrinsic reduction of depolarisation effects, they also show that the non-symmetrical shape of the thermal lens in unconventionally cut crystals might limit the achievable beam quality in laser oscillators.

The second option is to reduce the thermal gradients which cause these stress-induced birefringence effects. As shown in the work by Wilhelm et al. [539, 540], the maximum peak temperature of an end-pumped laser rod or slab can be reduced by the use of laser rods composed of several segments with different doping concentrations. The quantum defect and therefore the overall heat load in a Nd:YAG laser media can be reduced by more than 30% by changing the pump wavelength from 807 nm to 885 nm (see e.g. [462, 541]). Core doped rods can be used (see e.g. [542]) to achieve an easier and more stable fundamental mode operation. In these rods only the

inner core is doped and the outer core is used as a waveguide for the pump light comparable to a double clad fibre as described by Bedö et al. [543]. This concept is similar to mode selective pumping as the gain is only present in the doped inner core of the rod. However, it has the advantage that no high brightness pump source is required.

Optical fibre amplifiers have a large potential to offer single-frequency output at higher efficiencies and lower cost than solid-state amplifiers at similar power levels (see for example the overview paper by Limpert et al. [544]). Until several years ago, diode-pumped fibre amplifiers were limited to power levels of several Watts. This was both due to the unavailability of high brightness pump diodes as well as due to nonlinear effects in the fibre such as stimulated Raman scattering and stimulated Brillouin scattering (SBS). The invention of large mode-area (LMA) fibres and of photonic crystal fibres (PCF) has enabled output powers of single-mode fibre lasers to exceed 1 kW while retaining excellent efficiencies (see for example Jeong et al. [545]). The large effective core diameter of these fibres decreases the average intensity of the light at the laser wavelength in the fibre and thereby increases the threshold of nonlinear processes. The large inner cladding of the double-clad LMA fibres allows high power multi-mode pumps to be coupled into the fibre. Despite the large diameter of the active core, a clean single-mode output can be obtained by suppressing the higher order transverse modes by bending losses. A typical PCF geometry and a representative beam profile of such a fibre is shown in Fig. 194. The limiting factor for *narrow-linewidth* high-power fibre lasers for the use in GWDs is the onset of SBS.

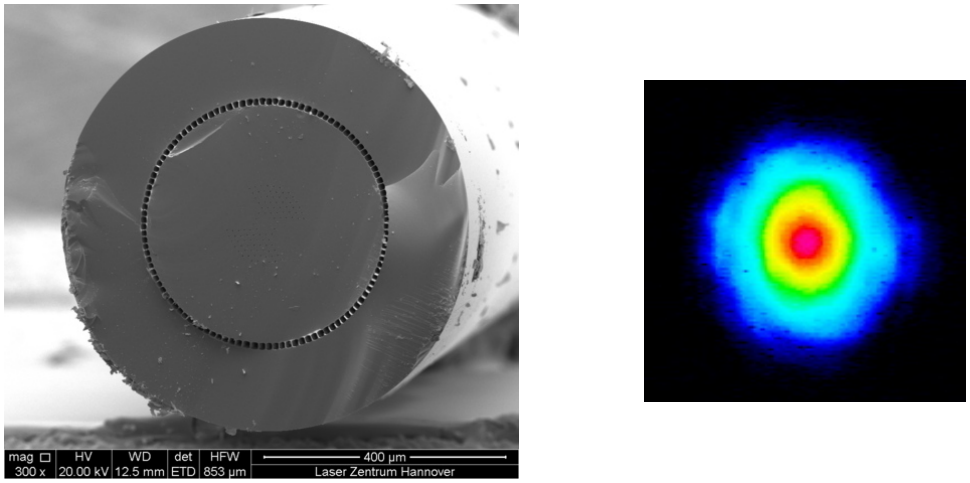

Figure 194: Typical geometry of a large-core photonic crystal fibre (left) and typical beam profile (right).

A state-of-the art single-frequency fibre amplifier system with 150 W of output power with a good output beam profile (92% in TEM_{00}) is described in [546]. With this system an optical-to-optical efficiency of 78% with respect to incident pump power was achieved with a good polarisation ratio of about 100/1. Recently, the output power of single-frequency, PCF-based, Ytterbium-doped fibre amplifiers has been scaled to more than 400 W of output power [547].

A different approach to realize LMA fibres with excellent output beam quality and simultaneously larger mode areas are multifilament-core (MFC) fibres with core regions consisting of many small doped filaments. In contrast to conventional multi-core design, the multifilament core fibres aim for strong coupling between smaller filaments resulting in the propagation of only one supermode by adequately choosing the diameter and spacing of the filaments. In the last years, MFC fibres with active and also with passive filaments were demonstrated, which enabled transversely single-mode output with a nearly Gaussian-shaped intensity mode profile [548, 549]. The main advantage of this new fibre type is the low effective core numerical aperture which can be achieved without the need for flattening the refractive index profile as it is crucial for PCFs. This is of particular importance for large index core materials like Erbium-Ytterbium codoped fibres for which this design approach allows for a precise reduction and control of the effective core index. Important properties of the MFC fibres, e.g. the low bending losses, can be explained using an equivalent step index based on the theory of the fundamental space

filling mode [550]. Recently, it has been demonstrated that a TEM_{00} mode content of more than 95% can be achieved with such an actively doped fibre [551]. In Fig. 195, both the calculated as well as the measured mode profile of an Erbium-Ytterbium codoped MFC fibre with 37 filaments is shown.

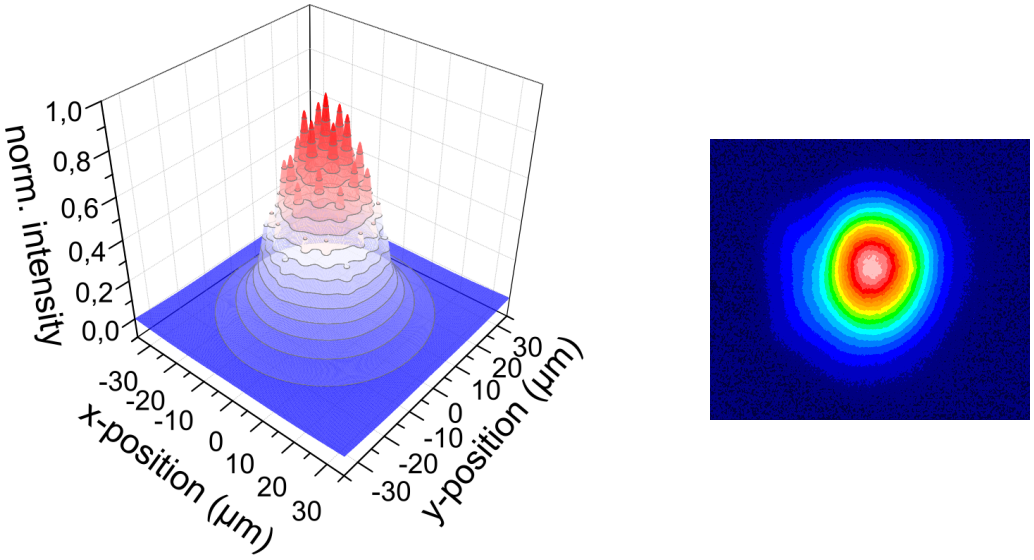

Figure 195: Calculated mode profile for an Er-Yb multifilament-core fibre with 37 filaments (left) and measured mode profile (right) with a fundamental Gaussian mode content of more than 95%.

Novel ideas to increase the SBS threshold are under investigation. A promising concept is to shift the Brillouin frequency along the fibre to lower the effective Brillouin gain for each frequency component. This could be achieved by temperature or strain gradients, or by varying doping concentrations along the fibre. Furthermore, fibres with specially designed transverse refractive index profiles are being developed to minimize the overlap of the optical and the acoustical fibre modes, also resulting in an effective reduction of the Brillouin gain.

Besides the power scaling aspect, the reliability and noise performance of high power fibre lasers need to be further analyzed and possibly improved to meet the requirements of third generation gravitational wave detectors. Especially thermal effects and contamination at the air-glass interface have to be considered. The main problem is the large light intensity at these interfaces which could be reduced by use of an undoped beam expansion section at the fibre ends or by all-fibre solutions for the pump-light coupling. One big advantage of fibre lasers is that they are compact and simple compared to the complex solid-state laser systems. Furthermore, modern splice techniques allow to produce monolithic all-fibre systems including the master oscillator, the high power stage and possibly even a mode-cleaning fibre, if required.

Erbium-doped fibre lasers emit around 1.56 μm where the absorption in silicon is small compared to the silica substrates currently used at 1 μm wavelength. For an efficient design with low nonlinear effects in single frequency operation, the Erbium-doped fibre should have high pump absorption and should be as short as possible. Unfortunately, the pump absorption cross sections of Erbium are about a factor of 10 lower than those of Ytterbium. In addition, quenching effects also limit the sensible doping concentrations to about a factor of 10 below that of Ytterbium. These combined factors result in about two orders of magnitude lower pump absorption of Erbium doped fibres, if similar fibre geometries as used with Ytterbium doped fibres are assumed. In order to avoid excessive fibre lengths, which is necessary to circumvent the onset of SBS, either the signal-core to pump-core ratio has to be adapted or the amplifier even has to be pumped into the single-mode signal core. For these reasons, pump sources with very high brightness or even single-mode beam quality are needed. This becomes even more obvious if the typically achieved optical-to-optical efficiencies of about 25%–30% (50% for 1480 nm pumping) are compared with the typical value of $> 70\%$ for Ytterbium. Recently, a single-mode output power of 81 W at 1480 nm was demonstrated with a Raman fibre laser [552] which can be used as a pump source for single-mode Er based systems. However, commercially available single-mode Raman fibre laser

modules are currently limited to an output power of 10–20 W.

In order to overcome these limitations, Yb codoping of Er-doped fibres and pumping at 980 nm can be used. This allows high pump absorption but also implicates a second gain band at the Yb wavelength around 1 μm. This second gain bands limits the achievable output power due to the onset of massive amplified spontaneous emission (ASE) which finally leads to pulsing instabilities of the amplifier system. The highest single-frequency output power of 151 W achieved with this concept was accompanied by more than 70 W of ASE at 1 μm [553]. Nevertheless, in recent experiments a new scheme was demonstrated by which the 1 μm oscillation in an Er-Yb codoped fibre amplifier could be effectively suppressed [554].

Concerning the direct generation or the amplification of spatial beam profiles other than the fundamental (fibre) mode, only very limited experimental results have been published. A good overview is given in the review article by Ramachandran et al. [555]. For the generation of specific higher order modes, the laser light is first coupled into the fundamental LP_{01} mode of a single-mode fibre. Then, an in-fibre long-period Bragg grating converts the LP_{01} into the desired LP_{0m} mode. This process can be very efficient with peak efficiencies of more then 99%. The usage of higher order modes in the optical fibres has several advantages compared to the fundamental mode. Firstly, the effective mode area is significantly enlarged and hence the threshold for SBS is increased. Furthermore, the higher order modes are less sensitive to mode distortions due to fibre bending or refractive index profile imperfections due to the fibre fabrication process. Recently, fibre amplifiers have been demonstrated employing this technique for the first time in an active fibre with several Watts of output power [556, 557]. However, all higher order LP_{0m} modes used have a central high intensity peak in common which is undesirable for the use in GWD [558]. Thus, some research on the generation of axisymmetric fibre modes with an intensity minimum in the centre as well as on the amplification of these modes will have to be carried out. Most probably, this will also involve some special design of active fibres in which the active dopant distribution favors the amplification of the mode of interest.

Box 5.11: Lasers for ET

While the step from first to second generation gravitational wave detectors required to scale the laser systems up by about a factor of 20, the step from second generation to ET will only require a much smaller scaling factor of about 4 for ET-HF. Research programs on ET lasers are already under way and no fundamental limits are known which are expected to prevent the realisation of the high power laser for ET-HF. The laser power required for ET-LF is with only about 5 W very small and currently already available.

Injection optics The Input Optics system (IO) of ET takes care of the optics downstream of the lasers. The whole system must deliver a beam with the required power, geometrical shape, frequency and angular stability at the Interferometer input.

Electro-Optic Modulators (EOM) should provide the needed RF phase or amplitude modulations (to sense longitudinal and angular degrees of freedom; see section 5.7.3). Two in-vacuum suspended input mode cleaners (IMC) in series will be used to geometrically clean the beam and reduce its amplitude fluctuations as well as geometrical fluctuations. The resonant IMC could also serve in the loop of laser frequency stabilization. After the IMC an intensity stabilization section will provide the signal for stabilizing the laser's relative intensity noise (RIN) and reach the requirements. An in-vacuum Faraday isolator (FI) will prevent interaction of the interferometer reflected light with the IMC and laser system. Finally, a mode matching telescope will be used to provide a beam with the correct size and wave front curvature for matching it into the interferometer. It is planned to use super-polished optics for ET-HF and ET-LF in order to lower as much as possible potential diffused light noise. Moreover the beam pointing noise created in components in free-space propagation (mirrors, lenses, EOM, FI, etc.) can be dominated by acoustic, seismic and thermal noise. Particular effort will be given to isolate the optics from seismic noise. Furthermore, several sensors used in the control loops will be placed on suspended benches inside the vacuum vessel of ET.

Input Mode Cleaner The laser light must be frequency- and spatially stabilized before it can be used in the interferometer. The input mode cleaner provides active frequency stabilization through feedback to the laser and passive frequency noise suppression above its cavity pole frequency. The input mode cleaner also reduces higher order modal content of the laser light, suppressing beam jitter by a factor depending of the cavity finesse.

The baseline configuration of the IMC for ET-HF is to use two 20-meter long IMC cavities placed in series (as done in GEO interferometer). Due to the high laser power that will be stored in the IMC cavity, radiation pressure effects and absorption in the IMC cavity input and output mirrors will be the main limiting effects. The radiation pressure effects will depend on the cavity finesse chosen. In Advanced Virgo, with about 60 kW power stored in this cavity it has been shown that the radiation pressure effect on the angular degrees of freedom is manageable by using mirrors of at least 3 kg weight [559]. This means that this effect could be overcome by increasing the IMC mirror weight or reducing the finesse if possible. For the lock acquisition of the cavity it is likely that we need to lock the cavity at a lower power and go to full power once the cavity is locked [559]. Radiation pressure noise (linked to power fluctuation in the cavity) could also be responsible for frequency noise since it can affect the length of the IMC cavity and the angular control of the IMC end mirror if the beam is not well centered on this mirror. In the linear regime, it has been shown that radiation pressure noise was not an issue for initial Virgo sensitivity [560] and Advanced Virgo [561]. Concerning input and output mirrors absorption, in order to avoid beam distortion induced by photothermal effects, a low-absorption fused silica grade with good homogeneity should be chosen as mirror substrate and coating absorption lower than 1 ppm is mandatory [562]. In order to cope with higher order Laguerre-Gauss modes, the resonant mode cleaner should be made with an even number of mirrors as explained in [563, 564]. Cavity parameters (finesse, round-trip losses and cavity pole) will have to be defined according to the beam jitter, amplitude and frequency noise requirements at the interferometer input.

There are two main differences between the input mode cleaners for ET-HF and ET-LF: First of all the optical power in the ET-LF IMC will be orders of magnitude lower than in the ET-HF IMC and therefore we expect to encounter fewer potential issues related to radiation pressure and thermal effects in the ET-LF IMC. Secondly the laser wavelength of the ET-LF IMC will be 1550 nm, which will allow us to strongly profit from synergies with the telecommunication sector. Therefore, we believe the realisation of the ET-LF IMC to be less challenging than the IMC for the ET high frequency interferometers.

Faraday isolator In order to avoid unwanted cross-coupling, light back-reflected by the interferometer should be picked up before being coupled back in the IMC cavities. The solution adopted in first and second generations of gravitational wave detectors is to install a Faraday isolator in vacuum on the beam path between the interferometer and the input mode cleaner cavity.

Faraday isolator for ET-HF: Faraday isolator designs have evolved to cope with the increase of power between first and second generation detectors. A R&D program put in place at the European Gravitational Observatory in collaboration with the Institute of Applied Physics (Nyzhni Novgorod Russia) has developed a Faraday isolator with reinforced magnetic field and using a thermal depolarization compensation technique [565]. This isolator uses Terbium Gallium Garnett (TGG) as magneto-optic material and the design has been optimized for thermal depolarization, thermal lensing and Verdet constant change compensation [566]. This device is able to achieve very good isolation performances (> 38 dB) in vacuum from low power up to 250 W laser power [567]. We could use this experience and the same kind of design and scale it up to get the expected performances of the Faraday isolator in the 1 kW power range. For ET-HF we could expect that the in-vacuum Faraday isolator should have the following characteristics:

- withstand high average power (1 kW) on long periods;
- an optical isolation higher than 30 dB at full power;
- residual thermal lensing resulting in a focal length higher than 100 m;
- provide good transmission (at least 95%)

Faraday isolator for ET-LF: In the telecom wavelength range, TGG cannot be used due to its higher absorption

at 1550 nm. Fortunately, in the field of telecommunications a lot of possible materials are available that can be used for Faraday isolators [568]. The main aspect that needs to be checked for ET-LF is ultra-high vacuum compatibility of a 1550 nm Faraday isolator.

RF-Electro optical modulation system In ET radio-frequency (RF) modulation of the laser beam will be used in the control of the interferometer, both for longitudinal and angular controls.

RF modulation system for ET-HF: The main difference between the Electro Optical Modulation (EOM) system to be used in ET-HF respect to first and second generation detectors is the laser power that the EOM system will have to withstand (up to 1 kW for ET-HF). Thermal effects become more significant [569] and the choice of an appropriate material (electro-optic crystal) becomes crucial to limit the consequences of these thermal effects on the EOM performance. Indeed, it is important to select the right material not only to limit wavefront aberrations but also to reduce local temperature fluctuations of the material. This heating can induce slow variations of the modulation index and therefore disturb the interferometer control. The ET requirements for the electro optical modulation system (oscillator phase noise, modulation index and modulation index noise) will have to be defined in the technical design, as many of these parameters will affect the driving electronics and signal generator choice.

RF modulation system for ET-LF: The experience of telecommunication field will be used extensively in the RF-modulation system of ET-LF. It is likely that integrated fibered optical components will be used to modulate the laser light.

Other high power compatible components The selection and development of high power compatible components suitable for ET-HF is essential. Experience acquired during the Advance Virgo highpower input optics R&D program should be a good starting point in the selection of waveplates, polarizers and for the design of high power low diffusing beam dumps [566, 567].

5.7.2 Detection system

Traditionally detection system of first and second generation gravitational wave detector includes all optical elements downstream the main interferometer (i.e. behind the signal recycling mirror), such as for instance the readout photodiodes and the output mode cleaner (OMC). In contrast, as described already described in section 5.5.3 ET will feature the injection of frequency dependent squeezed light from the back of the interferometer and there are lots of hardware components required for this purpose, such as for instance the squeezed light sources as well as the filter cavities. In this section we will focus on the traditional components of a the detection subsystem, i.e. the readout of the main gravitational wave signal and the output mode cleaner.

Readout options for the gravitational wave signal Figure 196 shows simplified schematics of three different readout methods applied to a basic Michelson interferometer. Usually Michelson interferometers used for gravitational wave detection are operated at the dark fringe, which has the advantage of providing good suppression of common mode noise and allows to make use of power recycling. The differential arm-length is controlled to give destructive interference at the output port: ideally no carrier light (f_c, red solid line) reaches the photo detector. A change of the differential arm length causes phase modulation sidebands, i.e. gravitational wave signal sidebands (blue dashed line). In contrast to the carrier light the gravitational wave signal sidebands interfere constructively at the beam splitter, exit the interferometer towards its output port and finally reach the photo detector. The absolute frequency of the gravitational signal sidebands is given by $f_{sig} = f_c \pm f_{gw}$, where f_{gw} is the frequency of the gravitational wave (usually in the audio-band) and f_c the frequency of the main laser light (carrier). Since f_{sig} is a few hundred terahertz, the photodiode cannot directly detect the gravitational wave signal, unless the presence of an optical local oscillator is ensured. Heterodyne, homodyne and DC-readout are three different concepts to ensure the presence of a low-noise optical local oscillator at the output port photodiode.

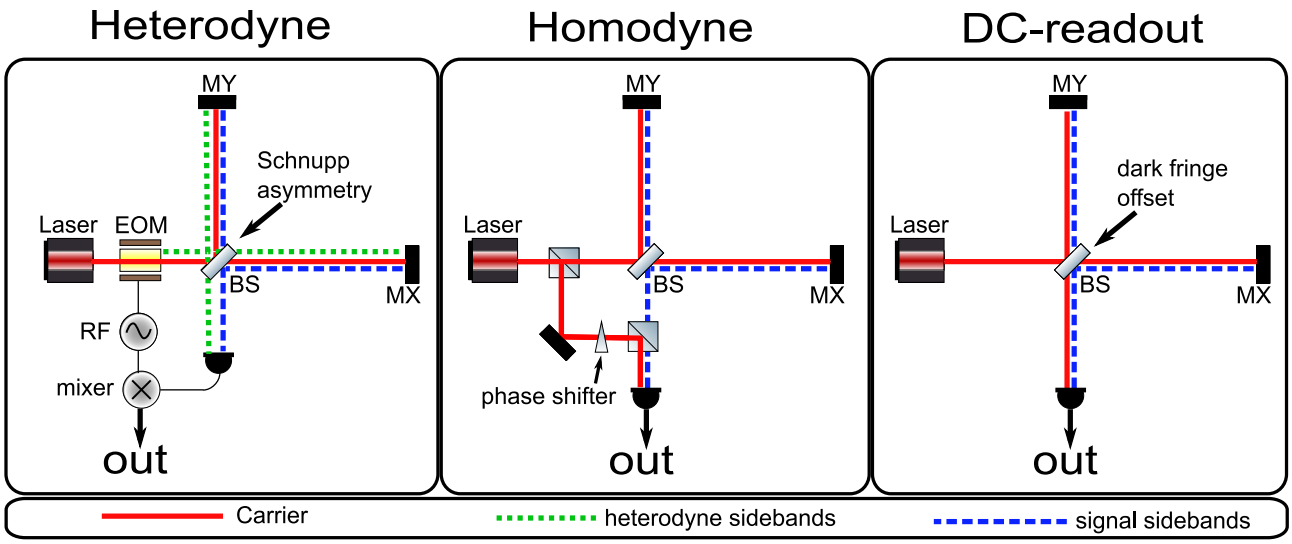

Figure 196: Illustration of three different readout methods of a Michelson interferometer: heterodyne, homodyne and DC-readout. A detailed explanation is given in the text.

In the heterodyne scheme, commonly used by the first generation gravitational wave detectors, radio frequency sidebands ($f_{\rm het}$, green dotted lines) are modulated onto the light at the input of the Michelson interferometer (Schnupp modulation [570]). Introducing a macroscopic arm length difference of several centimeter (so-called Schnupp asymmetry) allows the modulation sidebands to be transferred through the interferometer to the output port, where they serve as optical local oscillator for the differential arm length signal. The photo-current produced by the beat between the different optical field components (optical demodulation) contains a radio frequency component at $f_{\rm het} \pm f_{\rm gw}$. In a second demodulation process the photo-current is then electronically demodulated at $f_{\rm het}$ in order to finally derive a signal stream at $f_{\rm gw}$.

In the homodyne readout scheme (center plot of Figure 196) a small fraction of the carrier light is split off in front of the interferometer and guided directly to the output photo detector without passing through the interferometer. The big advantage of this form of homodyne readout is that a phase shifter, placed in the local oscillator path, allows an easy change of the optical demodulation phase, i.e. the readout quadrature, without any hardware changes. On the other hand homodyne readout has the disadvantage that the length and the alignment of the local-oscillator path needs to be highly stable. In practice this usually implies that the local-oscillator path length as well as its alignment need to be actively stabilized by a low-noise control system, and all components of the local-oscillator path must be seismically isolated inside a vacuum system. Due to these demanding noise and hardware requirements, so far there have been no serious plans to change the readout scheme of the currently operating gravitational wave detectors from heterodyne to homodyne readout.

DC-readout is a special case of homodyne readout which is much easier to combine with the existing elements of currently used gravitational wave detectors. In a DC-readout scheme the operating point of the Michelson interferometer is slightly shifted off the dark fringe, by introducing a so-called *dark-fringe offset*, thus a certain amount of carrier light leaves the interferometer at the output port and can serve as local oscillator. Compared with the previously described homodyne readout, DC-readout has the advantage that no additional local oscillator path outside the main interferometer is required. On the other hand, DC-readout offers no easy way to vary the phase of the optical demodulation.

DC-readout was already used in the first 'Michelson' interferometer ever by Michelson and Morley in 1887 [571]. It is probably the simplest way to read out a Michelson interferometer, but was considered to be unsuitable for the first generation of gravitational wave detectors due to the strong coupling of laser power noise. However, increased stability of the laser power inside future instruments gives hope for a renaissance of DC-readout for gravitational wave detectors, which was first proposed by Fritschel [572].

The next section briefly summarises the general advantages and disadvantages of DC-readout compared with heterodyne readout, especially taking into account the implications for an interferometer with tuned or detuned signal recycling [573].

Box 5.12: Motivation for using DC-readout in ET

DC-readout has several advantages over heterodyne readout:

1. DC-readout provides an increased signal to shot noise ratio compared to heterodyne readout [574]. This is due to the fact that in the homodyne detection the shot noise contribution from frequencies twice the heterodyne frequency does not exist.
2. In DC-readout a reduced number of beating light fields at the detection port potentially reduces and simplifies the cross-couplings of technical noise [573]. Especially the coupling of amplitude and phase noise of the heterodyne modulation is strongly reduced in a DC-readout scheme.
3. A simpler calibration procedure can be applied for DC-readout, because the GW-signal is present in a single data-stream even for detuned signal-recycling (and not spread over the two heterodyne quadratures as described in [575]).
4. As with DC-readout the main photodiode(s) and electronics for the detection do not need to be capable of handling RF signals, they can be simplified.
5. Large-area photodiodes may be used in DC-readout. These should offer reduced coupling of beam-pointing noise, due to decreased beam clipping and decreased influence of photo diode inhomogeneity (by averaging over a larger area).
6. As in the DC-readout configuration the local oscillator and the GW-signal pass the same optical system an optimal spatial overlap is guaranteed. (Due to thermal distortion current GW detectors employing arm cavities encountered the problem of imperfect spatial overlap of the carrier light (GW signal) and the heterodyne sidebands (local oscillator) [576])
7. Finally, the realization of a squeezed light enhanced interferometer is simpler using DC-readout rather than heterodyne readout. DC-readout requires squeezed light to be present only at frequencies in the GW signal bandwidth compared to heterodyne readout which requires squeezed light around twice the heterodyne frequency as well [577].

This long list of advantages has to be compared with the drawbacks of DC-readout. Even though power fluctuations of the carrier light (i.e. the local oscillator) are strongly filtered by the cavity poles of the power recycling cavity and the high-finesse arm cavities, the major disadvantage of DC-readout is an increased coupling of laser power noise. For the Einstein Telescope the advantages of DC-readout clearly way out the disadvantages and therefore DC-readout was chosen as baseline configuration for the gravitational wave readout.

Recently enhanced LIGO and GEO-HF have successfully demonstrated the application of DC-readout in long-baseline gravitational wave detectors. Furthermore, all advanced gravitational wave detectors plan to use DC-readout for the gravitational wave signal. Therefore, the commissioning of Advanced LIGO and Advanced Virgo is expected to greatly inform the technical design of the ET readout system.

Output mode cleaner The beam transmitted at the output port of each interferometer must be filtered by an Output Mode Cleaner cavity (OMC). The goal of the OMC is to filter the imperfections of the beam profile that are induced by beam mismatch, misalignment or astigmatism defects in the interferometer. Such defects couple a fraction of the main beam into spurious geometrical modes which do not carry information on differential arm motion. Therefore, by eliminating these spurious modes before the beam reaches the photodiodes, the OMC plays a crucial role in minimizing the shot noise.

For a DC-readout interferometer, only the carrier component of the beam is involved in the detection of a gravitational wave signal. On the other hand, modulation sidebands which are used for longitudinal and angular sensing in the mirror control loops do not play any role for detection. Therefore, the OMC should suppress the modulation side bands in order to minimize the shot noise and also to prevent the side band power noise from

spoiling the sensitivity. The main parameters to be defined for the OMC are: the geometry and the type of the cavity, the finesse, the length and the waist.

The favored geometry is a bow-tie cavity made of four reflective surfaces as shown in Figure 175. Two of these surfaces are curved in order to introduce a Gouy phase between different geometrical modes. Such cavity is compatible with the Laguerre-Gauss High Order mode technology, and would be suitable for both the ET-LF (TEM_{00} beam) and ET-HF (LG_{33} beam) instruments. A bow-tie cavity also allows a small incidence angle between the beam and the OMC surfaces. One can envision an incidence angle of the order of 10 degrees as it is foreseen for Advanced Virgo. This choice should make it possible to minimize the amount of back-scattered light without introducing too much astigmatism.

Two types of cavity can be envisioned: a monolithic cavity made of a few centimeters long crystal as it has been designed for Advanced Virgo ([578] and [579]) or a 'tombstone' design as for Advanced LIGO [580] or GEO600 [581, 582]. The tombstone OMC consists of four individual mirrors rigidly connected by a spacer and whose round-trip length can be of the order of 1 m. The main advantages and drawbacks of these designs are discussed below.

The monolithic design is a robust and compact solution that already benefits from a long and successful experience with the Virgo OMC. A monolithic OMC can be kept at resonance using a thermal length control based on a Peltier as actuator. The error signal can be obtained by modulating the OMC length using a small PZT actuator placed on top of the cavity. As it has been proven with the Virgo OMC, this system can be arranged so that its mechanical resonances lie well above the detector bandwidth [583]. Thus this device is very stable from a mechanical point of view. Another big advantage is a low thermal noise, which is an important criterion as OMC length fluctuations can spoil the sensitivity. A recent measurement with the Virgo interferometer was used to put an upper limit on the OMC length fluctuations due to thermal noise of 6×10^{-17} m/$\sqrt{\text{Hz}}$ at 100 Hz [579]. The main weakness of the monolithic design is the limitation on the length which cannot be increased too much in order to keep the thermal control simple and the mechanics stable. As the OMC length has a direct impact on the filtering performances of spurious geometrical modes and side bands, this criterion will have to be examined very carefully before making a final choice on the type of cavity. Another potential weakness of a monolithic OMC is the risk of thermal effects due to absorption of the laser power in the OMC substrate and thermal lensing. This risk becomes higher with the ET-HF instrument for which the power reaching the OMC should be four times larger than the expected power for Advanced Virgo. The characterization of thermal effects with the Advanced Virgo OMC will be very valuable to better assess this risk.

The tombstone design has been implemented in the Enhanced LIGO [580] and the GEO 600 [581, 582] interferometers. It is also being designed for the Advanced LIGO project [580]. The main advantage of the tombstone design is the absence of strong limitation on the cavity length, which could be of the order of 1 m. This offers stronger filtering performances with respect to a few centimeters long monolithic crystal of equal finesse. Also with this design there should be no risk associated to thermal effects due to the high laser power in ET-HF. The OMC length can be controlled by acting on the mirror positions with PZT actuators. Such actuators have a larger bandwidth but are likely to be noisier than the thermal control implemented for the Virgo monolithic OMC. The main weakness of the tombstone design is its higher mechanical complexity. For instance the enhanced LIGO detector has experienced some difficulties with the locking of its tombstone OMC. A more reliable actuation system is needed for ET. OMC mechanical resonances have been observed in the detection bandwidth of the enhanced LIGO and GEO 600 detectors. For the ET design mechanical resonances should be shifted to higher frequencies in order to not spoil the sensitivity. Moreover the length noise of such cavity could represent a risk that will be better assessed with the experience of GEO-HF and Advanced LIGO.

The choice between the monolithic or tombstone design will thus result from a trade-off between a conservative filtering of the side bands and a low length noise. The choice of the OMC finesse and length is driven by the filtering needed for the side bands. The main constraints on the filtering will be imposed by the sideband power noise which can limit the sensitivity if modulation sidebands are not sufficiently well suppressed. Keeping a similar design as for the Advanced Virgo OMC will lead to rather hard constraints on this noise: the relative intensity noise of the oscillator signal delivered by the generator should be kept below 10^{-8} $\text{Hz}^{-1/2}$ at 10 Hz for ET-LF, and in the range $10^{-9} - 10^{-8}$ $\text{Hz}^{-1/2}$ at 100 Hz for ET-HF. These specifications seem to be quite challenging. The experience that will be gained with Advanced Virgo and Advanced LIGO will help

understanding if they are achievable. In case the specifications on the side band power noise need to be relaxed, the finesse or length of the OMC cavity should be increased.

The choice of the finesse is limited by the amount of diffraction losses on the OMC mirrors. Assuming losses of the order of 30 *ppm* per face, one would need to choose a finesse below 260 in order to keep the total losses below 1%. A better evaluation of the expected diffraction losses on the OMC surfaces is needed to assess the limitation on the finesse.

The OMC radius of curvature will be chosen in order to sufficiently filter the spurious geometrical modes of the carrier and side bands. Its final choice will depend on the modulation frequencies selected for longitudinal and angular sensing. In order to prevent laser frequency noise to couple through the OMC, the main laser of ET-LF and ET-HF should be stabilized at low frequency using a rigid cavity.

The OMC needs to be associated to several other optical components. In order to limit the amount of back-scattered light a Faraday Isolator should be placed in front of the OMC. A telescope should be designed in order to tune with sufficient accuracy the beam matching and the beam alignment with respect to the OMC. The whole system should be seismically isolated and placed under vacuum in order to meet specifications on beam jitter [584].

5.7.3 Main control and alignment strategies

As a matter of fact, in interferometric GW detectors—the highly complex optical instruments they have grown—it is a crucial requirement for the multitude of their degrees-of-freedom (DOF) that they are held tightly at predefined operating points, for instance to allow for full internal power build up or to enable active null operation. For keeping the mirrors at their operating positions, electronic feedback control has proven as an essential tool, making a deterministic and reliable operation of a GW detector possible.

Box 5.13: Interferometric sensing and control for ET

The configurations of the ET main interferometers, featuring a dual-recycled Michelson interferometer with Fabry-Perot cavities in the arms, has been chosen to be similar to Advanced LIGO and Advanced Virgo. In addition the reflectivities and the resulting cavity finesse for the arm cavities and the recycling cavities will be within a factor of two of what is planned for the second generation interferometers. These choices have been made consciously in order to be able to transfer as much as possible the interferometric sensing and control concepts developed and implemented in second generation Gravitational wave detectors to ET.

The task of controlling an interferometer can further be sub-divided in the control of longitudinal DOF and alignment control. In the following we will first focus on aspects of controlling the longitudinal degrees of freedom (i.e. only variations along the axis of the optical mode in the interferometer will be considered) and in the later part discuss alignment control.

Fundamentals of length sensing and control A successful length sensing and control system for ET has to satisfy three basic requirements: First, starting from a random initial state it must bring the instrument to a predefined operating point ("lock acquisition"). Second, it must prevent disturbances of any kind from causing deviations of the instrument from its operating point by an amount larger than specified. Finally, it must provide a low-noise electronic signal which contains the GW signal. In this discussion we will focus on the first two aspects, while the GW readout has already been discussed in section 5.7.2.

A crucial element of a succesful longitudinal control scheme is the extraction of a complete set of signals which reflect the dynamical state of the longitudinal degrees-of-freedom and which, in particular, are a measure for the deviation of each of the interferometric degrees-of-freedom from its desired operating point. Generally, this is

achieved by employing variants of the fundamental Pound-Drever-Hall technique [585]. The Pound-Drever-Hall scheme builds on imprinting radio-frequency (RF) phase modulation sidebands on the carrier beam prior to its injection into the optical cavity to be controlled. Cavity length fluctuations are efficiently converted to carrier phase shifts, which occurs near resonance as a linear effect. The RF sidebands in contrast do not experience a phase shift, as their frequencies are generally chosen off-resonant in the cavity. Pure phase modulation is thus partially converted to amplitude modulation. Heterodyne readout of the reflected beam provides a signal which is a direct measure for the cavity's deviation from resonance and which can further serve as an error signal for electronic feedback controls.

Ideally, a sensing system would provide a number of independent outputs, one for each DOF in the detector. However, in practice error signals obtained from an interferometer by means of heterodyne detection show more or less strong coupling. This is acceptable as long as these signals are at least linearly independent, due to the fact that this class of signals can be electronically post-processed, i.e. linearly transformed, resulting in separated signals. The underlying transforms can easily be implemented in the form of matrices in digital data processing systems. However, care must be taken to provide rubustness of the transformations under parameter changes of the optical plant and the sensing electronics. This is why in practice optically separated signals are usually preferred over signals obtained via electronic separation. Further potential disadvantages of electronically separated signals are a reduced signal-to-noise ratio and more complex dynamics during lock acquisition [586]. Generally, providing too few modulation frequencies or extraction ports complicates the task of finding a set of independent length signals and, in the worst case, leaves the optical system underconstrained due to a lack of information about its internal state.

A valuable form of description for the design of a sensing scheme is the *sensing matrix*. The sensing matrix describes the relation between the interferometer's degrees-of-freedom and the signal extraction ports. In the ideal case this matrix would be diagonal which would read as all sensing signals being fully decoupled. Likewise, the control problem would decouple to a single-input single-output problem for each degree-of-freedom in the interferometer. Contrasting this, the signal mixing of length error signals one encounters in practice would yield non-vanishing off-diagonal elements in the sensing matrix. This is tolerable, as long as the off-diagonal elements are smaller in magnitude than the diagonal ones as in this case a technique referred to as *gain hierarchy* can be applied to solve the control problem. This technique is based on suppressing a large signal that appears in more than one port by closing a control loop around the DOF that causes it. A small signal, previously covered by the large one, can in this way be dissected from the signal mixture and serve as an error signal for another, by then uncontrolled, degree-of-freedom.

The classical approach of implementing servo controllors by means of analog electronics is driven from predominance more and more by digital control systems. At the expense of their higher cost and obvious bandwidth limitation, digital systems provide a high precision and low noise environment allowing for rapid design and easy duplication of solutions. Massively multiple-input multiple-output systems become feasible and instrument automation can be easily implemented. Unlike analog electronics digital servo systems exhibit a high immunity to environmental parameter changes which makes them predestinated for applications which require long-term stable operation. Despite all these obvious advantages, it is fair to say that digital system complexity, in practice, rivals analog controls.

Longitudinal sensing and control in Advanced generation detectors With increasing complexity and a growing number of degrees-of-freedom in the instruments comes the need for highly sophisticated length sensing and control schemes, which are substantial to setting the detector into operation. The interferometric topology that will be adopted by the Einstein Telescope is the cavity-enhanced dual recycling Michelson interferometer, which is also the underlying topology of the Advanced GW observatories currently under construction. In this section a review of central aspects of the sensing and control concepts of a typical Advanced generation GW observatory is given, focussing on Advanced LIGO [587] as an example. The optical setup is schematically depicted in Fig. 197.

For Advanced LIGO different modes of operation are foreseen, each of them involving e.g. different input laser power levels, signal recycling tunings, homodyne detection phases, etc., to yield optimum signal-to-noise ratio,

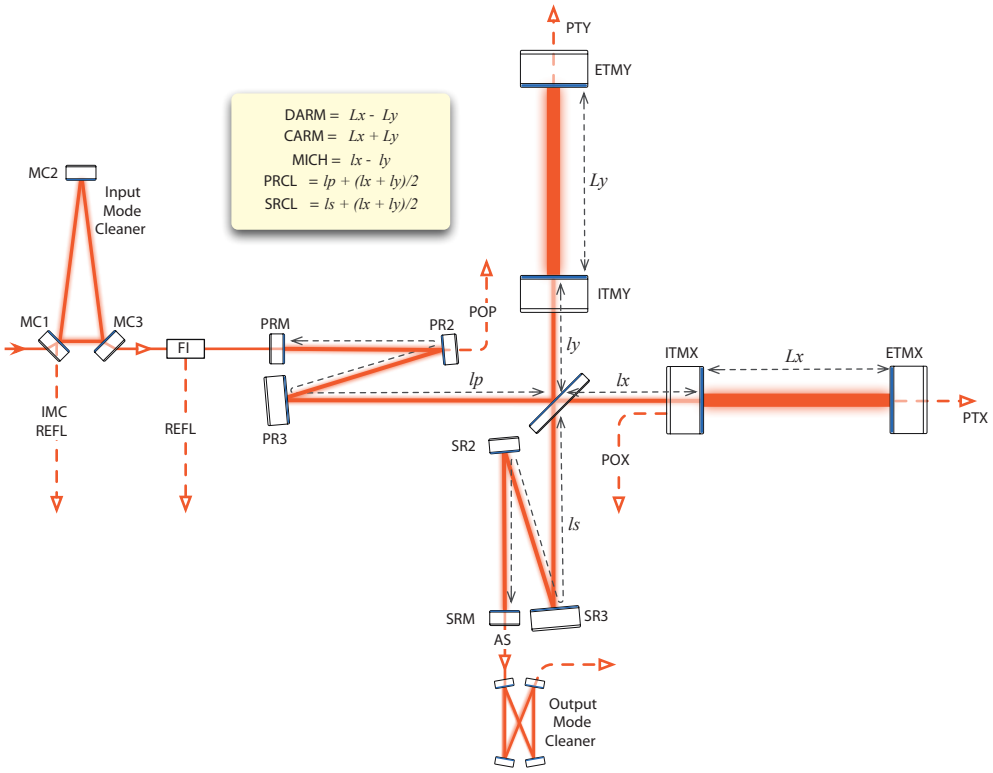

Figure 197: Schematic drawing of the Advanced LIGO optical layout, degrees-of-freedom and sensing ports [588]. Error signals for the control of the five longitudinal degrees-of-freedom are extracted from the four ports REFL, AS, POP and POX.

depending on the astrophysical source under investigation [588]. The main differential control requirement for Advanced LIGO is 10^{-15} m rms, yielding a shot noise limited sensitivity of $4 \times 10^{-21}\,\mathrm{m}/\sqrt{\mathrm{Hz}}$.

At the detector's operating point the carrier laser light is resonant in the power recycling cavity (PRC) and in the arm cavities. The signal recycling cavity (SRC) is tuned to carrier resonance only if the detector is operated in tuned mode. Two pairs of phase modulation sidebands, locked by a PLL, are imprinted on the input laser, forming the basis of the sensing scheme. The frequencies were chosen to be $f_1 = 9\,\mathrm{MHz}$ and $f_2 = 45\,\mathrm{MHz}$, both nearly anti-resonating in the arms to reduce arm-cavity induced phase shifts.Both pairs of modulation sidebands are resonant in the power recycling cavity. The signal recycling cavity, however, is arranged to be nearly resonant for the f_2 sidebands while the f_1 sidebands do not resonate.

A typical property of the recycling cavities is their potential to cause mixing of modulation sidebands which immediately leads to coupled error signals. To prevent this effect from rendering the control scheme more complicated than necessary it is crucial to arrange for a configuration that reduces this mixing to the largest possible extent.

The Schnupp asymmetry—a macroscopic offset in the arm lengths of the central Michelson—is set to 5 cm to provide nearly critical coupling of the f_2 sidebands in the dual recycling cavity, with the implication of simultaneous resonance of the power recycling and the signal recycling cavities for this sideband frequency. By choosing an appropriate value for the Schnupp asymmetry one can arrange for a large modulation sideband power ratio in the SRC, providing improved signal separation. In this case the resulting power ratio is of the order of 10^3, in favor of the f_2 sidebands.

A variety of ports in the interferometer are read out to obtain a complete set of control signals for all longitudinal degrees-of-freedom. Besides the asymmetric port (AS), signals are extracted from the symmetric port (REFL)

and from pick-off ports from within the power recycling cavity (POP) and a in reflection of one of the arm cavities (POX). These beams are directed to photodetectors and the resulting signals are in turn demodulated at f_1, f_2, $f_2 - f_1$ or $f_1 + f_2$, at appropriately set demodulation phases. Demodulation at the sum or difference frequency of two modulation sidebands, i.e. at their beat frequency, is a key concept in modern interferometric control system design and is often referred to as *double demodulation*.

The signal obtained in the symmetric port, after demodulation at the lower sideband frequency f_1 is used for common mode arm cavity (CARM) control. Consequently, the differential arm cavity mode control signal is obtained in the asymmetric port from the AS DC photodetector. For the DC readout scheme of the asymmetric port, which also contains the GW signal, a differential arm length (DARM) offset of the order of 10^{-11} m will be applied, yielding a DC power level in the asymmetric port of the order of 0.1 W of carrier light. The intra-cavity POP port yields signals for the PRC and the Michelson degrees-of-freedom, after demodulation at f_1 and f_2, respectively.

For controlling the signal recycling cavity, the optimum signal extraction port as well as the demodulation frequency depends on the mode of operation, i.e. the tuning of the SR cavity. Whereas for zero detuning an appropriate error signal can be extracted in the symmetric port in reflection of the interferometer or at the arm cavity pick off port, for detuned operation analyses have shown that double demodulation of the asymmetric port signal yields better error signals. Thus, if it is desired to continuously tune the SR from tuned mode to a detuned science mode, at a detuning of about 5 deg it is necessary to switch between error signals for the control of the signal recycling cavity.

The underlying sensing matrix shows well-separated error signals for the arm cavities' degrees-of-freedom. The power recycling cavity is sufficiently decoupled from the other degrees-of-freedom but shows strong coupling to the ports where the Michelson and signal recycling cavity error signals are obtained. The most worrisome degrees-of-fredom are the differential arm length of the central Michelson interferometer (MICH) and the signal recycling cavity length which exhibit comparably large amount of cross-coupling. However, control of the interferometer can be gained e.g. with a gain hierarchical approach in conjuction with the arm length stabilization system (ALS) which is discussed in Sec. 5.7.3.

The control signals derived from the error signals are applied to the end mirrors in the case of the DARM degree-of-freedom, to the beamsplitter for differential arm length of the central Michelson feedback and to the recycling mirrors for SRC and PRC length stabilization. However, the common mode arm cavity length control loop is the most elaborate one. The CARM error signal is fed back to the main laser via multiply cascaded frequency loops, providing the final level of frequency correction. The required unity gain frequencies of the servo controllers are of the order of tens of Hz for PRC, SRC and MICH, hundreds of Hz for DARM and tens of kHz for the CARM degree-of-freedom.

With the exception of the arm cavity common mode controller all servo loops are realized using digital controls. The more demanding (in terms of bandwidth) CARM servo will be implemented in analog electronics. The digital feedback loops are implemented in a custom-made real-time control system with typical sampling rates of up to 65536 samples per second at up to 18 bit resolution. Digital control systems have proven to be a powerful solution with high flexibility. Complex filter structures, e.g. with blending of sensors and signals, can be conveniently realized and changed on-the-fly with little effort.

Similar to the initial LIGO control scheme, correction paths are included in the Advanced LIGO scheme. Correction signals are filtered copies of sensing noise limited MICH and SRCL control signals. To cancel the effects of known couplings, correction signals are fed from SRCL to DARM and from MICH to DARM at a precision of 1%. An additional correction path will feed signals from PRCL to DARM, at a lower precision of 10%.

Detector lock acquisition Lock acquisition is the process of bringing an interferometer from its uncontrolled, initial state to a controlled state in which the instrument is fully operable. Contrasting the case of a servo loop operating near resonance, where the error signal for an optical cavity shows a linear response to length changes, during lock acquisition one has to generally deal with highly nonlinear signals. Servo loops are usually optimized

for control on resonance, resulting in a poor performance during acquisiton. The determining quantity in lock acquisition of an optical cavity system are the mirrors' relative velocities. Further, the *threshold velocity* is usually referred to as a measure which quantifies the performance of an acquisition scheme. By definition the threshold velocity is the maximal relative velocity of two cavity mirrors below which lock acquisition is successful. The threshold velocity strongly depends on the bandwidth of the underlying control loop. Only if the servo response time is suffiently short to follow the transient error signal it is capable of "capturing" an optic. As the probability for all DOF being simultaneously at their operating points is very small, a sequential approach must be taken, bringing the DOF to the locked state one after another.

The simplistic approach to lock acquisition, e.g. practiced in the early detector prototypes, is to wait for the instrument's DOF, driven by random ground motion, to move close to their operating points and then swiftly engage the control loops. As with this method lock acquisition of an interferometric GW detector would be a pure matter of coincidence more deliberate approaches were strongly desired. For initial LIGO an acquisition algorithm was developed which is based on a real-time estimate of the time-evolving sensing matrix, derived from measurable signals during lock acquisition [589]. With the implementation of this scheme on the LIGO digital control and data system lock of the detector was on average acquired on timescales of $\sim 1\,\mathrm{min}$. The Virgo approach to lock acquisition was to effectively decouple the instrument's DOF which is achieved by a deliberate misalignment of optics. This technique is often referred to as *variable finesse locking* [590]. Lock was usually acquired within a few minutes.

The Advanced LIGO quadruple suspensions provide isolation to the test masses with respect to ground motion at frequencies above 10 Hz. Even though the active internal seismic isolation (ISI) platforms provide additional low frequency isolation, low frequency disturbances are expected to cause significant test mass displacement of the order of $10^{-7}\mathrm{m}/\sqrt{\mathrm{Hz}}$ at 0.5 Hz. This is due to the fact that at the suspension system's resonance frequency or at lower frequency perturbations are not well attenuated and couple into the test masses' positions as displacement noise. Besides this, the test masses will have electrostatic actuators instead of coil-magnet actuators which were used in initial LIGO. Electrostatic actuators deliver lower actuation noise, at the expense of significantly lower actuation force they can exert on the test masses. The Advanced LIGO electostatic actuators are expected to saturate at forces of $\sim 200\,\mu\mathrm{N}$ [591]. This severely complicates the process of lock acquisition.

In order to ease the difficulties of lock acquisition in the Advanced detector generation, auxiliary laser based schemes will be employed to complement the well-established techniques. This discussion focusses on the Advanced LIGO ALS (arm length stabilization) system [592]. For Advanced Virgo it is anticipated to employ a similar scheme. Other systems to aid lock acquisition, that were considered for use in Advanced LIGO, such as the suspension point interferometer or digital interferometry are described in [593]. The underlying idea of ALS is to provide for more deterministic lock acquisition by locking the arm cavities independently of the remaining degrees-of-freedom. The ALS system builds on frequency doubled laser beams launched into the arm cavities through the end test masses for pre-stabilization of the interferometer arms, independent of the science laser circulating in the interferometer. By applying additional coatings on the arm cavity mirrors the properties of the arm cavities, as seen from the ALS, can be shaped in accordance to the pre-stabilizations scheme's requirements. The choice of reflectivities for the input mirror and the end mirror results in an overcoupled cavity for the auxiliary laser, seen from the end mirror. The Finesse of the arm cavities for the 532 nm ALS beams is ~ 100. A simplified schematic of the ALS principle setup is depicted in Fig. 198.

The initial step in the acquisition process is to hold the arm cavities on anti-resonance for the main science laser. In the next step the recycling cavities are brought to the locked state, before the ALS brings the arm cavities onto resonance with the main laser and hands over the control authority to the global interferometer sensing and control scheme. For effectiveness, the ALS must reduce the residual arm cavity length fluctuations to a displacement of no more than one cavity line width, which is approx. 1.3 nm in the case of the Advanced LIGO arm cavities. Estimations have shown that with ALS engaged a level of displacement fluctuations of 0.115 nm rms can be reached.

Technically, once the arm cavities are locked with the 532 nm beams, a heterodyne measurement is performed on the ALS beam transmitted by the x-arm cavity and a frequency doubled sample of the main laser beam. A second one is performed between the x-arm and the y-arm transmitted beams. These measurements yield common and differential mode error signals which are in turn fed back to the corresponding actuators. By

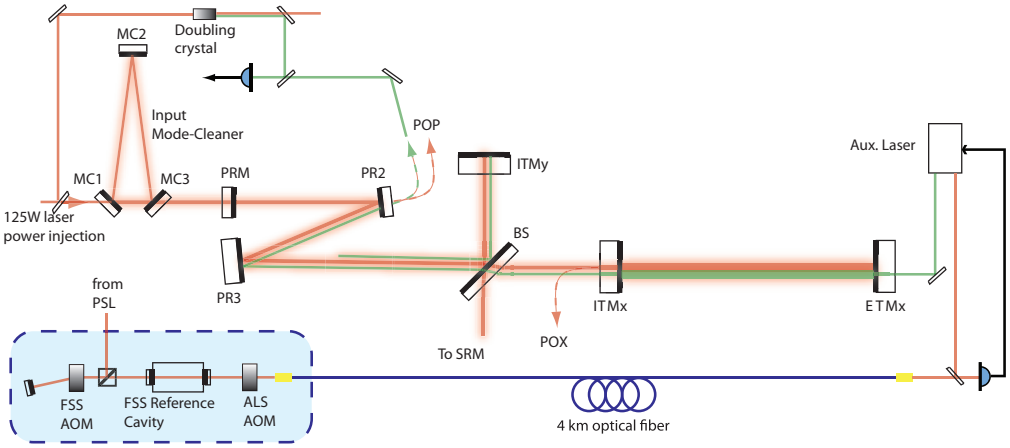

Figure 198: Schematic drawing of the Advanced LIGO arm length stabilization (ALS) subsystem [592]. The test mass motion is reduced prior to lock acquisition by a combined scheme of PDH reflection locking of an auxiliary laser to the arm cavities and hetorodyne detection of the transmitted beams. The optical fiber is necessary to provide an optical reference at the end stations, to lock the auxiliary lasers' phases to the science laser.

introducing a tunable offset into the heterodyne locking loop, the arm cavities can thus be adjusted to arbitrary tunings.

For a smooth transition from ALS arm cavity control to global control a robust phase-locked loop (PLL) is crucial, to provide a well-defined phase relationship between auxiliary lasers and the main science laser. Once the PLL is closed, the auxiliary lasers are locked to the arm cavities using PDH reflection locking. The resulting control signal acts on a voltage-controlled oscillator (VCO) which supplies the electronic local oscillator for the PLL. In this way the offset frequency of the auxiliary laser with respect to the reference is tuned. An analog servo is foreseen for this loop and is expected to have a bandwidth of a few kHz.

To provide a stable frequency standard for the auxiliary laser PLL, a technique based on the LISA (Laser Interferometer Space Antenna) back-link measurement is employed. Mullavey et al. [594] have experimentally demonstrated a scheme based on counter propagating two laser beams through an optical fiber and subsequent measurements of each of the outputs with LISA-style phasemeters. By subsequent combination of the output signals an error signal can be obtained which can be utilized to eliminate fiber induced phase noise. Their setup consisted of 4.6 km single mode optical fiber and two Nd:YAG lasers—operated in a master-slave configuration. To circumvent nonlinear forms of noise such as stimulated Brillouin scattering, the transmitted laser power was reduced to $\sim 50\,\mu$W. In the underlying bench top experiment a relative frequency noise of $0.5\,\mathrm{mHz}/\sqrt{\mathrm{Hz}}$ was reached for Fourier frequencies between 5 Hz and 20 Hz which is well below the Advanced LIGO requirements, with a margin of more than an order of magnitude.

Angular control - Automatic Alignment control system The angular control system has to be implemented in order to reduce the mirror misalignments in the frequency region in which the seismic attenuation system does not fulfill the alignment requirements, i.e. below the mechanical resonances, to reduce the fluctuations of the mirror angular positions with respect to the beam, to maintain the overall alignment of the optical elements, ensuring long data taking periods, and to reduce the noise at the output port. The mirror angular positions in data taking mode can not be locally controlled because the long term drifts of the local references spoil the overall alignment. After the lock has been acquired the angular control has to be switched to a global control system, the *Automatic Alignment*, which uses error signals derived from the interferometer itself with a modulation-demodulation technique based on differential wave front sensing. The control scheme chosen for the second and third generation of gravitational wave interferometer is a Ward-like scheme where the RF modulation frequencies are chosen to do not have any higher order modes resonating in the cavities [595].

The main differences between the third generation and the first generation of gravitational wave detectors, relevant for alignment control are:

- presence stable recycling cavities
- higher circulating power
- presence of signal recycling

These modifications will provide an improvement of the overall interferometer stability and sensitivity but also increase of complexity for the Automatic Alignment control system.

Stable Recycling cavities issue

The stable recycling cavities aim to make the potential higher order modes content to be less affected by thermal effects in the mirrors. This behaviour influences the Automatic Alignment control system since the amplitude of the alignment error signals is proportional to the amount of the $\mathrm{TEM}_{01/10}$ modes. For example in the case the recycling cavity with a Gouy phase of 15 deg the TEM_{01} mode is attenuated by a factor of about 6 while for 25 deg the attenuation factor is about 9. For this reason the choice of the recycling cavity Gouy phases has to be done taking into account both the stability requirements and the amount of first order higher order modes to ensure the angular controllability of the system.

High circulating power issue

In an high power interferometer *radiation pressure* plays an important role. The light beam acts on the mirror such as an optical spring whose strength increases with the power. This effect will be largest in the Fabry-Perot arm cavities, but the effect has also to be evaluated for the mirrors of the central interferometer.

Due to radiation pressure the two cavity mirrors become coupled and their angular motion must be described in terms of two linear combinations [596]. When the circulating power becomes large enough one of the angular modes can become dynamically unstable. As derived in [596], the interaction of the beam and the mirrors can be written in term of the stiffness matrix:

$$\mathbf{k} = \frac{2PL}{c(1-g_1g_2)} \begin{bmatrix} -g_2 & 1 \\ 1 & -g_1 \end{bmatrix} \tag{128}$$

where $g_i = 1 - L/R_i$ are the G-factors of the two mirrors. The eigenvectors and eigenvalues of the stiffness matrix determine the physical angular degrees of freedom and the corresponding stiffness applied to the mechanical system.

The normal stable situation corresponds to a positive stiffness of the system, given by the contribution of the mechanical stiffness of the mirror suspension and the extra-stiffness due to the radiation pressure, which gives a resonance made of a pair of complex poles with negative real part and quite large quality factor. The case of negative stiffness instead leads to an unstable system described with two real poles, one with positive and one with negative real part, with very close absolute frequency. The radiation pressure effects have then to be taken into account in the design of the control system.

Moreover the presence of the Signal Recycling mirror increases the number of degrees of freedom to control with respect the first generation of gravitational wave interferometers.

The design of the Automatic Alignment control system will be challenging because of the above mentioned issues and of the control accuracy and noise requirements to reach the targeted ET sensitivity. On the other hand all these effects and potential issues will be studied for the commissioning of the second generation interferometers, such as Advanced Virgo and Advanced LIGO, and therefore providing plentiful experience how to mitigate these difficulties.

5.7.4 Thermal effects and their compensation

Thermal lensing due to the absorption of the laser light in the core optics of gravitational wave interferometers can represent a limitation for their operational stability and sensitivity. This effect has already been observed in

the currently operating detectors (requiring the installation of compensation systems [597–599]) and will become more relevant in the second generation interferometers, due to the much higher circulating power. In case of ET xylophone configuration with a low-frequency cryogenic and a high-frequency room-temperature detector, the two interferometers show a different behaviour with respect to thermal effects.

Due to the low power circulating in the Fabry-Perot cavities and due to the thermal properties of silicon at low temperature (see table 11), thermal effects in ET-LF will be negligible: the thermal gradient due to the laser power absorption results to be less than 1 mK. On the contrary, the ET-HF interferometers will feature all the characteristics of an advanced detector (room temperature operation, high power and fused silica test masses, similar arm cavity finesse and recycling gains) and the only difference is the application of a LG_{33} beam profile instead of TEM_{00}.

In the test masses, the optical power is predominantly absorbed by the high-reflectivity coatings and converted into heat, producing a temperature gradient inside the substrate. While R&D activities to reduce coating absorptions are ongoing (see Sec. 5.9), values of about 0.6 ppm have been reported in literature [600]. Thus, considering 3 MW of optical power impinging on the test masses, the total absorbed power amounts to 1.8 W. This is a factor of three higher than expected in advanced detectors [601]. However, the resulting maximal temperature increase is less than 1 degree, as shown in figure 199, compared to about 2 degrees in the advanced detectors. This result is mainly due to the wider intensity distribution of the LG_{33}. By integration of the temperature field along the thickness of the test mass, it is possible to calculate the corresponding optical path length (OPL) increase. In figure 200 the expected ET-HF optical path increase is compared to the expectation for Advanced Virgo [601]: the use of LG_{33} modes will limit the increase of thermal effects with respect to advanced detectors to about 30%.

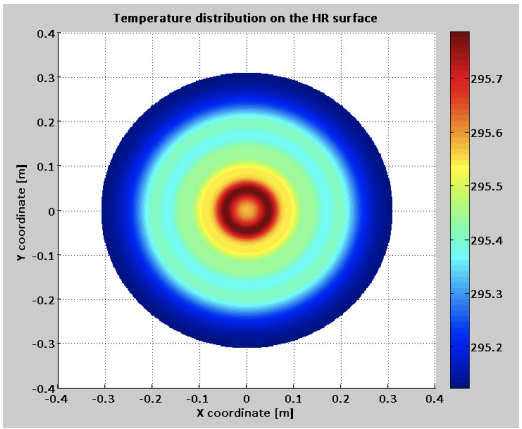

Figure 199: Temperature distribution in ET-D-HF test mass due to the absorption of 0.6 ppm of the arm cavity power.

Since the thermal effects expected for ET-HF are of the same order of magnitude as the ones expected for advanced detectors, it will possible to apply for ET the same thermal compensation system (TCS) as adopted for 2^{nd} generation interferometers. ET-HF could use a compensation plates (CP) in the recycling cavity, heated by CO_2 lasers, to cope with thermal lensing and a ring heater around each test mass to correct its thermally driven increase of radius of curvature. Figure 201 shows a sketch of a compensation plate and a ring heater around the test mass.

In order to optimize the compensation level, the CP heating pattern must account for the intensity profile of the interferometer beam. A heating pattern optimization code has been developed [602], consisting of a linear iterative optimization process based on a finite element analysis, that makes use of the OPL increase (ΔOPL) as error signal. At each iteration, the heating pattern for the next step is calculated from the previous one and from the corresponding OPL increase:

$$H_{\mathrm{path}}(n+1) = H_{\mathrm{path}}(n) + K_L \cdot \Delta\mathrm{OPL}(n), \tag{129}$$

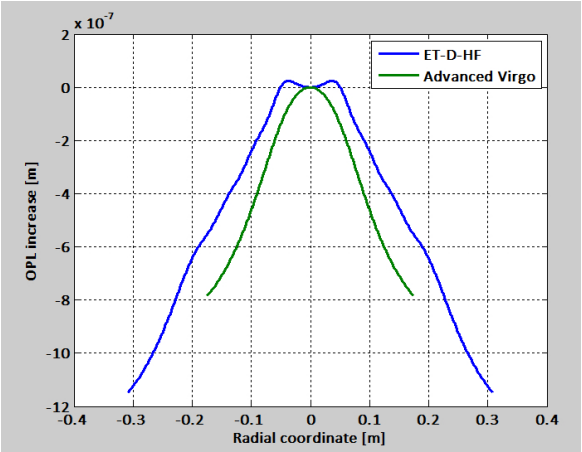

Figure 200: Optical path length (OPL) increase in ET-HF test mass (blue curve) compared to the expected values for Advanced Virgo (green curve).

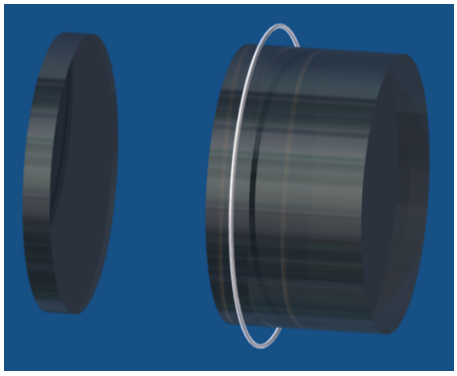

Figure 201: Sketch of the ET compensation plate and ring heater around the test mass (not in scale).

where, $H_{\rm path}$ is the CP heating pattern and K_L is the loop gain. The procedure is applied to the complete system made of the test mass, the compensation plate and ring heater. The result, when the compensation plate is placed sufficiently "far" from the ITM (thus there is no significant radiative coupling between the test mass and the compensation plate), is shown in Fig. 202. With this heating pattern, TCS can flatten the optical path lenght inside the input test mass substrate up to a diameter of 40 cm. This heating profile could be produced, for example, using scanning systems (for instance making use of galvos or crossed AOMs).

Since the ET infrastructure will comprise cryogenic facilities, it could be possible to exploit them to implement a different technique for the compensation of thermal effects. Such a system would aim to directly extract the heat deposited by the laser beam, before it has a chance to generate any deformation of the mirror. Localized heat extraction can be implemented via directional radiative cooling of the beam spot [603]. For this it is required to image a sufficiently cold black body on the beam spot (but not on the rest of the mirror), from a sufficiently large solid angle. Figure 203 shows a conceptual design of the system.

By placing parabolic collectors behind each cold spot, the radiative coupling with the mirror surface is improved and it is possible to achieve a strong reduction of the required size of the cold spot [604]. Such a scheme, named *parobolic mirrors radiative cooling* is shown in figure 204. The role of each reflector-collector couple is to build up a telescope that enlarges the radiative exchange surface of the cold target, as seen by the test mass center spot. This allows for the implementation of small cold surfaces with low cooling power and efficient temperature control.

The parobolic mirrors radiative cooling technique is being investigated [604] with the main aim of assessing

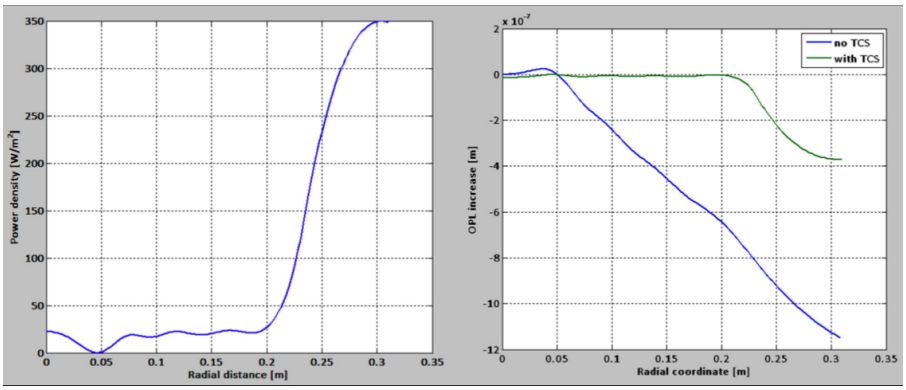

Figure 202: Left picture: optimized heating pattern. Right picture: compensated optical path length (green curve) compared to the uncompensated one (blue curve).

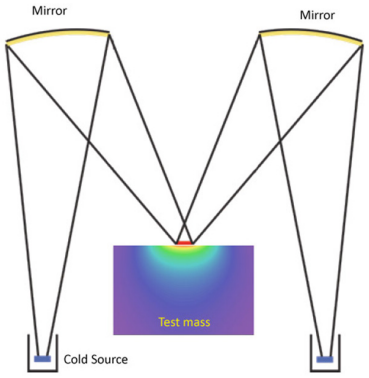

Figure 203: Conceptual scheme of the radiative cooling.

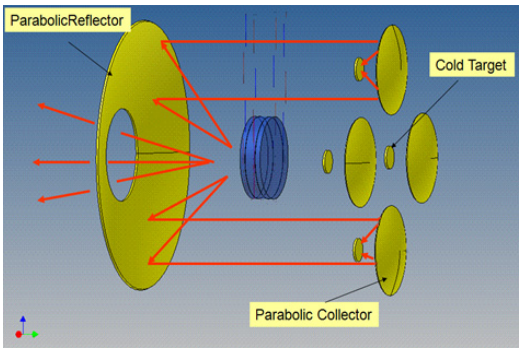

Figure 204: Scheme of the Parabolic Mirrors Radiative Cooling.

the capability of the system in producing proper cooling profiles. This is done in a test facility that allows the imaging system and the shape of the cold spots to vary in order to modify the cooling profile and to take the use of LG_{33} modes in ET-HF into account.

The same concept of radiative cooling can be clearly applied to image a warm source (or an array of sources) to produce heating profiles onto the periphery of the test mass. This could allow us, in principle, to avoid using compensation plates, provided that the noise injected by the heating system is compliant with the sensitivity requirements.

All these radiative techniques are at present under investigation. The CO_2 laser based TCS has already proven able to generate proper heating profiles. Again ET will be able to benefit from the vast experiences that will be gained by the commissioning of the TCS systems for Advanced Virgo and Advanced LIGO.

5.8 Rough cost evaluation

The main impact of the optical design on the cost is via the required infrastructure in terms of the vacuum system, tunnels and caverns. In addition the optical system yields direct costs for the high-quality optics and the auxiliary optical systems with their mechanical and electrical support systems The core elements of the interferometers are the test masses which need to be of considerable size and weight and must fulfil extremely stringent requirement for bulk and surface qualities.

The maximum available size for Suprasil 3001 today is the size of the 40 kg test masses for advanced LIGO. The heavier substrates envisaged for ET can presently only be made either of Suprasil 3002 which has inhomogeneities in the direction of the beam or from fused pieces of thinner Suprasil 3001. The price quoted by Heraeus for a substrate of 600 mm in diameter and 400 mm in thickness made of composite Suprasil 3001 is €700k which corresponds approximately to a price of €3.5k/kg. The end test masses can be made out of Suprasil 312 with a considerable lower cost per kilogramme, an estimate based on quotes for Advanced Virgo optics gives €1.6k/kg.

At present silicon is only available in Chzochalski grown crystals to a size of up to 450 mm.In Floating zone crystals the maximum size at present is 200 mm. The interest of the semiconductor industry in ultra-pure crystals is very limited and will most likely not drive the development of bigger size single crystals. Costs of silicon per kg are based on a quote by Simat and are comparable to the one of ultra-pure fused silica.

The cost estimates for polishing and coating of the mirrors are based on similar costs related to Advanced Virgo, up-scaled to include ion-beam polishing.

Further included in the optics cost are the main laser systems, optical benches in air and in vacuum for injecting the beam from the laser into the detectors, similar benches and components for extracting and detecting beams from the interferometers as well as the mechanical, optical and electronic components required for interferometer control purposes. We further count the cost for special optical subsystems such as the squeezed light source and the thermal compensation systems. These systems will be directly based on current systems and thus the costs have been estimated from the data for current and advanced detectors.

The total cost for the installation of the optical components of the first detector (two interferometers plus spares) has been computed as €37.6M. The total optics cost for all three detectors is estimated to be €60M. The nonlinear increase results from the fact that spare parts can be shared between detectors. The cost of the first detector is dominated by the main optics which account for €20.4M. The high-power laser system at 1064 nm and one medium power system at 1550 nm wavelength cost together €7M. The input and output optics require together another €7M. We also include €2.5M for control electronics and €600k for the thermal compensation system.

5.9 Technologies to be developed / R&D

5.9.1 Thermal noise reduction due to LG modes

Thermal noise will be limiting future generations of interferometric gravitational wave detectors in the central frequency band (where the detectors are most sensitive). In the case of the xylophone design, the cryogenic LF interferometer benefits from the low temperature so that the mirror thermal noise sits well below the quantum noise. However, in the case of the HF detector, we need to employ additional techniques to reduce the thermal noise below the ET requirement. Higher-order Laguerre-Gauss (LG) mode beams have been proposed and investigated for the reduction of mirror the thermal noise for the ET-HF interferometer [424, 425]. LG modes are solutions of the paraxial wave equation in cylindrical coordinates, in a similar way to the Hermite Gaussian modes which are the solutions in Cartesian coordinates. They have radial power distributions as shown in

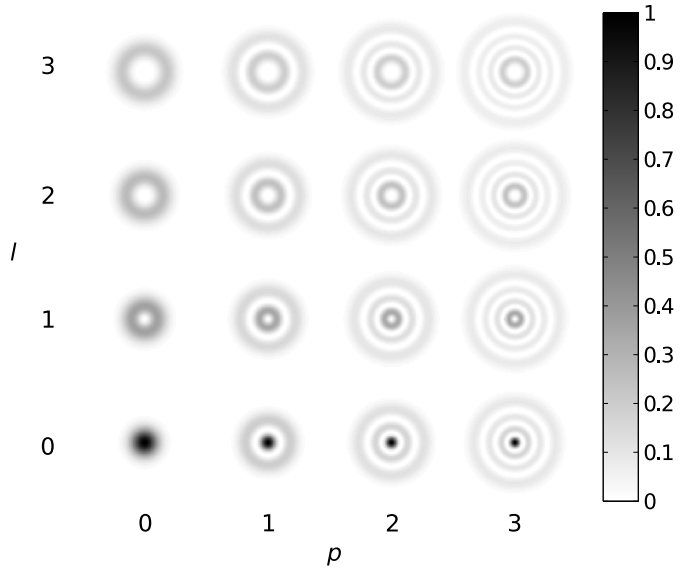

Figure 205: Power distributions of LG_{pl} mode. p is the radial mode index ($p \geq 0$), and l is the azimuthal mode index. The power distribution of LG_{00} mode is equivalent to that of the conventional TEM_{00} mode.

Fig. 205 which spreads the light power more evenly over the mirror surface (for a given amount of light lost over the mirror edge) than those of the conventional fundamental mode, therefore higher-order LG mode beams can be used to reduce the thermal noise without introducing higher clipping-losses. Also flat-top and conical beams have been proposed for future gravitational-wave detectors. However higher-order LG mode beams have the advantage that they have the spherical wave fronts and thus are compatible with conventional optics such as spherical mirrors and lenses. On the other hand, flat-top and conical beams require non-spherical complex mirrors. Non-spherical mirrors have been tested so far do not satisfy. angular alignment requirements [605]. Also, with current technology it is unclear if these mirrors can be manufactured with the same surface quality as spherical mirrors for which we have decades of experience. Previous investigations have shown that implementing LG_{33} modes in Advanced detectors could increase the inspiral range for NS binaries by a factor of two through the reduction of Brownian thermal noise in comparison to the fundamental LG_{00} mode [431]. In addition, higher-order LG beams are fully compatible with the conventional length and angular sensing signals. This fact indicates that changing over from the fundamental mode to the higher-order LG mode should not require any new control strategy. Ref. [431] analyzed the control signals using numerical simulation tools and found that the performance of the LG_{33} beam in tilt-to-longitudinal phase coupling, generation of angular control signals, and the corresponding control matrices, was equivalent to or better than that of the LG_{00} beam.

LG mode technology for gravitational wave detectors is currently in a transition phase from the theoretical and simulation investigation to the experimental investigation phase. The first table-top experiment has demonstrated the generation of a LG_{33} beam and the mode cleaner cavity performance with the generated LG_{33} beam [606]. The LG_{33} beam was generated by converting the LG_{00} beam to LG_{33} beam using a computer-controlled liquid-crystal-on-silicon spatial-light modulator (SLM). The PDH error signal was properly obtained with a LG_{33} beam, and successfully used to control the longitudinal degree of freedom of the mode-cleaner cavity. The mode purity of the generated LG_{33} beam was increased from 66% to 99% upon transmission through the linear mode cleaner, demonstrating that very high-purity LG_{33} mode light sources can be produced in this way. Further experimental investigations, using diffractive optical elements instead of SLM, are underway. A LG33 high-purity beam has been generated with a fused silica diffractive element and a linear mode-cleaner [607]. The ratio between the powers of the LG00 injected and the high-purity LG33 generated was 36%. By measuring the transmission of the setup for the LG00, it was possible to infer that the conversion efficiency specific to the LG33 was 49%. The generated LG33 mode was sent to a table-top Michelson interferometer, locked on the dark fringe.

However, LG modes pose one new challenge, namely mode degeneracy in optical cavities: Several modes of (l, p) exist with the same order, $2|l| + p$, and they have identical Gaussian beam parameters, such as radius of curvature and Gouy phase. Therefore these modes can all resonate in the same cavity, and can not rejected or cleaned away without adding unwanted complexity to the system, such as masks. These modes may contaminate the purity of the desired mode and may require a higher quality for the mirror surfaces. This effect does not occur for the fundamental mode, since there is only one mode the in zeroth order. Several research programs are currently underway to investigate mode degeneracy with numerical simulations and prototype interferometers.

5.9.2 Thermal noise reduction due to Khalili cavities and etalons

In 2005 Khalili proposed to replace the end mirror of an interferometric gravitational wave detector by a cavity (see fig. 206). The cavity is tuned to be in anti-resonance in order to provide a high reflectivity. The number of coating layers of the input mirror of the cavity is small while the number of of layers of the back mirror is high.

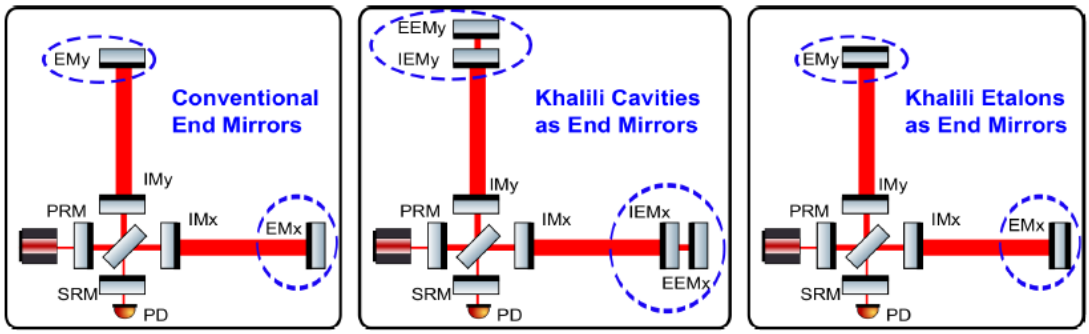

Figure 206: Schematic of an interferometer using a conventional mirror (left), Khalili cavity (middle) and Khalili etalon (right).

In a conventional mirror of an interferometric gravitational wave detector coating Brownian noise is the most dominating noise contribution. The coating Brownian noise is proportional to the mechanical loss as well as the thickness of the coatings layer. In a Khalili cavity the front mirror—where the laser beam senses thermal noise of the cavity—only contains a relatively thin coating. Hence the coating Brownian noise is smaller than a conventional mirror having the same reflectivity.

Keeping the Khalili cavity in its anti-resonant state involves complex control schemes which enhance the complexity of the total interferometer significantly. An alternative approach was proposed [608] where instead of using a cavity an etalon will be used (see fig. 206). This etalon can be thermally length controlled which simplifies the control. Additional noise sources like thermo-refractive noise and mechanical coupling between the two reflective coatings on the different ends of the etalons have been analysed and shown to be small enough to still lead to a thermal noise improvement compared to the conventional mirror.

A detailed analysis of the technical usability of a Khalili etalon is underway and upcoming experiments will demonstrate the usefulness of this approach.

5.9.3 Coating research

While silica:Ti-doped tantala coatings have thus-far proven to have the best combination of mechanical loss and optical properties at room temperature, the dissipation peaks in these materials at temperatures below 35 K are likely to reduce the improvement in coating thermal noise obtained from low temperature operation. Research into possible alternative coating materials is therefore ongoing. Hafnia (HfO_2) may be of particular interest as an alternative high index material as initial measurements have shown a significantly lower mechanical loss than tantala at temperatures below 150 K [609, 610], although these coatings were found to have high optical

absorption due to partial crystallisation. Crystallisation can be prevented by doping hafnia with silica, and there is evidence that this doping does not significantly affect the loss at room temperature. Further studies of the effects of heat-treatment and doping on the mechanical loss and optical properties of hafnia coatings are planned to assess the suitability of this material as a replacement of tantala.

Amorphous silicon can be used as the high-index component of a reflective coating suitable for use at 1550 nm. Experiments have shown that amorphous silicon coatings deposited by e-beam evaporation can have losses in the order of 10^{-5}, and that the low-temperature loss can be reduced by more than an order of magnitude by hydrogenation [611]. Additionally, the high refractive index of silicon reduces the number of layers needed for the same reflectivity. In order to achieve the same reflectivity in like a tantala-silica coating of 18 $\lambda/4$ doublets there are only 6 doublets of silicon-silica needed. Thus, the amount of coating material can be strongly reduced. Thus silicon may be a promising coating material for further investigation, potentially allowing for significant reductions in coating thermal noise. However, additional research is required. There are indications that the silicon-silica interface is chemically not stable. Oxygen starts diffusing from the silica into the silicon forming a silicon mono-oxide boundary layer. This layer might change the optical properties (reflectivity, scattering) of a potential HR stack made from these materials. Thus, a detailed investigation of optical properties of silicon-based optical coatings is required preferably at the desired operational temperature of the ET-LF detector at around 10 K.

Recent results have strongly indicated that the mechanical loss of coating materials may be strongly related to the local atomic structure. Various techniques are being used to study the structural properties of amorphous coating materials. One technique using electron diffraction Reduced Density Function (RDF) analysis and amorphous modelling allows models of the atomic structure to be obtained from experimental data [612]. Initial results for tantala coatings indicate increased ordering of the tantala structure as the heat-treatment temperature rises, and it seems likely that these changes may be responsible for the loss peaks observed to occur at higher heat-treatment temperatures. This work is ongoing, with the aim of developing a full understanding of the relationship between the coating atomic structure and the mechanical loss. A better understanding of the mechanical loss processes will influence the final coating choice (exact doping concentration, post-deposition treatment, annealing, etc.).

In a next future influence of annealing effect on high refractive index material should be tested. To know more about thin films and substrate materials at cryogenic temperatures, their mechanical losses and absorption investigations must be studied. Previous researches of standard coatings (Ti:Ta_2O_5 and SiO_2) have shown that the mechanical losses of both materials increase at 10 K compare to the value at 300 K. Research of other coating materials must be also developed to validate the usual $Ti : Ta_2O_5$ and SiO_2 thin films. Study of HfO_2, for example, was carried out at Glasgow. Several institutions participate to the mechanical losses measurement for different bulk and coating materials. The sharing of results between the different laboratories will permit to confirm the values and to develop a pretty good database of different materials. Finally, measurement of the silicon dn/dT parameters is also intended. Previous study gave this data at 30 K at 1500 nm [already cited], but not below. To know this value will guarantee the exact value of Substrate Thermo Refractive Noise of Silicon, which is, to date, only estimated.

Another point is the estimation of the influence of the coating on reflectivity and thermal noise. A first study performed with the software *TFCalc* for designing and manufacturing optical thin film coatings has demonstrated that a stack of 19 doublets of $Ti : Ta_2O_5$ and SiO_2 on a silicon substrate corresponds to a transmission of 4 ppm at a working wavelength of 1550 nm. The exact coating is $(HL)\_19HLL$ with H which corresponds to a high refractive index thin film (2.059 at 1550 nm) and L for the low refractive index thin film (1.4395 at 1550 nm).

Figure 207 describes the transmission of a stack $HB_{19}HBB$ on a silicon substrate versus a large range of wavelengths (the figure has been created with the software TFCalc).

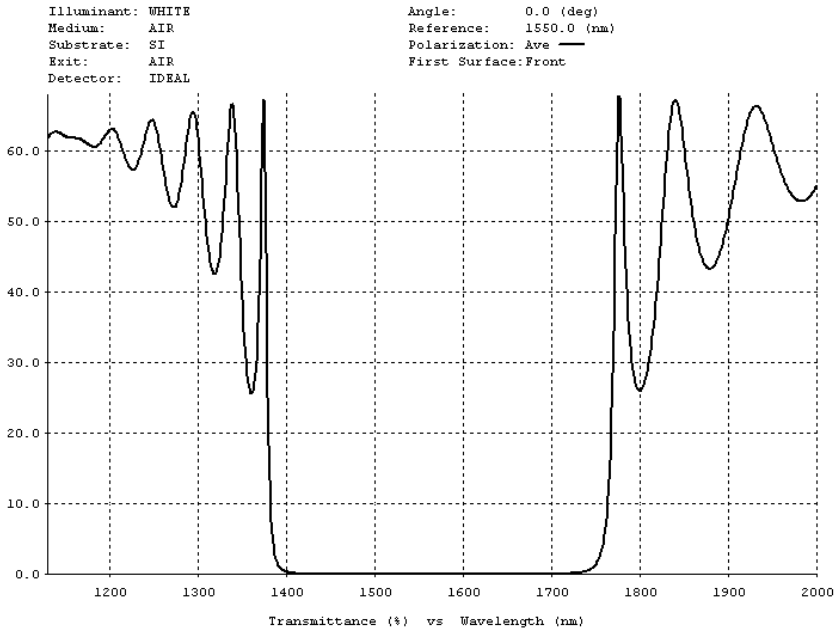

Figure 207: Transmission of stack $HB_{19}HBB$ on a silicon substrate vs wavelengths.

5.9.4 Waveguide grating mirrors

Test mass mirrors used in gravitational wave detectors are subject to several sources of thermal noise. A dominant contribution is given by Brownian thermal noise caused by mechanical loss of the high reflective multilayer coatings. These, conventionally, are made of up to 20 double layers of tantala (Ta_2O_5) and silica (SiO_2) each having a quarter wavelength optical thickness. Hence, concepts for a reduction of the mechanical lossy materials or for coating free mirrors are being investigated to provide alternative mirror architectures, in order to improve a detector sensitivity in its mid frequency band. For this purpose broadband waveguide grating (WG) structures have been proposed [613], which are based on resonant excitation of light fields in a nanostructured surface that theoretically allow for a perfect reflectivity under normal incidence, without implementing multilayer stacks.

The basic principle of WGs is shown in Fig. 208 using a ray picture [614].

WGs are basically constructed of a substrate with low index of refraction n_{L} and a nanostructered layer having a higher index of refraction n_{H}. The grating can be designed such that only specular reflection and three transmitted orders exist. The first order beams in the nanostructured layer are totally reflected at the substrate and partially coupled out at the surface. By adjusting the grating dimensions (optical properties) the outcoupled light fields can be forced to interfere constructively giving a perfect reflectivity. For dielectric materials Rigorous-Coupled-Wave Analysis (RCWA) [615] is a numerical method to investigate the optical properties of WGs, depending on their material and geometrical parameters, and was used to optimize waveguide gratings in terms

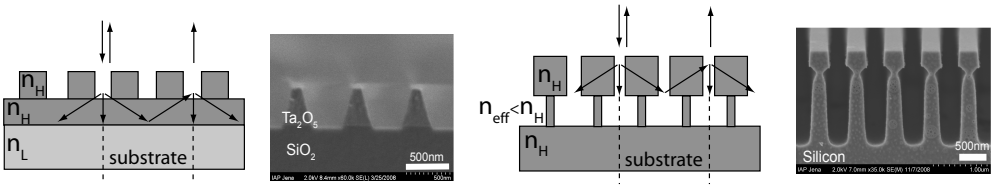

Figure 208: Single layer and monolithic waveguide grating architectures.

of parameter tolerant designs.

It was found that even a zero waveguide layer thickness (only ridges on top of a substrate) can show high reflectivity [613], which has experimentally been demonstrated using tantala ridges on a silica substrate for the prominent wavelength of 1064 nm [616]. The fabricated waveguide grating (see Fig. 208) was incoporated as a coupling mirror into a linear Fabry-Perot cavity together with a conventional high-reflectivity mirror. From the measured finesse of ≈ 660 the reflectivity of the waveguide grating was determined to be $(99.08 \pm 0.05)\,\%$.

Recent theoretical work [616] has shown that monolithic waveguide grating structures are also feasible by etching a T-shaped structure into a substrate (see Fig.208). Here, the lower grating is chosen to have a small fill factor (ratio of groove width to grating period) to act as an effective low index medium. This structure has been fabricated in silicon aiming at a high reflectivity for a laser wavelength of 1550 nm. Two etching steps were applied. In the first step the upper grating was defined via anisotropic etching and then protected on its sidewalls. In the second step, an isotropic etching was used to realize the low fill factor grating beneath. The reflectivity was determined in a table-top cavity setup to be $(99.79 \pm 0.01)\,\%$ [617] in full agreement with numerical simulations (RCWA) [615].

While the thermal noise models for conventional multilayer coatings and material parameters are well studied, the thermal noise performance of nanostructured surfaces is still to be investigated. It was experimentally shown that a nanostructured surface does not affect the mechanical quality of a substrate significantly [618]. However, the mechanical loss and other material parameters such as thermal conductivity of a nanostructure need to be further investigated in order to estimate the actual level of thermal noise. Also a direct measurement of thermal noise of a WG compared to a multilayer coating is of great interest.

Further, the fabrication process needs to be improved to meet the requirements for test masses used in gravitational wave detectors. Besides the optical quality in terms of high reflectivity and homogeneity over the grating area, techniques have to be developed to handle actual substrate dimensions. One approach being investigated is the bonding of a thin nanostructered wafer on a thick substrate.

5.9.5 Speedmeter topology

As mentioned in Section 5.5, speed meters can be considered for the ET interferometer due to their advantage in surpassing the quantum noise limit broadly in the low frequency region. However, little practical experience of speed meter technology has been accumulated, in contrast to well-studied Michelson-interferometer (MI) -type position-meter with currently operated gravitational-wave detectors. Practical speed meter characterization such as quantum noise surpass-ability and a capability to optical losses have to be examined in order to select the ET topology.

Speed-meters are realized by either MI-type or Sagnac-interferometer (SI) -type topology, and only a small part of them is experimentally demonstrated:

Michelson-interferometer type A typical configuration of a MI type speed meter [619, 620] is depicted in the left panel in Fig 209. The configuration employs an RSE interferometer with the sloshing cavity at the anti-symmetric port. The south port of the RSE part is kept to be the dark fringe (destructive interference between the north and east arms). When the end mirror of one cavity moves, some light goes through to the south port, and enters into the sloshing cavity. The light comes back from the sloshing cavity and enters the RSE part from the south port. This field is 180 degrees different in phase and cancels the position information, leaving only the phase shift proportional to the relative velocity of test masses. The sloshing cavity adds more complexity such as the length and alignment degrees of freedom to be controlled, compered with an RSE topology whose technology is mature and already being installed in, e.g., Advanced LIGO. Therefore, it is necessary to examine the practical capability of ET.

Sagnac-interferometer type The SI-type speed meter [418] is depicted in the right panel in Fig. 209. A SI is an more straightforward way to realize a speed meter than the MI-type. A basic SI is a ring interferometer (see

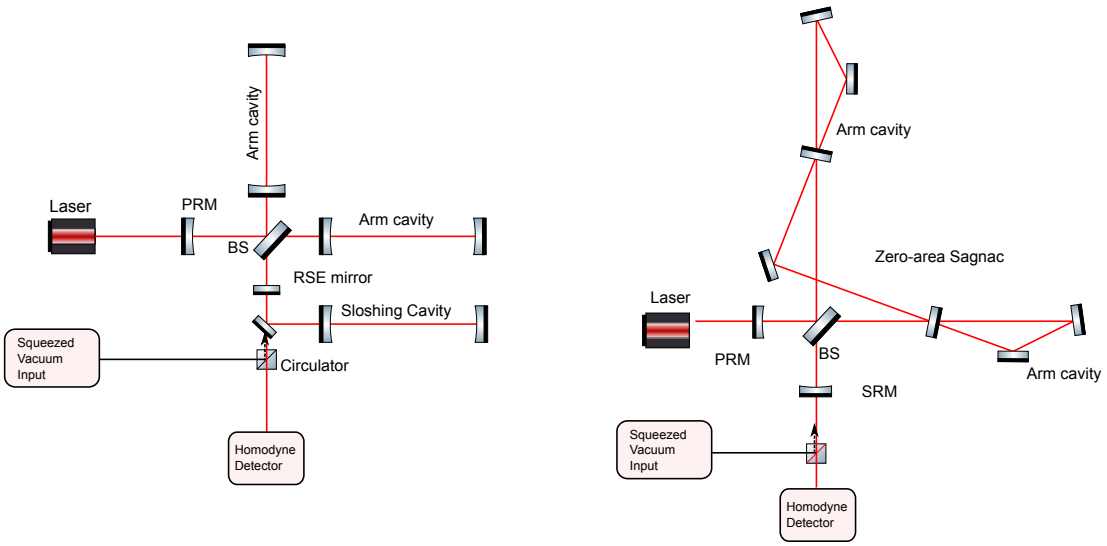

Figure 209: Left panel: An example configuration of a Michelson-interferometer-type speed meter. Right panel: An typical configuration of a Sagnac-interferometer-type speed meter with two ring cavities.

the middle panel in Fig. 162 in section 5.3) and it is a speed meter by itself. The laser light is split into two paths by a beam splitter, then one of the two light fields propagates the ring path in a clockwise direction whereas the other propogates in a counter-clockwise direction. These two fields interfere at the same beam splitter. The two fields experience the same path but at different timing depending on the path differences. Therefore the interference intensity depends only on the time dependent part of the test masses. For an ET topology, a zero-area SI in which the area enclosed by the two counter-propagating beams is zero, will be preferable because it is insensitive to the interferometer rotation.

Before it was realized that the speed meter is free from the quantum back-action noise, a Sagnac interferometer was investigated as a candidate topology for the ground based gravitational-wave detectors. The shot-noise-limited phase sensitivities were demonstrated by [422] and [621] at high or low frequency region, respectively.

The squeezed-vacuum will be necessary to be injected from the dark port to enhance the ability for surpassing the SQL in the broadband frequency region. This technique has been already demonstrated experimentally for a zero-area Sagnac interferometer by a table-top experiment [8]. The non-classical sensitivity improvement of up to 8.2 dB with a simple zero-area Sagnac interferometer was experimentally verified.

6 Overall budget and timeline considerations

The evolution toward the Einstein Telescope observatory has been, is and will be a long path. In the following subsections we will try to depict a possible roadmap for the realisation of the observatory and we will present a first budget of the project.

6.1 ET project timeline

The idea of a third generation GW detector born within the ILIAS project (http://www-ilias.cea.fr/, 2004–2008), supported by the European Commission within the Framework Programme 6 (FP6). In fact in that "Integration Activity", both a "Joint Research Activity" (JRA3 or "STREGA"), supporting R & D activities addressed to the thermal noise reduction, and a networking activity (N5-WP3), addressed to the studies for the third generation of GW detectors, have been implemented. On the same period, a first proposal (under FP6) for a "generic" design study for a third generation GW detector failed for lack of funding. In 2005, the European Science Foundation (ESF) supported an "Exploratory Workshop" (http://esf-gw.pg.infn.it/) specifically devoted to an European third generation GW observatory. This has been the right kick-off meeting to prepare the organization and clarify the targets of the successful proposal that bring to the funding, by the European Commission, under FP7, of the ET conceptual design study, object of this document.

The main target of this conceptual design, as mentioned in Sec. 1.1, is the demonstration of the feasibility of the ET project, through the definition of the requirements and main characteristics of the hosting site, the design of the key components of the research infrastructure, the indication of the possible technologies and the presentation of the detector design main elements. A rough cost evaluation is then reported to evaluate the financial feasibility of the ET project.

After the conceptual design phase, a series of difficult steps are expected. The first step is the consolidation of the design solving the several question marks currently present in many technologies needed for ET. In fact the detectors in the ET observatory will adopt technologies that aren't explored in the advanced detectors, like cryogenics, Silicon mirrors, different wavelength lasers, optical squeezing, gravity gradient noise subtraction techniques. The ET design consolidation needs, then, an intense R & D activity devoted to these technologies. The ET community must find the (human and financial) resources to support these activities; these resources should be a mix of national and international funds (i.e. like the ASPERA R & D funds). In parallel to the progresses of the technologies, the conceptual design needs to evolve in a technical design, describing in detail the components of the observatory. This phase of the project will need a correct framework and, because of the fact that the national funding agencies in Europe are fully engaged with the realisation of the advanced detectors, a possible choice is a networking or integration tool at European level (probably in FP8). To support this phase and to give a future to the ET project is, then, strongly recommended to inserted it in the list of the major research infrastructures (the so–called ESFRI roadmap) recommended by the "European Strategy Forum on Research Infrastructures" (ESFRI). Already part of the activities, necessary to achieve this target, has been performed inserting ET in the specialised roadmaps, like the GWIC roadmap (Fig. 210 or https://gwic.ligo.org/roadmap/) and the ASPERA roadmap http://www.aspera-eu.org/images/stories/files/Roadmap.pdf, but intense outreaching and proposition actions are still needed. In Fig. 210 the worldwide roadmap for the GW detectors, produced by GWIC, is shown; although it is a bit obsolete, being produced before the outcomes of this design study, it is useful to show the overall scenario where the ET project will evolve. In the Fig. 211 the expected steps of the ET project are shown, as elaborated within this conceptual design. Hence, after the current conceptual design, as previously mentioned, a technical design phase, supported by an intense R & D activity, is necessary. Then the ET project will need to define the best site location and to start a funding search activity. An *a priori* condition for the funding of the construction phase is the detection of a GW signal in the advanced detectors. To base the ET construction funding and start-up on a so intrinsically unpredictable event seems rather hazardous, but considering the installation and commissioning schedule of the advanced detectors and the promised sensitivity evolution, it is possible to predict a realistic time window for the GW signal from a BNS system in the 2015–2017 period. It will follow a site preparation phase, where all the legal and preliminary aspects of the land ownership acquirement are exploited. In parallel the production and test

of the first detector hardware components will start in the laboratories participating to the ET project. The site and infrastructures realisation will last for about four years, followed by the first ET detector installation. To save time, it is expected that part of the first detector installation (i.e. vacuum pipes deployment) could overlap with the latest infrastructure realisation activities. Thanks to the experience acquired with the initial GW detectors (that will be improved with the next commissioning of the advanced interferometers) it is possible to state that the commissioning phase will last at least for more than 3–4 years, with some early science data taking interlaced with the commissioning periods.

The ET observatory infrastructures and detectors are designed having as requirement the modularity of the components; this will allow sequential installation phases, interlaced with periods of data taking for the detectors, already operative in the ET site. In this way it will be also possible to upgrade the installed detectors when the technological progresses will make it convenient, maximising the duty cycle. This possibility underlines the main target of this study: to provide the design of a Research Infrastructure operative for decades and will be able to host evolving detectors.

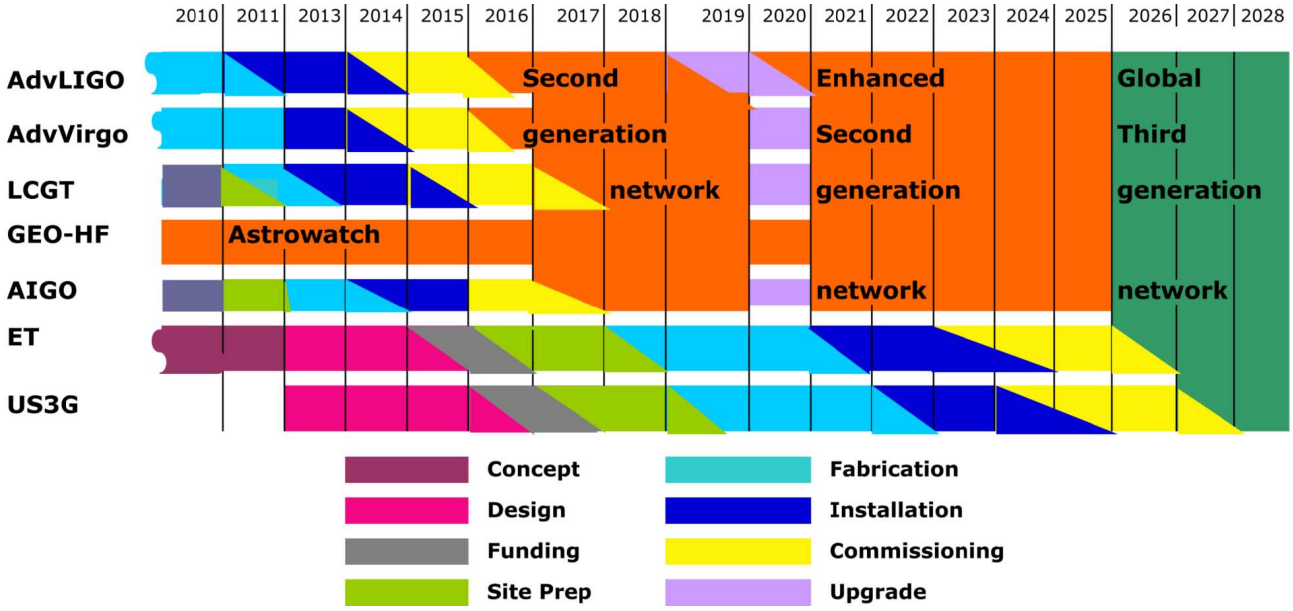

Figure 210: GWIC roadmap (rev. 30.1) showing the evolution of GW detectors in the World. The absolute timing for ET, shown in this figure, is a bit obsolete, being it produced before this design study

6.2 ET project preliminary cost evaluation

One of the main targets of this conceptual design study is a rough evaluation of the costs of the ET observatory. The level of detail of this document is not studied to provide a detailed cost table of the whole project, being this one of the deliverable of the technical design phase, but a cost evaluation, for each macro-systems composing the ET observatory, is provided. In table 212 the cost summary and the time distribution of the expenditures are shown, whereas in the following sections the cost evaluation is divided in to the five ET macro-systems. .

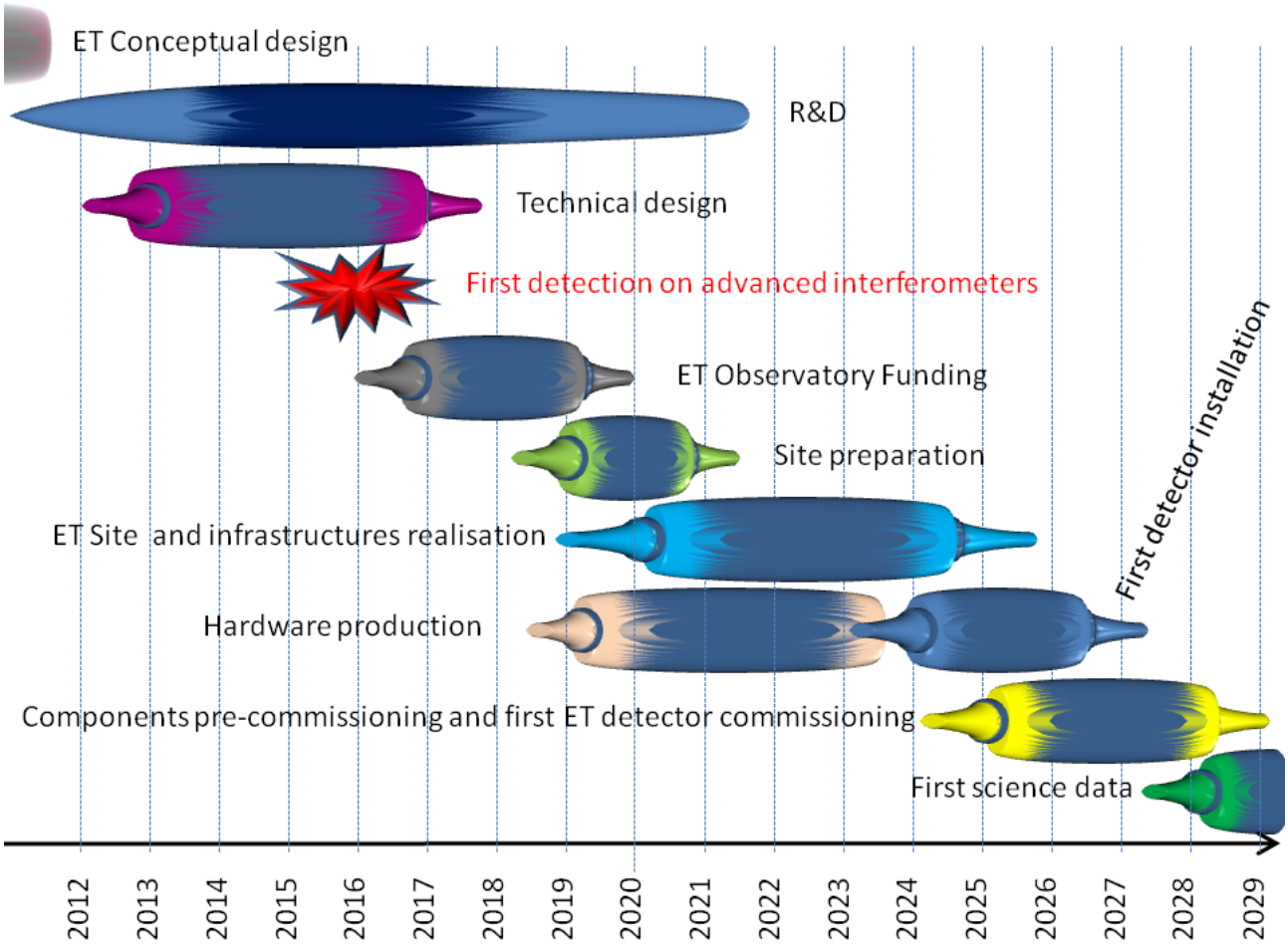

Figure 211: ET expected timeline. The incertitude in the start-stop of each activity is pictorially represented through the lateral appendixes to each horizontal bar.

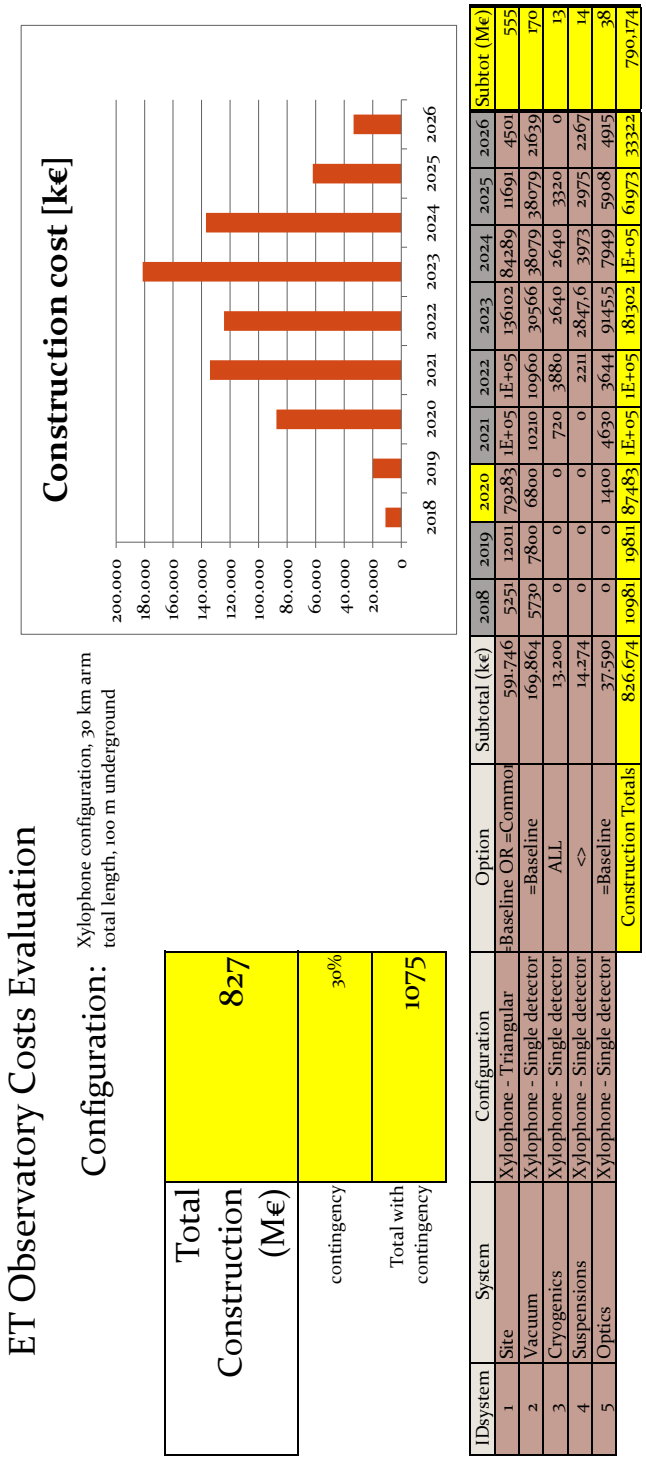

IDsystem	System	Configuration	Option	Subtotal (k€)	2018	2019	2020	2021	2022	2023	2024	2025	2026	Subtot (M€)
1	Site	Xylophone - Triangular	=Baseline OR =Commor	591.746	5251	12011	79283	1E+05	1E+05	136102	84289	11691	4501	555
2	Vacuum	Xylophone - Single detector	=Baseline	169.864	5730	7800	6800	10210	10960	30566	38079	38079	21639	170
3	Cryogenics	Xylophone - Single detector	ALL	13.200	0	0	0	720	3880	2640	2640	3320	0	13
4	Suspensions	Xylophone - Single detector	<>	14.274	0	0	0	0	2211	2847.6	3973	2975	2267	14
5	Optics	Xylophone - Single detector	=Baseline	37.590	0	0	1400	4630	3644	9145.5	7949	5908	4915	38
			Construction Totals	826.674	10981	19811	87483	1E+05	1E+05	181302	1E+05	61973	33322	790.174

Figure 212: ET observatory cost summary and expenditure time distribution

6.2.1 Infrastructure cost preliminary evaluation

The total estimated value for the infrastructure costs is 775 MEuro (in 2011 €). The cost is determined for a single xylophone detector mode. This configuration constitutes the phase I instrumentation of the project.

Phase II will be realized later and features a triple xylophone interferometer configuration.

The site specific costs are related to the direct costs for providing the infrastructure to site the observatory and are estimated at 592 MEuro (2011 value level). These costs include the underground civil facilities, services (electricity and water distribution), buildings and surface construction. The actual site-specific costs will depend on the location where the observatory is constructed, and the facilities that already exist at that location. For the estimates we have used 260 €/m^3 for the excavation costs. This includes digging cost, soil transportation and deposit, and finishing the floor and cavern walls with concrete. In addition, construction machines, running cost, maintenance, preparation and management costs are included. Several underground sites in Europe have been identified that comply with such costs, although a significant bandwidth applies. The number is also compliant with the site costs for LCGT in Japan.

The infrastructure costs include the direct costs for the safety and security systems, cooling and ventilation systems. Cost of the vacuum system and the cryogenic infrastructure are presented elsewhere. These costs are based on both the experience at GEO, Virgo and worldwide tenders.

A breakdown is given in Fig. 213. It is apparent that the main cost drivers are the underground site infrastructure: tunnels and caverns.

The observatory features more than 31 km of tunnel for housing the interferometers and their filter cavities. Each corner station has a main cavern and two satellite caverns that are connected by twin tunnels. The observatory will house one main site and two satellite sites. Surface buildings will be constructed at all sites and include control rooms, conference rooms, computing center, lunch area, science education center, cleanroom facilities, office buildings, mechanical and electronics workshops, air condition buildings, storage buildings, library, and auditorium. The main site will be fenced and guarded, and will have a visitor check in facility. Depending on the site, local lodging accommodation may be considered.

Services such as cooling and ventilation are of industrial standard type. However, there are several unusual constraints as humidity and temperature stability in underground areas that represent an engineering challenge. The dense stacking of equipment in precious underground space is a further consideration. Heat dissipating objects (*e.g.* cryogenic compressors, electronics) employ primary cooling water. All heat from the underground facilities must be rejected to the atmosphere through cooling towers. Other fluid networks involve drinking water, fire fighting water and seepage and waste water. With regard to ventilation air, the tunnels themselves are used as ducts. The system and quantity of air circulation must be optimised from the view of energy consumption. Low air flow is beneficial for noise reduction and for minimizing thermal effects.

Safety and security systems are crucial for personal safety and disaster prevention. Various causes of disasters must be considered (*e.g.* fires, electric power failure, cryogenic gas leaks, earthquake, terrorism). In all cases evacuation of personnel is required. Consequently, it is important that distances to safe places are minimized and that personnel is protected for several hours until rescue teams arrive. Emergency facilities must be carefully designed. Disaster prevention facilities include systems with emergency phones, emergency alarms, and fire alarms. Equipment such fire extinguishers, fire hydrant and water spray must be implemented. There has to be an active program of refuge instruction: evacuation routing, smoke facilities, and emergency illumination. A camera monitoring system must be implemented. While safety regulations are well established in law for surface facilities, this is not regulated by law in all countries for underground spaces (except in case of mining). In some cases special laws are established.

Site requirements that impact construction cost must be considered. These include topography and geological subterranean conditions. Factors such as horizontal versus vertical access to the underground facilities greatly affect the construction costs. Site availability and acquisition cost can vary greatly. Availability of existing support infrastructure is important. Underground laboratories as Laboratorio Nazionali del Gran Sasso LNGS (Italy), Laboratoire Souterrain de Mondane LSM (France), Laboratorio Subterraneo de Canfranc LSC (Spain) and Institute for Underground Science, Boulby mine (UK) provide extensive facilities for scientific and technical staff. This includes accommodations for resident staff (housing, schools, *etc.*), and visiting staff (lodging, transportation, *etc.*). For the same reason active or closed down mines may provide valuable facilities such as hosting shafts, electrical infrastructure, water pumps, and safety systems. In addition, they may provide local technical support and experienced technical staff. Other factors that determine the (cost of) the main

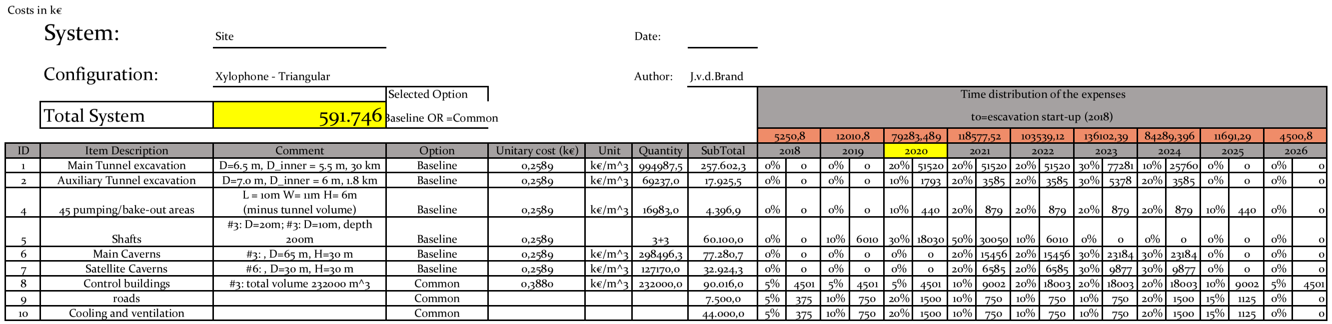

Costs in k€

System: Site

Date:

Configuration: Xylophone - Triangular

Author: J.v.d.Brand

Total System 591.746

Selected Option
Baseline OR =Common

								Time distribution of the expenses to=escavation start-up (2018)																	
								5250,8		12010,8		79283,489		118577,52		103539,12		136102,39		84289,396		11691,29		4500,8	
ID	Item Description	Comment	Option	Unitary cost (k€)	Unit	Quantity	SubTotal	2018		2019		2020		2021		2022		2023		2024		2025		2026	
1	Main Tunnel excavation	D=6.5 m, D_inner = 5.5 m, 30 km	Baseline	0,2589	k€/m^3	994987,5	257.602,3	0%	0	0%	0	20%	51520	20%	51520	20%	51520	30%	77281	10%	25760	0%	0	0%	0
2	Auxiliary Tunnel excavation	D=7.0 m, D_inner = 6 m, 1.8 km	Baseline	0,2589	k€/m^3	69237,0	17.925,5	0%	0	0%	0	10%	1793	20%	3585	20%	3585	30%	5378	20%	3585	0%	0	0%	0
4	45 pumping/bake-out areas	L = 10m W= 11m H= 6m (minus tunnel volume)	Baseline	0,2589	k€/m^3	16983,0	4.396,9	0%	0	0%	0	10%	440	20%	879	20%	879	20%	879	20%	879	10%	440	0%	0
5	Shafts	#3: D=20m; #3: D=10m, depth 200m	Baseline	0,2589		3+3	60.100,0	0%	0	10%	6010	30%	18030	50%	30050	10%	6010	0%	0	0%	0	0%	0	0%	0
6	Main Caverns	#3: , D=65 m, H=30 m	Baseline	0,2589	k€/m^3	298496,3	77.280,7	0%	0	0%	0	0%	0	20%	15456	20%	15456	30%	23184	30%	23184	0%	0	0%	0
7	Satellite Caverns	#6: , D=30 m, H=30 m	Baseline	0,2589	k€/m^3	127170,0	32.924,3	0%	0	0%	0	0%	0	20%	6585	20%	6585	30%	9877	30%	9877	0%	0	0%	0
8	Control buildings	#3: total volume 232000 m^3	Common	0,3880	k€/m^3	232000,0	90.016,0	5%	4501	5%	4501	5%	4501	10%	9002	20%	18003	20%	18003	20%	18003	10%	9002	5%	4501
9	roads		Common				7.500,0	5%	375	10%	750	20%	1500	10%	750	10%	750	10%	750	20%	1500	15%	1125	0%	0
10	Cooling and ventilation		Common				44.000,0	5%	375	10%	750	20%	1500	10%	750	10%	750	10%	750	20%	1500	15%	1125	0%	0

Figure 213: Partitioning of the site specific costs of the Infrastructure Reference Design for phase I of the Einstein Telescope observatory.

infrastructure design include groundwater conditions, hydrology and drainage which have an impact on the design of buildings and tunnels, accessibilities such as roads, railroad, distance to nearby supporting technical facilities, site utilities installations as power, water, and sewage. Finally, labour cost and proximity of soil waste and borrow areas must be considered.

Aside from construction costs, there are various factors impart the operation cost. These include the cost of electrical power, cost of local labour, heating and cooling requirements, maintenance, and travel time and cost for visiting staff. Environmental, health and safety plans must be put in place to assure the safety ofusers, staff and visitors to the Einstein Telescope observatory. These plans must comply with the relevant governmental and European standards and regulations. It is important to elevate the life-safety level above that in the mining and underground construction industries to one appropriate for researchers, students, and the public.

Risk must be minimized in the realization of the observatory. Risk factors include acquisition risk, risk from environmental sources such as earthquakes, floods and storms. Special attention must be paid to potential future man-made noise and vibration from development or industrial projects.

The explicit labor required to realize the construction project is estimated at xx million person-hours. It includes administration and project management, installation and testing. Part of the labor will be contracted and part will come from existing labor in collaborating institutions.

6.2.2 Vacuum cost preliminary evaluation

The largest contribution to the cost of the ET vacuum system comes from the vacuum pipes needed for the propagation of laser beams along the 10 km arms. The estimate of the ET vacuum pipe cost is based on past experience and on new information:

- cost and technique of fabrication and installation of the Virgo 6 km of pipe
- a new budgetary estimate by the Virgo pipe French producer (CNIM, http://www.cnim.com/)
- two successive budgetary estimates by a potential Australian supplier (Duraduct, http://www.stmduraduct.com/).

After meeting the Duraduct management and discussing deeply the matter, we decided to use their offer to estimate the cost of the ET vacuum pipe. This required to scaling appropriately the costs according to the various pipe diameters and specifications, that have been decided successively. This cost estimate may be confirmed or challenged if the "LIGO South" project will be achieved soon in Australia. The Virgo, LIGO and GEO600 experience have been very useful to evaluate technique and cost of supports and bake-out system. The cost of the towers has been evaluated on Virgo experience, due to the similarity of solutions, and on new budgetary estimates. The cost of pumps, valves and vacuum equipments has been evaluated on the basis of present market prices.

6.2.3 Cryogenic facilities and apparatuses cost preliminary evaluation

This part of the cost evaluation is based both on the experience of previous experiments and on preliminary evaluations by some external company.

A rough evaluation of the cost of the cryostat is based on the experience gained in the construction of the cryogenic apparatus for the resonant gravitational wave detectors EXPLORER and NAUTILUS. The cost of the nitrogen cryotraps is based on the Virgo experience. For the helium trap case we thank the CRIOTEC company, which helped us in the process of the cost assessment. The cost of the cryogenic solution based on extensive use of cryo-coolers (see Fig. 215) is based on the price market of such apparatuses made by the companies CRYOMECH (http://www.cryomech.com/, US) and Sumitomo (http://www.shicryogenics.com/, Japan).

For the cryogenic solution based on extensive use cryo-fluids the economics of 4.5 K refrigeration, cryo-distribution and storage systems have been evaluated. The experience gathered at CERN with the LEP [622] and LHC

projects [623], which have *de facto* turned the laboratory into a major world cryogenic center, has been considered. The recovered information have been updated taking into the account the price inflation of the Swiss currency. Then, this evaluation has been compared to that one performed for the cryogenic system planned for the International Linear Collider [624] and the educated guess done by the consulted experts of the Linde Kryotechnik AG (http://www.linde-kryotechnik.ch, Switzerland). The investment needed for the construction and the installation of the long flexible lines for the liquid helium transfer has been quoted, following the approach proposed in the CERN document [622, 623, 625, 626] for LHC, which is based on the evaluation of the multiplication factors to scale the present cost of stainless steel piping. They include engineering, installation and test costs of the transfer lines. The rough cost evaluation, using extensively cryogenic fluids, is about 18 millions of Euro.

Costs in k€

System: Vacuum

Date: 25/02/11

Configuration: Xylophone - Single detector

Author: Carlo Bradaschia

Total System	169864	Selected Option =Baseline

Time distribution of the expenses

to=escavation start-up (2018)

								5730		7800		6800		10210		10960		30566,4		38079,2		38079,2		21639,2	
ID	Item Description	Comment	Option	Unitary cost (k€)	Unit	Quantity	SubTotal	2018		2019		2020		2021		2022		2023		2024		2025		2026	
1	HF Vacuum Pipe	ϕ 0,9 m inst + supp + therm insul	Baseline	2070,00	km	20,0	41400,0	5%	2070	5%	2070	5%	2070	10%	4140	10%	4140	20%	8280	20%	8280	20%	8280	5%	2070
3	LFVacuum Pipe	ϕ 0,75 m inst + supp + therm insul	Baseline	1780,00	km	20,0	35600,0	5%	1780	5%	1780	5%	1780	10%	3560	10%	3560	20%	7120	20%	7120	20%	7120	5%	1780
4	Filter Cav.Vac. Pipe	ϕ 0,67 m inst + supp + therm insul	Baseline	1630,00	km	20,0	32600,0	0%	0	5%	1630	5%	1630	5%	1630	10%	3260	30%	9780	20%	6520	20%	6520	5%	1630
5	Pipe Factory	on site fabrication & 400°C firing	Baseline	1000,00		2,0	2000,0	50%	1000	50%	1000	0%	0	0%	0	0%	0	0%	0	0%	0	0%	0	0%	0
6	Baking Supply	15 kV-50 V	Baseline	220,00	km	20,0	4400,0	20%	880	30%	1320	30%	1320	20%	880	0%	0	0%	0	0%	0	0%	0	0%	0
7	High Tower	18 m x 2-2.5 m (Figs 196-7)	Baseline	1000,00	#	3,0	3000,0	0%	0	0%	0	0%	0	0%	0	0%	0	10%	300	30%	900	30%	900	30%	900
8	High Cryo-Tower	18 m x 2 m (cryog. excluded)	Baseline	1100,00		4,0	4400,0	0%	0	0%	0	0%	0	0%	0	0%	0	10%	440	30%	1320	30%	1320	30%	1320
9	Ancillary Cryo-Tower	6 m x 2 m (cryog. Excluded)	Baseline	300,00		4,0	1200,0	0%	0	0%	0	0%	0	0%	0	0%	0	10%	120	30%	360	30%	360	30%	360
10	Tower	10 m x 2 m	Baseline	500,00		11,0	5500,0	0%	0	0%	0	0%	0	0%	0	0%	0	10%	550	30%	1650	30%	1650	30%	1650
11	Filter Tower	8 m x 2.5 m	Baseline	500,00		3,0	1500,0	0%	0	0%	0	0%	0	0%	0	0%	0	10%	150	30%	450	30%	450	30%	450
12	Cryotrap	6 m x 0.9 m	Baseline	250,00		4,0	1000,0	0%	0	0%	0	0%	0	0%	0	0%	0	10%	100	30%	300	30%	300	30%	300
13	Large Valve	0,8 m aperture	Baseline	96,00		10,0	960,0	0%	0	0%	0	0%	0	0%	0	0%	0	10%	96	30%	288	30%	288	30%	288
14	Large Valve	0,65 m aperture	Baseline	40,00		14,0	560,0	0%	0	0%	0	0%	0	0%	0	0%	0	10%	56	30%	168	30%	168	30%	168
15	Large Valve	0,50 m aperture	Baseline	35,00		12,0	420,0	0%	0	0%	0	0%	0	0%	0	0%	0	10%	42	30%	126	30%	126	30%	126
16	Pseudo-valve	0,80-0,50 m aperture	Baseline	30,00		10,0	300,0	0%	0	0%	0	0%	0	0%	0	0%	0	10%	30	30%	90	30%	90	30%	90
17	Tower Link Tubes	0,75-0,9 m diameter	Baseline	40,00		13	520,0	0%	0	0%	0	0%	0	0%	0	0%	0	10%	52	30%	156	30%	156	30%	156
18	Pipe rough pumping	dry/roots	Baseline	100,00		1	100,0	0%	0	0%	0	0%	0	0%	0	0%	0	10%	10	30%	30	30%	30	30%	30
19	Pipe evacuation+bake	turbo+scroll+gauges+valves	Baseline	46,00		240	11040,0	0%	0	0%	0	0%	0	0%	0	0%	0	10%	1104	30%	3312	30%	3312	30%	3312
20	Pipe final pumping	Ti evap.+Ion+gauges+valves	Baseline	41,00		360	14760,0	0%	0	0%	0	0%	0	0%	0	0%	0	10%	1476	30%	4428	30%	4428	30%	4428
21	Pipe monitoring	Gauges+RGA	Baseline	100,00		6	600,0	0%	0	0%	0	0%	0	0%	0	0%	0	10%	60	30%	180	30%	180	30%	180
22	Pipe Vacuum Control	HW+SW+Cabling	Baseline	25,00		60	1500,0	0%	0	0%	0	0%	0	0%	0	0%	0	10%	150	30%	450	30%	450	30%	450
23	Tower Pumping & Control	scroll+turbo+ion+gauges+valves	Baseline	271,00		24	6504,0	0%	0	0%	0	0%	0	0%	0	0%	0	10%	650	30%	1951	30%	1951	30%	1951

Figure 214: Vacuum apparatuses and components cost summary and expenditure time distribution

6.2.4 Suspensions and payloads cost preliminary evaluation

The cost evaluation for the payloads and the local control is based on the experience acquired during the construction of the Virgo monolithic suspensions and during the realisation of a cryogenic payload prototype built on Virgo site. In both cases the the mirrors have a mass of 20kg. For this reason we have newly evaluated the costs of the materials for building heavier and, in the ET-LF case, cryo-compatible payload elements. In the case of the ET-LF interferometer the costs of the equipment for the temperature monitor with thermometers were added.

Costs in k€

System: Cryogenics — Date: 04/04/11

Configuration: Xylophone - Single detector — Author: P.Puppo

Total System	13600	Selected Option	=Baseline

									Time distribution of the expenses to=escavation start-up (2018)																							
									0		0		0		0		760		4000		2720		2720		3400		0			
ID	Item Description	Comment	Option	Unitary cost (k€)	Unit	Quantity	SubTotal		2018		2019		2020		2021		2022		2023		2024		2025		2026							
1	Cryogenerators	Cryomech/Sumitomo	Baseline	900,0	per tower	4,0	3600,0	0%	0	0%	0	0%	0	10%	360	30%	1080	20%	720	20%	720	20%	720	0%	0						
2	Cryo-Trap	Criotec colloquium 2 cryotrap in input towers	Baseline	1000,0	#	6,0	6000,0	0%	0	0%	0	0%	0	0%	0	30%	1800	20%	1200	20%	1200	30%	1800	0%	0						
3	Cryostats	Criotec colloquium	Baseline	800,0	per tower	4,0	3200,0	0%	0	0%	0	0%	0	10%	320	30%	960	20%	640	20%	640	20%	640	0%	0						
4	Cryogenic equipments	Cern and ILC experience	Baseline	200,0	per tower	4,0	800,0	0%	0	0%	0	0%	0	10%	80	20%	160	20%	160	20%	160	30%	240	0%	0						

Figure 215: Cryo-coolers based solution cost summary and expenditure time distribution

6.2.5 Optics cost preliminary evaluation

The main impact of the optical design on the cost is via the required infrastructure in terms of the vacuum system, tunnels and caverns. In addition the optical system yields direct costs for the high-quality optics and the auxiliary optical systems with their mechanical and electrical support systems The core elements of the interferometers are the test masses which need to be of considerable size and weight and must fulfil extremely stringent requirement for bulk and surface qualities.

The maximum available size for Suprasil 3001 today is the size of the 40 kg test masses for advanced LIGO. The heavier substrates envisaged for ET can presently only be made either of Suprasil 3002 which has inhomogeneities in the direction of the beam or from fused pieces of thinner Suprasil 3001. The price quoted by Heraeus for a substrate of 600 mm in diameter and 400 mm in thickness made of composite Suprasil 3001 is €700k which corresponds approximately to a price of €3.5k/kg. The end test masses can be made out of Suprasil 312 with a considerable lower cost per kilogramme, an estimate based on quotes for Advanced Virgo optics gives €1.6k/kg.

At present silicon is only available in Chzochalski grown crystals to a size of up to 450 mm.In Floating zone crystals the maximum size at present is 200 mm. The interest of the semiconductor industry in ultra-pure crystals is very limited and will most likely not drive the development of bigger size single crystals. Costs of silicon per kg are based on a quote by Simat and are comparable to the one of ultra-pure fused silica.

The cost estimates for polishing and coating of the mirrors are based on similar costs related to Advanced Virgo, up-scaled to include ion-beam polishing.

Further included in the optics cost are the main laser systems, optical benches in air and in vacuum for injecting the beam from the laser into the detectors, similar benches and components for extracting and detecting beams from the interferometers as well as the mechanical, optical and electronic components required for interferometer control purposes. We further count the cost for special optical subsystems such as the squeezed light source and the thermal compensation systems. These systems will be directly based on current systems and thus the costs have been estimated from the data for current and advanced detectors.

The total cost for the installation of the optical components of the first detector (two interferometers plus spares) has been computed as €37.6M. The total optics cost for all three detectors is estimated to be €60M. The nonlinear increase results from the fact that spare parts can be shared between detectors. The cost of the first detector is dominated by the main optics which account for €20.4M. The high-power laser system at 1064 nm and one medium power system at 1550 nm wavelength cost together €7M. The input and output optics require together another €7M. We also include €2.5M for control electronics and €600k for the thermal compensation system.

Costs in ke

System: Suspensions Date: 18/04/11

Configuration: Xylophone - Single detector Author: S.Braccini, P. Puppo, F.Frasconi

Total System	14274	Selected Option	<>

									Time distribution of the expenses to=escavation start -up (2018)																	
									0		0		0		0		2211		2847,6		3972,2		2974,8		2267,4	
ID	Item Description	Comment	Option	Unitary cost (ke)	Unit	Quantity	SubTotal		2018		2019		2020		2021		2022		2023		2024		2025		2026	
1	Super attenuator mechanics LF	17 meter, 6 filters	Baseline	430,0	#	9,0	3870,0	0%	0	0%	0	0%	0	0%	0	10%	387	20%	774	40%	1548	20%	774	10%	387
2	Super attenuator electronics LF	adV costs	Baseline	160,0	#	9,0	1440,0	0%	0	0%	0	0%	0	0%	0	10%	144	20%	288	40%	576	20%	288	10%	144
3	Cryogenic payload	Based on Cryo Pay prototype	Baseline	132,0	#	4,0	528,0	0%	0	0%	0	0%	0	0%	0	0%	0	20%	106	40%	158	40%	211	10%	53
4	Termometry	Based on Cryo Pay prototype	Baseline	9,0	#	4,0	36,0	0%	0	0%	0	0%	0	0%	0	0%	0	0%	0	30%	11	60%	22	10%	4
5	Local Control System	Based on Cryo Pay prototype	Baseline	30,0	#	4,0	120,0	0%	0	0%	0	0%	0	0%	0	20%	24	20%	24	20%	24	20%	24	20%	24
6	Standard payload	Based on Virgo+ payload	Baseline	165,0	#	14,0	2310,0	0%	0	0%	0	0%	0	0%	0	20%	462	20%	462	20%	462	20%	462	20%	462
7	Local Control System	Based on Virgo+ payload	Baseline	15,0	#	14,0	210,0	0%	0	0%	0	0%	0	0%	0	20%	42	20%	42	20%	42	20%	42	20%	42
8	Super attenuator mechanics HF	9 meter, 6 filters	Baseline	350,0	#	9,0	3150,0	0%	0	0%	0	0%	0	0%	0	20%	630	20%	630	20%	630	20%	630	20%	630
9	Super attenuator electronics HF	adV costs	Baseline	110,0	#	9,0	990,0	0%	0	0%	0	0%	0	0%	0	20%	198	20%	198	20%	198	20%	198	20%	198
10	Standard payload	Based on Virgo+ payload	Baseline	165,0	#	9,0	1485,0	0%	0	0%	0	0%	0	0%	0	20%	297	20%	297	20%	297	20%	297	20%	297
11	Local Control System	Based on Virgo+ payload	Baseline	15,0	#	9,0	135,0	0%	0	0%	0	0%	0	0%	0	20%	27	20%	27	20%	27	20%	27	20%	27

Figure 216: Suspensions cost summary (first detector) and expenditure time distribution

Costs in k€

System: Optics Date: 19/04/11

Configuration: Xylophone - Single detector Author: A.Freise, H.Lueck

Total System 37590 Selected Option =Baseline

								Time distribution of the expenses to=escavation start-up (2018)																	
								0		0		1400		4630		36435		9145.5		7948.5		5908		4914.5	
ID	Item Description	Comment	Option	Unitary cost (k€)	Unit	Quantity	SubTotal	2018		2019		2020		2021		2022		2023		2024		2025		2026	
1	main optics	first ITF installation	Baseline	20405.0		1.0	20405.0	0%	0	0%	0	0%	0	0%	0	0%	0	30%	6122	30%	6122	20%	4081	20%	4081
2	input optics	first ITF installation	Baseline	4935.0		1.0	4935.0	0%	0	0%	0	0%	0	0%	0	10%	494	40%	1974	20%	987	20%	987	10%	494
3	output optics	first ITF installation	Baseline	2100.0		1.0	2100.0	0%	0	0%	0	0%	0	30%	630	20%	420	20%	420	10%	210	10%	210	10%	210
4	laser	first ITF installation	Baseline	7000.0		1.0	7000.0	0%	0	0%	0	20%	1400	50%	3500	30%	2100	0%	0	0%	0	0%	0	0%	0
5	Control Electronics	first ITF installation	Baseline	2500.0		1.0	2500.0	0%	0	0%	0	0%	0	20%	500	20%	500	20%	500	20%	500	20%	500	0%	0
6	thermal compensation system	first ITF installation	Baseline	650.0		1.0	650.0	0%	0	0%	0	0%	0	0%	0	20%	130	20%	130	20%	130	20%	130	20%	130

Figure 217: Optics cost summary (first detector) and expenditure time distribution

Appendices

A Science Case

A.1 Detection Rate of BNS Systems in ET

Binary neutron stars have a relatively short *delay time,* the time between the formation of the binary system of massive stars and the merger [29]. Therefore, the coalescence rate roughly traces the star formation rate of the universe.

For example, assuming all gas forms stars similar to the present day Milky Way, the current Milky Way compact object merger rate allow us rescale the *total* star formation rate of the universe into an instantaneous merger rate per unit volume

$$\dot{\rho}_c(z) = \lambda \frac{SFR(z)}{1+z} \quad \text{with} \quad \dot{\rho}_c(0) = R_{\rm MW} n_{\rm MW} \tag{130}$$

In this expression, SFR is the star formation rate in $\mathrm{M}_\odot^{-1}$ Mpc^{-3} yr^{-1} (see for instance [28, 30]), and λ is the number of compact binary progenitors formed per unit of gas mass in $\mathrm{M}_\odot^{-1}$, assumed to be the same at all redshifts. The coalescence rate is normalized by the local rate at $z = 0$, obtained by multiplying the actual galactic rate $R_{\rm MW}$ in yr^{-1} and the local density of Milky Way equivalent galaxies $n_{\rm MW}$ in Mpc^{-3} is found by multiplying $\dot{\rho}_c$ by the gradient of comoving volume:

$$\frac{dR}{dz}(z) = \dot{\rho}_c(z) \frac{dV_c}{dz}(z). \tag{131}$$

Depending on the target sensitivity and beampattern of the ET network, the expected detection rate is roughly proportional to the integral of this rate up to some peak redshift. For most target ET sensitivities this limiting redshift $z_{\rm max}$ is greater than 1 for binary neutron stars, suggesting $O(10^6)$ detections per year. The enormous collections of events that ET-scale instruments will observe will permit high-precision modeling inaccessible with the sparse statistics available to smaller detectors.

A.2 The *Spin-Down Limit* signal amplitude

Under the assumption that the observed spin-down of a given neutron star is due to the emission of gravitational waves, a straightforward calculation leads to the so-called *spin-down limit* on the signal amplitude $h_0^{\rm sd}$:

$$h_0^{\rm sd} = 8.06 \times 10^{-19} \frac{I_{38}}{d_{kpc}} \sqrt{\frac{|\dot{f}_{\rm rot}|}{f_{\rm rot}}} \tag{132}$$

where $I_{38} = I/10^{38}\mathrm{kg\ m}^2$, d_{kpc} is the distance to the star in kpc, $\dot{f}_{rot}$ is the spin-down rate and $f_{\rm rot}$ is the spin frequency. The spin-down limit on the signal amplitude corresponds to an upper limit on the star's ellipticity of

$$\epsilon^{\rm sd} = 0.237 \left(\frac{h_0^{\rm sd}}{10^{-24}} \right) I_{38}^{-1} (f_{\rm rot}/\mathrm{Hz})^{-2}\, d_{\rm kpc}. \tag{133}$$

A.3 Search sensitivity to Continuous Wave sources

For targeted searches, that are based on coherent analysis methods, the minimum detectable signal amplitude is given by

$$h_{0,\rm min} \simeq 11.4 \sqrt{\frac{S_n(f)}{DT_{\rm obs}}}, \tag{134}$$

where $S_n(f)$ is the detector noise power-spectral density at a frequency f, $T_{\rm obs}$ is the observation time, and D is the number of detectors (assumed to have the same sensitivity at the frequency f). The factor of 11.4 corresponds to a false alarm rate of 1% and a false dismissal rate of 10% and its exact value depends on the specific analysis method.
For wide area searches, based on semi-coherent analysis methods, or on the alternation of coherent and incoherent steps, the minimum detectable signal amplitude is given by

$$h_{0,\rm min} \approx \frac{25}{N^{1/4}} \sqrt{\frac{S_n(f)}{DT_{\rm coh}}}\,. \tag{135}$$

Here $T_{\rm coh}$ is the time length of the piece of data coherently analyzed. This has been found to be a fairly good estimate (within $\sim 20\%$) of previous semi-coherent searches (see *e.g.* [270]). Note that in this case the minimum amplitude only decreases with the fourth root of the total observation time.

A.4 Measuring $w(z)$ Using GW and CMB Observations

To estimate the constraints on cosmological parameters from future Planck CMB data, one can consider the Fisher matrix

$$F_{ij}^{\rm CMB} = \sum_{\ell=2}^{\ell_{max}} \sum_{XX',YY'} \frac{\partial C_\ell^{XX'}}{\partial p_i} {\rm Cov}^{-1}(D_\ell^{XX'}, D_\ell^{YY'}) \frac{\partial C_\ell^{YY'}}{\partial p_j}, \tag{136}$$

wherer p_i are the cosmological parameters to be evaluated; $C_\ell^{XX'}$ are the CMB power spectra and $D_\ell^{XX'}$ their estimates; and ${\rm Cov}^{-1}$ is the inverse of the covariance matrix at given angular size ℓ and channels X, X' (T for temperature, E for polarization). For a detailed discussion we refer to [190].

Given a population of inspiral events, we can also associate a Fisher matrix to the set of events:

$$F_{ij}^{\rm GW} = \sum_k \frac{\partial_i(\ln D_{\rm L}(z_k))\partial_j(\ln D_{rmL}(z_k))}{\Delta \ln D_{\rm L}(z_k)}, \tag{137}$$

where ∂_i, ∂_j are partial derivatives with respect to cosmological parameters, and the k refer to individual events. This Fisher matrix can be combined with the one for the CMB as

$$F_{ij}^{\rm combined} = F_{ij}^{\rm GW} + F_{ij}^{\rm CMB}. \tag{138}$$

A.5 Sources of primordial stochastic GW background

A.5.1 Stochastic GW background in Pre-Big-Bang cosmology

The GW spectrum produced at the transition between the stringy phase and the radiation-dominated era is described as $\Omega_{\rm gw}(f) \sim f^3$ for $f < f_s$ and $\Omega_{\rm gw}(f) \sim f^{3-2\mu}$ for $f_s < f < f_1$ [627, 628]. The cutoff frequency f_1, which depends on string related parameters, has a typical value of 4.3×10^{10} Hz.

An upper limit on $\Omega_{\rm gw}$ is imposed by the Big Bang Nucleosynthesis (BBN) bound down to 10^{-10} Hz, corresponding to the horizon size at the time of BBN. Measurements of the light element abundances combined with the WMAP data gives $N_\nu < 4.4$ [629], which translates to $\Omega_{\rm gw} < 1.5 \times 10^{-5}$. Recent measurements of CMB anisotropy spectrum, galaxy power spectrum and of the Lyman-α forest give a bound of similar amplitude which extends down to 10^{-15} Hz, corresponding to the horizon size at the time of CMB decoupling [630].

A.5.2 GW background from cosmic string networks

The basic parameter describing a cosmic string netword is the string tension or energy per unit length $G\mu$, determined by the energy scale of the phase transition; in brane inflation this may take values from 10^{-6} down to 10^{-11}. The current limit from CMB and other cosmological probes is a few times 10^{-7} [631–633]. Fundamental strings also have a "reconnection probability" p significantly smaller than unity (the value for field-theoretic strings).

The properties of both field-theory and fundamental string networks can be summarized by parameters $\alpha < 1$ (size of newly-created loops relative to the Hubble horizon) and $\Gamma \sim 50$ (gravitational-wave luminosity of string loops). These are subject to uncertainty from numerical simulations. There are two limits: the "large loop" case where α is comparable to unity, for which the "plateau" value of $\Omega_{\rm gw}(f)$ may be estimated [634] as

$$\Omega_{\rm gw}(f) \sim 10^{-8}(G\mu/10^{-9})^{1/2} p^{-1} (0.2\Gamma\alpha)^{1/2}. \tag{139}$$

The "small loop" case is motivated if the size of loops is determined by gravitational backreaction, giving $\alpha \simeq \Gamma G\mu \ll 1$; deviations from this value [635] are parameterized by a factor ϵ. In Fig. 36 we use a recent evaluation [206] of the GW spectrum for $p = \epsilon = 1$.

Self-ordering dynamics of a scalar field may also result in a nearly "flat" spectrum [636], similar to that of cosmic strings, with an amplitude at the threshold of detectability for ET for a GUT scale phase transition.

A.5.3 Stochastic GW from cosmological phase transitions

The transition is characterized by the temperature T_* at which bubble nucleation occurs and the duration or characteristic timescale β^{-1}, assumed much shorter than a Hubble time H_*^{-1}. The present peak frequency and amplitude of GW are estimated as [637]

$$\begin{aligned} f_{\rm peak} &\simeq (5.2\times 10^{-8}\,{\rm Hz}) \frac{\beta}{H_*} \cdot \frac{T_*}{1\,{\rm GeV}} \left(\frac{g_*}{100}\right)^{1/6}, \\ \Omega_{\rm gw}(f_{\rm peak}) h_{100}^2 &\simeq (1.1\times 10^{-6}) \kappa \left(\frac{\alpha}{1+\alpha}\right)^2 \left(\frac{v^3}{0.24+v^3}\right) \left(\frac{H_*}{\beta}\right)^2 \left(\frac{100}{g_*}\right)^{1/3}, \end{aligned} \tag{140}$$

where α is a measure of the strength of the phase transition, κ is an "efficiency factor" for conversion of false vacuum energy to kinetic energy, and v is the speed of expansion of the bubbles. In the limit of a strongly first-order transition $\alpha \gg 1$, $v \to 1$ and $\kappa \to 1$, while β/H_* is expected to be of order 10^2. Turbulent plasma motion leads to similar values.

A.5.4 GW from reheating after hybrid inflation

In hybrid inflation the peak frequency and amplitude of the primordial GW background are estimated respectively as

$$\begin{aligned} f_{\rm peak} &\simeq (6\times 10^{10}\,{\rm Hz}) C g \lambda^{1/4}, \\ \Omega_{\rm gw}(f_{\rm peak}) h_{100}^2 &\simeq (2\times 10^{-6}) \left(\frac{v}{M_P}\right)^2 (Cg)^{-2}, \end{aligned} \tag{141}$$

for $g^2 \gtrsim \lambda$, where g is the coupling of the "Higgs" field to the inflaton, λ is its self-coupling and v its expectation value after symmetry-breaking; C is a constant determined by numerical simulation. When $g^2 \ll \lambda$ the relevant formulae are

$$\begin{aligned} f_{\rm peak} &\simeq (3\times 10^{10}\,{\rm Hz}) \frac{g}{\sqrt{\lambda}} \lambda^{1/4}, \\ \Omega_{\rm gw}(f_{\rm peak}) h_{100}^2 &\simeq (8\times 10^{-6}) \left(\frac{v}{M_P}\right)^2 \frac{\lambda}{g^2}. \end{aligned} \tag{142}$$

In Fig. 36 we plot the spectrum for the parameter values $\lambda = 2g^2 = 10^{-14}$, $v = 3 \times 10^{-7} M_P$.

A.6 Computational Challenges

A clear understanding of emerging computing technologies is essential to the success of any frontier science facility like ET. Our goal is to keep track of the developments and to shape and drive the technology with our own experiments in this emerging area. The next three Sections will discuss some of the key developments in computing that are relevant to ET.

A.6.1 Moore's Law

"Moore's Law is a violation of Murphy's Law. Everything gets better and better" [638]: this is how Gordon Moore commented the law, that bears his name, in 2005. Moore's law describes trend in the history of computing hardware. The law has been originally thought to describe the number of transistors that can be placed inexpensively on an integrated circuit. But now we see that this law can be applied also to the capabilities of many digital electronic devices, such as memory capacity, sensors and even the number and size of pixels in digital cameras, etc. There are in fact many other laws related to the Moore's one. Other laws predict, for example, hard disk storage cost per unit of information, or network capacity, or pixels per dollar, and more.

Gordon E. Moore formulated the law by a simple observation. In 1965 he noted that number of components in integrated circuits had doubled every two years from the invention of the integrated circuit in 1958. Thus, he predicted that the trend would continue "for at least ten years". Years after the law has been reformulated to take into account an higher growth, and the final formulation states that integrated circuits would double in performance every 18 months. Thus "Moore's first law" predicts an exponential rates for the transistor counts in a microprocessor: $P_n = P_0 \times 2^n$, where P_n is the predicted computer processing power in future years, P_0 is the actual computer processing power, and n the number of years divided by the doubling period, expressed in years. For transistors the doubling factor is 2 (every 2 years), while for processors' speed the doubling factor is 1.5 (every 18 months).

Moore's first law can be viewed just as an observation, but maybe there is even more. Maybe behind it there is a more deeper law, a law driving evolution of information and technology, of which the Moore's law is just a consequence. But up to now what it is clear is that this law has been widely accepted, and is used as a goal for both marketing and engineering departments of semiconductor manufacturers.

A.6.2 20 years of parallelization

Here we report some details about architecture innovation in the last 20 years by hardware manufacturers. We underline the implicit and explicit parallelization concept that has been used as a way to get around the problem of limitations in miniaturization and clock speed. A scalar processor is the simplest CPU that can be considered. It is capable of executing a single instruction per clock cycle and to manipulate one or two data items at a time. A superscalar processor is, instead, capable of intrinsic parallelism. Each instruction processes one data item, but multiple instructions and data are processed concurrently, having multiple redundant functional units within each CPU. In fact, modern superscalar processors includes multiple ALUs, multiple FPUs. Thus the dispatcher of the CPU reads instructions from memory and decides which ones can be run in parallel.

An important step forward has been the introduction (around 1998/1999) of one or more *SIMD* units by AMD and Intel. These units are used through the AMD's 3DNow and the Intel's Streaming SIMD Extensions (SSE) instruction set extension to perform basic vector operations (i.e. adding two vectors of float, in one step). The capability of executing more than one instruction per clock cycle is another level of parallelism introduced into superscalar CPU. The basic idea is to split each instruction into several micro-instructions, each executed by an indipendent functional unit of the pipeline. This approach permits a natural parallelism. In fact, usually when there are several instructions to be executed, as soon as the first functional unit has finished the execution of

the first micro-instruction, this is sent to the second unit. So the first functional unit of the pipeline is free to start the execution of the second instruction, and so on. Given a starting latency to fill the pipeline, the CPU can reach a steady state where N instructions are executed together for each clock cycle, where N is number of functional units (so called depth of the pipeline).

Another step in improving the efficiency of CPUs, has been the introduction of *Simultaneous multithreading (SMT)*, roughly about 2003-2004. Maybe one of the most famous implementation of this technique is the Intel's Hyper-Threading Technology. The HT, or HTT, works duplicating some sections of the processor pipeline. In this way the hyper-threading processor appears as two "logical" processors to the host operating system. This allows the operating system to schedule two threads or processes simultaneously.

Starting from 2005, multi-core CPUs have been introduced in the everyday computing architecture, both in the embedded and standard systems. This solution implements multiprocessing in a single physical package, namely the full processor, replicating the whole computing core. Different cores may or not share caches, and may implement message passing or shared-memory inter-core communication. The actual multi-core CPU implements up to four/six cores per package. In case of the multi-core CPU the performance gain is strictly related to the efficiency of the parallelized software. This is called Amdahl's law[639], it connects the parallelization efficiency with the fraction of the software that can be parallelized to run on multiple cores simultaneously.

A.6.3 Manycore architectures

The transition to many-cores systems seems to be the natural evolution of computational architecture. Many-core processors have a larger number of cores respect to traditional multi-processors, roughly in the range of several tens of cores. The actual state-of-the-art in many-core architecture is represented by GPU processors, where in a single package hundreds of computing cores are implemented. Here we would like to discuss decisions of major vendors of technology and their roadmaps, in order to show the trend in many-core architectures.

All major CPU processors manufactures, such as Intel and AMD, are researching and developing new innovative solutions in order to bypass the even more stringent technological challenges. In some sense GPU are the precursor of many-core architecture with several already marketed and used hardware devices. Even if these have been developed specifically for computer graphics this hardware is now widely used in other computing fields, proving a resounding success. Moreover, during 2010, Intel and AMD have published and made official communication about subsequent CPU generation. They report technological solutions that are following the path of increasing the number of computing core elements per CPU. In detail, AMD has declared to be close to releasing a new processors family based on Fusion [640]. AMD Fusion is the codename for next-generation microprocessor design and a product merging together AMD and ATI. Where AMD brings knowledge about CPU technology and ATI its own knowledge about Graphic Progessing Units, combining general processor execution as well as 3D geometry processing and other functions of modern GPUs into a single package.

The core of this new architecture are the APU (Accelerated Processing Units). This technology is expected to debut in the first half of 2011. Intel has recently declared during the New Orleans Supercomputing Conference its approach to the High Performance Computing, introducing the MIC (Many Integrated Core) solution [641], known with the name Knights Ferry. The Intel MIC architecture is derived from several Intel projects, including "Larrabee" [642] and such Intel Labs research projects as the Single-chip Cloud Computer [643, 644]. The architecture is based on chip containing 32 cores x86 at 22nm. Moreover, Intel has declared for 2012 the production of an higher solution based on 50 core 4 hyper-threading processor. One of the key point of the Intel solution is the code portability, being a x86 compatible architecture. Comparing Knights Ferry with GPU solution we have to remark that a CPU core is much more complex than a GPU core, providing for example SSE4, permitting 8 single precision operations per cycle per core. There are also other experiences in the market, such as Tilera products [645].

The previous statements indicate a clear direction about new processor products: *CPUs are evolving toward the direction of the many-core computing.* Each vendor is traducing this concept in different shapes (i.e. "homogeneous collections of general-purpose cores" rather than "computers using a variety of specialty cores"), but all agree on the need of increase significantly the parallelization level [646].

A deep change in hardware architecture will also require a deep change in software and algorithms. Without this effort it is impossible to extract the real power of these new computing resources.

A.6.4 Emerging technologies for distributed computing

One of the most famous definitions of the grid perfectly describes such design: "the grid is a flexible, secure, coordinated resource sharing among dynamic collections of individuals, institutions, and resources — what we refer to as virtual organizations" [647]. More precisely, the grid can be thought as a distributed system, where heterogeneous resources are geographically dispersed and connected by a network.

So grids represent a form of distributed computing facilities, where a "super virtual computer" is composed by many interconnected computing resources, like clusters, single workstations and traditional single supercomputers. The middleware (i.e. a collection of software libraries), like the operating system in a pc, gives to the user all the necessary instruments to use the grid in a transparent and secure way; it provides uniformity through a standard set of interfaces to the underlying resources. It is a layer of software between the network and the applications that provide services such as identification, authentication, authorization, directories, and security.

A working example of what we briefly described is the Worldwide LHC Computing Grid project (WLCG) [648], currently operates the world's largest scientific Grid, with over 140 computing centers in 34 countries contributing resources, including more than 10,000 CPUs and several Petabytes of storage. Cloud computing goes a step further in the direction of separating the user from the computing resources. This new computing paradigm represents also an improvement in the direction of the on-demand resource provisioning. Cloud computing generally means a collection of technologies enabling the final user to benefit of wide set of hardware and software remotely distributed.

We can compare the Cloud with the electric power network: when we switch on a light, or we plug in an electrical device into a wall socket, we are not aware from where the power comes from, and generally we do not care much about such details. Now we are thinking about a world in which computer power, storage and software capabilities, are as easily accessible as the electric power.

We can briefly summarize Cloud computing architecture as follows: The end user simply uses a specific service provided by a customer administrator. The administrator uses some interfaces to select a specific service (i.e. a virtual server or just some storage) and to administer the service (i.e. configure it, activate or deactivate the service, or maybe to ask for more computing power or storage). The service provider is the one that physically owns the real server, and the one who is in charge of providing transparent interface to manage the resources.

There are up to now several examples of working cloud infrastructures : Amazon Elastic Compute Cloud (EC2) (that allows users to rent and use virtual server for the scalable deployment of applications), Amazon S3 (Simple Storage Service, an online storage web service), Google App Engine (it is a platform for developing and hosting web applications in Google-managed data centers).

B Site and Infrastructure

B.1 Measurement methodology and data analysis

In order to measure the ambient seismic background low noise broadband seismometers are required. All seismic measurements were carried out using two measurement stations, each station consists of a Trillium 240 (T240) accelerometer and a data acquisition system. The T240 is a broadband low noise seismometer with a flat velocity response from 4 mHz to 35 Hz and a self noise below the low noise model from 0.01 to 10 Hz. Each seismometer is placed on top of a granite tile that is fixed to the solid rock floor with tile glue. A thermal and acoustic insulation cover is then placed over the seismometer. The read-out of the seismometers is done with a portable data acquisition system consisting of a 19 inch rack mounted computer with a National Instruments 18

bit DAQ card, a low noise amplifier, a battery UPS and a power supply to both the seismometer and amplifier. The seismometer produces a sensitive measurement of the ground velocity in 3 directions (north, east and vertical) and a number of diagnostic signals. The velocity channels are amplified by a factor of 105 to increase the resolution of the read-out system and passed through a low-pass filter with a -3 dB point at 30 Hz. The sampling rate is 128 Hz and every 128 seconds of data are written away into a single ascii data file by using a custom made LabView program.

The measurement noise of the seismic station is dominated by the self-noise of the T240 and the electronic noise from the pre-amplifer. The latter can be decomposed into voltage, thermal and current noise contributed by the first stage operational amplifier (op-amp), and ADC or quantization noise at the digitizer. The electronic noise at the input of the amplifier, can be modeled given the following equations [649];

$$E_{nn} = V_{00}\left(\frac{f_{cv}}{f}+1\right) + I_{00}\left(\frac{f_{ci}}{f}+1\right) r_p^2 + 4kTr_p + \frac{D_{nn}}{A_G^2} \quad V^2/\text{Hz} \tag{143}$$

$$D_{nn} = \left(\frac{2A}{2^n}\right)^2 \frac{1}{12 f_N} \quad V^2/\text{Hz}, \tag{144}$$

where, f_{cv} and f_{ci}, are the corner frequencies of op-amp voltage and current noise, V_{00} and I_{00}, the high frequency levels of op-amp voltage and current noise power spectral density. Boltzmann's constant is denote k, T is the temperature in Kelvin and appears in the op-amp Johnson or thermal noise contribution, r_p is the parallel combination of r_c and r_d and are the seismometer and shunt resistance respectively. Finally, the maximum amplitude of ADC input is A, A_G is the amplifier gain, f_N is the Nyquist frequency (related to the sampling frequency, $f_N = f_s/2$), and n the number of bits in the ADC.

Op-amp parameters					
Type	$V_{00}[V^2/\text{Hz}]$	f_{cv} [Hz]	I_{00} $[A^2/\text{Hz}]$	f_{cv} [Hz]	A_G gain
INA128	$6.4 \cdot 10^{17}$	10	$9 \cdot 10^{-26}$	200	105
ADC parameters					
Type	A [V]	Bits n	f_N [Hz]	r_c [Ω]	r_d [Ω]
NI 6289	10	18	64	300	10k

Table 16: Op-amp and ADC parameters used in the self-noise model calculations.

Fig. 218 shows the outcome of Eq. (143) with the seismic stations parameters (given in Tab. 16) along with the T240 self-noise provided by the manufacturer and the measured ADC and amplifier noise. The latter was obtained by short-circuiting the amplifier input with a impedance equal to that of the seismometer output (300 Ω). The ADC and amplifier noise is consistent with the expected values from Eq. (143), the dip in measured noise above 10 Hz is due to the seismometer response function. This suggests that the electronic noise is dominated by ADC noise. The total noise of the system stays below the NLNM between 0.03 and 8 Hz and is dominated by the T240 self-noise, except between 0.3 and 20 Hz where the amplifier electronic noise plays a dominate role.

The on-site seismic measurements were made over a period of 5 to 6 days. Care was taken to ensure that the measurement time includes at least a weekend and a number of week days. To characterize seismic measurements the amplitude of each frequency component of the velocity channels are calculated using Fourier analysis. In all of the following results a fast Fourier transform (FFT) was performed on stretches of 128 seconds of data to obtain an power spectral density (PSD) in $(\text{m}^2/\text{s}^4)/\text{Hz}$. The PSDs are averaged over a period of half an hour. Averaged PSD values are smoothed by taking the average of the PSD values in a constant relative bandwidth of 1/10 decade. (So for low frequencies the averaging is over only a few points, for high frequencies the averaging is over many more points). For comparison the new high and low noise models are also plotted. These models indicate theoretical values for extremely high and extremely low seismic noise locations respectively. Spectral variation plots are used here to not only show the amplitude of the seismic signal but also how much time, as a percentage, is spent at a certain level. This is indicated by the color of the plot. The spectral variation plots also contain three solid line plots to indicate the mode and the 90 and 10 % levels. The mode is the most

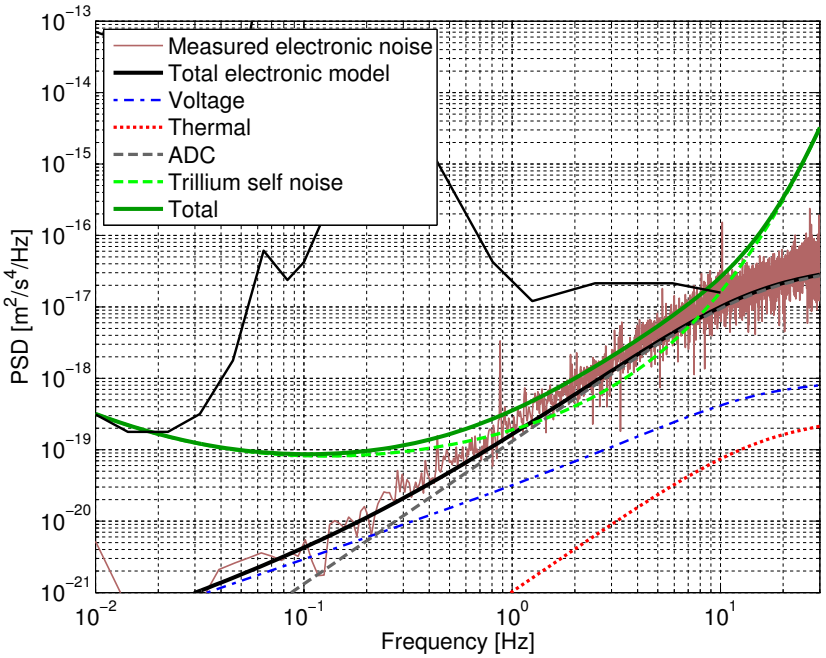

Figure 218: Noise characterization of the seismic data acquisition system. The main contributor to the electronica noise is ADC noise calculated from Eq. (143) and voltage noise from the first stage op-amp of the pre-amplifier. The Trillium 240 self-noise is provided by the manufacturer. The total noise is below the low noise model between 0.03 and 8 Hz.

common PSD value in each frequency bin, and 90 and 10 % levels indicate the point under which the PSD will stay for 90 or 10 % of the time, respectively.

B.2 Seismic measurement results

All the seismic measurements have been made possible with the dedication and help from a vast number of locals. To all the people (see also section 7) that have provided their expertise, time and assistance we would like to extend a sincere thank you.

Germany - Black forest

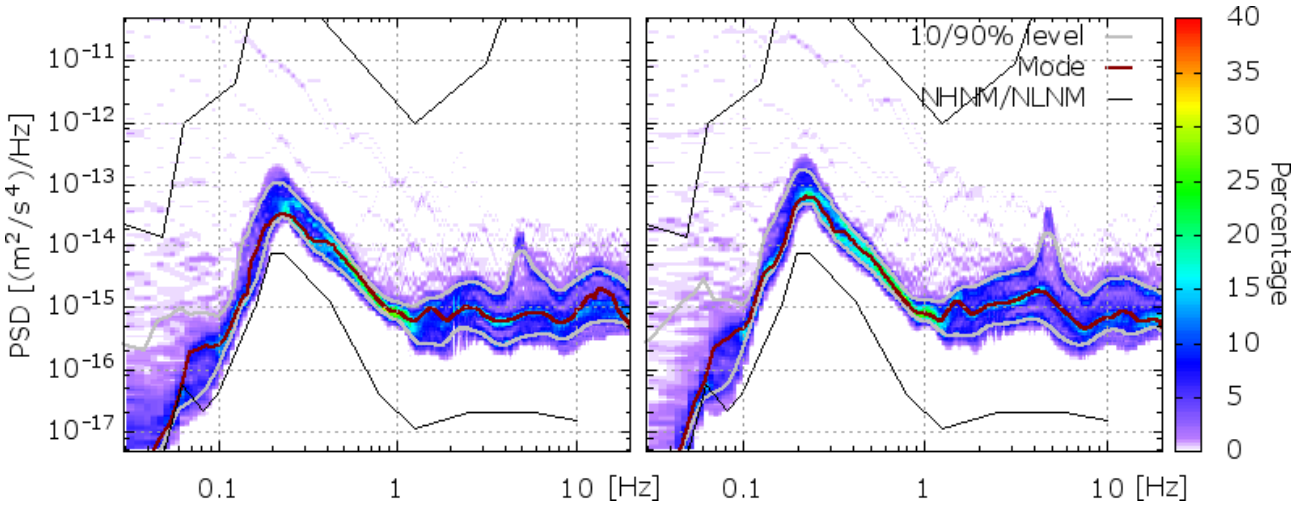

Figure 219: The horizontal component (left) and the vertical component (right) power spectral density plotted as a spectral variation from the Germany - Black forest site.

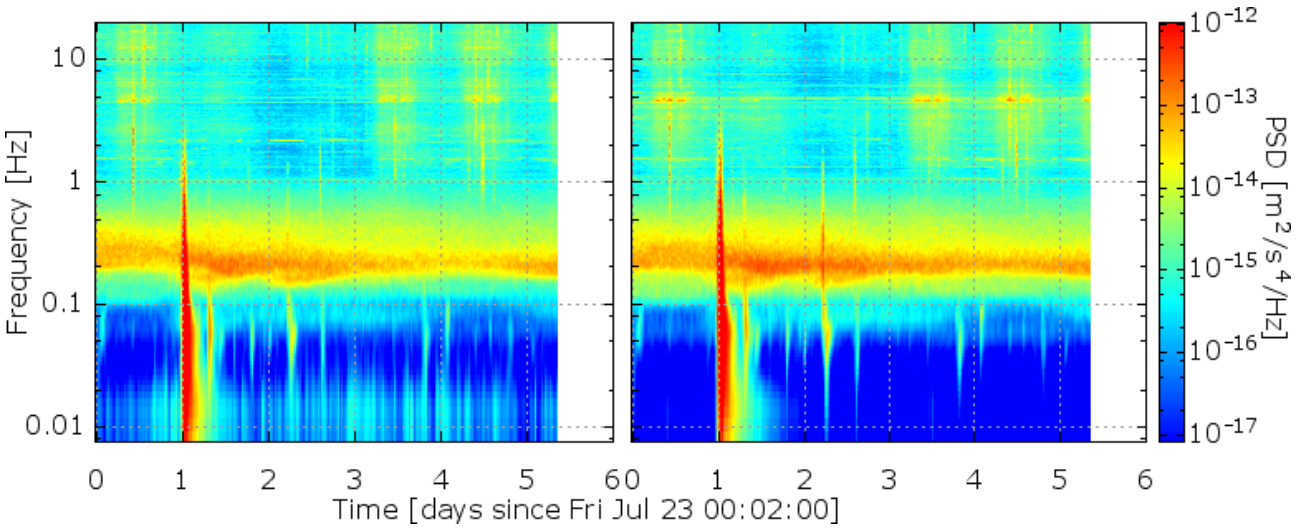

Figure 220: The spectrogram of the horizontal (left) and vertical (right) component from the Germany - Black forest site.

Spain - Laboratorio Subterréneo de Canfranc

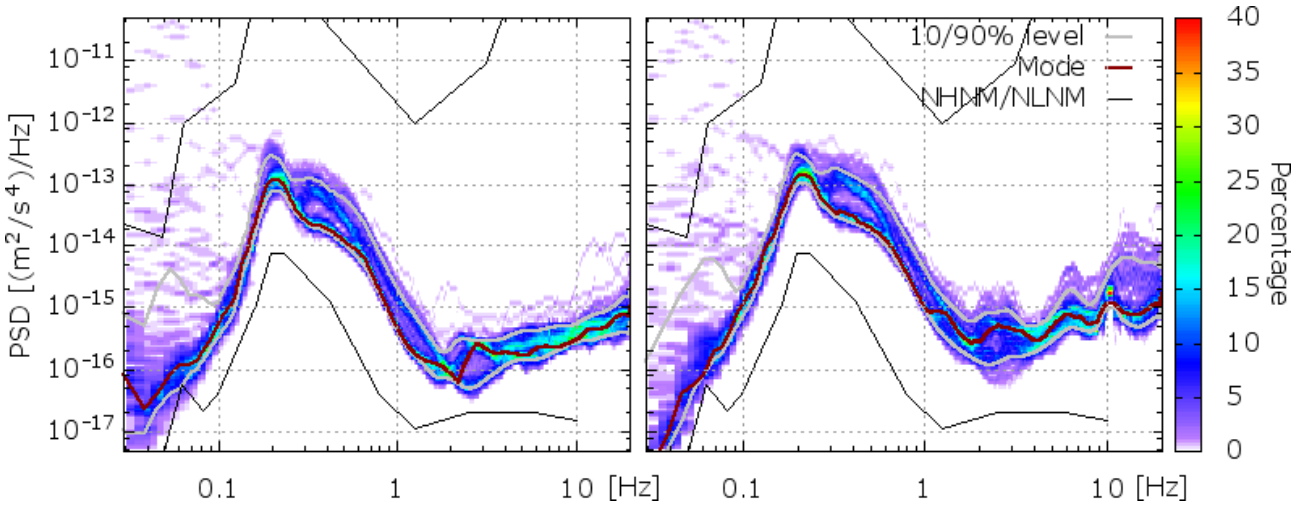

Figure 221: The horizontal component (left) and the vertical component (right) power spectral density plotted as a spectral variation from the Spain - Laboratorio Subterréneo de Canfranc site.

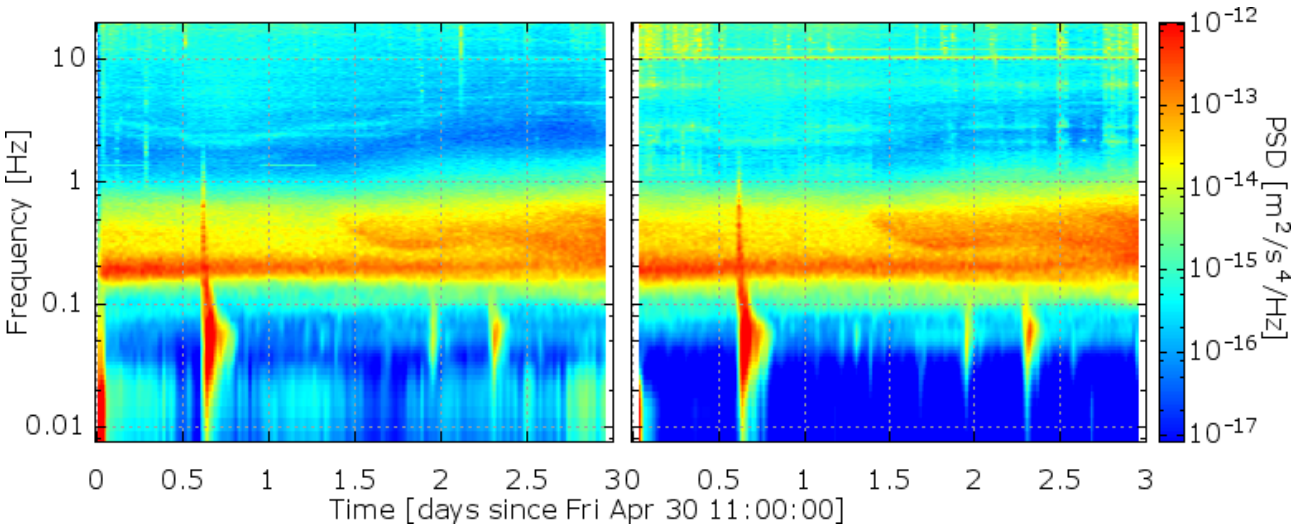

Figure 222: The spectrogram of the horizontal (left) and vertical (right) component from the Spain - Laboratorio SubterrÃ¡neo de Canfranc site.

Finland - Sumiainen

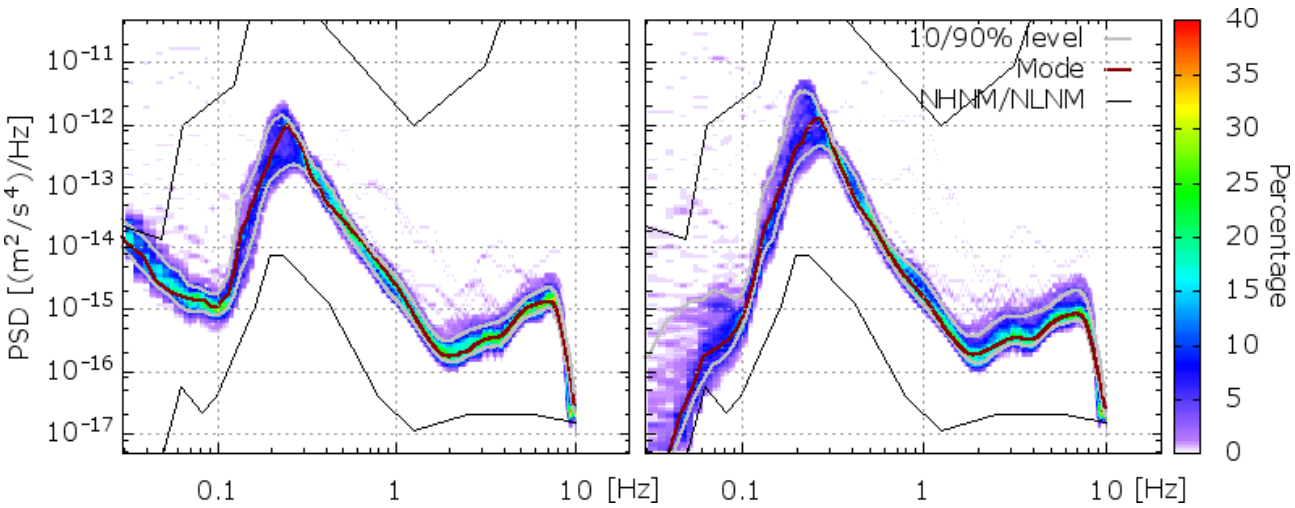

Figure 223: The horizontal component (left) and the vertical component (right) power spectral density plotted as a spectral variation from the Finland - Sumiainen site.

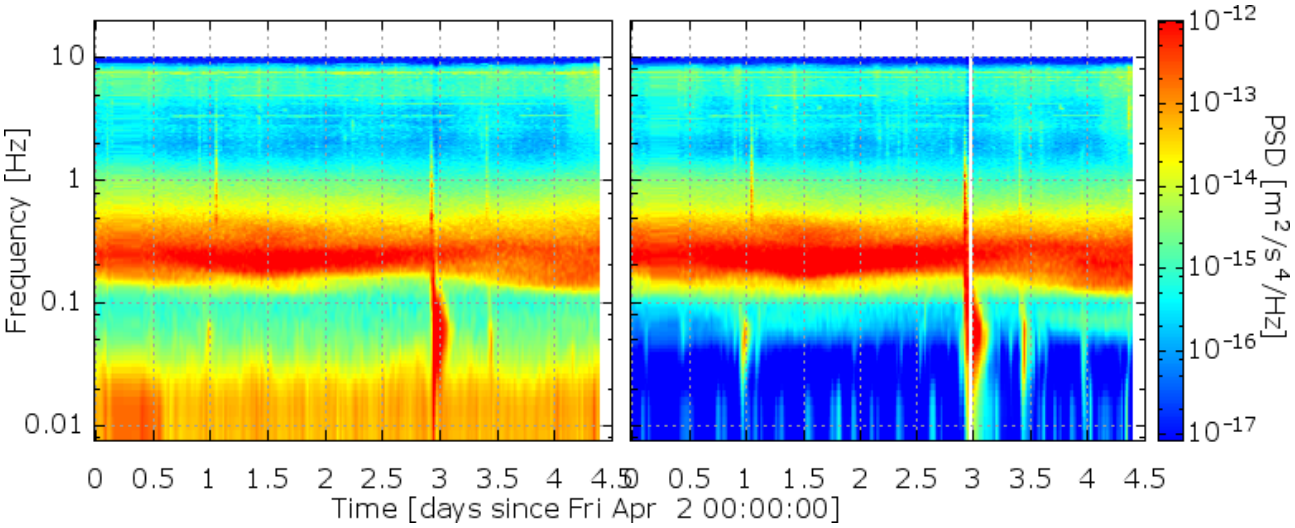

Figure 224: The spectrogram of the horizontal (left) and vertical (right) component from the Finland - Sumiainen site.

France - Frejus

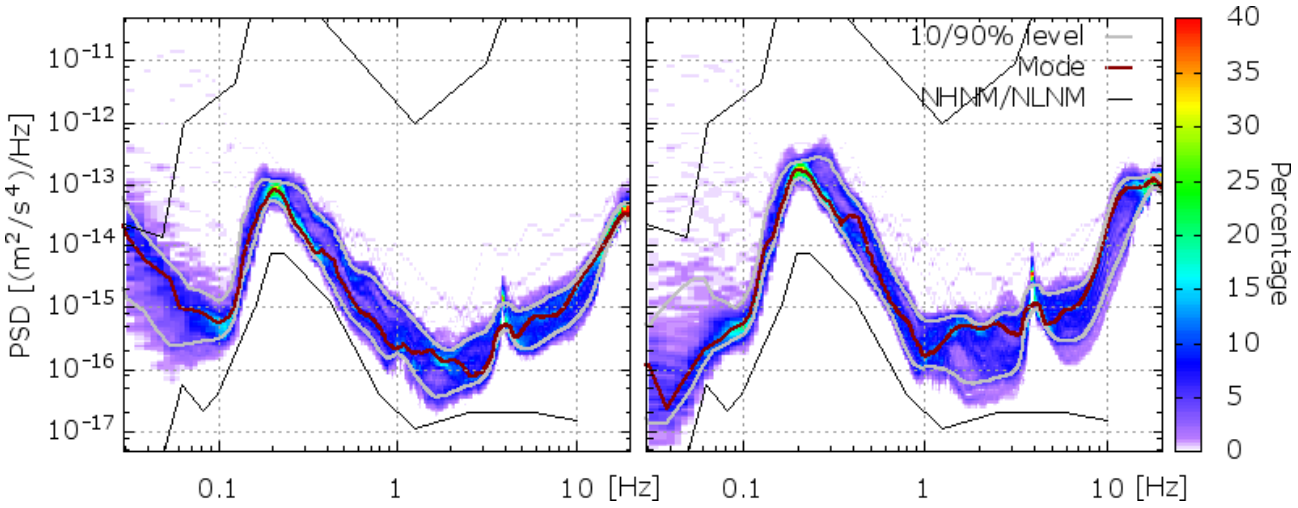

Figure 225: The horizontal component (left) and the vertical component (right) power spectral density plotted as a spectral variation from the France - Frejus site.

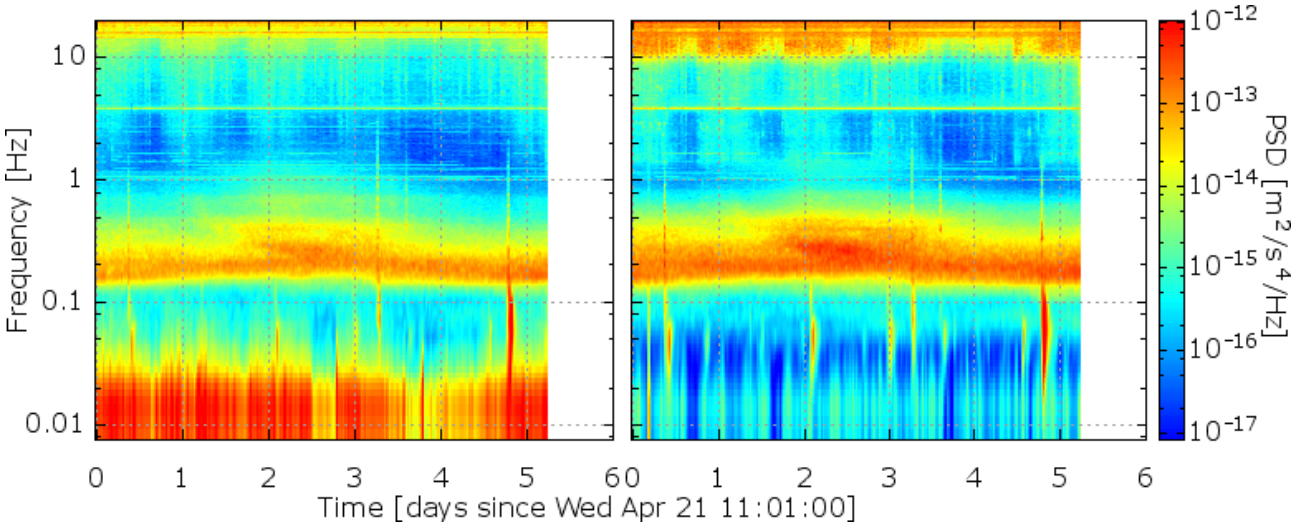

Figure 226: The spectrogram of the horizontal (left) and vertical (right) component from the France - Frejus site.

Italy - Gran Sasso

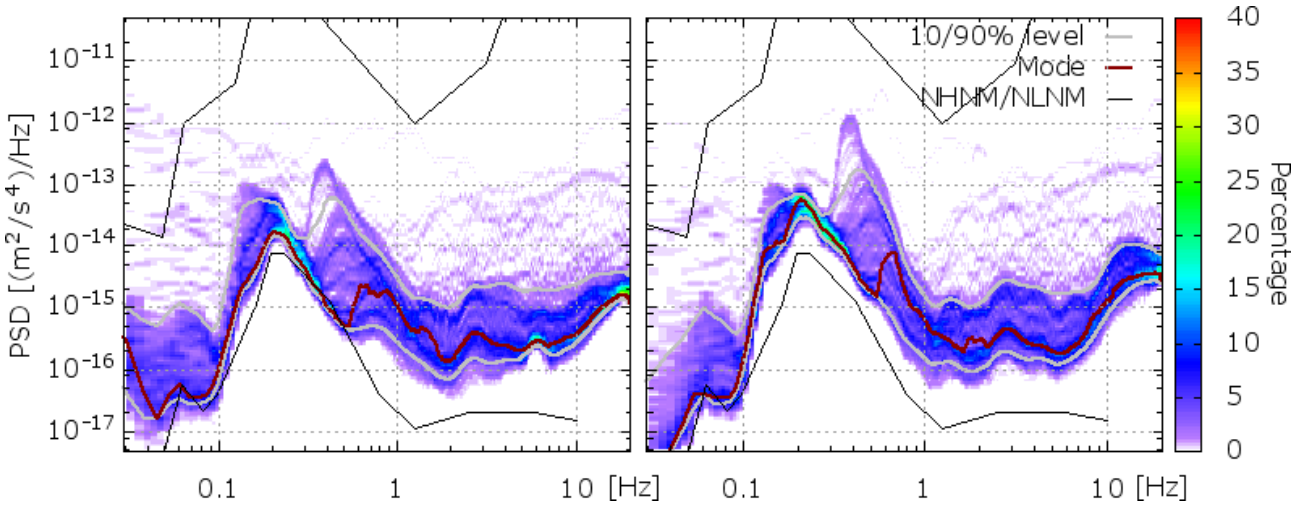

Figure 227: The horizontal component (left) and the vertical component (right) power spectral density plotted as a spectral variation from the Italy - Gran Sasso site.

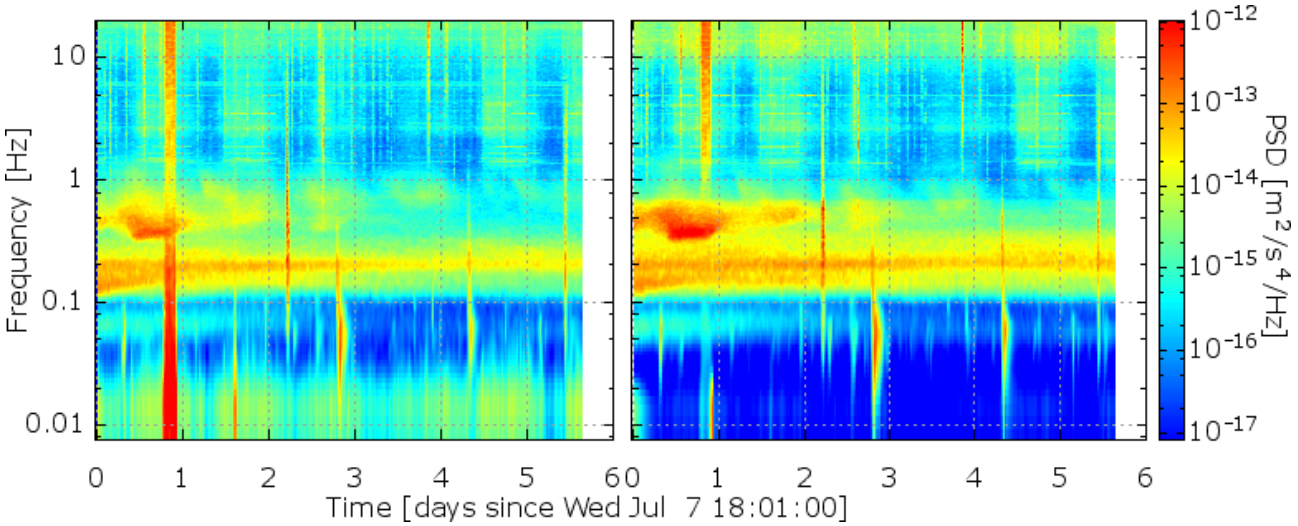

Figure 228: The spectrogram of the horizontal (left) and vertical (right) component from the Italy - Gran Sasso site.

Japan - Kamioka mine

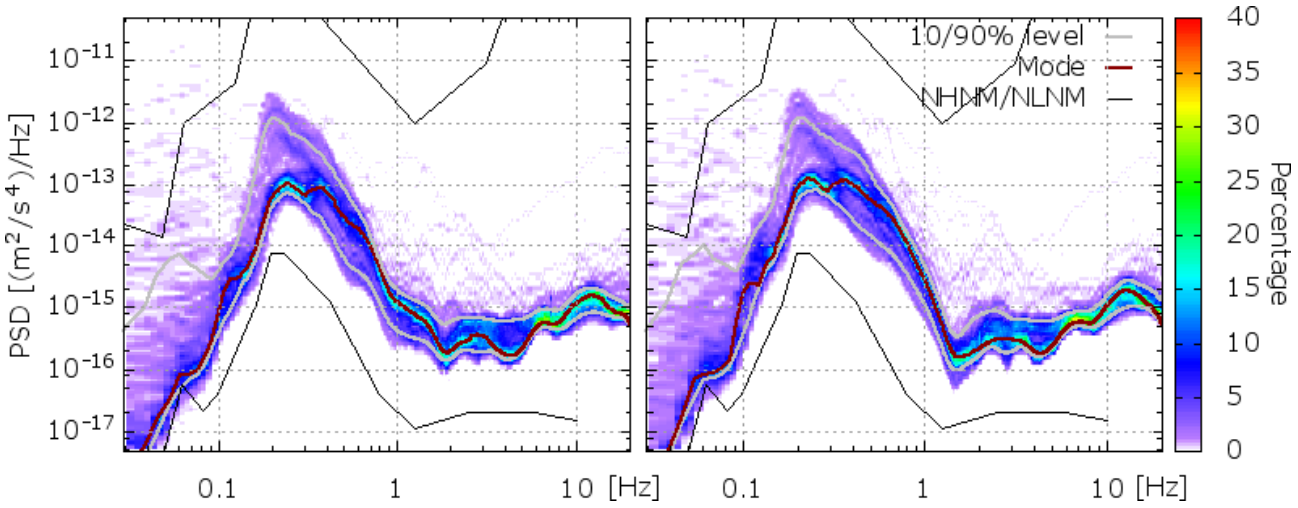

Figure 229: The horizontal component (left) and the vertical component (right) power spectral density plotted as a spectral variation from the Japan - Kamioka mine site.

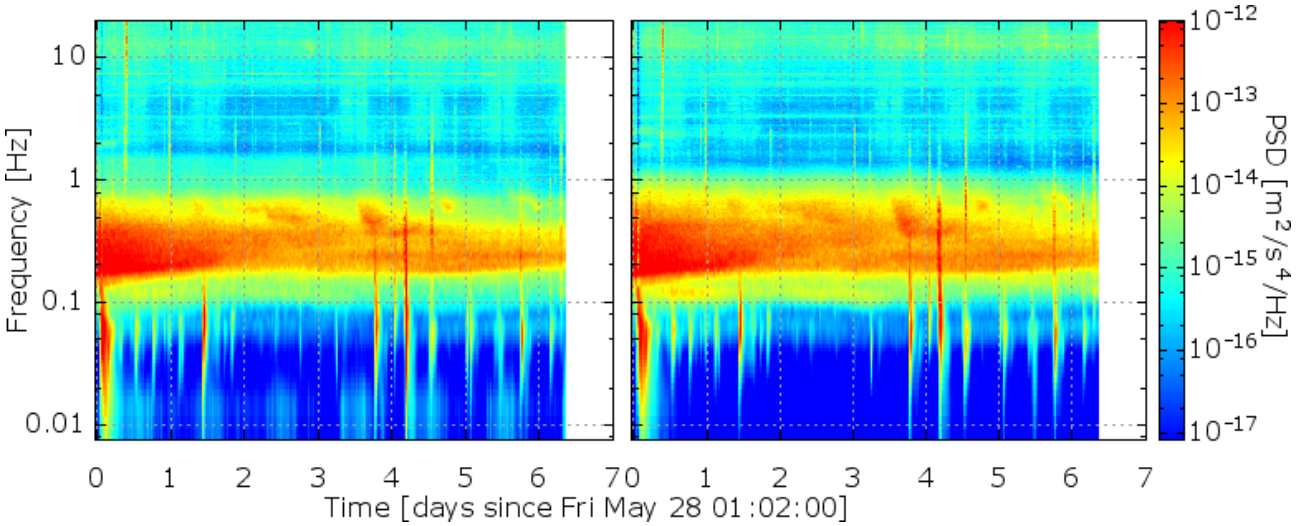

Figure 230: The spectrogram of the horizontal (left) and vertical (right) component from the Japan - Kamioka mine site.

Germany - Moxa

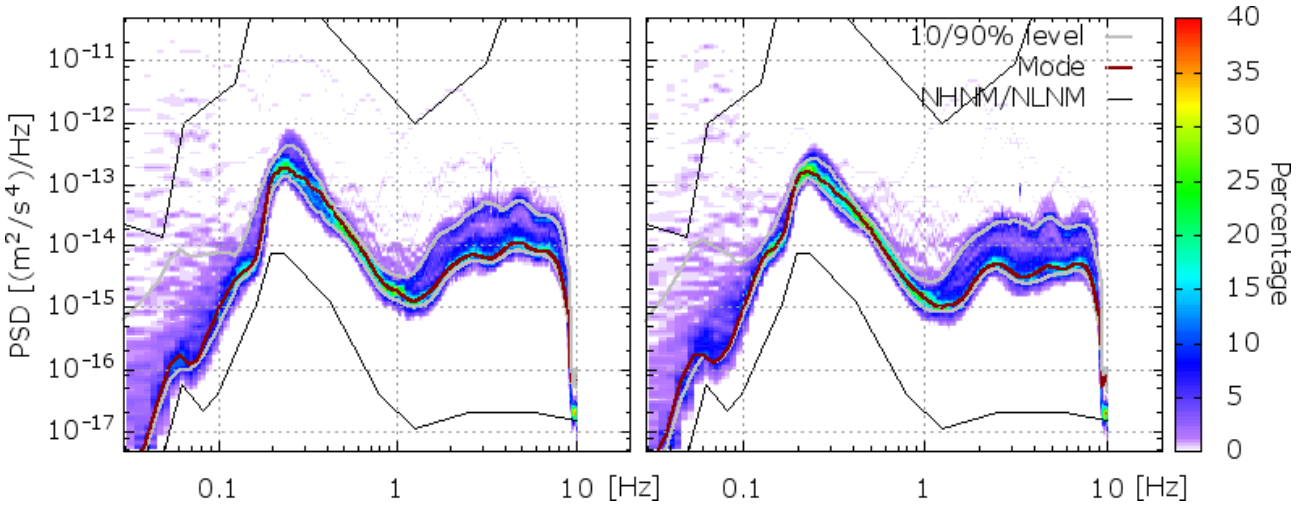

Figure 231: The horizontal component (left) and the vertical component (right) power spectral density plotted as a spectral variation from the Germany - Moxa site.

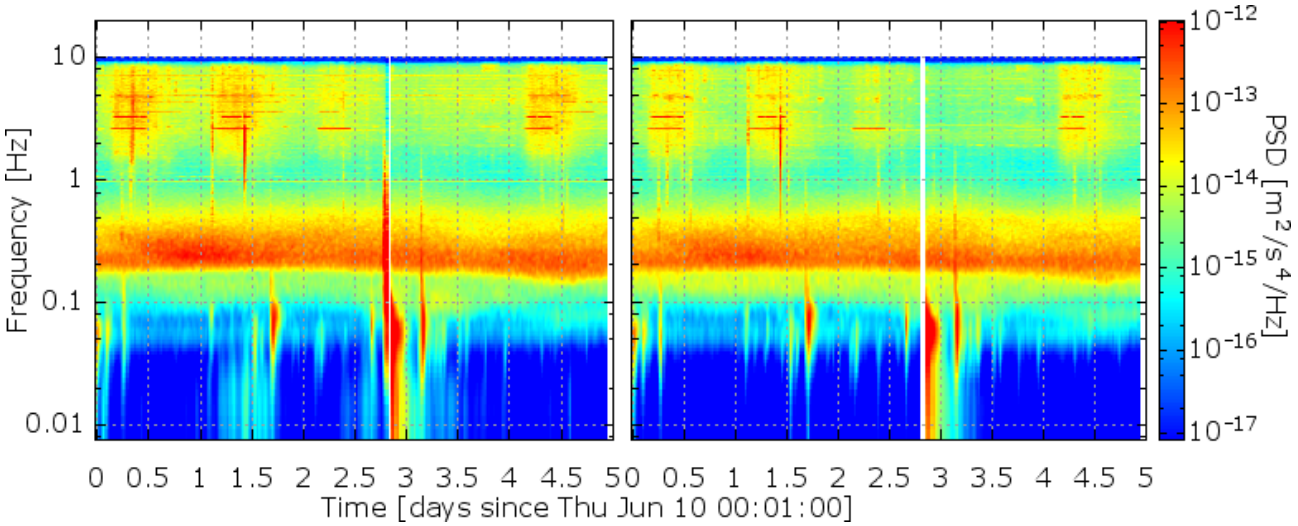

Figure 232: The spectrogram of the horizontal (left) and vertical (right) component from the Germany - Moxa site.

Netherlands - Heimansgroeve

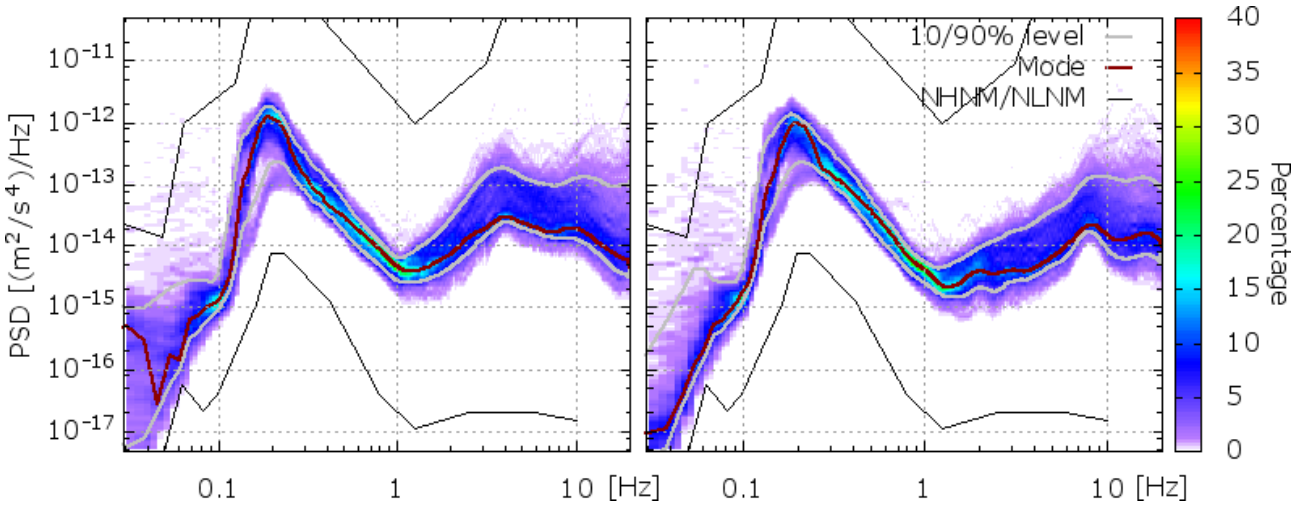

Figure 233: The horizontal component (left) and the vertical component (right) power spectral density plotted as a spectral variation from the Netherlands - Heimansgroeve site.

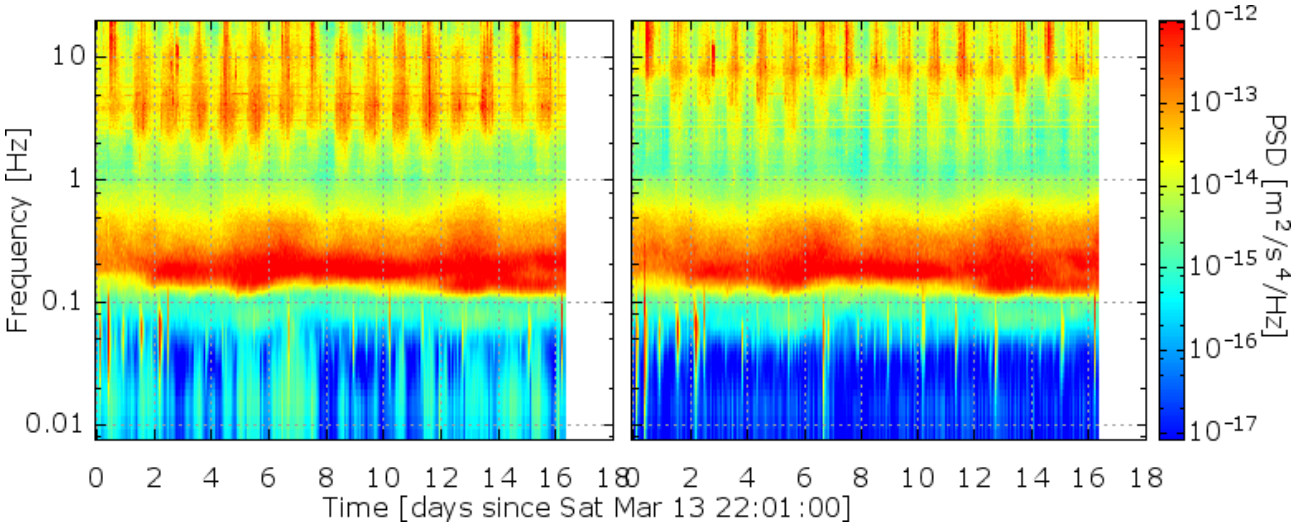

Figure 234: The spectrogram of the horizontal (left) and vertical (right) component from the Netherlands - Heimansgroeve site.

Romania - Slanic-Prahova

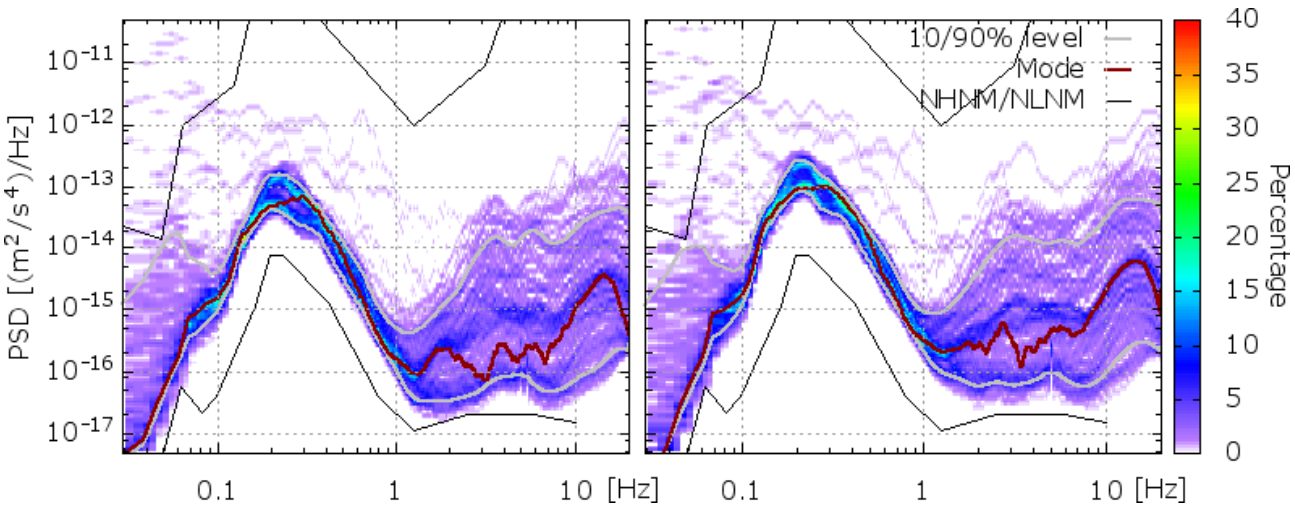

Figure 235: The horizontal component (left) and the vertical component (right) power spectral density plotted as a spectral variation from the Romania - Slanic-Prahova site.

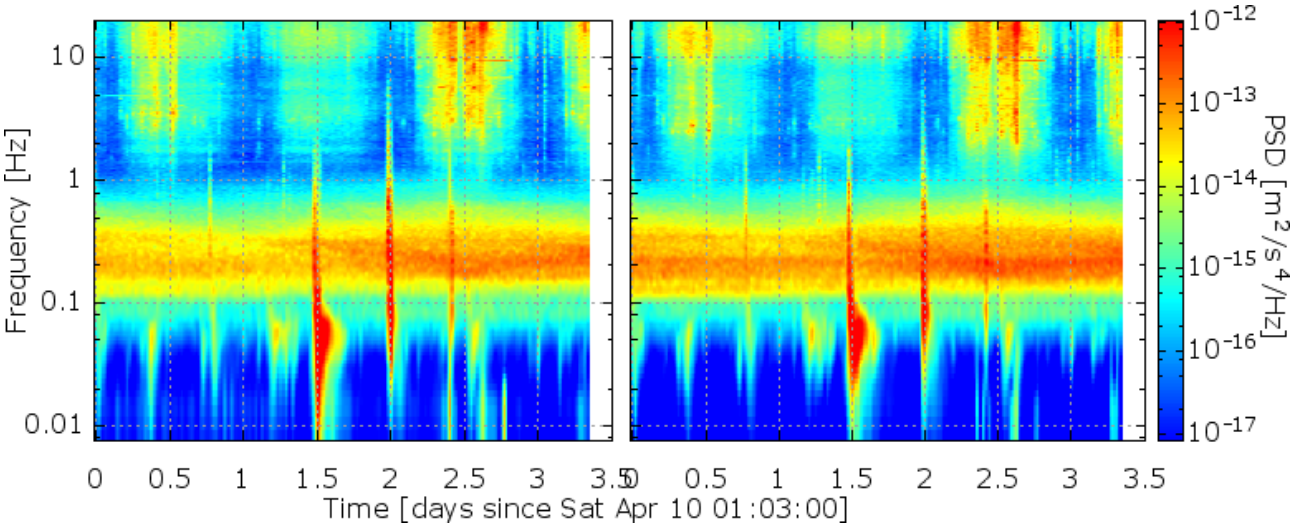

Figure 236: The spectrogram of the horizontal (left) and vertical (right) component from the Romania - Slanic-Prahova site.

Belgium - Mol

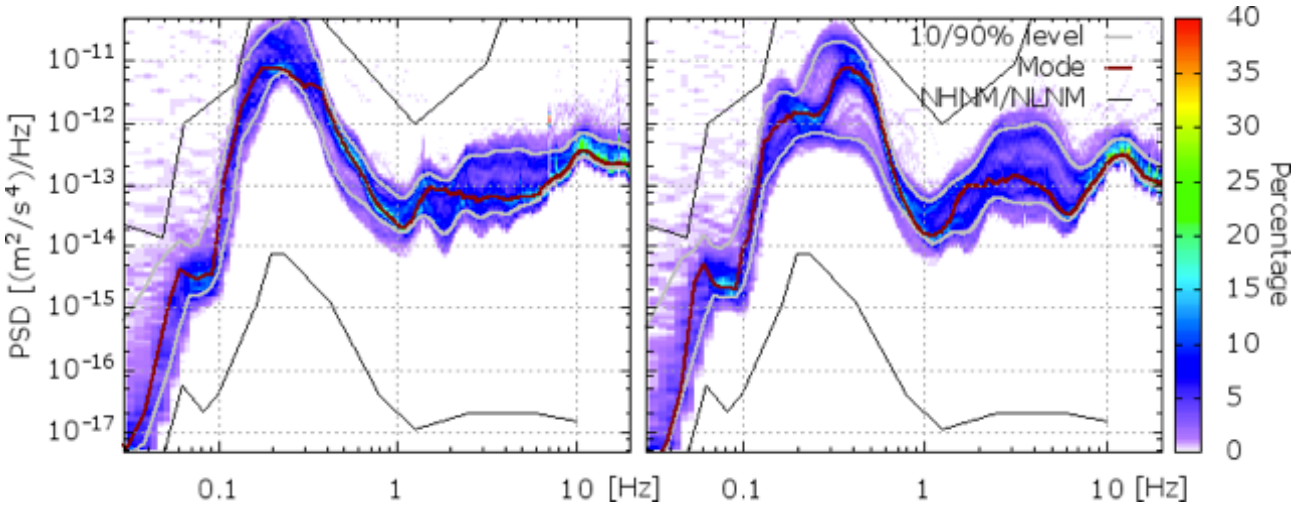

Figure 237: The horizontal component (left) and the vertical component (right) power spectral density plotted as a spectral variation from the Romania - Slanic-Prahova site.

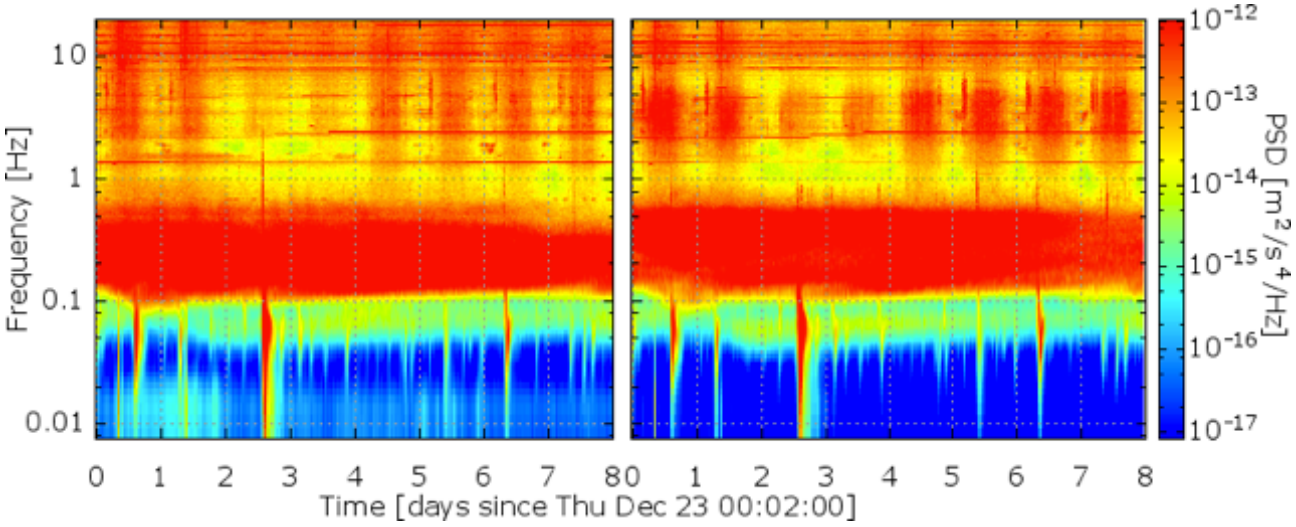

Figure 238: The spectrogram of the horizontal (left) and vertical (right) component from the Romania - Slanic-Prahova site.

B.3 The geometric configuration factor

The notation adopted here is that used in [650] and in [651]. The configuration factor from a differential area element dA_1 to a second element dA_2 is denoted by dF_{d1-d2}. In general, such a factor is given by

$$dF_{d1-d2} = \frac{\cos\theta_1 \, \cos\theta_2}{\pi S_{1-2}^2} \, dA_2 \tag{145}$$

where the quantities on the right-hand-side are shown in Fig. 239

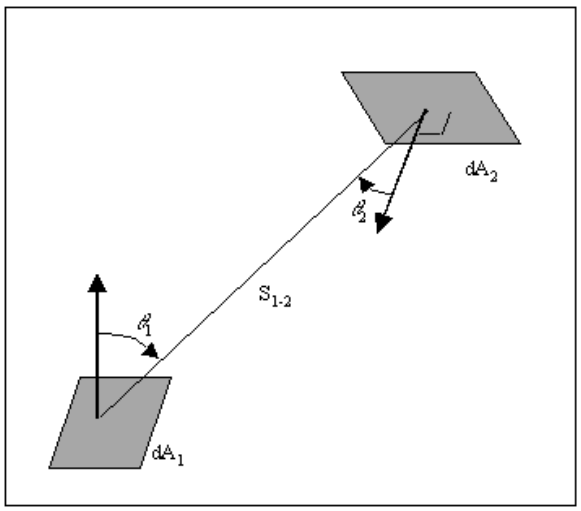

Figure 239: Defining geometry for configuration factor (from [651])

For the case of A1 and A2 both finite, the configuration factor is

$$F_{1-2} = \frac{1}{A_1} \int_{A_1} \int_{A_2} \frac{\cos\theta_1 \, \cos\theta_2}{\pi S_{1-2}^2} \, dA_2 \, dA_1 \tag{146}$$

leading to the reciprocity relation

$$A_1 F_{1-2} = A_2 F_{2-1} \tag{147}$$

For each section at fixed temperature we need to calculate the geometric factor of the interior surface of circular cylinder of radius R to a disk of radius r where $r < R$. The disk is perpendicular to axis of cylinder, and the axis of the cylinder passes through center of disk (see Fig. 240) [652, 653].

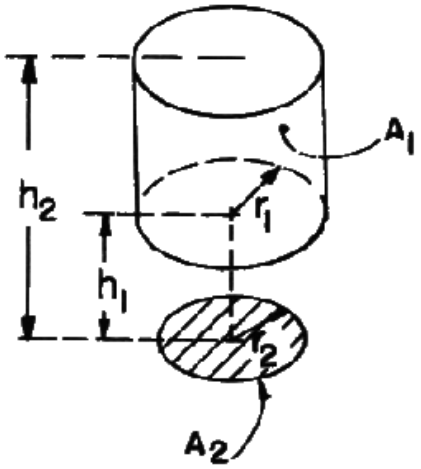

Figure 240: Defining symbols in eq.148 and eq.152 (from [651])

With the definitions:

$$R = \frac{r_1}{r_2} \tag{148}$$

$$H_1 = \frac{h_1}{r_2} \tag{149}$$

$$H_2 = \frac{h_2}{r_2} \tag{150}$$

$$X = H^2 + R^2 + 1 \tag{151}$$

the equation is:

$$F_{1-2} = \frac{1}{4R(H_2 - H_1)} \left[(X_1 - X_2) - (X_1^2 - 4R^2)^{1/2} + (X_2^2 - 4R^2)^{1/2} \right] \tag{152}$$

B.4 Diffusely emitting surfaces

On actual engineering surfaces it is reasonable, as a first approximation [650, 654], to represent the reflectance ρ as being divided into diffuse δ and mirror specular μ components:

$$\rho = \delta + \mu \tag{153}$$

In addition, we assume an opaque gray body, whose radiation is emitted diffusely according to Lambert's cosine law [650]. The emitted flux depends on the absolute temperature, T, of the surface, the surface emissivity, ϵ, and the Stefan-Boltzmann constant, σ, in the combination $\epsilon\sigma T^4$. Kirchoff's law states that the same surface element will absorb only the fraction ϵ of the incident radiation, while reflecting the fraction $\rho = 1 - \epsilon$, so that

$$\epsilon + \delta + \mu = 1 \tag{154}$$

In the diffuse limit ($\mu = 0$, $\rho = \delta$), we let G represent the radiant flux incident on a unit surface. Then for a diffusely emitting surface with a diffuse reflectance, δ, the radiosity, J, given by

$$J = \epsilon\sigma T^4 + \delta G \tag{155}$$

represents the diffusely distributed radiant flux leaving a unit surface element [655]. The net inward radiative heat flux, q, is then given the difference between the irradiation and the radiosity:

$$q = G - J \tag{156}$$

Using eq. 155 and eq. 156 we can eliminate J and obtain a general expression for the net inward heat flux into the opaque body based on G and T. From eq. 154 with $\mu = 0$ we get $\epsilon = 1 - \delta$, thus q is given by:

$$q = \epsilon \left(G - \sigma T^4 \right) \tag{157}$$

Starting from Eq. 157 the contribution to the thermal radiation heat transfer coming from diffuse reflectivity was calculated for the geometry given in Fig. 100 by a finite-element model.

B.5 Vacuum System Parameters

	ET-HF	ET-LF
Max residual pressure	$1.6 \cdot 10^{-10}$[mbar]	$1.6 \cdot 10^{-10}$[mbar]
Residual gas composition Hydrogen $1 \cdot 10^{-10}$[mbar] Water $5 \cdot 10^{-11}$[mbar] Others $1 \cdot 10^{-11}$[mbar]		
Residual gas noise	$0.8 \cdot 10^{-25}$[m $Hz^{-0.5}$]	$0.7 \cdot 10^{-25}$[m $Hz^{-0.5}$]
Vacuum enclosure material	304L Stainless Steel	304L Stainless Steel
Arm pipes diameter / length	0.9 m / 10 km	0.75 m / 10 km
Filter pipes diameter / length	0.6 m / 300 m (one pipe)	0.69 m / 10 km (two pipes)
Arm pipes bake-out	one week at 150 C	one week at 150 C
Pipes permanent pumping	5000 l/s every 500 m	5000 l/s every 50 0m
Cryotraps	10 m / 77 K	5 m / 4 K + 50 m / 77 K
Towers diameter / height	up to 3 m / 10 m	up to 3 m / 20 m

Table 17: Vacuum System Parameters

C Suspensions

C.1 Cryogenic compatibility of materials for Superattenuator construction

In this appendix some guide lines to select materials and components for the construction of a *Superattenuator* working in a cryogenic environment are reported. Doing this it will help in the understanding process of the interface problems linked to the presence of a cryogenic payload suspended from an anti-seismic system. During our investigation, based on data coming from literature and on some lab tests performed by Virgo collaboration, no preliminary hypothesis on the operating temperature has been done keeping the maximum flexibility. Even if some construction materials (stainless steel, $OFHC$ copper, etc.) can be used down to liquid helium temperature this does not represents a limiting factor of our investigation. However, for each element of the chain, it is necessary to perform a careful characterisation test of the thermal expansion coefficient. The presence of very sophisticated optics, indeed, requests a particular attention to avoid the environment contamination that needs to be carefully controlled. The conclusions of our activity, summarised in the following, are discussed in detail in [656].

- *Actuators*: the position of different elements of the suspension system, especially those ones close to the optical payload, must be moved for the interferometer control. Some commercial stepping motors designed for Ultra High Vacuum (UHV) and cryogenic applications are available, but they should be tested and qualified by a dedicated characterisation measurement performed in the standard working conditions. An AML motor has been tested successfully at Virgo down to a few Kelvin [$F.Frasconi$, $Private\ communication$]. Cryogenic lubricants should also be selected, avoiding those ones having chemical composition based on hydrocarbon and fluorine for possible contamination issues.
- *Cabling*: the great variety of control systems and sensors in Einstein Telescope will require a large number of electrical connections, that should have low thermal conductivity (to reduce heat exchange), low electrical resistivity (to reduce dissipation), high flexibility (to reduce noise injection) and low contamination. An optimization of conductors and insulator dimensions as a function of current and operating temperature is required. As detailed in [656], some low out-gassing samples tested in Virgo can be used at low temperatures: Pyre-Ml insulated wires, alumina insulated wires, Gore-Tex ribbons. While $Kapton$ and $PTFE$ insulation have been already tested for satellite applications.
- *Adhesives*: during the construction of the interferometer there will certainly be the need to bond several elements of Einstein Telescope. For this reason some adhesives could be selected and used. They must be able to withstand thermal cycling and match the thermal expansion coefficients of the bonded elements. The adhesives properties are strongly dependent on the specific batch and on the curing recipe (time and temperature). As shown in [656] several solutions are available for testing them down to liquid helium temperature, including epoxy and ceramic adhesives. Even if some of them have been tested on optical surfaces, the bonding strength, the thermal expansion coefficient, ageing and contamination issues on long

time scales must be measured by a dedicated research activity devoted to a precise characterisation of each adhesive.

- *Magnets*: the properties of magnetic materials are strongly dependent on the temperature. Ferrite and Alnico materials are not suited below 200 K because they change magnetic properties. Neodymium-Iron-Boron magnets show an increasing magnetic field going from room temperature down to 140-120 K while decreasing its value at lower temperature. Samarium-Cobalt magnets show a magnetic field slowly decreasing with decreasing temperature and they have been successfully used down to liquid helium temperature. A critical point is the "Barkhausen noise" that we are studying in a dedicated *R&D* activity for a precise characterisation, as reported in the coil -magnet actuator section.

As mentioned in the suspension chapter, another important topic deals with the creep noise of suspension elastic elements generated by the high stress applied. It has been already shown in the same section that the noise due to the dislocations motion and to their avalanche formation are typical events triggered by the temperature increasing, important only in the last stage(s) of the *Superattenuator*. The natural question is: what is the situation of this micro-glitch noise in a cryogenic environment? Even if creep is associated to an increment of the environmental temperature, cryogenic creep is not necessarily negligible, as observed for *OFHC* copper. Data from literature on this subject and relative to steels as reported in [657] are insufficient and scattered. Since most part of previous studies investigated transient creep, it is suggested to perform very long term tests before using this material in a cryogenic environment. In [657] typical apparatus to measure creep in a cryogenic environment are outlined. An *R&D* program is required only if in the final design of Einstein Telescope some elastic elements will operate at low temperature.

C.2 Geometric anti-springs as seismic attenuation filters

An evolution of the Virgo mechanical filter to be used as vertical seismic noise suppression system, has been developed at Caltech [351], AEI and NIKHEF. The anti-spring effect of this new technolgy is based on a particular geometry of the elastic elements, the blades, mounted on a metallic disk and forming the so called *Geometric Anti-Springs* (GAS) filter. Seismic filters based on this effect have been successfully employed in the TAMA interferometer [658] and now the GAS solution represents the baseline option for the optical components suspensions of the cryogenic and underground gravitational waves detector LCGT at Kamioka in Japan.

The GAS filter, shown in Fig. 241, consists of a set of radially arranged cantilever spring blades clamped at the base to a common frame disk and opposing each other via a central ring or keystone.

The blades are machined with a flat triangular shape while they become bended as soon as a suitable load is applied on their bases pushing the mechanical structure toward the filter center. Since these elastic elements are compressed with a very high stress, (up to 1.8 GPa) the material choice for their construction plays a fondamental role. To this purpose the Maraging steel [348] has been selected because it guarantees low creep noise level, low deformability and high thermal stability under high stress applied. Each filter is an adjustable spring formed by a crown of curved cantilever blades compressed each against the other: the constrained radial stress creates an anti-spring effect (geometric anti-spring) [659] that allows a low effective stiffness to be achieved in the vertical direction when the nominal load is hung.

The main features of the GAS filters are:

- Compact design with a limited number of mechanical elements;
- UHV compatible;
- Fast assembly and tuning;
- Possibility to implement an active control (e.g. electro-magnetic antispring EMAS) with LVDT sensor and a voice coil actuator integrated into the design;
- Excellent attenuation performance when carefully tuned and operated under vacuum.

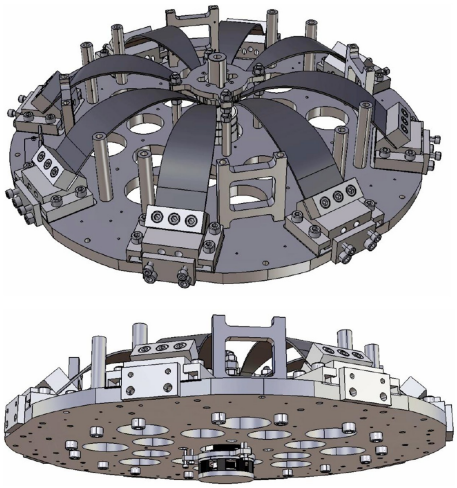

Figure 241: A 3D rendering view of a GAS filter used as seismic isolation system for the 10 m long interferometer at AEI Hannover. The same technology is used by the NIKHEF group for the the optical bench of the light injection in the interfrometer of Advanced Virgo. A voice coil actuator, visible on the bottom part of the figure, is located in the center of the filter.

A photo of a geometric anti-spring assembled at NIKHEF and an LCGT prototype is shown in Fig. 242.

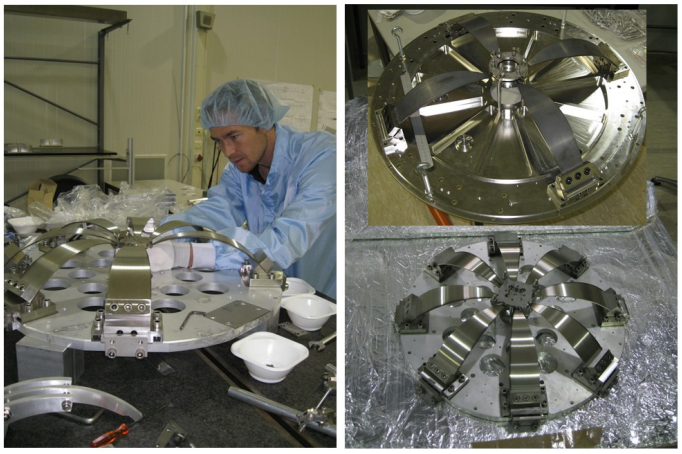

Figure 242: Pictures of the GAS filter prototypes. The left and top right panels show a filter built and tested at NIKHEF for the Virgo external injection bench [660]. The bottom right panel shows a prototype for LCGT suspension.

A vertical cut-off frequency down to 0.30 Hz have been obtained through a fine mechanical adjustment of the compression rate while longer natural period can be achieved by applying positive feedback (the so-called electro-magnetic anti-spring - EMAS). The performance of a GAS filter is shown in Fig. 243 where a comparison between the model and the measurements performed using a system with three blades is reported. In the plot a seismic attenuation performance of -60 dB at about 10 Hz is visible while an isolation level down to -80 dB (at frequncy higher than 10 Hz) can be reached by using a set of overcompensating wands [661].

Finite element analysis (FEA) [662] and a measurements campaign on a GAS filter prototype are in progress in AEI Hannover and NIKHEF. They provide valuable input for the GAS filter fine tuning and its behaviour as a function of the environmental temperature. Detailed studies on a filter prototype for LCGT project and with different blades shapes are also in progress at NIKHEF.

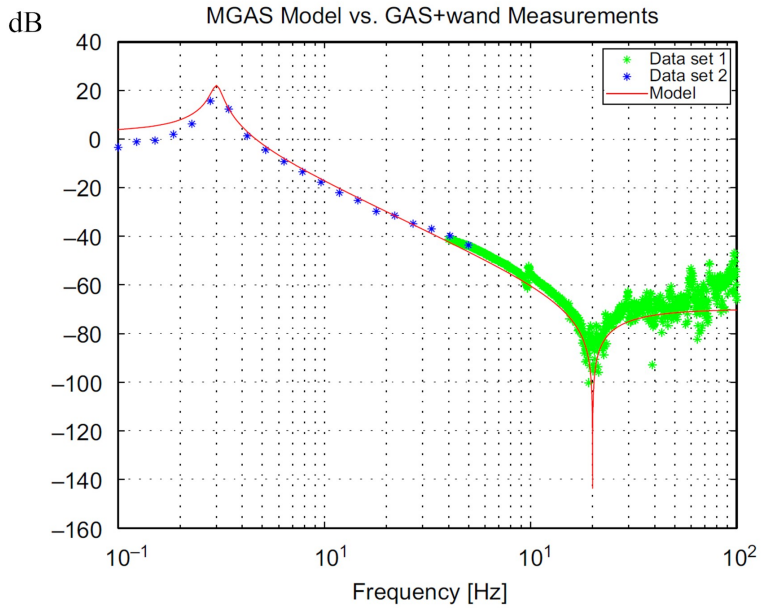

Figure 243: Vertical attenuation performance of a GAS filter with overcompensating wands [661]

C.3 The LIGO active seismic filters

In the the Advanced LIGO project the seismic noise suppression problem has been fixed using a different approach [6]. The suspension chain has been designed including an in-vacuum two-stage active isolation system where the inner modes are reduced by sensing the stage motion and applying forces in feedback loops.

The in-vacuum attenuator provides isolation above about 0.2 Hz and consists of two-stages platforms connected to each other by springs. Each stage is supported by three maraging steel blade springs and short pendulums from the stage above it to provide vertical and horizontal compliance in six degrees of freedom (see fig. 244 left side). Contained in each stage are six position sensors and six seismometers which collectively measure motion in all degrees of freedom. The signals from these detectors are feed-back to magnetic actuators to reduce the motion of the platforms. The rigid body modes of these stages are between 1.3 and 7 Hz, while the unity gain frequency of the control loop will be at about 25 Hz. Together, these stages provide isolation of about a factor of 300 at 1 Hz and about 3000 at 10 Hz, in amplitude. The second stage contains an optical table, from which the suspension and test mass are supported.

The Advanced LIGO test masses will be supported by suspensions that hang below the seismic isolation platforms. These suspensions are multistage pendulums with a final stage consisting of the test mass hanging on fused silica fibers. They will provide additional passive isolation, allow for necessary control forces to be applied without adding excess noise, and minimize the effect of thermal noise.

In addition to the main quadruple suspension chain that supports the test mass, there will also be a nearly identical reaction chain placed 5 mm behind it (see fig. 244 right side). This chain will allow control forces for global angular and longitudinal degrees of freedom to be applied from a quiet platform. These forces will be hierarchically used, with large forces applied with coils and magnets between both the upper intermediate and penultimate masses but with fine control forces applied with an electrostatic drive (ESD). The ESD is a gold pattern deposited on the face of the final reaction mass and applies forces to the test mass with an electrostatic field. Local damping of all the low frequency suspension modes will be done with co-located sensors and actuators on the top mass to insure that any sensing noise will be well isolated from the test mass.

The main feature of this suspension, shorter than the Virgo Superattenuator, is represented by the fact that the final isolation requirements are reached with a system based mainly on an active hierarchical control.

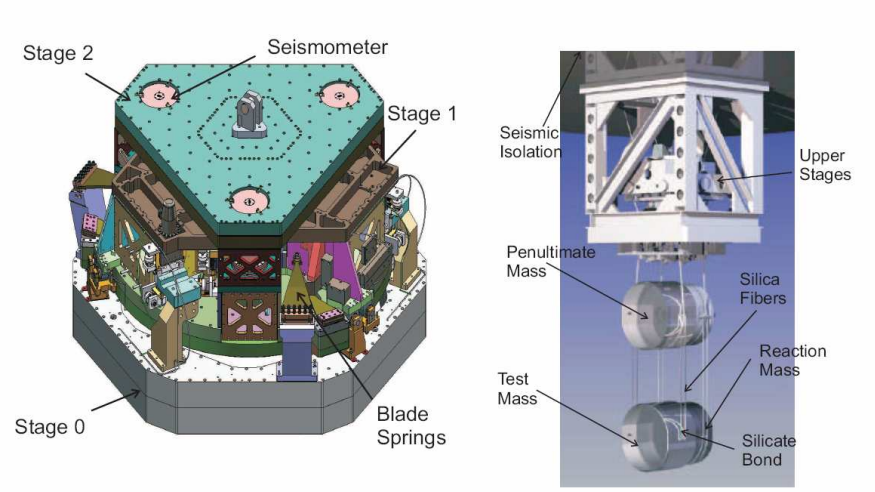

Figure 244: Internal stages of the large vacuum chamber seismic isolation system (left side). Advanced LIGO suspension: the test mass connected at the bottom to the penultimate mass above it with silica fibers. On right side, the reaction mass behind the test mass is visible

D Optics

D.1 Table of layout parameters

	ET-HF	**ET-LF**
Approximate frequency range	10–10^4 Hz	1–250 Hz
Detection scheme	DC readout	DC readout
Input power (after IMC)	500 W	3 W
Laser wavelength	1064 nm	1550 nm
Beam shape	LG_{33}	TEM_{00}
ARM CAVITIES		
Arm length	10 km	10 km
Opening angle	60 °	60 °
Arm power	3 MW	18 kW
Temperature	290 K	10 K
Mirror material	fused silica	silicon
Mirror diameter	62 cm	>45 cm
Mirror thickness	30 cm	about 50 cm
Mirror mass	200 kg	211 kg
Beam radius (at mirror)	7.2 cm	9.0 cm
Beam waist (symmetric cavity)	2.51 cm	2.9 cm
RoC (symmetric cavity)	5690 m	5580 m
Scatter loss per surface	37.5 ppm	37.5 ppm
Finesse	880	880
Reflective coating ITM	tantala/silica	tantala/silica
	8 $\lambda/4$ doublets	9 $\lambda/4$ doublets
Reflective coating ETM	tantala/silica	tantala/silica
	17 $\lambda/4$ doublets	18 $\lambda/4$ doublets
Transmission ITM	7000 ppm	7000 ppm
Transmission ETM	6 ppm	6 ppm
CENTRAL INTERFEROMETER		
SR-phase	tuned (0.0)	detuned (0.6)
Focussing element	in or near the ITM	in or near the ITM
	focal length = 303 m	focal length = 303 m
Distance ITM–BS	300 m	300 m
Distance BS–MPR	10 m	10 m
Recycling cavity length	310 m	310 m
Beam size on BS	4.7 mm	6 mm
Beam size on MPR	2.7 mm	3.4 mm
Recycling gain	21.6	21.6
Recycling cavity free spectral range	484 kHz	484 kHz
Round-trip Guoy phase	10.5 °	9.6 °
mode separation frequency	28 kHz	26 kHz
Recycling cavity temperature	room temperature	room temperature
Beam splitter material	fused silica	fused silica
Transmission PRM	4.6 %	4.6 %
Transmission SRM	10 %	20 %
FILTER CAVITIES		

	ET-HF	**ET-LF**
Quantum noise suppression	frequency-dependent squeezing	frequency-dependent squeezing
Filter cavities	1×300 m	2×10 km
Half-bandwidth	5.7 Hz	5.7 Hz and 1.5 Hz
Detuning	25.4 Hz	25.4 Hz and 6.6 Hz
Round-trip loss	75 ppm	75 ppm

D.2 Quantum noise features of different topologies

Within the design study, there have been carried out many optimizations of the quantum noise of different detectors towards different astrophysical sources. In the following example noise curves are given which are optimized towards the detection of neutron star binary inspirals, as carried out in Ref. [663]. Furthermore, those examples are attempts to realize the ambitious sensitivity goal of the Einstein telescope gravitational-wave detector – in terms of the quantum noise – with a single interferometer, where the total circulating optical power is limited to 3 MW, the arm length to 10 km and the test-mass weight to a few hundred kilograms.

The first candidate among the different types of detectors is the **simple position meter**: here we gather the Michelson interferometer topology w/o or w/ arm cavities, w/o or w/ power-recycling, w/o or w/ tuned signal-recycling. The installation of a power-recycling cavity (by putting an additional mirror at the bright port

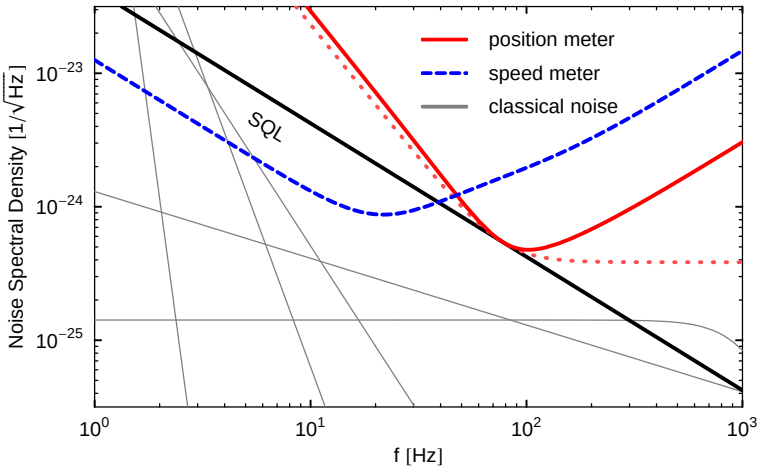

Figure 245: Example quantum noise spectral densities for position meter (solid curve), with adiabatically eliminated cavity mode (dotted curve) and for a speed meter (dashed curve): 10 km arms; 3 MW optical power; 120 kg test-masses. Example noise budget (gray curves): seismic and gravity gradient noise reduced by a huge amount compared to advanced detectors; suspension thermal noise (coating thermal noise) reduced by a factor of 10 (4.5) in amplitude compared to estimations for Advanced LIGO detector.

of the interferometer) and the use of cavities in the arms of the interferometer, both increase the circulating optical power inside the interferometer. As a consequence, they force up the interaction strength between the laser field and the test-masses and reduce the shot noise (dominating at high frequencies) but at the same time increase the radiation-pressure noise (dominating at low frequencies). From another point of view (namely when the required circulating optical power in the arms is fixed) the power-recycling technique can help to lower the required input power, while using arm cavities can additionally lower the optical power which has to pass the beam splitter preventing thermal effects in the transmissive optics to become a major problem and also minimizing the bright port / dark port coupling due to the beam splitter motion [664]. The use of arm cavities additionally increases the signal-susceptibility within the finite bandwidth of the optical arm resonators, but decreases it above the optical bandwidth making the shot noise spectral density raise towards higher frequencies and therefore decreasing the bandwidth of the gravitational-wave detector. Signal-recycling,

as proposed by Meers [665], can increase the bandwidth of the gravitational-wave detector by creating an effective bandwidth. Here an additional mirror, the so-called signal-recycling mirror, is placed at the dark output port of the interferometer, reflecting parts of the signal modulation fields back into the interferometer and forming a signal-recycling cavity either together with the end mirrors of a simple Michelson interferometer or with the input mirrors of the interferometer's arm cavities. The signal becomes recycled which basically means that it is amplified due to an increase in interaction time between the laser field and the mirrors. If the signal-recycling cavity is tuned with respect to the laser frequency, the optical resonator (or the two coupled optical resonators in a Michelson interferometer with arm-cavities) have an (effective) bandwidth which can be greater than the original bandwidth of the arm-cavities. In such a detector the quantum noise depends mostly on the optical power circulating in the interferometer, the bandwidth and length of the cavities and the test-mass weight, which altogether define the measurement frequency, i.e. the frequency where the quantum noise touches the standard quantum limit. The strength of the quantum noise is basically shuffled between high and low frequencies by shifting the measurement frequency towards higher frequencies. All first generation laser-interferometric gravitational-wave detectors (LIGO [2], VIRGO [666] and TAMA [667]) so far have been constructed as simple position meters. In Fig. 245 we see example quantum noise curves for a simple position meter and the standard quantum limit for such a detector with 10 km long arms and 120 kg test-masses. The quantum noise spectral densities are plotted for 3 MW circulating optical power in the arms for a detector with an effective 50 Hz cavity-bandwidth (solid curve) and for a detector with adiabatically eliminated cavity mode (dotted curve).

Furthermore, the different contributions of an example classical noise budget for a third generation detector with classical noise reduction techniques as described within this design study are additionally adumbrated in Fig. 245 and show a big gap between the assumed classical noise budget and the standard quantum limit. It is obvious that such a simple position meter would be totally dominated by the quantum noise, i.e. a waste of efforts in the classical noise reduction, and therefore not suitable to reach the sensitivity goal of the Einstein Telescope gravitational-wave detector. For more details refer to e.g. Ref. [663] and references therein.

When the signal-recycling cavity is neither resonant nor anti-resonant with respect to the carrier frequency, the technique is called detuned signal-recycling. In this case the sensitivity of the interferometer is enhanced around the (effective) optical resonance frequency. The signal-recycling technique was already successfully tested in a 30 m prototype gravitational-wave detector [668, 669], in table-top experiments [670, 671] and has been implemented into the GEO600 detector [672]. Additionally, the optomechanical coupling in the arm cavities of a Michelson interferometer with detuned signal-recycling can induce a restoring force onto the differential motion of the arm-cavities mirrors—the optical spring effect [673], which can up-shift the mechanical resonance frequency into the detection band. We will call such a device an **optical spring interferometer** [673–676]. Here the sensitivity of the detector is further enhanced around the second resonance, the optical spring resonance. This quantum-noise reduction technique belongs to the second group of methods as defined in Sec. 5.5. The optical spring effect has been demonstrated in a 40 m prototype gravitational-wave detector [671] and in several table-top experiments [677]. Furthermore, the Advanced LIGO detector [5] will very likely make use of the optical spring effect in order to improve the sensitivity. In Fig. 246 example noise curves for such an optical spring interferometer are given. For the optical spring interferometer the optimal quantum noise—optimal for the specific wave-form of neutron star binary inspirals—becomes very narrowly peaked around 100 Hz [663]. Also for different astrophysical sources the optimal quantum noise spectral density is rather narrowband than broadband. Note that the concept of the optical spring interferometer can be extended to double optical spring interferometer [676] or even multiples optical spring interferometer, where a second (or multiple) additional frequency-shifted carrier is injected into the interferometer, creating additional optical springs which can be used to enhance the sensitivity and additionally stabilize the optomechanical system within the detection band.

A third detector option is to use an optical **speed meter** [678]. The idea of using speed meter detectors was to totally avoid the quantum back-action of the measurement. At first glance it seems to be very promising to reach this goal by measuring the speed of the test-masses, because it is usually proportional to the momentum, which, as a conserved quantity, cannot introduce any back-action noise. But once the detector couples to the speed, it has been shown that in this case the conjugate momentum is actually not proportional to the speed of the test object [428]. Nevertheless, a speed meter is able to surpass the standard quantum limit broadbandly by removing the (frequency-independent) radiation-pressure noise from the measurement output. The dashed

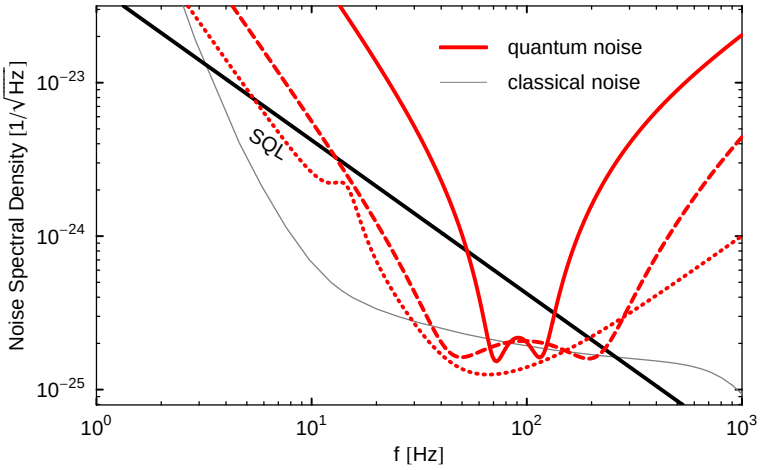

Figure 246: Example quantum noise spectral densities for a Michelson interferometer with arm cavities (10 km; 3 MW optical power; 120 kg test-mass mirrors) and detuned signal-recycling (136 Hz effective detuning; 16 Hz effective bandwidth; $2\pi/3$ detection angle)—no input-squeezing (solid curve), no optical loss. Dashed curve: with 10 dB frequency-dependent input-squeezing (208 Hz effective detuning; 120 Hz effective bandwidth; $0.44\,\pi$ detection angle) and 75 ppm loss in each 10 km filter cavity. Dotted curve: variational output with 10 dB frequency-independent input-squeezing (4 Hz effective detuning, 180 Hz effective bandwidth) and 75 ppm loss in each 10 km filter cavity.

curve in Fig. 245 shows a typical example for a quantum noise curve of a speed meter interferometer—here with 10 km long arms, 120 kg test-masses, 3 MW circulating optical power in a 35 Hz-bandwidth cavity. There exist different proposed designs of how to realize a speed meter with different topologies: it is possible to turn a Michelson interferometer topology into a speed meter by adding a sloshing cavity [619, 620] to the interferometer at the dark output port, where the signal sloshes back and forth, realizing a time-delayed sensing of the test-mass position. Another option is to use polarizing optics and build up a speed meter from a Michelson interferometer topology by either re-sending the signal into the interferometer multiple times [679] or by circulating the light through the two arms [680] of the Michelson-like setup. The most obvious way to realize an optical speed meter, however, is by using a Sagnac topology with triangular or rectangular ring cavities in the (folded) arms [8, 418, 681]. Ignoring the influence of optical losses, all those different speed meter realizations have the same quantum noise performance [418] even though they have different technical advantages and disadvantages. The specific quantum-noise feature of a speed meter is that it has a flat response to the radiation-pressure noise at low frequencies [418], providing a constant back-action free detection quadrature. The measurement can therefore be made shot-noise limited at lower frequencies but with a decreasing signal transfer [422] (cf. Fig. 245). A detuned signal-recycling cavity turns a speed meter interferometer into an **optical inertia interferometer** [681]: the optomechanical coupling influences the dynamics of the test-masses – it modifies their dynamical mass by introducing an optical inertia. In Fig. 247 we see the quantum noise of a signal-recycled Sagnac interferometer, which provides high sensitivity mainly in the low-frequency regime, due to the speed meter effect, while the detuned signal-recycling broadens the sensitivity curve by opening it a little more to the high-frequency regime [663]. Note that the optical inertia can become in principle even negative and then can cancel the mechanical inertia. The hope is that in this way one can create a test object which has a high resonance-type mechanical susceptibility in a broad frequency band. Such a situation can also be found in the double optical spring interferometer, by exploiting the frequency dependence of the two optical springs [682].

Finally, the last option for the main interferometer, which we want to review here, the **optical transducer** [683–686], is totally different compared to the others in terms of the readout method: the idea of such schemes is not to measure the phase shift of the laser field via monitoring the outgoing modulations fields at the dark port of an interferometer but to measure the redistribution of optical energy directly inside an interferometer by converting the gravitational-wave strain via radiation pressure into real mirror motion. This motion should

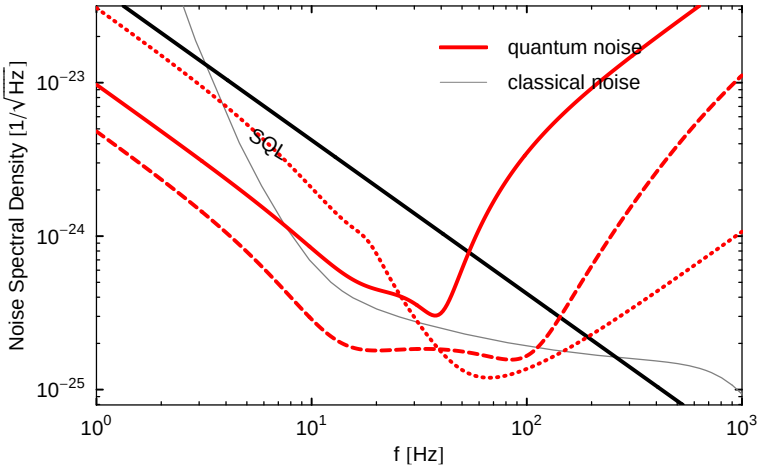

Figure 247: Example quantum noise spectral densities for a Sagnac interferometer with ring cavities (10 km; 3 MW optical power; 100 Hz bandwidth; 120 kg test-mass mirrors) and detuned signal-recycling (42 Hz effective detuning; 0.475 π detection angle)—no input-squeezing (solid curve), no optical loss. Dashed curve: with 10 dB frequency-dependent squeezed input (150 Hz bandwidth; 95 Hz effective detuning; 0.475 π detection angle) and 75 ppm loss in each 10 km filter cavity. Dotted curve: variational output with 10 dB frequency-independent squeezed input (50 Hz bandwidth; 0.5 Hz effective detuning) and 75 ppm loss in each 10 km filter cavity.

then be sensed by an additional highly sensitive local meter. The overall sensitivity to gravitational waves for such a transducer scheme depends not only on the transducer ability of the main interferometer but also on the sensitivity of the local meter. Several optical realizations have been proposed: the initial idea was to construct an optical bar, as an optical analog to an mechanical bar resonator. Later this topology was extended to the optical lever scheme [685], where the interaction strength is enhanced by the use of arm cavities. Furthermore, it had been realized before that also a detuned signal-recycled Michelson interferometer with arm cavities effectively functions as an optical bar at low frequencies, where the gravitational-wave strain is converted into mirror motion of the input mirrors of the arm cavities. In this case even the realization of a local meter is straightforward: a second frequency-shifted carrier can be inserted into the interferometer, which is anti-resonant in the arm cavities, and therefore forming a small interferometer with the arm-cavity input mirrors as its end mirrors. This local readout scheme [686] is a combination of an optical bar interferometer and a optical spring interferometer, where the two outputs can be combined in an ideal way to enhance the sensitivity at lower frequencies (optical bar) and simultaneously at higher frequencies (detuned signal-recycled Michelson).

All these different main interferometer detectors can be equipped with a technique which is usually called **input-squeezing**. The use of squeezed states of light for improving the sensitivity of gravitational-wave detectors was first proposed in 1981 by Caves [438]. He showed that the quantum noise limited sensitivity in a shot noise dominated interferometer can be enhanced by the injection of broadband (frequency-independent) squeezed fields into the interferometers signal port. Accordingly at a point, where the interferometer performance will be limited by the amount of the achievable circulating light power and the thermal load in its optics squeezed field injection can be used to either relax the high power requirement or increase the sensitivity further. The reduction of shot noise by the aid of squeezing was later experimentally shown in Refs. [447, 448, 478] (cf. Sec. 5.5.3). However, at first view the enhancement of an interferometers sensitivity with frequency independent squeezing (squeezed light with a fixed quadrature angle) can only be achieved in a certain frequency range. This is a direct consequence of the Heisenberg uncertainty principle. Considering a simple position meter, the quantum noise in its phase quadrature (shot noise) can be reduced by the amount of squeezing. Unfortunately, the quantum noise in the amplitude quadrature (radiation pressure noise) will be increased by the same amount enhancing the noise at low frequencies. Later it was revealed by Unruh [487] and others [452, 455, 488] that squeezed field injection with frequency dependent squeezing angle allows an overall quantum noise reduction including the radiation pressure noise. Motivated by the work of Unruh and Jackel & Reynaud the use of additional

input and output optics—namely filter cavities—was proposed by Kimble *et al.* [436]. Applying these filters (commonly referred to as Kimble-filters) converts a conventional interferometer into a broadband quantum non-demolition interferometer (cf. Sec. 5.5.4). The filters allow the preparation of squeezed states providing a frequency-dependent squeezed quadrature which is adapted to the interferometers quadrature rotation. The injection of such a prepared squeezed state leads to a quantum noise reduction over the entire detection band. The investigation of Kimble *et al.* was restricted to simple position meters. It was shown by Harms *et al.* [477] and Buonanno & Chen [687] that such filters applied to optical spring interferometers also allow a broadband quantum noise reduction by squeezed light. Unfortunately, quite generally two low-loss, narrow-bandwidth, and therefore long-baseline optical filter cavities are necessary to prepare the squeezed states in an optimum way. The generation of frequency-dependent squeezing utilizing one filter cavity was experimentally characterized by Chelkowski *et al.* [688] followed by the shot noise reduction of a table-top dual-recycled Michelson interferometer demonstrated by Vahlbruch *et al.* [479]. Another way to achieve an enhancement in the high frequency range without drastically worsen the low frequency sensitivity by avoiding the use of multiple long base-line filter cavities was proposed by Corbitt *et al.* [689]. Here, the use of a tuned Fabry-Perot cavity with two partly transparent mirrors was suggested acting has high-pass filters (termed amplitude filters within this context) for the squeezed field. In reflection of this filter cavity the squeezing at sideband frequencies beyond the filter cavity bandwidth is preserved whereas at low frequencies the squeezing is lost and replaced by ordinary vacuum noise. Since any optical loss of the filters mainly affects the transmitted part, the baseline of the filters can be chosen comparatively small. It has already been realized quite early that there is a transition region between the reduced noise at high frequencies and the non-increased noise at low frequencies, were the sensitivity is degraded. Later, this degradation was explained by information loss at the end mirror of the filter cavity and an additional homodyne detection was proposed to capture this information [690]. Furthermore, it has been proposed to inject additional squeezed vacuum though the filter cavity end mirror and thus suppress also the low-frequency radiation-pressure noise [691]. However, these techniques are more useful for simple position meters and are intended to be installed as a low-cost add-on during the life cycle of the second generation detectors [692], since the rotation of the squeezing ellipse around the optical resonance of optical spring interferometers cannot be compensated by these filters leading to a deceased sensitivity which can be even below that of the interferometer without input-squeezing. For speed meter interferometer the quantum noise can be reduced by input-squeezing analogously to a position meter with filter cavities [620]. But here it is also possible to achieve an enhancement at lower frequencies without drastically worsen the high frequency sensitivity avoiding the use of filter cavities [8]. Furthermore, it has been experimentally verified that the shot-noise limited sensitivity of a zero-area Sagnac interferometer can be enhanced by input-squeezing [8]. In Fig. 246 and Fig. 247 one finds examples of quantum noise spectral densities (dashed curves) for the optical spring and speed meter interferometer with frequency-dependent input squeezing in the ideal case of no optical loss.

Additionally, all main interferometer detectors can be equipped with a balanced homodyne detection and with the **variational-output** technique, which was invented conceptually in the early 1990s by Vyatchanin, Matsko and Zubova [693, 694] and later substantiated by Kimble *et al.* [436]. Here filter cavities are used to make the quadrature angle of the detected output field frequency dependent and therefore realize a broadband evasion of the radiation-pressure noise. Even though the most efficient combination of frequency-dependent input-squeezing and variational-output for the optical spring interferometer cannot be realized with Kimble-filters, different semi-optimal configuration have been found [687]. Especially at low frequencies, variational output with frequency-independent input-squeezing can in principle improve the sensitivity much more than frequency-dependent input-squeezing, but on the other hand optical losses in the filter cavities for the variational-output become even more severe [436, 695]. When the radiation-pressure noise is strong, it is required to bring enough of the quadrature without signal-content into the output in order to cancel the radiation-pressure noise and this introduces significantly higher noise due to optical losses. Moreover, optical losses in the filters remove parts at low frequencies of the already weak signal from the output. In Fig. 246 and Fig. 247 there are examples for quantum noise spectral densities (dotted curves) of variational readout interferometers in the ideal case of no optical loss given. For more details refer to Ref. [663].

D.3 Filter cavities

The necessity of filter cavities for a broadband quantum noise reduction with a squeezed state of light was described in Secs. 5.5.4 and App. D.2. In the following sections, the technical requirements for these optical filters are discussed. An important point is the required baseline length of these filter cavities in view of their optical round-trip loss (App. D.3.1). The tolerances of the determined design parameters will be discussed in App. D.3.3. Furthermore, in App. D.3.4 the optical layout with regard to the round-trip loss that will be mainly caused by scattering by the mirror surface defects is treated. Finally, the degradation of the squeezing level due to noise couplings (e.g. displacement noise in the filter cavities) will be analysed in Sec. D.3.5, leading to further estimates for the requirements.

D.3.1 Restrictions for the baseline length of the filter cavity

In this Section we start with a description of the influence of optical round-trip loss on the filter cavities performance in dependence of their baseline length and half-bandwidth. The required half-bandwidth γ_{fc} and detuning Φ_{fc} (note that we will define them as angular frequencies) of the filter cavities giving the optimal frequency-dependent squeezing angle are determined by the interferometer configuration and its induced phase-space rotation of light fields entering the interferometers output port.

Generally, any round-trip loss will degrade the squeezing level at sideband frequencies being resonant in the filter cavity (cf. Sec. 5.5.4). For a given power round-trip loss $l^2_{\mathrm{rt,fc}}$ (mainly caused by scattering) the resulting loss in reflection of the filter cavity increases with a decreasing baseline length L_{fc} of the filter. As well, for a certain length L_{fc} and a certain round-trip loss $l^2_{\mathrm{rt,fc}}$ the loss imposed on the squeezed field increases with a decreasing half-bandwidth γ_{fc} that needs to be realized.

Starting from the expression for the half-bandwidth of a lossy cavity

$$\gamma_{\mathrm{fc}} = \frac{c}{2L_{\mathrm{fc}}} \arccos\left(1 - \frac{(1-\rho_{\mathrm{c}}\sqrt{1-l^2_{\mathrm{rt,fc}}})^2}{2\rho_{\mathrm{c}}\sqrt{1-l^2_{\mathrm{rt,fc}}}}\right) \tag{158}$$

one can derive the filter cavity's coupling mirror power reflectance $R_{\mathrm{c}} = \rho_{\mathrm{c}}^2$ that is required to achieve the targeted half-bandwidth. One obtains

$$\rho_{\mathrm{c}} = \frac{1}{\sqrt{1-l^2_{\mathrm{rt,fc}}}}\left[2 - \cos(\mathcal{F}') - \sqrt{\cos^2(\mathcal{F}') - 4\cos(\mathcal{F}') + 3}\right] \tag{159}$$

with

$$\mathcal{F}' = \frac{2\gamma_{\mathrm{fc}}L_{\mathrm{fc}}}{c} = \frac{\gamma_{\mathrm{fc}}}{\mathrm{FSR}_{\mathrm{fc}}} = \frac{\pi}{\mathcal{F}_{\mathrm{fc}}}\,. \tag{160}$$

Graph e) in Fig. 248 shows the value for $R_{\mathrm{c}} = \rho_{\mathrm{c}}^2$ according to Eq. (159). In the underlying calculations the baseline length L_{fc} and the round-trip loss $l^2_{\mathrm{rt,fc}}$ were considered with 10 km and 75 ppm, respectively. The tuning of the filter cavity was exemplary set to $\Phi_{\mathrm{fc}} = \gamma_{\mathrm{fc}}L_{\mathrm{fc}}/c$. It can be seen, that for small half-bandwidths γ_{fc} the reflectance R_{c} comes close to unity. Correspondingly, the resulting finesse rises as shown in Graph d). It can be seen from Eq. (159) that there are two fundamental restrictions for the choice of the filter cavity length. First, for great values of the finesse (i.e. for small half-bandwidths) we obtain

$$\lim_{\gamma_{\mathrm{fc}}\to 0}\rho_{\mathrm{c}} = \frac{1}{\sqrt{1-l^2_{\mathrm{rt,fc}}}} > 1 \tag{161}$$

which does not represent a physical solution. Thus, there must exist a value L_{min} such that for $L_{\mathrm{min}} < L_{\mathrm{fc}}$ we always have $\rho_{\mathrm{c}} < 1$. The expression for L_{min} can be derived to

$$L_{\mathrm{min}} = \frac{c}{2\gamma_{\mathrm{fc}}}\arccos\left[2 - \frac{2-l^2_{\mathrm{rt,fc}}}{2\sqrt{1-l^2_{\mathrm{rt,fc}}}}\right]\,. \tag{162}$$

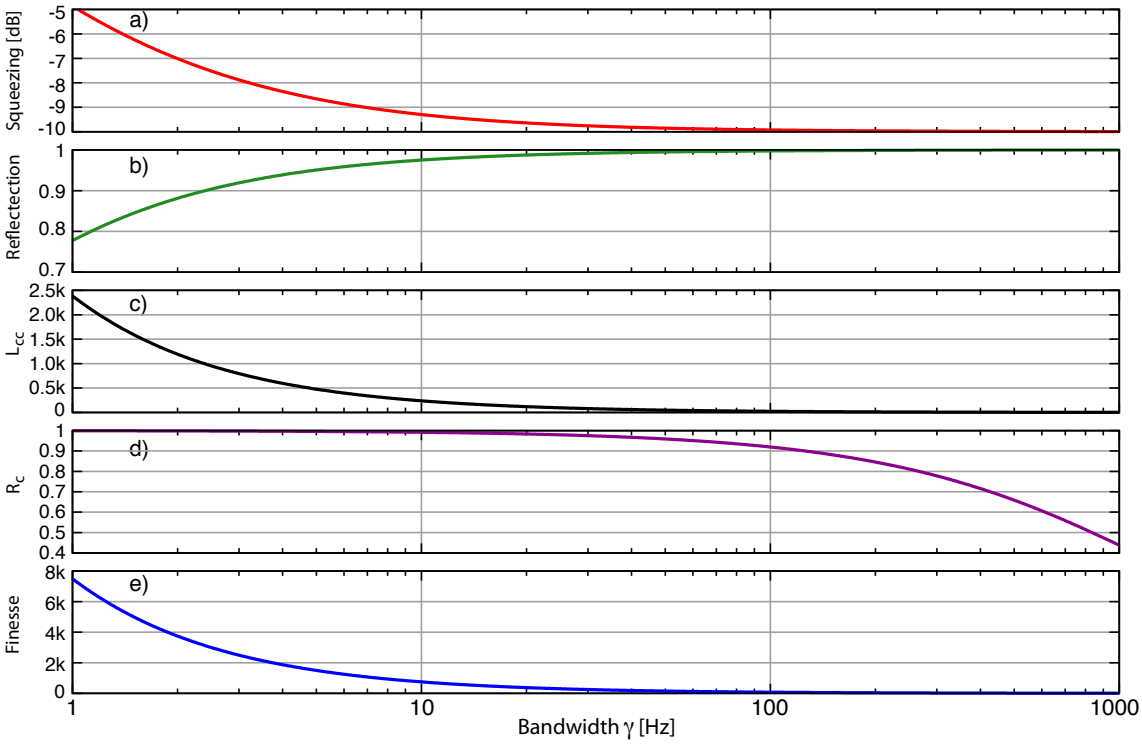

Figure 248: Filter cavity properties in dependence of its half-bandwidth γ_{fc}. a) the remaining detectable squeezing level in reflection of the filter cavity and b) its reflectance at the frequency $\Omega = \Phi_{\mathrm{fc}} L_{\mathrm{fc}}/c$. In c) the value for L_{cc} is shown according to Eq. (163). Curve d) shows the finesse and e) the coupling mirror reflectance R_{c} given by Eq. (159). For all traces a filter cavity length $L_{\mathrm{fc}} = 10\,\mathrm{km}$ and a round-trip loss $l^2_{\mathrm{rt,fc}} = 75\,\mathrm{ppm}$ was assumed. An initial pure 10 dB squeezed state was considered. It can be seen that the impact of the round-trip loss becomes significant for $\gamma_{\mathrm{fc}} < 2\pi \cdot 10\,\mathrm{Hz}$.

Second, for $L_{\rm fc} < L_{\rm cc}$ we obtain $\rho_{\rm c} > \sqrt{1-l_{\rm rt,fc}^2}$ and the filter cavity becomes under-coupled. But even in the most general case, the interferometer represents an over-coupled cavity. Hence, an under-coupled filter cavity with $L_{\rm fc} < L_{\rm cc}$ can not provide the phase-space rotation required for the generation of the optimal squeezing angle.

To keep $\rho_{\rm c} < \sqrt{1-l_{\rm rt,fc}^2}$ the filter cavity length needs to be

$$L_{\rm fc} > L_{\rm cc} = \frac{c}{2\gamma_{\rm fc}} \arccos\left[2 - \frac{1+(1-l_{\rm rt,fc}^2)^2}{2(1-l_{\rm rt,fc}^2)}\right] \tag{163}$$

Note that for $L_{\rm fc} = L_{\rm cc}$ the filter cavity is critically coupled (impedance matched) and the loss in its reflection is maximum. Therefore, to preserve the squeezing in reflection of the filter cavities its length should be chosen with $L_{\rm fc} \gg L_{\rm cc}$. This fact becomes obvious when looking at graph a) and b) of Fig. 248. They show the squeezing level in reflection of the filter cavity and the according reflectance of the filter cavity at its resonance frequency, respectively. At small half-bandwidths the value for $L_{\rm cc}$ (graph c)) is of the order of the filter cavity's baseline length $L_{\rm fc} = 10\,\text{km}$ and hence the reflectance and accordingly the remaining squeezing level are considerably reduced.

In Fig. 173 the filter cavity performance is shown depending on its baseline length $L_{\rm fc}$. In the corresponding calculations we assumed the target half-bandwidth with $\gamma_{\rm fc} = 2\pi \cdot 1.4\,\text{Hz}$ and the target detuning with $\Phi_{\rm fc_1} = 2\pi \cdot 6.6\,\text{Hz} \cdot L_{\rm fc_1}/c$. Note, that these values are approximately the requirements for one of the filter cavities that needs to be realised in the ET-LF detector [434]. Again, the round-trip loss was considered of 75 ppm and the initial squeezing level of 10 dB. Graph a) demonstrates, that even with a filter cavity length of 10 km the amount of squeezing is already reduced by a factor of about 4 dB. For lengths smaller than about 2.5 km the unbalanced loss for upper and lower squeezing sidebands results in a noise enhancement (anti-squeezing) when compared to vacuum noise in reflection of the filter cavity. At the critical length $L_{\rm fc} = L_{\rm cc} \approx 1239\,\text{m}$ this enhancement becomes maximum and corresponds to about 5 dB anti-squeezing. For lengths smaller than $L_{\rm cc}$ the noise level drops and squeezing can be achieved again (grey shaded area II) until it reaches at $L_{\rm fc} = L_{\rm min}$ the initial level of 10 dB. However, in this region the filter is under-coupled and does not yield the required phase-space rotation of the squeezed field. This can be understood when considering the extreme case for $L_{\rm fc} = L_{\rm min}$. Here, $R_{\rm c}$ is equal to one and the filter cavity can be replaced by an ordinary mirror that has no frequency dependence. Again, it can be deduced that a filter cavity length $L_{\rm fc} \gg L_{\rm cc}$ needs to be realised in order to preserve the squeezing. In addition, the high finesse of a short cavity might pose a problem for the lock acquisition in the environment of a gravitational-wave detector where the optics needs to be suspended.

So far in Figs. 248 and 173 the squeezing level was shown in reflection of the considered filter cavities at its resonance frequency. Here the (frequency-dependent) imposed loss is maximum. Now, for exemplification Fig. 249 shows squeezing spectra obtained after the reflection at two subsequent filter cavities FC_1 and FC_2.

The considered half-bandwidths and tunings of these filters are those needed for the ET-LF detector. The length of the cavities were considered with $L_{\rm fc_1} = L_{\rm fc_2} = 2\,\text{km}$ (red curve), $L_{\rm fc_1} = L_{\rm fc_2} = 5\,\text{km}$ (blue curve) and $L_{\rm fc_1} = L_{\rm fc_2} = 10\,\text{km}$ (green curve), respectively.

The calculations and exemplary filter properties considered within this Section imply that in 3rd generation gravitational-wave detectors such as the Einstein Telescope, where filter cavities with half-bandwidths in the range of $\gamma_{\rm fc} \approx 2\pi \cdot 1 - 2\pi \cdot 5\,\text{Hz}$ will be required, the baseline length of these filters needs to be in the order of a few kilometers. This contrasts to the results presented in [691] for the Advanced LIGO detector. As for the Advanced LIGO configuration filter cavities with half-bandwidths in the order of $2\pi \cdot 50 - 2\pi \cdot 200\,\text{Hz}$ will be required, a considerable sensitivity increase by the injection of frequency-dependent squeezed light can already be achieved if filter cavities with lengths in the order of 100 m are utilised. Certainly, our exemplary calculations are based on a conservative assumption of 75 ppm for the round-trip loss of the filter cavities, but even if optimistic values of $l_{\rm rt,fc}^2 = 20\,\text{ppm}$ are considered, the corresponding values for the critical lengths will be $L_{\rm cc,fc_1} = 330\,\text{m}$ and $L_{\rm cc,fc_2} = 84\,\text{m}$, respectively. As shown in Figs. 248 and 173 the respective length $L_{\rm fc}$ should be at least 10 times greater than $L_{\rm cc}$. I.e. for the ET-LF detector the length of the two required filter cavities should be 10 km. In contrast, it can be shown that for the ET-HF detector a filter with a length of about

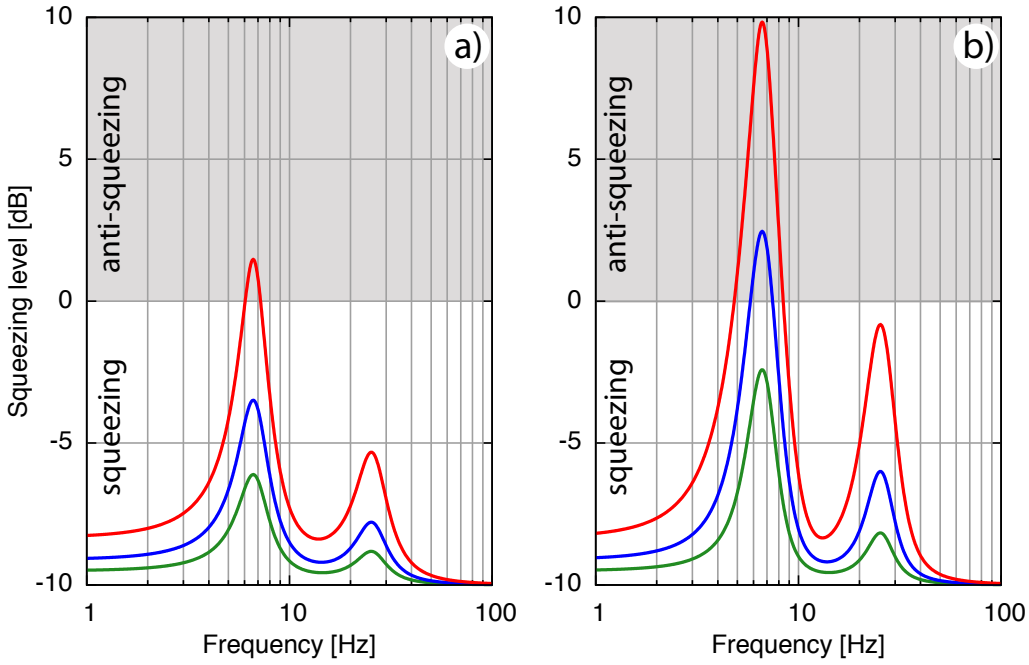

Figure 249: The figure shows the remaining squeezing level after subsequent reflection at two filter cavities FC_1 and FC_2. In graph a) an initial pure 10 dB squeezed state was considered and 75 ppm round-trip loss in each cavity. Additionally, in graph b) optical loss of 9 % outside the filter cavities was considered. Thus, an initial pure 20 dB squeezed state is necessary to achieve 10 dB detectable squeezing. In both cases, three length of the cavities were considered. The green curves are obtained for $L_{\mathrm{fc}_1} = L_{\mathrm{fc}_2} = 10\,\mathrm{km}$, the blue one for $L_{\mathrm{fc}_1} = L_{\mathrm{fc}_2} = 5\,\mathrm{km}$ and the red one for $L_{\mathrm{fc}_1} = L_{\mathrm{fc}_2} = 2\,\mathrm{km}$. The filter parameters are approximately those that are required for a broadband quantum noise reduction in the ET-LF detector, i.e. $\gamma_{\mathrm{fc}_1} = 2\pi \cdot 1.4\,\mathrm{Hz}$, $\Phi_{\mathrm{fc}_1} = 2\pi \cdot 6.6\,\mathrm{Hz} \cdot L_{\mathrm{fc}_1}/c$ and $\gamma_{\mathrm{fc}_1} = 2\pi \cdot 5.7\,\mathrm{Hz}$, $\Phi_{\mathrm{fc}_1} = -2\pi \cdot 25.4\,\mathrm{Hz} \cdot L_{\mathrm{fc}_1}/c$, respectively. Please note, that from this comparison it can be deduced, that the tolerable loss in the filters needs to be determined also in view of the injected anti-squeezing.

500 m is sufficient. This filter will be required for an optimisation of the squeezed quadrature in the radiation pressure noise dominated frequency band. However, in this frequency band other noise sources dominates the quantum noise. For that it is satisfactory to adapt the squeezing level to the level of these noise sources which will be possible with a comparatively short filter cavity.

The former investigation demonstrated that the round-trip loss ultimately restricts the minimal allowed baseline length and consistently the performance of the filter cavities. As it is expected that the round-trip loss of the filters will be dominated by scattering at imperfect mirror surfaces, the optical layout needs to be designed such that the amount of scattering is as much as possible reduced. The scattering in different optical layouts is treated in Sec. 5.5.4.

D.3.2 Determination of the required filter parameters

In publications by Purdue and Chen [620] and Harms [477] treating the frequency dependent squeezed light injection, some analytical expressions were derived showing first the need for filter cavities and second allow for a calculation of the required number, bandwidth and tuning of filter cavities. In these works the interferometer quantum noise transfer function was derived using the Caves-Schumacher two-photon formalism [696]. The interferometer quantum noise transfer function is then described by a 2×2-matrix $\mathbf{T}$ (refer to Eq. (3) in [477]). From this matrix the required frequency-dependent squeezing angle $\lambda(\Omega)$ can be derived according to Eq. (16) in [477]

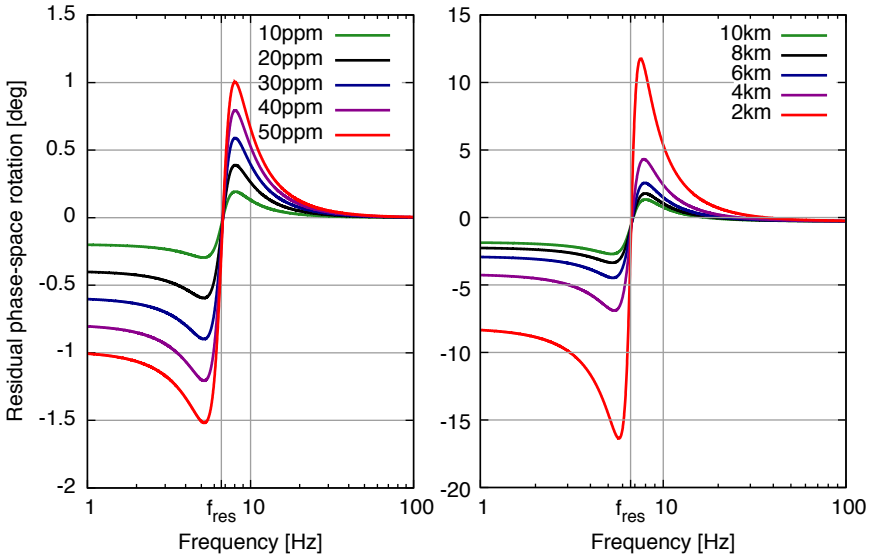

Figure 250: The figure demonstrates, that the phase-space rotation of a Fabry-Perot cavity is not only determined by its resonance frequency and bandwidth (here exemplary set to 6.628 Hz and 1.44448 Hz, respectively, for all cases), but also by its round-trip loss (left for a length of 10 km) and its baseline length (right for losses of 75 ppm).

$$\lambda(\Omega) = \arctan\left(-\frac{T_{11}\cos\zeta + T_{21}\sin\zeta}{T_{12}\cos\zeta + T_{22}\sin\zeta}\right) . \tag{164}$$

Here, Ω is the angular sideband frequency and ζ the read-out angle. It was shown in [620], that with a combination of Fabry-Perot cavities the required frequency dependent angle $\lambda(\Omega)$ can be realized. It has the form [620]

$$\tan\lambda(\Omega) = \frac{\sum_{k=0}^{n} B_k \Omega^{2k}}{\sum_{k=0}^{n} A_k \Omega^{2k}} \text{, with } |A_n + \mathrm{i}B_n| > 0 \tag{165}$$

From the corresponding characteristic equation

$$\sum_{k=0}^{n} (A_k + \mathrm{i}B_k)\,\Omega^{2k} = 0 \tag{166}$$

the required bandwidth and tuning of the filter cavities can be obtained. They are given by the $2n$ roots (in n pairs with a positive imaginary part) of Eq. (166). However, these calculations are based on the assumption of a lossless main interferometer, an infinite small signal-recycling cavity length, an expansion in powers of the light's angular frequency and the approximated expression for a cavity's half-bandwidth $\gamma = c\tau_c/(4L)$. Thus, in general they allow just for a precise estimation for the required parameters.

Furthermore it is demonstrated in Fig. 250, that it is not sufficient to realize filter cavities having the bandwidth and tuning determined by Eq. (166). First, the impact of optical loss was considered. Therefore, the phase-space rotation in reflection of a cavity with a half-bandwidth $\gamma = 2\pi \cdot 1.44448\,\mathrm{Hz}$ and a tuning according to $f_{\mathrm{res}} = 6.628\,\mathrm{Hz}$ is calculated for different values of the round-trip loss. The length was set to 10 km. The results are shown in the left graph of Fig. 250. It can be seen that the deviation of the phase-space rotation related to the lossless case increases with increasing optical loss. Similarly, the rotation in reflection depends on the baseline length of the cavity. This fact is shown in the right graph of Fig. 250. Here, the round-trip loss was set to 75 ppm for all cases.

Especially under consideration of optical intra-cavity round-trip loss and a finite baseline length of the filter cavities as well as the signal-recycling cavity, there is no possibility to determine the optimal filter cavities

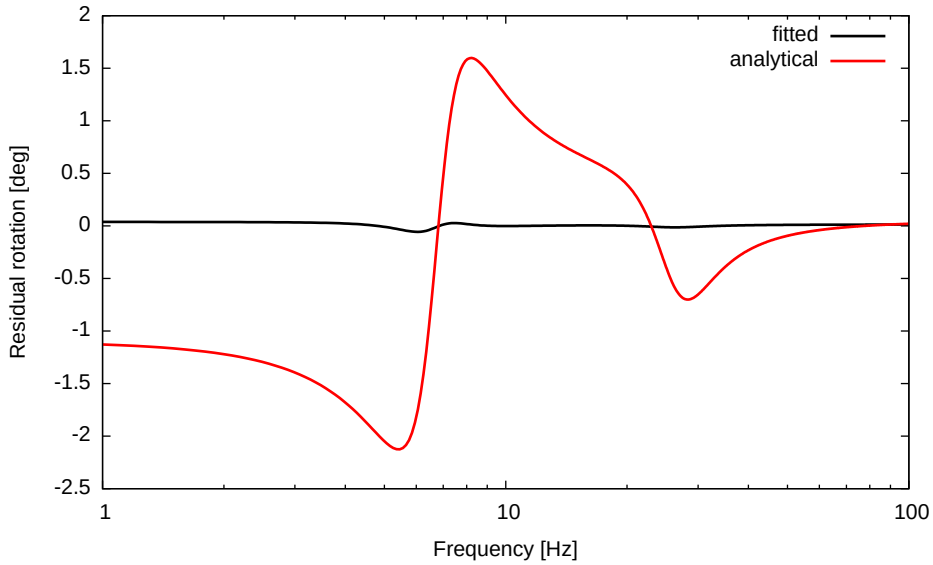

Figure 251: The figure shows the residual rotation of the injected squeezing, if the filter cavities are realized with parameters determined in accordance to Eq. (166) (red curve) and those determined by a fit (black curve). After fitting the parameters, the residual rotation is less than 0.2 deg.

parameters analytically. Thus, the parameters for the filter cavities were fitted with respect to the residual phase-space rotation of injected squeezed field. Fig. 251 compares the results for the parameters determined in accordance to Eq. 166 (red curve) and those determined by the fit (black curve) for the ET-D LF detector. The corresponding filter cavity parameters are listed in Tab. 19

Box D.1: Determination of the required filter parameters

	tuning [Hz] (fitted / analytical)	half-bandwidth [Hz] (fitted / analytical)
FC_1	-25.4255 / -25.3592	5.76766 / 5.68148
FC_2	6.6167 / 6.6280	1.53135 / 1.44448

Table 19: Deduced design parameters for the ET-D LF Filter-cavities.

	tuning [Hz] (fitted / analytical)	half-bandwidth [Hz] (fitted / analytical)
FC_1	– / -25.3592	– / 5.68148

Table 20: Deduced design parameters for the ET-D HF Filter-cavities.

D.3.3 Robustness of the design parameters

In this section we illustrate the effect of a deviation from the determined design parameters. We will concentrate on the most obvious quantities, that will potentially change the properties of the filter, i.e.

1. the reflectance factors of the used mirrors,
2. the round-trip loss,
3. the macroscopic length, and
4. the resonance frequency.

The first three quantities affect the bandwidth of the filter cavity and thus the required phase-space rotation around the targeted resonance frequency. A deviation from the design values of these quantities could not be compensated if the filter cavity is realised as single resonator. An adaption of the filters bandwidth would be possible if coupled resonators—e.g. a linearly coupled three-mirror cavity—are utilised. Although it should be always possible to tune the filter cavity to the required resonance frequency, for the sake of completeness we treat a potential mismatch within this section. From the results the requirements for the length stabilisation with regard to displacement noise could be determined.

We start from the set of design parameters for the length, the detuning and the mirror reflectance factors yielding the bandwidth and phase-space rotation of the two filter cavities that are required for ET-C LF. These parameters are listed in Table 21. The analysis of the impact on the achievable squeezing levels for a certain mismatch of the bandwidths will give the allowable tolerances of theses parameters.

Parameter	FC_1	FC_2
length L_{fc} [km]	10	10
half-bandwidth γ_{fc} [Hz]	$2\pi \cdot 1.4$	$2\pi \cdot 5.7$
resonance frequency f_{res} [Hz]	$2\pi \cdot 6.6$	$-2\pi \cdot 25.4$
detuning Φ_{fc} [°]	≈ 0.1369	≈ 0.3026
round-trip loss $l_{rt,fc}$ [ppm]	75	75
coupling mirror reflectance R_c	99.8864 %	99.5323 %

Table 21: Design parameters / estimates for the two filter cavities FC_1 and FC_2 needed in the ET-C LF detector.

To demonstrate the effect of a mismatched bandwidth we calculate the squeezing spectra after reflection at two subsequent resonators– the required filter cavity and an auxiliary cavity which models the interferometer. For the filter cavity the design parameters (and a certain deviation of them) as listed in Table 21 are assumed. The auxiliary one has a bandwidth and detuning that models the transfer function and thus the phase-space rotation of the interferometer. Consistently, no phase-space rotation occur after subsequent reflection at these resonators if their bandwidths are matched. Note, that the auxiliary resonator is assumed to be loss-free so that the imperfections in the squeezing spectra can be clearly traced back to the respective deviation of the filter cavities design parameters. For a first illustration of the effect of a mismatched filter cavity bandwidth, Fig. 252 shows the squeezing level (top) and the residual phase-space rotation (bottom) after subsequent reflection at both cavities. Note that here *both* cavities were assumed to be loss-free.

Fig. 253 shows the performance of the filter cavities (FC_1 and FC_2) required for the ET- LF detector. Their bandwidth was varied according to a deviation of 1 % to 5 % from the designed value. In these plots, the round-trip loss of the filter cavities was considered to be 75 ppm.

D.3.4 Scattering light noise in optical cavities

We have estimated the amount of scattering in long baseline cavities between the suspended optics for different cavities geometries to test whether this particular class of scattering has any influence on the selection of the optical resonator for ET filter cavities. The four cavity geometries depicted in Fig. 254 were considered.

At the detection port, a photodetector detects the light field as

$$P_{out} = EE^*. \tag{167}$$

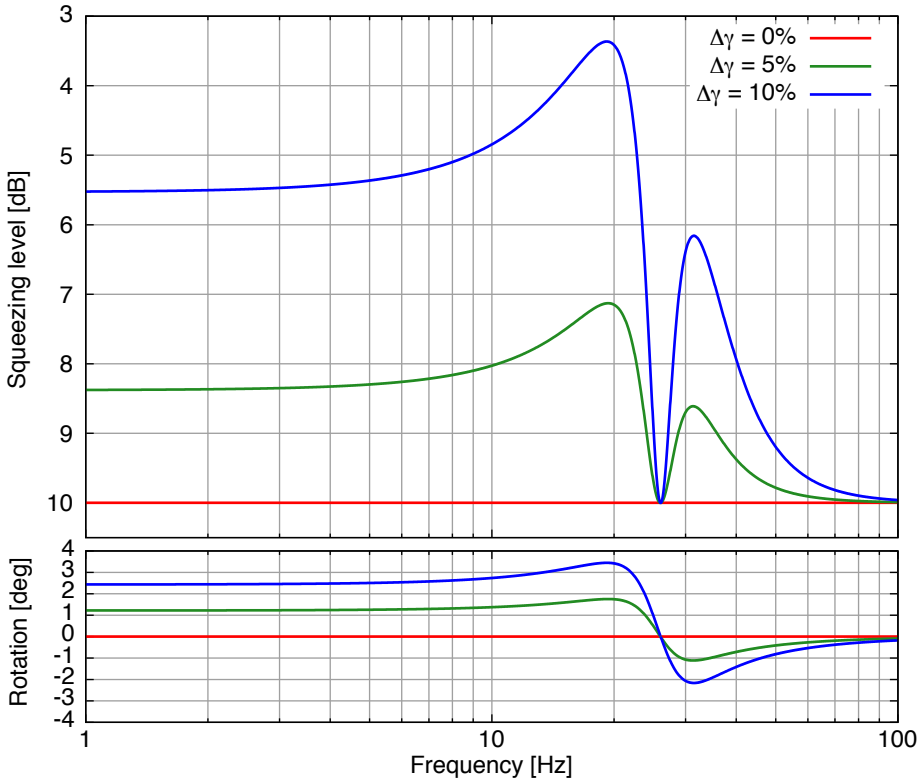

Figure 252: The figure illustrates the effect of a deviation of the required bandwidth. The lower graph shows the resulting residual phase-space rotation of the squeezing ellipse, the upper graph the according squeezing levels. Please note that the filter cavities are assumed to be lossless. Thus, the degradation of the squeezing level can be clearly traced back to the residual phase-space rotation.

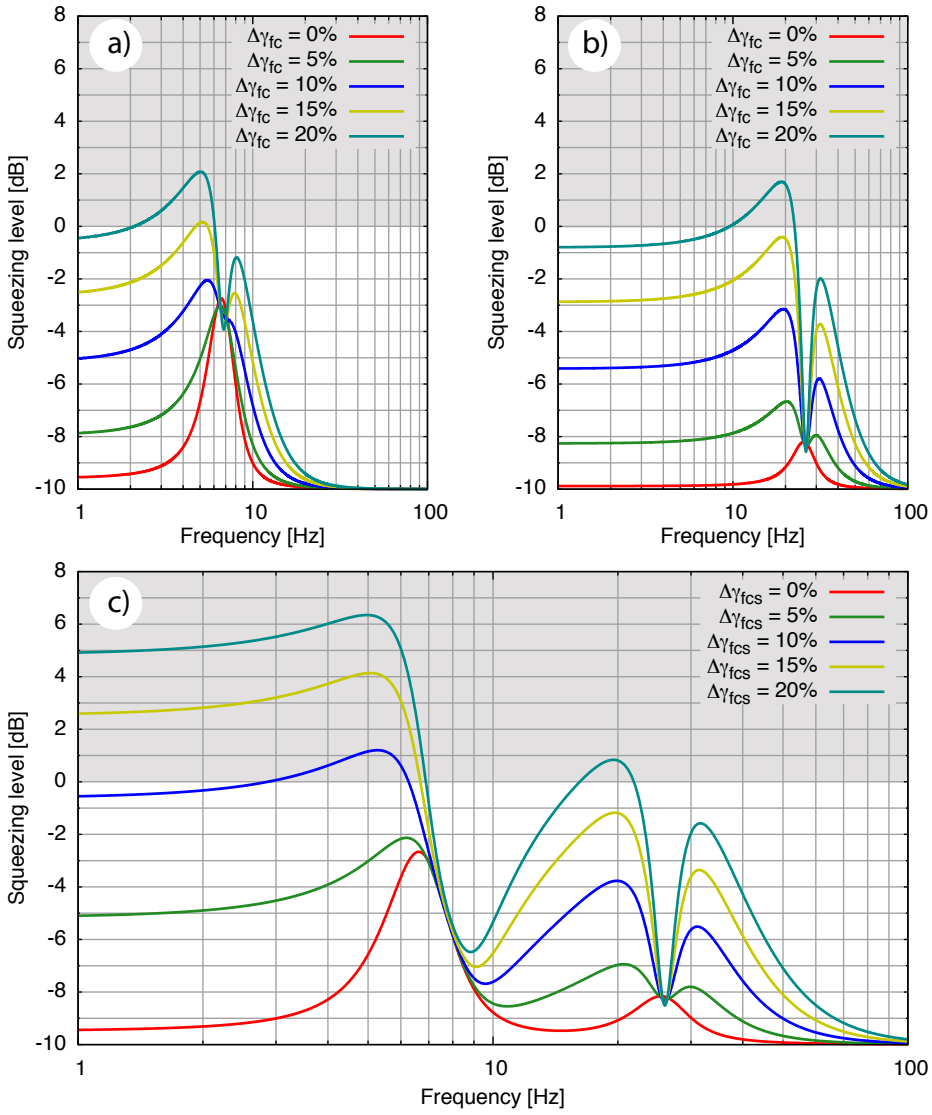

Figure 253: The figure shows the squeezing spectra for a deviation of the designed bandwidth of a) the single FC_1 and b) the single FC_2. Graph c) shows the spectra if both filter cavities are considered. In all cases, the filter cavity round-trip loss was considered to be 75 ppm.

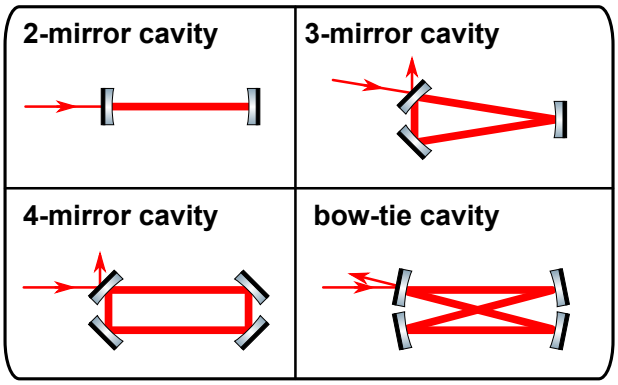

Figure 254: The scattering-light effects for four geometries, (1) Two-mirror cavity, (2) triangular cavity, (3) rectangular cavity, and (4) bow-tie cavity, are analysed.

In addition to the cavity fundamental mode E_c, we also consider a complex field δE which occurs due to scattering, thus we write

$$E = E_c + \delta E. \tag{168}$$

The detected field is proportional to

$$\begin{aligned} P_{\rm det} &\propto (E_c + \delta E)(E_c^* + \delta E^*) &(169)\\ &\propto |E_c|^2 + |\delta E|^2 + E_c \delta E^* + E_c^* \delta E &(170)\end{aligned}$$

where the first term is the power of the main mode, and the second term is the power of the scattering filed which is the second order term and assumed to be negligible. Only the cross terms between the fundamental and complex scatter field affects the sensitivity. Considering the x-y plane, the cross term, or coupling factor, is written as

$$X = \int_{-\infty}^{\infty}\int_{-\infty}^{\infty} E_c(x,y,z)\delta E^*(x,y,z){\rm d}x{\rm d}y, \tag{171}$$

where the z axis is the main beam propagation direction, and $E_{\rm cav}(x,y,z_{\rm cav})$ is the Gaussian field which is the resonant mode in the cavity,

$$E_{\rm c}(x,y,z) = \sqrt{\frac{k_0}{\pi z_R}}\frac{iz_R}{z+iz_R}\exp\left[\frac{-ik_0(x^2+y^2)}{2(z+iz_R)}\right] \tag{172}$$

where z_R is the Rayleigh range of the cavity resonant mode and k_0 is the wave number of the laser source.

Here, we consider three simplified scenarios of scattering processes, in order to estimate the scattered light levels in candidate ET cavities; direct back scattering, diagonal path scattering, and the Gaussian tail effect. The three processes will be evaluated and compared between the four cavity geometries: a two-mirror cavity, triangular cavity, rectangular cavity, and bow-tie cavity, as shown in Fig. 254.

(a) Direct back scattering When the main beam is reflected by a mirror, some of the main light field is scattered back by the non-uniform distribution of the mirror surface. The scattered field can couple with the cavity resonant mode in the opposite direction with respect to the propagation direction of the main beam. The direct back scattering scenario considers only coupling which occurs after scattering by just one mirror. In general, when the wavefront of the scattered light is changed by deformations of the mirror surfaces, the scattering into any direction is given by the Fourier transform of the mirror surface figure. For mirror surface deformations with longer spatial wavelengths the scattering angle will be smaller. A typical mirror surface has

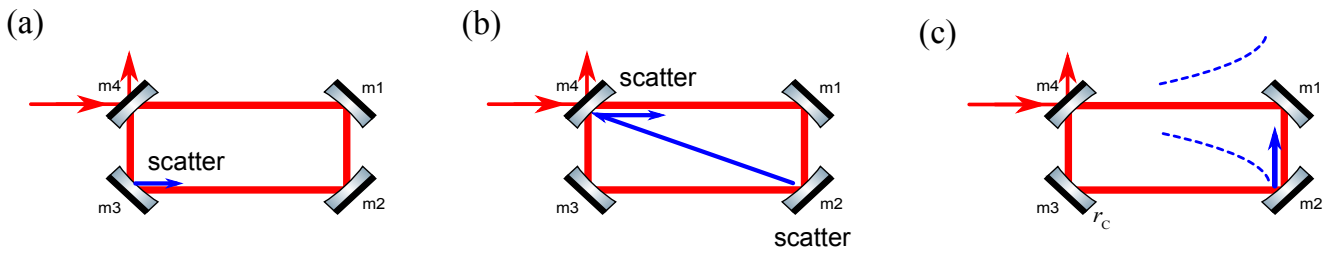

Figure 255: Three scattering processes considered in this analysis. (a) An exemplary field of the direct back scattering. It occurs at all mirrors in each geometry except in the two-mirror cavity. (b) Diagonal path scattering. In the rectangular cavity, the diagonal paths in the rectangular geometry create spurious paths. (c) Gaussian tail effect. In the rectangular and bow-tie cavities, the tail of the Gaussian field may interact with the wrong mirror, is partially reflected. This reflected field couples into the main Gaussian beam.

more long spatial wavelength deformations than short spatial wavelength deformations, therefore the power scattered into large angles should be very small.

To evaluate the coupling factor, the scattered field is written as

$$\delta E(x,y,z) = \eta(\phi) E_{\rm c}(x,y,-z)\, \exp\Big[-2ik_0 x \tan\alpha + \frac{ik_0(x^2+y^2)}{2r_C}\Big], \tag{173}$$

where the exponential factor describes the phase delay due to the mirror angle α with respect to the mirror normal, and the radius of curvature of the mirror r_C is taken into account as the phase delay due to the reflection surface geometry.

In Eq. (173), $\eta_n(\phi_n)$ is an amplitude, or efficiency of the scattering process. We assumed η using the bidirectional reflectance distribution function (BRDF) which describes the scattering intensity distribution of a mirror as follows: The amplitude of the field scattered at angle ϕ_n is written as

$$\eta(\phi) \quad = \quad \sqrt{P(\phi)}. \tag{174}$$

where $P(\phi)$ is the field power that reaches the reflecting mirror surface at the end of the diagonal path. The power can be estimated using the BRDF as,

$$P(\phi) \sim P_0 \mathrm{BRDF}(\phi) dS \tag{175}$$

where P_0 is the incident light power, dS is the solid angle of the second mirror, which receives the scattered light, from the first mirror. As the BRDF of the ET mirrors is unknown, we use a measured BRDF of an Advanced LIGO mirror [697]

$$\mathrm{BRDF}(\phi) \quad = \quad \frac{10^{-20}\pi^2}{\lambda^3 \phi[\mathrm{m}^{-3}\mathrm{rad}^{-1}] + 0.0016\lambda\phi^3[\mathrm{m}^{-1}\mathrm{rad}^{-3}]}. \tag{176}$$

as plotted in Fig. 256. Note that this is a BRDF of a silica mirror of Advanced LIGO and might be an overestimate for the advanced mirrors of ET. Also, the BRDF is valid when the incoming beam is perpendicular to the mirror surface, which is different from our situation. The bidirectional reflectance distribution might alter in our case, in which the incoming beam and the mirror normal have an angle.

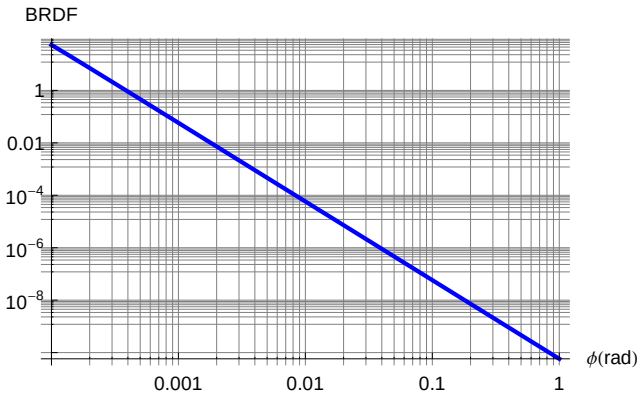

Figure 256: A bidirectional reflectance distribution function (BRDF) of an Advanced LIGO mirror. The BRDF describes an angular distribution of a scattered light power per unit solid angle. It was used to assume the scattering efficiency for the diagonal path scattering process.

Substituting Eq. (173) into Eq. (171), we obtain the coupling coefficient as

$$X_1 = \frac{\eta(\phi)k_0 z_R}{\pi(z^2+z_R^2)}\int_\infty^\infty\int_\infty^\infty \exp\Big[-\frac{k_0 z_R(x^2+y^2)}{z^2+z_R^2} - ik_0\Big\{\frac{x^2+y^2}{2r_C}+2x\tan\alpha\Big\}\Big]\mathrm{d}x\mathrm{d}y. \tag{177}$$

(b) Diagonal path scattering In the rectangular cavity, the diagonal lines of the rectangular geometry can become scattered light paths. When the main beam illuminates a mirror, scattered light fields are produced by the mirror surface distribution. The scattered light experiences further scattering or reflection incidents. There can be many possible spurious paths during this process. In Fig. 257, all the possible routes with 2 incidents are shown, while only one example path is shown for other paths with 3 to 5 incidents. Each route might have one or more spurious paths because each incident is either from scattering or reflection. For example, a 3-incident route of m1 - m3 - m4 has possible paths of m1 (large angle scattering) - m3 (small-angle and short-path scattering) - m4 (small angle scattering), and m1 (large angle scattering) - m3 (reflection) - m4 (small-angle and short-path scattering), and m1 (large angle scattering) - m2 (small-angle and short-path scattering) - m3 (reflection). Here, we consider such spurious paths with up to 5 incidents.

The total number of possible paths were counted in the following way: (i) Spurious paths with up to 5 incidents of scatter and/or reflection were considered. (ii) At the end of the path, the scattered field couples into the main beam in the normal propagating direction. (iii) Direct back scatter was not considered because it is assumed to be smaller than the coupling in the normal direction at the small angle (iv) scattered light does not propagate along the long path without coupling into the main beam. The total number of the possible spurious paths are 4 paths (all of which are shown in the Fig. 257), 10 paths, 12 paths, and 16 paths were found for 3, 4, and 5 incidents, respectively. To obtain the result, all contributions from all paths are statistically summed.

The efficiency of the scattering power is large when the scattering angle, which is the angle made with the main beam path, is small, and the efficiency is small when the scattering angle is large. Therefore, the amplitude of the scattered field depends on the propagation path and the spurious path. Here we assume the amplitude using BRDF which is a function of the scattering angle again.

Assuming the scattered field to be a plane wave as a rough approximation, one can write the scattered field of each path as

$$\delta E(x,y,z) = \prod_{n=1}^{N}\eta_n(\phi_n)\,\exp\Big[-ik_0\Big\{R_d+\frac{x^2+y^2}{2r_C}\Big\}\Big]. \tag{178}$$

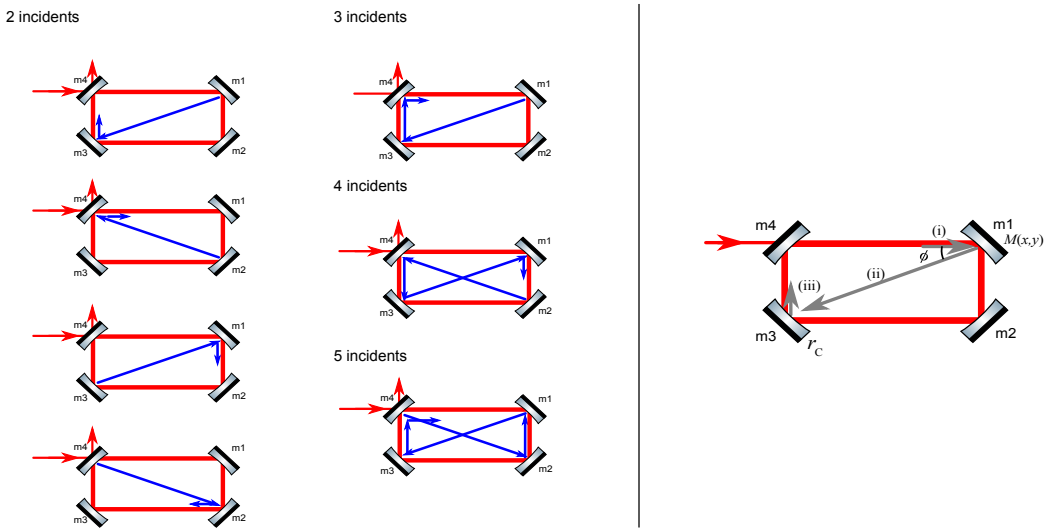

Figure 257: Above left: Possible routes of the diagonal path scattering. After the scattered light is emitted by one mirror, the field propagates along the diagonal path or the shorter path in the rectangular, then is scattered again or reflected by another mirror, and finally couples to the main beam. Until coupling into the main beam, the route is composed of a number of scattering and/or reflection incidents. Depending on which small angle, large angle scattering, or reflection incident, one route might have different combinations of spurious paths. Here, spurious routes with up to 5 incidents were considered. All possible paths with two incidents are depicted on the left, while only one example route is shown for 3, 4 and 5 incidents. Above right: Example view of small angle scattering and of large angle scattering. (i) The scattered light is emitted when the main beam hits m1. (ii) The scattered light propagates along the diagonal line. This incident is considered as the large angle scattering which has a small scattering efficiency because this diagonal path is at almost 90 degrees from the main path after the reflection at m1. (iii) The scattered field is scattered again at a small angle with respect to the main beam. This is considered as the small angle scattering as this path coupling into the main beam is at a very small angle compared with the reflected path resulting from the diagonal path (from m1). Depending on whether the scattering angle is large or small, the corresponding scattering efficiency is taken into account.

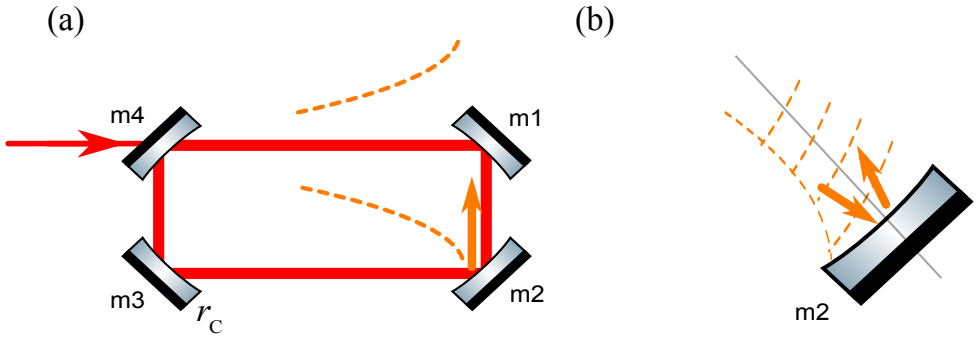

Figure 258: (a) An example dagram of the Gaussian tail effect. This process will occur at each mirror in the rectangular and bow-tie cavities. (b) Detailed diagram of the wave fronts at the tail of Gaussian field. In the picture, the incident angle and the reflection angle is slightly different from the approximated picture (a).

where R_d is the total path length from the emission point to the coupling point, and r_C is the radius of curvature of a mirror when the scattered filed couples into the cavity, N is the total incidence number, and $\eta_n(\phi_n)$ is the amplitude (or efficiency) of the nth incident of scattering or reflection, assumed by BRDF and the scattering angles.

Substituting Eq. (178) into Eq. (171), the coupling coefficient is derived as

$$X_2 = \sqrt{\frac{k_0 z_R}{\pi}} \frac{\prod_{n=1}^{N} \eta_n(\phi_n)}{(z_R + i z_{\rm cav})} \int_\infty^\infty \int_\infty^\infty \exp\Big[-ik_0\Big\{R_d + \frac{x^2+y^2}{2r_C} - \frac{x^2+y^2}{2(z_{\rm cav} - i z_R)}\Big\}\Big] {\rm d}x{\rm d}y. \tag{179}$$

(c) Gaussian tail effect In the rectangular and bow-tie cavities, the tail of the Gaussian field may reach the wrong mirror, for example as shown in Fig. 258 (a), and is partially reflected. This reflected field couples into the main Gaussian beam. Note that this is also a simplified picture. As shown in Fig. 258 (b), the wave front at the edge of the main field faces a different direction compared with the wave front at the center of the beam, therefore, the reflection angle may differ from the main beam path. However, for a simple estimation, we approximate that the Gaussian tail field is reflected and directly couples into the main mode. The rectangular or bow-tie cavity has four fields to be considered since this process can occur at each mirror.

When a mirror (therefore the coupling point) is a distance L away in the x direction from the main beam, the coupling field is written as

$$\delta E(x, y, z) = E_c(x + L_s, y, z_{\rm sc}). \tag{180}$$

The coupling coefficient is

$$X_4 = \frac{-k_0 z_R}{\pi (i z_{\rm cav} + z_R)(i z_{\rm sc} - z_R)} \int_\infty^\infty \int_\infty^\infty \exp\Big[-ik_0\Big\{\frac{x^2+y^2}{2(iz_R - z_{\rm cav})} + \frac{(L_s+x)^2+y^2}{2(iz_R - z_{\rm sc})}\Big\}\Big] {\rm d}x{\rm d}y. \tag{181}$$

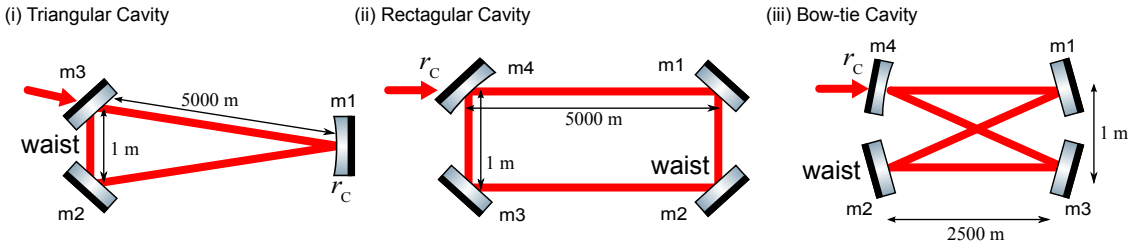

Figure 259: Cavity designs used for the numerical calculation. The cavities have a round trip length of approximately 10 km, and a beam waist at the middle point of the path.

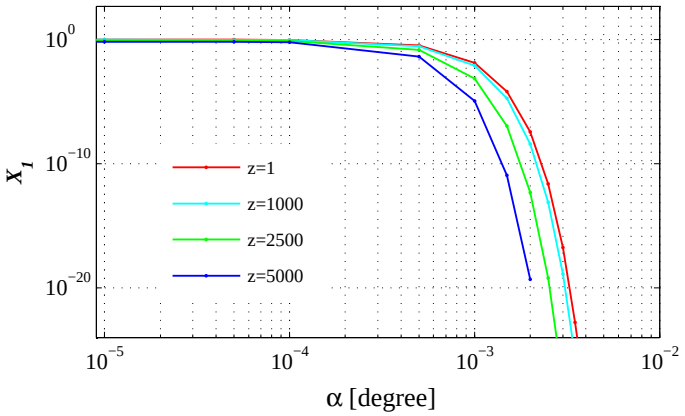

Figure 260: The coupling factor X_1 (direct back scattering) over the mirror angle where the scattering process occurs. The coupling factor rapidly goes to zero after 10^{-3} degrees.

Numerical evaluation In order to numerically calculate the coupling coefficient, we assume that the round trip of a cavity is about 10 km, and the waist position of the laser beam is at the middle point of the round trip for all the geometries, as shown in Fig. 259. The triangular cavity is an isosceles triangle with two 5 km arms and with a 1 m base, and the beam waist is at the middle of the short path. The rectangular cavity has long and short paths of 5 km and 1 m respectively, and the beam waist is at m2 in Fig. 259. The bow-tie cavity has four paths of 2.5 km and the separation between the closer mirrors is assumed to be 1 m. For mode-matching, each mirror was assumed to be either flat or to have a radius of curvature r_C.

• Direct back scattering: Fig. 260 shows the plot of X_1 over the mirror angle α for four coupling locations (z=1, 1000, 2500, and 5000). X_1 strongly depends on the angle between the mirror normal and the propagation direction of the beam, α. The coupling coefficient rapidly approaches zero when the angle is larger than 10^{-3} degrees. This is because the coupling between the two fields is very small when the wavefront of one field is delayed by the mirror surface with the incident angle while the other field is not delayed. Since the mirror angles of all the ring cavities have much larger α, the direct back-scattering is negligible in ET cavities although arbitrary scattering angles (i.e. arbitrary scattering efficiencies η) are considered here.

• Diagonal path scattering: From the assumption using BRDF and the scattering angles when the longer and the shorter path lengths of the rectangular cavity are 10 km and 1 m respectively, the amplitude of the small angle scatter is $\eta(\phi_s) = 3.8 \times 10^{-8}$, of the large angle scatter is $\eta(\phi_s) = 7.5 \times 10^{-6}$, and of the small-and-short scatter is $\eta(\phi_{SS}) = 4.1 \times 10^{-5}$. Adding the coupling coefficients of all the possible paths up to 5 incidents, the total coupling coefficient was calculated to be 4.7×10^{-11} when the intra cavity power is normalised as unity. Therefore, one should be careful to consider the scattering field propagating along the diagonal paths in the rectangular cavity. In order to block the diagonal paths, placing baffles inside the rectangular geometry will be

Type	direct-back scattering	Diagonal	Gauss. Tail
Two-mirror	N/A	N/A	N/A
Triangular	0	N/A	N/A
Rectangular	0	4.7×10^{-11}	0
Bow-tie	0	N/A	0

Table 22: Summary of the scattering process for each geometry without an amplification factor of the cavity. The numbers are in amplitudes while the light power is normalised to be unity inside the cavity.

useful to prevent the scattered light coupling into the cavity mode.

• Gaussian tail effect: The Gaussian tail effect is found to be negligible with the optical parameters considered here. In numerical simulations a length of 1 m for the shorter paths in rectangular or bow-tie cavities was found to be sufficient for the effect to be negligible.

Table 22 shows a summary of the numerical evaluation. The two-mirror cavity is the best configuration from the scattered-light point of view because there are no spurious paths in the geometry. For the other three configurations, the direct back scattering and the Gaussian tail effect were found to be negligible. One should be careful to consider the scattering field propagating along the diagonal paths in the rectangular cavity. If this geometry is to be used, the placement of baffles inside the rectangular geometry will be necessary to prevent the scattered light from propagating along the paths.

D.3.5 Noise couplings

In this section several noise mechanisms that potentially limit the detected squeezing levels are discussed. First, we discuss the effect of phase noise in the squeezing path. Assuming a self-homodyning readout (DC readout) of the interferometers signal field, the DC part of the interferometer output field serves as local oscillator. The quadrature of the signal field that is read out is determined by its relative phase with regard to this local oscillator. In order to reduce the quantum noise of this measurement, the relative phase of the injected squeezed field needs to be chosen such that the squeezed quadrature coincides with the readout quadrature. This required phase relation gets disturbed due to e.g. vibrating optical components in the squeezing path (displacement noise) or residual high frequency phase modulations that probably will be required for control purposes. If the measurement time is greater than the period of the phase jitter period, the homodyne read out is not a pure measurement of a certain quadrature ζ (e.g. the squeezed quadrature) but the integral over some span of $\zeta + \delta\zeta$. In this case, a certain fraction of the noise in the anti-squeezed quadrature is mixed into the measurement that was intended to be a measurement of the squeezed quadrature. It is obvious, that such a *phase diffused squeezed state* results in a degraded squeezing level. Accordingly, an upper limit for the overall tolerable phase noise in the squeezing path needs to be deduced with regard to the targeted quantum noise reduction of 10 dB.

The influence of phase noise on the squeezed field can be nicely illustrated by the accordant Wigner functions. We start from the Wigner function of a squeezed state that has a certain orientation (determined by the quadrature angle φ) in phase-space. It is given by

$$W(X_{1,\varphi}, X_{2,\varphi}, \varphi) = \frac{1}{2\pi\sqrt{V_s V_a}} \exp\left[-\frac{X_{1,\varphi}^2}{2V_s} - \frac{X_{2,\varphi}^2}{2V_a}\right] . \tag{182}$$

Here V_s and V_a denotes the variances in the squeezed and anti-squeezed quadrature, respectively (e.g. for a pure 10 dB squeezed state $V_s = 0.1$ and $V_a = 10$ if normalised to the variance of the vacuum state $V_{\mathrm{vac}} = 1$). The orientation in phase-space is accounted for by setting

$$X_{1,\varphi} = X_1 \cos(\varphi) - X_2 \sin(\varphi) \tag{183}$$
$$X_{2,\varphi} = X_1 \sin(\varphi) + X_2 \cos(\varphi) . \tag{184}$$

Here, the local oscillator serves as reference for the phase-space with its amplitude (X_1) and phase quadrature (X_2). The corresponding probability distribution in the amplitude quadrature (X_1) can be obtained from the Wigner function by integrating over X_2. One obtains

$$P_{X_1} = \int_{-\infty}^{\infty} W_d(X_1, X_2) dX_2 \tag{185}$$

$$= \frac{1}{\sqrt{2\pi V_{X_1}(\varphi)}} \exp\left[-\frac{X_1^2}{2V_{X_1}(\varphi)}\right] . \tag{186}$$

with the variance of the amplitude quadrature

$$V_{X_1}(\varphi) = V_s \cos^2(\varphi) + V_a \sin^2(\varphi) \tag{187}$$

$$= \frac{1}{2}\left[V_s + V_a + (V_s - V_a)\cos(2\varphi)\right] . \tag{188}$$

Now, to describe a phase-diffused squeezed state, the quadrature angle φ needs to be replaced by a probability density for the phase denoted as $\Phi(\varphi)$. Then, the Wigner function is given by

$$W_d(X_1, X_2) = \int \Phi(\varphi) W_d(X_1, X_2, \varphi) d\varphi . \tag{189}$$

Again, the corresponding probability distribution in the amplitude quadrature (X_1) can be obtained from the Wigner function by integrating over X_2

$$P_{X_1,d} = \int_{-\infty}^{\infty} W_d(X_1, X_2) dX_2 . \tag{190}$$

Accordingly, the variance of a phase-diffused squeezed state is given by

$$V_{X_1,d} = \int_{-\infty}^{\infty} \Phi(\varphi) V_{X_1} d\varphi \Leftrightarrow \int_{-\infty}^{\infty} P_{X_1,d} X_1^2 dX_1 . \tag{191}$$

In Fig. 261 four Wigner functions (top) and the corresponding probability distribution in the X_1-quadrature (bottom) are shown. We assumed a Gaussian-distributed phase noise, i.e,

$$\Phi(\varphi) = \frac{1}{\sqrt{2\pi\sigma^2}} \exp\left(-\frac{\varphi^2}{2\sigma^2}\right) . \tag{192}$$

Note that no specific assumptions on the spectral distribution of the phase noise have been made. In order to deduce the value of the variance of φ from a measured spectrum of the phase noise the integral over the full observation bandwidth has to be taken.

We have considered phase noise with a standard deviation σ of 0 (no phase noise), 0.3, 0.6 and 0.9 rad (from left to right in Fig. 261). The initial squeezed state (left figures) was assumed with $V_s = 0.1$ and $V_a = 10$, i.e. as a pure 10 dB squeezed state. The degradation of the squeezing level due to phase noise becomes obvious from the comparison with the probability distribution of a vacuum state (grey traces in the bottom graphs). The probability distributions are labelled with the corresponding squeezing level. For strong phase noise the initial squeezing is destroyed and the noise in the amplitude quadrature is even enhanced when compared to the vacuum noise (shot noise).

The illustration in Fig. 261 implies that the larger the anti-squeezing level, the larger the effect of phase noise. In fact, in order to achieve the targeted quantum noise reduction of 10 dB, a squeezed light source needs to

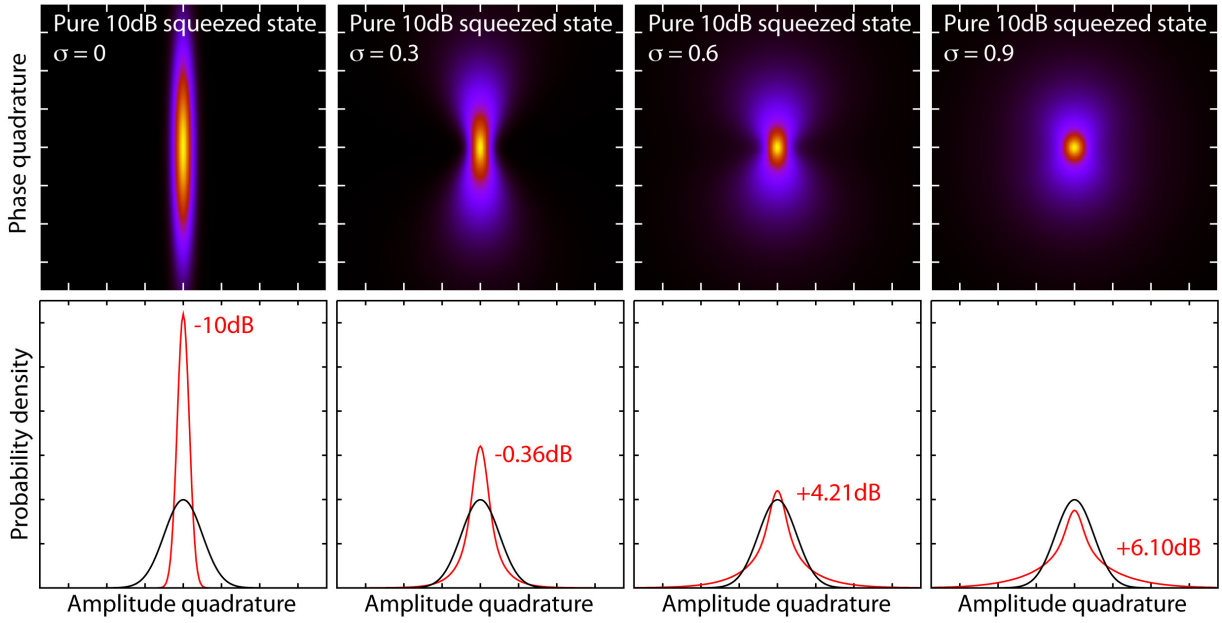

Figure 261: Illustration of the influence of a Gaussian distributed phase noise on the squeezed state. **Top:** Wigner functions for phase noise with a standard deviation σ of 0, 0.3, 0.6, 0.9 rad. The initial, pure squeezed state was assumed with 10 dB. **Bottom:** The probability distribution of the phase diffused squeezed states and the corresponding squeezing levels (red curves and red labels, respectively) in the amplitude quadrature (X_1). For comparison, the distribution of a vacuum state is shown (grey curves).

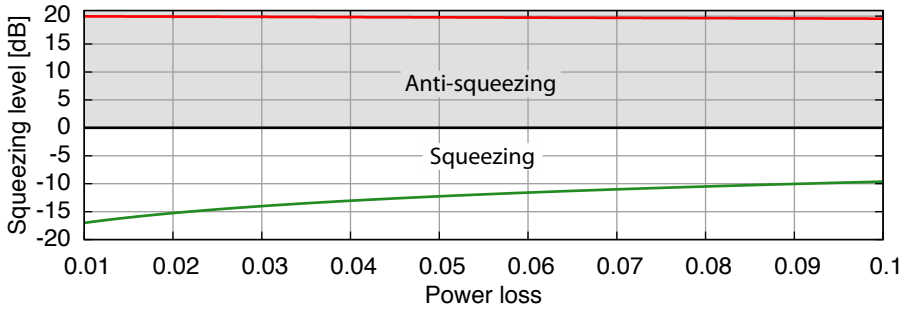

Figure 262: The degradation of the squeezing and anti-squeezing levels due to optical loss for an initially pure (no loss) 20 dB squeezed state.

be utilised that generates considerably more than 10 dB (anti-)squeezing to compensate for possible loss. If an overall optical loss of up to 10 % in the squeezing path (including 1 % loss in the squeezed light source itself) is assumed, an initially pure 20 dB squeezed state needs to be generated. The degradation of the squeezing (and anti-squeezing) level with optical loss is shown in Fig. 262. Whereas the squeezing level is strongly affected by optical loss, the anti-squeezing level is not considerably reduced. Considering an overall optical loss of 10 % the squeezing level is reduced from 20 dB to about 9.6 dB, but the anti-squeezing level is still about 19.5 dB. In Fig. 263 the effect of phase noise on an initial 20 dB squeezed state is illustrated, for which optical loss of 1 %, 3 %, 5 % and 10 % was considered. Here the phase noise was assumed with a standard deviation of $\sigma = 0.3\,rad$. Again, the top graphs show the Wigner functions and the bottom graphs the probability distribution in the amplitude quadrature. Here, in each case three traces are plotted. The red trace is the distribution of the phase diffused squeezed state and the black one that of a vacuum state. The grey curves correspond to the distribution without phase noise, i.e. the degradation of the squeezing level only due to the considered optical loss can be deduced. Again, it can be seen that the high phase noise destroys the squeezing. In each case, the

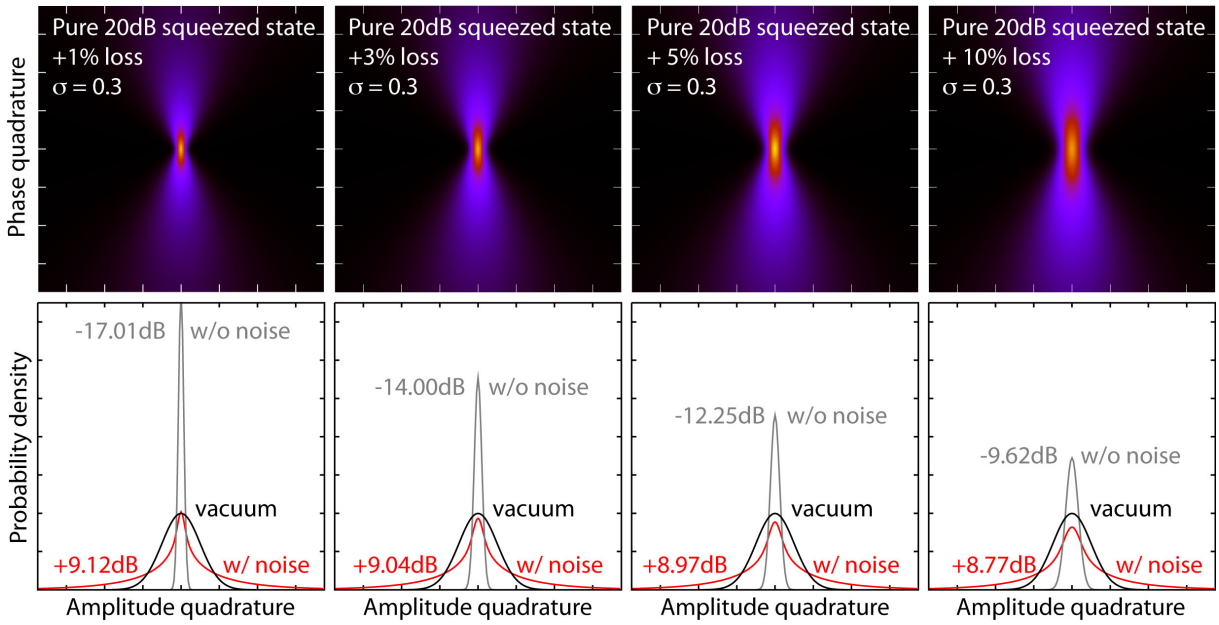

Figure 263: The degradation of the squeezing and anti-squeezing levels due to optical loss for an initially pure (no loss) 20 dB squeezed state. **Top:** Wigner functions for phase noise with a standard deviation σ of 0.3 rad and losses of 1%,3%,5%, and 10%. The initial, pure squeezed state was assumed with 20 dB. **Bottom:** The probability distribution of the phase diffused squeezed states and the corresponding squeezing levels (red curves and red labels, respectively) in the amplitude quadrature (X_1). For comparison, the distribution of a vacuum state (black curves) and the squeezed state without phase noise but with optical losses (grey curves) is shown.

resulting noise level is considerably enhanced when compared to the shot noise level. Please note that although the squeezing levels in the undisturbed case are $\geq$10 dB, the high anti-squeezing level of almost 20 dB leeds to higher noise levels when compared to the pure 10 dB squeezed state (refer to Fig. 261). I.e. in presence of phase noise the achievable squeezing level can be optimized by reducing the anti-squeezing (and thus the squeezing) generated by the squeezed light source. On the other hand, that means that in presence of considerable phase noise a compensation of optical loss in the squeezing path is not possible by enhancing the squeezing (and thus the anti-squeezing) generated in the squeezed light source.

In the previous investigation comparatively high values for the phase noise was considered for illustration purposes. Such high values are not expected to be present in a realistic experimental environment. However, the upper limit for the overall phase noise in the squeezing path depends on the squeezed state, that is generated by the squeezed light source. Table 23 lists the allowed phase noise (i.e. its standard deviation) for several conditioned squeezed states. The states were constituted for several values of the optical power loss l^2 such that the squeezing level without phase noise is 10 dB. The required squeezing that needs to be generated inside the squeezed light source can be calculated according to

$$V_s = 0.1 - l^2 \quad \text{and} \quad V_a = \frac{1}{V_s}. \tag{193}$$

We relate the upper limit $\sigma_{\max}$ for the phase noise to a squeezing level that is reduced to 9 dB due to the phase noise. As the phase noise is assumed to be Gaussian-distributed with zero mean, Eq. (191) can be solved giving

$$V_{X_1,d} = \frac{1}{2}\left[V_s + V_a + (V_s - V_a)\exp\left(-2\sigma^2\right)\right]. \tag{194}$$

Soving Eq. (194) for σ yields

$$\sigma = \sqrt{-\frac{1}{2}\log\left[\frac{2V_{X_1,d} - V_s - V_a}{V_s - V_a}\right]}. \tag{195}$$

optical loss [%]	initial squeezing [dB]	squeezing [dB]	anti-squeezing [dB]	$\sigma_{\max}[rad]$
1	-10.41	-10	10.37	0.049
3	-11.41	-10	11.29	0.044
5	-12.79	-10	12.58	0.038
9	-19.59	-10	19.19	0.018
10	$-\infty$	-10	∞	0
20	$-\infty$	-6.99	∞	0

Table 23: The table lists the squeezing and anti-squeezing levels and the tolerable maximum mean phase noise for several values of optical loss.

From this equation the tolerable phase noise characterised by σ_{max} can be calculated for the targeted variance $V_{X_1,d} = 0.1$ and squeezing level of 10 dB, respectively. It turns out that for realistic values of squeezing and anti-squeezing the squeezing phase will have to be stabilised with respect to the phase of the local oscillator of the interferometer, but the phase stability requirements are fairly easy to fulfil. The resulting requirements on the stability of the length of the filter cavity are increased roughly by the finesse of the cavity, but are also rather easily met.

D.4 Thermal noise of the ET-LF interferometer

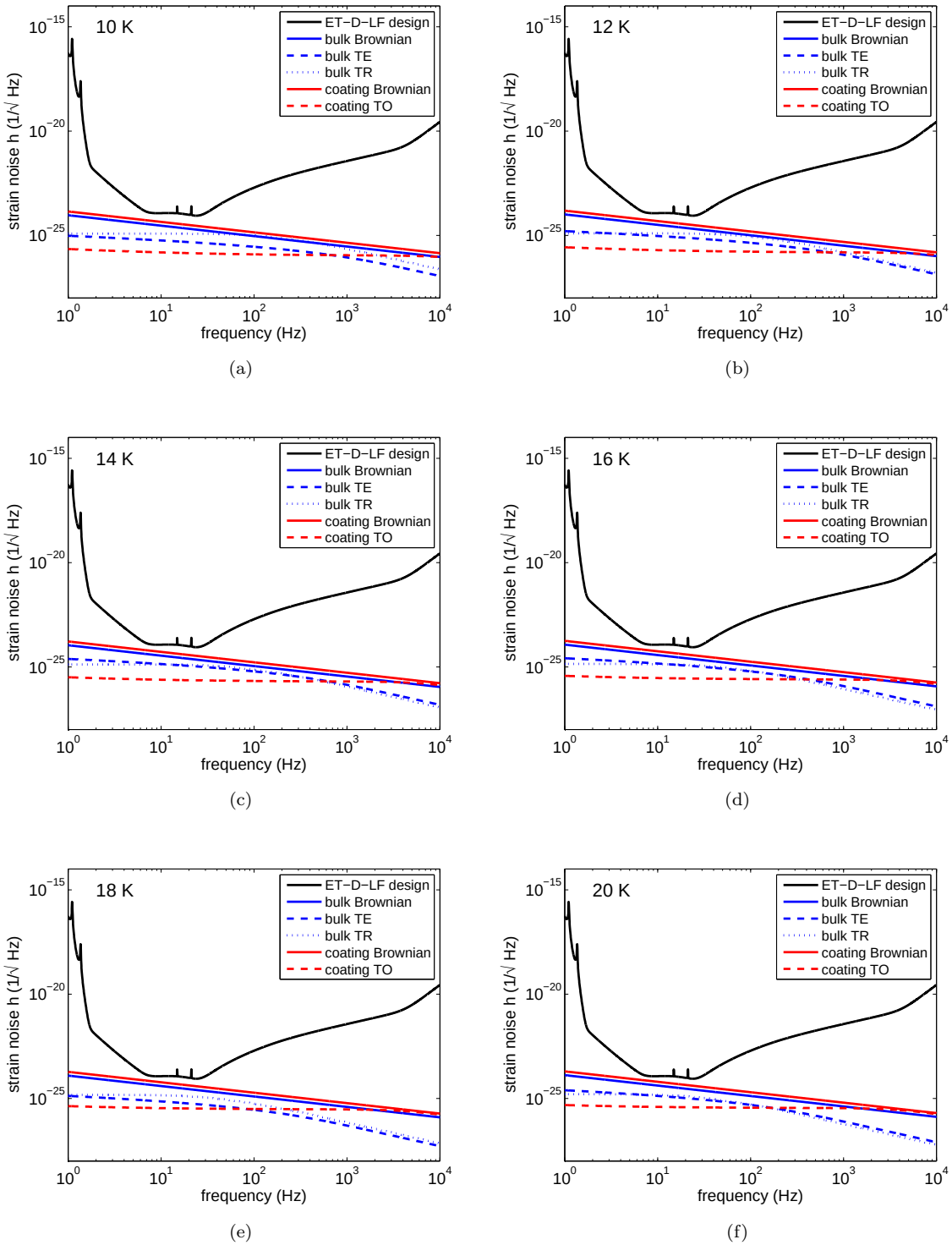

Figure 264: Evolution of the total thermal noise of the ET-LF interferometer in dependence of the operating temperature. (a) - 10 K, (b) - 12 K, (c) - 14 K, (d) - 16 K, (e) - 18 K, (f) - 20 K.

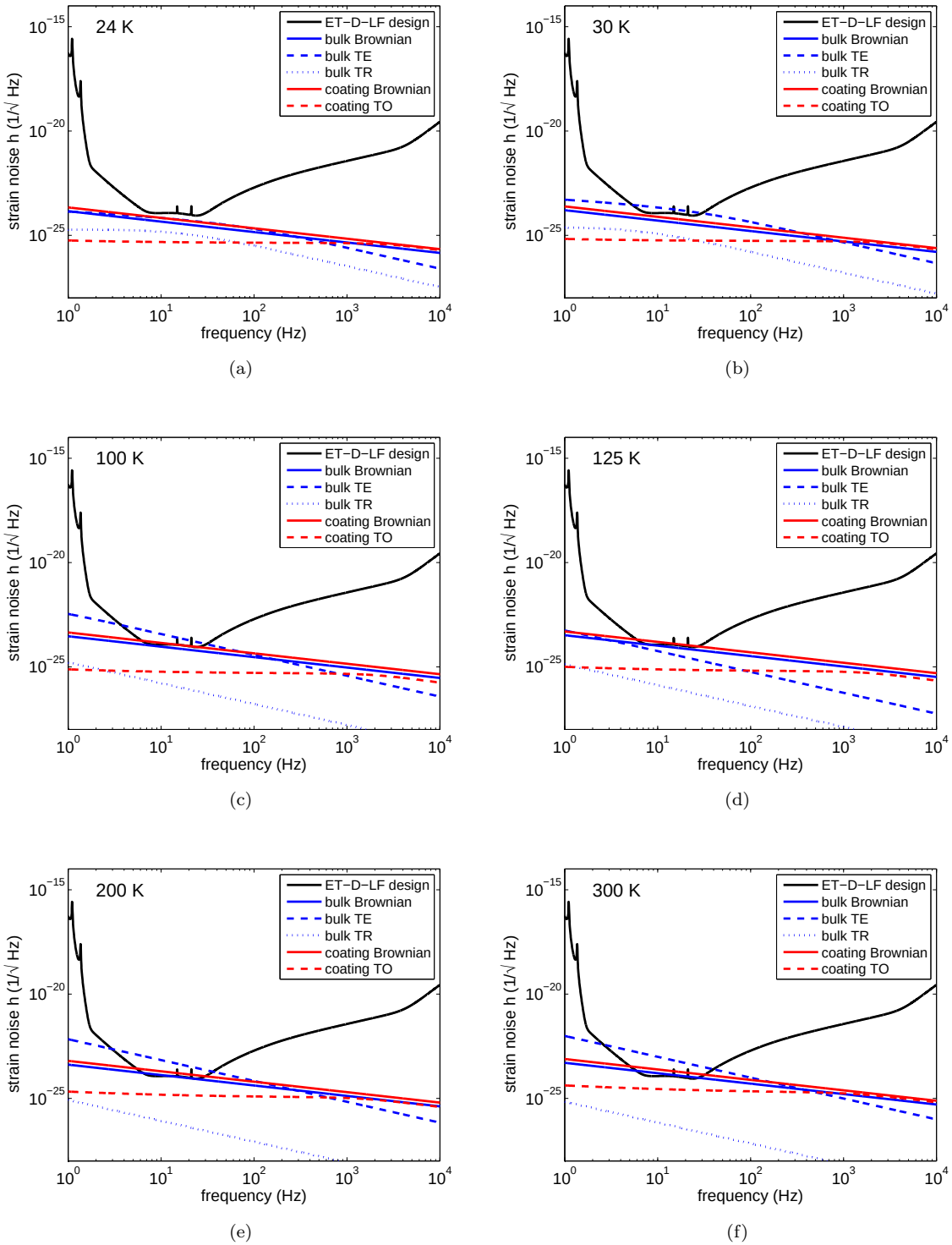

Figure 265: Evolution of the total thermal noise of the ET-LF interferometer in dependence of the operating temperature. (a) - 24 K, (b) - 30 K, (c) - 100 K, (d) - 125 K, (e) - 200 K, (f) - 300 K.

D.5 Parametric instability

Parametric instability is one of the important issues in future interferometric detectors [698]. Such interferometers have at least a few km length arm cavities. The spectral distance between optical modes in these long cavities are on the order of 10 kHz. This value is comparable with the frequencies of elastic modes of the cavity mirrors. In such cases, the parametric instability becomes a serious problem in the stable operation of interferometers. A small thermally driven elastic vibration modulates the light and excites the transverse optical modes of the cavity which is called Stokes modes. These excited optical modes apply modulated radiation pressure on the mirrors. This makes the amplitude of the elastic modes larger. At last, the elastic modes and optical Stokes modes which is different from injected beam oscillate largely. This is the parametric instability.

The formula of the parametric instability of a Fabry-Perot cavity (without anti-Stokes modes) is derived in Ref. [698]. If the parametric gain R of an elastic mode is larger than unity, that mode is unstable. The formula of R is

$$R = \sum_{\text{optical mode}} \frac{4PQ_{\mathrm{m}}Q_{\mathrm{o}}}{McL{\omega_{\mathrm{m}}}^2} \frac{\Lambda_{\mathrm{o}}}{1+\Delta\omega^2/{\delta_{\mathrm{o}}}^2}, \tag{196}$$

where $P, Q_{\mathrm{m}}, Q_{\mathrm{o}}, M, c, L, \omega_{\mathrm{m}}, \Delta\omega$, and δ_{o} are the optical power in the cavity, the Q-values of the elastic and optical modes, the mass of the mirror, the speed of light, the cavity length, the angular frequency of the elastic mode, the angular frequency difference between the elastic and optical modes, and the half-width angular frequency of the optical mode, respectively. The value Λ_{o} represents the spatial overlap between the optical and elastic modes. If the shapes of the optical and elastic modes are similar, Λ_{o} is on the order of unity. If the shapes are not similar, Λ_{o} is almost zero. When the shapes and frequencies of the optical and elastic modes are similar ($\Lambda_{\mathrm{o}} \sim 1, \Delta\omega \sim 0$), R will become several thousands in second generation projects; Advanced LIGO and Advanced Virgo. In these projects, the effect of parametric instability is a serious problem [699, 700].

Here, the parametric instability of the Einstein Telescope (ET) interferometer is discussed. This instability depends on the specification of the interferometer. However, details of the design are considered and discussed now. Therefore, outlines of the instability of the ET interferometer, preliminary calculation results, and future work are shown. In order to simplify the discussion, only the instability of a Fabry-Perot cavity is considered. The effect of power and signal recycling (or resonant sideband extraction) techniques are not taken into account.

At first, we consider the parametric instabilities in Advanced LIGO as an example of the second generation. At second, the parametric instability in ET is discussed (outline of instability in ET and the preliminary results of calculation are shown). At third, how to suppress the instability of the ET arm cavity is considered. The last part is devoted to a summary (and future work).

Parametric instability of the second generation interferometers

As example of the second generation interferometers, the Advanced LIGO is considered. The specifications of Advanced Virgo are similar. Table 24 gives the specifications of Advanced LIGO in Refs. [699–701] (after these references, the specifications of Advanced LIGO were changed).

Study of the instability in Advanced LIGO by a group at the University of Western Australia [699, 700] is reviewed briefly. They investigated what happens when the curvature of a mirror is changed. The curvature of the other mirror is the default value given in Table 24. Reference [700] shows the curvature dependence of the unstable mode number. The number of the unstable modes of mirror cavity is between 20 and 60 (it must be noted that this number increases if the higher elastic modes are taken into account). Reference [699] shows that the maximum of R in the various elastic modes strongly depends on the mirror curvature. Even a shift of only a few meters in the mirror curvature causes a drastic change of the maximum R. The requirement of the accuracy in the mirror curvature in Advanced LIGO is difficult to be achieved.

Parametric instability of Einstein Telescope: Specifications of Einstein Telescope

Here, the parametric instability of the ET is considered. The details of the ET interferometer are not decided now. Here, we adopt parameters of ET-C [434]. These parameters are summarized in Table 24. Parameters of ET-D [489] (this is newer than ET-C) are similar to those of ET-C. The difference does not change the paremetric instability. The comparison with old sensitivity, ET-B [427, 702], is also discussed here.

	Advanced LIGO	ET-C-HF	ET-C-LF
Laser beam profile	Gaussian	LG33	Gaussian
Wavelength(λ)	1064 nm	1064 nm	1550 nm
Cavity length(L)	4000 m	10000 m	10000 m
Front mirror curvature radius(R_1)	2076 m	5643 m	6109 m
End mirror curvature radius(R_2)	2076 m	5643 m	6109 m
Beam radius at the mirrors(w_i)	60 mm	72.5 mm	120 mm
Finesse ($\mathcal{F}$)	1250	850	850
Power in a cavity(P)	0.83 MW	3 MW	18 kW
Mirror material	Fused silica	Fused silica	Silicon
Sound velocity in mirror (v)	5.7 km/s	5.7 km/s	8.4 km/s
Density of mirror (ρ)	2.2 g/cm^3	2.2 g/cm^3	2.3 g/cm^3
Mirror mass(M)	40 kg	200 kg	211 kg
Mirror diameter(r)	340 mm	620 mm	620 mm
Mirror thickness(t)	200 mm	300 mm	300 mm
Mirror temperature(T)	300 K	300 K	10 K

Table 24: Specification of Advanced LIGO [699–701], and ET-C [434].

Parametric instability of Einstein Telescope: Maximum of R of Einstein Telescope

The strength of instability R is written as

$$R \propto \frac{4PQ_\mathrm{m}Q_\mathrm{o}}{McL{\omega_\mathrm{m}}^2}. \tag{197}$$

Let us compare the maximum R of ET with that of Advanced LIGO. It is supposed that Q_m is the same. We must take the difference of power P and mass M into account. It must be noted that the ratio Q_o/L is proportional to the factor $\mathcal{F}/\lambda$. The resonant frequency ω_m is inversely propotional to the mirror size. It is assumed that scale of mirror is propotional to the third root of mirror volume (ratio of mass to density). We should consider the material difference in the case of ET-LF. The resonant frequency of mirror ω_m is inversely propotional to the sound velocity.

The ratio of R of ET-HF to that of Advanced LIGO is

$$\left(\frac{3\mathrm{MW}}{0.83\mathrm{MW}}\right)\left(\frac{850}{1250}\right)\left(\frac{40\mathrm{kg}}{200\mathrm{kg}}\right)\left(\frac{200\mathrm{kg}}{40\mathrm{kg}}\right)^{2/3} = 1.4. \tag{198}$$

The ratio of R of ET-LF to that of Advanced LIGO is

$$\left(\frac{18\mathrm{kW}}{0.83\mathrm{MW}}\right)\left(\frac{850}{1250}\frac{1064\ \mathrm{nm}}{1550\ \mathrm{nm}}\right)\left(\frac{40\mathrm{kg}}{211\mathrm{kg}}\right)\left(\frac{211\mathrm{kg}}{40\mathrm{kg}}\frac{2.2\mathrm{g/cm}^2}{2.3\mathrm{g/cm}^3}\right)^{2/3}\left(\frac{5.7\mathrm{km/s}}{8.4\mathrm{km/s}}\right)^2 = 2.6\times10^{-3}. \tag{199}$$

The maximum of R in Advanced LIGO is on the order of 100 [700]. Therefore, the parametric instability of ET-LF is not a problem. On the other hand, maximum R of ET-HF is comparable with that of Advanced LIGO. We will discuss parametric instability of only ET-HF.

Parametric instability of Einstein Telescope: Number of unstable modes of ET-C-HF

The number of unstable modes are proportional to the product of elastic mode density and optical mode density. The mode density of the elastic mode is proportional to the cubic of the ratio of the mirror size to the sound velocity. Thus, the elastic mode density of ET-HF is 5 times larger than that of Advanced LIGO because of the difference of mirror size.

The ratio of the optical transverse mode interval to the free spectrum range is described as

$$\frac{1}{\pi}\cos^{-1}\sqrt{g_1 g_2}, \tag{200}$$

$$g_n = 1 - \frac{L}{R_n}. \tag{201}$$

There are 8 and 4 transverse optical modes in a free spectrum range of Advanced LIGO and ET-HF interferometers. Since the cavity of ET is 2.5 times longer, the free spectrum range is 2.5 times smaller. Therefore, the optical mode density of the ET-HF interferometer is 1.4 times larger. The reason why the optical mode density of ET-HF is comparable with that of Advanced LIGO nevertheless the cavity length of ET-HF is longer stems from the difference of beam shape, TEM_{00} and LG_{33}. Since the beam in Advanced LIGO is Gaussian (TEM_{00}), a larger beam radius implies smaller interval between optical transverse modes. On the other hand, ET-HF adopts the LG33 mode, higher optical transverse mode. The radius of higher mode is larger than that of TEM00. Thus, it is not necessary to increase the radius of fundamental mode (TEM_{00}). This effect cancels that of longer length of cavity.

In total, the number of the instable modes, which is proportional to the product of the elastic and optical mode densities, of the ET-HF interferometer is 7 times larger than that of the Advanced LIGO interferometer. The main reason of the difference of Advanced LIGO and ET-HF is that of size of mirrors.

Parametric instability of Einstein Telescope: Mirror curvature dependence of ET-C-HF

The instability strength R is a function of the transverse optical mode frequencies. How the curvature variation affects the n-th optical transverse mode was calculated. The result is $1.2n$ Hz/m in ET-HF. This value is smaller than that of Advanced LIGO ($15n$ Hz/m). The longer baseline and adopting LG33 mode make mirror curvature dependence of instability smaller.

Parametric instability of Einstein Telescope: Comparison with ET-B

Here parametric instability of ET-B [427], which is sensitivity in old design, is compared with that of ET-C (the details about parametric instability of ET-B is discussed in Ref. [702]). From point of view of parametric instability, ET-C is better than ET-B. Obviously, the first reason is that ET-C-LF has no serious problem about this instability. The second reason is that ET-C-HF has (about 4 times) less instable modes and (about 3 times) weaker mirror curvature dependence. This is because of the difference of beam shape; Gaussian beam (TEM00) in ET-B and LG33 in ET-C-HF.

Parametric instability of Einstein Telescope: Preliminary results of calculation for parametric instability of ET-C-HF using finite element method

The preliminary calculation for instability of ET-C-HF using finite element method is introduced here. At first, it must be noted that further investigation is necessary. We consider all elastic modes below 30 kHz (twice times the free spectral range of cavity). The anti-Stokes modes are taken into account. Therefore, Eq. (196) should be rewritten as [703]

$$R = \sum_{\text{optical mode}} \frac{4PQ_{\mathrm{m}}Q_{\mathrm{o}}}{McL{\omega_{\mathrm{m}}}^2}\frac{\Lambda_{\mathrm{o}}}{1+\Delta\omega^2/{\delta_{\mathrm{o}}}^2} - \sum_{\text{optical mode(anti)}} \frac{4PQ_{\mathrm{m}}Q_{\mathrm{o(anti)}}}{McL{\omega_{\mathrm{m}}}^2}\frac{\Lambda_{\mathrm{o(anti)}}}{1+\Delta\omega^2_{\mathrm{anti}}/{\delta_{\mathrm{o(anti)}}}^2}, \tag{202}$$

The number of unstable modes is only 5. One of the reasons is that some Stokes modes are canceled by anti-Stokes modes effectively. If the anti-Stokes modes are neglected, there are 17 unstable modes. In this calculation, the splitting of the degenerated elastic mode due to imperfectness of mirrors is not taken into account [704, 705]. Since this effect increases the number of unstable modes, it should be considered in a next step.

We calculated the instability with the other mirror curvature. The curvature of one mirror is changed. The new curvature is 5743 m. In this case, the number of unstable modes is 5. So, the number of unstable modes does not depend on mirror curvature supporting the conclusion of the previous discussion.

Instability suppression in ET-C-HF

Although the strength of the instability of the ET-HF interferometer is comparable with that of Advanced LIGO, the number of the unstable modes is 7 times larger. The three methods for the instability suppression in Advanced LIGO are being studied [700, 706, 707]. Let us consider whether these three methods (thermal tuning method, feedback control, Q reduction of elastic modes) are appropriate for ET (the tranquilizer cavity [708] is one of the other methods. However, this is not introduced here).

Instability suppression in ET-C-HF: Thermal tuning method

In the thermal tuning method [700], a part of the mirror is heated for curvature control. Since R depends on the curvature, the suppression of R should be possible by this manner. However, this method is not useful in ET-HF because the mirror curvature dependence of parametric instability is 10 times smaller than that of Advanced LIGO.

Instability suppression in ET-C-HF: Feedback control

It is possible to control the light or the mirror so that the parametric instabilities would be actively suppressed [700, 707]. If the number of unstable modes is smaller, feedback control is easier. However, these are more difficult (active) methods than Q reduction (passive method) of the elastic modes, especially, if there are many unstable modes. Therefore, it is good that almost all modes are suppressed by passive method and that only strong instable modes are supressed by active method.

Instability suppression in ET-C-HF: Q reduction of elastic modes

This is a useful method [706] for ET. The value of R is proportional to the Q-value of the elastic mode, $Q_{\rm m}$, as shown in Eq. (196). The Q-values of fused silica are about 10^8 [709]. The maximum R of ET is comparable with that of Advanced LIGO, on the order of 100 hundreds at most [700]. If the Q-values of the ET-HF mirrors become 10^6, almost all modes become stable. Since the mechanical loss concentrated far from the beam spot has a small contribution to the thermal noise [710, 711], we should be able to apply additional loss on a barrel surface [706, 712]. The thermal noise caused by loss on barrel surface is $4.3\times10^{-25}/\sqrt{\rm Hz}$ at 100 Hz (details are described in Appendix after the summary of parametric instability). This is comparable with ET-HF sensitivity. However, this estimation is not precious (in order to simplify the discussion, it is assumed that laser beam is Gaussian although it is LG33). We should investigate thermal noise introduced by loss on barrel surface.

We are able to introduce the loss on the barrel surface by the coating Ta_2O_5, which is a popular material for the reflective coating of the mirrors. According to Ref. [713], the loss angle of the SiO_2/Ta_2O_5 coating is $(4\sim6)\times10^{-4}$ between 4 K and 300 K. Since the loss of this coating is dominated by that of Ta_2O_5 [714], the loss angle of Ta_2O_5 is $(8\sim12)\times10^{-4}$. If the barrel loss dominates the mirror Q, it would be expressed as [711]

$$\frac{1}{Q_{\rm m}} \sim \frac{E_{\rm Ta_2O_5}}{E_{\rm substrate}}\frac{2d}{R}\phi, \tag{203}$$

where $E_{\rm Ta_2O_5}, E_{\rm substrate}, d, R, \phi$ are the Young's moduli of Ta_2O_5 and the mirror substrate, the thickness of the Ta_2O_5 layer, the mirror radius and the loss angle of Ta_2O_5, respectively. These values are summarized in Table 25 [434, 713]. In order to arrive at Q-values of $Q_{\rm m}\sim10^6$, the Ta_2O_5 coating thickness d must be 80 μm in the case of ET-HF.

Young's modulus of the Ta_2O_5 ($E_{\rm Ta_2O_5}$)	1.4×10^{11} Pa
Young's modulus of the fused silica	7.2×10^{10} Pa
Mirror radius (R)	31 cm
Loss angle of Ta_2O_5 (ϕ)	10^{-3}

Table 25: Specification of the coating [434, 713].

Recently, another method to reduce Q-values of elastic mode (using electrostatic actuator) is proposed [715]. It should be considered in near future.

Box D.2: Summary

The parametric instability of ET-C is discussed (it is expected that the result of ET-D is similar). The instability of ET-C-LF is not a serious issue because of the small light power. The maximum strength of instability of ET-C-HF is comparable to that of Advanced LIGO. The mirror curvature depepndence of ET-C-HF instability is about 10 times weaker than that of Advanced LIGO because of longer baseline and LG33 beam. However, the instable mode number is 7 times larger (In order to evaluate a precise number, the calculation using finite element method is necessary. This calculation is in progress). This is mainly owing to the larger mirrors of ET. We should investigate how to suppress. Feedback control and Q reduction of elastic modes are candidates.

Appendix A : Mirror scale dependence of thermal noise by barrel surface loss

The ET mirror is larger than the Advanced LIGO mirror. We must consider the size effect on the thermal noise by the loss on the barrel surface. In order to simplify the discussion, it is supposed that the mirror and laser beam of ET are similar to those of Advanced LIGO (although the beam of ET-HF is LG33, not Gaussian). In short, the difference between ET and Advanced LIGO mirrors is only the scale. The ratio of beam radius to mirror radius is the same. Under these assumptions, Q-values of mirrors are independent of the mirror scale, a. According to Ref. [710], the amplitude of the thermal noise $\sqrt{G_{\rm coating}}$ is described as

$$\sqrt{G_{\rm coating}} \propto \sqrt{W_{\rm diss}}, \tag{204}$$

where $W_{\rm diss}$ is the dissipated power when the pressure of which the profile $p(r)$ is the same as the laser beam is applied on the mirror flat surface. If the loss is the structure damping, the dissipated power is proportional to the elastic energy in the loss layer on the barrel surface;

$$W_{\rm diss} \propto \int_{\rm barrel\ surface} \mathcal{E} dS \times d, \tag{205}$$

where $\mathcal{E}$ and d are the elastic energy density and the thickness of the loss layer. The problem is how $W_{\rm diss}$ depends on the mirror scale a. Since the mirrors are similar, dS and d are described as

$$dS \propto a^2, \tag{206}$$
$$d \propto a. \tag{207}$$

The elastic energy density $\mathcal{E}$ is proportional to the square of the strain tensor. The strain tensor is proportional to the pressure on the flat surface p. This pressure is inverse proportional to the square of the scale. In short, the elastic energy density is written as

$$\mathcal{E} \propto p^2 \propto \frac{1}{a^4}. \tag{208}$$

We are able to obtain the relationship between the thermal noise and the mirror scale;

$$\sqrt{G_{\rm coating}} \propto \sqrt{\frac{1}{a^4} \times a^2 \times a} = \sqrt{\frac{1}{a}}. \tag{209}$$

Above discussion is based on the assumption that the ratio of the beam radius to mirror radius is constant. If the mirror size is fixed, the thermal noise by the barrel loss is independent of the beam size [711]. Therefore, the thermal noise by the barrel surface coating is inverse proportional to the square root of the mirror scale.

The thermal noise caused by surface coating for instability supression is evaluated. The thermal noise by the holes with loss on the barrel surface is investigated in Ref. [712]. The size of their mirror is 150 mm in diameter and 60 mm in thickness. The mass is 2.3 kg. Since the mass of ET-HF is 200 kg, the size of ET-HF mirror is about $(200/2.33)^{1/3} \sim 4.4$ times larger. The beam radius of ET-HF is 72.5 mm. If the ratio of beam radius

to mirror radius is the same, the beam radius of ET-HF corresponds to 1.6 cm in Ref. [712]. Figure 4 of Ref. [712] shows that mirror thermal noise (displacement) with 1.6 cm radius beam is about 10^{-20} m/$\sqrt{\text{Hz}}$ at 100 Hz. Since there are 4 mirrors and cavity length is 10 km, it corresponds to a strain noise amplitude of 2×10^{-24} /$\sqrt{\text{Hz}}$. We should take correction of size, Eq. (209), into account. The Q-values of mirror with this loss in Ref. [712] is $1/(10^{-2} \times 5 \times 10^{-4}) = 2 \times 10^5$. Since we assume that Q-value is 10^6, we should take this difference into account. In total,

$$2 \times 10^{-24} \ /\sqrt{\text{Hz}} \times \sqrt{\frac{1}{4.4}} \times \sqrt{\frac{2 \times 10^5}{10^6}} = 4.3 \times 10^{-25} \ \sqrt{\text{Hz}} \tag{210}$$

This value is comparable with the ET-HF sensitivity. However, this evaluation is not precise. For example, we assumed that beam is Gaussian. However, ET-HF will adopt LG beam. These effects should be investigated.

D.6 Holographic noise

It is currently widely assumed that the holographic principle, developed by G. 't Hooft [716] and L. Susskind [717], should be the fundamental constituent part of any unified theory of quantum gravity. It says that that the physical theory defined in the space-time of dimensionality D is equivalent to another theory defined on the boundary of dimensionality $D-1$. The most known mathematical realization of holographic principle is the AdS/CFT correspondence by J. Maldacena: string theory in anti-de Sitter space-time is equivalent to conformal field theory on its boundary [718]. It follows from the holographic principle that if the volumetric system can be described by the theory on the boundary, then the maximal number of volumetric degrees of freedom should not exceed the number of their "images" on the boundary. Since the "classical" field-theoretical informational content of the region of space is defined by its volume, such a description contains much more degrees of freedom than allowed by the holographic entropy bound. Therefore, our 3-dimensional world must be "blurry" in order to match the number of degrees of freedom inscribed on some 2-dimensional holographic surfaces. The holographic uncertainty is a particular (highly speculative) hypothesis proposed by C. Hogan about how the holographic principle works in a flat space-time [414]. He posited that in order to preserve the holographic nature of space time, it must have diffractive nature described by the wave functions of transversal position distribution of matter-energy [719], i.e. the transversal coordinates of two particles (test masses) separated by a distance L in a longitudinal direction should no longer commute: $[\hat{x}_1, \hat{x}_2] = il_{\text{P}}L$, where the commutator is defined on the light-like geodesics only. The corresponding uncertainty relation reads $\Delta x_1 \Delta x_2 \geq l_{\text{P}}L$ meaning that the relative transversal positions of two test masses cannot be measured with infinite precision. The holographic uncertainty relation implies that the measurement of the transversal position of a single test mass with the optical signals will yield uncertain results with $\Delta x \geq \sqrt{l_{\text{P}}L}$, where L stands for the distance the light wave travels between the two measurements. This holographic fuzziness with associated uncertainty Δx should be seen in precise interferometry, otherwise it would be possible to distinguish more test-mass configurations than is allowed by the holographic entropy bound. Thus, in a Michelson interferometer the measurement of the beam-splitter transversal position relative to the direction of the incident laser beam should yield uncertain results. Uncertain measurement results produce fluctuating time series, i.e. the noise called holographic noise. The minimal level of expected holographic noise corresponds to the Gaussian space-time wave functions which minimizes the holographic uncertainty relation, much like in usual quantum mechanics. In the frequency region $f \ll c/L$ holographic noise power spectral density is frequency-independent and equals to $S(f) = 2t_{\text{P}}L^2/\pi$, or effective metric strain $h(f) = \sqrt{S(f)/L^2} = \sqrt{2t_{\text{P}}/\pi} = 1.84 \times 10^{-22}/\sqrt{\text{Hz}}$ with t_{P} standing for Planck time. Holographic noise prediction is thus fixed with no free parameters, therefore the hypothesis can be either confirmed or ruled out experimentally. Holographic noise signatures are currently being looked for in the noise spectrum of GEO-600 interferometer. However, the available sensitivity does not allow to make unambiguous conclusions. Since the space-time wave function universally defines the transversal distribution of mass-energy, holographic noise should exhibit particular cross-correlation features. Namely, two closely positioned interferometers should produce correlated measurements of the holographic displacement, because they occupy nearly the same space-time volume and thus holographic motion of their test masses (beam-splitter, in particular) is defined by nearly the same wave function. If the two interferometers are aligned along their arms and are displaced by $\Delta L \ll L$ along one of them, then the cross-correlation spectral density equals to $S(f) = 2t_{\text{P}}L^2[1 - (\Delta L/L)]/\pi$. This

expected feature of the holographic noise is to be tested in the Fermilab holometer which is currently under construction [720]. For a Michelson interferometer with cavities in the arms, the effective metric strain equals to $h(f) = N^{-1}\sqrt{S(f)/L^2} = N^{-1}\sqrt{2t_{\rm P}/\pi} = N^{-1}1.84\times10^{-22}/\sqrt{\rm Hz}$, where N is the average number of photon round trips inside the cavities. The reason for the N^{-1} factor is that the cavities effectively lengthen the arms for the gravitational waves (this holds true for the frequencies $f \lesssim c/2LN$), thus amplifying the response to the gravitational waves, but do not change the beam-splitter holographic displacement spectrum [414]. With planned transmittances of the arm-cavities input mirror and the end mirror of 7000 and 10 ppm, respectively, the number of photon round-trips inside the ET cavities equals to $N \approx 277$, thus lowering the holographic metric strain to $h(f) \approx 0.66\times10^{-24}/\sqrt{\rm Hz}$. The development of sound theoretical models and experimental test are under way. If it turns out that the holographic noise is a serious issue for the Einstein telescope gravitational-wave detector, the optical design (e.g. cavity finesse) has to be adapted.

D.7 Displacement-noise-free interferometry

Most of the dominant noise sources in laser interferometric gravitational-wave detection can be related to the class of displacement noise: seismic noise, gravity-gradient noise, various thermal noise sources, even the quantum back-action noise. Each method of suppression or elimination of displacement noise is usually suited for control of only one kind of noise: seismic isolation, measurement and partial cancellation of gravity gradients, cryogenics, quantum-noise-reduction schemes. Displacement-noise-free interferometry (DFI) is the method of displacement noise cancellation which aims at simultaneous elimination of the information about all position fluctuations of the test masses, but leaving a certain amount of information about gravitational waves. All known DFI schemes can be divided into two categories: schemes with complete and partial displacement noise cancellation. Complete displacement noise cancellation relies on the distributed nature of gravitational waves. While displacement noise imprints on the optical phase only at the moments of the laser beam reflection at the test masses (localized effect), gravitational waves affect the laser beam along its optical path (distributed effect). From the viewpoint of some local observer the interaction of the gravitational wave with the interferometer adds up to two effects [721]: the motion of the test masses in the gravitational-wave tidal force-field (which is indistinguishable from the action of fluctuating forces, therefore it is a localized effect) and the direct coupling between the gravitational wave and light (distributed red-shift effect). DFI implies the cancellation of displacement noises along with the localized part of the gravitational-wave effect, leaving the distributed red-shift effect in the interferometer response. Since the latter one has the order of $O[h(L/\lambda_{\rm GW})^2]$ (where h is the gravitational-wave amplitude, L is the interferometer linear scale and $\lambda_{\rm GW}$ is the gravitational wavelength), DFI has much weaker gravitational-wave susceptibility than conventional gravitational-wave detectors in the long-wavelength regime $L \ll \lambda_{\rm GW}$. Complete displacement noise cancellation can be achieved in an interferometer with large enough number of test masses by properly combining several response signals [722]. For instance, 2- and 3-dimensional setups composed of two Mach-Zehnder interferometer topologies sharing the beam-splitters [723]. The gravitational-wave response of the 2-dimensional scheme has the order of $O[h(L/\lambda_{\rm GW})^3]$, while the one of the 3-dimensional scheme is of the order of $O[h(L/\lambda_{\rm GW})^2]$. For comparison, the gravitational-wave response of the conventional Michelson interferometer is $O[h(L/\lambda_{\rm GW})^0]$. Implementation of time-delay devices, while improving the strength of the gravitational-wave response, limits the sensitivity by adding noise [724]. Another class of DFI schemes with partial displacement noise cancellation aims on keeping strong enough gravitational-wave susceptibility, with either $O[h(L/\lambda_{\rm GW})^0]$ or $O[h(L/\lambda_{\rm GW})^1]$ leading orders in the response. This can be achieved with linear Fabry-Perot cavities, ring cavities, etc. A single Fabry-Perot cavity, double-pumped through both mirrors, allows elimination of their displacement noise in the proper linear combination of the responses, however, the sensitivity remains limited due to laser noise and displacement noise of all the auxiliary optics [725]. Modification of this scheme with two cavities placed symmetrically allows complete displacement noise cancellation but does not allow laser noise cancellation [726]. In a symmetric double Michelson interferometer with the arm-cavities the sensitivity is limited by the noise of the local oscillators used for detection of the transmitted waves in the arms; in addition, this scheme requires placing several mirrors rigidly on a single common platform, which is very impractical [727]. Double pumping of the resonant ring cavity allows cancellation of its mirrors noise and laser noise, but cannot deal with displacement noise of the mirrors and beam-splitters used to produce the pumping waves [728]. To summarize, all detectors with either complete or partial displacement noise can-

cellation consist of combinations of many different topologies and therefore differ in general significantly from the conventional detectors especially in terms of the complexity and either have very weak gravitational-wave susceptibility or impractical requirements (like rigid platforms) to operate, or suffer from uncancelled noises, thus making them hardly advantageous over the conventional non-DFI topologies.

D.8 Alternative to laser interferometry: atomic sensor

It is in principle also possible to utilize light pulse atom interferometry to detect gravitational waves. Light pulse atom interferometry can be thought of as a comparison of time kept by internal atom clocks and optical wave of the laser. The incoming gravitational wave changes the rate of time which can be seen in an interferometer phase shift. The major advantage of the atom-light interferometry over conventional optical interferometry is that the atoms, playing the role of inertial sensors, are not subjected to the external fluctuations in comparison with the mirrors, and thus do not require sophisticated vibration isolation techniques. A phase shift measurement in an atomic interferometer consists of three steps [729]: first, the atomic cloud is prepared, cooled to sub-microkelvin temperatures and then launched. Atoms in the cloud are in the $|\text{ground}\rangle$ state and are freely falling after the launch. In the second phase light pulses are applied. The "beamsplitter" $\pi/2$-pulse places atoms in the superposition of two states: $1/\sqrt{2}|\text{ground}\rangle + 1/\sqrt{2}|\text{excited}\rangle$. Since the internal state of the atom is correlated with its momentum, atoms in ground and excited states acquire different velocities, and thus both states become temporarily and spatially separated. After some time the "mirror" π-pulse exchanges the two components of the superposition: $|\text{ground}\rangle \to |\text{excited}\rangle$, $|\text{excited}\rangle \to |\text{ground}\rangle$, so that the atoms will finally overlap. Finally, the second "beam-splitter" $\pi/2$-pulse makes the two branches of the atom wave function interfere, in full similarity to a Mach-Zehnder interferometer. The third phase of interferometry is detection. The interference pattern can be extracted by measuring the population of atoms in a given state, for instance, in the excited state. The measured phase shift results from both the free-fall evolution of the quantum state along each path in interferometer and from the local phase of the laser which is imprinted on the atoms at the moments laser pulses are applied. Since laser sources and atomic interferometer can be separated by a significant spatial distance, the incoming gravitational wave modulates the latter, thus causing the modulation of the arrival time of the laser pulses which enters the measured atomic phase shift. A terrestrial based gravitational-wave detection with light-atom interferometry can be realized in a vertical shaft with the linear scale of $\sim 1\,\text{km}$. Two atomic interferometers of the linear scale of $\sim 10\,\text{m}$ are placed on the top and the bottom of the shaft and are operated by common lasers. With a reasonable measurement repetition time, a ground-based setup will have its peak susceptibility to the gravitational waves around $\sim 1\,\text{Hz}$, which is very interesting form the astrophysical point of view. Such a setup allows performing differential measurements between two atomic interferometers, which significantly suppresses the vibrational and optical noises of the lasers. The vibration of the optical trap which leads to different launch velocities is of less importance, since the initial "beam-splitter" pulse is applied after the atoms are launched. However, spread in velocities will enter the measurement error through the gravity-gradients, since in the nonuniform gravitational field atoms moving along different trajectories experience different gravitational forces. Gravity-gradients seem to be one of the major limiting factors towards the increase of the sensitivity. Other noises sources come from the variations of the magnetic field which change the atoms energy levels, coupling of the Earth rotation to the fluctuating transversal velocity of the optical trap. One of the dominating noise sources with the technique currently available is the atomic shot noise. It can be lowered by implementation of the sources with more intense atom fluxes and/or preparation of the atoms in squeezed states. Although light pulse atom interferometry has already found applications in atomic clocks, metrology, gyroscopes, gradiometers and gravimeters, its implementation in gravitational-wave detection requires detailed and comprehensive study and further development of the noise-lowering techniques. With the current available technologies atomic interferometers cannot provide the same level of sensitivity as the well-developed optical interferometers.

E Properties

Mechanical, optical and thermal properties at room and cryogenic temperature have been reported in the references [495, 513]. The following tables and graphs will summarise the different parameters taken into account for thermal noise simulations for the LF and HF interferometers. Generally, at cryogenic temperatures we have listed the values at 10 K unless otherwise stated.

E.1 Optics properties data base

The following tables report different optical parameters of bulk and coating materials at room and cryogenic temperature that have been used within this design study.

The bulk materials under investigation for the Einstein Telescope are silicon, sapphire and fused silica. Fused silica is known to be the best currently available optical material at room temperature. For the cryogenic case, silicon and sapphire are the two candidate materials. The detailed discussion of the materials under investigation can be found in Sec. 5.6.

Material		Fused silica	Silicon	Sapphire
Absorption	ppm	0.25 [730]	0.032 @ 1450 nm [505]	50 [731]
Thermo-optic coefficient β	$(10^{-6}/\mathrm{K})$	10	13	-
Refractive index n		1.45	3.45 @ 1550 nm	1.75

Table 26: Optical bulk material properties at room temperature. The refractive index is given at 1064 nm for fused silica and sapphire.

Material		Fused silica	Silicon	Sapphire
Absorption	ppm	-	-	90 [496]
Thermo-optic coefficientβ	$(10^{-6}/\mathrm{K})$	1.01 @ 30 K	5.8 @ 30 K	0.09 @ 4 K
Refractive index n		1.44876 @ 30 K	3.45 @ 30 K	1.75

Table 27: Optical bulk material properties at cryogenic temperatures. Parameters are given at 10 K unless otherwise specified. The refractive index of fused silica and sapphire is given at 1064 nm whereas for silicon at 1550 nm.

Several coating materials have been tested as HR coating materials and results have been reported in literature. A report has been devoted to summarize all these parameters values [495].

Material		SiO_2	Al_2O_3	$Ti:Ta_2O_5$	Ta_2O_5	TiO_2	Nb_2O_5	ZrO_2	
Absorption	ppm	0.3 [732]	-	0.5 [732]	1.22 [732]	-	2.2 [732]	11 [732]	
Thermo-optic coefficientβ	$(10^{-6}\mathrm{K})$	8	13	14	2.3	-1.8	14.3	100	
refractive index n		1.45 [732]	1.58	2.06 [732]	2.035 [732]	2.11 [733]	2.21 [732]	2.1 [732]	1.985

Table 28: Optical coating material properties at room temperature – refractive indices n are given at 1064 nm.

Material		SiO_2	Al_2O_3	Ta_2O_5	TiO_2	HfO_2
Absorption	ppm	-	-	-	-	-
Thermo-optic coefficient β	$(10^{-6}K)$	1.01	-	-	-	-
Refractive index @ 1064 nm		1.44876 @ 30 K	-	2.05	-	-

Table 29: Optical coating material properties at cryogenic temperatures. Parameters are given at 10 K unless otherwise specified.

E.2 Mechanical properties of optical materials

The mechanical properties like the Young's modulus, the mass density, Poisson's ratio as well as the mechanical loss angle play an important role in the determination of the Brownian thermal noise contribution. These values are summarised in this section for the bulk and coating materials discussed in this design study – both at room temperature as well as cryogenic temperatures. Apart from the mechanical loss angle all mechanical properties are only weakly temperature dependent and thus assumed to be temperature independent. The mechanical loss is strongly temperature dependent and thus differently taken into account at different temperatures.

The references for the different values can be found in [495, 513] unless otherwise stated.

Material		Fused silica	Si(100)	Si(110)	Si(111)	Sapphire
Loss Angle (290 K)		4×10^{-10}	1×10^{-8}	1×10^{-8}	1×10^{-8}	2×10^{-9}
Loss Angle (10 K)		1×10^{-3}	1×10^{-9}	1×10^{-9}	1×10^{-9}	4×10^{-9} @ 4.2 K
Density ρ	(kg/m^3)	2200	2330	2330	2330	3980
Young Modulus E	(GPa)	72	130	169	188	400
Poisson ratio		0.17	0.22	0.22	0.22	0.235

Table 30: Mechanical bulk material properties at room temperature as well as cryogenic temperatures.

Material		SiO_2	Al_2O_3
Loss Angle		0.5×10^{-4}	2.4×10^{-4}
Density ρ	(kg/m^3)	2200	3700
Young Modulus E	(GPa)	60	210
Poisson ratio		0.17	0.22

Table 31: Low refractive index materials – Mechanical properties at room temperature.

Material		$Ti:Ta_2O_5$	Ta_2O_5	TiO_2	Nb_2O_5	ZrO_2	HfO_2
Loss Angle		2×10^{-4}	3.8×10^{-4}	6.3×10^{-3}	4.6×10^{-4}	2.3×10^{-4}	5.9×10^{-4}
Density ρ	(kg/m^3)	6425	6850	4230	4590	6000	8000
Young Modulus E	(GPa)	140	140	290	68	200	380
Poisson ratio		0.23	0.23	0.28	0.2	0.27	0.2

Table 32: High refractive index materials – Mechanical properties at room temperature.

Material		SiO_2	Al_2O_3	Ti:Ta_2O_5	TiO_2	HfO_2
Loss Angle		5×10^{-4}	-	3.8×10^{-4}	5.6×10^{-3} @ 77 K	2.2×10^{-4}
Density ρ	(kg/m^3)	2200	3700	6425	4269 @ 73 K	-
Young Modulus E	(GPa)	60	356	140	290	-
Poisson ratio		0.159	0.2	0.21	0.253	-

Table 33: Mechanical coating material properties at cryogenic temperatures. Parameters are given at 10 K unless otherwise specified.

E.3 Thermal properties of optical materials

This section summarises the thermal properties of bulk and coating materials at room and cryogenic temperatures. These parameters influence the thermo-elastic and thermo-refractive noise contributions from the different components.

The references for the different values can be found in [495, 513] unless otherwise stated.

Material		Fused silica	Silicon	Sapphire
Thermal conductivity k_{th}	(W/m K)	1.38	130-160	33
Specific heat C	(J/kg K)	746	711	770
Thermal expansion α	(10^{-6}/K)	0.51	2.54	5.1

Table 34: Thermal bulk material properties at room temperature.

Material		Fused silica	Silicon	Sapphire
Thermal conductivity k_{th}	(W/m K)	0.4	2330	1500 @ 12.5 K
Specific heat C	(J/kg K)	3	0.276	9.34×10^{-2} @ 10 K
Thermal expansion α	(1/K)	-0.25×10^{-6}	4.85×10^{-10}	5.3×10^{-10}

Table 35: Thermal bulk material properties at cryogenic temperatures.

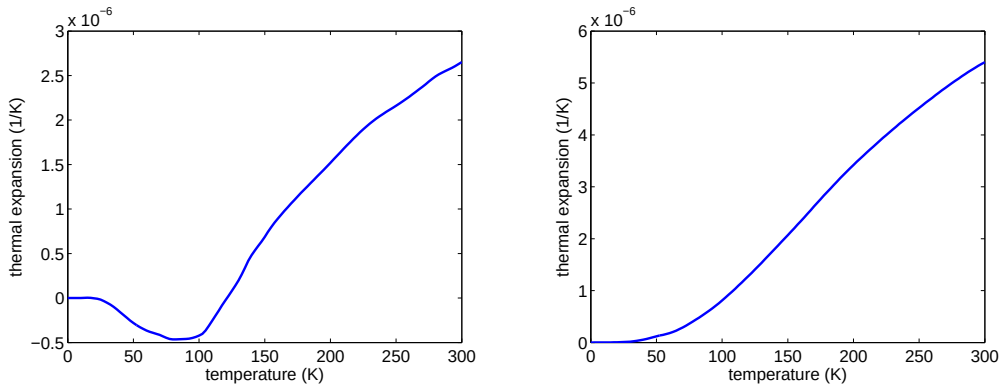

(a) (b)

Figure 266: Dependence of the coefficient of thermal expansion for silicon (a) and sapphire (b) as a function of temperature.

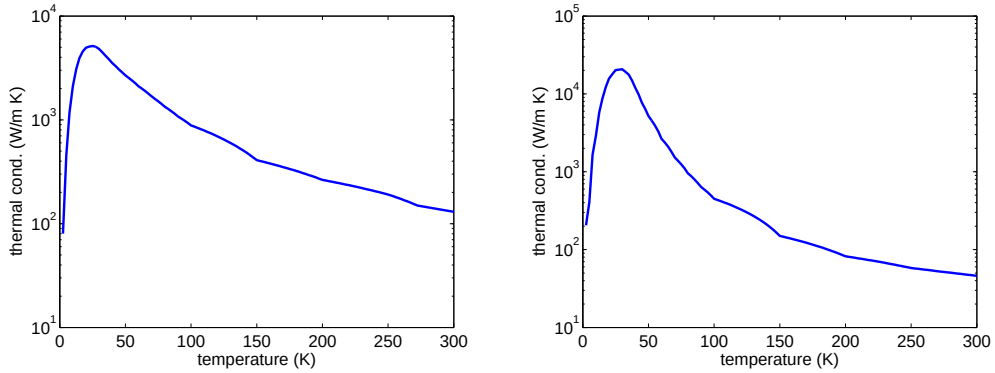

(a) (b)

Figure 267: Dependence of the thermal conductivity of silicon (a) and sapphire (b) as a function of temperature.

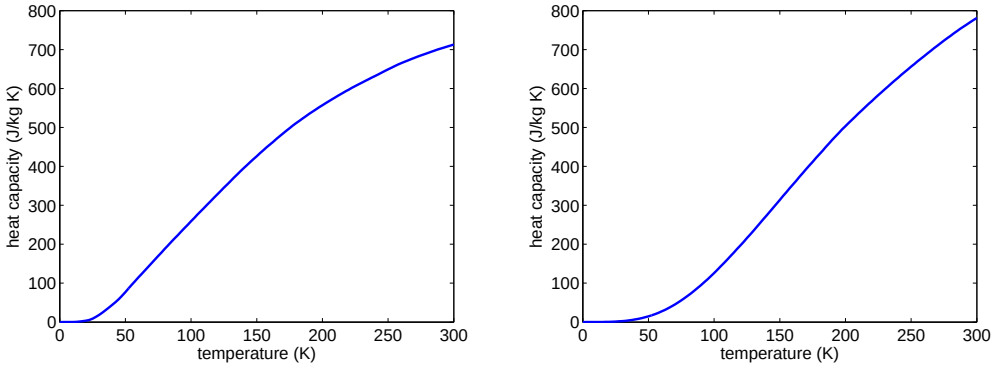

(a) (b)

Figure 268: Dependence of the heat capacity of silicon (a) and sapphire (b) as a function of temperature.

Material		SiO_2	Al_2O_3
Thermal conductivity k_{th}	(W/m K)	0.5	3.3
Specific heat C	(J/kg K)	746	310
Thermal expansion α	(10^{-6}/K)	0.51	8.4

Table 36: Thermal properties of low refractive index materials at room temperature.

Material		Ti:Ta_2O_5	Ta_2O_5	TiO_2	Nb_2O_5	ZrO_2	HfO_2
Thermal conductivity k_{th}	(W/m K)	0.6	0.6	0.45	1	1.09	1.2
Specific heat C	(J/kg K)	269	306	130	590	26	16.7
Thermal expansion α	(10^{-6}/K)	3.6	3.6	50	5.8	10.3	3.8

Table 37: Thermal properties of high refractive index materials at room temperature.

Material		SiO_2	Al_2O_3	$Ti:Ta_2O_5$	TiO_2	HfO_2
Thermal conductivity k_{th}	(W/m K)	0.13	5	-	500	-
Specific heat C	(J/kg K)	1-7	0.1	3.17 @ 50 K	0.012	-
Thermal expansion α	(10^{-6}/K)	-0.25	0.6 @ 100 K	-	6.5 @ 100 K	-

Table 38: Thermal coating material properties at cryogenic temperatures. All parameters are given at 10 K unless otherwise stated.

7 Acknowledgements

The research leading to these results has received funding from the European Community's Seventh Framework Programme (FP7/2007–2013) under grant agreement n 211743.

We thank the whole ET science team for the excellent activities during the design study phase and for the great support in producing this document.

We also thank the German Centre for Quantum Engineering and Space-Time Research, QUEST, for support.

This work is part of the research programme of the Foundation for Fundamental Research on Matter (FOM), which is financially supported by the Netherlands Organisation for Scientific Research (NWO).

All the seismic measurements have been made possible with the dedication and help from a vast number of locals. To all the people that have provided their expertise, time and assistance we would like to extend a sincere thank you. Due to the extent of the research it is impractical to list all those people but we would like to thank a few people in particular. For fruitful discussions and advice as well as facilitating measurements at the Heimansgroeve we thank Reinoud Sleeman and his colleagues from the KNMI. We also acknowledge their help in obtaining data from the Virtual European Broadband Seismograph Network (VEBSN). The measurements in Hungary were generously supported by members of the Research Institute for Particle and Nuclear Physics, Budapest, and the mining company MECSEK-ÖKO. For assistance during the measurements in Romania we are grateful to Romul Mircea Margineanu and the Salrom mining company. The Frejus tunnel measurements were kindly facilitated by Michel Zampaolo of the Laboratoire Souterrain de Modane. We thank Alessandro Bettini and Jose Jimenez of the Canfranc Underground Laboratory for their help during measurements in Spain. We are grateful to the colleagues from the University "Sapienza" and the miners of IGEA spa, for access to the Sardinian site. We would also like to thank Eugenio Coccia and Benedetto Gallese for their help during measurements at the Gran Sasso underground laboratory. We are very grateful to Rudolf Widmer-Schnidrig, Thomas Forbinger and Walter Zuern of the Black Forest Observatory for the interesting discussions and access to their laboratory. We acknowledge Guido Nuijton for his thoughts on sites in Finland. For measurements carried out at the CLIO site in Japan we thank Uchiyama Takashi, Osamu Miyakawa and Miyoki Shinji for their external help. Ricardo de Salvo and friends at the Italkali mine in Sicilie kindly assisted the measurements there. Finally we would like to acknowledge the help of EURIDICE staff members, Philippe van Marcke and Kris Moerkens, during measurements in Belgium.

We thank R.Prix for helping with Fig. 19.

References

[1] H. Grote for the LIGO Scientific Collaboration, "The status of GEO 600," *Classical and Quantum Gravity*, vol. 25 (11), p. 114043 (9pp), 2008. 8

[2] B. Abbott et al. (LIGO Scientific Collaboration), "LIGO: the Laser Interferometer Gravitational-Wave Observatory," *Reports on Progress in Physics*, vol. 72 (7), p. 076901, 2009. 8, 349

[3] K. Arai and the TAMA Collaboration, "Recent progress of TAMA300," *Journal of Physics: Conference Series*, vol. 120 (3), p. 032010, 2008. 8

[4] F. Acernese et al., "Status of Virgo," *Classical and Quantum Gravity*, vol. 25 (11), p. 114045 (8pp), 2008. 8

[5] D. S. for the Advanced LIGO Team, "Advanced LIGO Reference Design," 2009. 8, 246, 349

[6] G. M. Harry and the LIGO Scientific Collaboration, "Advanced LIGO: the next generation of gravitational wave detectors," *Classical and Quantum Gravity*, vol. 27 (8), p. 084006, 2010. 8, 196, 251, 259, 345

[7] . The VIRGO Collaboration, "Advanced Virgo Baseline Design," Virgo Technical Report VIR-0027A-09, 2009. 8, 174, 246

[8] T. Eberle et al., "Quantum enhancement of the zero-area Sagnac interferometer topology for gravitational wave detection," *Phys. Rev. Lett.*, 2010. 16, 253, 254, 307, 350, 352

[9] S. E. Woosley and E. Baron, "The collapse of white dwarfs to neutron stars," *Astrophys. J.*, vol. 391, pp. 228–235, 1992. 24

[10] B. Schutz, *A First Course in General Relativity*, Cambridge University Press, Cambridge; New York, 2nd edn., 2009. 26

[11] B. Sathyaprakash and B. F. Schutz, "Physics, Astrophysics and Cosmology with Gravitational Waves," *Living Reviews in Relativity*, vol. 12 (2), 2009. 27

[12] N. Andersson et al., "Gravitational waves from neutron stars: promises and challenges," *General Relativity and Gravitation*, vol. 43, pp. 409–436, 2011. 27

[13] K. Arun, B. Iyer, B. Sathyaprakash, and P. Sundararajan, "Parameter estimation of inspiralling compact binaries using 3.5 post-Newtonian gravitational wave phasing: The nonspinning case," *Phys. Rev. D*, vol. 71, 084008, 2005. 29

[14] A. Vecchio, "LISA observations of rapidly spinning massive black hole binary systems," *Phys. Rev.*, vol. D70, p. 042001, 2004.

[15] M. van der Sluys et al., "Parameter estimation of spinning binary inspirals using Markov-chain Monte Carlo," *Class. Quant. Grav.*, vol. 25, p. 184011, 2008.

[16] R. Lang and S. Hughes, "Measuring coalescing massive binary black holes with gravitational waves: The impact of spin-induced precession," *Phys. Rev. D*, vol. 74, 122001, 2006. 29

[17] C. Van Den Broeck and A. Sengupta, "Binary black hole spectroscopy," *Class. Quantum Grav.*, vol. 24, pp. 1089–1114, 2007. 29

[18] C. V. D. Broeck and A. S. Sengupta, "Phenomenology of amplitude-corrected post-Newtonian gravitational waveforms for compact binary inspiral: I. Signal-to-noise ratios," *Classical and Quantum Gravity*, vol. 24, pp. 155–176, 2007.

[19] K. Arun, B. Iyer, B. Sathyaprakash, S. Sinha, and C. Van Den Broeck, "Higher signal harmonics, LISA's angular resolution and dark energy," *Phys. Rev. D*, vol. 76, 104016, 2007. 29

[20] F. Pretorius, "Evolution of binary black hole spacetimes," *Phys. Rev. Lett.*, vol. 95, 121101, 2005. 29

[21] M. Campanelli, C. Lousto, P. Marronetti, and Y. Zlochower, "Accurate evolutions of orbiting black-hole binaries without excision," *Phys. Rev. Lett.*, vol. 96, 111101, 2006.

[22] J. Baker, J. Centrella, D.-I. Choi, M. Koppitz, and J. van Meter, "Gravitational wave extraction from an inspiraling configuration of merging black holes," *Phys. Rev. Lett.*, vol. 96, 111102, 2006. 29

[23] M. Hannam, "Status of black-hole-binary simulations for gravitational-wave detection," *arXiv:0901.2931 [gr-qc]*, 2009. 30

[24] L. Santamaria et al., "Matching post-Newtonian and numerical relativity waveforms: systematic errors and a new phenomenological model for non-precessing black hole binaries," *Phys. Rev.*, vol. D82, p. 064016, 2010. 31

[25] M. Burgay et al., "An increased estimate of the merger rate of double neutron stars from observations of a highly relativistic system," *Nature*, vol. 426, pp. 531–533, 2003. 31

[26] C. Kim, V. Kalogera, and D. R. Lorimer, "The Probability Distribution of Binary Pulsar Coalescence Rates. I. Double Neutron Star Systems in the Galactic Field," *Astrophys. J.*, vol. 584, pp. 985–995, 2003.

[27] C. Kim, V. Kalogera, and D. R. Lorimer, "Effect of PSR J0737-3039 on the DNS Merger Rate and Implications for GW Detection," in "A life with stars," 2006. 31

[28] A. M. Hopkins and J. F. Beacom, "On the Normalization of the Cosmic Star Formation History," *Astrophys. J.*, vol. 651, pp. 142–154, 2006. 31, 68, 69, 322, 426

[29] T. Regimbau and S. A. Hughes, "Gravitational-wave confusion background from cosmological compact binaries: Implications for future terrestrial detectors," *Phys. Rev. D*, vol. 79 (6), pp. 062002–+, 2009. 31, 67, 322

[30] R. O'Shaughnessy, V. Kalogera, and K. Belcynski, "Binary compact object coalescence rates: The role of elliptical galaxies," *(arXiv:0908.3635)*, 2009. 31, 322

[31] R. O'Shaughnessy, V. Kalogera, and C. Belczynski, "Short GRBs I: Predictions from population synthesis for a heterogeneous universe," *Astrophys. J.*, vol. 675, p. 566, 2008. 31

[32] K. Belczynski et al., "Compact Object Modeling with the StarTrack population synthesis code," *Astrophys.J. Suppl.*, vol. 174, pp. 223–260, 2008. 31

[33] K. Kulczycki, T. Bulik, K. Belczyński, and B. Rudak, "VIRGO sensitivity to binary coalescences and the Population III black hole binaries," *Astron. Astrophys.*, vol. 459, pp. 1001–1006, 2006.

[34] R. O'Shaughnessy, C. Kim, V. Kalogera, and K. Belczynski, "Constraining population synthesis models via observations of compact-object binaries and supernovae," *Astrophys. J.*, vol. 672, p. 479, 2008.

[35] K. Belczynski, R. E. Taam, V. Kalogera, F. A. Rasio, and T. Bulik, "On the rarity of double black hole binaries: Consequences for gravitational-wave detection," *Astrophys. J.*, vol. 662, p. 504, 2007. 31

[36] K. Belczynski et al., "On the Maximum Mass of Stellar Black Holes," *The Astrophysical Journal*, vol. 714 (2), p. 1217, 2010. 31

[37] K. Belczynski, D. H. Hartmann, C. L. Fryer, D. E. Holz, and B. O'Shea, "On the Origin of the Highest Redshift Gamma-Ray Bursts," *The Astrophysical Journal*, vol. 708 (1), p. 117, 2010. 31, 32

[38] R. O'Shaughnessy, R. Kopparapu, and K. Belczynski, "Impact of star formation inhomogeneities on merger rates and interpretation of LIGO results," *submitted to Astrophys. J.*, 2008. 31

[39] T. Bulik, K. Belczynski, and A. Prestwich, "IC10 X-1/NGC300 X-1: The Very Immediate Progenitors of BH-BH Binaries," *Astrophys. J.*, vol. 730, pp. 140–+, 2011. 32

[40] R. O'Shaughnessy, R. O'Leary, and F. Rasio, "Dynamical Interactions and the Black Hole Merger Rate of the Universe," *Phys. Rev. D*, vol. 76, p. 061504, 2007. 32

[41] A. Sadowski et al., "The Total Merger Rate of Compact Object Binaries in the Local Universe," *Astrophys. J.*, vol. 676, pp. 1162–1169, 2008.

[42] S. F. Portegies Zwart and S. L. McMillan, "Black Hole Mergers in the Universe," *Astrophys. J.*, vol. 528, pp. L17–L20, 2000. 32

[43] B. F. Schutz, "Determining the Hubble constant from gravitational wave observations," *Nature (London)*, vol. 323, p. 310, 1986. 32, 47

[44] M. C. Miller and E. J. M. Colbert, "Intermediate-Mass Black Holes," *International Journal of Modern Physics D*, vol. 13, pp. 1–64, 2004. 33

[45] M. C. Miller, "Intermediate-Mass Black Holes as LISA Sources," *ArXiv e-prints*, 2008, 0812.3028. 33

[46] S. A. Farrell, N. A. Webb, D. Barret, O. Godet, and J. M. Rodrigues, "An intermediate-mass black hole of over 500 solar masses in the galaxy ESO243-49," *Nature*, vol. 460, pp. 73–75, 2009. 33

[47] I. Mandel, D. A. Brown, J. R. Gair, and M. C. Miller, "Rates and Characteristics of Intermediate Mass Ratio Inspirals Detectable by Advanced LIGO," *Astrophys. J.*, vol. 681, pp. 1431–1447, 2008. 33, 48

[48] J. R. Gair, I. Mandel, M. C. Miller, and M. Volonteri, "Exploring intermediate and massive black-hole binaries with the Einstein Telescope," *Gen. Rel. Grav.*, vol. 43, p. 485, 2011, 0907.5450. 33, 48

[49] J. M. Fregeau, S. L. Larson, M. C. Miller, R. O'Shaughnessy, and F. A. Rasio, "Observing IMBH-IMBH Binary Coalescences via Gravitational Radiation," *Astrophysical Journal Letters*, vol. 646, pp. L135–L138, 2006. 33

[50] P. Amaro-Seoane et al., "Intermediate and Extreme Mass-Ratio Inspirals – Astrophysics, Science Applications and Detection using LISA," *Class. Quant. Grav.*, vol. 24, pp. R113–R170, 2007. 33, 48

[51] P. Amaro-Seoane and L. Santamaria, "Detection of IMBHs with ground-based gravitational wave observatories: A biography of a binary of black holes, from birth to death," *Astrophys. J.*, vol. 722, pp. 1197–1206, 2010. 33

[52] P. Jaranowski, A. Krolak, and B. F. Schutz, "Data analysis of gravitational-wave signals from spinning neutron stars. I: The signal and its detection," *Phys. Rev.*, vol. D58, p. 063001, 1998. 33, 234

[53] B. Abbott et al. (LIGO Scientific Collaboration), "Limits on gravitational wave emission from selected pulsars using LIGO data," *Phys. Rev. Lett.*, vol. 94, 181103, 2005. 34

[54] B. Abbott et al. (LIGO Scientific Collaboration), "Upper limits on gravitational wave emission from 78 radio pulsars," *Phys. Rev. D*, vol. 76, 042001, 2007.

[55] B. Abbott et al., "Beating the Spin-Down Limit on Gravitational Wave Emission from the Crab Pulsar," *The Astrophysical Journal Letters*, vol. 683 (1), p. L45, 2008. 34

[56] B. A. et al, "Searches for gravitational waves from known pulsars with S5 LIGO data," *Astrophys.J.*, vol. 713, pp. 671–685, 2010, * Brief entry *. 34

[57] E. Chassande-Mottin, M. Hendry, P. Sutton, and S. Márka, "Multimessenger astronomy with the Einstein Telescope," *General Relativity and Gravitation*, vol. 43, pp. 437–464, 2011, 10.1007/s10714-010-1019-z. 37, 38, 57

[58] S. Ando, F. Beacom, and H. Yüksel, "Detection of Neutrinos from Supernovae in Nearby Galaxies," *Phys. Rev. Lett.*, vol. 95, p. 171101, 2005. 37, 59, 60

[59] C. D. Ott, "TOPICAL REVIEW: The gravitational-wave signature of core-collapse supernovae," *Class. Quantum Grav.*, vol. 26, p. 063001, 2009. 37, 57, 59, 60

[60] C. Fryer and K. New, "Gravitational Waves from Gravitational Collapse," *Living Rev. Relativity*, vol. 14, lrr-2003-2, 2011. 37

[61] H. Dimmelmeier, C. D. Ott, A. Marek, and H.-T. Janka, "Gravitational wave burst signal from core collapse of rotating stars," *Phys. Rev. D.*, vol. 78, p. 064056, 2008. 37, 60

[62] J. W. Murphy, C. D. Ott, and A. Burrows, "A Model for Gravitational Wave Emission from Neutrino-Driven Core-Collapse Supernovae," *Astrophys. J.*, vol. 707, p. 1173, 2009. 60

[63] A. Marek, H.-T. Janka, and E. Müller, "Equation-of-state dependent features in shock-oscillation modulated neutrino and gravitational-wave signals from supernovae," *Astron. Astrophys.*, vol. 496, p. 475, 2009. 60

[64] S. Scheidegger, R. Käppeli, S. C. Whitehouse, T. Fischer, and M. Liebendörfer, "The influence of model parameters on the prediction of gravitational wave signals from stellar core collapse," *Astron. Astrophys.*, vol. 514, p. A51, 2010. 37, 60

[65] J. Hjorth et al., "A very energetic supernova associated with the gamma-ray burst of 29 March 2003," *Nature*, vol. 423, pp. 847–850, 2003. 38, 56

[66] S. Woosley, "Gamma-ray bursts from stellar mass accretion disks around black holes," *Astrophys. J.*, vol. 405, pp. 273–277, 1993. 38

[67] A. MacFadyen and S. Woosley, "Collapsars: Gamma-ray bursts and explosions in 'failed supernovae'," *Astrophys. J.*, vol. 524, pp. 262–289, 1999. 38

[68] M. B. Davies, A. King, S. Rosswog, and G. Wynn, "Gamma-Ray Bursts, Supernova Kicks, and Gravitational Radiation," *The Astrophysical Journal Letters*, vol. 579 (2), p. L63, 2002. 38, 57

[69] A. King et al., *The Astrophysical Journal Letters*, vol. 630 (2), p. L113, 2005.

[70] A. L. Piro and E. Pfahl, "Fragmentation of Collapsar Disks and the Production of Gravitational Waves," *Astrophys. J.*, vol. 658, p. 1173, 2007. 38, 57, 60

[71] M. H. P. M. van Putten et al., "Gravitational radiation from gamma-ray burst-supernovae as observational opportunities for LIGO and VIRGO," *Phys. Rev. D*, vol. 69 (4), p. 044007, 2004. 38, 57

[72] N. Andersson and K. Kokkotas, "Towards gravitational wave asteroseismology," *Mon. Not. R. Astron. Soc.*, vol. 299, pp. 1059–1068, 1998. 38, 39, 53, 58

[73] N. Andersson, "TOPICAL REVIEW: Gravitational waves from instabilities in relativistic stars," *Classical and Quantum Gravity*, vol. 20, pp. 105–+, 2003. 38, 54

[74] F. Gavriil et al., "Magnetar-Like Emission from the Young Pulsar in Kes 75," *Science*, vol. 319, pp. 1802–1805, 2008. 39

[75] N. Andersson and G. Comer, "Relativistic Fluid Dynamics: Physics for Many Different Scales," *Living Rev. Relativity*, vol. 10, lrr-2007-1, 2007. 39, 40, 53

[76] A. Watts and T. Strohmayer, "High frequency oscillations during magnetar flares," *Astrophys. Space Sci.*, vol. 308, pp. 625–629, 2007. 39

[77] L. Samuelsson and N. Andersson, "Neutron star asteroseismology. Axial crust oscillations in the Cowling approximation," *MNRAS*, vol. 374, pp. 256–268, 2007. 39

[78] S. Chandrasekhar, "Solutions of two problems in the theory of gravitational radiation," *Phys. Rev. Lett.*, vol. 24, p. 611, 1970. 39

[79] J. Friedman and B. Schutz, "Secular instability of rotating newtonian stars," *Astrophys. J.*, vol. 222, pp. 281–296, 1978. 39

[80] L. Lindblom and S. Detweiler, "On the secular instabilities of the Maclaurin spheroids," *Astrophys. J.*, vol. 211, pp. 565–567, 1977. 40

[81] L. Lindblom and G. Mendell, "Does gravitational radiation limit the angular velocities of superfluid neutron stars?" *Astrophys. J.*, vol. 444, pp. 804–809, 1995. 40

[82] N. Stergioulas and J. Friedman, "Nonaxisymmetric Neutral Modes in Rotating Relativistic Stars," *Astrophys. J.*, vol. 492, p. 301, 1998. 40

[83] L. Lindblom, B. Owen, and S. Morsink, "Gravitational radiation instability in hot young neutron stars," *Phys. Rev. Lett.*, vol. 80, pp. 4843–4846, 1998. 40, 75

[84] N. Andersson, K. Kokkotas, and B. Schutz, "Gravitational radiation limit on the spin of young neutron stars," *Astrophys. J.*, vol. 510, pp. 846–853, 1999.

[85] B. J. Owen et al., "Gravitational waves from hot young rapidly rotating neutron stars," *Phys. Rev. D*, vol. 58, 084020, 1998. 40, 75

[86] L. Lindblom and B. J. Owen, "Effect of hyperon bulk viscosity on neutron-star r-modes," *Phys. Rev. D*, vol. 65, 063006, 2002. 40

[87] B. Lackey, M. Nayyar, and B. Owen, "Observational constraints on hyperons in neutron stars," *Phys. Rev. D*, vol. 73, 024021, 2006. 40

[88] R. Bondarescu, S. A. Teukolsky, and I. Wasserman, "Spinning down newborn neutron stars: Nonlinear development of the r-mode instability," *Phys. Rev. D*, vol. 79 (10), pp. 104003–+, 2009. 40, 54, 55

[89] B. Allen and J. Romano, "Detecting a stochastic background of gravitational radiation: Signal processing strategies and sensitivities," *Phys. Rev. D*, vol. 59, 102001, 1999. 41, 76

[90] K. Thorne, "Gravitational radiation," in S. Hawking and W. Israel, eds., "Three Hundred Years of Gravitation," pp. 330–458, Cambridge University Press, Cambridge; New York, 1987. 41, 42

[91] B. Pagel, "Helium and Big Bang nucleosynthesis," *Phys. Rep.*, vol. 333, pp. 433–447, 2000. 42

[92] G. Steigman, "Primordial Nucleosynthesis in the Precision Cosmology Era," *Annu. Rev. Nucl. Part. Sci.*, vol. 57, pp. 463–491, 2007. 42

[93] B. Abbott et al., "An Upper Limit on the Stochastic Gravitational-Wave Background of Cosmological Origin," *Nature*, vol. 460, p. 990, 2009. 42

[94] C. Will, "Bounding the mass of the graviton using gravitional-wave observations of inspiralling compact binaries," *Phys. Rev. D*, vol. 57, p. 2061, 1998. 44

[95] K. G. Arun and C. M. Will, "Bounding the mass of the graviton with gravitational waves: Effect of higher harmonics in gravitational waveform templates," *Class. Quant. Grav.*, vol. 26, p. 155002, 2009. 44, 45

[96] C. Brans and R. H. Dicke, "Mach's Principle and a Relativistic Theory of Gravitation," *Phys. Rev.*, vol. 124 (3), pp. 925–935, 1961. 45

[97] B. Bertotti, L. Iess, and P. Tortora, "A test of general relativity using radio links with the Cassini spacecraft," *Nature*, vol. 425, p. 374, 2003. 45

[98] C. M. Will, "Testing scalar - tensor gravity with gravitational wave observations of inspiraling compact binaries," *Phys. Rev.*, vol. **D** 50, pp. 6058–6067, 1994. 45

[99] A. Królak, K. Kokkotas, and G. Schäfer, "Estimation of the post-Newtonian parameters in the gravitational-wave emission of a coalescing binary," *Phys. Rev. D*, vol. 52, pp. 2089–2111, 1995. 45

[100] C. M. Will, *Theory and experiments in gravitational physics*, Cambridge University Press, New York, USA, 1981. 45

[101] K. Arun, M. Iyer, Qusailah, and B. Sathyaprakash, "Testing post-Newtonian theory with gravitational waves," *Class. Quantum Grav.*, vol. 23, pp. L37–L43, 2006. 46

[102] K. Arun, B. Iyer, M. Qusailah, and B. Sathyaprakash, "Probing the non-linear structure of general relativity with black hole binaries," *Phys. Rev. D*, vol. 74, p. 024006, 2007.

[103] C. Mishra, K. Arun, B. Iyer, and B. Sathyaprakash, "Parameterized tests of post-Newtonian theory using Advanced LIGO and Einstein Telescope," *Phys. Rev. D*, vol. 82, p. 064010, 2010. 46

[104] P. J. E. Peebles and B. Ratra, "The cosmological constant and dark energy," *Rev. Mod. Phys.*, vol. 75, pp. 559–606, 2003. 47

[105] E. Komatsu et al., "Seven-Year Wilkinson Microwave Anisotropy Probe (WMAP) Observations: Cosmological Interpretation," *Astrophys. J. Suppl. Ser.*, vol. 192, p. 18, 2011. 47

[106] B. Carter, "Axisymmetric black hole has only two degrees of freedom." *Phys. Rev. Lett.*, vol. 26, pp. 331–333, 1971. 48

[107] F. D. Ryan, "Gravitational waves from the inspiral of a compact object into a massive, axisymmetric body with arbitrary multipole moments," *Phys. Rev. D*, vol. 52, pp. 5707–5718, 1995. 48, 49

[108] D. A. Brown et al., "Prospects for Detection of Gravitational Waves from Intermediate-Mass-Ratio Inspirals," *Phys. Rev. Lett.*, vol. 99 (20), p. 201102, 2007. 48, 49

[109] E. A. Huerta and J. R. Gair, "Intermediate-mass-ratio inspirals in the Einstein Telescope. I. Signal-to-noise ratio calculations," *Phys. Rev. D*, vol. 83 (4), p. 044020, 2011. 48

[110] O. Dreyer et al., "Black Hole Spectroscopy: Testing General Relativity through Gravitational Wave Observations," *Class. Quantum Grav.*, vol. 21, p. 787, 2004. 49

[111] E. Berti, V. Cardoso, and C. Will, "Gravitational-wave spectroscopy of massive black holes with the space interferometer LISA," *Phys. Rev. D*, vol. 73, 064030, 2006.

[112] E. Berti, J. Cardoso, V. Cardoso, and M. Cavagliá, "Matched filtering and parameter estimation of ringdown waveforms," *Phys. Rev.*, vol. D76, p. 104044, 2007. 49

[113] F. D. Ryan, "Spinning boson stars with large self-interaction," *Phys. Rev. D*, vol. 55, pp. 6081–6091, 1997. 49

[114] R. Penrose, "Gravitational Collapse: the Role of General Relativity," *Nuovo Cimento Rivista Serie*, vol. 1, p. 252, 1969. 50

[115] M. Kesden, J. Gair, and M. Kamionkowski, "Gravitational-wave signature of an inspiral into a supermassive horizonless object," *Phys. Rev. D*, vol. 71 (4), p. 044015, 2005. 50

[116] D. Lorimer, "Binary and Millisecond Pulsars," *Living Rev. Relativity*, vol. 8, lrr-2005-7, 2005. 51

[117] J. M. Lattimer and M. Prakash, "Neutron star observations: Prognosis for equation of state constraints," *J. Phys. Rep.*, vol. 442, pp. 109–165, 2007. 51

[118] T. Klähn et al., "Constraints on the high-density nuclear equation of state from the p henomenology of compact stars and heavy-ion collisions," *Phys. Rev. C*, vol. 74 (3), p. 035802, 2006.

[119] D. Page and S. Reddy, "Dense Matter in Compact Stars: Theoretical Developments and Observational Constraints," *Ann. Rev. Nucl. Part. Sci.*, vol. 56, pp. 327–374, 2006. 51

[120] H. Dimmelmeier, C. Ott, H.-T. Janka, A. Marek, and E. Müller, "Generic Gravitational Wave Signals from the Collapse of Rotating Stellar Cores," *Phys. Rev. Lett.*, vol. 98, 251101, 2007. 51, 75

[121] A. Marek, H.-T. Janka, and E. Müller, "Equation-of-state dependent features in shock-oscillation modulated neutrino and gravitational-wave signals from supernovae," *AAP*, vol. 496, pp. 475–494, 2009. 51

[122] B. J. Owen, "Maximum elastic deformations of compact stars with exotic equations of state," *Phys. Rev. Lett.*, vol. 95, p. 211101, 2005. 51, 58

[123] A. Watts, B. Krishnan, L. Bildsten, and B. Schutz, "Detecting gravitational wave emission from the known accreting neutron stars," 2008. 51

[124] X. Zhuge, J. M. Centrella, and S. L. W. McMillan, "Gravitational radiation from the coalescence of binary neutron stars: Effects due to the equation of state, spin, and mass ratio," *Phys. Rev. D*, vol. 54 (12), pp. 7261–7277, 1996. 51

[125] F. A. Rasio and S. L. Shapiro, "Coalescing Binary Neutron Stars," *Class. Quantum Grav.*, vol. 16, p. R1, 1999.

[126] É. É. Flanagan and T. Hinderer, "Constraining neutron-star tidal Love numbers with gravitational-wave detectors," *Phys. Rev. D*, vol. 77 (2), p. 021502, 2008.

[127] J. S. Read, B. D. Lackey, B. J. Owen, and J. L. Friedman, "Constraints on a phenomenologically parameterized neutron- star equation of state," *Phys. Rev.*, vol. D79, p. 124032, 2009. 52

[128] J. S. Read et al., "Measuring the neutron star equation of state with gravitational wave observations," *Phys. Rev.*, vol. D79, p. 124033, 2009. 51, 52

[129] M. Bejger et al., "Impact of the nuclear equation of state on the last orbits of binary neutron stars," *Astron. Astrophys.*, vol. 431, pp. 297–306, 2005. 51

[130] M. Shibata, K. Taniguchi, and K. Uryū, "Merger of binary neutron stars with realistic equations of state in full general relativity," *Phys. Rev. D*, vol. 71, p. 084021, 2005.

[131] M. Shibata, "Constraining Nuclear Equations of State Using Gravitational Waves from Hypermassive Neutron Stars," *Phys. Rev. Lett.*, vol. 94 (20), p. 201101, 2005. 53

[132] R. Oechslin and H. T. Janka, "Torus formation in neutron star mergers and well-localized short gamma-ray burst," *Mon. Not. R. Astron. Soc.*, vol. 368, p. 1489, 2006.

[133] R. Oechslin and H. T. Janka, "Gravitational Waves from Relativistic Neutron-Star Mergers with Mycrophysical Equations of State," *Phys. Rev. Lett.*, vol. 99, p. 121102, 2007.

[134] T. Yamamoto, M. Shibata, and K. Taniguchi, "Simulating coalescing compact binaries by a new code SACRA," *Phys. Rev. D*, vol. 78, pp. 064054–1–38, 2008.

[135] L. Baiotti, B. Giacomazzo, and L. Rezzolla, "Accurate evolutions of inspiralling neutron-star binaries: prompt and delayed collapse to black hole," *Phys. Rev. D*, vol. 78, p. 084033, 2008. 51

[136] L. Baiotti, B. Giacomazzo, and L. Rezzolla, "Accurate evolutions of inspiralling neutron-star binaries: assessment of the truncation error," *Class. Quantum Grav., in press, arXiv:0901.4955*, 2009. 51

[137] J. A. Faber, T. W. Baumgarte, S. L. Shapiro, K. Taniguchi, and F. A. Rasio, "The Dynamical Evolution of Black Hole-Neutron Star Binaries in General Relativity: Simulations of Tidal Disruption," *Phys. Rev. D*, vol. 73, p. 024012, 2006, astro-ph/0511366. 51

[138] M. Shibata and K. Taniguchi, "Merger of black hole and neutron star in general relativity: Tidal disruption, torus mass, and gravitational waves," *Phys. Rev. D*, vol. 77 (8), p. 084015, 2008.

[139] M. Shibata, K. Kyutoku, T. Yamamoto, and K. Taniguchi, "Gravitational waves from black hole-neutron star binaries I: Classification of waveforms," *Phys. Rev.*, vol. D79, p. 044030, 2009. 51

[140] B. Giacomazzo, L. Rezzolla, and L. Baiotti, "The influence of magnetic fields on the gravitational-wave emission from binary neutron stars," *arXiv:0901.2722*, vol. , 2009. 53

[141] P. W. Anderson and N. Itoh, "Pulsar glitches and restlessness as a hard superfluidity phenomenon," *Nature*, vol. 256, pp. 25–27, 1975. 53

[142] C. M. Espinoza, A. G. Lyne, B. W. Stappers, and M. Kramer, "A study of 315 glitches in the rotation of 102 pulsars," 2011, * Temporary entry *. 53

[143] M. Ruderman, "Crust-breaking by neutron superfluids and the Vela pulsar glitches," *Astrophys. J.*, vol. 203, pp. 213–222, 1976. 53

[144] G. McDonald, *A Review of Pulsar Glitch Mechanisms*, Ph.D. thesis, University of Johannesburg, South Africa, 2007. 53

[145] N. Andersson, G. Comer, and R. Prix, "The Superfluid two - stream instability and pulsar glitches," *MNRAS*, 2002. 54

[146] N. Andersson, G. Comer, and R. Prix, "Are pulsar glitches triggered by a superfluid two-stream instability?" *Phys.Rev.Lett.*, vol. 90, p. 091101, 2003. 54

[147] P. M. Sa and B. Tome, "The influence of differential rotation on the detectability of gravitational waves from the r-mode instability," *Phys. Rev.*, vol. D74, p. 044011, 2006. 55

[148] P. M. Sa and B. Tome, "Gravitational waves from r-modes," *Astrophys. Space Sci.*, vol. 308, pp. 557–561, 2007. 55

[149] C. Kouveliotou et al., "Identification of two classes of gamma-ray bursts," *Astrophys. J. Lett.*, vol. 413, pp. L101–L104, 1993. 56

[150] C. J. Conselice et al., "Gamma-Ray Burst-Selected High-Redshift Galaxies: Comparison to Field Galaxy Populations to z 3," *The Astrophysical Journal*, vol. 633 (1), p. 29, 2005. 56

[151] T. J. Galama et al., "An unusual supernova in the error box of the gamma-ray burst of 25 April 1998," *Nature*, vol. 395, p. 670, 1998. 56

[152] S. R. Kulkarni et al., "Radio emission from the unusual supernova 1998bw and its association with the gamma-ray burst of 25 April 1998," *Nature*, vol. 395, p. 663, 1998.

[153] S. Campana et al., "The association of GRB 060218 with a supernova and the evolution of the shock wave," *Nature*, vol. 442, 2006. 56

[154] S. E. Woosley, *Astrophys. J.*, vol. 405, p. 273, 1993. 56

[155] K. Iwamoto et al., *Nature*, vol. 395, p. 672, 1998. 56

[156] J. S. Bloom and J. X. Prochaska, "Constraints on the Diverse Progenitors of GRBs from the Large-Scale Environments," *AIP Conf. Proc.*, vol. 836, pp. 473–482, 2006. 56

[157] J. S. Bloom et al., *Astrophys. J.*, vol. 654, 2007. 56

[158] E. Nakar, A. Gal-Yam, T. Piran, and D. B. Fox, "The Distances of Short-Hard Gamma-Ray Bursts and the Soft Gamma-Ray Repeater Connection," *Astrophys. J.*, vol. 640, pp. 849–853, 2006. 56, 62

[159] R. Chapman, R. S. Priddey, and N. R. Tanvir, "Short gamma-ray bursts from SGR giant flares and neutron star mergers: two populations are better than one," *Mon. Not. R. Astron. Soc.*, p. 430, 2009. 56, 57

[160] B. Abbott et al. (LIGO Scientific Collaboration), "Analysis of LIGO data for gravitational waves from binary neutron stars," *Phys. Rev. D*, vol. 69, 122001, 2004. 56

[161] B. Abbott et al. (LIGO Scientific Collaboration), "Search for gravitational waves from galactic and extra-galactic binary neutron stars," *Phys. Rev. D*, vol. 72, 082001, 2005. 56

[162] B. Abbott et al. (LIGO Scientific Collaboration) and K. Hurley, "Implications for the Origin of GRB 070201 from LIGO Observations," *Astrophys. J.*, vol. 681, pp. 1419–1430, 2008. 56, 57, 58

[163] J. Abadie et al., "Search for Gravitational-wave Inspiral Signals Associated with Short Gamma-ray Bursts During LIGO's Fifth and Virgo's First Science Run," *The Astrophysical Journal*, vol. 715 (2), p. 1453, 2010. 57

[164] K. Hurley et al., "An exceptionally bright flare from SGR 1806-20 and the origins of short-duration γ-ray bursts," *Nature*, vol. 434, pp. 1098–1103, 2005. 57

[165] N. R. Tanvir, R. Chapman, A. J. Levan, and R. S. Priddey, "An origin in the local Universe for some short γ-ray bursts," *Nature*, vol. 438, pp. 991–993, 2005. 57

[166] A. J. Levan et al., "On the nature of the short-duration GRB 050906," *Mon. Not. R. Astron. Soc.*, vol. 384, pp. 541–547, 2008. 57

[167] D. Frederiks et al., "GRB 051103 and GRB 070201 as Giant Flares from SGRs in Nearby Galaxies," in M. Galassi, D. Palmer, and E. Fenimore, eds., "American Institute of Physics Conference Series," vol. 1000 of *American Institute of Physics Conference Series*, pp. 271–275, 2008. 57

[168] E. O. Ofek et al., "GRB 070201: A Possible Soft Gamma-Ray Repeater in M31," *Astrophys. J.*, vol. 681, pp. 1464–1469, 2008. 57

[169] J. A. de Freitas Pacheco, *Astronomy and Astrophysics*, vol. 336, p. 397, 1998. 58

[170] R. Price and K. S. Thorne, "Non-Radial Pulsation of General-Relativistic Stellar Models. II. Properties of the Gravitational Waves," *Astrophys. J.*, vol. 155, p. 163, 1969. 58

[171] O. Benhar, "Neutron star matter equation of state and gravitational wave emission," *Mod. Phys. Lett. A*, vol. 20, pp. 2335–2349, 2005. 58

[172] K. Ioka, *Mon. Not. R. Astron. Soc.*, vol. 327, p. 639, 2001. 58

[173] H. A. Bethe, "Supernova mechanisms," *Rev. Mod. Phys.*, vol. 62 (4), pp. 801–866, 1990. 59

[174] H.-T. Janka, K. Langanke, A. Marek, G. Martínez-Pinedo, and B. Müller, *Phys. Rep.*, vol. 442, p. 38, 2007. 59

[175] C. D. Ott, "Probing the Core-Collapse Supernova Mechanism with Gravitational Waves," *Class.Quant.Grav.*, vol. 26, p. 204015, 2009. 59

[176] S. Ando and J. F. Beacom, "Revealing the Supernova Gamma-Ray Burst Connection with TeV Neutrinos," *Phys. Rev. Lett.*, vol. 95 (6), p. 061103, 2005. 60, 426

[177] L. Blanchet and T. Damour, "Hereditary effects in gravitational radiation," *Phys.Rev.*, vol. D46, pp. 4304–4319, 1992. 59

[178] D. Christodoulou, "Nonlinear nature of gravitation and gravitational wave experiments," *Phys.Rev.Lett.*, vol. 67, pp. 1486–1489, 1991. 59

[179] P. J. Sutton et al., "X-Pipeline: an analysis package for autonomous gravitational-wave burst searches," *New Journal of Physics*, vol. 12 (5), p. 053034, 2010. 59

[180] P. Kalmus and L. Santamaria, "Private communication," 2011. 59

[181] K. N. Yakunin et al., "Gravitational Waves from Core Collapse Supernovae," *Class. Quant. Grav.*, vol. 27, p. 194005, 2010. 60

[182] A. Burrows, E. Livne, L. Dessart, C. D. Ott, and J. Murphy, "A New Mechanism for Core-Collapse Supernova Explosions," *Astrophys. J.*, vol. 640, p. 878, 2006. 60

[183] C. D. Ott et al., "Dynamics and Gravitational Wave Signature of Collapsar Formation," *Phys. Rev. Lett.*, vol. 106, p. 161103, 2011. 60

[184] C. Fryer, D. Holz, and S. Hughes, "Gravitational Wave Emission from Core Collapse of Massive Stars," *Astrophys. J.*, vol. 565, p. 430, 2002. 60

[185] L. E. Strigari, J. F. Beacom, T. P. Walker, and P. Zhang, "The concordance cosmic star formation rate: implications from and for the supernova neutrino and gamma ray backgrounds," *JCAP*, vol. 4, p. 17, 2005. 60

[186] B. Sathyaprakash, B. Schutz, and C. Van Den Broeck, "Cosmography with the Einstein Telescope," *Class.Quant.Grav.*, vol. 27, p. 215006, 2010, * Brief entry *. 62

[187] K. Levenberg, "A method for the Solution of Certain Non-Linear Problems in Least Squares," *The Quarterly of Applied Mathematics*, vol. 2, pp. 164–168, 1944. 63

[188] D. Marquardt, "An algorithm for Least-Squares Estimation of Nonlinear Parameters," *SIAM Journal on Applied Mathematics*, vol. 11, 431, 1963. 63

[189] S. Nissanke, D. Holz, S. Hughes, N. Dalal, and J. Sievers, "Exploring short gamma-ray bursts as gravitational wave standard sirens," *Astrophys. J.*, vol. 725, pp. 496–514, 2010. 64

[190] W. Zhao, C. Van Den Broeck, D. Baskaran, and T. Li, "Determination of Dark Energy by the Einstein Telescope: Comparing with CMB, BAO and SNIa Observations," http://arxiv.org/abs/1009.0206. 65, 323

[191] A. Heavens, B. Panter, R. Jimenez, and J. Dunlop, "The Complete star formation history of the universe," *Nature*, vol. 428, p. 625, 2004. 66

[192] V. Lipunov, K. Postnov, and M. Prokhorov, *MNRAS*, vol. 288, p. 245, 1997. 67

[193] K. Belczynski and T. Bulik, *Astronomy and Astrophysics*, vol. 346, p. 91, 1999. 67

[194] K. Nagamine, J. Ostriker, M. Fukugita, and R. Cen, "The History of Cosmological Star Formation: Three Independent Approaches and a Critical Test Using the Extragalactic Background," *Astrophys. J.*, vol. 653, pp. 881–893, 2006. 68, 69, 426

[195] M. Fardal, N. Katz, D. Weinberg, and R. Davé, "On the Evolutionary History of Stars and their Fossil Mass and Light," *MNRAS*, vol. 379, pp. 985–1002, 2007. 68, 69, 426

[196] S. Wilkins, N. Trentham, and A. Hopkins, *MNRAS*, vol. 385, p. 687, 2008. 68, 69, 426

[197] A. Sesana, M. Volonteri, and F. Haardt, "The imprint of massive black hole formation models on the LISA data stream," *Mon. Not. R. Astron. Soc.*, vol. 377, pp. 1711–1716, 2007. 70, 71

[198] P. Madau and M. J. Rees, "Massive Black Holes as Population III Remnants," *Astrophys. J. Lett.*, vol. 551, pp. L27–L30, 2001. 70

[199] S. M. Koushiappas, J. S. Bullock, and A. Dekel, "Massive black hole seeds from low angular momentum material," *Mon. Not. R. Astron. Soc.*, vol. 354, pp. 292–304, 2004. 70

[200] M. C. Begelman, M. Volonteri, and M. J. Rees, "Formation of supermassive black holes by direct collapse in pre-galactic haloes," *Mon. Not. R. Astron. Soc.*, vol. 370, pp. 289–298, 2006. 70

[201] P. Bender et al. (LISA Study Team), "LISA. Laser Interferometer Space Antenna for the detection and observation of gravitational waves. An international project in the field of Fundamental Physics in Space. Pre-Phase A report. Second Edition," Tech. rep., Max-Planck-Institut für Quantenoptik, Garching, 1998. 70

[202] M. Volonteri, F. Haardt, and P. Madau, "The Assembly and Merging History of Supermassive Black Holes in Hierarchical Models of Galaxy Formation," *Astrophys. J.*, vol. 582, pp. 559–573, 2003. 70

[203] M. Volonteri, R. Salvaterra, and F. Haardt, "Constraints on the accretion history of massive black holes from faint X-ray counts," *Mon. Not. R. Astron. Soc.*, vol. 373, pp. 121–127, 2006. 70

[204] A. Sesana, J. Gair, I. Mandel, and A. Vecchio, "Observing Gravitational Waves from the First Generation of Black Holes," *Astrophys. J. Lett.*, vol. 698, pp. L129–L132, 2009. 70, 71

[205] B. Allen, "The Stochastic Gravity-Wave Background: Sources and Detection," in J.-A. Marck and J.-P. Lasota, eds., "Relativistic Gravitation and Gravitational Radiation," Cambridge Contemporary Astrophysics, pp. 373–418, 1997. 71

[206] X. Siemens, V. Mandic, and J. Creighton, "Gravitational wave stochastic background from cosmic (super)strings," *Phys. Rev. Lett.*, vol. 98, p. 111101, 2007. 72, 324, 426

[207] C. D. Ott, A. Burrows, L. Dessart, and E. Livne, "A New Mechanism for Gravitational-Wave Emission in Core-Collapse Supernovae," *Physical Review Letters*, vol. 96 (20), p. 201102, 2006. 72, 75, 427

[208] Y.-I. Sekiguchi and M. Shibata, "Axisymmetric collapse simulations of rotating massive stellar cores in full general relativity: Numerical study for prompt black hole formation," *Phys. Rev. D*, vol. 71 (8), pp. 084013–+, 2005. 72, 75, 427

[209] D. H. Lyth, "What would we learn by detecting a gravitational wave signal in the cosmic microwave background anisotropy?" *Phys. Rev. Lett.*, vol. 78, pp. 1861–1863, 1997. 71

[210] M. S. Turner, "Detectability of inflation-produced gravitational waves," *Phys. Rev.*, vol. D55, pp. 435–439, 1997. 71

[211] S. Kuroyanagi, T. Chiba, and N. Sugiyama, "Imprint of inflation dynamics on the spectrum of the primordial gravitational wave background," *Phys. Rev.*, vol. D79, p. 103501, 2009. 71

[212] L. Grishchuk, "The implications of the microwave background anisotropies for laser-interferometer-tested gravitational waves," *Class. Quantum Grav.*, vol. 14, pp. 1445–1454, 1997. 71

[213] L. A. Boyle and A. Buonanno, "Relating gravitational wave constraints from primordial nucleosynthesis, pulsar timing, laser interferometers, and the CMB: implications for the early universe," *Phys. Rev.*, vol. D78, p. 043531, 2008. 71

[214] L. A. Boyle, P. J. Steinhardt, and N. Turok, "The cosmic gravitational wave background in a cyclic universe," *Phys. Rev.*, vol. D69, p. 127302, 2004. 71

[215] M. Gasperini and G. Veneziano, "Pre - big bang in string cosmology," *Astropart. Phys.*, vol. 1, pp. 317–339, 1993. 71

[216] M. Gasperini and G. Veneziano, "The pre-big bang scenario in string cosmology," *Phys. Rept.*, vol. 373, pp. 1–212, 2003. 71

[217] C. Cartier, E. J. Copeland, and M. Gasperini, "Gravitational waves in non-singular string cosmologies," *Nucl. Phys.*, vol. B607, pp. 406–428, 2001. 73

[218] M. B. Hindmarsh and T. W. B. Kibble, "Cosmic strings," *Rept. Prog. Phys.*, vol. 58, pp. 477–562, 1995. 73

[219] G. R. Dvali and S. H. Tye, "Brane inflation," *Phys. Lett.*, vol. B450, pp. 72–82, 1999. 73

[220] S. Sarangi and S. H. Tye, "Cosmic string production towards the end of brane inflation," *Phys. Lett.*, vol. B536, pp. 185–192, 2002. 73

[221] C. Caprini, R. Durrer, T. Konstandin, and G. Servant, "General properties of the gravitational wave spectrum from phase transitions," *Phys. Rev. D*, vol. 79 (8), p. 083519, 2009. 73

[222] C. Grojean and G. Servant, "Gravitational Waves from Phase Transitions at the Electroweak Scale and Beyond," *Phys. Rev.*, vol. D75, p. 043507, 2007. 73

[223] A. Kosowsky, A. Mack, and T. Kahniashvili, "Gravitational radiation from cosmological turbulence," *Phys. Rev.*, vol. D66, p. 024030, 2002. 73

[224] T. Kahniashvili, A. Kosowsky, G. Gogoberidze, and Y. Maravin, "Detectability of Gravitational Waves from Phase Transitions," *Phys. Rev.*, vol. D78, p. 043003, 2008. 73

[225] L. Randall and G. Servant, "Gravitational waves from warped spacetime," *J. High Energy Phys.*, vol. 2007 (05), 054, 2007. 73

[226] N. J. Craig, "Gravitational Waves from Supersymmetry Breaking," 2009. 73

[227] R. Easther and E. A. Lim, "Stochastic gravitational wave production after inflation," *JCAP*, vol. 0604, p. 010, 2006. 73

[228] J.-F. Dufaux, A. Bergman, G. N. Felder, L. Kofman, and J.-P. Uzan, "Theory and Numerics of Gravitational Waves from Preheating after Inflation," *Phys. Rev.*, vol. D76, p. 123517, 2007. 73

[229] J. Garcia-Bellido, D. G. Figueroa, and A. Sastre, "A Gravitational Wave Background from Reheating after Hybrid Inflation," *Phys. Rev.*, vol. D77, p. 043517, 2008. 74

[230] J.-F. Dufaux, G. N. Felder, L. Kofman, and O. Navros, "Gravity Waves from Tachyonic Preheating after Hybrid Inflation," *JCAP*, vol. 0903, p. 001, 2009. 74

[231] J.-F. Dufaux, "Gravity Waves from the Nonperturbative Decay of Condensates along Supersymmetric Flat Directions," *Phys. Rev. Lett.*, vol. 103, p. 041301, 2009. 74

[232] T. Regimbau, "The astrophysical gravitational wave stochastic background," *Research in Astronomy and Astrophysics*, vol. 11, pp. 369–390, 2011. 74

[233] R. Schneider, V. Ferrari, S. Matarrese, and S. Portegies Zwart, "Gravitational waves from cosmological compact binaries," *Mon. Not. R. Astron. Soc.*, vol. 324, p. 797, 2001. 74

[234] T. Regimbau and J. A. de Freitas Pacheco, "Stochastic Background from Coalescences of Neutron Star-Neutron Star Binaries," *Astrophys. J.*, vol. 642, pp. 455–461, 2006.

[235] T. Regimbau and B. Chauvineau, "A stochastic background from extra-galactic double neutron stars," *Classical and Quantum Gravity*, vol. 24, pp. 627–+, 2007.

[236] T. Regimbau and V. Mandic, "Astrophysical sources of a stochastic gravitational-wave background," *Classical and Quantum Gravity*, vol. 25 (18), pp. 184018–+, 2008. 74

[237] S. Marassi, R. Schneider, and V. Ferrari, "Gravitational wave backgrounds and the cosmic transition from Population III to Population II stars," *ArXiv e-prints*, 2009. 74

[238] L. Tornatore, A. Ferrara, and R. Schneider, "Population III stars: hidden or disappeared?" *Mon. Not. R. Astron. Soc.*, vol. 382, pp. 945–950, 2007. 74

[239] Y. Suwa, T. Takiwaki, K. Kotake, and K. Sato, "Gravitational Wave Background from Population III Stars," *Astrophys. J. Lett.*, vol. 665, pp. L43–L46, 2007. 74

[240] E. Müller, M. Rampp, R. Buras, H.-T. Janka, and D. H. Shoemaker, "Toward Gravitational Wave Signals from Realistic Core-Collapse Supernova Models," *Astrophys. J.*, vol. 603, pp. 221–230, 2004. 75

[241] X. Zhu, E. Howell, and D. Blair, "Observational upper limits on the gravitational wave production of core collapse supernovae," *Mon. Not. R. Astron. Soc.*, vol. 409, pp. L132–L136, 2010. 75

[242] C. D. Ott, A. Burrows, E. Livne, and R. Walder, "Gravitational Waves from Axisymmetric, Rotating Stellar Core Collapse," *Astrophysical Journal*, vol. 600, pp. 834–864, 2004. 75

[243] D. Brown, *Phys. Rev. D*, vol. 62, p. 084024, 2000. 75

[244] K. C. B. New, J. M. Centrella, and J. E. Tohline, "Gravitational Waves from Long-Duration Simulations of the Dynamical Bar Instability," *Phys. Rev. D*, vol. 62 (064019), 2000.

[245] M. Shibata, W. Baumgarte, and S. Shapiro, *Astrophys. J.*, vol. 542, p. 453, 2000.

[246] M. Saijo, M. Shibata, W. Baumgarte, and S. Shapiro, *Astrophys. J.*, vol. 548, p. 919, 2001.

[247] L. Baiotti, R. D. Pietri, G. M. Manca, and L. Rezzolla, "Accurate simulations of the dynamical bar-mode instability in full general relativity," *Phys. Rev. D*, vol. 75, p. 044023, 2007. 75

[248] M. Shibata and Y. Sekiguchi, "Three-dimensional simulations of stellar core collapse in full general relativity: Nonaxisymmetric dynamical instabilities," *Phys. Rev. D*, vol. 71, p. 024014, 2005. 75

[249] V. Ferrari, S. Matarrese, and R. Schneider, "Stochastic background of gravitational waves generated by a cosmological population of young, rapidly rotating neutron stars," *Mon. Not. Roy. Astron. Soc.*, vol. 303, p. 258, 1999. 75

[250] D. Lai and S. L. Shapiro, "Gravitational radiation from rapidly rotating nascent neutron stars," *Astrophys. J.*, vol. 442, p. 259, 1995. 75

[251] T. Regimbau and J. A. de Freitas Pacheco, "Gravitation wave emission from radio pulsars revisited," *Astronomy and Astrophysics*, vol. 359, pp. 242–250, 2000. 76

[252] C.-A. Faucher-Giguère and V. M. Kaspi, "Birth and Evolution of Isolated Radio Pulsars," *Astrophys. J.*, vol. 643, pp. 332–355, 2006.

[253] R. Soria, R. Perna, D. Pooley, and L. Stella, "How rapidly do neutron stars spin at birth?" 2008. 76

[254] R. C. Duncan and C. Thompson, "Formation of very strongly magnetized neutron stars - implications for gamma-ray bursts," *Astrophys. J.*, vol. 392, p. L9, 1992. 76

[255] C. Thompson and R. C. Duncan, "Neutron star dynamos and the origins of pulsar magnetism," *Astrophys. J.*, vol. 408, p. 194, 1993. 76

[256] T. Regimbau and J. A. de Freitas Pacheco, "Gravitational wave background from magnetars," *Astron. Astrophys.*, vol. 447, pp. 1–7, 2006. 76

[257] B. Sathyaprakash and S. Dhurandhar, "Choice of filters for the detection of gravitational waves from coalescing binaries," *Phys. Rev. D*, vol. 44, pp. 3819–3834, 1991. 77

[258] R. Balasubramanian, B. Sathyaprakash, and S. Dhurandhar, "Gravitational waves from coalescing binaries: Detection strategies and Monte Carlo estimation of parameters," *Phys. Rev. D*, vol. 53, pp. 3033–3055, 1996.

[259] B. Owen, "Search templates for gravitational waves from inspiralling binaries: Choise of template spacing," *Phys. Rev. D*, vol. 53, pp. 6749–6761, 1996.

[260] B. Owen and B. Sathyaprakash, "Matched filtering of gravitational waves from inspiraling compact binaries: Computational cost and template placement," *Phys. Rev. D*, vol. 60, 022002, 1999.

[261] S. Babak, R. Balasubramanian, D. Churches, T. Cokelaer, and B. S. Sathyaprakash, "A template bank to search for gravitational waves from inspiralling compact binaries. I: physical models," *Class. Quant. Grav*, vol. 23, 5477, 2006. 77

[262] E. Thrane et al., "Probing the anisotropies of a stochastic gravitational-wave background using a network of ground-based laser interferometers," 2009. 78

[263] L. S. Collaboration, "Searching for a Stochastic Background of Gravitational Waves with LIGO," 2006. 78

[264] L. S. Collaboration and the Virgo Collaboration, "An Upper Limit on the Stochastic Gravitational-Wave Background of Cosmological Origin," 2009. 78

[265] B. Abbott et al. (LIGO Scientific Collaboration), "Upper limit map of a background of gravitational waves," 2007. 78

[266] Y. Itoh, M. A. Papa, B. Krishnan, and S. X., "Chi-square test on candidate events from CW signal coherent searches," *Class.Quant.Grav.*, vol. 21, p. S1667, 2004. 79

[267] S. V. Dhurandhar and A. Vecchio, "Searching for continuous gravitational wave sources in binary systems," *Phys.Rev.D*, vol. 63, p. 122001, 2001. 79

[268] P. R. Brady, T. Creighton, C. Cutler, and B. F. Schutz, "Searching for periodic sources with LIGO," *Phys.Rev. D*, vol. 57, p. 2101, 1998. 79

[269] R. P. Brady and T. Creighton, "Searching for periodic sources with LIGO. II: Hierarchical searches," *Phys. Rev. D*, vol. 61, p. 082001, 2000. 79

[270] B. Abbott et al. (LIGO Scientific Collaboration), "First all-sky upper limits from LIGO on the strength of periodic gravitational waves using the Hough transform," *Phys. Rev. D*, vol. 72, 102004, 2005. 80, 323

[271] P. et al., *Quantum Grav.*, vol. 72, S1255.S1264, 102004, 2005. 80

[272] S. Klimenko et al., "Localization of gravitational wave sources with networks of advanced detectors," 2011. 80

[273] M. H. van Putten et al., "Prospects for true calorimetry on Kerr black holes in core-collapse supernovae and mergers," 2011. 81

[274] "Moore's law," . 81

[275] J. Richards, "Will computers reach top speed by 2020," http://technology.timesonline.co.uk/tol/news/tech_and_web/article2489053.ece. 81

[276] S. Pat Gelsinger and co-GM of Intel's Digital Enterprise Group (DEG), http://java.sys-con.com/node/557154. 82

[277] B. L., "cuInspiral: prototype gravitational waves detection pipeline fully coded on GPU using CUDA," *arXiv, submitted to Computational Physics*, 2010. 83

[278] D. Cipullo, ""Implementazione e studio di algoritmi per generazione di segnali gravitazionali in ambiente CUDA e OPENCL", Tesi di laurea in informatica - University of Perugia," 2011. 83

[279] S. L. L. Fontana Relatori: Servoli L., Bosi L., ""Utilizzo di MPI e Pthread nella parallelizzazione multi-GPU di algoritmi di identificazione di segnali gravitazionali", Tesi di laurea in informatica - University of Perugia," 2011. 83

[280] E. S. Hans Meuer, Jack Dongarra and H. Simon, "TOP500 Supercomputer Sites," http://www.top500.org/. 83

[281] A. Petiteau, Y. Shang, S. Babak, and F. Feroz, "The search for spinning black hole binaries in mock LISA data using a genetic algorithm," *Phys. Rev. D*, vol. 81, 104016, 2010. 85

[282] P.-Y. Bard et al., "SESAME: Site effects assessment using ambient excitations." Tech. rep., 2003, final report WP08. 93

[283] B. Gutenberg, "Microseisms," *Advances in Geophysics*, vol. 5, pp. 53–92, 1958.

[284] M. Asten, "Arrays estimators and the use of microseisms for reconnaissance of sedimentary basins," *Bulletin of the Seismological Society of America*, vol. 68, pp. 1623 – 1636, 2002.

[285] L. Peck, "Overview of Seismic Noise and its relevance to Personnel detections," ERDC/CRREL TR-08-5, US Army Corps of Engineers, 2008, engineer Research and Development Center. 93

[286] J. Peterson, "Observations and modeling of seismic background noise," Open-File report 93-322, 1993. 93, 427

[287] J. Peterson, "Preliminary observations of noise spectra at the SRO and ASRO stations." Open-File report 80-992, 1980. 94

[288] R. Schofield et al., "Source and propagation of the predominant 1-50 Hz seismic signal from off-site at LIGO-Hanford," LIGO Scientific Collaboration Meeting, LIGO Hanford Observatory, Hanford, Washington, 15-17 August 2000., 2000. 96

[289] I. Fiori, L. Holloway, and F. Paoletti, "Studies of the 1 - 4 Hz seism," Internal Virgo Note (VIR-NOT-FIR-1390-251). 96

[290] D. Coward, D. Blair, R. Burman, , and C. Zhao., "Vehicle-induced seismic effects at a gravitational wave observatory," *Review of Scientific Instruments*, vol. 74, pp. 4846 – 4854, 2003. 96

[291] C. Young, "A comparison of the high-frequency (>1Hz) surface and subsurface noise environment at three sites in the United States," *Bull. of the Seism. Soc. of America*, vol. 86, pp. 1516–1528, 1996. 96, 98

[292] 97, 427

[293] M. Withers et al., "High-frequency analysis of seismic background noise as a function of wind speed and shallow depth," *Bulletin of the Seismological Society of America*, vol. 86, pp. 1507 – 1515, 1996. 98

[294] 98, 427

[295] D. E. McNamara, "Ambient Noise Levels in the Continental United States," *Bull. Seism. Soc. Am.*, vol. 94, pp. 1517–1527, 2004. 99, 100, 427

[296] "OneGeology," http://onegeology.org/. 99

[297] M. Steinwachs, *Systematische Untersuchung der kurxperiodischen seismischen Boderumruhe in der Bundesrepublik Deutschland*, Geologisches Jahrbuch, Geophysik E3 Hannover, 1974. 99

[298] M. Beker et al., "Improving the sensitivity of future GW observatories in the 1Hz band: Newtonian and seismic noise," *General Relativity and Gravitation*, pp. 1–34, 2010, 10.1007/s10714-010-1011-7. 102, 112

[299] P. R. Saulson, "Terrestrial gravitational noise on a gravitational wave antenna," *Phys. Rev. D*, vol. 30 (4), pp. 732–736, 1984. 103, 106

[300] M. Beccaria et al., "Relevance of Newtonian seismic noise for the VIRGO interferometer sensitivity," *Classical and Quantum Gravity*, vol. 15, pp. 3339–3362, 1998. 123, 169

[301] S. A. Hughes and K. S. Thorne, "Seismic gravity-gradient noise in interferometric gravitational-wave detectors," *Phys. Rev. D*, vol. 58 (12), p. 122002, 1998. 103, 104, 106

[302] "Comsol Multiphysics version 3.5a," 2009. 104

[303] M. Schevenels, *The impact of uncertain dynamic soil characteristics on the prediction of ground vibrations.*, Ph.D. thesis, Katholieke Universiteit Leuven, 2007. 104

[304] J. Achenbach, *Wave Propagation in Elastic Solids*, pp. 187–194, North-Holland, Amsterdam, 1973. 104

[305] W. Hassan and P. B. Nagy, *J. Acoust. Soc. Am.*, vol. 104, p. 3107, 1998. 104

[306] R. Woods, "Screening the surface waves in soils," *Proceedings of ASCE*, vol. 94, pp. 951–979, 1968. 104

[307] D.-S. Kim and J.-S. Lee, "Propagation and attenuation characteristics of various ground vibrations," *Soil Dyn. and Earthq. Eng.*, vol. 19, pp. 115–126, 2000. 104

[308] A. Caticha and R. Preuss, "Maximum entropy and bayesian data analysis: entropic priors," *Phys. Rev. E*, vol. 70, p. 046127. 107

[309] K. Pepper, R. Adhikari, and P. Willems, "Newtonian Noise simulation and suppression for gravitational-wave interferometers," Tech. rep., Caltech, 2007. 112

[310] H. J, R. DeSalvo, S. Dorsher, and V. Mandic, "Simulation of underground gravity gradients from stochastic seismic fields," *Phys. Lett. D*, vol. 80, p. 12, 2009. 112

[311] K. S. Thorne and C. J. Winstein, "Human gravity-gradient noise in interferometric gravitational-wave detectors," *Phys. Rev. D*, vol. 60 (8), p. 082001, 1999. 114

[312] E. Marchetti and M. Mazzoni, "Evidence of oceanic microseism as a source of low frequency seismic signal recorded at Virgo," 2004. 118

[313] "Foundation for education and training on tunnelling and underground space use," IRACET Foundation, 2010. 131

[314] 131, 132, 430

[315] G. Cella, "Residual pressure noise evaluation," http://wwwcascina.virgo.infn.it/advirgo/biweekly/2008/2008-06/cella_190608.ppt, 2008, virgo internal document. 139

[316] J.-Y. Vinet et al., "Scattered light noise in gravitational interferometric detectors: A statistical approach," *Phys.Rev.*, vol. D 56, p. 6085, 1997. 143

[317] J.-Y. Vinet, V. Brisson, and S. Braccini, "Scattered light noise in gravitational wave interferometric detectors: Coherent effects," *Phys.Rev.*, vol. D 54, p. 1276, 1996. 143

[318] C. Ho, R. Powell, and P. Liley, "Thermal Conductivity of the Elements," *J. Phys. Chem. Ref. Data*, vol. 1, p. 279, 1972. 152, 153, 430

[319] T. Tomaru et al., "Conduction Effect of Thermal Radiation in a Metal Shield Pipe in a Cryostat for a Cryogenic Interferometric Gravitational Wave Detector," 2007, arXiv:0711.0839v1. 157

[320] T. Tomaru et al., "Reduction of Heat Load of LCGT Cryostat," *Journal of Physics: Conference Series*, vol. 122, p. 012009, 2008, 7th Edoardo Amaldi Conference on Gravitational Waves, Sydney, Australia, July 2007. 157

[321] D. Mosher and S. J. Stephanakis, "X-ray "light pipes"," *Applied Physics Letters*, vol. 29 (2), pp. 105–107, 1976. 157

[322] M. E.I., T. A.A., and S. M.P., "Low temperature expansion pulse tubes," in "Advanced in Cryogenic Engineering," vol. 29, pp. 629–637, Plenum Press, New York, 1984. 160

[323] Z. Sh., W. P., and C. Zh., "Double inlet pulse tube refrigerators: an important improvement," *Cryogenics*, vol. 30, p. 514, 1990. 160

[324] K. Kuroda et al., "Large-Scale Cryogenic Gravitational Wave Telescope," *International Journal of Modern Physics D*, vol. 8 (5), pp. 557–579, 1999. 161

[325] T. Tomaru et al., "Vibration analysis of cryocoolers," *Cryogenics*, vol. 44, pp. 309–317, 2004. 161

[326] S. Caparrelli et al., "Vibration-free cryostat for low-noise applications of a pulse tube cryocooler," *Review of Scientific Instruments*, vol. 77 (9), 2006. 161, 174

[327] S. Riabzev, A. Veprik, H. Vilenchik, and N. Pundak, "Vibration generation in a pulse tube refrigerator," *Cryogenics*, vol. 49 (1), 2009. 161

[328] "AttoCube," http://www.attocube.com/attoCRYO/attoDRY1000.htm. 161, 162

[329] T. Suzuki et al., "Pulse tube cryocooler with self-cancellation of cold stage vibration," 2006. 161, 168, 430

[330] K. S. H. Blessing, Ph. Lebrun, "Very low-loss liquid helium transfer with long fexible cryogenic lines," Cern lep-ma/89-38, CERN, 1989. 166, 430

[331] P. Astone et al., "Noise behaviour of the Explorer gravitational wave antenna during the transition to the superfluid phase," *Cryogenics*, vol. 32, pp. 668–670, 1992. 166

[332] P. Puppo and F. Ricci, "Cryogenics and Einstein Telescope," *General Relativity and Gravitation*, vol. 43 (2), pp. 657–669, 2010. 167

[333] T. Koettig et al., "Application of novel regenerator material within a coaxial two-stage pulse tube refrigerator," in Boulder, ed., "Advances in Cryogenic Engineering: Transactions of the Cryogenic Engineering Conference - CEC," vol. 53 of *AIP Conference Proceedings, Vol. 985 (2008) 235-242.*, AIP, 2008. 167

[334] N. Jiang, U. Lindemann, F. Giebeler, and G. Thummes, "A 3He pulse tube cooler operating down to 1.27 K," *Cryogenics*, vol. 44, pp. 809 –816, 2004. 168

[335] "Einstein Telescope Home Page," . 169

[336] F. Ricci, "Low Temperature and Future Gravitational Wave experiments," in J. Dumarchez and J. T. Thanh, eds., "Gravitational Waves and Experimental Gravity," vol. Proc. XLII Rencontres de Moriond 2007, pp. 177–182, The Gioi Publishers, Hanoi, Vietnam, 2007. 172

[337] F. Acernese et al., "Measurements of Superattenuator seismic isolation by Virgo interferometer," *Astroparticle Physics*, vol. 33 (3), pp. 182 – 189, 2010. 174, 182, 183, 431

[338] M. Punturo, "The Virgo sensitivity curve," *Virgo Technical Report*, vol. VIR-NOT-PER-1390-51, 2004. 175, 430

[339] F. Acernese et al., "Properties of seismic noise at the Virgo site," *Classical and Quantum Gravity*, vol. 21 (5), p. S433, 2004. 175

[340] M. Ohashi et al., "Laser Interferometer in the Kamioka mine," *Proceedings of the 28th International Cosmic Ray Conference, Tsukuba, Japan, Universal Academy Press*, 2003. 175

[341] M. G. Beker et al., "Selection criteria for ET candidate sites (Einstein Telescope Working Group 1 Report)," *ET Scientific Note*, vol. ET-030-09, 2009. 175

[342] G. Ballardin et al., "Measurement of the transfer function of the steering filter of the Virgo super attenuator suspension," *Review of Scientific Instruments*, vol. 72 (9), pp. 3635–3642, 2001. 178, 181, 182

[343] T. V. Collaboration, "VIRGO Final Design," *E.T.S.*, vol. E.T.S, Pisa, Italy, 1995. 178

[344] G. Losurdo et al., "An inverted pendulum preisolator stage for the VIRGO suspension system," *Review of Scientific Instruments*, vol. 70 (5), pp. 2507–2515, 1999. 179

[345] G. Losurdo et al., "Inertial control of the mirror suspensions of the VIRGO interferometer for gravitational wave detection," *Review of Scientific Instruments*, vol. 72 (9), pp. 3653–3661, 2001. 179

[346] M. Beccaria et al., "Extending the VIRGO gravitational wave detection band down to a few Hz: metal blade springs and magnetic antisprings," *Nuclear Instruments and Methods in Physics Research Section A: Accelerators, Spectrometers, Detectors and Associated Equipment*, vol. 394 (3), pp. 397 – 408, 1997. 180, 181

[347] M. Beccaria et al., "The creep problem in the VIRGO suspensions: a possible solution using Maraging steel," *Nuclear Instruments and Methods in Physics Research Section A: Accelerators, Spectrometers, Detectors and Associated Equipment*, vol. 404 (2-3), pp. 455 – 469, 1998. 180

[348] S. Braccini et al., "The maraging-steel blades of the Virgo super attenuator," *Measurement Science and Technology*, vol. 11 (5), p. 467, 2000. 180, 343

[349] A. Delapierre and F. Frasconi, "Stress distribution on the suspension wires of the Virgo superattenuator," Virgo Internal Note VIR-TRE-PIS-4600-137, INFN, 1997. 180

[350] S. Braccini et al., "An improvement in the VIRGO Super Attenuator for interferometric detection of gravitational waves: The use of a magnetic antispring," *Review of Scientific Instruments*, vol. 64 (2), pp. 310–313, 1993. 181

[351] G. Cella et al., "Monolithic geometric anti-spring blades," *Nuclear Instr. and Methods in Phys. Res. A*, pp. 502–519, 2005. 181, 343

[352] S. Braccini on behalf of the ET-WG2, "Einstein Telescope - Seismic Isolation Design Study," 2010, Talk at the WP2-WP3 joint meeting (Jena). 182, 184, 188, 431

[353] W. H. P. and, *Numerical Recipes in C*, Cambridge University Press, 2008. 183

[354] F. Marchesoni, "Self-organized criticality and dislocation damping," *Journal of Alloys and Compounds*, vol. 211-212, pp. 124 – 127, 1994, 10th International Conference on Internal Friction and Ultrasonic Attenuation in Solids. 186

[355] A. Bernardini et al., "Suspension last stages for the mirrors of the Virgo interferometric gravitational wave antennas," *Review of Scientific Instruments*, vol. 70 (8), pp. 3463–3472, 1999. 195, 213

[356] M. V. Plissi et al., "Aspects of the suspension system for GEO 600," *Review of Scientific Instruments*, vol. 69 (8), pp. 3055–3061, 1998. 196, 259

[357] B. Willke et al., "The GEO 600 gravitational wave detector," *Classical and Quantum Gravity*, vol. 19 (7), p. 1377, 2002. 196, 259

[358] N. A. Robertson et al., "Quadruple suspension design for Advanced LIGO," *Classical and Quantum Gravity*, vol. 19 (15), p. 4043, 2002. 196, 259

[359] A. Cumming et al., "Finite element modelling of the mechanical loss of silica suspension fibres for advanced gravitational wave detectors," *Classical and Quantum Gravity*, vol. 26 (21), p. 215012, 2009. 196, 259

[360] Y. S. Touloukian and C. Y. Ho, "Thermophysical Properties of Matter," in "Vol. 1 - Thermal Conductivity - Metallic Elements and Alloys," Plenum, 1970. 197, 198, 263, 432

[361] Y. S. Touloukian and C. Y. Ho, "Thermophysical Properties of Matter," in "Vol. 2 - Conductivity - Nonmetallic Solids," Plenum, 1970. 197, 263, 432

[362] T. Uchiyama et al., "Mechanical quality factor of a sapphire fiber at cryogenic temperatures," *Physics Letters A*, vol. 273 (5-6), pp. 310 – 315, 2000. 197

[363] T. Tomaru et al., "Maximum heat transfer along a sapphire suspension fiber for a cryogenic interferometric gravitational wave detector," *Physics Letters A*, vol. 301 (3-4), pp. 215–219, 2002.

[364] T. Suzuki et al., "Thermal Conductance through Sapphire-Sapphire Bonding," in "International Cosmic Ray Conference," vol. 5 of *International Cosmic Ray Conference*, pp. 3131–+, 2003. 197

[365] A. Dari, F. Travasso, H. Vocca, and L. Gammaitoni, "Breaking strength tests on silicon and sapphire bondings for gravitational wave detectors," *Classical and Quantum Gravity*, vol. 27 (4), p. 045010, 2010. 197, 260, 261

[366] A. A. van Veggel et al., "Strength testing and SEM imaging of hydroxide-catalysis bonds between silicon," *Classical and Quantum Gravity*, vol. 26 (17), p. 175007, 2009. 197, 222, 261

[367] M. Alshourbagy et al., "First characterization of silicon crystalline fibers produced with the μ-pulling technique for future gravitational wave detectors," *Rev. Sci. Instrum.*, vol. 77, p. 044502, 2006. 197, 200, 220

[368] S. Reid et al., "Mechanical dissipation in silicon flexures," *Physics Letters A*, vol. 351 (4-5), pp. 205 – 211, 2006. 197, 199, 201

[369] J. Callaway, "Model for Lattice Thermal Conductivity at Low Temperatures," *Phys. Rev.*, vol. 113 (4), pp. 1046–1051, 1959. 198

[370] J. Callaway and H. C. von Baeyer, "Effect of Point Imperfections on Lattice Thermal Conductivity," *Phys. Rev.*, vol. 120 (4), pp. 1149–1154, 1960. 198

[371] T. Ruf et al., "Thermal conductivity of isotopically enriched silicon," *Solid State Communications*, vol. 115 (5), pp. 243 – 247, 2000. 198, 432

[372] D. T. Morelli, J. P. Heremans, and G. A. Slack, "Estimation of the isotope effect on the lattice thermal conductivity of group IV and group III-V semiconductors," *Phys. Rev. B*, vol. 66 (19), p. 195304, 2002. 198

[373] Y. S. Touloukian and C. Y. Ho, "Thermophysical Properties of Matter," in "Vol. 4 - Specific Heat - Metallic Elements and Alloys," Plenum, 1970. 199

[374] Y. S. Touloukian and C. Y. Ho, "Thermophysical Properties of Matter," in "Vol. 5 - Specific Heat - Nonmetallic Solids," Plenum, 1970. 199, 263

[375] Y. S. Touloukian and C. Y. Ho, "Thermophysical Properties of Matter," in "Vol. 12 - Thermal Expansion - Metallic Elements and Alloys," Plenum, 1970. 199

[376] Y. S. Touloukian and C. Y. Ho, "Thermophysical Properties of Matter," in "Vol. 13 - Thermal Expansion - Nonmetallic Solids," Plenum, 1970. 199, 263

[377] D. F. McGuigan et al., "Measurements of the mechanical Q of single-crystal silicon at low temperatures," *Journal of Low Temperature Physics*, vol. 30, pp. 621–629, 1978, 10.1007/BF00116202. 199, 200, 220, 261, 263, 432

[378] S. Rowan et al., "Investigation of mechanical loss factors of some candidate materials for the test masses of gravitational wave detectors," *Physics Letters A*, vol. 265 (1-2), pp. 5 – 11, 2000. 263

[379] S. Rowan et al., "Test mass materials for a new generation of gravitational wave detectors," in "Proceedings of SPIE," vol. 4856, 2003. 261

[380] R. Nawrodt et al., "High mechanical Q-factor measurements on silicon bulk samples," *Journal of Physics: Conference Series*, vol. 122 (1), p. 012008, 2008. 262, 263, 434

[381] R. Nawrodt et al., "Investigation of mechanical losses of thin silicon flexures at low temperatures," *arXiv:1003.2893v1*, 2010. 199, 200, 223, 432

[382] S. Rowan et al., "The quality factor of natural fused quartz ribbons over a frequency range from 6 to 160 Hz," *Physics Letters A*, vol. 227 (3-4), pp. 153 – 158, 1997. 199

[383] A. Heptonstall, G. Cagnoli, J. Hough, and S. Rowan, "Characterisation of mechanical loss in synthetic fused silica ribbons," *Physics Letters A*, vol. 354 (5-6), pp. 353 – 359, 2006.

[384] A. M. Gretarsson and G. M. Harry, "Dissipation of mechanical energy in fused silica fibers," *Review of Scientific Instruments*, vol. 70 (10), pp. 4081–4087, 1999.

[385] S. D. Penn et al., "High quality factor measured in fused silica," *Review of Scientific Instruments*, vol. 72 (9), pp. 3670–3673, 2001.

[386] S. D. Penn et al., "Frequency and surface dependence of the mechanical loss in fused silica," *Phys. Lett. A*, vol. 352 (1-2), pp. 3–6, 2006. 199, 259, 263

[387] I. Martin et al., "Measurements of a low-temperature mechanical dissipation peak in a single layer of Ta_2O_5 doped with TiO_2." *Classical and Quantum Gravity*, vol. 25, p. 055005, 2008. 201, 265

[388] I. W. Martin et al., "Comparison of the temperature dependence of the mechanical dissipation in thin films of Ta_2O_5 and Ta_2O_5 doped with TiO_2," *Classical and Quantum Gravity*, vol. 26 (15), p. 155012, 2009.

[389] I. W. Martin et al., "Effect of heat treatment on mechanical dissipation in Ta2O5 coatings," *Classical and Quantum Gravity*, vol. 27 (22), p. 225020, 2010. 201, 265

[390] F. Piergiovanni, M. Punturo, and P. Puppo, "The thermal noise of the Virgo+ and Virgo Advanced Last Stage Suspension (The PPP effect)," Tech. rep., 2009. 202, 203, 208

[391] P. Puppo, "A thermal noise model for a branched system of harmonic oscillators," *Journal of Physics: Conference Series*, vol. 228 (1), p. 012031, 2010. 202

[392] S. Amadori et al., "Low temperature anelasticity in Ti6Al4V alloy and Ti6Al4V-SiCf composite," *Materials Science and Engineering: A*, vol. 521-522, pp. 340 – 342, 2009, 15th International Conference on Internal Friction and Mechanical Spectroscopy. 203

[393] A. Caticha and R. Preuss, "Maximum entropy and Bayesian data analysis: Entropic prior distributions," 2004. 213

[394] P. Falferi, "Testing the intrinsic noise of a coil-magnet actuator for cryogenic gravitational wave interferometers," *Class. Quant. Grav.*, vol. in press, 2011, accepted for publication. 213

[395] M. Hewitson et al., "Calibration of GEO 600 for the S1 science run," *Class. Quantum Grav.*, vol. 20, pp. S885–S893, 2003. 217

[396] P. Amico et al., "Mechanical quality factor of mirror substrates for VIRGO," *Class. Quantum Grav.*, vol. 19, pp. 1663–1668, 2002. 217

[397] S. Grasso et al., "Electrostatic systems for fine control of mirror orientation in interferometric GW antennas," *Physics Letters A*, vol. 244, pp. 360–370, 1998. 218

[398] M. J. Mortonson, C. C. Vassiliou, D. J. Ottaway, D. H. Shoemaker, and G. M. Harrya, "Effects of electrical charging on the mechanical Q of a fused silica disk," *Review of Scientifi Instruments*, vol. 74, pp. 4840–4845, 2003. 218

[399] M. Hewitson et al., "Charge measurement and mitigation for the main test masses of the GEO 600 gravitational wave observatory," *Class. Quantum Grav.*, vol. 24, 2007. 218

[400] R. D. Rosa, F. Garufi, L. Milano, S. Mosca, and G. Persichetti, "Characterization of electrostatic actuators for suspended mirror control with modulated bias," *Jou. of Physics: Conf. Series*, vol. 228, p. 012018, 2010. 218

[401] F. Acernese et al., "Application of a hybrid modular acquisition system to the control of a suspended interferometer with electrostatic actuators," *Jou. of Physics: Conf. Series*, vol. 122, p. 012011, 2008. 218

[402] C. Lam and D. Douglas, "Internal friction measurements in Boron-doped single-crystal silicon," *Physics Letters*, vol. 85, pp. 41 – 42, 1981. 220

[403] L. Lagonigro et al., "Low loss silicon fibers for photonics applications," *Appl. Phys. Lett.*, 2010. 220

[404] A. Toncelli, 2010, private communication. 221

[405] N. L. Beveridge et al., "Low-temperature strength tests and SEM imaging of hydroxide catalysis bonds in silicon," *Classical and Quantum Gravity*, vol. 28 (8), p. 085014, 2011. 222

[406] J. Yang, T. Ono, and M. Esashi, "Surface effects and high quality factors in ultrathin single-crystal silicon cantilevers," *Appl. Phys. Lett.*, vol. 77, pp. 3860–3862, 2000. 223

[407] K. Y. Yasumura et al., "Quality Factors in Micron- and Submicron-Thick Cantilevers," *J. of Microelectromechanical Systems*, vol. 9, pp. 117–125, 2000.

[408] J. Yang, T. One, and M. Esashi, "Energy Dissipation in Submicrometer Thick Single-Crystal Silicon Cantilevers," *J. of Microelectromechanical Systems*, vol. 11, pp. 775–783, 2002. 223

[409] J. Liu, L. Ju, and D. Blair, "Vibration isolation performance of an ultra-low frequency folded pendulum resonator," *Phys. Lett. A*, vol. 228, pp. 243–249, 1997. 224, 225

[410] A. Bertolini et al., "Mechanical design of a single axis monolithic accelerometer for advanced seismic attenuation systems," *Nucl. Instr. and Meth.*, vol. 556, pp. 616–623, 2006. 224, 225

[411] F. Acernese et al., "New tunable mechanical monolithic horizontal seismometer for low frequency seismic noise measurement," in P. of SPIE, ed., "Sensors and Smart Structures Technologies for Civil, Mechanical, and Aerospace Systems," vol. 7647, 2008. 224, 225

[412] F. Acernese, R. D. Rosa, G. Giordano, R. Romano, and F. Barone, "Mechanical monolithic horizontal sensor for low frequency seismic noise measurement," *Rev. Sci. Instrum.*, vol. 79, p. 074501, 2008. 224, 225

[413] F.Basti et al., "A cryogenic payload for the 3rd generation of gravitational wave interferometers." *submitted to Astrophys. J.*, 2011. 228

[414] C. Hogan, "Holographic Noise in Interferometers," arXiv:0905.4803v8, 2009. 233, 380, 381

[415] A. Freise et al., "Triple Michelson interferometer for a third-generation gravitational wave detector," *Classical and Quantum Gravity*, vol. 26 (8), p. 085012, 2009. 233, 235, 237

[416] W. Winkler et al., eds., *Plans for a large gravitational wave antenna in Germany*, 1985. 234

[417] Y. Gürsel and M. Tinto, "Near optimal solution to the inverse problem for gravitational-wave bursts," *Phys. Rev. D*, vol. 40, pp. 3884–3938, 1989. 235

[418] Y. Chen, "Sagnac interferometer as a speed-meter-type, quantum-nondemolition gravitational-wave detector," *Phys. Rev. D*, vol. 67, p. 122004, 2003. 235, 237, 241, 306, 350

[419] S. L. Danilishin and F. Y. Khalili, "Practical design of the optical lever intracavity topology of gravitational-wave detectors," *Phys. Rev. D*, vol. 73 (2), pp. 022002–+, 2006.

[420] Y. Chen et al., "Interferometers for Displacement-Noise-Free Gravitational-Wave Detection," *Physical Review Letters*, vol. 97 (15), pp. 151103–+, 2006. 235

[421] S. Chelkowski, "A Topology Review: The Sagnac Effect," 2009, talk at Hannover ET-WP3 meeting. 237

[422] K.-X. Sun, M. M. Fejer, E. Gustafson, and R. L. Byer, "Sagnac Interferometer for Gravitational-Wave Detection," *Phys. Rev. Lett.*, vol. 76 (17), pp. 3053–3056, 1996. 237, 307, 350

[423] J. Mizuno, A. Rüdiger, R. Schilling, W. Winkler, and K. Danzmann, "Frequency response of Michelson- and Sagnac-based interferometers," *Optics Communications*, vol. 138 (4-6), pp. 383–393, 1997. 237

[424] B. Mours, E. Tournefier, and J.-Y. Vinet, "Thermal noise reduction in interferometric gravitational wave antennas: using high order TEM modes," *Classical and Quantum Gravity*, vol. 23, pp. 5777–5784, 2006. 238, 301

[425] J.-Y. Vinet, "Reducing thermal effects in mirros of advanced gravitational wave interferometric detectors," *Class. Quantum Grav.*, vol. 24 (15), pp. 3897–3910, 2007. 238, 278, 301

[426] A. Freise and K. Strain, "Interferometer Techniques for Gravitational-Wave Detection," *Living Reviews in Relativity*, vol. 13, pp. 1–+, 2010. 238

[427] S. Hild, S. Chelkowski, and A. Freise, "Pushing towards the ET sensitivity using 'conventional' technology," *arXiv:0810.0604v2 [gr-qc]*, 2008. 240, 375, 377

[428] F. Y. Khalili, "The optical lever intracavity readout scheme for gravitational-wave antennae," *Phys. Lett. A*, vol. 298, p. 308, 2002. 241, 349

[429] D. Shoemaker, "Future limits to sensitivity," 2001, g010026-00-G. 241

[430] G. Conforto and R. DeSalvo, "Proposal for lower frequency companions for the advanced LIGO Gravitational Wave Interferometric Detectors," *Nuclear Instruments and Methods in Physics Research Section A: Accelerators, Spectrometers, Detectors and Associated Equipment*, vol. 518 (1-2), pp. 228–232, 2004, frontier Detectors for Frontier Physics: Proceedin. 241

[431] S. Chelkowski, S. Hild, and A. Freise, "Prospects of higher-order Laguerre-Gauss modes in future gravitational wave detectors," *Phys. Rev. D*, vol. 79 (12), p. 122002, 2009. 243, 302

[432] V. B. Braginsky, "Classical and quantum restrictions on detection of weak distributions of a macroscopic oscillator," *Sov. Phys. JETP*, vol. 26, p. 831, 1968. 245

[433] V. B. Braginsky and F. Y. Khalili, *Quantum measurement*, Cambridge University Press, 1999. 245, 250

[434] S. Hild et al., "A xylophone configuration for a third-generation gravitational wave detector," *Classical and Quantum Gravity*, vol. 27, p. 015003, 2010. 246, 355, 375, 376, 378, 440

[435] V. B. Braginsky et al., "Noise in gravitational-wave detectors and other classical-force measurements is not influenced by test-mass quantization," *Phys. Rev. D*, vol. 67 (8), p. 082001, 2003. 246

[436] H. J. Kimble, Y. Levin, A. B. Matsko, K. S. Thorne, and S. P. Vyatchanin, "Conversion of conventional gravitational-wave interferometers into quantum nondemolition interferometers by modifying their input and/or output optics," *Phys. Rev. D*, vol. 65 (2), p. 022002, 2001. 246, 352

[437] R. Schnabel, N. Mavalvala, D. E. McClelland, and P. K. Lam, "Quantum metrology for gravitational wave astronomy," *Nature Communications*, vol. 1.121, 10.1038/ncomms1122, 2010. 248

[438] C. M. Caves, "Quantum-mechanical noise in an interferometer," *Phys. Rev. D*, vol. 23 (8), pp. 1693–1708, 1981. 248, 250, 251, 351

[439] H. Vahlbruch, *Squeezed Light for Gravitational Wave Astronomy*, Ph.D. thesis, Leibniz Universität Hannover, 2008. 249, 254

[440] H. P. Yuen, "Two-photon coherent states of the radiation field," *Phys. Rev. A*, vol. 13 (6), pp. 2226–2243, 1976. 249

[441] D. F. Walls, "Squeezed states of light," *Nature*, vol. 306, pp. 141–146, 1983. 250

[442] G. Breitenbach, S. Schiller, and J. Mlynek, "Measurement of the quantum states of squeezed light," *Nature*, vol. 387, pp. 471–475, 1997.

[443] V. V. Dodonov, "'Nonclassical' states in quantum optics: a 'squeezed' review of the first 75 years," *Journal of Optics B: Quantum Semiclass.*, vol. 4, pp. R1–R33, 2002. 249

[444] C. C. Gerry and P. L. Knight, *Introductory quantum optics*, Cambridge University Press, 2004. 249, 250, 252

[445] J. DiGuglielmo, B. Hage, A. Franzen, J. Fiurášek, and R. Schnabel, "Experimental characterization of Gaussian quantum-communication channels," *Phys. Rev. A*, vol. 76 (1), p. 012323, 2007. 250

[446] R. E. Slusher, L. W. Hollberg, B. Yurke, J. C. Mertz, and J. F. Valley, "Observation of Squeezed States Generated by Four-Wave Mixing in an Optical Cavity," *Phys. Rev. Lett.*, vol. 55 (22), pp. 2409–2412, 1985. 250, 251, 252

[447] M. Xiao, L.-A. Wu, and H. J. Kimble, "Precision measurement beyond the shot-noise limit," *Phys. Rev. Lett.*, vol. 59 (3), pp. 278–281, 1987. 250, 351

[448] P. Grangier, R. E. Slusher, B. Yurke, and A. LaPorta, "Squeezed-light enhanced polarization interferometer," *Phys. Rev. Lett.*, vol. 59 (19), pp. 2153–2156, 1987. 250, 351

[449] C. M. Caves, "Quantum-Mechanical Radiation-Pressure Fluctuations in an Interferometer," *Phys. Rev. Lett.*, vol. 45 (2), pp. 75–79, 1980. 250

[450] K. S. Thorne, R. W. P. Drever, C. M. Caves, M. Zimmermann, and V. D. Sandberg, "Quantum Nondemolition Measurements of Harmonic Oscillators," *Phys. Rev. Lett.*, vol. 40 (11), pp. 667–671, 1978. 250

[451] V. B. Braginsky and F. Y. Khalili, "Quantum nondemolition measurements: the route from toys to tools," *Rev. Mod. Phys.*, vol. 68 (1), pp. 1–11, 1996. 250

[452] H. P. Yuen, "Contractive States and the Standard Quantum Limit for Monitoring Free-Mass Positions," *Phys. Rev. Lett.*, vol. 51 (9), pp. 719–722, 1983. 250, 255, 351

[453] W. G. Unruh, *Quantum noise in the interferometer detector*, Plenum, 1983. 250

[454] C. M. Caves, "Defense of the Standard Quantum Limit for Free-Mass Position," *Phys. Rev. Lett.*, vol. 54 (23), pp. 2465–2468, 1985. 250

[455] M. T. Jaekel and S. Reynaud, "Quantum Limits in Interferometric Measurements," *Europhys. Lett.*, vol. 13 (4), pp. 301–306, 1990. 250, 351

[456] D. Vitali et al., "Optomechanical Entanglement between a Movable Mirror and a Cavity Field," *Phys. Rev. Lett.*, vol. 98 (3), p. 030405, 2007. 250

[457] S. Pirandola, D. Vitali, P. Tombesi, and S. Lloyd, "Macroscopic Entanglement by Entanglement Swapping," *Phys. Rev. Lett.*, vol. 97 (15), p. 150403, 2006. 251

[458] H. Müller-Ebhardt, H. Rehbein, R. Schnabel, K. Danzmann, and Y. Chen, "Entanglement of Macroscopic Test Masses and the Standard Quantum Limit in Laser Interferometry," *Phys. Rev. Lett.*, vol. 100 (1), p. 013601, 2008. 251

[459] R. M. Shelby, M. D. Levenson, S. H. Perlmutter, R. G. DeVoe, and D. F. Walls, "Broad-Band Parametric Deamplification of Quantum Noise in an Optical Fiber," *Phys. Rev. Lett.*, vol. 57 (6), pp. 691–694, 1986. 251, 252

[460] L.-A. Wu, H. J. Kimble, J. L. Hall, and H. Wu, "Generation of Squeezed States by Parametric Down Conversion," *Phys. Rev. Lett.*, vol. 57 (20), pp. 2520–2523, 1986. 251, 252

[461] H. Bachor and T. C. Ralph, *A Guide to Experiments in Quantum Optics*, Wiley-VCH, 2004. 251, 252

[462] M. Frede, R. Wilhelm, and D. Kracht, "250 W end-pumped Nd:YAG laser with direct pumping into the upper laser level," *Optics Letters*, vol. 31, pp. 3618–3619, 2006. 251, 282

[463] A. Furusawa et al., "Unconditional Quantum Teleportation," *Science*, vol. 282 (5389), pp. 706–709, 1998. 251

[464] W. P. Bowen et al., "Experimental investigation of continuous-variable quantum teleportation," *Phys. Rev. A*, vol. 67 (3), p. 032302, 2003.

[465] K. Schneider, M. Lang, J. Mlynek, and S. Schiller, "Generation of strongly squeezed continuous-wave light at 1064 nm," *Opt. Express*, vol. 2 (3), pp. 59–64, 1998.

[466] P. K. Lam et al., "Optimization and transfer of vacuum squeezing from an optical parametric oscillator," *Journal of Optics B: Quantum and Semiclassical Optics*, vol. 1 (4), p. 469, 1999. 251

[467] M. D. Reid and P. D. Drummond, "Correlations in nondegenerate parametric oscillation: Squeezing in the presence of phase diffusion," *Phys. Rev. A*, vol. 40 (8), pp. 4493–4506, 1989. 252

[468] H. Vahlbruch et al., "The GEO 600 squeezed light source," *Classical and Quantum Gravity*, vol. 27 (8), p. 084027, 2010. 253, 254, 434

[469] W. P. Bowen, R. Schnabel, N. Treps, H.-A. Bachor, and P. K. Lam, "Recovery of continuous wave squeezing at low frequencies," *Journal of Optics B: Quantum and Semiclassical Optics*, vol. 4 (6), p. 421, 2002. 252

[470] R. Schnabel et al., "Squeezed light at sideband frequencies below 100 kHz from a single OPA," *Optics Communications*, vol. 240 (1-3), pp. 185 – 190, 2004. 252

[471] K. McKenzie et al., "Squeezing in the Audio Gravitational-Wave Detection Band," *Phys. Rev. Lett.*, vol. 93 (16), p. 161105, 2004. 252

[472] K. McKenzie et al., "Quantum noise locking," *Journal of Optics B: Quantum and Semiclassical Optics*, vol. 7 (10), p. S421, 2005. 252

[473] H. Vahlbruch et al., "Coherent Control of Vacuum Squeezing in the Gravitational-Wave Detection Band," *Physical Review Letters*, vol. 97 (1), 011101, 2006. 252

[474] H. Vahlbruch, S. Chelkowski, K. Danzmann, and R. Schnabel, "Quantum engineering of squeezed states for quantum communication and metrology," *New Journal of Physics*, vol. 9 (10), p. 371, 2007. 252

[475] K. McKenzie, M. B. Gray, P. K. Lam, and D. E. McClelland, "Technical limitations to homodyne detection at audio frequencies," *Appl. Opt.*, vol. 46 (17), pp. 3389–3395, 2007. 253

[476] J. Gea-Banacloche and G. Leuchs, "Squeezed States for Interferometric Gravitational-wave Detectors," *Journal of Modern Optics*, vol. 34 (6), pp. 798–811, 1987. 253

[477] J. Harms et al., "Squeezed-input, optical-spring, signal-recycled gravitational-wave detectors," *Phys. Rev. D*, vol. 68 (4), p. 042001, 2003. 253, 352, 356

[478] K. McKenzie, D. A. Shaddock, D. E. McClelland, B. C. Buchler, and P. K. Lam, "Experimental Demonstration of a Squeezing-Enhanced Power-Recycled Michelson Interferometer for Gravitational Wave Detection," *Phys. Rev. Lett.*, vol. 88 (23), p. 231102, 2002. 253, 351

[479] H. Vahlbruch et al., "Demonstration of a Squeezed-Light-Enhanced Power- and Signal-Recycled Michelson Interferometer," *Phys. Rev. Lett.*, vol. 95 (21), 211102, 2005. 253, 352

[480] K. Goda et al., "A quantum-enhanced prototype gravitational-wave detector," *Nature Physics*, vol. 4, pp. 472–476, 2008. 253

[481] R. Schnabel, "Gravitational wave detectors: Squeezing up the sensitivity," *Nat Phys*, vol. 4, pp. 440–441, 2008. 253

[482] Y. Takeno, M. Yukawa, H. Yonezawa, and A. Furusawa, "Observation of -9 dB quadrature squeezing with improvement of phase stability in homodyne measurement," *Opt. Express*, vol. 15 (7), pp. 4321–4327, 2007. 253

[483] H. Vahlbruch et al., "Observation of Squeezed Light with 10-dB Quantum-Noise Reduction," *Physical Review Letters*, vol. 100 (3), 033602, 2008.

[484] E. S. Polzik, "Quantum physics: The squeeze goes on," *Nature*, vol. 453, pp. 45–46, 2008. 253

[485] M. Mehmet et al., "Observation of cw squeezed light at 1550 nm," *Opt. Lett.*, vol. 34 (7), pp. 1060–1062, 2009. 254

[486] K. McKenzie, M. B. Gray, S. Gossler, P. K. Lam, and D. E. McClelland, "Squeezed state generation for interferometric gravitational-wave detection," *Classical and Quantum Gravity*, vol. 23 (8), p. S245, 2006. 254

[487] W. G. Unruh, *Quantum Optics, Experimental Gravitation and Measurement Theory*, chap. 6, p. 647, Plenum, New York, 1982. 255, 351

[488] A. F. Pace, M. J. Collett, and D. F. Walls, "Quantum limits in interferometric detection of gravitational radiation," *Phys. Rev. A*, vol. 47 (4), pp. 3173–3189, 1993. 255, 351

[489] S. Hild et al., "Sensitivity Studies for Third-Generation Gravitational Wave Observatories," arXiv:1012.0908[gr-qc], 2010. 255, 274, 375

[490] J. M. Mackowski, "Coating principle," *Optics in Astrophysics, NATO Science Series*, vol. 198, pp. 327–342, 2005. 259, 263

[491] E. Tournefier, "News from Virgo: present status and future upgrades," in2p3-00422110, version 1, 2009. 259

[492] M. Lorenzini and the Virgo Collaboration, "The monolithic suspension for the Virgo interferometer," *Classical and Quantum Gravity*, vol. 27 (8), p. 084021, 2010. 259

[493] O. L. Anderson and H. E. Bömmel, "Ultrasonic Absorption in Fused Silica at Low Temperatures and High Frequencies," *Journal of the American Ceramic Society*, vol. 38 (4), pp. 125–131, 1955. 260

[494] C. Schwarz et al., "Cryogenic Setup for Q-factor measurements on bulk materials for future gravitational wave detectors," in H.-M. Chang and other, eds., "Proceedings of ICEC22-ICMC2008," The Korea Institute of Applied Superconductivity and Cryogenics, 2009. 260, 263

[495] J. Franc et al., "Mirror thermal noise in laser interferometer gravitational wave detectors operating at room and cryogenic temperatures," ET document ET 09021, 2009. 260, 263, 265, 383, 384, 385

[496] T. Tomaru et al., "Cryogenic measurement of the optical absorption coefficient in sapphire crystals at 1.064μm for the large-scale cryogenic gravitational wave telescope," *Physics Letters A*, vol. 283 (1-2), pp. 80–84, 2001. 260, 383

[497] C. T. Taylor, M. Notcutt, E. K. Wong, A. G. Mann, and D. G. Blair, "Measurement of the coefficient of thermal expansion of a cryogenic, all-sapphire, Fabry-Perot optical cavity," *Optics Communications*, vol. 131 (4-6), pp. 311 – 314, 1996. 260

[498] T. Uchiyama et al., "Mechanical quality factor of a cryogenic sapphire test mass for gravitational wave detectors," *Physics Letters A*, vol. 261 (1-2), pp. 5–11, 1999. 260, 263

[499] A. L. Alexandrovski, M. M. Fejer, and R. K. Route, "Effect of annealing on the light absorption in sapphire," in "Gravitational Waves - 3rd Edoardo Amaldi Conference," 2000. 260

[500] . LCGT collaboration, "LCGT design document (ver. 3)," Tech. rep., JGW-T0400030, 2009. 260

[501] M. Tokunari, T. Saito, S. Miyoki, M. Ohashi, and K. Kuroda, "Optical properties measurement of an Al2 O3 mirror substrate for the Large-Scale Cryogenic Gravitational Wave Telescope (LCGT)," *Class. Quantum Grav.*, vol. 27, p. 185015, 2010. 260

[502] A. S. Nowick and B. S. Berry, *"Anelastic Relaxation in Crystalline Solids"*, Academic Press, 1972. 260

[503] M. Punturo et al., "The third generation of gravitational wave observatories and their science reach," *Classical and Quantum Gravity*, vol. 27 (8), p. 084007, 2010. 261

[504] J. Software, "Material Properties Data Base," . 261, 263

[505] M. A. Green and M. J. Keevers, "Optical properties of intrinsic silicon at 300 K," *Progress in Photovoltaics: Research and Applications*, vol. 3, pp. 189–192, 1995. 261, 383

[506] M. J. Keevers and M. A. Green, "Absorption edge of silicon from solar cell spectral response measurements," *Applied Physics*, vol. 66, 1995. 262

[507] B. J. Frey, D. B. Leviton, and T. J. Madison, "Temperature-dependent refractive index of silicon and germanium," in "SPIE Conference Series," vol. 6273, 2006. 262, 263, 273

[508] G. K. White and M. L. Minges, "Thermophysical Properties of Some Key Solids," *International Journal of Thermophysics*, vol. 15, pp. 1333–1343, 1994, 10.1007/BF01458841. 263

[509] R. Hull, *Properties of Crystalline Silicon*, The Institution of Engineering and Technology, 1999. 263

[510] T. Tomaru et al., "Thermal lensing in cryogenic sapphire substrates," *Classical and Quantum Gravity*, vol. 19, p. 2045, 2002. 263, 273

[511] D. B. Leviton and B. J. Frey, "Temperature-dependent absolute refractive index measurements of synthetic fused silica," vol. 6273, p. 62732K, SPIE, 2006. 263

[512] I. H. Malitson, "Refraction and Dispersion of Synthetic Sapphire," *J. Opt. Soc. Am.*, vol. 52 (12), pp. 1377–1379, 1962. 263

[513] R. Nawrodt et al., "Mirror thermal noise calculation for ET," ET document ET 09027, 2009. 263, 265, 268, 383, 384, 385

[514] G. M. Harry et al., "Thermal noise in interferometric gravitational wave detectors due to dielectric optical coatings," *Classical and Quantum Gravity*, vol. 19 (5), p. 897, 2002. 267, 270

[515] G. M. Harry et al., "Thermal noise from optical coatings in gravitational wave detectors," *Appl. Opt.*, vol. 45 (7), pp. 1569–1574, 2006. 267, 270

[516] V. B. Braginsky, M. L. Gorodetsky, and S. P. Vyatchanin, "Thermodynamical fluctuations and photothermal shot noise in gravitational wave antennae," *Physics Letters A*, vol. 264 (1), pp. 1 – 10, 1999. 268

[517] M. Cerdonio, L. Conti, A. Heidmann, and M. Pinard, "Thermoelastic effects at low temperatures and quantum limits in displacement measurements," *Phys. Rev. D*, vol. 63 (8), p. 082003, 2001. 268

[518] F. Bondu, P. Hello, and J.-Y. Vinet, "Thermal noise in mirrors of interferometric gravitational wave antennas," *Physics Letters A*, vol. 246 (3-4), pp. 227 – 236, 1998. 270

[519] Y. T. Liu and K. S. Thorne, "Thermoelastic noise and homogeneous thermal noise in finite sized gravitational-wave test masses," *Phys. Rev. D*, vol. 62 (12), p. 122002, 2000. 270

[520] M. Evans et al., "Thermo-optic noise in coated mirrors for high-precision optical measurements," *Phys. Rev. D*, vol. 78, p. 102003, 2008. 271

[521] V. B. Braginsky and S. V. Vyatchanin, "Corner reflectors and quantum non-demolition measurements in gravitational wave antennae," *Physics Letters A*, vol. 324, pp. 345–360, 2004. 272

[522] B. Benthem and Y. Levin, "Thermorefractive and thermomechanical noise in the beamsplitter of the GEO600 gravitational-wave interferometer," *Phys. Rev. D*, vol. 80, 2009. 272, 276

[523] J. Franc, J. Degallaix, and R. Flaminio, "Substrate thermo-refractive noise for future cryogenic gravitational wave detector," ET-00095A-10, 2010. 273

[524] B. Caron et al., "SIESTA, a time domain, general purpose simulation program for the VIRGO experiment," *Astroparticle Physics*, vol. 10, pp. 369–386, 1999. 280

[525] M. Galimberti, "Requirements for ET arm cavity mirrors," 2010, talk at WP2-WP3 joint meeting, Jena. 280

[526] M. Galimberti and R. Flaminio, "Surface specifications for ET mirrors: state of the art," ET-0133A-10, 2010.

[527] M. Galimberti and R. Flaminio, "Mirror requirements for 3rd generation GW detectors," 2010, talk at GWADW 2010, Kyoto. 280, 281

[528] G. Billingsley, "Advanced LIGO Core Optics, expanding the imagination. . . ," LIGO Document G1100216-v2, 2011. 281

[529] R. Bonnand, M. Galimberti, J. Degallaix, R. Flaminio, and L. Pinard., "Simulations for AdV. Mirror Specifications: High Spatial Frequency & Corrective Coating," Virgo Note VIR-0088A-11, 2011. 281

[530] C. Bond, "Laguerre-Gauss mode degeneracy in gravitational wave detectors," 2010, (Fourth Year Project Report, Internal document). 281

[531] J. Deile, R. Brockmann, and D. Havrilla, "Current Status and Most Recent Developments of Industrial High Power Disk Lasers," in "Conference on Lasers and Electro-Optics/International Quantum Electronics Conference," p. CThA4, Optical Society of America, 2009. 282

[532] Y. Kalisky and O. Kalisky, "The status of high-power lasers and their applications in the battlefield," *Optical Engineering*, vol. 49 (9), 091003, 2010. 282

[533] A. Giesen and J. Speiser, "Fifteen Years of Work on Thin-Disk Lasers: Results and Scaling Laws," *IEEE Journal of Selected Topics in Quantum Electronics*, vol. 13 (3), pp. 598–609, 2007. 282

[534] Q. Lü et al., "A novel approach for compensation of birefringence in cylindrical Nd:YAG rods," *Optical and Quantum Electronics*, vol. 28, pp. 59–69, 1996. 282

[535] W. Koechner and D. K. Rice, "Birefringence of YAG:Nd laser rods as a function of growth direction," *Journal of the Optical Society of America*, vol. 61, pp. 758–766, 1971. 282

[536] L. N. Soms, A. A. Tarasov, and V. V. Shashkin, "Problem of depolarization of linearly polarized light by a YAG: Nd^{3+} laser-active element under thermally induced birefringence conditions," *Soviet Journal of Quantum Electronics*, vol. 10, pp. 350–351, 1980. 282

[537] I. Shoji and T. Taira, "Intrinsic reduction of the depolarization loss in solid-state lasers by use of a (110)-cut $Y_3Al_5O_{12}$ crystal," *Applied Physics Letters*, vol. 80, pp. 3048–3050, 2002. 282

[538] O. Puncken et al., "Intrinsic reduction of the depolarization in Nd:YAG crystals," *Optics Express*, vol. 18, pp. 20461–20474, 2010. 282

[539] R. Wilhelm, D. Freiburg, M. Frede, D. Kracht, and C. Fallnich, "Design and comparison of composite rod crystals for power scaling of diode end-pumped Nd:YAG lasers," *Optics Express*, vol. 17, pp. 8229–8236, 2009. 282

[540] R. Wilhelm, M. Frede, and D. Kracht, "Power Scaling of End-Pumped Solid-State Rod Lasers by Longitudinal Dopant Concentration Gradients," *IEEE Journal of Quantum Electronics*, vol. 44, pp. 232–244, 2008. 282

[541] R. Lavi and S. Jackel, "Thermally Boosted Pumping of Neodymium Lasers," *Applied Optics*, vol. 39, pp. 3093–3098, 2000. 282

[542] D. Kracht, D. Freiburg, R. Wilhelm, M. Frede, and C. Fallnich, "Core-doped Ceramic Nd:YAG Laser," *Optics Express*, vol. 14, pp. 2690–2694, 2006. 282

[543] S. Bedö, W. Lüthy, and H. P. Weber, "The effective absorption coefficient in double-clad fibres," *Optics Communications*, vol. 99, pp. 331–335, 1993. 283

[544] J. Limpert et al., "The rising power of fiber lasers and amplifiers," *IEEE J. of Selected Topics in Quantum Electronics*, vol. 13, pp. 537–545, 2007. 283

[545] Y. Jeong, J. K. Sahu, D. N. Payne, and J. Nilsson, "Ytterbium-doped large-core fibre laser with 1kW of continuous-wave output power," *Electronics Letters*, vol. 40, pp. 470–472, 2004. 283

[546] M. Hildebrandt, M. Frede, P. Kwee, B. Willke, and D. Kracht, "Single-frequency master-oscillator photonic crystal fiber amplifier with 148 W output power," *Optics Express*, vol. 14, pp. 11071–11076, 2006. 283

[547] C. Robin, I. Dajani, C. Vergien, C. Zeringue, and T. M. Shay, "Experimental and theoretical studies of single frequency PCF amplifier with output of 400 W," in K. Tankala, ed., "Fiber Lasers VII: Technology, Systems, and Applications," vol. 7580, p. 75801I, SPIE, 2010. 283

[548] G. Canat et al., "Multifilament-core fibers for high energy pulse amplification at 1.5 μm with excellent beam quality," *Optics Letters*, vol. 33, pp. 2701–2703, 2008. 283

[549] M. M. Vogel, M. Abdou-Ahmed, A. Voss, and T. Graf, "Very-large-mode-area, single-mode multicore fiber," *Optics Letters*, vol. 34, pp. 2876–2878, 2009. 283

[550] G. Canat, R. Spittel, S. Jetschke, L. Lombard, and P. Bourdon, "Analysis of the multifilament core fiber using the effective index theory," *Optics Express*, vol. 18, pp. 4644–4654, 2010. 284

[551] V. Kuhn et al., "Experimental Comparison of Fundamental Mode Content in Er:Yb-Codoped LMA Fibers with Multifilament- and Pedestal-Design Cores," *Journal of Lightwave Technology*, vol. PP (99), pp. 1–1, 2010. 284

[552] J. W. Nicholson et al., "Raman fiber laser with 81 W output power at 1480 nm," *Optics Letters*, vol. 35, pp. 3069–3071, 2010. 284

[553] Y. Jeong, J. K. Sahu, D. B. S. Soh, C. A. Codemard, and J. Nilsson, "High-power tunable single-frequency single-mode erbium:ytterbium codoped large-core fiber master-oscillator power amplifier source," *Optics Letters*, vol. 30, pp. 2997–2999, 2005. 285

[554] V. Kuhn, P. Wessels, J. Neumann, and D. Kracht, "Stabilization and power scaling of cladding pumped Er:Yb-codoped fiber amplifier via auxiliary signal at 1064 nm," *Optics Express*, vol. 17, pp. 18304–18311, 2009. 285

[555] S. Ramachandran et al., "Ultra-large effective-area, higher-order mode fibers: a new strategy for high-power lasers," *Laser & Photonics Reviews*, vol. 2, pp. 429–448, 2008. 285

[556] J. W. Nicholson et al., "Nanosecond Pulse Amplification in a Higher-Order-Mode Erbium-Doped Fiber Amplifier," in "Conference on Lasers and Electro-Optics," p. CPDB5, Optical Society of America, 2010. 285

[557] J. W. Nicholson et al., "A higher-order-mode Erbium-doped-fiber amplifier," *Opt. Express*, vol. 18 (17), pp. 17651–17657, 2010. 285

[558] J.-Y. Vinet, "On Special Optical Modes and Thermal Issues in Advanced Gravitational Wave Interferometric Detectors," *Living Reviews in Relativity*, vol. 12 (5), 2009. 285

[559] E. Genin, M. Mantovani, and P. Ruggi, "Advanced Virgo INJ: Radiation pressure effects in the Advanced Virgo IMC longitudinal and angular directions," 2009. 286

[560] M. Punturo, "Radiation pressure effects on Virgo mode cleaner," Tech. rep., VIR-NOT-PER-1390-284, 2004. 286

[561] B. Canuel et al., "AdV INJ: Preliminary design study," Tech. rep., VIR-0023A-09, 2009. 286

[562] E. Genin, J. Marque, B. Swinkels, and G. Vajente, "Virgo Input Mode Cleaner: Optical characterization," 2010. 286

[563] M. Barsuglia, "Some considerations about Laguerre-Gaussian modes for advanced Virgo," Tech. rep., Presentation at AdV bi-weekly meeting July 1, 2008. 286

[564] S. Chelkowski, "Advanced Virgo with higher order LG modes, implications for mirror radii of curvature," Tech. rep., Presentation at Virgo week July 2008,VIR-0668A-08, 2008. 286

[565] E. Khazanov et al., "Compensation of Thermally Induced Modal Distortions in Faraday Isolators," *IEEE Journal of Quantum Electronics*, vol. 40, p. 10, 2004. 286

[566] B. Canuel, R. Day, E. Genin, F. Nocera, and F. Paoletti, "High power input optics R+D: Final report," Tech. rep., VIR-0296A-10, 2010. 286, 287

[567] E. Genin, "Advanced Virgo INJ: Faraday isolator, electro-optical modulator, high power beam dump and input mode-cleaner," 2010. 286, 287

[568] N. Mavalvala et al., "Lasers and optics: looking towards third generation gravitational wave detectors," *General Relativity and Gravitation*, 2010. 287

[569] J. D. Mansell et al., *Appl.Opt*, vol. 40, pp. 366–374, 2001. 287

[570] L. Schnupp, "Presentation at European Collaboration Meeting on Interferometric Detection of Gravitational Waves," 1988, (Sorrent, Italy, Oct 1988). 288

[571] A. Michelson and E. Morley, "On the Relative Motion of the Earth and the Luminiferous Ether," *Am. J.Sci. (3rd series)*, vol. 34, pp. 333–345, 1887. 288

[572] P. Fritschel, "talk at Technical Plenary Session of the LSC meeting 2003," 2003. 288

[573] S. Hild et al., "Demonstration and comparison of tuned and detuned signal recycling in a large-scale gravitational wave detector," *Classical and Quantum Gravity*, vol. 24 (6), pp. 1513–1523, 2007. 289

[574] A. Buonanno, Y. Chen, and N. Mavalvala, "Quantum noise in laser-interferometer gravitational-wave detectors with a heterodyne readout scheme," *Phys. Rev. D*, vol. 67 (12), p. 122005, 2003. 289

[575] M. Hewitson et al., "Optimal time-domain combination of the two calibrated output quadratures of GEO 600," *Classical and Quantum Gravity*, vol. 22, pp. 4253–4261, 2005. 289

[576] R. Lawrence et al., "Adaptive thermal compensation of test masses in advanced LIGO," *Class. Quantum Grav.*, vol. 19, p. 1803, 2002. 289

[577] V. Chickarmane et al., "Squeezed light in a frontal-phase-modulated signal-recycled interferometer," *Phys. Rev. A*, vol. 57, pp. 3898–3912, 1998. 289

[578] E. Tournefier, "Advanced Virgo output mode cleaner: specifications," Tech. Rep. VIR-NOT-071A-08, 2008. 290

[579] R. Gouaty, G. L. Corre, B. Mours, L. Rolland, and E. Tournefier, "Advanced Virgo output mode cleaner: revision of the specifications," Tech. Rep. VIR-0020A-11, Virgo, 2011. 290

[580] S. J. Waldman, "Output Mode Cleaner Design," Tech. Rep. LIGO-T1000276-v1, LIGO, 2010. 290

[581] J. Degallaix et al., "Commissioning of the tuned DC readout at GEO 600," *J. Phys.: Conf. Ser.*, vol. 228, p. 012013, 2010. 290

[582] M. Prijatelj et al., "Control and automatic alignment of the output mode cleaner of GEO 600," *J. Phys.: Conf. Ser.*, vol. 228, p. 012014, 2010. 290

[583] L. Derome, "New mode cleaner support test," Tech. Rep. VIR-0045A-07, Virgo, 1997. 290

[584] L. Rolland, R. Gouaty, G. L. Corre, B. Mours, and E. Tournefier, "Constraints on the Advanced Virgo detection bench jitter from OMC alignment," Tech. Rep. VIR-0054A-11, Virgo, 2011. 291

[585] R. W. P. Drever, J. L. Hall, F. V. Kowalski, J. Hough, and G. M. Ford, "Laser Phase and Frequency Stabilization Using an Optical Resonator," *Appl. Phys. B*, vol. 31, p. 97, 1983. 292

[586] S. Sato, S. Kawamura, K. Kokeyama, F. Kawazoe, and K. Somiya, "Diagonalization of the length sensing matrix of a dual recycled laser interferometer gravitational wave antenna," *Phys. Rev. D*, vol. 75 (8), p. 082004, 2007. 292

[587] "Advanced LIGO," . 292

[588] R. Abbott et al., "Advanced LIGO Length Sensing and Control Final Design," Tech. rep., 2010. 293

[589] M. Evans et al., "Lock acquisition of a gravitational-wave interferometer," *Optics Letters*, vol. 27, p. 598, 2002. 295

[590] F. Acernese et al., "The variable finesse locking technique," *Classical and Quantum Gravity*, vol. 23 (8), p. S85, 2006. 295

[591] L. Barsotti and M. Evans, "Lock Acquisition study for Advanced LIGO," 2010. 295

[592] M. Evans et al., "Advanced LIGO Arm Length Stabilization System Design," Tech. rep., 2010. 295, 296, 435

[593] B. Slagmolen et al., "Advanced LIGO Arm Cavity Pre-Lock Acquisition System," Tech. rep., 2008. 295

[594] A. J. Mullavey, B. J. J. Slagmolen, D. A. Shaddock, and D. E. McClelland, "Stable transfer of an optical frequency standard via a 4.6 km optical fiber," *Optics Express*, vol. 18, pp. 5213–5220, 2010. 296

[595] E. Morrison et al., *Appl. Opt.*, vol. 33, p. 504, 1994. 296

[596] J. Sidles and D. Sigg, "Optical torques in suspended Fabry-Perot interferometers," *Phys. Lett. A*, vol. 354, pp. 167–172. 297

[597] P. Willems et al., "LIGO-G0900182-v1 - Thermal Compensation in Enhanced LIGO," Tech. rep., 2009. 298

[598] T. Accadia et al., "A Thermal Compensation System for the gravitational wave detector Virgo," *In Proceedings of the 12th Marcell Grossmann Meeting, Paris, July 2009, in press*, 2010.

[599] T. Accadia et al., "Commissioning status of the Virgo interferometer," *Class. Quantum Grav.*, vol. 27, 2010. 298

[600] L. Pinard, "VIR-0555A-09 - AdV substrates technical readiness review," Tech. rep., 2009. 298

[601] V. Fafone and A. Rocchi, "VIR-0669B-08 - TCS update," Tech. rep., 2008. 298

[602] A. Rocchi, "Compensation of thermal effects in future detectors," Talk to the Gravitational-Wave Advanced Detector Workshop, Kyoto, May, 2010. 298

[603] C. J. Kamp et al., "Directional radiative cooling thermal compensation for gravitational wave interferometer mirrors," *Nucl. Instrum. Methods A*, vol. 607, 2009. 299

[604] E. Coccia et al., "VIR-0302A-10 - Investigation on the Directional Radiative Cooling," Tech. rep., 2010. 299

[605] P. Savov and S. Vyatchanin, "Estimate of tilt instability of mesa-beam and Gaussian-beam modes for advanced LIGO," *Phys. Rev. D*, vol. 74, p. 082002, 2006. 302

[606] P. Fulda, K. Kokeyama, S. Chelkowski, and A. Freise, "Experimental demonstration of higher-order Laguerre-Gauss mode interferometry," *Phys. Rev. D*, vol. 82 (1), p. 012002, 2010. 302

[607] M. Granata, C. Buy, R. Ward, and M. Barsuglia, "Higher-Order Laguerre-Gauss Mode Generation and Interferometry for Gravitational Wave Detectors," *Phys. Rev. Lett.*, vol. 105 (23), p. 231102, 2010. 302

[608] K. Somiya et al., "Reduction of coating thermal noise by using an etalon," *Physics Letters A*, vol. 375 (11), pp. 1363 – 1374, 2011. 303

[609] M. Abernathy et al., "in preparation," . 303

[610] E. Chalkley, *Investigations of the properties of materials for the optics and suspensions of future gravitational wave detectors*, Ph.D. thesis, University of Glasgow, 2010. 303

[611] X. Liu and R. O. Pohl, "Low-energy excitations in amorphous films of silicon and germanium," *Phys. Rev. B*, vol. 58, pp. 9067–9081, 1998. 304

[612] R. Bassiri et al., "Probing the atomic structure of amorphous Ta_2O_5 coatings," *Appl. Phys. Lett.*, vol. 98, p. 031904, 2011. 304

[613] A. Bunkowski, O. Burmeister, D. Friedrich, K. Danzmann, and R. Schnabel, "High reflectivity grating waveguide coatings for 1064 nm," *Classical and Quantum Gravity*, vol. 23, pp. 7297–7303, 2006. 305, 306

[614] D. Rosenblatt, A. Sharon, and A. A. Friesem, "Resonant Grating Waveguide Structures," *IEEE JOURNAL OF QUANTUM ELECTRONICS*, vol. 33, p. 11, 1997. 305

[615] M. G. Moharam and T. K. Gaylord, "Rigorous coupled-wave analysis of planar-grating diffraction," *J. Opt. Soc. Am*, vol. 71, pp. Issue. 7, 811–818, 1981. 305, 306

[616] F. Brückner et al., "Demonstration of a cavity coupler based on a resonant waveguide grating," *Opt. Express*, vol. 17 (1), pp. 163–169, 2009. 306

[617] F. Bruckner et al., "Realization of a Monolithic High-Reflectivity Cavity Mirror from a Single Silicon Crystal," *Physical Review Letters*, vol. 104, p. 163903, 2010. 306

[618] R. Nawrodt et al., "Mechanical Q-factor measurements on a test mass with a structured surface," *New Journal of Physics*, vol. 9, pp. 225–+, 2007. 306

[619] P. Purdue, "Analysis of a quantum nondemolition speed-meter interferometer," *Phys. Rev. D*, vol. 66, p. 022001, 2002. 306, 350

[620] P. Purdue and Y. Chen, "Practical speed meter designs for quantum nondemolition gravitational-wave interferometers," *Phys. Rev. D*, vol. 66, p. 122004, 2002. 306, 350, 352, 356, 357

[621] R. L. B. Peter T Beyersdorf and M. M. Fejer, "Results from the Stanford 10 m Sagnac interferometer," *Class. Quantum Grav.*, vol. 19, pp. 1585–1589, 2002. 307

[622] "Specification, installation and commissioning of a large industrial control system for the LEP2 cryogenics," *Nuclear Instruments and Methods in Physics Research Section A: Accelerators, Spectrometers, Detectors and Associated Equipment*, vol. 352 (1-2), pp. 467 – 470, 1994. 314, 315

[623] P. Lebrun, "Cryogenic refrigeration for the LHC," Communication at the MaTeFu Spring Training School Cadarache, 2009. 315

[624] T. Peterson, "ILC Cryogenic Systems Reference Design," Presentation at the ILC meeting at SLAC, 2007. 315

[625] H. K. Kuhn and M. Pellin, "Advant OCS controls cryogenic installations of CERN's particle accelerator," *ABB Rev.*, vol. 5, pp. 18–23, 1999. 315

[626] S. Claudet, P. Gayet, P. Lebrun, L. Tavian, and U. Wagner, "Economics of Large Helium Cryogenic Systems: experience from Recent Projects at CERN," Tech. Rep. LHC-Project-Report-317. CERN-LHC-Project-Report-317, CERN, Geneva, 1999. 315

[627] A. Buonanno, M. Maggiore, and C. Ungarelli, "Spectrum of relic gravitational waves in string cosmology," *Phys. Rev. D*, vol. 55, pp. 3330–3336, 1997. 323

[628] V. Mandic and A. Buonanno, "Accessibility of the Pre-Big-Bang Models to LIGO," *Phys. Rev.*, vol. D73, p. 063008, 2006. 323

[629] R. H. Cyburt, B. D. Fields, K. A. Olive, and E. Skillman, "New BBN limits on Physics Beyond the Standard Model from He4," *Astropart. Phys.*, vol. 23, pp. 313–323, 2005. 323

[630] T. L. Smith, E. Pierpaoli, and M. Kamionkowski, "A new cosmic microwave background constraint to primordial gravitational waves," *Phys. Rev. Lett.*, vol. 97, p. 021301, 2006. 323

[631] L. Pogosian, S. H. Tye, I. Wasserman, and M. Wyman, "Observational constraints on cosmic string production during brane inflation," *Phys. Rev.*, vol. D68, p. 023506, 2003. 324

[632] R. A. Battye, B. Garbrecht, and A. Moss, "Constraints on supersymmetric models of hybrid inflation," *JCAP*, vol. 0609, p. 007, 2006.

[633] N. Bevis, M. Hindmarsh, M. Kunz, and J. Urrestilla, "Fitting CMB data with cosmic strings and inflation," *Phys. Rev. Lett.*, vol. 100, p. 021301, 2008. 324

[634] C. J. Hogan, "Gravitational waves from light cosmic strings: Backgrounds and bursts with large loops," *Phys. Rev.*, vol. D74, p. 043526, 2006. 324

[635] T. Damour and A. Vilenkin, "Gravitational radiation from cosmic (super)strings: Bursts, stochastic background, and observational windows," *Phys. Rev. D*, vol. 71, 063510, 2005. 324

[636] E. Fenu, D. G. Figueroa, R. Durrer, and J. Garcia-Bellido, "Gravitational waves from self-ordering scalar fields," *JCAP*, vol. 0910, p. 005, 2009. 324

[637] M. Kamionkowski, A. Kosowsky, and M. S. Turner, "Gravitational radiation from first order phase transitions," *Phys. Rev.*, vol. D49, pp. 2837–2851, 1994. 324

[638] ""Moore's Law at 40 . Happy birthday"," http://economist.com/displaystory.cfm?storyi_id=3798505.Retrieved2006-06-24), . 325

[639] A. G., "Validity of the Simplre Processor Approach to Achieving large scale computing Capabilities," AFIPS Conference Proceedings(30) (483-485), 1967. 326

[640] "AMD White Paper: AMD Fusion Family of APUs," 2010. 326

[641] S. Nadathur et al., "Fast Sort on CPUs, GPUs and Intel MIC Architectures," Technical Report, Intel Labs, 2010. 326

[642] "Silicon Technology," . 326

[643] "The SCC Platform Overview," 2010. 326

[644] ""Single-chip Cloud Computer" An experimental many-core processor from Intel Labs," Symposium in Santa Clara, 2010. 326

[645] "Tilera website," http://www.tilera.com. 326

[646] M. Azimi et al., "Integration Challenges and Tradeoffs for Tera-scale Architectures," Intel Technology Journal http://www.intel.com/technology/itj/2007/v11i3/1-integration/1-abstract.htm, 2007. 326

[647] S. T. I. Foster, C. Kesselman, "The anatomy of the Grid," *Int. Journal of Supercomputer Application*, vol. 15, p. 3, 2001. 327

[648] "LHC Computing Grid Technical Site," . 327

[649] P. Rodgers, "Self-Noise spectra for 34 common electromagnetic seismometer/pre-amplifier pairs," *Bull. Seism. Soc. Am.*, vol. 84, pp. 222–228, 1994. 328

[650] J. R. Howell and R. Siegel, *Thermal Radiation Heat Transfer*, Taylor and Francis-Hemisphere, Washington, 3rd edn., 1992. 339, 341

[651] J. Howell, "A Catalog of Radiation Heat Transfer Configuration Factors, 3rd edition," Http://www.engr.uky.edu/rtl/Catalog/. 339, 340, 437

[652] J. R. Howell and R. Siegel, *Thermal Radiation Heat Transfer*, Taylor and Francis-Hemisphere, Washington, 4th edn., 2001. 340

[653] A. J. Buschman and C. M. Pittman, "Configuration factors for exchange of radiant energy between axisymmetrical sections of cylinders, cones, and hemispheres and their bases," Tech. Rep. D-944, NASA, 1961. 340

[654] E. M. Sparrow and S. L. Lin, "Radiation heat transfer at a surface having both specular and diffuse reflectance components," *Int. J. Heat Mass Transfer*, vol. 8, pp. 769–779, 1965. 341

[655] D. S. Tsai and W. Strieder, "Radiation across and down a Cylindrical Pore Having both Specular and Diffuse Reflectance Components," *Ind. Eng. Chem. Fundam*, vol. 25 (2), pp. 244–249, 1986. 341

[656] R. Poggiani, "Materials and components of possible interest for cryogenic operation of Einstein Telescope," *Einstein Telescope Note*, vol. ET-026-9, 2009. 342

[657] R. Poggiani, "Cryogenic Properties of Steels," *Einstein Telescope Note*, vol. ET-102A-10, 2010. 343

[658] Y. Aso, *PhD. thesis*, Master's thesis, University of Tokyo, 2006. 343

[659] A. Bertolini, G. Cella, R. DeSalvo, and V. Sannibale, "Seismic noise filters, vertical resonance frequency reduction with geometric anti-springs: a feasibility study," *Nuclear Instruments and Methods in Physics Research*, (435), pp. 475–483, 1999. 343

[660] M. Blom and mblom@nikhef.nl, "private communication," 2011. 344, 437

[661] A. Stochino et al., "Nuclear Instr. and Methods in Phys. Res. A," *The Seismic Attenuation System (SAS) for the Advanced LIGO gravitational wave interferometric detectors*, vol. 598, pp. 737–753, 2009. 344, 345, 437

[662] E. Hennes and ehennes@nikhef.nl, "private communication," 2011. 344

[663] H. Müller-Ebhardt et al., "Review of quantum non-demolition schemes for the Einstein Telescope," https://tds.ego-gw.it/itf/tds/file.php?callFile=ET-010-09.pdf, 2009, eT-010-09. 348, 349, 350, 352

[664] J. Harms, R. Schnabel, and K. Danzmann, "Finite mass beam splitter in high power interferometers," *Phys. Rev. D*, vol. 70, p. 102001, 2004. 348

[665] B. J. Meers, "Recycling in laser-interferometric gravitational-wave detectors," *Phys. Rev. D*, vol. 38, p. 2317, 1988. 349

[666] L. D. Fiore and the VIRGO collaboration, "The present status of the VIRGO Central Interferometer," *Class. Quant. Grav.*, vol. 19, p. 1421, 2002. 349

[667] M. Ando and the TAMA collaboration, "Stable Operation of a 300-m Laser Interferometer with Sufficient Sensitivity to Detect Gravitational-Wave Events within Our Galaxy," *Phys. Rev. Lett.*, vol. 86, p. 3950, 2001. 349

[668] G. Heinzel et al., "Experimental Demonstration of a Suspended Dual Recycling Interferometer for Gravitational Wave Detection," *Phys. Rev. Lett.*, vol. 81, p. 5493, 1998. 349

[669] A. Freise et al., "Demonstration of detuned dual recycling at the Garching 30 m laser interferometer," *Physics Letters A*, vol. 277 (3), pp. 135 – 142, 2000. 349

[670] K. Somiya et al., "Development of a frequency-detuned interferometer as a prototype experiment for next-generation gravitational-wave detectors," *Appl. Opt.*, vol. 44, p. 3179, 2005. 349

[671] O. Miyakawa et al., "Measurement of optical response of a detuned resonant sideband extraction gravitational wave detector," *Phys. Rev. D*, vol. 74, p. 022001, 2006. 349

[672] H. Grote et al., "Dual recycling for GEO 600," *Class. Quantum Grav.*, vol. 21, p. S473, 2004. 349

[673] A. Buonanno and Y. Chen, "Quantum noise in second generation, signal-recycled laser interferometric gravitational-wave detectors," *Phys. Rev. D*, vol. 64, p. 042006, 2001. 349

[674] A. Buonanno and Y. Chen, "Signal recycled laser-interferometer gravitational-wave detectors as optical springs," *Phys. Rev. D*, vol. 65, p. 042001, 2002.

[675] A. Buonanno and Y. Chen, "Scaling law in signal recycled laser-interferometer gravitational-wave detectors," *Phys. Rev. D*, vol. 67, p. 062002, 2003.

[676] H. Rehbein et al., "Double optical spring enhancement for gravitational wave detectors," *Phys. Rev. D*, vol. 78, p. 062003, 2008. 349

[677] T. Corbitt et al., "An All-Optical Trap for a Gram-Scale Mirror," *Phys. Rev. Lett.*, vol. 98 (15), p. 150802, 2007. 349

[678] F. Y. Khalili and Y. Levin, "Speed meter as a quantum nondemolition measuring device for force," *Phys. Rev. D*, vol. 54, p. 4735, 1996. 349

[679] K. McKenzie, "Private communication," 2008. 350

[680] S. L. Danilishin, "Sensitivity limitations in optical speed meter topology of gravitational-wave antennas," *Phys. Rev. D*, vol. 69, p. 102003, 2004. 350

[681] H. Müller-Ebhardt, *On quantum effects in the dynamics of macroscopic test masses*, Ph.D. thesis, Leibniz Universität Hannover, 2009. 350

[682] F. Khalili et al., "Negative optical inertia for enhancing the sensitivity of future gravitational-wave detectors," *Phys. Rev. D*, vol. 83 (6), p. 062003, 2011. 350

[683] V. B. Braginsky and F. Y. Khalili, "Nonlinear meter for the gravitational wave antenna," *Phys. Lett. A*, vol. 218, p. 167, 1996. 350

[684] V. B. Braginsky, M. L. Gorodetsky, and F. Y. Khalili, "Optical bars in gravitational wave antennas," *Phys. Lett. A*, vol. 232, p. 340, 1997.

[685] F. Y. Khalili, "Quantum speedmeter and laser interferometric gravitational-wave antennae," http://arxiv.org/abs/gr-qc/0211088v1, 2002. 351

[686] H. Rehbein et al., "Local readout enhancement for detuned signal-recycling interferometers," *Phys. Rev. D*, vol. 76, p. 062002, 2007. 350, 351

[687] A. Buonanno and Y. Chen, "Improving the sensitivity to gravitational-wave sources by modifying the input-output optics of advanced interferometers," *Phys. Rev. D*, vol. 69 (10), p. 102004, 2004. 352

[688] S. Chelkowski et al., "Experimental characterization of frequency-dependent squeezed light," *Phys. Rev. A*, vol. 71 (1), 013806, 2005. 352

[689] T. Corbitt, N. Mavalvala, and S. Whitcomb, "Optical cavities as amplitude filters for squeezed fields," *Phys. Rev. D*, vol. 70 (2), p. 022002, 2004. 352

[690] F. Y. Khalili, "Increasing future gravitational-wave detectors' sensitivity by means of amplitude filter cavities and quantum entanglement," *Phys. Rev. D*, vol. 77 (6), p. 062003, 2008. 352

[691] F. Y. Khalili, H. Miao, and Y. Chen, "Increasing the sensitivity of future gravitational-wave detectors with double squeezed-input," *Phys. Rev. D*, vol. 80 (4), p. 042006, 2009. 352, 355

[692] F. Y. Khalili, "Optimal configurations of filter cavity in future gravitational-wave detectors," 2010. 352

[693] S. P. Vyatchanin and A. B. Matsko, *JETP*, vol. 77, p. 218, 1993. 352

[694] S. P. Vyatchanin and E. A. Zubova, "Quantum variation measurement of a force," *Physics Letters A*, vol. 201 (4), pp. 269–274, 1995. 352

[695] Y. Chen, S. L. Danilishin, F. Y. Khalili, and H. Müeller-Ebhardt, "QND measurements for future gravitational-wave detectors," *Gen. Relativ. Gravit.*, 2010. 352

[696] C. M. Caves and B. L. Schumaker, "New formalism for two-photon quantum optics. I. Quadrature phases and squeezed states," *Phys. Rev. A*, vol. 31 (5), pp. 3068–3092, 1985. 356

[697] H. Yamamoto, California Institute of Technology, Private Communication. 363

[698] V. B. Braginsky, S. Strigin, and S. Vyatchanin, "Parametric oscillatory instability in Fabry-Perot interferometer," *Phys. Lett. A*, vol. 287, pp. 331–338, 2001. 375

[699] L. Ju, S. Gras, C. Zhao, J. Degallaix, and D. Blair, "Multiple modes contributions to parametric instabilities in advanced laser interferometer gravitational wave detectors," *Phys. Lett. A*, vol. 354, pp. 360–365, 2006. 375, 376, 440

[700] L. Ju et al., "Comparison of parametric instabilities for different test mass materials in advanced gravitational wave interferometers," *Phys. Lett. A*, vol. 355, pp. 419–426, 2006. 375, 376, 378

[701] C. Zhao, L. Ju, J. Degallaix, S. Gras, and D. Blair, "Parametric Instabilities and Their Control in Advanced Interferometer Gravitational-Wave Detectors," *Phys. Rev. Lett.*, vol. 94, p. 121102, 2005. 375, 376, 440

[702] K. Yamamoto, "Parametric instability of a cavity of Einstein Telescope," 2009. 375, 377

[703] W. Kells and E. D'Ambrosio, "Considerations on parametric instability in Fabry-Perot interferometer," *Phys. Lett. A*, vol. 299, pp. 326–330, 2002. 377

[704] S. Strigin, D. Blair, S. Gras, and S. Vyatchanin, "Numerical calculations of elastic modes frequencies for parametric oscillatory instability in Advanced LIGO interferometer," *Phys. Lett. A*, vol. 372, pp. 5727–5731, 2008. 377

[705] S. Strigin, "Elastic modes frequencies in the mirrors with "ears" for parametric oscillatory instability in advanced LIGO interferometer," *Phys. Lett. A*, vol. 372, pp. 6305–6308, 2008. 377

[706] S. Gras, C. Zhao, L. Ju, and D. Blair, "Preliminary investigation on a passive method for parametric instability control in advanced gravitational wave detectors," *J. Phys.: Conf. Ser.* , vol. 32, pp. 251–258, 2006. 378

[707] L. Ju et al., "Strategies for the control of parametric instability in advanced gravitational wave detectors," *Class. Qauntm Grav.*, vol. 26, p. 015002, 2009. 378

[708] V. Braginsky and S. Vyatchanin, "Low quantum noise tranquilizer for Fabry?Perot interferometer," *Phys. Lett. A*, vol. 293, pp. 228–234, 2002. 378

[709] K. Numata et al., "Systematic measurement of the intrinsic losses in various kinds of bulk fused silica," *Phys. Lett. A*, vol. 327, pp. 263–271, 2004. 378

[710] Y. Levin, "Internal thermal noise in the LIGO test masses: A direct approach," *Phys. Rev. D*, vol. 57, pp. 659–663, 1998. 378, 379

[711] K. Yamamoto, M. Ando, K. Kawabe, and K. Tsubono, "Thermal noise caused by an inhomogeneous loss in the mirrors used in the gravitational wave detector," *Phys. Lett. A*, vol. 305, pp. 18–25, 2002. 378, 379

[712] S. Gras, D. Blair, , and L. Ju, "Thermal noise dependence on equatorial losses in the mirrors of an interferometric gravitational wave detector," *Phys. Lett. A*, vol. 333, pp. 1–7, 2004. 378, 379, 380

[713] K. Yamamoto et al., "Measurement of the mechanical loss of a cooled reflective coating for gravitational wave detection," *Phys. Rev. D*, vol. 74 (2), p. 022002, 2006. 378, 440

[714] S. D. Penn et al., "Mechanical loss in tantala/silica dielectric mirror coatings," *Class. Quantum Grav.*, vol. 20, pp. 2917–2928, 2003. 378

[715] J. Miller et al., "Damping parametric instabilities in future gravitational wave detectors by means of electrostatic actuators," *Phys. Lett. A*, vol. 375, pp. 788–794, 2011. 378

[716] G. Hooft, "Dimensional Reduction in Quantum Gravity," arXiv:gr-qc/9310026v2, 1993. 380

[717] L. Susskind, "The World as a Hologram," *J. Math. Phys.*, vol. 36, p. 6377, 1995. 380

[718] J. Maldacena, "The Large N Limit of Superconformal Field Theories and Supergravity," *Adv. Theor. Math. Phys.*, vol. 2, 1998. 380

[719] C. Hogan and M. Jackson, "Holographic geometry and noise in matrix theory," *Phys. Rev. D*, vol. 79, 2009. 380

[720] C. Hogan et al., "The Fermilab Holometer. A program to measure Planck scale indeterminacy," 2009. 381

[721] M. Rakhmanov, "Response of test masses to gravitational waves in the local Lorentz gauge," *Phys. Rev. D*, vol. 71, 2005. 381

[722] Y. Chen and S. Kawamura, "Displacement- and Timing-Noise Free Gravitational-Wave Detection," *Phys. Rev. Lett.*, vol. 96, 2006. 381

[723] Y. Chen et al., "Interferometers for Displacement-Noise-Free Gravitational-Wave Detection," *Phys. Rev. Lett.*, vol. 97, 2006. 381

[724] K. Somiya et al., "Utility investigation of artificial time delay in displacement-noise-free interferometers," *Phys. Rev. D*, vol. 76, 2007. 381

[725] S. Tarabrin and S. Vyatchanin, "Displacement-noise-free gravitational-wave detection with a single Fabry-Perot cavity: a toy model," *Phys. Lett. A*, vol. 372, 2008. 381

[726] A. Rakhubovsky and S. Vyatchanin, "Displacement-noise-free gravitational-wave detection with two Fabry-Perot cavities," *Phys. Lett. A*, vol. 373, 2008. 381

[727] S. Tarabrin and S. Vyatchanin, "Double Michelson/Fabry-Perot interferometer for laser- and displacement-noise-free gravitational-wave detection," arXiv:0904.3296v1, 2009. 381

[728] S. Vyatchanin, "Displacement-noise-free resonant speed meter for gravitational-wave detection," arXiv:0808.3445v1, 2008. 381

[729] S. Dimopoulos et al., "Atomic gravitational wave interferometric sensor," *Phys. Rev. D*, vol. 78, 2008. 382

[730] S. Hild et al., "Measurement of a low-absorption sample of OH-reduced fused silica," *Applied Optics*, vol. 45 (28), pp. 7269–7272, 2006. 383

[731] Z. Yan et al., "Study of rayleigh scattering absorption and birefringence of large size bulk single crystal," *Applied Optics*, vol. 45, p. 2631, 2006. 383

[732] R. Flaminio et al., "A study of coating mechanical and optical losses inview of reducing mirror thermal noise in gravitational wave detectors," *Class. Quantum Grav.*, vol. 27, p. 084030, 2010. 383

[733] M. K. Song et al., "Influence of Deposition Method on Refractive Index of SiO2 and TiO2 Thin Films for Anti-reflective Multilayers," *Journal of the Korean Ceramic Society*, vol. 45, pp. 524–530, 2008. 383

[734] G. Dai, Y. Chen, J. Lu, Z. Shen, and X. Ni, "Analysis of laser induced thermal mechanical relationship of HfO2/SiO2 high reflective optical thin film at 1064 nm," *CHINESE OPTICS LETTERS*, vol. 7, 2009. 383

List of Figures

List of Tables

List of Boxes

Nomenclature

Abbreviations

AIGO	Australian International Gravitational Observatory
aLIGO	The advanced LIGO observatory
ALS	Arm Length Stabilisation
ALU	Arithmetic and Logical Unit
APU	Accelerated Processing Unit
ASE	Amplified Spontaneous Emission
ASPERA	AStroParticle ERAnet (http://www.aspera-eu.org/)
BBH	Binary Black Hole
BBN	Big Bang Nucleosynthesis
BD	Brans-Dicke (theory), an alternative to general relativity
BH	Black Hole
BHD	Balanced Homodyne Detector
BNS	Binary Neutron Star
BS	Beam Splitter
CARM	Common Mode Arm Length
CCD	Charge-Coupled Device
CCH	Cosmic Censorship Hypothesis
CCSN	Core Collapse Supernova
CERN	European Organization for Nuclear Research
CLIO	Cryogenic Laser Interferometer Observatory: A prototype gravitational wave detector in Japan
CMB	Cosmic Microwave Background radiation
CMP	Chip-Level Multiprocessing
CP	Compensation Plate
CPU	Central Processing Unit
CTE	Coefficient of Thermal Expansion
cWB	coherent Wave Burst
CW	Continuous Waves
CZ	Czochralski
DARM	Differential Arm Length
DE	Dark Energy
DEG	Digital Enterprise Group
DESY	German Electron Synchrotron
DM	Dark Matter

DOF	Degree(s) Of Freedom
EA	Electrostatic Actuators
EC2	Amazon Elastic Compute Cloud
EDM	Electric Discharge Machining
eLIGO	The enhanced LIGO observatory
EM	Electromagnetic
EM	End Mirrors
EMRI	Extreme Mass Ratio Inspiral
EOM	Electro-Optic Modulator
EoS	Equation of State
ESFRI	European Strategy Forum on Research Infrastructures
ET	Einstein Telescope
ETM	End Test Mass
FDT	Fluctuation Dissipation Theorem
FC	Filter Cavity
FFT	Fast Fourier Transform
FI	Faraday Isolator
Flops	Floating point operations per second (a common measure of the computing system speed)
FP7	Seventh Framework Programme: "Framework programmes (FPs) are the main financial tools through which the European Union supports research and development activities covering almost all scientific disciplines (http://cordis.europa.eu/fp7/home_en.html).
FP	Folded Pendulum
FPU	Floating Point Unit
FS	Fused Silica
FZ	Float Zone
GAE	Google App Engine
GA	Genetic Algorithm
GAS	Geometric Anti-Spring
GIPC	Global Inverted-Pendulum Control
GPU	Graphic Processing Unit
GRB	Gamma-Ray Burst
GR	General Relativity
GUT	Grand Unified Theory
GWD	Gravitational Wave Detector
GW	Gravitational Wave
GWIC	Gravitational Wave International Committee (https://gwic.ligo.org/)

HADES	High Activity Disposal Experimental Site, an underground research facility studying geological disposal of radioactive waste
HF	High Frequency
HPC	High Performance Computer
HTT	Hyper-Threading Technology, called also HT
IBS	Ion Beam Sputtering
IFO	Interferometer
ILC	International Linear Collider
IMBH	Intermediate Mass Black Hole
IMC	Input Mode Cleaner
IM	Input Mirrors
IMRI	Intermediate Mass Ratio Inspiral
IO	Input Optics
IO	Input/Output
IP	Inverted Pendulum
ITM	Input Test Mass
KNMI	Royal Dutch Meteorological Institute
kpc	Kiloparsec, $1\,\mathrm{kpc} = 10^3\,\mathrm{pc}$
LCGT	Large Scale Cryogenic Gravitational Wave Telescope: a second-generation gravitational wave detector under construction in Japan
LF	Low Frequency
LG	Laguerre-Gauss
LHC	Large Hadron Collider
LIGO	Laser Interferometer Gravitational-Wave Observatory
LISA	Laser Space Interferometer Antenna
LMA	Large Mode Area (fibre)
LMXB	Low Mass X-ray Binaries
LNGS	Laboratori Nazionali del Gran Sasso
LSM	Laboratory for Surface Modification
LSO	Last Stable Orbit
LSS	Last Stage Suspension
LVDT	Linear Variable Differential Transformers
MBH	Massive Black Hole
MCMC	Markov Chain Monte Carlo method
MEMS	Micro-Electric Mechanical Systems
MFC	Multifilament-Core (fibre)

MHMC	Metropolis Hastings Monte Carlo method
MIC	Many Integrated Core
MI	Michelson Interferometer
Mpc	Megaparsec, $1\,\mathrm{Mpc} = 10^6\,\mathrm{pc}$
MRM	Marionette Reference Mass
MWIR	Mid Infrared
NHNM	New High Noise Model
NIR	Near Infrared
NLNM	New Low Noise Model
NSBH	Neutron Star – Black Hole
NS	Neutron Star
OMC	Output Mode Cleaner
OPA	Optical Parametric Amplification
OPL	Optical Path Length
ORFEUS	Observatories and Research Facilities for EUropean Seismology
PCF	Photonic Crystal Fibre
pc	Parsec, a unit of distance; $1\,\mathrm{pc} = 3.086 \times 10^{16}\,\mathrm{m}$
PLL	Phase Locked Loop
PN	Post-Newtonian, an approximation to Einstein's field equations
ppm	Parts per million
PRC	Power Recycling Cavity
PRM	Power Recycling Mirror
PR	Power Recycling
PSD	Power Spectral Density
PT	Pulse Tube cryogenic refrigerator
QND	Quantum Non-Demolition
R&D	Research and Development
RDF	Reduced Density Function
RF	Radio Frequency
RIN	Relative Intensity Noise
RM	Recoil Mass or Reference Mass
rms	Root-mean-square
ROC	Radius Of Curvature
RPSD	Root PSD
RSE	Resonant Sideband Extraction
S3	Amazon Simple Storage Service

S5	LIGO's Fifth Science Run
SAN	Storage Attached Network
SA	Super-Attenuator
SBS	Stimulated Brillouin Scattering
SFR	Star Formation Rate
SGR	Soft Gamma Repeaters
SHG	Second Harmonic Generation
SIMD	Single Instruction, Multiple Data
SI	Sagnac Interferometer
SMBH	Super Massive Black Hole
SMT	Simultaneous multithreading
SNR	Signal to Noise Ratio
SN	Supernova
SQL	Standard Quantum Limit
SQUID	Superconducting Quantum Interference Device, a magnetometer based on Josephson effect
SRC	Signal Recycling Cavity
SR	Signal Recycling
SRS	Stimulated Raman Scattering
SSE4	Streaming SIMD Extensions version 4
SSE	intel's Streaming SIMD Extension
SUSY	Supersymmetry
TCS	Thermal Compensation System
TEM	Transverse Electromagnetic
TE	Thermo-Elastic
UHV	Ultra-high vacuum
WLCG	Worldwide LHC Computing Grid

Glossary

Top500	Top500 is a project which ranks and details twice a year the 500 (non-distributed) most powerful known computer systems in the world.
ATNF	The Australia Telescope National Facility Pulsar Catalog is a catalog of known pulsars.
Compact binary	A compact binary is an astronomical binary consisting of a pair of compact stars
Compact star	Throughout this document a compact star stands for a neutron star or a black hole
CMOS	Complementary metal-oxide-semiconductor is a technology for constructing integrated circuits like microprocessors, static RAM, ...
Dual Recycling	Using Power- and Signal-Recycling at the same time

ET-A An ET design curve, as described in the introduction

ET-B An ET design curve, as described in the introduction

ET-C An ET design curve, as described in the introduction

ET-D An ET design curve, as described in the introduction

ET-HF The high frequency ET detector in the xylophone design

ET-LF The low frequency ET detector in the xylophone design

FLRW The Friedmann-Lemaitre-Robertson-Walker metric is an exact solution of Einstein's field equations of general relativity

G1 The GEO600 detector near Hannover in Germany

GEO600 The GEO600 detector located near Hannover in Germany

H1 The LIGO 4-kilometre interferometer at Hanford, USA

H2 The LIGO 2-kilometre interferometer at Hanford, USA

Horizon Distance The distance at which a gravitational wave detector would measure a matched-filter signal-to-noise ratio of 8 for an optimally oriented (i.e. face-on) compact binary source located in a direction perpendicular to the plane of the detector

InfiniBand is a switched fabric communications link used in high-performance computing and enterprise data centers. It is especially used in connections between processor nodes and high performance I/O nodes such as storage device.

JDEM The Joint Dark Energy Mission, a proposed space based observatory, designed to explore the properties of dark energy and measure how cosmic expansion has changed over time

L1 The LIGO 4-kilometre interferometer at Livingston Parish, Louisiana, USA

Multi-Core Multi-core processors are single components with two or more independent actual processors, called cores

Power Recycling Re-using the light reflected back to the interferometer input by placing a mirror there and resonantly enhancing the circulating light power. Has the same effect as using a more powerful laser.

QND Typically the term quantum nondemolition (QND) measurement is used to describe a measurement of a quantum system which preserves the integrity of the system and the value of the measured observable. In the literature on gravitational wave detectors this term is often used to describe a variety of interferometer schemes in which shot noise and radiation pressure noise can be simultaneously suppressed. Such systems are typically not performing a strict QND measurement, thus they may more appropriately be referred to as Quantum Noise Reduction (QNR) systems.

REGIO The REGIO database of Eurostat contains the statistical information of the major financial and social aspects of the European Union

RHIC The Relativistic Heavy Ion Collider

Resonant Sideband Extraction The same technique as SR but operated anti-resonant, i.e. widening and/or detuning the bandwidth by reducing the reflectivity of the compound mirror formed by the inboard cavity mirror and the SR mirror.

Signal Recycling Resonantly enhancing the GW signals exiting the interferometer through the output port by placing a mirror there. This increases the sensitivity at the cost of the bandwidth. With a different (anti-resonant) tuning the same technique can be used for widening the bandwidth at the expense of the sensitivity (RSE). SR can optimize the sensitivity for an arbitrary frequency.

SNAP The SuperNova Acceleration Probe, a proposed space observatory designed to measure the expansion of the universe and discover the nature of dark energy

URCA An URCA process is one that emits neutrinos and is believed to take part in the cooling of BHs and NSs.

V1 The Virgo gravitational wave detector in Italy

Vacuum fluctuations Fluctuations that result from the quantum nature of an electromagnetic field even at the lowest possible energy level (zero mean energy = vacuum).

Virgo Virgo is a 3-kilometre gravitational wave detector located near Pisa, Italy

Wigner function The Wigner function is a quasi-probability density distribution in phase space describing the probability of an outcome of a measurement of phase and amplitude of a quantized harmonic oscillator. For a light field in a quantum noise limited classical state, i.e. a coherent state, the fluctuations are equally distributed between amplitude and phase. Equi-probability lines of the Wigner function would be circles. In a squeezed state fluctuations in one quadrature are decreased at the cost of increased fluctuations in the other quadrature thereby obeying Heisenberg's Uncertainty relation. For squeezed states, the equi-probability lines of the Wigner function become ellipses.

WMAP The Wilkinson Microwave Anisotropy Probe, a NASA Explorer mission that launched June 2001 to make fundamental measurements of cosmology

Symbols

Please note that some symbols might stand for more than one quantity depending on the context

c Speed of light

D_{L} Luminosity distance to the source

$\mathcal{F}'$ $\pi/\mathcal{F}_{\mathrm{fc}}$

$\mathcal{F}_{\mathrm{fc}}$ Finesse of a filter cavity

Φ_{fc} Detuning of a filter cavity

f_{res} Resonance frequency

$F_{\times}$ Detector response to $\times$ polarized GWs

F_{+} Detector response to + polarized GWs

γ_{fc} Half-bandwidth (pole-frequency) of a filter cavity

h Gravitational wave amplitude, usually denoting the detector response

i Imaginary unit

$\lambda(\Omega)$ Frequency-dependent squeezing angle

L Geometric length

L_{fc} Baseline length of a filter cavity

$l_{\mathrm{rt,fc}}$ Optical amplitude round-trip loss in a filter cavity

L_{cc} Critical length of a filter cavity

L_{min} Minimum possible length of a filter cavity that can be realised to match the target bandwidth in presence of optical loss

SLM	Spatial-Light modulator
M	Total mass of a binary or a black hole
ν	Symmetric mass ratio: for a binary composed of compact stars of masses m_1 and m_2 the symmetric mass ratio is $\nu = m_1 m_2/(m_1+m_2)^2$.
Ω	Angular sideband frequency
P	Probability distribution
$\rho_{\rm c}$	Amplitude reflectance factor of a filter cavity's coupling mirror
$R_{\rm c}$	Power reflectance factor ($\rho_{\rm c}^2$) of a filter cavity's coupling mirror
σ	Standard deviation
$\mathbf{T}$	2×2-matrix describing the input-output relation of an optical device
$\tau_{\rm c}$	Amplitude transmittance of a cavity's coupling mirror
V	Variance
V_a	Variance in the anti-squeezed quadrature
V_s	Variance in the squeezed quadrature
W	Wigner function
X_1	Amplitude quadrature
X_2	Phase quadrature
ζ	Homodyning angle
z	Cosmological redshift to the source

Impressum

Publisher:
European Gravitational Observatory, Via E. Amaldi 56021 S. Stefano a Macerata - Cascina (PI), Italy

Print:
STYLGRAFICA, Viale Etruria 1/2, Cascina, (PI), Italy

Image credits:
title page with content from: http://hubblesite.org/gallery/album/entire/pr1996001c/
Credit: R. Williams (STScI), the Hubble Deep Field Team and NASA

Printed: Cascina, June 28, 2011

Contacts

http://www.et-gw.eu

France:

- Raffaele Flaminio r.flaminio@lma.in2p3.fr

Germany:

- Harald Lück harald.lueck@aei.mpg.de

Italy:

- Federico Ferrini federico.ferrini@ego-gw.it
- Michele Punturo michele.punturo@pg.infn.it
- Fulvio Ricci Fulvio.Ricci@roma1.infn.it

The Netherlands:

- J.F.J. van den Brand jo@nikhef.nl

United Kingdom:

- Andreas Freise adf@star.sr.bham.ac.uk
- B. S. Sathyaprakash B.Sathyaprakash@astro.cf.ac.uk

The ET Science Team